Gigatonne-scale reduction of CO$_2$ emissions via mineralization using iron and steel slags

鉄鋼スラグを用いた鉱化によるギガトンスケールの CO$_2$ 排出削減に関する研究

July 2019

Corey Adam MYERS

マイヤズ コーリ アダム

Gigatonne-scale reduction of CO$_2$ emissions via mineralization using iron and steel slags

鉄鋼スラグを用いた鉱化によるギガトンスケールの CO$_2$ 排出削減に関する研究

July 2019

Waseda University

Graduate School of Creative Science and Engineering,

Department of Modern Mechanical Engineering,

Research on Exergy Engineering

Corey Adam MYERS

マイヤズ コーリ アダム

Table of Contents

Chapter 1: Introduction and motivation

This dissertation was produced from the viewpoint that technical solutions alone are not sufficient to realize the greenhouse gas emissions reductions and removal of extant CO_2 necessary to avoid the severe human suffering and loss of planetary stability projected to occur over the coming decades due to anthropogenic climate change. There is now ample evidence showing that despite human civilization being at stake, society as a whole will not adopt the necessary climate change mitigation measures if they run counter to the short-term desires of individuals, companies, and politicians. Unfortunately, this is not the whole of the problem. In the rare instances where social pressure, political will, and commercial interests align to support available mitigation methods, the pace of implementation is discouragingly slow compared to what is needed for even mildly good odds at avoiding climatic catastrophe. The causes of this sluggishness are varied and intrinsically case-dependent, but the result is an unambiguous global tardiness in addressing climate change. Depressingly, it is becoming increasingly likely that the shared scientific narrative of the likely rates and impacts of climate change are probably a 'best-case scenario'. Put bluntly, what appears to be a just barely achievable task (i.e., maintaining the global mean temperature rise below 2 ˚C) may in fact already be a lost cause. This potential is due to the complex interactions and feedbacks in the earth system causing highly non-linear transitions when pushed out of a stable climatic configuration; colloquially these are known as 'tipping points'.

These three issues, 1) the need for technologies to account for human nature, 2) the need to accelerate technology adoption, and 3) the looming uncertainties in climatic feedbacks are the setting upon which this research was built. This dissertation focusses on passive CO_2 mineralization of the solid, inorganic waste called slag. The technologies and methods described herein directly apply to only a small fraction of anthropogenic emissions; namely, a portion of the CO_2 associated with the production of iron and steel. However, the lessons learned are also applicable to reducing emissions from cement production and realizing carbon dioxide removal via enhanced weathering, thereby carrying potential for much larger impacts. Additionally, the design principles used to develop and guide this work are generally applicable to all forms of climate change mitigation and should be considered to accelerate the adoption of mitigation methods and technologies.

This dissertation is structured as shown in **Fig. 1-1**. Chapter 1 continues with a brief discussion of the state of climate change, the history of climate change mitigation efforts, and the design principles used in this work. Discussion of these areas are fundamental as the ultimate goal is stabilization of the Earth's climate in a condition consistent with supporting the needs of modern society. Chapter 2 provides background on the iron and steelmaking process and in particular focusses on the solid waste called 'slag'. In Chapter 2, two methods to utilize slag to reduce CO_2 emissions are introduced: molten centrifugal separation and in-container solidification. Both methods begin when slag exits the ironmaking or steelmaking furnace as a solid. Chapter 3 discusses the prediction of molten slag properties and solidification using traditional methods and the development of deep neural networks to provide improved, and hitherto unobtainable, predictions. The ability to predict molten slag properties is central to the design of the centrifugal and slow-solidification methods proposed in this dissertation; Chapter 4 delves into the design of said processes. After solidification, grinding and separation of slag minerals is necessary for efficient utilization; Chapter 5 focusses on the calculation of the surface energy and critical stress intensity of common slag minerals. Additionally, Chapter 5 introduces a novel, low-energy comminution technique called solid-state quenching. Following

grinding, a portion of slag may be used to mineralize CO_2 as climatically-stable calcium and magnesium carbonates. In Chapter 6, the trait controlling mineralization rates, the CO_2 diffusion coefficient, is empirically determined for common slag minerals. Chapter 6 also provides several modifications to the Shrinking Core Model to increase accuracy. A new theory to quantify inter-mineral occlusion in heterogeneous ensembles, 'mineral locking', is also provided in Chapter 6. Chapter 7 aggregates the novel data and methods from the previous chapters to estimate the effectiveness of the slag-based CO_2 mineralization methods. These methods are also used to evaluate direct, gas-solid CO_2 mineralization of extant solid wastes and natural minerals in Chapter 7. In Chapter 8, each method is applied globally taking into account technology adoption and diffusion rates to evaluate the potential impact on climate change mitigation. Additionally, Chapter 8 provides a cost and revenue analysis to evaluate the financial potential of each method. Chapter 9 provides a summary of the essential findings, novel methods, and remaining work from this dissertation.
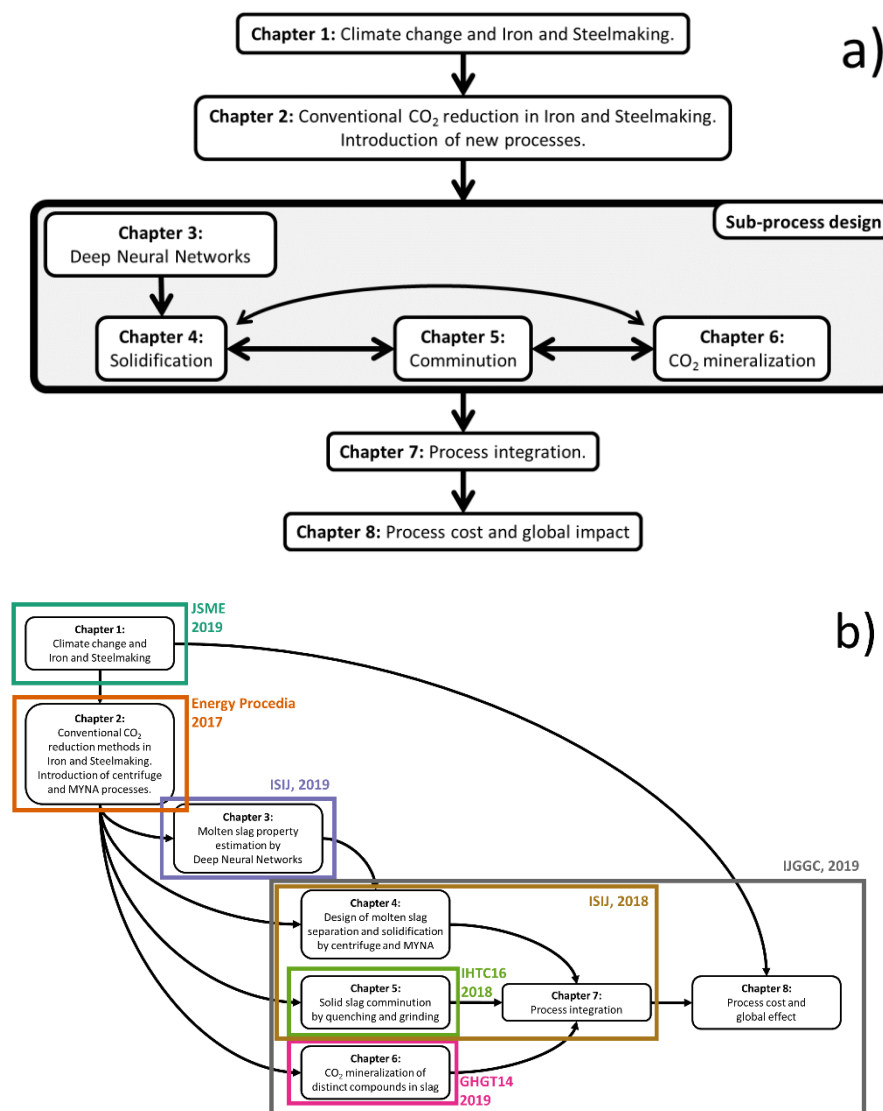
Fig. 1-1. The a) general flow of this dissertation and the b) relevant published papers and conference proceedings.

Chapter highlights

- Climate change is already negatively impacting all environmental services upon which human civilization depends.
- The rate of anthropogenic greenhouse gas emissions continues to increase.
- Current global anthropogenic greenhouse gas emissions are >50 gigatonnes of CO_2 equivalent per year.
- Several climatic and biological tipping points have already been crossed.
- Tipping points are not known ahead of time; in the near future, the Earth may enter into a 'hothouse Earth' regime, commensurate with global-scale extinctions.
- Ignoring population growth and increased per capita consumption, full utilization of renewable energy across all sectors of society will still result in >20 gigatonnes of CO_2 equivalent per year.
- The bulk of 'difficult to decarbonize' emissions are due to long-distance transport and production of iron and steel, cement, and chemicals.
- Negative emissions technologies are necessary to limit global mean surface temperature to 1.5 ˚C warming over pre-industrial levels by 2100.
- If rapid reductions in anthropogenic greenhouse gases does not begin by 2030, then negative emissions technologies become necessary to limit global mean surface temperature to 2 ˚C warming over pre-industrial levels by 2100.
- Anthropogonic emissions must become net zero by mid-century, with negative emissions technologies adopted at a scale of ~5-15 gigatonnes CO_2/y by 2100.
- The most-often cited negative emission technologies (i.e., bioenergy with CO_2 capture and storage and direct air capture with CO_2 capture and storage) are limited by biogenic, societal, and financial barriers.
- The necessary scale of negative emissions decreases as emissions in 'difficult to decarbonize sectors' are reduced.
- From a technical standpoint, CO_2 capture and storage can remove emissions from iron and steel, cement, and chemicals production.
- CO_2 capture and storage has been technically viable for 90 years, the lack of adoption is due to political and economic frameworks.
- A profitable method for CO_2 reduction could circumvent political issues, resulting in rapid technological adoption.
- A profitable CO_2 reduction technology is particularly important for the difficult to decarbonize iron and steel industry.

Publications relevant to this chapter

- CCS、CCUS のレビューと技術展望 〜コスト、量的寄与、リスクの観点から〜. 日本機械学会誌、 第 122 巻　第 1203 号 特集　二酸化炭素分離回収と貯留・固定および利用技術 p.8-13 (2019), Takao Nakagaki and **Corey Myers**.

1.1. Climate change

The danger that climate change poses is made clear by its name; the best climate in which to build and maintain a large, complex society is a stable climate. Societies have been built around the local geography, natural resources, and hazards present. Any alteration to these features inherently requires a modification of the underpinnings of society, with larger alterations necessarily causing greater upheavals. The International Panel on Climate Change (IPPC) has thoroughly proven that current anthropogenically-induced climate change is caused by an alteration of the Earth's energy budget due to an accumulation of CO_2 and other greenhouse gases in the atmosphere [IPCC AR5 WG1, 2013]. Interestingly, many of the major extinction events in Earth's history appear to be due to large and/or rapid changes in the atmospheric content of CO_2 [Rothman, 2017]. In past events where CO_2 was rapidly drawn down, the mechanism is likely to have been the weathering of rocks by land plants, the deposition of calcifying biota in the oceans, and burial of biota forming modern day coal deposits [Brannen, 2016]. However, the vast majority of major extinctions are instigated by an accumulation of CO_2 in the atmosphere. The release of CO_2 from large igneous provinces and fossil deposits by volcanic intrusion appears to be a common mechanism. Even so, anthropogenic climate change is unique in the geologic record in terms of the pace of CO_2 release. Current anthropogenic CO_2 emissions of 37.1 $GtCO_2$/y are roughly 17.5 times faster than the next closest event in the geologic record: the Paleocene-Eocene Thermal Maximum (PETM) [Gutjahr et al., 2017; Global Carbon Project, 2018]. At current emission rates, the atmospheric CO_2 concentrations will return to that of the PETM [Gingerich, 2019]. It is worth noting the PETM resulted in a near complete loss of oceanic life in the mid latitudes [Frieling et al., 2017]. Regardless of source, the accumulation of atmospheric CO_2 increases the absorption and reradiation of solar irradiance and thus increases the Earth's mean surface temperature (i.e., the greenhouse effect). Absent the greenhouse effect, Earth's mean surface temperature is controlled by the total solar irradiance (TSI), its albedo (A), and the Stefan-Boltzmann constant (σ). Due to energy conservation the outgoing radiation at the top of the atmosphere must match the TSI resulting in **Eq. 1-1**.

$$Mean\ Surface\ Temperature\ = \left[\frac{TSI(1-A)}{4\sigma}\right]^{1/4} = 256\ K \qquad (1-1)$$

The current TSI is ~1,368 W/m^2 and A is 0.29 [Stephens et al., 2015]. The rotating, spherical nature of Earth is the source of the factor of 4. The greenhouse effect accounts for the 33 K difference between the estimated temperature of **Eq. 1-1** and the observed surface temperature of the Earth. The greenhouse effect is dominated by water vapor, clouds, and non-condensing greenhouse gasses (GHG) such as CO_2, CH_4, and N_2O. The particular temperatures, pressures, and feedbacks of the Earth system make non-condensing GHG the primary climatic control knob with water vapor and clouds acting as feedbacks [Alley, 2013]. Over the course of the past 500 million years CO_2 has likely been the dominant greenhouse gas; roughly 80% of the GHG forcing is attributed to CO_2 over the glacial-interglacial period [Köhler et al., 2010]. **Figure 1-2** shows the various natural and anthropogenic influences on the temperature of the Earth over the past ~170 years. Anthropogenic GHGs are clearly the primary driver of temperature increase. Other anthropogenic GHGs, in particular CH_4, are of consequence to climate due to their strong radiative forcing (**Fig. 1-3**) [Allen et al., 2016]. However, the half-life of CH_4 decomposition in the atmosphere is 8.6 years [Muller and Muller, 2017], meaning

that unlike CO_2 it does not continue to accumulate and persist under scenarios of falling emissions (**Fig. 1-4**). Some recent evidence suggests the natural decomposition of CH_4 in the atmosphere is slowing, possibly due to a reduction in global hydroxyl concentrations [Turner et al., 2017].
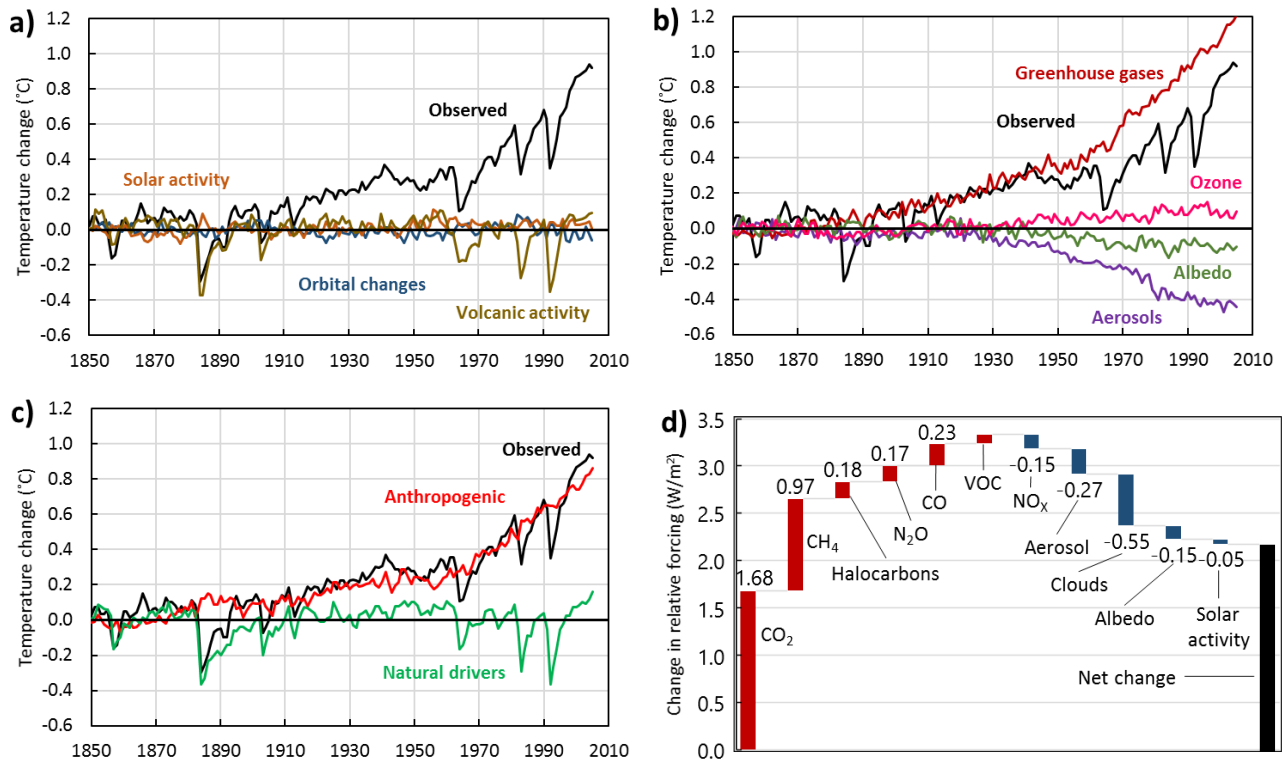
Fig. 1-2. Observed forcings on Earth's mean surface temperature attributable to a) various natural occurrences, b) various anthropogenic activity, c) total natural and anthropogenic forcings, and d) the cumulative change in relative forcings since 1750 [Hansen et al., 2011; IPCC AR5 WG1, 2013].
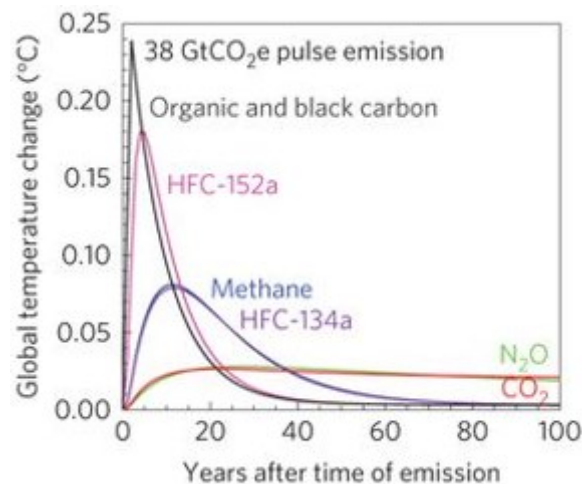
Fig. 1-3. The radiative forcing of various non-condensable GHGs. Reprinted with permission, copyright 2016, Springer [Allen et al., 2016].
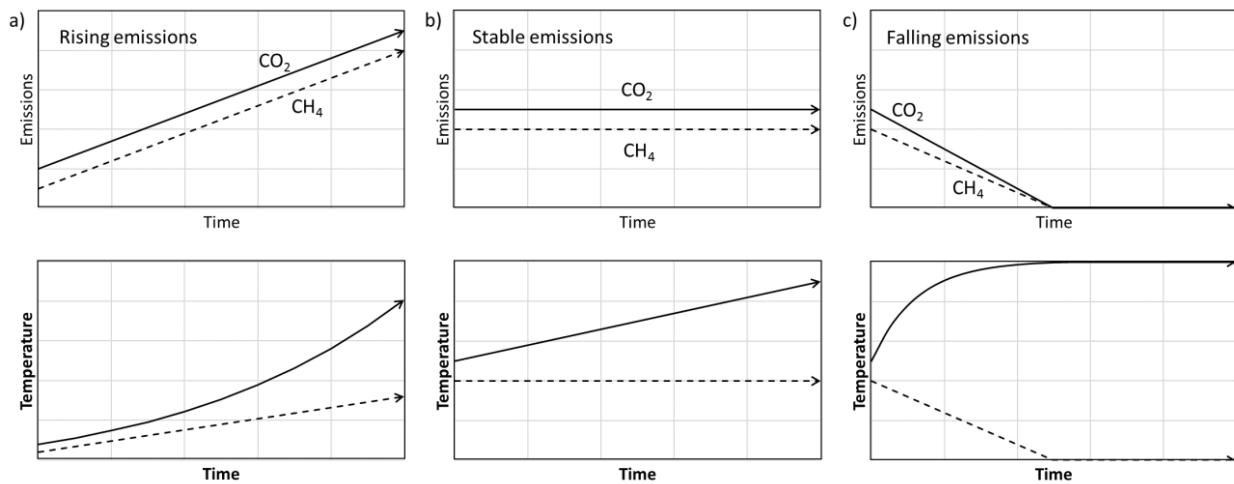
Fig. 1-4. A qualitative representation of the connection between CO_2 (solid lines) and CH_4 (dashed lines) emissions (upper graphs) and temperature (lower graphs) for a) rising emissions, b) stable emissions, and c) falling emissions [Allen et al., 2018].

The increase in global mean temperature impacts other aspects of the Earth that can amplify or dampen the warming effect. For example, increase in temperature melts ice at the poles, decreasing the albedo (i.e., white ice is converted to dark water and land) and thus increasing the amount of solar irradiance retained. On the other hand, increased CO_2 and temperature increases the rate of weathering of (Ca/Mg)-bearing rocks, thereby increasing the rate of atmospheric CO_2 draw down, in-turn lowering radiative forcing. However, the Earth is not purely rock, water, and ice; the large stocks of living and dead biomass (i.e., the pedosphere) play a significant role in the overall climate (**Fig. 1-5**). Geological and theoretical evidence suggests that the coevolution of the biotic and abiotic systems has led to an increase climatic and biotic stability [Gao et al., 2016; Goyal and Maslov, 2018; Lenton et al., 2018; Rothman, 2017]. Likewise, the average response of the Earth climatic system to a doubling of CO_2 (so-called Earth Climate Sensitivity: ECS) has been shown to increase as the average global temperature increases [Shaffer et al., 2016]. Moreover, as the ECS is an emergent, global scale behavior that depends on specific conditions and history, its value is inherently probabilistic, with current best estimates containing large fat tails that represent mass extinction level catastrophe at a doubling of CO_2 from preindustrial levels (**Fig. 1-6**; **Fig. 1-7**).
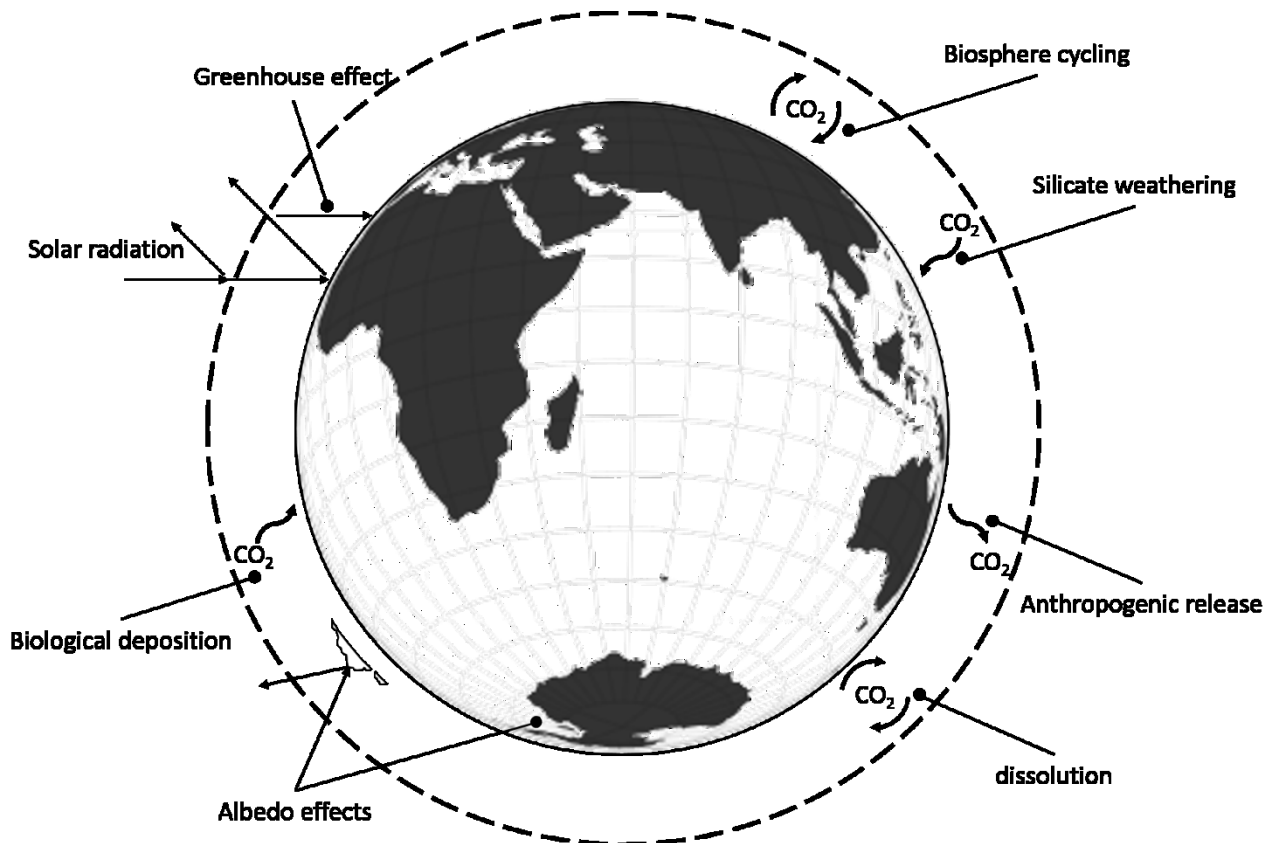
Fig. 1-5. Drivers and feedbacks of the Earth's climate system.

In aggregate, the pushing of the Earth system to higher CO_2 levels and concurrent reduction in biodiversity (both due to climate change and from other human activities) threatens to move the planet past one or more tipping points from which it cannot recover to the current environment. Such sudden and irreversible tipping points exists for both biological systems [Beaugrand et al., 2019; Sánchez-Bayo and Wyckhuys, 2019; Smale et al., 2019] and climatic patterns [Jones and Ricketts, 2017; Schneider et al., 2019]. As the Earth's climate is intrinsically linked to abiotic and biotic influences, consideration of these feedbacks are necessary [Neumann et al., 2019; Strona and Bradshaw, 2018]. Unfortunately, the difficulty of modeling such feedbacks has resulted in their exclusion from climatic models until recently. Consideration of feedbacks has consistently shown the climate to be more sensitive to increased GHG concentrations and warming than traditionally thought [Bodman et al., 2016; Caldeira and Cvijanovic, 2014; Golledge et al., 2019; Green et al., 2019].
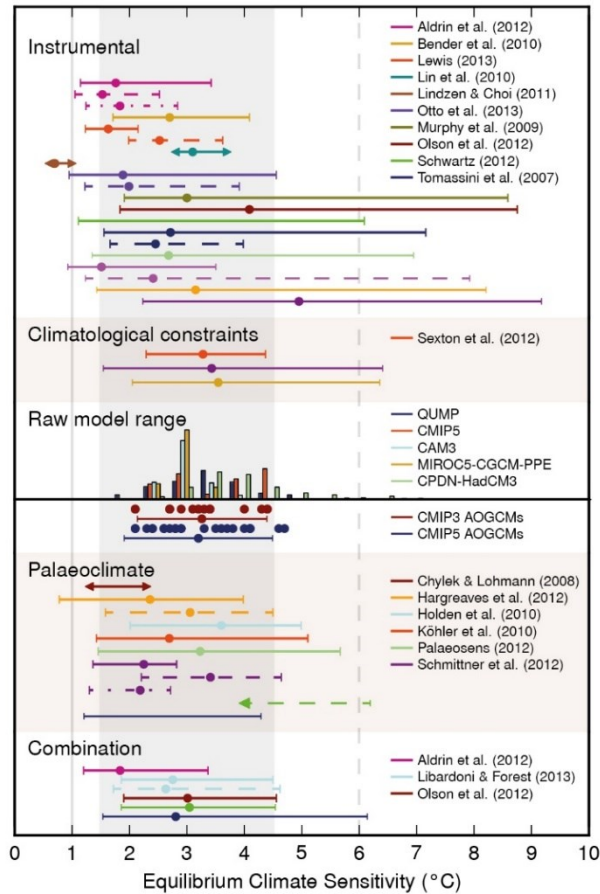
Fig. 1-6. The range of ECS constrained by various lines of empirical and theoretical evidence [IPCC AR5 WG1, 2013]
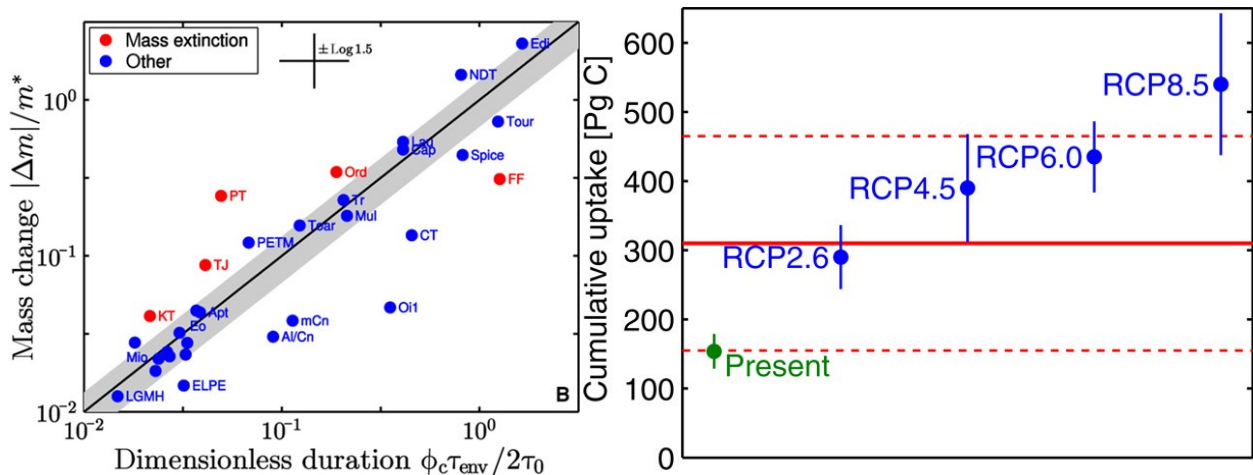
Fig. 1-7. The cumulative carbon release extent and rate for the major extinctions in Earth's history (left graph) and the current and potential future anthropogenic releases (right graph). Reprinted with permission from AAAS [Rothman, 2017].

Examination of the temperature response to changes in CO_2 emissions shows that reaching net zero emissions will stabilize the Earth's temperature, but removal of carbon dioxide from the atmosphere (CDR; alternatively, negative emissions technology: NET) will be necessary to reduce the CO_2 concentrations and temperatures to moderately safe levels in timescales relevant to human

civilization. Due to feedbacks from the ocean and biomass sinks, continuous application of NETs will be necessary until the total quantity of NETs matches the sum historical CO_2 emissions (**Fig. 1-8**) [IPCC AR5 WG1, 2013].
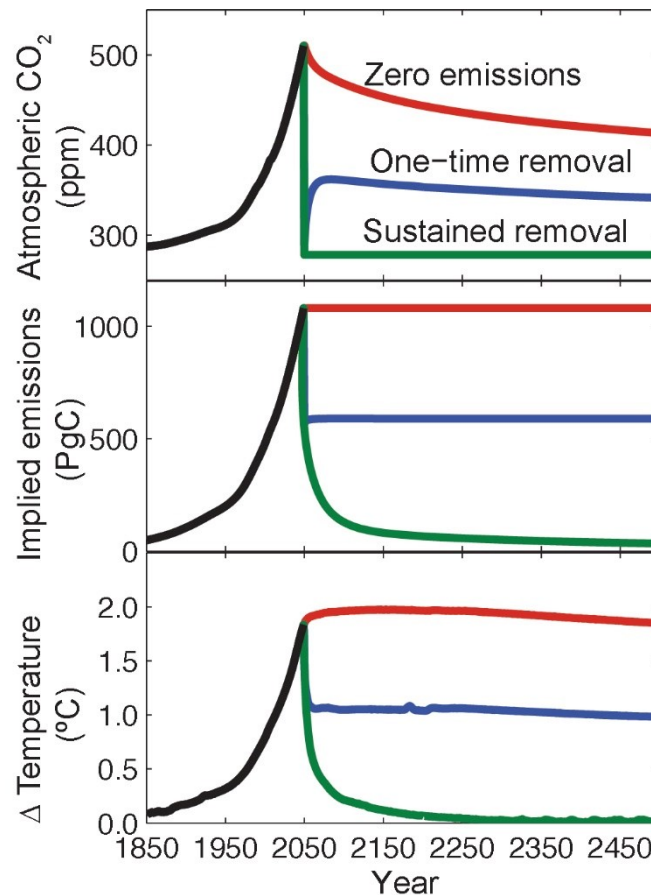
Fig. 1-8. The temporal change in mean surface temperature that coincides with zero emissions, a onetime removal of all atmospheric CO_2, and sustained removal of all atmospheric CO_2 [IPCC AR5 WG1, 2013].

It must be emphasized that while attempts to mitigate climate change are taking place, the climate is already undergoing significant changes. For example, the quantity of CO_2 predicted to be lost by organic carbon stocks by 2100 under 2 °C of warming will result in an additional 0.24-0.66 °C of warming (**Table 1-1**). This significantly intensifies and complicates the climate change challenge and emphasizes the need to act quickly and forcefully before climatic feedbacks become too intense to rectify.

Table 1-1. Carbon cycle feedbacks from biota. Reprinted with permission from PNAS [Steffan et al., 2018].

Feedback	Stock size, GtCO$_2$ (min-max)	Strength of feedback by 2100, °C (min-max)
Permafrost thawing	165 (73 - 293)	0.09 (0.04 - 0.16)
Relative weakening of land and ocean physiological C sinks	- - -	0.25 (0.13–0.37)
Increased bacterial respiration in the ocean	12	0.02
Amazon forest dieback	25 (15 – 55)	0.05 (0.03–0.11)
Boreal forest dieback	30 (10 – 40)	0.06 (0.02–0.10)
Total	232 (110 – 400)	0.47 (0.24–0.66)

The strength of the feedback is estimated at 2100 for an ~2 °C warming.

1.1.1. Impacts to 2100

Anthropogenically-induced climate change now poses an existential threat to modern civilization if not addressed quickly and vigorously. As shown in **Fig. 1-9**, the effects of climate change impact all environmental services on which human society depends [Mora et al., 2018; Zscheischler et al., 2018]. Currently, 467 aspects of human society are undergoing negative impact from climate change. In addition to the loss of environmental services such as water availability, arable land, and food stocks, climate change induces risks to the built environment from extreme weather and fundamental alteration of local terrain. The changing of climatic regions also induces risks that local societies are not adapted to confront (e.g., expansion of vector-borne disease regions). The loss of food and water security, infrastructure, traditional employment opportunities, and the increased strain on shared institutions is also projected to increase the extent and pace of human migration and conflict. By 2100, a large portion of the world's population is projected to be assaulted by multiple, concurrent climatic strains (**Fig. 1-10**). These interconnected risks are being increasingly appreciated by society's political and economic leaders as evidenced by change in attitudes towards risk probability and impact (**Fig. 1-11**) [WEF, 2019]. It is notable that the primary risks that are not directly labeled as 'environmental' (i.e., water, food, and migration) will be primarily driven by climate-change, with essentially all risks somehow intensified by climate change (**Fig. 1-12**).
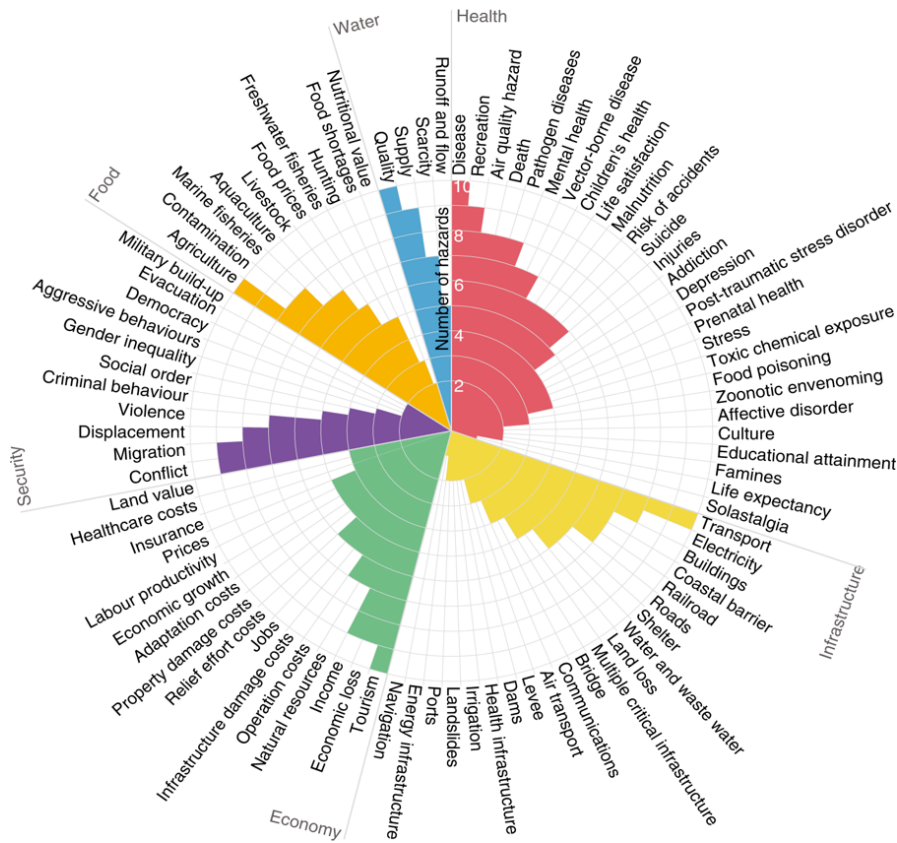
Fig. 1-9. The plethora of current negative impacts on human society resulting from anthropogenic climate change. Reprinted with permission from Springer Nature [Mora et al., 2018].
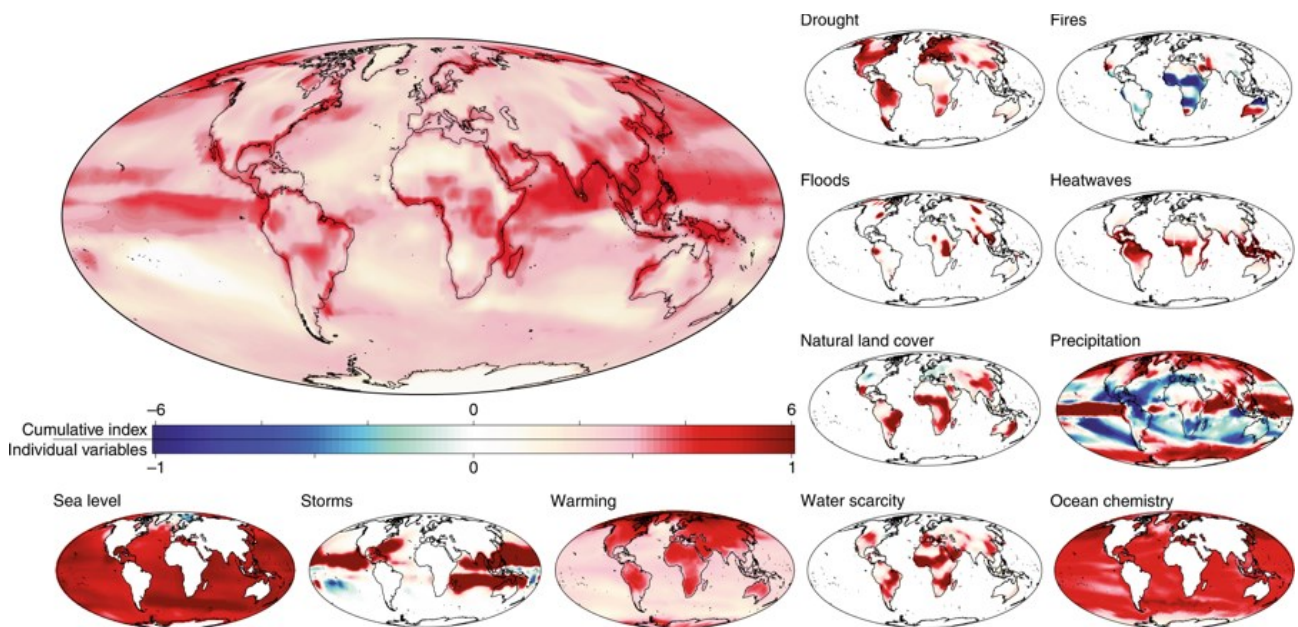
Fig. 1-10. The number of concurrent, cumulative climate impacts in 2100 (large, upper left inset) and the alteration in magnitude for major climate impact categories in 2100 (small insets). Reprinted with permission from Springer Nature [Mora et al., 2018].

Fig. 1-11. The evolution of climate risks as the most likely and impact global risks [WEF, 2019].
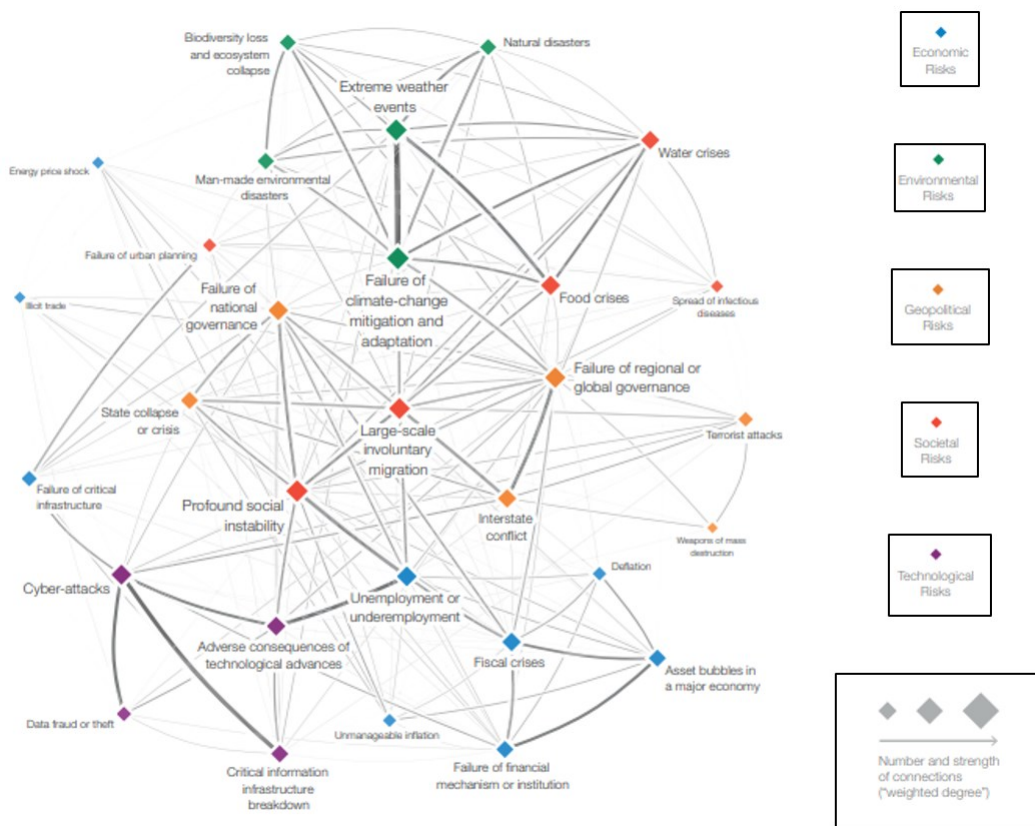
Fig. 1-12. The interconnected nature of global risks, with the role of climate change as a risk multiplier [WEF, 2019].

1.1.2. 2DS and 1.5 ˚C scenarios

The degree of human suffering and economic loss from climate change is intrinsically linked to the severity and rate of climatic changes. These dangers roughly scale with the amount of mean surface temperature increase, which in turn correlates with the total amount total amount of CO_2 released (**Fig. 1-13**). The current international ambition set out by the Paris Agreement is to limit global mean surface temperature increase over pre-industrial levels to well below 2 ˚C (2DS), and to make efforts to limit warming to 1.5 ˚C (B2DS) [UN, 2015a]. Given the amount of CO_2 already released by human activities, the net CO_2 budget to 2100 (starting from 2016) to stay below 1.5 ˚C and 2 ˚C is likely 210 $GtCO_2$ and 810 $GtCO_2$, respectively [Luderer et al., 2018]. Without the usage of NETs, this implies a reduction of current emissions of 37.1 $GtCO_2$/y by ~5% and ~27% year-on-year in order to meet 2DS and B2DS, respectively (**Fig. 1-14**). As shown in **Fig. 1-15**, delaying mitigation efforts rapidly increases the rate at which emissions reductions must occur.
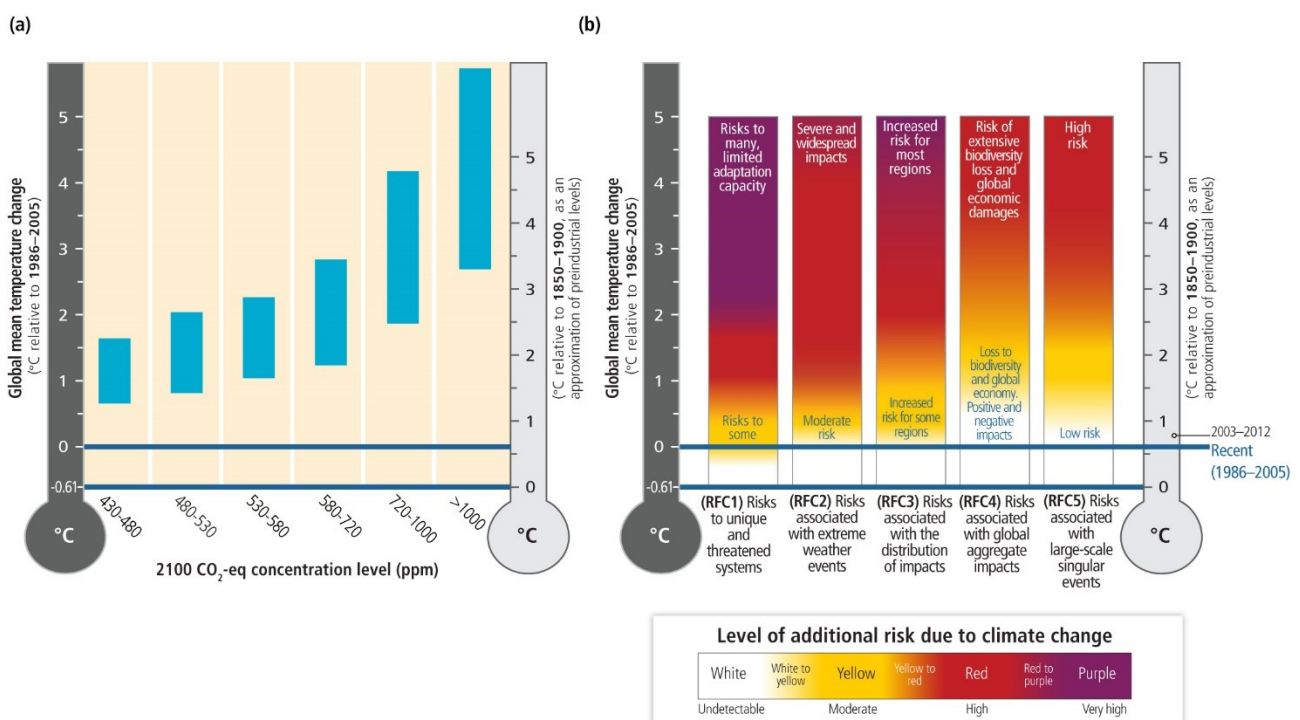
Fig. 1-13. The global mean temperature change a) as a function of atmospheric CO_2 concentration, and b) as it relates to risks to human society [IPCC AR5 WG2, 2013].
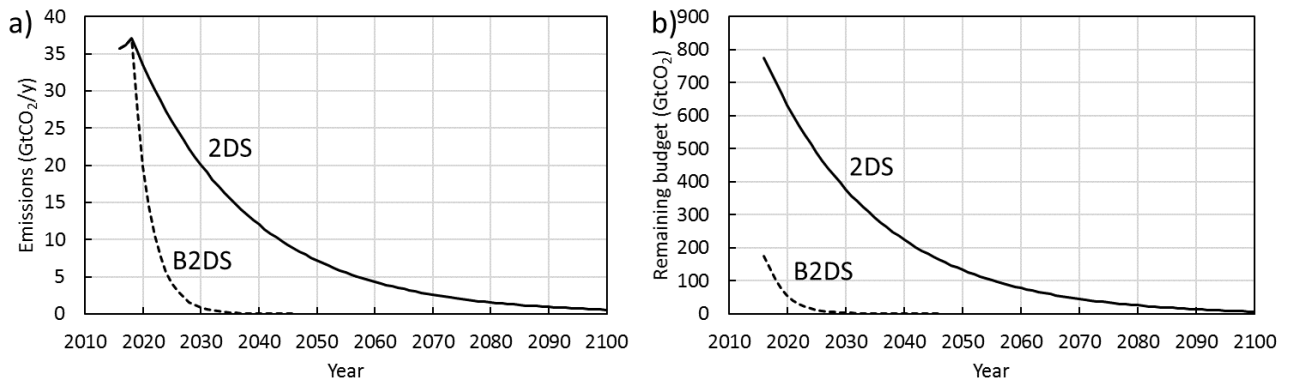
Fig. 1-14. The implied a) reduction in CO_2 emissions and b) remaining carbon budget if NETs are unavailable to meet the Paris Agreement climate goals.
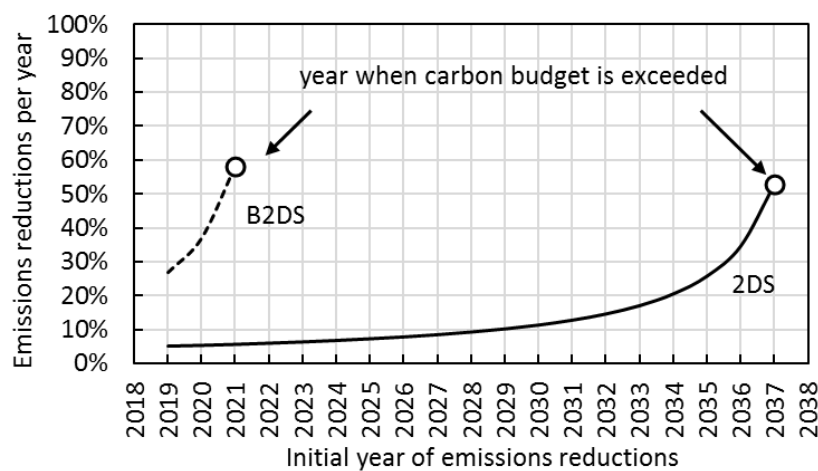
Fig. 1-15. The increase in mitigation effort (yearly emissions reduction) that comes with a delay in emissions reductions.

However, as summarized in **Table 1-2**, many CO_2 sources lack methods for decarbonization (e.g., iron and steelmaking, cement manufacture, agriculture); the continued CO_2 emissions from such sectors forces the application of NETs [Kaya et al., 2019]. The magnitude of NETs adoption depends strongly on assumptions about future emissions and socioeconomic factors. However, the majority of estimates suggest NETs at the gigatonne CO_2 per year scale by 2100, with cumulative NETs by 2100 reaching many hundreds to over a thousand gigatonnes of CO_2 for both B2DS and 2DS [Nemet et al., 2018].

An additional area of concern is the fact that climate projections such as those used for the IPCC special report on meeting B2DS do not take into account reductions in air pollution, natural climate cycles, and the reality of rising emissions (**Fig. 1-16**) [Xu et al., 2018]. Reduction in aerosols (SO_X and NO_X) concurrently increases the amount of solar irradiance reaching the surface, thereby enhancing warming. Removal of aerosols without any alteration to GHG emissions would increase mean surface temperatures by 0.5 ˚C [Hienola et al., 2018]. Natural oceanic cycles of the Pacific and Atlantic oceans may result in less heat being drawn into the deep oceans (i.e., higher atmospheric temperatures). Since 1971, 90% of the excess heat from anthropogenic climate change has been taken up by the oceans [Zanna et al., 2018]. The Interdecadal Pacific Oscillation appears to be entering its positive phase, which will result in increased surface temperatures, in particular over North America and the

equitorial Pacific region [Meehl et al., 2016]. Concurrently, the mixing of surface and deep waters by the Atlantic meridional overturning circulation appears to be weakening [Caesar e al., 2018]; a phenomenon that would result in increased heat retention in the atmosphere. Finally, the IPCC special report on 1.5 ˚C, and ostensibly most climate projections, assume a 0.2 ˚C per decade temperature increase. However, current emissions suggest that temperatures will increase at 0.25-0.32 ˚C per decade [Smith et al., 2018]. This underprediction by conventional models is further intensified by the fact that, according to empirical data, the assumed ECS is likely conservatively low [Brown and Caldiera, 2017], and that the ECS will increase as climate change progresses [Andrews et al., 2018].
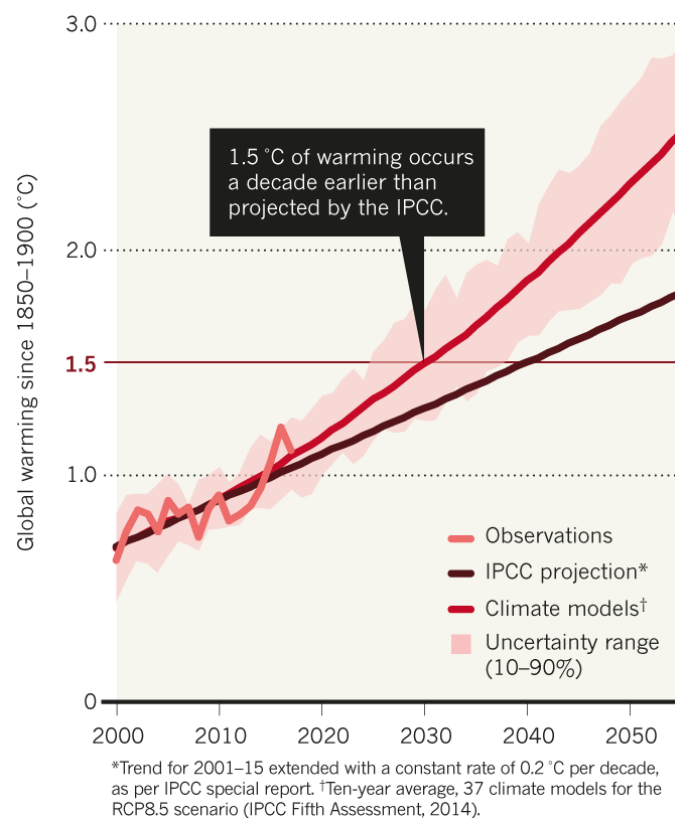
Fig. 1-16. The underestimation of temperature increase in models aggregated by the IPCC special report [Xu et al., 2018].

1.1.3. Sustainable development goals

Climate change is viewed as a problem due to the value humans place on human life, happiness, and the natural environment. Therefore, a climate change mitigation strategy that inflicts unnecessary death and suffering cannot be accepted. As such, climate change mitigation efforts must be considered in tandem with efforts to reduce poverty, inequality, conflict, and their associated effects. There is a striking lack of ethics included in IAMs, the primary instrument used to evaluate efforts to fight climate change [Lenzi et al., 2018]. To help rectify this weakness, the goals of society are laid out in the United Nations Sustainable Development Goals (SDGs) as summarized in **Fig. 1-17** [UN, 2014]. The 17 SDGs contain 169 targets and 230 indicators of progress. While most of the SDGs align with efforts to fight climate change (e.g., increased gender equality leads to a decreased birth rate and thus less anthropogenic CO_2), the SDGs in general require a higher quality of living and thus

larger per capita energy expenditure. Nevertheless, projections of potential future societies in line with the SDGs result in the lowest climate mitigation challenges [Riahi et al., 2017].

Fig. 1-17. The 17 UN SDGs that are expected by policy makers to occur concurrent to climate change mitigation efforts.

1.1.4. Equity

Equity in the climate change mitigation and adaptation community has often centered around attribution of emissions (i.e., historical vs. contemporary) and what constitutes a fair allocation of contribution of resources to resolving the issue. Developed countries argue that developed countries should reduce emissions commensurate with their population while developing countries argue that they deserve to enjoy the same quality of life that developed countries gained through the dumping of carbon dioxide. These arguments can be summarized by the differences between **Fig. 1-18a** and **Fig. 1-18b** [Chancel and Piketty, 2015].
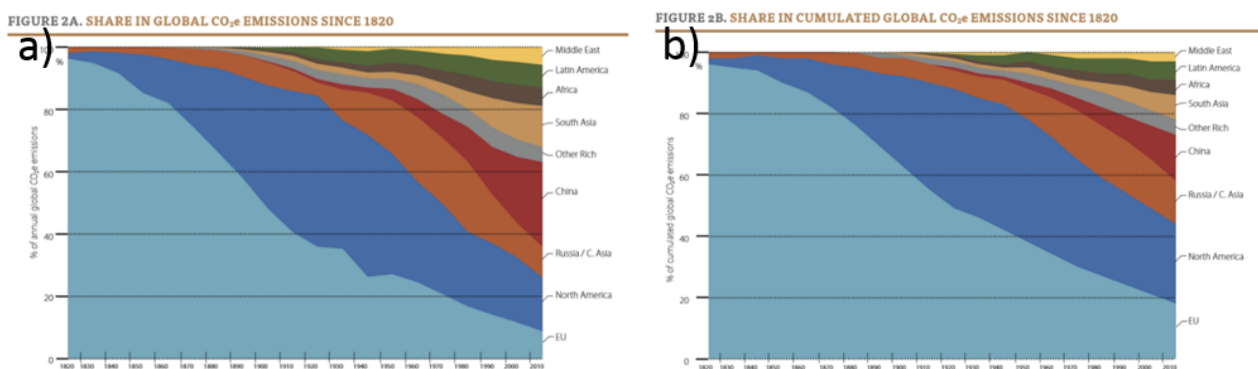
Fig. 1-18. The distribution of CO_2 emissions by country a) per year, and b) cumulative [Chancel and Piketty, 2015].

However, an additional axis of responsibility exists that is rarely discussed; namely, the inequality of CO_2 emissions mirroring economic inequality. For example, if the richest 10% of the global population lived at the per capita CO_2 emissions of the average EU citizen, global CO_2 emissions would fall by 30% [Anderson, 2019]. Roughly 50% of emissions can be attributed to the richest 10% of the global population, whose per capita CO_2 dumping is 60 times that of the poorest 10% (**Fig. 1-19**) [Gore, 2015].
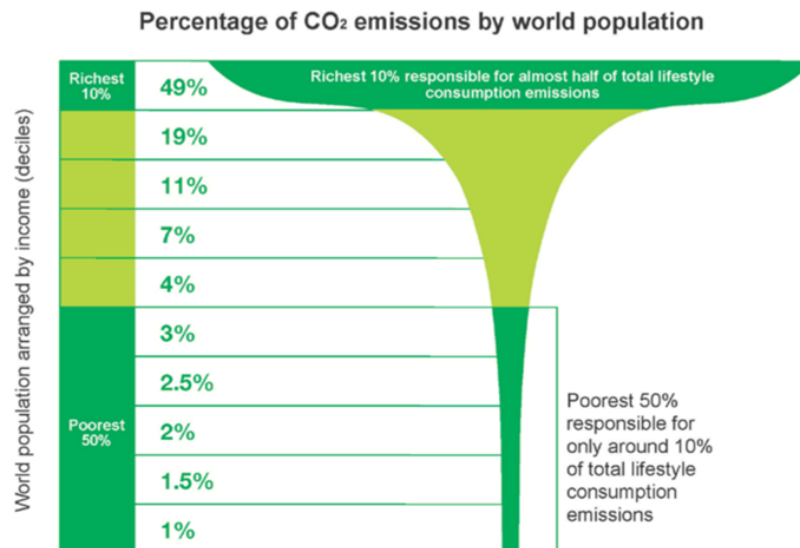
Fig. 1-19. The inequality of CO_2 emissions from personal consumption by economic class [Gore, 2015].

The fact that those negotiating climate change regulations are overwhelming part of the global rich, and often directly financially benefit from the richest and most carbon intensive individuals and companies is beyond troublesome. It should be unsurprising that the responsibility of the global rich goes unheralded. It should be noted that the magnitude of climate change makes global, coordinated action advantageous as opposed to a knitwork of individual efforts. As such, what is needed is for governments to put in measures to reduce the high end of the carbon dumping inequality, and use those gains to develop the technology, infrastructure, and markets to drive global scale climate change mitigation and adaptation.

Perhaps more upsetting is the disproportionate impact climate change will have on the global poor. The poor are more likely to depend financially on environmental services, are less likely to have the financial and technological means to adapt to and withstand climate impacts, and are inherently separated from the ruling class by their economic position. These effects are magnified by issues of systemic inequality such as sexism, racism, and xenophobia. Therefore, climate change as a crisis of the commons is a misnomer, as the access to capital and influence are not equally distributed among people. The distribution of CO_2 emissions attributable to personal consumption within countries is provided in **Fig. 1-20** [Gore, 2015].
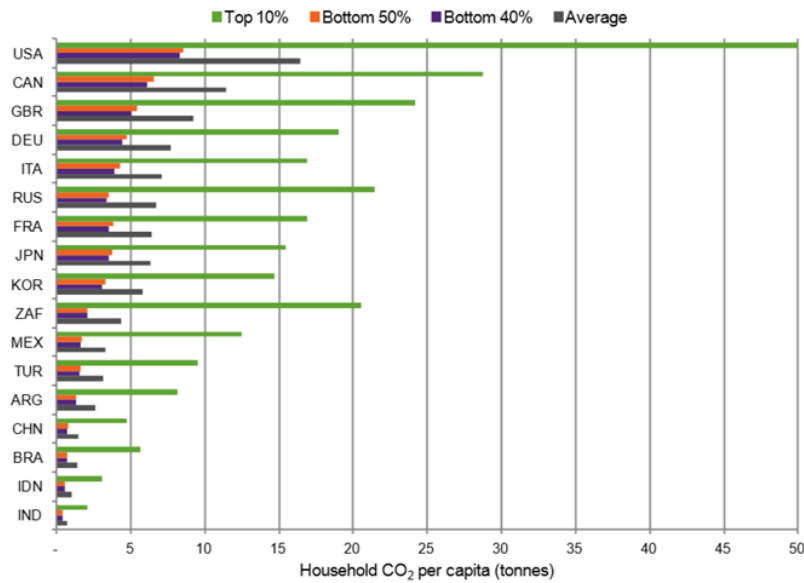
Fig. 1-20. Inequality in emissions within countries by economic level [Gore, 2015].

1.1.5. Mitigation and adaptation

This dissertation, as is the case for most research about fighting climate change, attacks the issue from the standpoint of mitigation; in other words, reducing the magnitude of climate change through emissions reductions and removal of previously released carbon dioxide. However, mitigations efforts have proven unsuccessful. Projections indicate that even under the most optimistic scenarios there will be severe climatic instability and the associated environmental impact and human suffering. For example, by the 2080's, most cities will be in new climatic zones, equivalent to contemporary cities 100's of kilometers closer to the equator than their current position [Fitzpatrick and Dunn, 2019]; this will stress infrastructure that has been developed for a specific climate. In fact, over 500 million people will be at risk of heat death due to wet bulb temperatures exceeding 35 ˚C [Im et al., 2017; Kang and Eltahir, 2018; Mora et al., 2017; Russo et al., 2017]. At least 2 billion people will be without a supply of fresh water [Wester et al., 2019]. Hundreds of millions of people will need to migrate due to sea level rise [Brown et al., 2018a; Nicholls et al., 2011; Tamura et al., 2019]. Though the costs of abatement are always lower than the damages they prevent, the window for applying mitigation techniques is rapidly closing [Lamontagne et al., 2019].

Given these facts, the other major mode of fighting climate change, adaptation, is also necessary. Adaptation involves reducing vulnerability to the changes that will occur, increasing the resilience of human and natural systems towards disruptive events and trends while preserving their basic functions, and increasing the adaptive capacity of individuals, communities, and systems towards harmful events and potentially beneficial opportunities. These goals are distinctly qualitative and intrinsically case-dependent [Leiter et al., 2017]. Moreover, the very character of climate change is to cause the foundations of society from which goals are set, to become fluid and difficult to predict. Acknowledging this difficulty, county-level reporting of adaptation efforts take the form of self-determined National Adaptation Plans (NAP). The primary purpose of NAPs are to enable the poorest and least-developed countries to report their medium- and long-term needs such that richer and more developed countries may provide support.

The effort to develop a common global framework for addressing adaptation is still in the early stages of development as stated in the 2017 United Nations Adaptation Gap Report "*The global goal on adaptation is multifaceted and unspecified in terms of targets and indicators at national and global levels*" [UNEP, 2017]. This fact is evidenced by the bulk of the work focusing on defining terminology and developing suitable descriptive and flexible metrics for evaluation. However, concrete progress on adaptation exists in the Sendai Framework for Disaster Risk Reduction [UN, 2015b]. The core concept of the Sendai Framework is to build resilience into systems instead of managing risks as they unfold. The framework includes seven targets measurable by 38 indicators. Importantly, the indicators are linked to and coherent with the SDGs; in particular, making cities and settlements resilient (SDG11), global climate change action (SDG 13), and ending poverty (SDG 1). Moreover, a focus is placed on strengthening cooperation between countries, including a continuous financial and technological support to poor and developing countries. Underlying this focus is the need to instill trust between parties without being overly regulatory, punitive, or burdensome. To achieve such a system requires transparent and complete communication between parties, which is embodied in the call for periodically updated communication on adaptation efforts (e.g., NAP, as part of the NDC, or other national communication). Likewise, rich and developed countries shall report what financial and technology transfer capabilities they have to offer to poor and developing countries.

The goals of the Sendai Framework on Disaster Prevention in terms of the behavior of countries is mirrored in the field of game theory. In order for a collective of actors to share limited resources most efficiently, each actor must reduce their gains by not cheating the agreed upon system of sharing. However, when the stresses of climate change begin to become sever, or when the impacts are unevenly distributed, there will be a natural tendency to act in short term self-interest. Such behavior can rapidly upend the delicate balance of a shared system. Moreover, the desire for national sovereignty drastically reduces the ability of the collective to punish those that cheat the system. The problem is further aggravated by the potential for climate change to be unadaptable in large swaths of the world due to such issues as heat death [Mora et al., 2017], water scarcity [Wester et al., 2019], rising seas [UCCRN, 2018], ecosystem collapse [Penn et al., 2018], and the like. Note that no area of the world appears to be outside the realm of negative impacts from climate change: the coasts are more prone the effects of sea level rise and natural disasters while the inland and high elevations are more prone to temperature and humidity increase [Mani et al., 2018; Pepin et al., 2015]. The dubious assumption of the adaptation community is that all areas of the world can maintain their current quality of life if sufficient preventative measures are taken now. However, it is overwhelming likely that large amounts of human migration will occur due to climate change [Abel et al., 2019]. Thus, adaptation should include handling the stresses on systems that come with sudden influxes or effluxes of people.

From the less optimistic perspective of adaptation that comes from the climate change science and mitigation community, adaptation is not a panacea, but rather another lever to reduce climate change effects. Adaptation works to increase the climate change society can handle before crumbling, and mitigation acts to reduce the magnitude of events that adaptive systems must handle.

1.2. Current GHG sources and options

As of 2016, there remained between 430 and 1000 $GtCO_2$ emissions allowable to meet 2DS (median 810 $GtCO_2$). For a >66% chance of meeting 2DS, global anthropogenic GHG emissions must match natural and engineered sinks by mid-century; additionally, NETs must reach the ~10 $GtCO_2$/y

scale by 2100, with ~5 $GtCO_2$/y necessary by 2050 [Nemet et al., 2018]. NETs are required to pay the debt of historical excess emissions and to offset sectors that are particularly difficult to decarbonize. Given the novelty of NETs, it is undoubtedly favorable to reduce emissions as rapidly as possible, with NETs being used as compensatory lever. Current direct and indirect GHG emissions are shown in **Fig. 1-21** including CO_2, CH_4, N_2O, and fluorinated gases in terms of an equivalent CO_2 radiative forcing (CO_2eq); the effects of aerosols and particulates are not included. Though CO_2 from power, industry, and transportation are the main drivers of climate change, the effects of trace gases and indirect emissions increases the annual CO_2eq emissions from 35.76 to 53.14 $GtCO_2$eq in 2016.
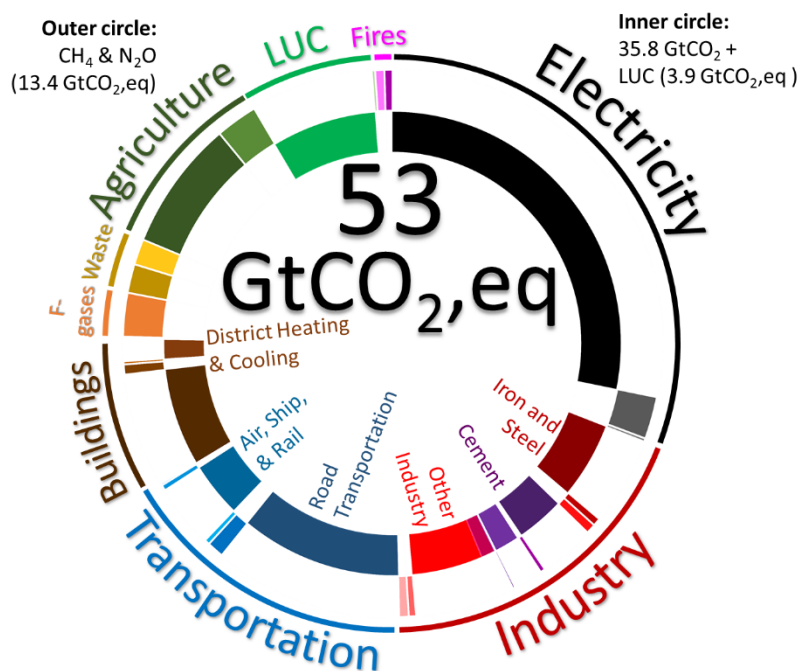
Fig. 1-21. The anthropogenic GHG sources in 2016.

The ability of renewable energy (RE) and electrification to provide the needed GHG reduction by sector is provided in **Fig. 1-22**; not accounted for in **Fig. 1-22** are the potential large increases in flux from the biogenic carbon sinks due to climate change. There are also options to address certain emissions that do not rely on RE or electrification. These methods break down into alteration of human behavior and regeneration of natural carbon sinks. Alteration of human behavior is distilled by the concept of reduce, reuse, and recycle (RRR). The reduction of consumption across all sectors of society would apply a strong downward trend to CO_2 emissions. At the level of the individual, RRR can be realized most strongly by the reduction in: number of children, air travel, and consumption beef and dairy products [Shepon et al., 2018]. At the level of companies and municipalities, RRR means increasing the efficiency of buildings and equipment, reducing new construction, building and manufacturing with less materials, increasing recycling of high CO_2-intensity materials (e.g., metals, cement, glass, plastics), and divesting from companies engaged in fossil fuel extraction. At the scale of countries and international companies, RRR can be realized by increasing education, eliminating fossil fuel subsidies, reducing wealth inequality, and reducing the offshoring of manufacturing to countries with high CO_2 intensities.

reliable energy
coke, limestone, & heat
clinker & heat
H2 & heat
long-haul transport
DHC
waste
agriculture

20 GtCO$_2$,eq
if applied in 2016

Handled by renewable energy

Requires CCS/CCU/CCUS
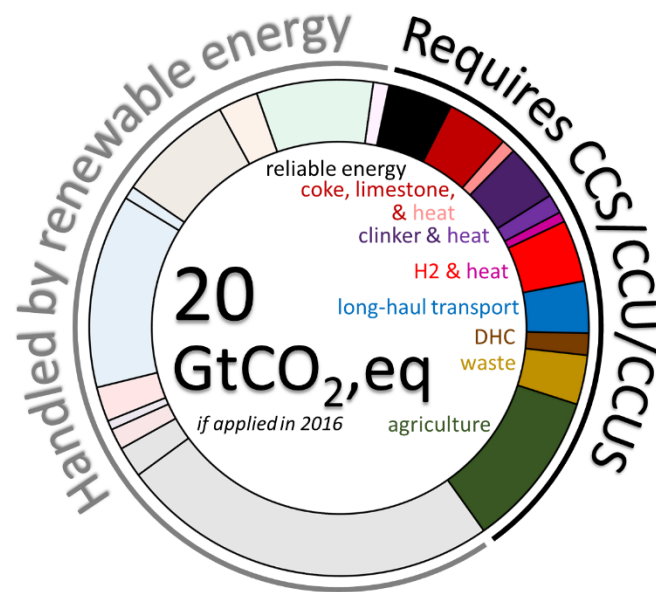
Fig. 1-22. The breakdown of current GHG sources that have clear pathways to removal by application of renewable energy (grayed-out colors) and those that require some form of CCS, CCU, or CCUS (bold colors).

A variety of methods are available for the restoration of natural carbon stocks. Roughly 590 GtCO$_2$ (~1/3 of all anthropogenic emissions since 1850) are a result of land use change (LUC) and the loss of carbon from soils [Lawrence et al., 2018]. The natural environment (i.e., sans human influence) provides the largest magnitude carbon storage [Huang et al., 2018]. Efforts to increase carbon storage in soils are fraught with uncertainty [Sulman et al., 2018]; moreover, even if carbon storage can be enhanced over natural levels, such a soil condition requires continual effort to prevent re-release of carbon from the saturated soils [Smith, 2016]. Soil carbon sequestration (SCS) is technically feasible simply by allowing land to lay fallow; however, this comes at an economic cost to various entities that may wish to utilize the land for economically productive activities. The largest of these interests are for agriculture and grazing. However, an outsized portion of land is used as pasture for cows and to produce feed for livestock (**Fig. 1-23**) [Merrill and Leatherby, 2018]. Therefore, for SCS to have a meaningful impact, it will be necessary to alter the dietary habits of a large number of individuals.
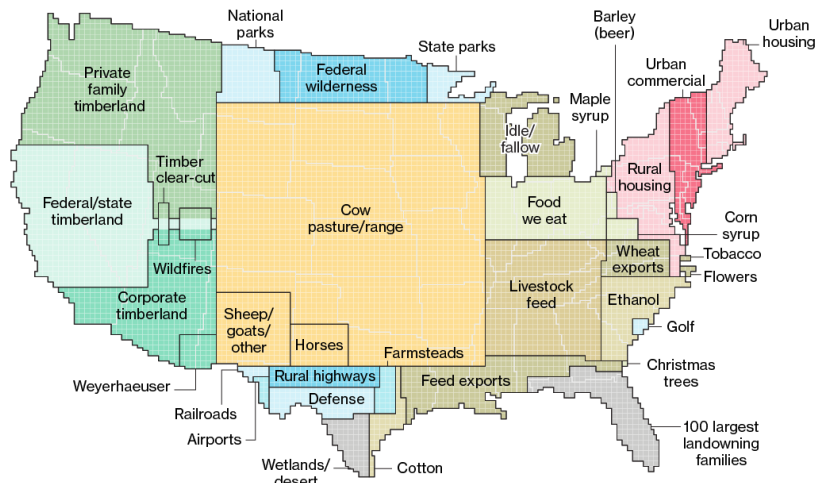
Fig. 1-23. The breakdown of land usage within the contiguous United States [Merrill and Leatherby, 2018].

In addition to increasing the carbon content of soils by allowing for the restoration of natural biota, the active reforestation of deforested areas (RF) and afforestation (AF) of certain environments is a low cost, low risk method to increase natural carbon stocks. Afforestation and reforestation provide benefits beyond NETs such as soil stability and increased air quality. However, the interconnected nature of the soil and biota systems means that simple accounting of the carbon content in planted trees is insufficient to determine the net CO_2 change of the environment. It is possible to increase CO_2 emissions through AF/RF due to changes in the inherent biota and soils that occurs when trees are actively introduced. Moreover, trees alter the albedo of the landscape, causing a warming effect that in some scenarios may completely offset the cooling effect from removal of CO_2 [Popkins, 2018]. It is also worth remembering that climate change will alter the physiological activity of plants; current research suggests that climate change will reduce the primary production of plants [Kovenock and Swann, 2018; Reich et al., 2018]. Therefore, depending on AF/RF for NETs may not be as robust of a method as it initially seems.

An additional 'natural' method to drawn down CO_2 is to increase the rate at which natural rocks react with atmospheric and aqueous CO_2 (i.e., weathering). So-called enhanced weathering (EW) generally focusses on aqueous dissolution of magnesium and calcium silicate rocks via biological activity in soils [Renforth et al., 2015] or mixing with ocean water [Montserrat et al., 2017; Moosdorf et al., 2014]. The extremely slow rate of dissolution requires substantial grinding and extraction of large quantities of material to have globally-relevant impacts. While generally slower and less efficient than biological methods, the resultant form of carbon (as calcium and magnesium carbonates) is stable in the Earth environment.

Amongst the remaining GHG emissions (i.e., not related to agriculture and LUC), the power and road transport sectors are likely to be the technically and financially easiest to decarbonize due to the rapidly decreasing price of RE (primarily wind and solar photovoltaics: PV) and Lithium-ion batteries (LiB) [Diesendorf and Ellitson, 2018; Ram et al., 2017]. Due to the inherent variability of RE, decarbonization of the power sector will become increasingly more difficult and expensive as RE penetration increases [Sepulveda et al., 2018]. Load-following power (e.g., natural gas peakers) will likely be replaced by a combination of demand response, purpose-built 100 MW to GW-scale batteries (mechanical, electrochemical, thermal, and chemical), and storage supply in the grid from

electric vehicles (EV) and home/commercial battery systems [ARPA-e, 2018; Thornhill, 2018]. Even so, most current projections suggest RE penetration will be financially limited to ~80% even with the advent of regional high voltage direct current transmission networks (HVDC) [Clack et al., 2017; Walsh et al., 2017]. The remaining energy will need to be provided by sources that can meet demand regardless of season and for long durations, namely: nuclear energy, bioenergy, fossil fuel power plants with CO_2 capture and storage (CCS), and long-term energy storage technologies such as pumped hydropower, flow batteries, and synthetic fuels like H_2.

Due to the lower cost of ownership of EVs compared to internal combustion engine (ICE) vehicles, the road transportation sector will become increasingly decarbonized in-line with decarbonization of utility-scale power generation. This is projected to include long-haul trucking due to increased performance of LiB and large potential benefits from next-generation batteries (e.g., lithium sulfur and lithium metal batteries) [IEA, 2018a]. Short-haul shipping (e.g., ferries, tug boats, barges) and aviation (<300-500 kilometers) are projected to convert to electric [Dowling, 2018; Lambert, 2018]. Long-haul rail, shipping, and aviation will require higher energy densities than can be provided by LiB; potential low carbon fuel sources are biofuels, synthetic fuels, and low CO_2 footprint H_2 [Davis et al., 2018].

The main energy loads of the domestic and commercial building sectors (space heating/cooling, water heating/cooling, and cooking) are amenable to low cost electric alternatives to fossil fuel-based technologies. Additionally, natural-gas infrastructure could be repurposed to utilize low CO_2 footprint H_2 [Sadler et al., 2016]. Fluorinated gases are primarily used in air conditioning systems and so are amenable to regulatory phase-out; however, the lower effectiveness of alternatives may lead to reductions in cooling efficiency. The building sector is also ripe for application of demand response and efficiency gains [Moon and Lee, 2018].

The heat requirement of the industrial sector is less amenable to RE and electrification due to the high temperatures required [Philibert, 2017]. The high temperature heat needed by industry could be provided by biofuels, synthetic fuels, or low CO_2 footprint H_2. Hydrogen-based furnaces will require engineering to avoid production of thermal NO_X and to adjust the control scheme due to differences in the adiabatic flame temperature, flame speed, and diluent makeup.

Low CO_2 footprint H_2 is a necessary component of many solution pathways and can be derived from RE-powered electrolysis, traditional H_2 generation from fossil fuels connected to CCS infrastructure, or through microalgae and/or bacterial fermentation. The energetic load of electrolysis-derived H_2 remains prohibitively high [IRENA, 2018a]. H_2 generated via photobiolysis from microalgae remains at energy efficiencies of ~1% due to Oxygen sensitivity and inhomogeneous illumination [Sambusiti et al., 2015]. Pairing microalgae H_2 production with dark fermentation using anaerobic bacteria can increase H_2 production rates; however, anaerobic digestion is thermodynamically limited to 33% conversion of the organic substrate with the remaining material typically comprising an organic waste stream [Nagarajan et al., 2017]. The low efficiency limits the scale to available organic waste streams.

The GHG emissions of the waste sector can be dramatically reduced by incineration of wastes instead of landfilling practices (i.e., proactively forming CO_2 instead of CH_4). Combined with CCS, waste incineration could be a net zero (if waste is generated from fossil-fuel derived material) or a net negative technology option (if waste is derived from biogenically sourced material).

Decarbonization of the industrial sector, in particular iron and steel making (ISM) and cement production, remain technically and financially problematic [Davis et al., 2018]. The production of

these materials inherently generates CO_2 as part of the process chemistry. In ISM, limestone is decomposed to remove impurities from molten metal, coke is used to reduce iron ore to metallic iron, and coke provides the process heat. In cement production, limestone is thermally decomposed to CaO by way of burning fossil fuels. Increased recycling of scrap in ISM, usage of alternatives to clinker in cement, and improved civil engineering can reduce the CO_2 emissions from cement and ISM. Alternative cement formulations, including but not limited to geopolymers and Mg-based cements could reduce the CO_2 footprint of cement manufacture, though full-chain life cycle assessments remain lacking. Moreover, the nature of civil engineering projects makes the industry risk adverse, and there is little financial incentive to utilize novel cement formulations [Neuhoff et al., 2014a]. Re-mineralization of CO_2 during the cement curing process is a promising method [Zhang et al., 2017]. Nevertheless, a CO_2 capture step will be necessary to implement CO_2 curing. Research has also indicated that cement naturally takes up CO_2 as it ages, particularly when it is crushed during demolition [Xi et al., 2016]. Reduction of CO_2 emissions from ISM is typically viewed to be contingent upon application of CO_2 capture and storage (CCS) or application of NETs to offset emissions [Neuhoff et al., 2014b]. Emissions stemming from ISM and cement accounted for 2.64 and 2.5 $GtCO_2eq$ in 2016, respectively [Olivier et al., 2017]. ISM production is projected to increase ~1.4-2.0 times 2016 levels by 2050 [Oda et al., 2013], similar increases in cement production can be reasonably expected.

Table 1-2 summarizes the connection between sectors requiring emissions reduction and potential solutions. All sectors can potentially utilize NETs to offset emissions; though the scale of NETs required to offset all remaining emissions will likely generate other global crises such as competition for water, land, and energy [Heck et al., 2018]. Lifestyle changes (e.g., less meat consumption, less international travel, fewer children) can dramatically reduce the load placed on technology, though this requires a change to the underlying mechanism that has led to climate change: the failure of individuals and institutions to grasp that they do not live in an environment, but are part of an environment. CCS is the most widely available and technologically mature mechanism to reduce emissions, though CCS has struggled with timing and financing to set-up the full capture, transport, and storage infrastructure. 'Green fuels' are also a prevalent solution to reducing CO_2 emissions, in particular for dispersed emissions (e.g., aviation) and high heat uses (e.g., furnaces). However, these fuels require either CCS, extremely low cost RE, or technological breakthroughs to deliver on the promise of low CO_2 emissions.

Table 1-2. The reliance of difficult to decarbonize sectors on various mitigation methods.

	3R	LUM[1]	Excess RE	Nuclear	Biomass	New technology	CCS	Mineralization[2]	NETs	Energy storage[3]	Green fuels
Dispatchable PP	✓			✓	✓		✓	✓	✓	✓	✓
Waste	✓				✓[4]		✓	✓	✓		
DH&C	✓				✓[4]				✓	✓	✓
Air, ship, rail	✓								✓		✓
Other industry	✓						✓		✓		✓
ISM	✓				✓	✓[5]	✓	✓	✓		
ISM finishing	✓						✓		✓		✓
Cement	✓					✓[6]	✓	✓	✓		
Cement heat	✓						✓		✓		✓
Minerals	✓						✓		✓		✓
Agriculture	✓	✓				✓[7]			✓		
Legacy CO$_2$		✓							✓		
Green fuels											
H$_2$			✓	✓		✓	✓				
Biofuels		✓			✓	✓					
PtG			✓				✓[8]				H$_2$

1 Land use management (LUM) refers to practices to retain natural levels of carbon in local biological sinks
2 Mineralization of CO$_2$ into environmentally stable carbonate (e.g., CaCO$_3$, MgCO$_3$, etc.)
3 Energy storage includes 'green fuels', mechanical (e.g., PHS, CAES), electrochemical (e.g., Li-ion batteries, flow batteries), and thermal (e.g., stored solids, molten salt) storage.
4 Incineration of waste coupled with CCS can supplement the energy and DH&C sectors while reducing CO$_2$ emissions. If products are generated from renewable carbon sources, then negative emissions are possible.
5 e.g., H$_2$-based steelmaking, electrolytic cells, etc.
6 e.g., calcium aluminate, geopolymers, super-sulfated, etc.
7 e.g., indoor hydroponics, CO$_2$ fertilization from point sources, genetic engineering, etc.
8 CO$_2$ capture and transportation infrastructure necessary; Permanent CO$_2$ storage not needed.

The position of CCS as a lynchpin in mitigating climate change is further highlighted by **Fig. 1-24**, which shows only a small portion of integrated assessment models (IAM) can meet 2DS without CCS [IPCC AR5 SYR, 2014]. In IAMs that do meet 2DS without CCS, the cost of mitigating climate change is increased substantially; the source of the cost increase is primarily due to the industrial sector. In reality, the cost of CCS is only relative to a baseline condition of the unaccounted-for costs of carbon pollution on society. Compared to shadow carbon prices deemed necessary in IAMs, CCS is a cheap option [Budinis et al., 2018].

2100 concentrations (ppm CO$_2$-eq)	Mitigation cost increases in scenarios with limited availability of technologies [d] [% increase in total discounted [e] mitigation costs (2015–2100) relative to default technology assumptions]				Mitigation cost increases due to delayed additional mitigation until 2030 [% increase in mitigation costs relative to immediate mitigation]	
	no CCS	nuclear phase out	limited solar/wind	limited bioenergy	medium term costs (2030–2050)	long term costs (2050–2100)
450 (430 to 480)	138% (29 to 297%) [4]	7% (4 to 18%) [8]	6% (2 to 29%) [8]	64% (44 to 78%) [8]	44% (2 to 78%) [29]	37% (16 to 82%) [29]
500 (480 to 530)	not available (n.a.)	n.a.	n.a.	n.a.		
550 (530 to 580)	39% (18 to 78%) [11]	13% (2 to 23%) [10]	8% (5 to 15%) [10]	18% (4 to 66%) [12]	15% (3 to 32%)	16% (5 to 24%)
580 to 650	n.a.	n.a.	n.a.	n.a.		

Symbol legend—fraction of models successful in producing scenarios (numbers indicate the number of successful models)

- : all models successful
- : between 80 and 100% of models successful
- : between 50 and 80% of models successful
- : less than 50% of models successful

Fig. 1-24. The shadow reliance of climate mitigation methods on application of CCS to meet 2DS and to do so cheaply [IPCC AR5 SYR, 2014].

1.2.1. Negative emissions

Figure 1-25 provides the potential NETs technologies and interdependencies. Negative emissions technologies are segregated based on the CO$_2$ storage mechanism: storage in the biosphere, storage in underground formations, or storage as a stable mineral. **Figure 1-25** also shows potential uses of CO$_2$ (i.e., CO$_2$ Capture and Utilization: CCU) such as chemical production. The goal of NETs is to stabilize the concentration of CO$_2$ in the atmosphere at a level commensurate with a habitable Earth. To that end, prospective technologies must demonstrate net zero or net negative CO$_2$ emissions when the system control boundary is the planet and the timescale is on the order of millennia. The storage of CO$_2$ in biological material or as organic products (e.g., plastics, chemicals) are inherently unstable and prone to release. On the other hand, underground storage and CO$_2$ mineralization sequester CO$_2$ from the atmosphere functionally indefinitely. Underground storage is separated into bioenergy with CCS (BECCS), enhanced oil recovery with CCS (EOR-CCS), direct air CO$_2$ capture with storage (DACCS), and bio-industry with CCS (BICCS). Bioenergy with CCS and BICCS require detailed temporospatial life cycle analysis to account for the change in CO$_2$ flux into the biosphere sink, alteration of the non-targeted biomass, and emissions from transportation, processing, and utilization of biomass [Bui et al., 2018; DeCicco and Schlesinger, 2018; Fajardy and Mac Dowell, 2017; Harper et al., 2018; Sterman et al., 2018]. Enhanced oil recovery with CCS can potentially provide substantial storage of CO$_2$. However, the generation of additional fossil fuels significantly reduces the net CO$_2$ reduction efficiency. Moreover, to remain net-negative, EOR-CCS requires inefficient use of CO$_2$ as an oil recovery agent, calling into question its real-world application [Mac Dowell et al., 2017]. Direct air CCS avoids issues of requiring CO$_2$ transport infrastructure and spatial mismatches between CO$_2$ sources and storage sites; however, the large energy demand and spatial footprint means that the financial viability and flexibility of DACCS remains to be proven [Fuss et al., 2018; Keith et al., 2018]. Storage of CO$_2$ as stable calcium and/or magnesium carbonates can be achieved in below ground CO$_2$ storage formations (in-situ) or above ground using rocks or brine as the feedstock (ex-situ). In-situ mineralization has been proven at scale but requires large quantities of water and

dramatically reduces the CO_2 storage capacity of a formation [Gunnarsson et al., 2018]. In-situ mineralization over the course of hundreds to thousands of years may be expected in some formations even when CO_2 is injected are a supercritical fluid. Ex-situ mineralization is generally energy intensive and suffers from low conversion efficiencies when the CO_2 footprint of chemicals and process parameters are considered. Enhanced weathering suffers from the tradeoff between accelerating the rate of CO_2 drawdown and maintaining a high net CO_2 drawdown.

Figure 1-25 demonstrates the competition between most NETs and CCU for land, water, nutrients, and biomass. Importantly, these are also required by agriculture, energy, and industry; setting the stage for the so-called 'water-energy-food' nexus. An additional axis should be added to the problem: land. Currently, human activities compete over access and utilization of land, inclusion of land-based NETs activities will only heighten this struggle [Creutzig et al., 2018]. It should also be noted that the concurrent application of BECCS/BICCS and SCS/AF/RF is not additive; any alteration to the natural habitat reduces the natural CO_2 storage capacity [Dooley et al., 2018; Krause et al., 2017; Turner et al., 2018]. Moreover, human intervention reduces the efficacy of environmental services, further stressing the natural environment on which society relies. Even under ideal conditions where landscape engineering increases storage capacity, this storage will only last as long as the application of maintenance to the site.
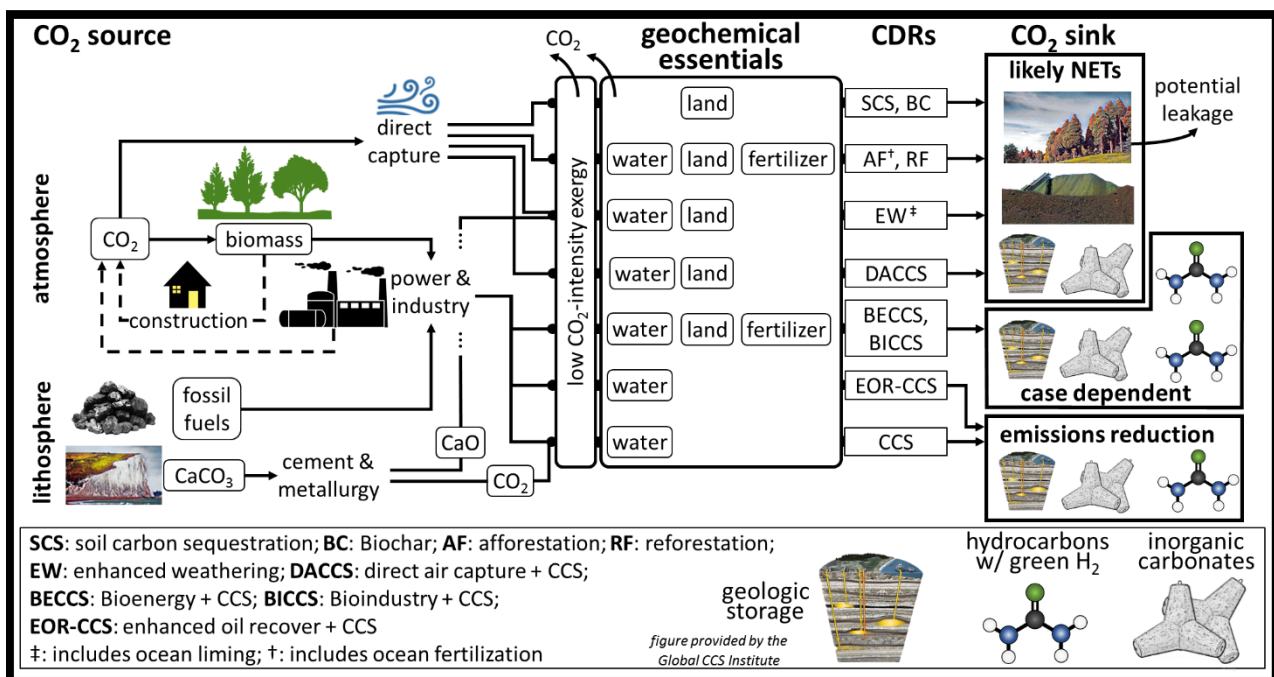
Fig. 1-25. The shared reliance across NETs on water and land.

The output of some NETs can be utilized by other NETs. Namely, BECCS and EOR-CCS may provide low CO_2 energy that can be used by DACCS, EW, and ex-situ CO_2 mineralization. Enhanced weathering can provide nutrients and support to soils to reduce the need for fertilizers and irrigation. Carbon dioxide mineralization using brines can provide fresh water that is needed by all other NETs methods.

A long-term constraint to the usefulness of CCS and CCUS as NETs is the supply of high concentration CO_2. Currently, high concentration CO_2 streams are available due to the continued use of fossil carbon resources in power and industry. Given the implementation of CCS to the power sector has been constrained by financial issues, it is hard to imagine that BECCS will be financially

attractive to power generators. Biomass-fired power plants are inherently less efficient due to the lower fuel value of biomass. Moreover, under a high biomass utilization scenario, the competition for land may increase the cost of biomass. In such a future, the supply of high concentration CO_2 may be limited to the industrial sector (cement, iron and steel, pulp and paper, chemicals, and waste incineration). If carbon-containing resources are biologically sourced and the processes are coupled to CCS or CCUS then they may function as NETs. The CCS and CCUS technologies that can address difficult to decarbonize sectors and legacy CO_2 emissions are provided in **Table 1-3** along with the feasible global adoption rate and associated water, energy, and land usage.

Table 1-3. The scale and impacts of the major negative emissions technologies

Method	Scale[‡] [$GtCO_2/y$]	Water Use [$\times 10^9 \, m^3$]	Energy Use [EJ]	Land [$km^2 \times 10^3$]
BECCS	$0.5 - 5$	$58 - 1158$	$7 - 70$ (*generation*)	$157 - 2895$
DACCS	$05. - 5$	$4 - 41$	$6 - 65$	*Negligible*
BioISM-CCS	$4.5 - 6.7$	$332 - 645$	*NA*	$875 - 1612$
Cement CCS	$2.0 - 3.3$	$17 - 27$	*NA*	$210 - 387$
CCS-EOR	$0.4 - 5$	$3 - 41$	$2 - 30$ (*generation*)	*NA*
Brine mineralization	$0.4 - 1.8$	$82 - 417$ (*generation*)	$3 - 23$	*Negligible*
EW	$2 - 4$	$1 - 2$	$8 - 15$	$55 - 109$
AR	$0.5 - 3.6$	$46 - 330$	*NA*	$397 - 2858$
SCS	$2 - 5$	*NA*	*NA*	$1532 - 3830$

‡ *in 2050*

1.3. History of climate change mitigation efforts

    Figure 1-26 displays the history of global annual anthropogenic CO_2 emissions against major moments in human civilization's understanding of climate change. What can be observed from **Fig. 1-26** is that despite growing knowledge of climate change and increasing rhetoric about mitigating its worst effects, humans still collectively are emitting more and more GHG each year.
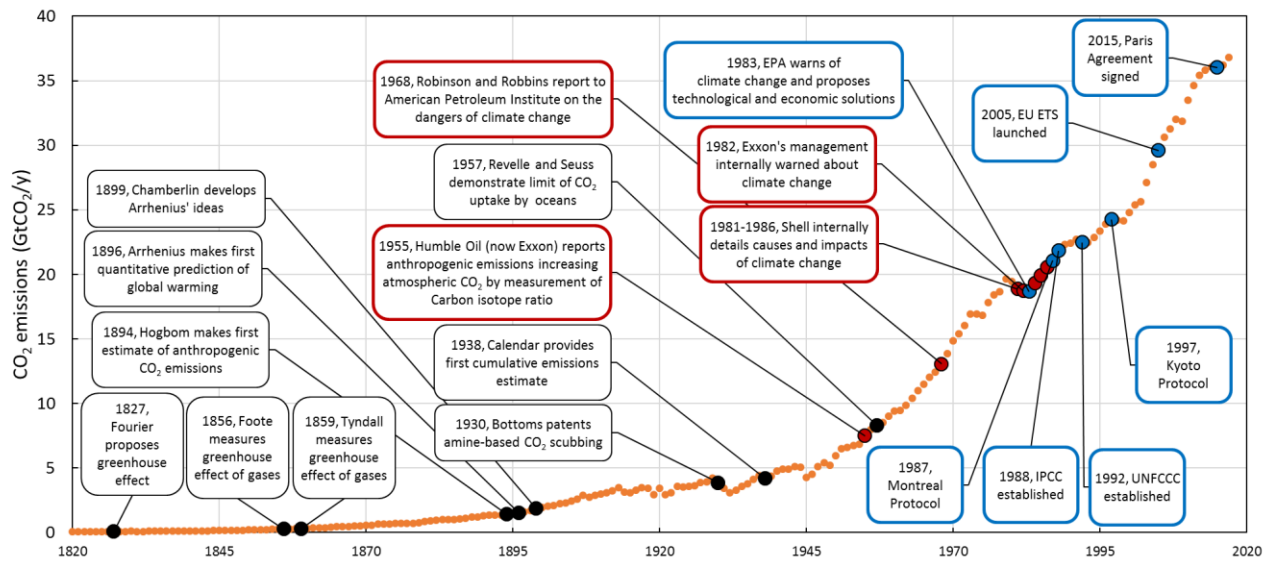
Fig. 1-26. History of knowledge about climate change and policy efforts to limit/reduce CO_2 emissions plotted against actual anthropogenic CO_2 emissions. Annual emissions are orange dots, independent scientific knowledge is in black, knowledge within companies is in red, government knowledge and intervention is in blue.

1.3.1. Technology

Without argument, CCS has played the biggest role in proposed and realized climate change mitigation strategies purposefully advanced by humans. A method to purify CO_2 from industrial gases using an amine-based capture column followed by a stripping column was patented in 1930 and is strikingly similar to current implementations (**Fig. 1-27**) [Bottoms, 1930]. The process was first proposed as a method to fight climate change in 1980 by Albanese and Steinberg (**Fig. 1-28**). After purification, the CO_2 is pressurized for transport (typically by pipeline) to a geological storage site, where it is pumped into a porous formation for permanent storage (**Fig. 1-29**). This method has been occurring relatively unchanged since the mid 1970's primarily for the enhanced recovery of oil from geological formation (EOR). Storage of CO_2 into underground formations has been heavily researched and even in highly faulted sites that would be deemed unsuitable for CO_2 storage, analysis shows that leakage rates would be insignificant in terms of deteriorating the climate change mitigation impact or on direct human and environmental health [Miocic et al., 2019]. Instead, the biggest risk to underground CO_2 storage is likely public or regulatory backlash from false positive anomalous events [Romanak, 2019].
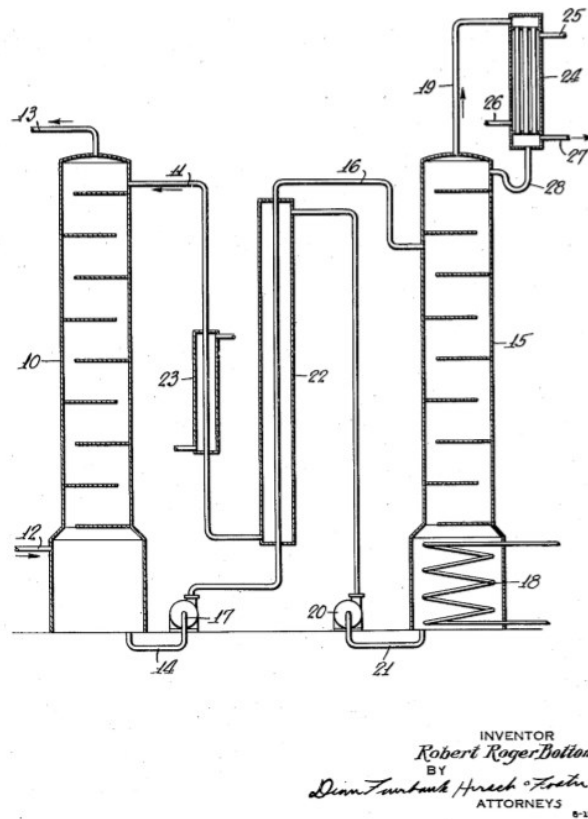
Fig. 1-27. Bottom's design for acid gas removal from flue gas streams. The design incoporates a capture column, stripper column, and heat exchanger clearly similar to current CO_2 capture designs [Bottoms, 1930].
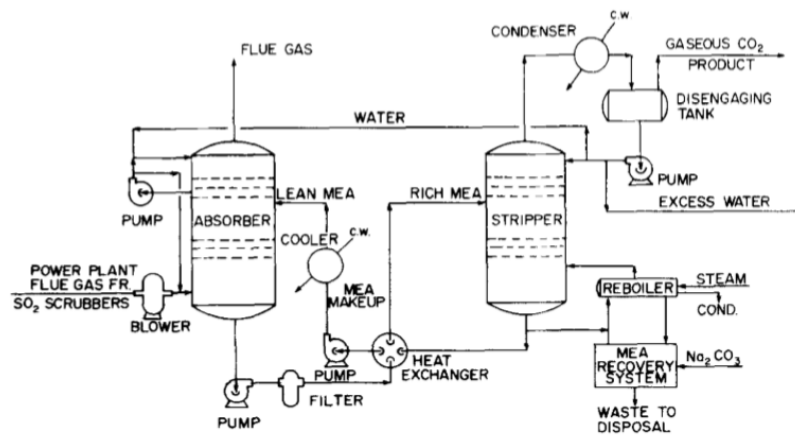
Fig. 7. Flowsheet for CO_2 absorption recovery from power plant flue gas using MEA.

Fig. 1-28. The CO_2 capture system design proposed by Albanese and Steinberg in 1980 to address growing anthropogenic CO_2 emissions [Albanese and Steinberg, 1980].
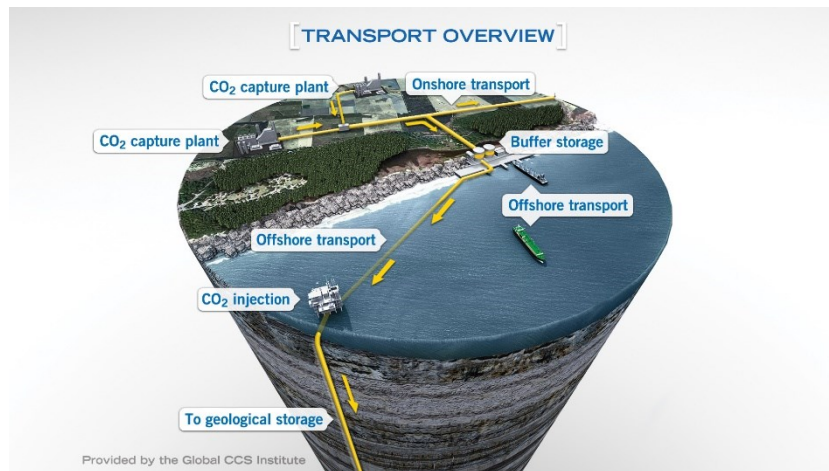
Fig. 1-29. Schematic of the flow of CO_2 from source to storage. Image provided by the Global CCS Institute.

Figure 1-30 plots the historical data on CCS implementation, including pilot and full-scale projects [GCCSI, 2017]. Following the historical trends, CCS may provide between 100's of megatonnes to over a gigatonne of CO_2 storage per year by 2050. Given that in the energy system, even rapidly expanding technologies switch from exponential growth to liner growth at roughly 1% of the market, the exponential growth to 2050 is overly optimistic [Kramer and Haigh, 2009]. Under the range of IAMs covered in the IPCC Special Report on 1.5 ˚C, by 2050 CCS is implemented at 5-10 $GtCO_2/y$ [IPCC, 2018]. Projections from fossil fuel companies suggest that CCS may reach 1.5% of emissions in 2050, far short of what is required for 2DS and B2DS [DNV-GL, 2018]. It should be further noted that the net CO_2 storage of EOR (included in **Fig. 1-30**) is much less than the necessary implementation scale of CCS. This is because EOR generates additional fossil fuels and may in fact increase CO_2 emissions dependent on the details of the injection and storage practices. However, even under ideal assumptions, the historical data on CCS suggests it will not provide the necessary amount of CO_2 removal required to meet 2DS. The cause of this mismatch between necessary deployment and actual adoption has roots in economics, politics, and social pressures.
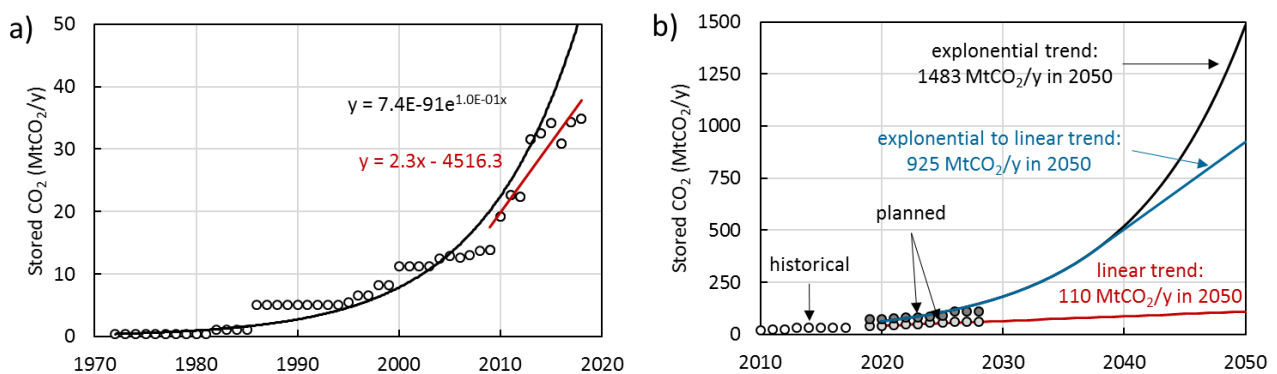
Fig. 1-30. Trends in a) deployment of CCS b) extended to 2050.

1.3.2. Politics and economics

Political recognition of the severity of climate change was highlighted by the Paris Agreement, which has the stated goal of "limit anthropogenic climate change to well below 2 °C and pursue

efforts to limit the temperature increase to 1.5 °C above pre-industrial levels". The 2DS and B2DS scenarios connote an unrealistic level of confidence in the human understanding and management of feedbacks in the Earth system [Sulman et al., 2018; Gasser et al., 2018; Kovenock and Swann, 2018], but are nevertheless useful insofar as they provide a concrete goal for society to work towards in unison. However, the political aspiration of 2DS and B2DS are inconsistent with political commitments for greenhouse gas (GHG) emissions reductions laid out in the nationally determined contributions (NDCs) [Raftery et al., 2017; Rogelj et al., 2016]. **Table 1-4** summarizes the gap in CO_2 emissions between pledged reductions and those necessary to be on track to reach the goal of 2DS and B2DS [UN, 2018]. By 2030 the gap will reach 15 and 32 $GtCO_2$,eq for 2DS and B2DS, respectively; the share of this gap is not uniform across countries. **Figure 1-31** demonstrates the mean surface temperature increase that would result in 2100 if all countries took climate change mitigation action at the levels currently implemented by each country [du Pont and Meinshausen, 2018]. In other words, **Fig. 1-31** is the temperature that each country's current actions indicate is acceptable for 2100.

Table 1-4. The breakdown of temperature outcomes and emissions gaps based on various future policy scenarios [UN, 2018].

Scenario	Global emissions in 2030, $GtCO_2$,eq	Estimated temperature outcome in degrees C (in 2100)			2030 emissions gap in $GtCO_2$,eq ($10^{th} - 90^{th}$ percentile)		
		>50% chance	>66% chance	>90% chance	Below 2 ˚C	Below 1.8 ˚C	Below 1.5 ˚C (in 2100)
No policy	65 (60-70)	---	---	---	---	---	---
Current policy	59 (56-60)	---	---	---	18 (16-20)	24 (22-25)	35 (32-36)
Unconditional NDCs	56 (52-58)	---	---	---	15 (12-17)	21 (17-23)	32 (28-34)
Conditional NDCs	53 (49-55)	---	---	---	13 (9-15)	19 (15-20)	29 (26-31)
Below 2 ˚C (66% chance)	40 (38-45)	Peak: 1.7 -1.8 (1.6 -1.7)	Peak: 1.9 -2.0 (1.8 -1.9)	Peak: 2.4 -2.6 (2.3 -2.5)	---	---	---
Below 1.8 ˚C (66% chance)	34 (30-40)	Peak: 1.6 -1.7 (1.3 -1.6)	Peak: 1.7 -1.8 (1.5 -1.7)	Peak: 2.1 -2.3 (1.9 -2.2)	---	---	---
Below 1.5 ˚C in 2100 (66% chance)	24 (22-30)	Peak: 1.5 -1.6 (1.2 -1.3)	Peak: 1.6 -1.7 (1.4 -1.5)	Peak: 2.0 -2.1 (1.8 -1.9)	---	---	---
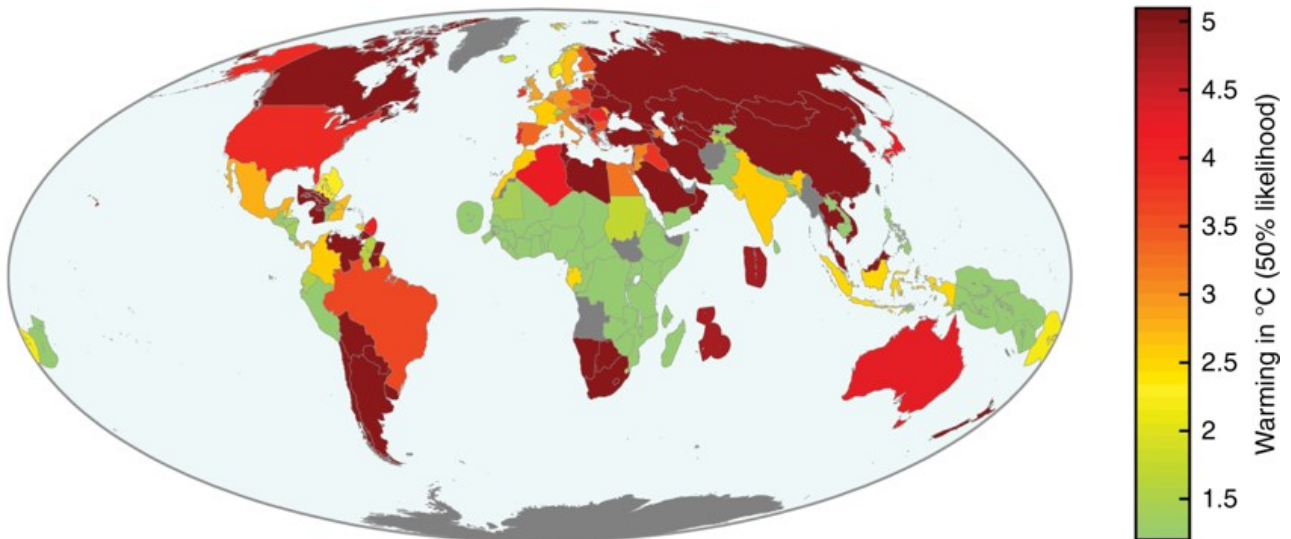
Fig. 1-31. Acceptable temperature in 2100 as indicated by each country's current climate change mitigation efforts [du Pont and Meinhausen, 2018].

Along with reports from the IPCC, authoritative documents from governments [USGCRP, 2017], non-governmental organizations [IRENA, 2018b], and independent scientists [Millar et al., 2017; Peters et al., 2017] have made clear the general timeline and pace of emissions reductions necessary to meet 2DS and B2DS require a concerted, consistent global effort unmatched in human history. Simply stated, anthropogenic GHG sources must match GHG sinks in the second half of the century with active removal of CO_2 from the atmosphere at the gigatonne per year scale. The difficulty in mitigating global warming is now dominated not by the need for technical solutions, but rather by meeting the necessary pace of technology scale-up and global adoption.

Meeting 2DS is dependent on a rapid scale-up of net zero and net negative CO_2 technologies. While technical solutions exist for various CO_2 emitting industries, the pace of adoption varies substantially; for example, global wind and solar power installations have increased at a rate of 13.9%/y over the past 5 years while global nuclear power generation has remained stalled at 2500 TWh for the past 20 years [Jackson et al., 2018]. The root causes of this disparity are decidedly non-technical, depending primarily on the incentives and risks for individual actors to adopt a technology. The key differences in adoption rate relate to the project scale, degree of regulatory oversight, and awareness from society. Much of the success of RE and LiB can be attributed to the learning-by-doing framework of innovation. This methodology is only possible because small-scale projects can be rapidly realized with small capital investments and limited risk; this paradoxically leads to more rapid successful application at larger plants [Nemet, 2006]. Additionally, little-to-no regulatory oversight is necessary for such small-scale projects. Carbon capture and storage projects require the siting of an appropriate geologic storage location, the development of transport infrastructure, adequate supply of CO_2, installation of CO_2 capture, buy-in from the public in the storage, transport, and capture locations, regulatory approval, and potentially navigating issues of international law. This process is inherently long-term with large upfront costs and numerous failure points, similar to issues seen in the development of nuclear power plants. This longer lead time and higher risk suppresses the degree and pace of innovation, largely reducing the potential for the steep price declines seen in RE and LiB.

Innovative CCS methods that ameliorate the cost, time, regulatory, and perception issues will be necessary for CCS to make the significant impact on CO_2 emissions necessary to meet 2DS. Net zero technologies and NETs that can take advantage of learning-by-doing are more likely to play a leading role in meeting 2DS, not because of being inherently superior technologies, but because of the higher pace of scale-up and price reduction. Methods that can act as innovations to current services or products are more likely to be absorbed by extant companies, accelerating technological dispersion and uptake. Moreover, modifications to existent methods are more likely to avoid regulatory issues while also being more easily marketable to the public simply as an environmentally friendly alternative as opposed to an unknown commodity. For methods that directly compete with extant products or services, they will need to either provide significant benefits or provide distinct co-benefits not provided by current methods (e.g., waste treatment).

The key barrier typically posited to the rapid scale-up and deployment of climate mitigation methods is the unpriced nature of GHG emissions. **Figure 1-32** shows the distribution of carbon prices for energy related emissions in the OECD and G20 countries [UN, 2018]. Roughly 50% of emissions have essentially no carbon price. Inclusion of industrial CO_2 emissions would further depress the average price of carbon. The developed world shares the largest moral obligation to reduce emissions given the historical usage of CO_2 dumping as means to realize economic growth and the continued high per capita CO_2 emissions. Moreover, increase of the energy usage by the developing world will substantially improve the quality of life for billions; it is hard to argue that minor discomfort on the globally rich is too high a price to pay for the health and basic humanity of the globally poor. Nevertheless, accounting for emissions from developing countries results in 85% of global emissions being unpriced and the vast majority of remaining emissions being priced at less than $10/tonne-$CO_2$ as shown in **Fig. 1-33** [World Bank, 2018]. The globalized nature of many products means that without an international, uniformly imposed carbon price, there is a negative incentive to realize a zero and negative CO_2 society. The large increase in carbon price as time progresses needed to realize deep decarbonization and NETs is also of concern (**Fig. 1-34**).
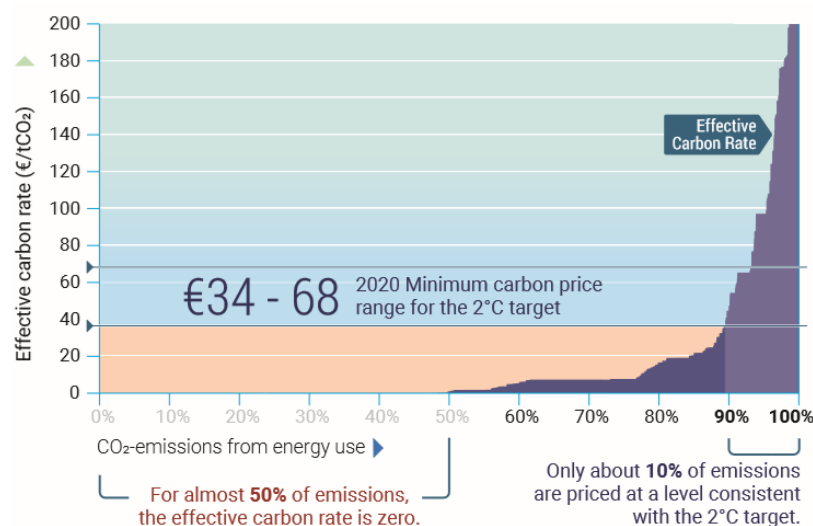
Fig. 1-32. The carbon price for energy-related emission in G20 and OECD countries [UN, 2018].
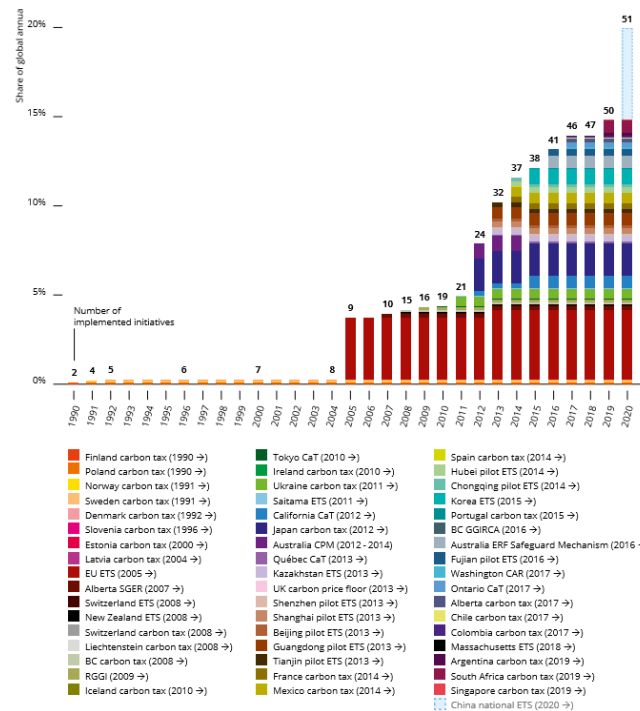
Fig. 1-33. The progression of taxed carbon over time [World Bank, 2018].
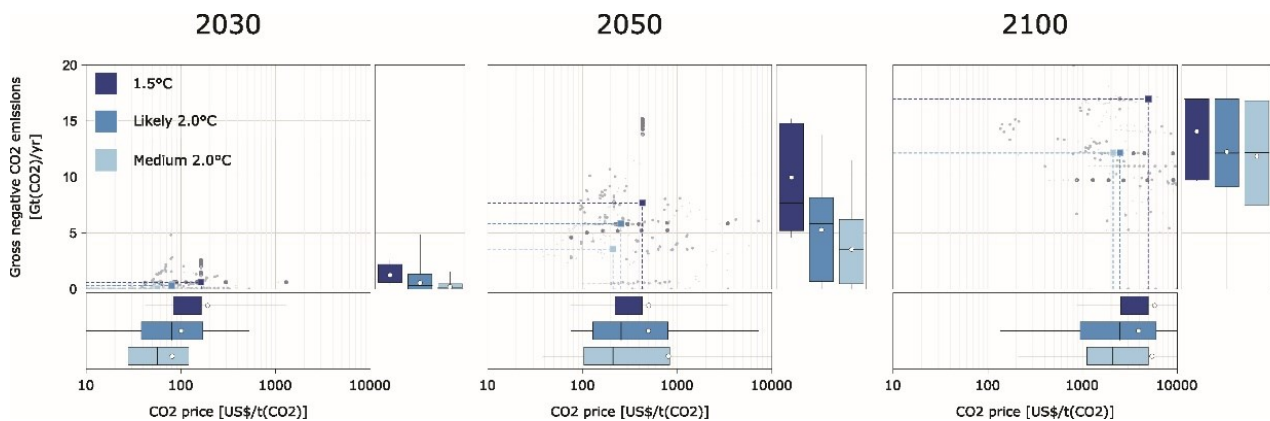
Fig. 1-34. The necessary price on carbon in order to realize NETs at levels consistence with B2DS and 2DS [Nemet et al., 2018].

All IAMs that meet 2DS or B2DS have either an explicit carbon price or a shadow carbon price (SCP). The reasons for using SCP instead of the full cost of damages of current emission of CO_2 (or other GHG) over its lifetime (i.e., the social cost of carbon: SCC) are essentially that other country's emissions cannot be controlled, and that climate change impacts are path dependent [Price et al., 2007]. Frankly, these are evasions that allow economists and policy-makers to avoid confronting the true cost of climate change. Most economists and politicians conclude the SCC to be on the order of $40/t-$CO_2$ [Havranek et al., 2015]. However, these estimates are at odds with those of scientists, whose estimates are generally 20 to 30 times high [Nordhaus, 1994]. Though this data is 25 years old, it is worth recalling that the economic theory used in IAMs has gone unchanged in the last quarter century, while the scientific estimates of climate change-induced damages has only increased. Moreover, the nature of the climatic system is that it contains non-linearities, tipping points, and time delays which generate a complex risk profile [Stern et al., 2006]. Accounting for such

discontinuities in the risk profile generates a minimum estimate for the current SCC to ~$125 per tonne CO_2 [Van Den Bergh and Botzen, 2014], with most estimates closer to ~$1,000 per tonne CO_2 [Ackerman and Stanton, 2012; Dietz and Stern, 2015; Hwang et al., 2016; Pycroft et al., 2011]. It is odd however to put a price on the maintenance of modern civilization. The question of the cost-benefit analysis of preventing the collapse of society is on its face ridiculous. This is captured by the 'dismal theorem' which puts the upper limit of SCC as infinite [Weitzman, 2009]. In other words, value only has meaning when there is a civilization to apply it.

Regardless of whether the price of carbon is in the tens or hundreds of dollars, all models are assuming a government supported effort by the very nature of introducing a SCC or SCP. Whether this government support is directed and implemented by the public or private sector is of secondary importance to the fact that government support exists. However, even at this late date, no government has implemented a climate change mitigation policy (through direct involvement or construction of a market) of sufficient strength to meet the targets of the Paris Agreement.

A key issue left largely unaddressed in the climate change mitigation modeling field is the use of equilibrium state economic models in the modeling of the transition of the energy and other sectors to a zero-carbon society [Hoekstra et al., 2017]. Prior to considering the application to climate change, it should be noted the fundamental assumption of equilibrium economic models (i.e., convergence to equilibrium) fails in complicated settings with competing interests [Pangallo et al., 2019]. Addressing climate change means, at a minimum, a system-level change of the energy, industrial, transportation, and agricultural sectors. The pace and degree of change required fundamentally challenges numerous powerful, entrenched interests and bumps against aspects of everyday life for the common person. As such, the core assumptions of equilibrium state economic models are plainly erroneous. Equilibrium models are path independent, top-down models [Burfisher, 2017], purposefully analogous to classical physics models such as the ideal gas law [Mosini, 2008]. Equilibrium models assume that the complexity of individuals, companies, cultures, governments, and the like can be modeled by a few simplified 'actors' [Fagiolo and Roventini, 2016], and that these actors only attempt to maximize a definable utility function. Actors further contain complete and precise knowledge of the market and its impacts on their own utility. Manipulation of actors by other actors, aspects not directly linked to the utility function (e.g., status, morals, marketing), and spatiotemporal concerns (e.g., future generations, information diffusion time) are all irrelevant in equilibrium economic models. Likewise, the markets themselves are treated as ideal, with no political influence, gaming of the system, incumbent resistance, and the like. The sum effect of using equilibrium state models is the poor performance of predicting rapid transitions that can come from development of currently immature technologies. This type of result is highlighted nicely by the consistently poor performance of the World Energy Model used by the International Energy Agency in their annual 'Energy Outlook' report [IEA, 2018b]. **Figure 1-35** displays the performance of this model against actual new installations of solar photovoltaic systems [Hoekstra, 2017].
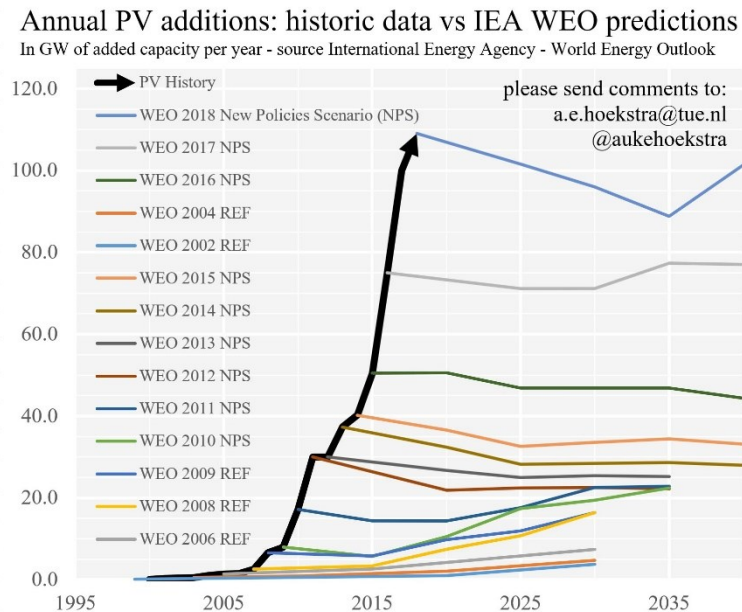
Fig. 1-35. An example (World Energy Model of IEA) of the poor performance of equilibrium economic models in predicting disruptive technologies (e.g., Solar PV) [Hoekstra, 2017].

Despite the fact that many economists now dismiss equilibrium theory out of hand [Ackerman, 2002; Krugman, 2009], the promising adoption of complex adaptive system models and agent-based models by the economic field and energy fields [Balint et al., 2017], and the meshing of such models with climate change models [Lamperti et al., 2018], there remains no non-equilibrium economic IAMs included in IPCC reports. Therefore, guidance for investment into climate change mitigation and adaptation pathways remains built on an economic foundation that has been proven incompetent in modeling transitions, upheavals, and uncertainties which are the foundational effects of climate change and efforts to reduce its impacts.

1.3.3. Success stories

Success in climate change mitigation strategies is limited to increased efficiency across all sectors, the development of RE (primarily solar PV and wind), LiB, and electrification of road transport. Notably, these areas provide benefits over current competing technologies in terms of performance and cost. Solar PV (**Fig. 1-36**), wind (**Fig. 1-37**), and LiB (**Fig. 1-38**) have seen rapid recent improvement only due to the cumulative effects of a long history of learning by doing, boot-strapping from small-scale, supportive government policies [Breetz et al., 2018], and only recently economies of scale [IRENA, 2016; Schmidt et al., 2017]. These results suggest that investment in large CO_2 emissions reductions projects may be paradoxically misguided. Rather, major reductions in CO_2 emissions can be achieved by pushing towards 100% of power being generated from RE with storage [Brown et al., 2018b; Creutzig et al., 2017; Lovins et al., 2018; van Sluisveld et al., 2018] and progressively taxing the rich [Otto et al., 2019] to fund education of women [Samir and Lutz, 2017] and investment in CO_2 mitigation technologies and NCS [Griscom et al., 2017]. These distributed methods are generally less favored by economic predictions due to the inherent difficulty of modeling, but actually constitute the low-hanging fruit of climate change policies.
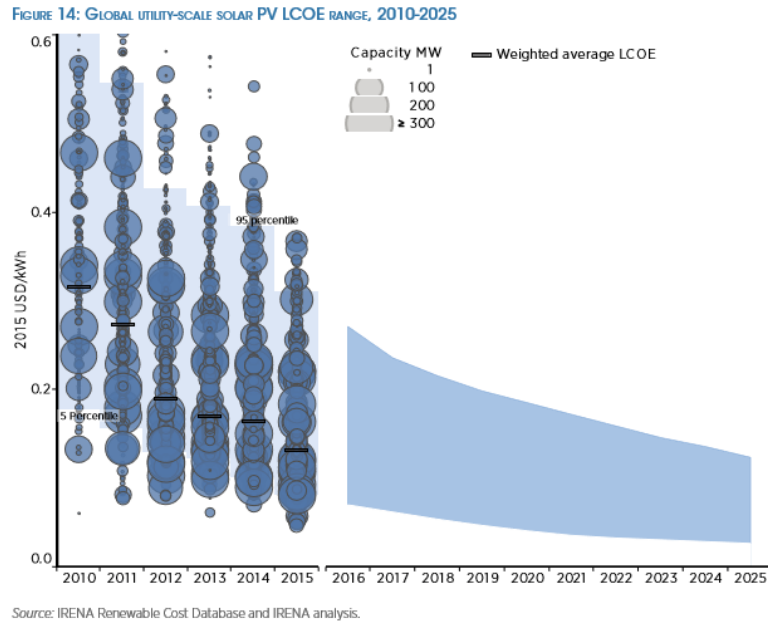
Fig. 1-36. The historical and potential future cost reduction of solar PV [IRENA, 2016]
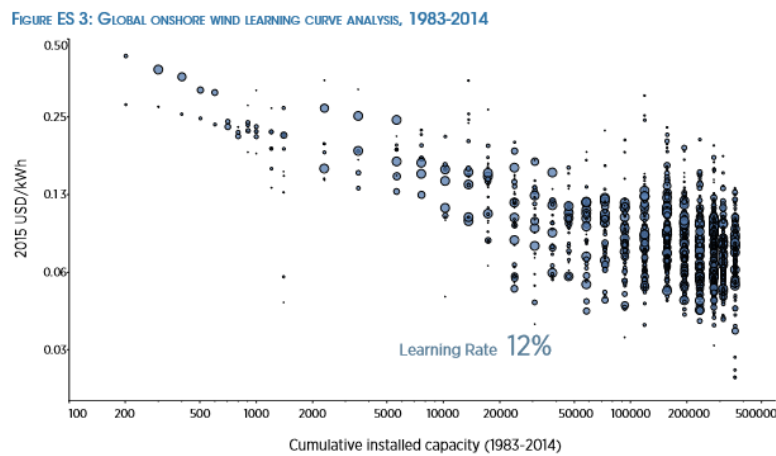
Fig. 1-37. The historical learning curve for onshore wind energy showing a learning rate of 12% [IRENA, 2016].
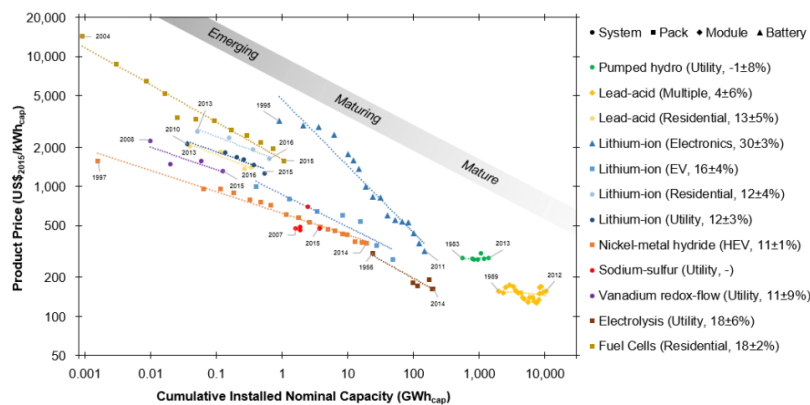
Fig. 1-38. The historical learning curve for various energy storage options including lithium ion batteries [Schmidt et al., 2017].

1.4. Design principles to meet the climate change challenge

Over a hundred years since recognition of the greenhouse effect, 90 years since the advent of technologies to address it, 65 years since major GHG emitters recognized its dangers, and 30 years since the world's leaders have committed to preventing it, humanity continues to accelerate towards a climatic catastrophe. Evaluating humanity's progress in light of the cumulative time, effort, intellectual capital, and money expended leaves much to be desired. Prior to any further technology development, it seems that the principles guiding said development should be expounded. It may be that certain technologies are fully technically realizable but not socially, economically, or politically palatable. Likewise, some solutions may seem attractive socioeconomically, but run afoul of technical scrutiny. Below, the guiding principles used in the development of the technologies within this dissertation are explained.

1.4.1. Societal

- *Profitability.* Provide a profit motive to capture and stabilize CO_2 that does not rely on political regulation. This allows for the dispersed, rapid adoption of NETs necessary to meet 2DS and B2DS.

- *Scalable Products.* Given that profitability is achieved through product sales, product markets must be able to withstand the supply influx associated with gigatonne-scale NETs without substantial loss in value.

- *Diverse Products.* A diverse set of products should be generated to de-risk future demand change due to unforeseen innovations, regulations, and societal change.

- *Leverage of Extant Regulated Wastes.* The treatment/disposal cost and fines of an extant regulated waste is built into the source market. Co-treatment of CO_2 with regulated waste provides the opportunity for revenue (in the form of a waste treatment/liability fee) or a free input stream.

- *Tangible* CO_2 *Storage.* Concerns from citizens over CO_2 storage largely stem from ignorance and the imperceptible nature of CO_2 stored underground. For scientists and engineers, the lack of impact on daily life is a key advantage of CO_2 capture and storage (CCS). For the average citizen the simultaneous knowledge that CO_2 is underground and that its current behavior is opaque to them may lead to apprehension. Mineralization of CO_2 into rocks allows the public to see and physically handle the material; its inertness and benign nature become immediately intuitive.

1.4.2. Technical

- *System Independence.* Any reliance on externally-generated materials or energy increases the risk of carbon leakage; this is especially true given the geographic heterogeneity in the pace and extent of decarbonization of energy and industry.

- *Preference for Electricity and Low Temperature Heat.* Given the need for system independence, heavy utilization of chemicals/consumables is financially unfeasible as these would require on-site production. Off-grid heat and electricity can be generated through renewable energy with battery storage with minimal cost and complication. Methods based on low temperature heat allows for utilization of local waste heat where available.

- *Utilization of Solar Photovoltaics (PV) and Li-ion Batteries.* System independence and the use of electricity and low-quality heat imply that an off-grid, variable scale, low CO_2 intensity power supply is necessary. Solar PV paired with Li-ion batteries provide these features with the additional benefit of substantial learning rates projected to continue as production scale and field of application increases.

- *Complete Additive Recycling.* Any loss in additive will require external input or internal production. The former option increases chances of carbon leakage, the latter substantially increases system cost and complexity.
- *Small-scale Systems and Learning-by-doing.* Small-scale applications should be plentiful, and the lessons should be applicable to larger scale systems. Small-scale systems allow for rapid process improvement and innovation with low financial risk. Small-scale projects also increase the aptitude of the field while de-risking larger projects for financial institutions.

1.5.   Slag-based CO_2 emissions reductions in the context of climate change

This dissertation focusses on using the solid waste of iron and steelmaking (so-called, 'slag') to reduce CO_2 emissions. Given that iron and steelmaking accounts for less than 10% of current anthropogenic emissions, and slag can only reduce ISM emissions by ~10%, it is fair to question the significance of this dissertation. Clearly, slag-based CO_2 emissions reduction cannot halt or even significantly slow climate change on its own. In truth, no available or proposed technology can single-handedly solve climate change. Rather, slag-based CO_2 emissions reduction targets a portion of emissions (i.e., iron and steelmaking) that currently does not have a technologically and financially viable pathway to emissions reduction. Review of **Fig. 1-22** will reveal that the energy sector has a viable pathway to net zero CO_2 emissions within a relatively short time frame while the industrial sectors remain problematic. Every tonne of CO_2 from industrial sources that remains unabated requires an additional tonne of 'negative emissions', a technology portfolio that, as of yet, remains unproven at scale. As such, focusing on these industrial emissions have the added benefit of reducing the risk that NETs fail to materialize.

In addition to targeting a difficult to decarbonize sector, the realization of direct, gas-solid CO_2 mineralization of slags opens up a range of other large-scale CO_2 mineralization feedstocks; namely: demolition waste and natural rocks. Carbonation of demolition waste helps to offset legacy CO_2 emissions from cement production. If direct, gas-solid mineralization of natural rocks can be achieved at reasonable time scales and costs, it would represent a NET many times the size of all potential fossil fuel emissions. In short, slag-based CO_2 emissions reduction is important for the direct emissions reductions, but also acts as a stepping stone to larger-scale emissions reduction.

Chapter-specific symbol and abbreviation list

2DS: 2 degrees Celsius scenario

A: albedo

AF: Afforestation

B2DS: 1.5 degree Celsius scenario

BECCS: Bioenergy with CCS

BICCS: Bio-industry with CCS

CCU: CO_2 capture and utilization

CCS: CO_2 capture and storage

CCUS: CO_2 capture, utilization, and storage

CDR: Carbon dioxide removal

CO_2eq: CO_2 equivalent radiative forcing

DACCS: Direct air capture with CO_2 storage

ECS: Earth climate sensitivity

EOR: Enhanced oil recovery

EW: Enhanced weathering

GHG: greenhouse gas

IAM: Integrated assessment model

ISM: Iron and steelmaking

LiB: Lithium-ion battery

NAP: National adaptation plan

NDC: Nationally determined contributions

NET: Negative emission technology

PETM: Paleocene-Eocene Thermal Maximum

RE: Renewable energy

RF: Reforestation

RRR: Reduce, reuse, recycle

SCC: Social cost of carbon

SCP: Shadow carbon price

SCS: Soil carbon sequestration

SDG: Sustainable development goals

TSI: total solar irradiance

σ: Stefan-Boltzmann constant

References

Abel, G.J., Brottrager, M., Cuaresma, J.C. and Muttarak, R., 2019. Climate, conflict and forced migration. Global Environmental Change, 54, pp.239-249.

Ackerman, F., 2002. Still dead after all these years: interpreting the failure of general equilibrium theory. Journal of Economic Methodology, 9(2), pp.119-139.

Ackerman, F. and Stanton, E., 2012. Climate risks and carbon prices: Revising the social cost of carbon. Economics: The Open-Access, Open-Assessment E-Journal, 6, pp.1-25.

Albanese, A.S. and Steinberg, M., 1980. Environmental control technology for atmospheric carbon dioxide. Energy, 5(7), pp.641-664.

Allen, M.R., Fuglestvedt, J.S., Shine, K.P., Reisinger, A., Pierrehumbert, R.T. and Forster, P.M., 2016. New use of global warming potentials to compare cumulative and short-lived climate pollutants. Nature Climate Change, 6(8), p.773.

Allen, M.R., Shine, K.P., Fuglestvedt, J.S., Millar, R.J., Cain, M., Frame, D.J. and Macey, A.H., 2018. A solution to the misrepresentations of CO 2-equivalent emissions of short-lived climate pollutants under ambitious mitigation. Climate and Atmospheric Science, 1(1), p.16.

Alley, R., 2013. The Carbon Control Knob. Island Press.

Anderson, K., 2019. Climate's holy trinity: how cogency, tenacity & courage could yet deliver on our Paris 2°C commitment. Presentation at Oxford Climate Society, January 24, 2019.

Andrews, T., Gregory, J.M., Paynter, D., Silvers, L.G., Zhou, C., Mauritsen, T., Webb, M.J., Armour, K.C., Forster, P.M. and Titchner, H., 2018. Accounting for changing temperature patterns increases historical estimates of climate sensitivity. Geophysical Research Letters, 45(16), pp.8490-8499.

ARPA-e, 2018. Duration Addition to electricitY Storage (DAYS) project description.

Balint, T., Lamperti, F., Mandel, A., Napoletano, M., Roventini, A. and Sapio, A., 2017. Complexity and the economics of climate change: a survey and a look forward. Ecological Economics, 138, pp.252-265.

Beaugrand, G., Conversi, A., Atkinson, A., Cloern, J., Chiba, S., Fonda-Umani, S., Kirby, R.R., Greene, C.H., Goberville, E., Otto, S.A. and Reid, P.C., 2019. Prediction of unprecedented biological shifts in the global ocean. Nature Climate Change, 9(3), p.237.

Bodman, R.W., Rayner, P.J. and Jones, R.N., 2016. How do carbon cycle uncertainties affect IPCC temperature projections?. Atmospheric Science Letters, 17(3), pp.236-242.

Bottoms, R.R., Girdler Corp, 1930. Process for separating acidic gases. U.S. Patent 1,783,901.

Brannen, P., 2016. The Ends of the World. One world Publications.

Breetz, H., Mildenberger, M. and Stokes, L., 2018. The political logics of clean energy transitions. Business and Politics, 20(4), pp.492-522.

Brown, P.T. and Caldeira, K., 2017. Greater future global warming inferred from Earth's recent energy budget. Nature, 552(7683), p.45.

Brown, S., Nicholls, R.J., Goodwin, P., Haigh, I.D., Lincke, D., Vafeidis, A.T. and Hinkel, J., 2018a. Quantifying land and people exposed to sea‐level rise with no mitigation and 1.5 C and 2.0 C rise in global temperatures to year 2300. Earth's Future, 6(3), pp.583-600.

Brown, T.W., Bischof-Niemz, T., Blok, K., Breyer, C., Lund, H. and Mathiesen, B.V., 2018b. Response to 'Burden of proof: A comprehensive review of the feasibility of 100% renewable-electricity systems'. Renewable and Sustainable Energy Reviews, 92, pp.834-847.

Budinis, S., Krevor, S., Mac Dowell, N., Brandon, N. and Hawkes, A., 2018. An assessment of CCS costs, barriers and potential. Energy strategy reviews, 22, pp.61-81.

Bui, M., Fajardy, M. and Mac Dowell, N., 2018. Bio-energy with carbon capture and storage (BECCS): Opportunities for performance improvement. Fuel, 213, pp.164-175.

Burfisher, M.E., 2017. Introduction to computable general equilibrium models. Cambridge University Press.

Caesar, L., Rahmstorf, S., Robinson, A., Feulner, G. and Saba, V., 2018. Observed fingerprint of a weakening Atlantic Ocean overturning circulation. Nature, 556(7700), p.191.

Caldeira, K. and Cvijanovic, I., 2014. Estimating the contribution of sea ice response to climate sensitivity in a climate model. Journal of Climate, 27(22), pp.8597-8607.

Chancel, L. and Piketty, T., 2015. Carbon and Inequality from Kyoto to Paris: Trends in the global inequality of carbon emissions (1998-2013) and prospects for an equitable adaptation fund. Paris school of economics.

Clack, C.T., Qvist, S.A., Apt, J., Bazilian, M., Brandt, A.R., Caldeira, K., Davis, S.J., Diakov, V., Handschy, M.A., Hines, P.D. and Jaramillo, P., 2017. Evaluation of a proposal for reliable low-cost grid power with 100% wind, water, and solar. Proceedings of the National Academy of Sciences, 114(26), pp.6722-6727.

Creutzig, F., Agoston, P., Goldschmidt, J.C., Luderer, G., Nemet, G. and Pietzcker, R.C., 2017. The underestimated potential of solar energy to mitigate climate change. Nature Energy, 2(9), p.17140.

Creutzig, F., d'Amour, C.B., Weddige, U., Fuss, S., Beringer, T., Gläser, A., Kalkuhl, M., Steckel, J.C., Radebach, A. and Edenhofer, O., 2019. Assessing human and environmental pressures of global land-use change 2000–2010. Global Sustainability, 2.

Davis, S.J., Lewis, N.S., Shaner, M., Aggarwal, S., Arent, D., Azevedo, I.L., Benson, S.M., Bradley, T., Brouwer, J., Chiang, Y.M. and Clack, C.T., 2018. Net-zero emissions energy systems. Science, 360(6396), p.eaas9793.

DeCicco, J.M. and Schlesinger, W.H., 2018. Opinion: Reconsidering bioenergy given the urgency of climate protection. Proceedings of the National Academy of Sciences, 115(39), pp.9642-9645.

Diesendorf, M. and Elliston, B., 2018. The feasibility of 100% renewable electricity systems: A response to critics. Renewable and Sustainable Energy Reviews, 93, pp.318-330.

Dietz, S. and Stern, N., 2015. Endogenous growth, convexity of damage and climate risk: how Nordhaus' framework supports deep cuts in carbon emissions. The Economic Journal, 125(583), pp.574-620.

DNV-GL, 2018. Energy Transition Outlook 2018: A global and regional forecast to 2050.

Dooley, K., Christoff, P. and Nicholas, K.A., 2018. Co-producing climate policy and negative emissions: trade-offs for sustainable land-use. Global Sustainability, 1.

Dowling, S., 2018. Norway's plan for a fleet of electric planes. BBC. Accessed January 9, 2019.

du Pont, Y.R. and Meinshausen, M., 2018. Warming assessment of the bottom-up Paris Agreement emissions pledges. Nature communications, 9(1), p.4810.

Fajardy, M. and Mac Dowell, N., 2017. Can BECCS deliver sustainable and resource efficient negative emissions?. Energy & Environmental Science, 10(6), pp.1389-1426.

Fagiolo, G. and Roventini, A., 2016. Macroeconomic policy in dsge and agent-based models redux: New developments and challenges ahead.

Fitzpatrick, M.C. and Dunn, R.R., 2019. Contemporary climatic analogs for 540 North American urban areas in the late 21st century. Nature communications, 10(1), p.614.

Frieling, J., Gebhardt, H., Huber, M., Adekeye, O.A., Akande, S.O., Reichart, G.J., Middelburg, J.J., Schouten, S. and Sluijs, A., 2017. Extreme warmth and heat-stressed plankton in the tropics during the Paleocene-Eocene Thermal Maximum. Science advances, 3(3), p.e1600891.

Fuss, S., Lamb, W.F., Callaghan, M.W., Hilaire, J., Creutzig, F., Amann, T., Beringer, T., de Oliveira Garcia, W., Hartmann, J., Khanna, T. and Luderer, G., 2018. Negative emissions—Part 2: Costs, potentials and side effects. Environmental Research Letters, 13(6), p.063002.

Gao, J., Barzel, B. and Barabási, A.L., 2016. Universal resilience patterns in complex networks. Nature, 530(7590), p.307.

Gasser, T., Kechiar, M., Ciais, P., Burke, E., Kleinen, T., Zhu, D., Huang, Y., Ekici, A. and Obersteiner, M., 2018, April. Path-dependent reduction in emission budgets caused by permafrost CO2 and CH4 release. In EGU General Assembly Conference Abstracts (Vol. 20, p. 14234).

GCCSI, 2017. The global status of CCS: 2017.

Gingerich, P.D., 2019. Temporal Scaling of Carbon Emission and Accumulation Rates: Modern Anthropogenic Emissions Compared to Estimates of PETM‐Onset Accumulation. Paleoceanography and Paleoclimatology.

Global Carbon Project, 2017. Supplemental data of Global Carbon Budget 2017 (Version 1.0) [Data set]. Global Carbon Project

Golledge, N.R., Keller, E.D., Gomez, N., Naughten, K.A., Bernales, J., Trusel, L.D. and Edwards, T.L., 2019. Global environmental consequences of twenty-first-century ice-sheet melt. Nature, 566(7742), p.65.

Gore, T., 2015. Extreme Carbon Inequality: Why the Paris climate deal must put the poorest, lowest emitting and most vulnerable people first.

Goyal, A. and Maslov, S., 2018. Diversity, stability, and reproducibility in stochastically assembled microbial ecosystems. Physical review letters, 120(15), p.158102.

Green, J.K., Seneviratne, S.I., Berg, A.M., Findell, K.L., Hagemann, S., Lawrence, D.M. and Gentine, P., 2019. Large influence of soil moisture on long-term terrestrial carbon uptake. Nature, 565(7740), p.476.

Griscom, B.W., Adams, J., Ellis, P.W., Houghton, R.A., Lomax, G., Miteva, D.A., Schlesinger, W.H., Shoch, D., Siikamäki, J.V., Smith, P. and Woodbury, P., 2017. Natural climate solutions. Proceedings of the National Academy of Sciences, 114(44), pp.11645-11650.

Gunnarsson, I., Aradóttir, E.S., Oelkers, E.H., Clark, D.E., Arnarson, M.Þ., Sigfússon, B., Snæbjörnsdóttir, S.Ó., Matter, J.M., Stute, M., Júlíusson, B.M. and Gíslason, S.R., 2018. The rapid and cost-effective capture and subsurface mineral storage of carbon and sulfur at the CarbFix2 site. International Journal of Greenhouse Gas Control, 79, pp.117-126.

Gutjahr, M., Ridgwell, A., Sexton, P.F., Anagnostou, E., Pearson, P.N., Pälike, H., Norris, R.D., Thomas, E. and Foster, G.L., 2017. Very large release of mostly volcanic carbon during the Palaeocene–Eocene Thermal Maximum. Nature, 548(7669), p.573.

Hansen, J., Sato, M., Kharecha, P. and Schuckmann, K.V., 2011. Earth's energy imbalance and implications. Atmospheric Chemistry and Physics, 11(24), pp.13421-13449.

Harper, A.B., Powell, T., Cox, P.M., House, J., Huntingford, C., Lenton, T.M., Sitch, S., Burke, E., Chadburn, S.E., Collins, W.J. and Comyn-Platt, E., 2018. Land-use emissions play a critical role in land-based mitigation for Paris climate targets. Nature communications, 9(1), p.2938.

Havranek, T., Irsova, Z., Janda, K. and Zilberman, D., 2015. Selective reporting and the social cost of carbon. Energy Economics, 51, pp.394-406.

Heck, V., Gerten, D., Lucht, W. and Popp, A., 2018. Biomass-based negative emissions difficult to reconcile with planetary boundaries. Nature Climate Change, 8(2), p.151.

Hienola, A., Partanen, A.I., Pietikäinen, J.P., O'Donnell, D., Korhonen, H., Matthews, H.D. and Laaksonen, A., 2018. The impact of aerosol emissions on the 1.5° C pathways. Environmental Research Letters, 13(4), p.044011.

Hoekstra, A., 2018. Photovoltaic growth: reality versus projections of the International Energy Agency – with 2018 update. https://steinbuch.wordpress.com/2017/06/12/photovoltaic-growth-reality-versus-projections-of-the-international-energy-agency/. Retrieved February 2, 2019.

Hoekstra, A., Steinbuch, M. and Verbong, G., 2017. Creating agent-based energy transition management models that can uncover profitable pathways to climate change mitigation. Complexity, 2017.

Huang, Y., Chen, Y., Castro-Izaguirre, N., Baruffol, M., Brezzi, M., Lang, A., Li, Y., Härdtle, W., von Oheimb, G., Yang, X. and Liu, X., 2018. Impacts of species richness on productivity in a large-scale subtropical forest experiment. Science, 362(6410), pp.80-83.

Hwang, I.C., Tol, R.S. and Hofkes, M.W., 2016. Fat-tailed risk about climate change and climate policy. Energy Policy, 89, pp.25-35.

IEA, 2018a. Global EV outlook 2018. International Energy Agency.

IEA, 2018b. World Energy Outlook 2018. International Energy Agency.

Im, E.S., Pal, J.S. and Eltahir, E.A., 2017. Deadly heat waves projected in the densely populated agricultural regions of South Asia. Science advances, 3(8), p.e1603322.

IPCC, 2013. Climate Change 2013: The Physical Science Basis. Contribution of Working Group I to the Fifth Assessment Report of the Intergovernmental Panel on Climate Change [Stocker, T.F., D. Qin, G.-K. Plattner, M. Tignor, S.K. Allen, J. Boschung, A. Nauels, Y. Xia, V. Bex and P.M. Midgley (eds.)]. Cambridge University Press, Cambridge, United Kingdom and New York, NY, USA, 1535 pp.

IPCC, 2014. Climate Change 2014: Impacts, Adaptation, and Vulnerability. Part A: Global and Sectoral Aspects. Contribution of Working Group II to the Fifth Assessment Report of the Intergovernmental Panel on Climate Change [Field, C.B., V.R. Barros, D.J. Dokken, K.J. Mach, M.D. Mastrandrea, T.E. Bilir, M. Chatterjee, K.L. Ebi, Y.O. Estrada, R.C. Genova, B. Girma, E.S. Kissel, A.N. Levy, S. MacCracken, P.R. Mastrandrea, and L.L.White (eds.)]. Cambridge University Press, Cambridge, United Kingdom and New York, NY, USA, 1132 pp.

IPCC, 2014: Climate Change 2014: Synthesis Report. Contribution of Working Groups I, II and III to the Fifth Assessment Report of the Intergovernmental Panel on Climate Change [Core Writing Team, R.K. Pachauri and L.A. Meyer (eds.)]. IPCC, Geneva, Switzerland, 151 pp.

IPCC, 2018: J. Rogelj, D. Shindell, K. Jiang, S. Fifita, P. Forster, V. Ginzburg, C. Handa, H. Kheshgi, S. Kobayashi, E. Kriegler, L. Mundaca, R. Séférian, M. V. Vilariño, 2018, Mitigation pathways compatible with 1.5°C in the context of sustainable development. In: Global warming of 1.5°C. An IPCC Special Report on the impacts of global warming of 1.5°C above pre-industrial levels and related global greenhouse gas emission pathways, in the context of strengthening the global response to the threat of climate change, sustainable development, and efforts to eradicate poverty [V. Masson-Delmotte, P. Zhai, H. O. Pörtner, D. Roberts, J. Skea, P. R. Shukla, A. Pirani,

W. Moufouma-Okia, C. Péan, R. Pidcock, S. Connors, J. B. R. Matthews, Y. Chen, X. Zhou, M. I. Gomis, E. Lonnoy, T. Maycock, M. Tignor, T. Waterfield (eds.)].

IRENA, 2016. The Power to Change: Solar and Wind Cost Reduction Potential to 2025. International Renewable Energy Agency, Abu Dhabi.

IRENA, 2018a. Hydrogen from renewable power: Technology outlook for the energy transition, International Renewable Energy Agency, Abu Dhabi.

IRENA, 2018b, Global Energy Transformation: A roadmap to 2050, International Renewable Energy Agency, Abu Dhabi.

Jackson, R.B., Le Quéré, C., Andrew, R.M., Canadell, J.G., Korsbakken, J.I., Liu, Z., Peters, G.P. and Zheng, B., 2018. Global energy growth is outpacing decarbonization. Environmental Research Letters, 13(12), p.120401.

Jones, R. and Ricketts, J., 2016. Reconciling the signal and noise of atmospheric warming on decadal timescales. Earth Systems Dynamics, 8, pp.177-210.

Kang, S. and Eltahir, E.A., 2018. North China Plain threatened by deadly heatwaves due to climate change and irrigation. Nature communications, 9(1), p.2894.

Kaya, Y., Yamaguchi, M. and Geden, O., 2019. Towards net zero CO_2 emissions without relying on massive carbon dioxide removal. Sustainability Science, pp.1-5.

Keith, D.W., Holmes, G., Angelo, D.S. and Heidel, K., 2018. A Process for Capturing CO_2 from the Atmosphere. Joule.

Köhler, P., Bintanja, R., Fischer, H., Joos, F., Knutti, R., Lohmann, G. and Masson-Delmotte, V., 2010. What caused Earth's temperature variations during the last 800,000 years? Data-based evidence on radiative forcing and constraints on climate sensitivity. Quaternary Science Reviews, 29(1-2), pp.129-145.

Kovenock, M. and Swann, A.L., 2018. Leaf trait acclimation amplifies simulated climate warming in response to elevated carbon dioxide. Global Biogeochemical Cycles, 32(10), pp.1437-1448.

Kramer, G.J. and Haigh, M., 2009. No quick switch to low-carbon energy. Nature, 462(7273), p.568.

Krause, A., Pugh, T.A., Bayer, A.D., Li, W., Leung, F., Bondeau, A., Doelman, J.C., Humpenöder, F., Anthoni, P., Bodirsky, B.L. and Ciais, P., 2018. Large uncertainty in carbon uptake potential of land‐based climate‐change mitigation efforts. Global change biology, 24(7), pp.3025-3038.

Krugman, P., 2009. How Did Economists Get It So Wrong? The New York Times.

Lambert, F., 2018. All-electric ferry cuts emissions by 95% and costs by 80%, brings in 53 additional orders. Electrek. Accessed January 9, 2019.

Lamontagne, J.R., Reed, P.M., Marangoni, G., Keller, K., and Garner, G.G., 2019. Robust abatement pathways to tolerable climate futures require immediate global action. Nature Climate Change, Letter.

Lamperti, F., Dosi, G., Napoletano, M., Roventini, A. and Sapio, A., 2018. Faraway, so close: coupled climate and economic dynamics in an agent-based integrated assessment model. Ecological Economics, 150, pp.315-339.

Lawrence, P.J., Lawrence, D.M. and Hurtt, G.C., 2018. Attributing the Carbon Cycle Impacts of CMIP5 Historical and Future Land Use and Land Cover Change in the Community Earth System Model (CESM1). Journal of Geophysical Research: Biogeosciences, 123(5), pp.1732-1755.

Leiter, T. and Olivier, J., 2017. Synergies in monitoring the implementation of the Paris Agreement, the SDGs and the Sendai Framework. Policy Brief. Deutsche Gesellschaft für Internationale Zusammenarbeit (GIZ) GmbH.

Lenton, T.M., Daines, S.J., Dyke, J.G., Nicholson, A.E., Wilkinson, D.M. and Williams, H.T., 2018. Selection for Gaia across multiple scales. Trends in ecology & evolution.

Lenzi, D., Lamb, W.F., Hilaire, J., Kowarsch, M. and Minx, J.C., 2018. Weigh the ethics of plans to mop up carbon dioxide. Nature, 561(7723), pp.303-305.

Lovins, A.B., Palazzi, T., Laemel, R. and Goldfield, E., 2018. Relative deployment rates of renewable and nuclear power: A cautionary tale of two metrics. Energy Research & Social Science, 38, pp.188-192.

Mac Dowell, N., Fennell, P.S., Shah, N. and Maitland, G.C., 2017. The role of CO_2 capture and utilization in mitigating climate change. Nature Climate Change, 7(4), p.243.

Mani, M., Bandyopadhyay, S., Chonabayashi, S., Markandya, A., and Mosier, T., 2018. South Asia's Hotspots: The Impact of Temperature and Precipitation Changes on Living Standards. South Asia Development Matters. Washington, DC: World Bank.

Meehl, G.A., Hu, A. and Teng, H., 2016. Initialized decadal prediction for transition to positive phase of the Interdecadal Pacific Oscillation. Nature communications, 7, p.11718.

Merrill, D. and Leatherby, L., 2018. Here's how America uses its land. Bloomberg. Accessed January 9, 2019.

Millar, R.J., Fuglestvedt, J.S., Friedlingstein, P., Rogelj, J., Grubb, M.J., Matthews, H.D., Skeie, R.B., Forster, P.M., Frame, D.J. and Allen, M.R., 2017. Emission budgets and pathways consistent with limiting warming to 1.5 C. Nature Geoscience, 10(10), p.741.

Miocic, J.M., Gilfillan, S.M., Frank, N., Schroeder-Ritzrau, A., Burnside, N.M. and Haszeldine, R.S., 2019. 420,000 year assessment of fault leakage rates shows geological carbon storage is secure. Scientific Reports, 9(1), p.769.

Montserrat, F., Renforth, P., Hartmann, J., Leermakers, M., Knops, P. and Meysman, F.J., 2017. Olivine dissolution in seawater: implications for CO_2 sequestration through enhanced weathering in coastal environments. Environmental science & technology, 51(7), pp.3960-3972.

Moon, S. and Lee, J.W., 2018. Multi-residential demand response scheduling with multi-class appliances in smart grid. IEEE transactions on smart grid, 9(4), pp.2518-2528.

Moosdorf, N., Renforth, P. and Hartmann, J., 2014. Carbon dioxide efficiency of terrestrial enhanced weathering. Environmental science & technology, 48(9), pp.4809-4816.

Mora, C., Dousset, B., Caldwell, I.R., Powell, F.E., Geronimo, R.C., Bielecki, C.R., Counsell, C.W., Dietrich, B.S., Johnston, E.T., Louis, L.V. and Lucas, M.P., 2017. Global risk of deadly heat. Nature Climate Change, 7(7), p.501.

Mora, C., Spirandelli, D., Franklin, E.C., Lynham, J., Kantar, M.B., Miles, W., Smith, C.Z., Freel, K., Moy, J., Louis, L.V. and Barba, E.W., 2018. Broad threat to humanity from cumulative climate hazards intensified by greenhouse gas emissions. Nature Climate Change, 8(12), p.1062.

Mosini, V. ed., 2008. Equilibrium in economics: scope and limits. Routledge.

Muller, R.A. and Muller, E.A., 2017. Fugitive Methane and the Role of Atmospheric Half-Life. Geoinformatics & Geostatistics: An Overview, 2017.

Nagarajan, D., Lee, D.J., Kondo, A. and Chang, J.S., 2017. Recent insights into biohydrogen production by microalgae - From biophotolysis to dark fermentation. Bioresource technology, 227, pp.373-387.

Nemet, G.F., 2006. Behind the learning curve: Quantifying the sources of cost reductions in photovoltaics. Energy Policy, 34(17), pp.3218-3232.

Nemet, G.F., Callaghan, M.W., Creutzig, F., Fuss, S., Hartmann, J., Hilaire, J., Lamb, W.F., Minx, J.C., Rogers, S. and Smith, P., 2018. Negative emissions—Part 3: Innovation and upscaling. Environmental Research Letters, 13(6), p.063003.

Neuhoff, K., Vanderborght, B., Ancygier, A., Atasoy, A.T., Haussner, M., Ismer, R., Mack, B., Martin, R., Nagore, S., Ponssard, J.P. and Quirion, P., 2014a. Carbon Control and Competitiveness Post 2020: The Cement Report. FINAL REPORT, February 2014.

Neuhoff, K., Vanderborght, B., Ancygier, A., Atasoy, A.T., Haussner, M., Ismer, R., Mack, B., Martin, R., Nagore, S., Ponssard, J.P. and Quirion, P., 2014b. Carbon Control and Competitiveness Post 2020: The Steel Report. FINAL REPORT, February 2014.

Neumann, R.B., Moorberg, C.J., Lundquist, J.D., Turner, J.C., Waldrop, M.P., McFarland, J.W., Euskirchen, E.S., Edgar, C.W. and Turetsky, M.R., 2019. Warming effects of spring rainfall increase methane emissions from thawing permafrost. Geophysical Research Letters.

Nicholls, R.J., Marinova, N., Lowe, J.A., Brown, S., Vellinga, P., De Gusmao, D., Hinkel, J. and Tol, R.S., 2011. Sea-level rise and its possible impacts given a 'beyond 4 C world'in the twenty-first century. Philosophical Transactions of the Royal Society A: Mathematical, Physical and Engineering Sciences, 369(1934), pp.161-181.

Nordhaus, W.D., 1994. Expert opinion on climatic change. American Scientist, 82(1), pp.45-51.

Oda, J., Akimoto, K. and Tomoda, T., 2013. Long-term global availability of steel scrap. Resources, Conservation and Recycling, 81, pp.81-91.

Olivier, J.G.J., Schure, K.M., Peters, J.A.H.W., 2017. Trends in global CO2 and total greenhouse gas emissions: 2017 Report. PBL Netherlands Environmental Assessment Agency The Hague, 2017.

Otto, I.M., Kim, K.M., Dubrovsky, N. and Lucht, W., 2019. Shift the focus from the super-poor to the super-rich. Nature Climate Change, 9(2), p.82.

Pangallo, M., Heinrich, T. and Farmer, J.D., 2019. Best reply structure and equilibrium convergence in generic games. Science advances, 5(2), p.eaat1328.

Penn, J.L., Deutsch, C., Payne, J.L. and Sperling, E.A., 2018. Temperature-dependent hypoxia explains biogeography and severity of end-Permian marine mass extinction. Science, 362(6419), p.eaat1327.

Pepin, N., Bradley, R.S., Diaz, H.F., Baraër, M., Caceres, E.B., Forsythe, N., Fowler, H., Greenwood, G., Hashmi, M.Z., Liu, X.D. and Miller, J.R., 2015. Elevation-dependent warming in mountain regions of the world. Nature Climate Change, 5(5), p.424.

Peters, G.P., Andrew, R.M., Canadell, J.G., Fuss, S., Jackson, R.B., Korsbakken, J.I., Le Quéré, C. and Nakicenovic, N., 2017. Key indicators to track current progress and future ambition of the Paris Agreement. Nature Climate Change, 7(2), p.118.

Philibert, C., 2017. Renewable Energy for Industry: From green energy to green materials and fuels. IEA Insights series 2017.

Popkins, G., 2018. The forest question. Nature, (565), p.280-282.

Price, R., Thornton, S. and Nelson, S., 2007. The social cost of carbon and the shadow price of carbon: what they are, and how to use them in economic appraisal in the UK.

Pycroft, J., Vergano, L., Hope, C., Paci, D. and Ciscar, J., 2011. A tale of tails: Uncertainty and the social cost of carbon dioxide. European Commission, Spain.

Raftery, A.E., Zimmer, A., Frierson, D.M., Startz, R. and Liu, P., 2017. Less than 2 C warming by 2100 unlikely. Nature Climate Change, 7(9), p.637.

Ram, M., Bogdanov, D., Aghahosseini, A., Oyewo, S., Gulagi, A., Child, M. and Breyer, C., 2017. Global energy system based on 100% renewable energy—power sector. Lappeenranta University of Technology and Energy Watch Group: Lappeenranta, Finland.

Reich, P.B., Hobbie, S.E., Lee, T.D. and Pastore, M.A., 2018. Unexpected reversal of C3 versus C4 grass response to elevated CO2 during a 20-year field experiment. Science, 360(6386), pp.317-320.

Renforth, P., von Strandmann, P.P. and Henderson, G.M., 2015. The dissolution of olivine added to soil: Implications for enhanced weathering. Applied Geochemistry, 61, pp.109-118.

Riahi, K., Van Vuuren, D.P., Kriegler, E., Edmonds, J., O'neill, B.C., Fujimori, S., Bauer, N., Calvin, K., Dellink, R., Fricko, O. and Lutz, W., 2017. The shared socioeconomic pathways and their energy, land use, and greenhouse gas emissions implications: an overview. Global Environmental Change, 42, pp.153-168.

Rogelj, J., Den Elzen, M., Höhne, N., Fransen, T., Fekete, H., Winkler, H., Schaeffer, R., Sha, F., Riahi, K. and Meinshausen, M., 2016. Paris Agreement climate proposals need a boost to keep warming well below 2 C. Nature, 534(7609), p.631.

Romanak, K, 2019. Risk assessment on CO_2 leakage at CO_2 storage sites. CCS Technical Workshop, Tokyo, Japan, January 16, 2019.

Rothman, D.H., 2017. Thresholds of catastrophe in the Earth system. Science Advances, 3(9), p.e1700906.

Russo, S., Sillmann, J. and Sterl, A., 2017. Humid heat waves at different warming levels. Scientific reports, 7(1), p.7477.

Sadler, D., Cargill, A., Crowther, M., Rennie, A., Watt, J., Burton, S., Haines, M., Trapps, J., Hand, M., Pomroy, R., Haggerty, K., Summerfield, I., Evans, M., 2016. H21 Leeds City Gate Full Report - Northern Gas Networks.

Sambusiti, C., Bellucci, M., Zabaniotou, A., Beneduce, L. and Monlau, F., 2015. Algae as promising feedstocks for fermentative biohydrogen production according to a biorefinery approach: a comprehensive review. Renewable and Sustainable Energy Reviews, 44, pp.20-36.

Samir, K.C. and Lutz, W., 2017. The human core of the shared socioeconomic pathways: Population scenarios by age, sex and level of education for all countries to 2100. Global Environmental Change, 42, pp.181-192.

Sánchez-Bayo, F. and Wyckhuys, K.A., 2019. Worldwide decline of the entomofauna: A review of its drivers. Biological Conservation, 232, pp.8-27.

Schmidt, O., Hawkes, A., Gambhir, A. and Staffell, I., 2017. The future cost of electrical energy storage based on experience rates. Nature Energy, 2(8), p.17110.

Schneider, T., Kaul, C.M. and Pressel, K.G., 2019. Possible climate transitions from breakup of stratocumulus decks under greenhouse warming. Nature Geoscience, 12(3), p.163.

Sepulveda, N.A., Jenkins, J.D., de Sisternes, F.J. and Lester, R.K., 2018. The role of firm low-carbon electricity resources in deep decarbonization of power generation. Joule, 2(11), pp.2403-2420.

Shaffer, G., Huber, M., Rondanelli, R. and Pepke Pedersen, J.O., 2016. Deep time evidence for climate sensitivity increase with warming. Geophysical Research Letters, 43(12), pp.6538-6545.

Shepon, A., Eshel, G., Noor, E. and Milo, R., 2018. The opportunity cost of animal based diets exceeds all food losses. Proceedings of the National Academy of Sciences, p.201713820.

Smale, D.A., Wernberg, T., Oliver, E.C., Thomsen, M., Harvey, B.P., Straub, S.C., Burrows, M.T., Alexander, L.V., Benthuysen, J.A., Donat, M.G. and Feng, M., 2019. Marine heatwaves threaten global biodiversity and the provision of ecosystem services. Nature Climate Change, p.1.

Smith, D.M., Scaife, A.A., Hawkins, E., Bilbao, R., Boer, G.J., Caian, M., Caron, L.P., Danabasoglu, G., Delworth, T., Doblas‐Reyes, F.J. and Doescher, R., 2018. Predicted chance that global warming will temporarily exceed 1.5 C. Geophysical Research Letters.

Smith, P., 2016. Soil carbon sequestration and biochar as negative emission technologies. Global Change Biology, 22(3), pp.1315-1324.

Stephens, G.L., O'Brien, D., Webster, P.J., Pilewski, P., Kato, S. and Li, J.L., 2015. The albedo of Earth. Reviews of geophysics, 53(1), pp.141-163.

Steffen, W., Rockström, J., Richardson, K., Lenton, T.M., Folke, C., Liverman, D., Summerhayes, C.P., Barnosky, A.D., Cornell, S.E., Crucifix, M. and Donges, J.F., 2018. Trajectories of the Earth System in the Anthropocene. Proceedings of the National Academy of Sciences, 115(33), pp.8252-8259.

Sterman, J.D., Siegel, L. and Rooney-Varga, J.N., 2018. Does replacing coal with wood lower CO2 emissions? Dynamic lifecycle analysis of wood bioenergy. Environmental Research Letters, 13(1), p.015007.

Stern, N., Peters, S., Bakhshi, V., Bowen, A., Cameron, C., Catovsky, S., Crane, D., Cruickshank, S., Dietz, S. and Edmonson, N., 2006. Stern Review: The economics of climate change (Vol. 30, p. 2006). London: HM treasury.

Strona, G. and Bradshaw, C.J., 2018. Co-extinctions annihilate planetary life during extreme environmental change. Scientific reports, 8(1), p.16724.

Sulman, B.N., Moore, J.A., Abramoff, R., Averill, C., Kivlin, S., Georgiou, K., Sridhar, B., Hartman, M.D., Wang, G., Wieder, W.R. and Bradford, M.A., 2018. Multiple models and experiments underscore large uncertainty in soil carbon dynamics. Biogeochemistry, 141(2), pp.109-123.

Tamura, M., Kumano, N., Yotsukuri, M. and Yokoki, H., 2019. Global assessment of the effectiveness of adaptation in coastal areas based on RCP/SSP scenarios. Climatic Change, pp.1-15.

Thornhill, J., 2018. Musk's Outback Success Points to Bright Future for Battery Storage. Bloomberg. Accessed January 9, 2019.

Turner, A.J., Frankenberg, C., Wennberg, P.O. and Jacob, D.J., 2017. Ambiguity in the causes for decadal trends in atmospheric methane and hydroxyl. Proceedings of the National Academy of Sciences, 114(21), pp.5367-5372.

Turner, P.A., Mach, K.J., Lobell, D.B., Benson, S.M., Baik, E., Sanchez, D.L. and Field, C.B., 2018. The global overlap of bioenergy and carbon sequestration potential. Climatic change, 148(1-2), pp.1-10.

UCCRN, 2018. Impact 2050: The Future of Cities Under Climate Change. UCCRN Technical Report.

UN, 2014. Transforming our world: the 2030 Agenda for Sustainable Development, A/RES/70/1.

UN, 2015a. Conference of the Parties on its twenty-first session, FCCC/CP/2015/10/Add.1.

UN, 2015b. Sendai Framework for Disaster Risk Reduction 2015 – 2030.

UN, 2018. Emissions gap report 2018, DEW/2210/NA.

UNEP 2017. The Adaptation Gap Report 2017. United Nations Environment Programme (UNEP), Nairobi, Kenya.

USGCRP, 2017. Climate Science Special Report: Fourth National Climate Assessment, Volume I [Wuebbles, D.J., D.W. Fahey, K.A. Hibbard, D.J. Dokken, B.C. Stewart, and T.K. Maycock (eds.)]. U.S. Global Change Research Program, Washington, DC, USA, 470 pp., doi: 10.7930/J0J964J6.

Van Den Bergh, J.C. and Botzen, W.J., 2014. A lower bound to the social cost of CO 2 emissions. Nature climate change, 4(4), p.253.

van Sluisveld, M.A., Harmsen, M.J., van Vuuren, D.P., Bosetti, V., Wilson, C. and Van Der Zwaan, B., 2018. Comparing future patterns of energy system change in 2 C scenarios to expert projections. Global Environmental Change, 50, pp.201-211.

Walsh, B., Ciais, P., Janssens, I.A., Penuelas, J., Riahi, K., Rydzak, F., van Vuuren, D.P. and Obersteiner, M., 2017. Pathways for balancing CO 2 emissions and sinks. Nature communications, 8, p.14856.

Weitzman, M.L., 2009. On modeling and interpreting the economics of catastrophic climate change. The Review of Economics and Statistics, 91(1), pp.1-19.

Wester, P., Mishra, A., Mukherji, A., Shrestha, A.B. (eds), 2019. The Hindu Kush Himalaya Assessment - Mountains, Climate Change, Sustainability and People. Springer Nature.

World Bank, 2018. State and trends in Carbon pricing 2018.

World Economic Forum, 2019. The Global Risks Report 2019: 14th Edition.

Xi, F., Davis, S.J., Ciais, P., Crawford-Brown, D., Guan, D., Pade, C., Shi, T., Syddall, M., Lv, J., Ji, L. and Bing, L., 2016. Substantial global carbon uptake by cement carbonation. Nature geoscience, 9(12), p.880.

Xu, Y., Ramanathan, V. and Victor, D.G., 2018. Global warming will happen faster than we think.

Zanna, L., Khatiwala, S., Gregory, J., Ison, J. and Heimbach, P., 2018. Global reconstruction of historical ocean heat storage and transport. Proceedings of the National Academy of Sciences of the United States of America.

Zscheischler, J., Westra, S., Hurk, B.J., Seneviratne, S.I., Ward, P.J., Pitman, A., AghaKouchak, A., Bresch, D.N., Leonard, M., Wahl, T. and Zhang, X., 2018. Future climate risk from compound events. Nature Climate Change, p.1.

Zhang, D., Ghouleh, Z. and Shao, Y., 2017. Review on carbonation curing of cement-based materials. Journal of CO2 Utilization, 21, pp.119-131.

Chapter 2: Background of Ironmaking and Steelmaking

After the power sector, iron and steelmaking (ISM) represents the largest quantity of point source CO_2 emissions in the world. Emissions stemming from ISM accounted for 2.64 GtCO₂eq in 2016 [Olivier et al., 2017] with ISM production projected to increase ~1.4-2.0 times 2016 levels by 2050 [Oda et al., 2013]. The production of steel is dominated by the integrated Blast Furnace-Basic Oxygen Furnace (BF-BOF) and the Electric Arc Furnace (EAF) (**Fig. 2-1 and Fig. 2-2**). These processes are highly optimized with substantial integration and reuse of waste products making further efficiency improvements challenging (**Table 2-1**) [Fruehan et al., 2000]. In other words, aspects of the ISM process that seem wasteful in terms of CO_2 emissions are necessary for product quality or maintaining cost competitiveness.
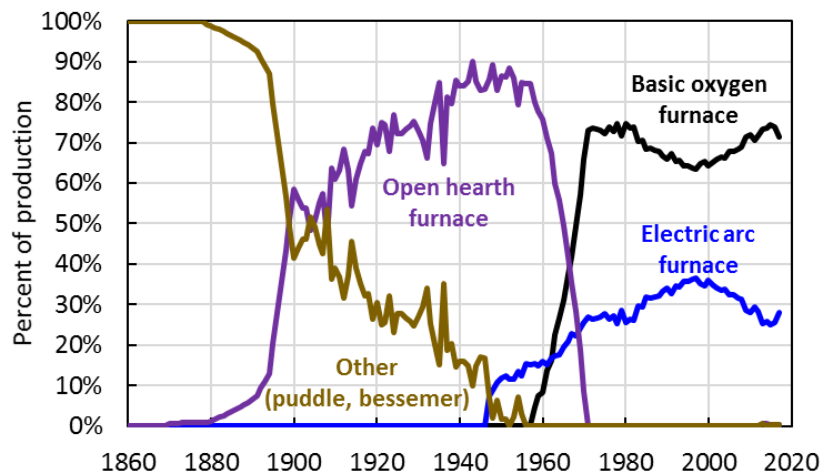
Fig. 2-1. The history of steelmaking processes since the late 19th century [Grubler, 1998; World Steel Association, 2018].
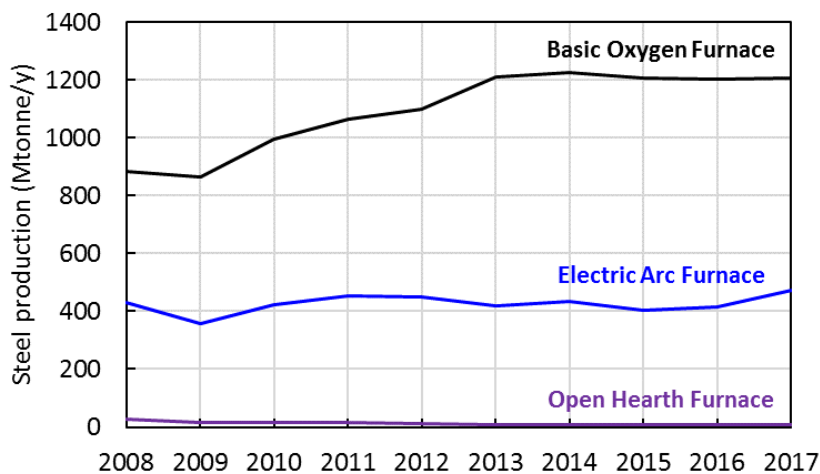
Fig. 2-2. The recent global production of steel by process type [World Steel Association, 2018].

Table 2-1. Comparison of the actual energy and CO_2 intensity of the ISM process with theoretical and practical minimums [Freuhan et al., 2000].

Process (product)	Energy Intensity (GJ/t-product) Theoretical minimum Practical minimum Actual	CO_2 Intensity (kgCO$_2$/t-product) Theoretical minimum Practical minimum Actual
Blast Furnace (crude iron)	9.8 10.4 $13 - 14$	1091 1158 $1447 - 1559$
Basic Oxygen Furnace (liquid steel)	7.9 8.2 $10.5 - 11.5$	144 144 $189 - 207$
Electric Arc Furnace (liquid steel)	1.3 1.6 $2.1 - 2.4$	225 277 $364 - 416$
Hot rolling	0.03 0.9 $0.1 - 3.2$	2 50 $110 - 132$
Cold rolling	0.02 0.02 $1.0 - 1.4$	4 4 $173 - 243$

The ISM process has undergone significant changes and improvements over the last 100 years [Emi, 2015], with the bellows furnaces of ancient China and crucible furnaces of ancient India being replaced by open hearth furnaces (OHF), Bessemer furnaces, the modern Blast Furnace (BF) and Basic Oxygen Furnace (BOF), Electric Arc Furnaces (EAF), and directly reduced iron (DRI). In the modern ISM processes, the primary CO_2 sources are coke and flux. Coke is used to reduce iron ore generating gaseous CO_2 as a by-product. Additionally, calcium carbonate is decomposed to CaO and gaseous CO_2; the CaO is used to remove impurities from molten metal. Innovation continues in ISM as evidenced by major projects such as 'Ultra Low CO_2 Steelmaking' (ULCOS) in the European Union, the 'CO_2 Ultimate Reduction in Steelmaking Process by Innovative Technology for Cool Earth by 2050' (COURSE 50) in Japan, and work by the American Iron and Steel Institute (AISI) in the United States [Junjie, 2018]. **Figure 2-3** outlines the major lines of research of these programs. Currently, four manufacturing technologies that may lower the CO_2 intensity of ISM are at a significant degree of maturity: 1) top gas recirculated blast furnace (TGRBF), 2) advanced directly reduced iron supplied to electric arc furnace (DRI-EAF), 3) solid-state reduction (COREX), and 4) advanced smelting reduction (HIsmelt, HIsarna) [IEAGHG, 2018].
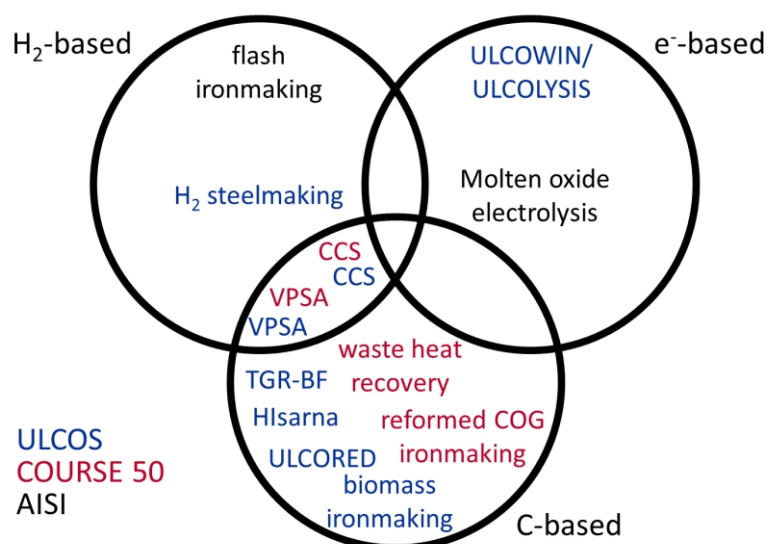
Fig. 2-3. Major research tracks of ULCOS, COURSE 50, and AISI to reduce the CO_2 intensity of ISM.

In the TGRBF process, CO_2 is removed from the BF gas, leaving a CO/H_2-rich gas which is re-injected into the BF. Typically, pure oxygen is also blown into the BF to reduce dilution by N_2. In essence, the TGRBF process increases the utilization of the chemical reduction potential of coke.

In the DRI-EAF process, the reduction of iron ore is achieved in a solid state generally by way of reaction with CH_4, CO, and H_2. The reduced iron is feed to an EAF along with scrap for steelmaking. The process can be intensified by replacing air in the process with pure O_2 to yield a pure CO_2 off-gas. There is a subgroup of DRI processes that use H_2 derived from electrolysis of water instead of from fossil sources. However, it should be noted that the energy consumption of H_2 production via electrolysis of water needed to match current ISM production levels would nearly double all energy production, making the full-scale practicality of such methods suspect [Wyns et al., 2018].

The COREX process utilizes separate reactors to achieve reduction and smelting. The main benefit of COREX is the removal of the coking and sintering processes. On the other hand, the ratio of fuel to ore is increased compared to extant processes.

Similar to COREX, advanced smelting reduction processes avoid the coking and sintering steps, but reactions occur in a single vessel. In advanced smelting reduction methods, melting and partial reduction of ore occur in a cyclone above the molten metal bath. Preheating and partial pyrolysis of coal occurs in the bath along with the final reduction of iron oxides to metallic iron.

Though the novel, low-CO_2 ISM methods described above are under development, and a plethora of other technologies that aim to leverage renewable energy (RE) are being examined [Philibert, 2017], the large scale of traditional ISM facilities means that existing assets will likely be used to their end of life [Kuramochi, 2017]. This financial reality calls into question the wisdom of waiting for the next generation of facilities [Arens et al., 2017]. A growing area of interest is using biological resources in place of coal as a reductant source in ISM. In a simplified theoretical framework, use of biomass would generate CO_2-neutral steel as the carbon was sourced from the atmosphere instead of fossil reserves. However, several complications make the concept of CO_2-neutral bio-ISM untenable. Firstly, flux sources are not covered by biological production. Secondly, it is yet to be seen whether existing ISM facilities can be used with biological reductant, or if biological reductant can be

reliably used in processing at all [Suopajärvi et al., 2018]. Moreover, the competition for biological sources means that purposeful agriculture would need to increase to meet demand, decreasing carbon stocks in the biosphere and soils. Moreover, the spatial mismatch between biological production and steel production means that a multitude of carbon leakage risks exist across the supply chain.

Reducing CO_2 emissions while maintaining ISM assets can be accomplished by post combustion capture (PCC) of CO_2 with permanent storage in underground geologic formations (CCS). Though technically mature, research continues along many avenues in an effort to reduce the cost of CCS [Wang et al., 2015]; nevertheless, overall costs have remained essentially flat for the last 10 years [Rubin et al., 2015]. This cost is problematic for application to the ISM industry; iron and steelmaking have a particularly low profit margin and exposure to global competition. As such, even minor efficiency reductions or cost increases threaten the financial solvency of most ISM facilities [Silva and de Carvalho 2015]. A functioning global price on carbon (e.g., carbon taxes, carbon border adjustments, etc.) would provide the economic certainty for ISM to invest in CO_2 capture while also driving the development of CCS infrastructure. The same economic difficulties exist for bio-ISM, where the price of biological reductant makes the process unfeasibly expensive [Mandova et al., 2019]. Without such organized, directed international effort, the ISM industry requires a CO_2 reduction technology that can be implemented at close to no capital or operating expense, is robustly CO_2 negative cradle-to-grave, and has minimal external dependencies.

The co-generated solid waste of ISM called 'slag' provides the opportunity to meet these requirements for ~10% of ISM's CO_2 emissions. However, any utilization of slag must not reduce the quality or rate of metal produced in ISM and must not negatively impact ISM equipment. In other words, the slag utilization process must begin after the slag has been separated from the furnace and metallic melt.

Chapter highlights

- Iron and steelmaking depends fundamentally on a reducing agent, which currently is limited to carbon-based compounds in industrial-scale systems.
- The large amount of sunk capital in iron and steelmaking facilities financially discourages operators from adopting new equipment.
- The low profit margins and global nature of the iron and steel industry means that CO_2 reduction technologies that increase the cost of production are unlikely to be adopted without strict regulatory action and/or strong government subsidies.
- The solid waste of iron and steelmaking (called, 'slag') can potentially offset roughly 10% of current CO_2 emissions from iron and steelmaking via conversion of the calcium and magnesium content to carbonates.
- Slag is a highly variable, heterogeneous mineral mélange that varies by iron and steelmaking process type, between facilities, within a facility over time, and as a function of the method of cooling from the molten to solid state.
- CO_2 mineralization has been researched for 30 years with little progress.
- The heterogeneous nature of slags results in occlusion of reactive species by unreactive species (so called: 'mineral locking'). Quantification of mineral locking has been overlooked by the research community, resulting in a lack of progress in efficient mineralization processes.
- Direct, gas-solid CO_2 mineralization was largely abandoned 15 years ago due to 'slow kinetics'. The tests that led to this conclusion either made unjustified assumptions about, or failed to account for, the effect of temperature, CO_2 concentration, and relative humidity.
- Multistep methods, aqueous reactions, chemical/thermal/mechanical activation, and extreme operating conditions have been used to accelerate mineralization reactions. However, the associated CO_2 emissions generally make such processes net CO_2 emitters.
- Two methods that overcome the effects of mineral locking are proposed: 1) centrifugal separation, and 2) slow solidification with solid-state quenching. Both methods begin the slag treatment process design while slag is still molten.
- A method to passively mineralization slag via direct, gas-solid reaction is also proposed. The process uses flue gas or the atmosphere as a CO_2 source, operates at 30 ˚C, and a relative humidity of 90%.

Publications relevant to this chapter

- Enhanced recovery process of calcium oxide and metals from steelmaking slag with net carbon sequestration, Energy Procedia Vol. 114 p.6246-6255 (2017), **Corey Myers**, Takao Nakagaki, and Takuya Mitamura.

2.1. Iron and steelmaking process

The BF-BOF and EAF processes and equipment are briefly described prior to discussing how slag can be utilized for CO_2 reduction without negatively impacting the upstream processes. Alternative ISM methods (e.g., direct reduced iron, COREX) are not discussed due to their currently small market share. Modifications to the internal operations of BF-BOF and EAF processes (e.g., top gas recycling) that do not significantly impact slag quantity or composition are not discussed. The ISM process contains roughly 4 steps:

1. Preparation of raw materials,
2. Reduction of iron ore to iron (ironmaking),
3. Refining of iron to steel (steelmaking), and
4. Forming and finishing (casting, reheating, and rolling).

The forming and finishing tasks happen separate from slag and are thus not discussed. The chemistry of ironmaking and steelmaking results in off-gases with substantial fuel value; these gases are typically fed to a power plant for production of electricity used elsewhere in the process. **Figure 2-4** provides the general connections between the sub-operations comprising ISM via BF-BOF.
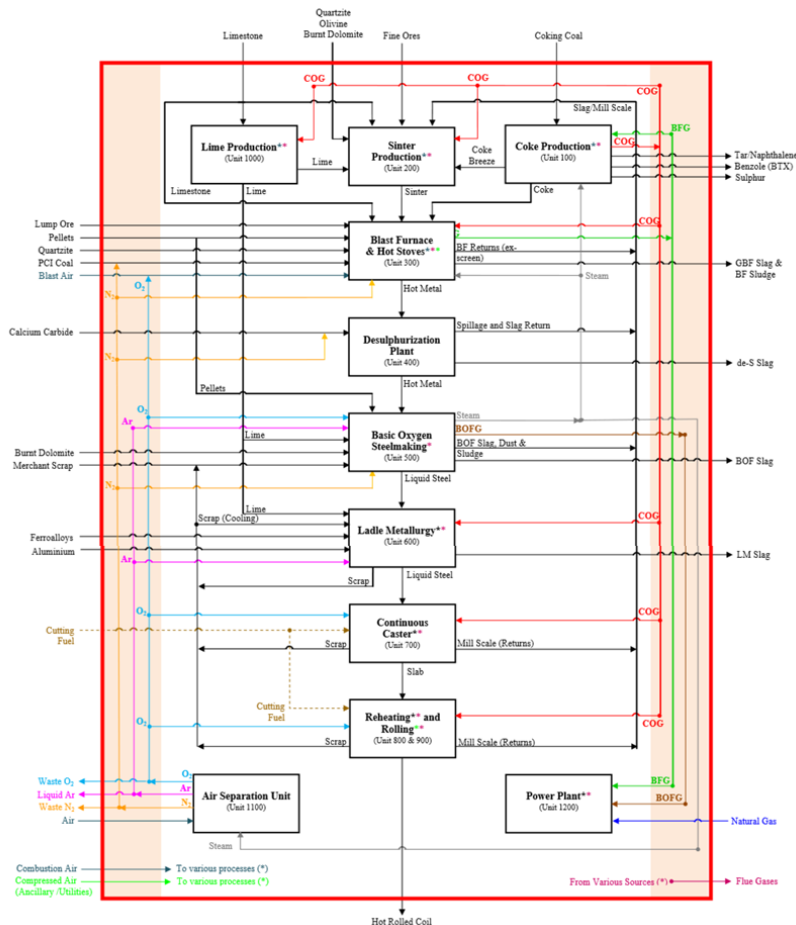
Fig. 2-4. The material flows between the subprocess of ISM [IEAGHG, 2013a].

2.1.1. Materials preparation

The solid input materials to ISM are iron ore, scrap metal, coal, and flux. Each input is pretreated prior to introduction to the furnace.

Iron Ore

Iron ore is a category encompassing various iron oxides (Fe_3O_4, Fe_2O_3, $FeO \cdot OH$, $FeCO_3$, etc.) which typically also contains some amount of non-ferrous material such as silicates and aluminates (termed: gangue). Mined iron ore is ground and mixed to generate a homogeneous chemical composition. The homogenized iron ore is then sintered or pelletized prior to introduction into the furnace. Pore spaces that exist between the agglomerates produced by sintering or pelletization allow for the upward flow of gas within the ironmaking furnace. In the sintering process, finely-ground coke, flux material (typically limestone), and in-house wastes (e.g., iron oxide from rolling operations, slag dust) are added to the ground iron ore prior to igniting the mixture at ~1300 ˚C to generate a solid product. By premixing the materials, the chemical homogeneity within the ironmaking furnace is increased and operations can remain close to the platonic conditions assumed in design specifications. In the case of pelletization, iron ore is blended with a binder (e.g., bentonite) and flux (typically limestone) prior to forming into balls and baking at ~1315 ˚C. This process generates a hard, dense solid with the benefits of a premixed composition.

Steel Scrap

In the steelmaking process, steel scrap is mixed with hot metal generated from ironmaking to control temperature and the total carbon content. Introduction of steel scrap is done in both the BOF and EAF processes. As ironmaking requires substantial coal for heat and ore reduction, usage of scrap significantly reduces the CO_2 intensity of the overall ISM process. Scrap is generated both in-house and purchased from recyclers. In-house scrap is derived from the imperfections in the production and finishing of iron and steel. Such imperfections include metal entrained in slag, cuttings, flakes from rolling, dust, and material rejected by quality control. The EAF can generally utilize higher proportions of scrap than the BOF, though both methods are sensitive to tramp elements (e.g., Al, B, Pb) in the scrap.

Coal

Coal provides the chemical reduction potential and process heat needed to convert iron oxides into metallic iron; it also provides the carbon that will eventually become part of the metal product. Bituminous grade coal is converted to a form suitable for ISM called 'coke'. Compared to bituminous grade coal, coke contains much less volatile material and is more porous. Along with its use as the fuel and reducing agent, coke acts as a porous support for the iron ore and flux within the BF furnace. Coke allows gases to pass up the furnace and contact the solid inputs, generating the iron reduction reactions. Due to its use as a physical support mechanism, coke requires not only specific thermochemical properties, but also physical strength, hardness, and porosity.

To convert coal to coke, it is first crushed and gravity-separated to remove low quality coal and various gangue material. The crushed coal is then heated under non-oxidizing conditions at ~1200 ˚C for ~20 hours. This process drives off volatile materials without converting the carbon content to gaseous products. The generated coke is then quenched in water to prevent burning when contacting air. Quenched coke is ground, and the fines are often mixed with ore and flux in the sintering process.

Flux

Flux is a broad category of materials that are used to react with and remove gangue materials (e.g., SiO_2, P_2O_5) from the metallic melt. After binding with gangue, the flux becomes a buoyant liquid that

floats atop the metallic melt. This disparate material is called 'slag'. Based on the chemical principle of 'like dissolves like', and given that gangue is generally composed of oxides, fluxes are also typically oxides. For recovery of 'acidic' impurities (e.g., SiO_2, P_2O_5) a basic flux is added (e.g., CaO). Analogously, removal of 'basic' impurities is achieved with an 'acidic' flux. The BF-BOF and EAF processes primarily utilize basic fluxes in the form of limestone ($CaCO_3$), dolomite ($MgCO_3 \cdot CaCO_3$), lime (CaO), and burnt dolomite ($MgO \cdot CaO$). Oxides are generally preferred as the decomposition of carbonates is highly endothermic and effects control of the furnace temperature. 'Acidic' fluxes such as quartzite (SiO_2) and olivine (Mg_2SiO_4) are used primarily for precise control of slag properties (e.g., basicity, viscosity).

Refractory

Refractory material lines the internal walls of the BF, BOF, and EAF. Refractory is often somewhat dissolved by the thermochemistry within the furnace and is transferred into the slag phase. The BF hearth (containing carbon-saturated liquid iron) is generally carbon-lined. To resist attack from basic slag, the steelmaking furnaces are typically magnesia-lined (MgO). Furnaces are often equipped with a water-cooled jacket to reduce the rate of attack by molten species. The lower temperatures near the refractory-slag interface may generate a layer of solidified slag that acts to protect the furnace from dissolution. Equipment that handles and transports molten slag or metal after exiting the steelmaking furnace (e.g., ladles, torpedo cars, etc.) are generally magnesia-lined (MgO), zirconia-lined (ZrO_2), or alumina-lined (Al_2O_3).

Alloying Materials

Compounds added to generate specific metallic properties may be captured by slag to some degree. Typical alloying elements not found in large quantities elsewhere in the ISM process are B, Co, Cr, Mo, Mn, Ni, Ti, and W.

2.1.2. Ironmaking

Conversion of iron ore to metallic iron occurs in the blast furnace. Input materials are fed continuously into the top of the BF while hot air (sometimes moisture-controlled and oxygen-enriched) and supplemental fuels are injected through tuyeres near the bottom of the furnace (**Fig. 2-5**). Molten slag and molten metallic iron flow down to the bottom of the furnace through the thermal reserve zone and are periodically removed through tapholes. The produced metal is commonly termed 'crude iron' or 'pig iron' and contains a large carbon content (~4%). Almost all crude iron is sent in a molten state called 'hot metal' (~1450 °C) to a steelmaking process for further refinement.
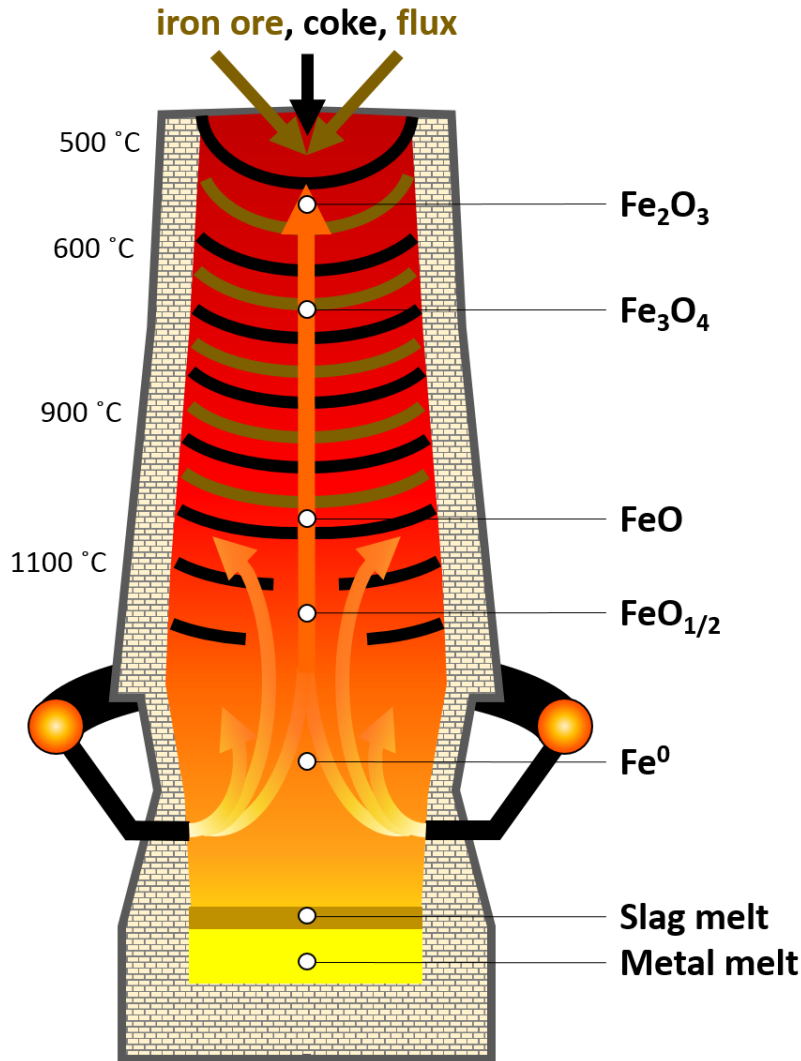
Fig. 2-5. Schematic of a blast furnace.

The thermochemical process of ironmaking is captured by a series of reduction steps of iron oxides by carbon and carbon monoxide. The representative chemical reactions are shown in **Eq. (2-1)** through **Eq. (2-4)**. Carbon from coke is oxidized to CO_2 by injected oxygen, releasing heat. This heat drives the melting of the input materials (i.e., ore, flux, and gangue). The generated CO_2 is subsequently reduced by endothermic reaction with the excess carbon in the coke, forming CO. Carbon monoxide acts to reduce iron oxides to metallic iron. Any H_2 present from the moisture in injected gases and supplemental fuels also serves to reduce iron oxides.

$$Fe_2O_3 + CO \rightarrow 2FeO + CO_2 \text{ @}400-700\text{ °C} \qquad (2-1)$$

$$FeO + CO \rightarrow Fe + CO_2 \text{ @}700-1000\text{ °C} \qquad (2-2)$$

$$2FeO + C + CO_2 \rightarrow 2Fe + 2CO_2 \text{ @}1000-1400\text{ °C} \qquad (2-3)$$

$$Fe^0 + C \rightarrow carburization\text{: melts as eutectic @}1400-1450\text{ °C} \qquad (2-4)$$
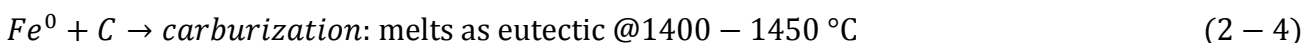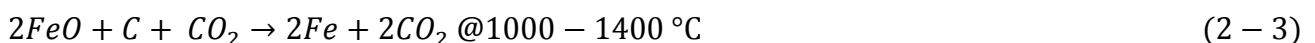
Metallic iron melts at 1537 ˚C, but the presence of C results in a low melting point eutectic of ~1150 ˚C (**Fig. 2-6**). Even so, the metallic iron is maintained at ~1500 ˚C in the furnace in order to generate the low viscosity necessary to remove the molten metal by pouring (so-called 'tapping'). Molten metal flows into refractory-lined, torpedo-shaped containers which are moved by rail to the steelmaking or other refining processes.
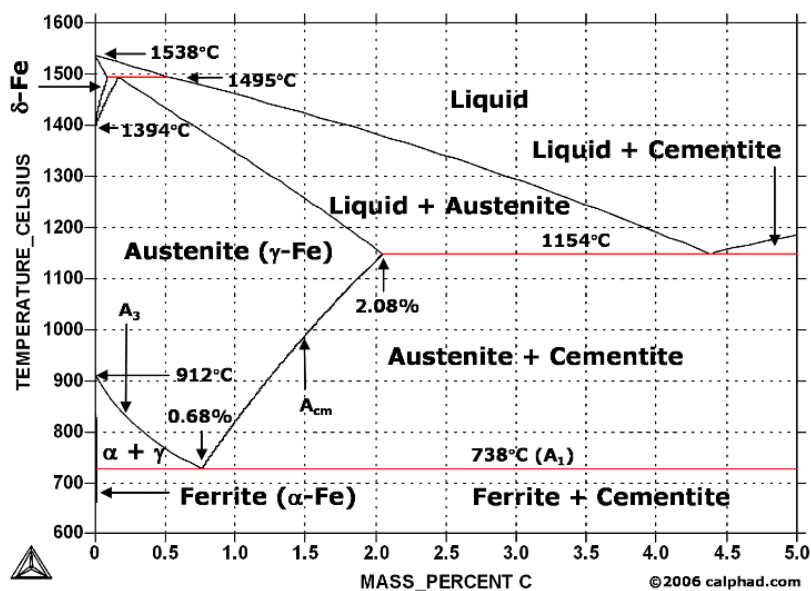
Fig. 2-6. The phase diagram of the Fe-C system [Bale et al., 2016].

2.1.3. Steelmaking

The refining of crude iron to steel involves the reduction of the carbon content (generally to <1%) and addition of alloying elements. Current steelmaking is dominated by the BOF and EAF processes. In the BOF process, a high-velocity lance injects pure oxygen into the furnace, causing the excess carbon content to be oxidized. The EAF process is fundamentally different from the BOF process; an electric arc generated between two in-furnace electrodes passes through the solid material, causing it to melt and impurities to be oxidized. This oxidation is achieved through oxygen injection, though the amount of oxygen required is typically less than the BOF process due to the main charge being scrap instead of crude steel (i.e., lower overall carbon content). Electric arc furnaces can be run using direct current or alternating current. In direct current EAFs, the current passes from the electrodes to an electrode in the hearth; in alternating current EAFs, the current routes between electrodes lowered into the furnace. The graphite electrodes are consumed by the process at a rate of ~1-2 kg-electrode per tonne of steel produced.

The removal of non-carbon impurities occurs through oxidation and interaction with the flux (prototypically, CaO). As silicon is more easily oxidized than iron, it is readily removed. Meanwhile, Zinc is eliminated from the melt as a fume. On the other hand, copper, nickel, and tin are difficult to remove due to their higher stability than iron in an oxidizing environment. The removal of other impurities (e.g., manganese, phosphorous) is dependent on the slag chemistry and temperature. After oxidation, addition of some additives can scavenge oxygen from the melt and subsequently separate as a slag. It is also common to remove impurities through agitation with inert gas and vacuum de-gassing. Even so, the difficulty in impurity removal results in a slag that typically contains

a high percentage of iron as FeO. In the EAF process, slag foaming by the release of CO is promoted as it creates a thermally insulating layer.

2.1.4. By-products

Off-gases

The thermochemistry of ironmaking results in off-gases enriched in CO and H_2; as such, blast furnace gases contain significant fuel value and are used to generate electricity in an on-site power plant. Along with gaseous components, the flue gases of both ironmaking and steelmaking contain elutriated dust particles which are high in iron content. To retrieve this resource, the flue gas passes through filter bags, scrubbers, and electrostatic precipitators. The retrieved dust is generally sent to the sintering or pelletizing process.

The chemical composition of the various flue gases in the BF-BOF ISM process are provided in **Table 2-2**. A notable difference between ISM and other point source CO_2 emitters (e.g., power plants, cement kilns) is the large number of flue gas streams with disparate compositions. Mixing of the flue gases is possible but adds significant complexity in terms of piping and the control of the gas composition to match the process flow of ISM. Additionally, review of **Table 2-3** shows that the CO_2 concentration varies significantly between flue gas streams. The sinter production and the reheating furnace contain particularly low CO_2 concentrations. Homogenization of the flue gases therefore dilutes the high CO_2 concentration streams, increasing the specific energy of CO_2 capture. Additionally, as the sizing of CO_2 capture equipment is dictated by the overall gas flow rate, removal of the low CO_2 concentration streams would result in ~78% smaller equipment with a reduced capital expense (CAPEX) and operating expense (OPEX). Given that CCS is necessary to reduce ISM CO_2 emissions and that ISM is sensitive to cost, it is imperative to develop methods that can allow these low CO_2 concentration flue gases to be omitted from CCS activities.

Table 2-2. ISM flue gas composition.

	Hot stove	Power plant	Lime production	Coke production	Reheating furnace	Sinter production	EAF
CO_2	27.30%	26.43%	19.41%	14.77%	4.59%	4.81%	10.00%
N_2	65.52%	65.88%	60.24%	69.47%	71.86%	72.65%	58.00%
O_2	0.80%	0.71%	7.77%	5.00%	7.20%	14.90%	0.00%
H_2O	6.38%	6.98%	12.58%	10.76%	16.34%	6.90%	0.00%
CO	0.00%	0.00%	0.00%	0.00%	0.00%	0.74%	30.00%
H_2	0.00%	0.00%	0.00%	0.00%	0.00%	0.00%	2.00%

Table 2-3. BF-BOF flue gas CO_2 content.

Stream	Stream-specific CO_2 concentration (mol%)	Contribution to ISM CO_2 emissions (%)	Contribution to ISM flue gas volume (mol%)
Hot stove	27.3%	23.7%	17.2%
Power plant	26.4%	56.1%	42.0%
Lime production	19.4%	4.1%	4.2%
Coke production	14.8%	10.9%	14.6%
Reheating furnace	4.8%	3.3%	7.9%
Sinter production	4.6%	1.9%	14.2%
All streams merged	19.8%	100%	100%
Reheating and sinter streams removed	24.1%	90.7%	78%

Generation of slag

The majority of flux is introduced with the sintered or pelletized ore as (Ca/Mg)O. Some limestone or dolomite may be added directly to the furnace for precise operational control. Directly added flux rapidly decomposes endothermically to MgO at 350 ˚C and CaO at 825 ˚C. The calcium and magnesium oxide reacts with SiO_2, Al_2O_3, and other impurities in the fusion zone of the furnace, generating molten slag. The impurities comprising slag besides sulfur and phosphorous are largely insoluble in the metallic melt and thus remain in the buoyant molten slag layer. Sulfur removal requires high temperature contact between sulfur-impregnated iron, carbon, and a basic slag to generate CaS (this occurs primarily in the hearth). Phosphorous oxides are reduced in the furnace and the elemental phosphorus readily dissolves in iron; like sulfur, removal of phosphorous requires a basic slag. The slag composition is typically maintained near low temperature eutectics to avoid potential solidification within the furnace. Along with controlling the melting point, the viscosity and basicity of slag are the primary considerations when designing the slag composition. Slag is normally maintained at ~1550 ˚C in order to preserve a low viscosity that allows passage of metal through the slag and easy removal of slag by pouring. In general, upon tapping the furnace, the slag is either dumped in pits to generate large granules or rapidly cooled by high pressure water jet spray prior to grinding for reuse as an additive in cement production.

2.2. CO_2 reduction efforts in iron and steelmaking

Reduction of emissions in ISM occurs along four basic routes: 1) the ever-present societal action of reduce, reuse, and recycle (RRR), 2) increased efficiency in the current ISM process, 3) modifications and innovations to allow continued use of existing assets, and 4) novel ironmaking and steelmaking processes that inherently have lower CO_2 intensities.

Increasing RRR means designing structures and products that require less metal, increased maintenance and refurbishment of existing assets, and finding 'second-life' and beyond usages for metals prior to recycling as scrap to the steelmaking process. Though these actions may have implications for the quality and type of metals produced, they do not directly affect the ISM process itself. As such, they are not discussed in detail here. Other strategies to reduce ISM emissions do have direct implications for ISM operations; from the perspective of the ISM industry, the exposure to global markets without a global coverage of a carbon price makes investment in CO_2 reduction

technologies a purely regulatory requirement, instead of a win-win proposition [Neuhoff et al., 2014]. Moreover, there is a lack of niche markets in the ISM industry that may provide the coverage for high-risk, high-capital development of new CO_2 reduction methods or ISM processes [Smith and Raven, 2012]. Without such markets, immature, small-scale novel processes are immediately exposed to competition with highly developed, large-scale, entrenched processes. This uneven playing field makes rapid uptake and diffusion of low CO_2 ISM difficult. Even if local conditions help foster investment into novel technologies, the low margins of ISM means that most new processes or equipment require a payback period of 2-4 years to be considered for adoption at facilities. This standard is particularly difficult for low CO_2 technologies to achieve.

An additional hurdle to rapid uptake of low-CO_2 ISM is that the ideal product of a novel ISM process is indistinguishable from conventional products. Moreover, iron and steel typically constitute only a portion of another product. As such, the purchasing decision for low CO_2 ISM is disconnected from individual consumers. The undifferentiated and opaque nature of iron and steel makes consumer-based choice of the low CO_2 option more challenging than, for example, electric vehicles [Hoekstra and Refa, 2017]. The lack of coverage from niche markets, a global carbon price, or steady government support for full-scale operations means that CO_2 reduction technologies need to be low-risk, low-capital, and viable independent of regulatory policy. At the same time, given the scale of CO_2 emissions in ISM and the necessary pace of reduction, processes must be easily scalable and modifiable to fit 'on the ground' conditions.

A looming issue for the ISM is the need to reduce overall CO_2 emissions while iron and steel production is projected to increase. The root cause of the growth in ISM is the macro trend of per capita steel utilization as a function of per capita GDP. Developed countries tend towards a steady-state steel stock of roughly 10 tonnes per person [Müller et al., 2011]. The current global steel stock is ~4 tonnes per person; thus, along with the projected population growth to 9.7-12.9 billion people by 2100 [UN, 2015], there is the projected per capita increase in steel stock. Thus, even with the inclusion of best available technology, extensive scrap recycling, and next-generation processes and equipment, further efforts are projected to be necessary to reduce the ISM industry's CO_2 footprint to be in line with 2DS [JISF, 2018a]. The IEA predicts that by 2050 such novel processes need to supply reductions of ~623 $MtCO_2/y$ to stay on a 6DS path, and ~765 $MtCO_2/y$ to remain consistent with 2DS [West, 2015].

2.2.1. Process efficiency

Increasing efficiency in the extant ISM facilities varies greatly by region. Highly developed countries such as Japan maintain efficiencies close to theoretical maximums [RITE, 2008], while developing nations often have less strict environmental regulation or enforcement and accordingly have less efficient ISM processes in aggregate (e.g., China). This effect is due to process efficiency as well as the relative amount of BOF and EAF plants [Hasanbeigi et al., 2014]. Increased efficiency in ISM hinges primarily upon increased purity and homogeneity of input materials, reuse of fuel value in exhaust gases, recovery of materials lost during processing (e.g., iron oxide from rolling operations, iron dust), and the recovery of heat from the multitude of high temperature sources in the process.

2.2.2. Scrap recycling

Scrap recycling is traditionally defined as the recovery of metal after production and reuse in the steelmaking process. This metal may come from in-house losses (i.e., accidental entrainment in slag), losses during finishing and fabrication (e.g., cuttings), and from products at their end of life (EOL) in society. Roughly 27% of produced metal does not enter into the market as products; roughly 70-90%

of this 'new scrap' is recycled. Roughly 15% of EOL product scrap is never recovered, while less than 10% of structural scrap is permanently lost [Enkvist and Klevnas, 2019]. Scrap recycling drastically reduces the energy demand and CO_2 emissions per unit steel, as the input material is chemically much closer to the desired product composition. However, the degree of global EOL recycling of steel is already 83% [Pauliuk et al., 2013a] and exceeds 90% in some countries [Almemark and Hallberg, 2012]. As such, the reduction in emissions due to scrap recycling is expected to asymptotically decline as the market is saturated with scrap. Moreover, a few barriers exist for a complete closure of the steel cycle. A large portion (4-5%) of recovered scrap is lost to the slag phase during the re-melting process [Pauliuk et al., 2013b; Price, 2009]. Moreover, increasing concentration of tramp elements due to specialized metal production causes a downcycling of metal [Reck and Graedel, 2012]. The most daunting tramp element in steel recycling is copper, which already exceeds acceptable concentrations in OECD scrap for many major product groups [Daehn et al., 2017]. Copper cannot be removed from steel in traditional steel refining processes, and so represents a permanent downgrading of the metal quality [Ohno et al., 2014]. Additional tramp elements such as Nickel and tin also must be addressed as their increasing content represents a degradation of steel quality, and thus the continued need for primary iron and steel production, with the associated higher CO_2 emissions.

An additional 'scrap' type is hydrocarbon material that is considered waste by society but still contains fuel value or reductive potential in the ISM process. This category of scrap is dominated by waste plastics and tires [JISF, 2018b]; utilization of this low entropy resource not only lowers the net CO_2 intensity of society, but also removes the environmental impacts of these materials.

2.2.3. Fuel switching

The primary production of iron is the largest source of CO_2 emissions in ISM, driven mainly by the use of coal as the reducing agent. An alternative reduction method using CH_4 (natural gas: NG) in place of coal generates iron pellets and briquettes (called 'directly reduced iron': DRI) which are subsequently feed into an EAF for steel production. This method lowers the emissions relative to the BF-BOF route by ~20-30% but requires investment in completely new assets or imported DRI. Moreover, the stated reductions are overly optimistic as the CO_2eq intensity of NG does not include emissions during the extraction and refinement process, raising emissions by ~60% [Alvarez et al., 2018].

The economic incentive for DRI depends on the availability of EAF, the relative price of coal, NG, and any relevant carbon price. With the accelerating reduction in coal-fired power plants, and the increase in NG peakers to stabilize grids with high RE penetration, the cost of fuel to operate DRI compared to a BF may offset the financial incentives from climate change regulation.

Another fuel alternative to coal is the use of biomass in the traditional BF-BOF process. In its natural state, woody biomass is unsuitable for replacement of coal in ISM due to a high moisture content, low bulk energy density, differences in the ratio of hydrogen, carbon, and oxygen, and for some species, excessive amounts of problematic tramp elements [Suopajärvi et al., 2018]. However, biomass can be upgraded to chemical compositions suitable for ISM by way of drying, pyrolysis, and charcoaling. Likewise, careful control of wood species, and the portion of wood used, can reduce the quantity of unwanted elements. Physical requirements such as hardness and porosity also seem to be technically achievable with biomass [Wei et al., 2017]. However, biomass utilization at the scale needed to meaningfully impact global ISM emissions represents a large appropriation of land for the purpose of ISM. Given the need for precise control of the input material, such biomass-based ISM

would likely involve only a few woody species. Such alterations to natural ecosystems, especially the replacement of diverse environments with monocultures, results in large CO_2 emissions from the soils [Huang et al., 2018]. Likewise, even with an unrealistically ideal cycling of CO_2 between the atmosphere and the dedicated biomass, and ignoring ecosystem feedbacks, there would be a large upfront CO_2 emissions debt from the initial removal of mature forest [DeCicco and Schlesinger, 2018; Sterman et al., 2018]. These environmental feedbacks, along with the full chain of biomass production, upgrading, and transport, may very well eliminate the assumed CO_2 emissions reductions of biomass-based ISM [Fajardy and Mac Dowell, 2017].

Regardless of whether biomass-based ISM can overcome the technical and environmental challenges it faces, the largest hurdle is the cost of biomass. Competition for biomass from other industries, and the competition for land to produce biomass makes it prices restrictively high for use in ISM [Mandova et al., 2018; Suopajärvi et al., 2017].

2.2.4. CCS

Carbon dioxide capture and storage from ISM is an attractive option for reducing CO_2 emissions as it does not require changes to the furnace operation or structure. However, application of CCS to ISM is more challenging than to power plants. This difficulty is due to the in large part to the multiple off-gas streams spread across the BF-BOF process. Each stream has different chemical composition and generation schedule [IEAGHG, 2013b]. As such, the decision to separately capture CO_2 from each stream or to merge streams is not straightforward and is highly case-dependent. Moreover, many ISM facilities are old, with varying degrees of retrofitting and maintenance. The non-standardized nature of process configurations, combined with the non-uniform nature of the input materials, means that the impurity in the off-gases is variable between ISM facilities. Given the degradative effects of long-term exposure to impurities (e.g., sulfur, iron ions) on amine solvents, utilization of CCS in ISM has a large long-term risk profile. The further issues associated with CCS usage for any industry are also present for ISM (e.g., availability and timing of transport and storage infrastructure). Typical costs for applying CCS to ISM are around \$65-120/t-CO_2, with reductions due to learning effects to \$55/t-CO_2 by 2050 under a robust adoption scenario [Leeson et al., 2017].

2.2.5. Novel production methods

Several novel ISM processes with lower CO_2 emissions than the BF-BOF process are currently under development, with the goal for implementation near the middle of the century. Electrolysis-based ISM removes the need for carbon as a reductant of iron ore, but the net CO_2 emissions are fundamentally dependent on the CO_2 intensity of electricity generation. Hydrogen steelmaking uses H_2 in place of coal or natural gas as the reducing agent for iron ore. Subsequently, the iron is converted to steel in an EAF. Again, the production of H_2 requires substantial energy, so the CO_2 intensity of energy generation still controls the true CO_2 footprint of the process. The issue with these methods is the requirement for low CO_2 electricity above and beyond what is needed for RE to offset fossil fuel-based energy production. For example, the final energy consumption for ferrous metal production in the European Union was 2.05 EJ in 2016 [Eurostat, 2018]. A low emissions pathway would see European Union electricity demand from ISM of 400-500 TWh by 2050 [Wyns et al., 2018]. Given that the European Union produces roughly 10% of global steel, the amount of additional RE required is staggering.

Methods that do not rely heavily on RE involve either process intensification (e.g., HIsarna) or improved recycling of the exhaust gases (top gas recycling: TGR) from the BF furnace such that the full reduction potential of the injected carbon is utilized (e.g., SMART steelmaking) [Hisashige et al.,

2019]. The HIsarna process utilizes a novel reactor design, so is prone to the difficulties of market penetration discussed earlier. The SMART steelmaking process and other systems that can be applied during maintenance operations are more likely to see wide adoption.

2.3. Slag

Slag is the waste stream that results from the combination of impurities in the various inputs and the flux. It is primarily composed of calcium silicates in the case of ironmaking and calcium ferrites in the case of steelmaking, however a large quantity of other elements are ubiquitously present in slag and significantly impact molten and solid phase properties. In the furnace, slag is molten and therefore effectively homogeneous at the macroscopic scale. Slag solidification and cooling occur outside of the furnace and thus represent a potential pathway for engineering intervention. The rate of solidification and cooling of slag fundamentally alters its mineralogy and micromorphology.

2.3.1. Elemental composition

The elemental composition of slag is controlled by ISM operators to maintain desired properties in terms of impurity removal, metals by-pass, heat transfer, furnace protection, and removability from the furnace. However, as the inputs to ISM are naturally occurring materials (ores and coal), there is always some degree of undesired or unexpected inclusions. Typical slags contain on the order of 10-20 elements at detectable concentrations. This imbues molten slag with a complexity that is difficult to completely account for via preemptive engineering. Nevertheless, a large body of research has been undertaken by the ISM field to determine the physical mechanisms, or at least consistent correlations, connecting slag composition to slag characteristics. Due to this concerted effort, a large body of data exists in the literature on extant slag composition.

A review of the literature was performed to evaluate the range of elemental compositions for slags generated in the BF, BOF, and EAF processes. Data from 35 papers covering the period of 1977-2016 representing slag from BF, BOF, and EAF furnaces was aggregated. The relative distribution of each element is shown in **Fig. 2-7**. The compositions are graphed on three ternary diagrams: CaO-SiO_2-FeO, CaO-SiO_2-Al_2O_3, and CaO-MgO-SiO_2 in **Fig. 2-8**.
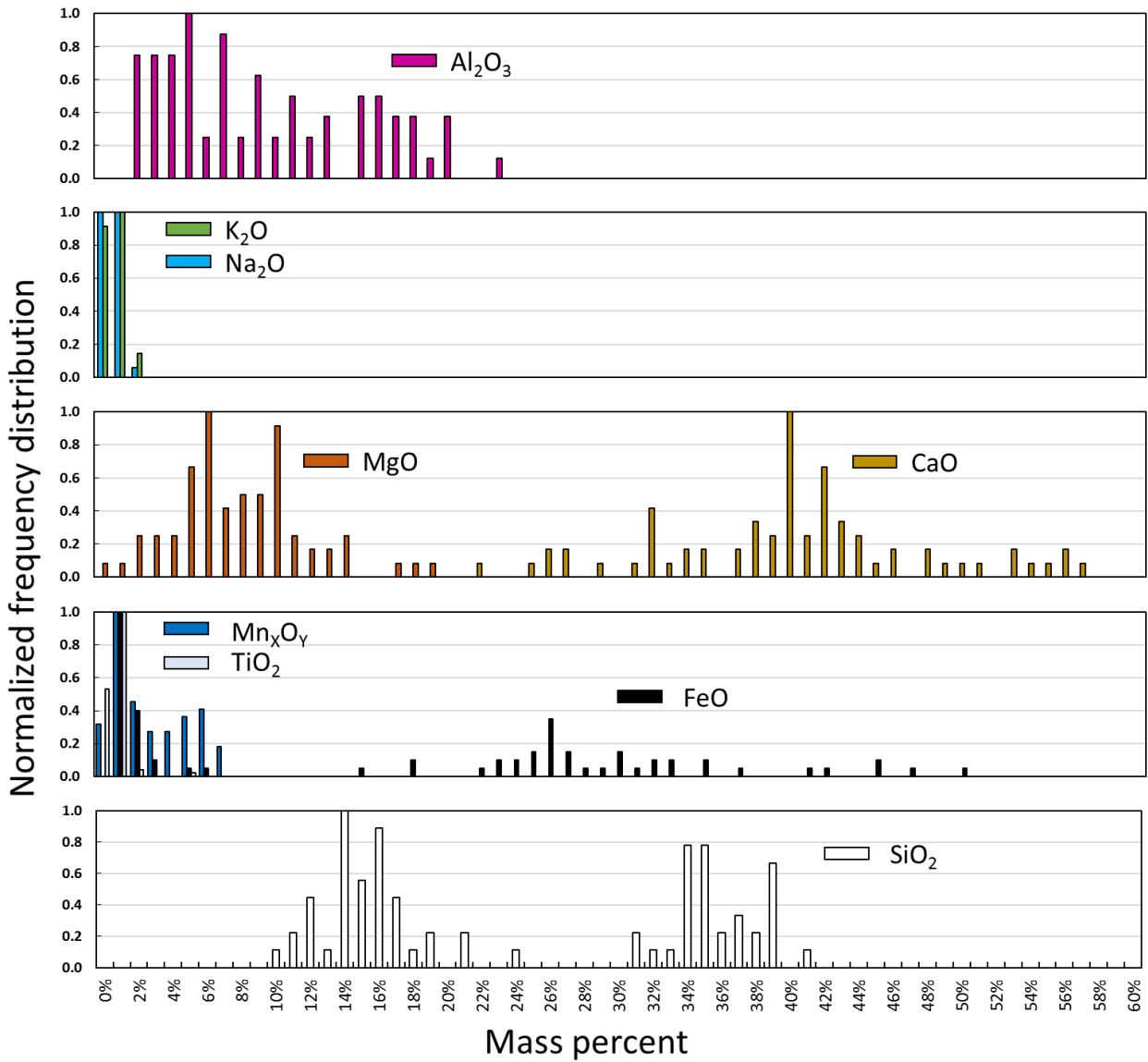
Fig. 2-7. The distribution of elements within extant ISM slags.
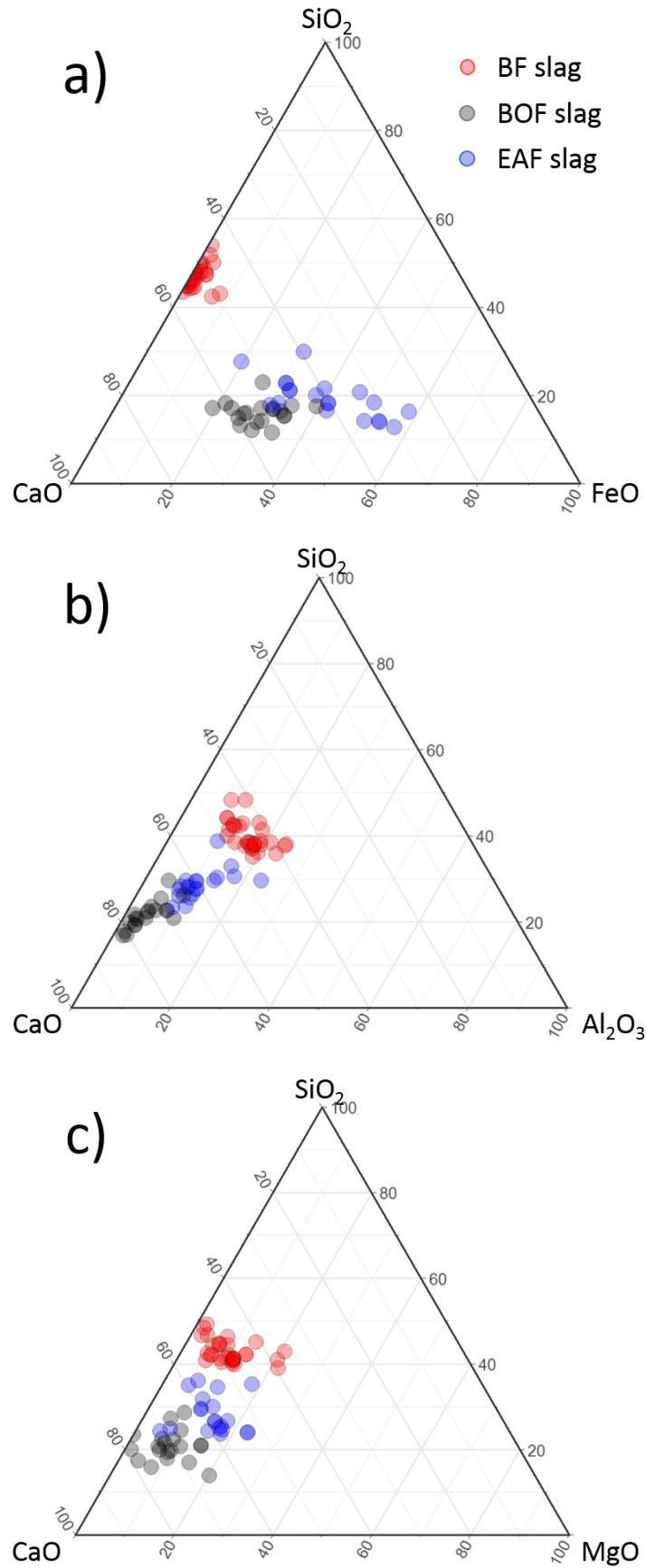
Fig. 2-8. The distribution of elements in solid, extant BF, BOF, and EAF slags in terms of the a) CaO-SiO$_2$-FeO ternary, b) CaO-SiO$_2$-Al$_2$O$_3$ ternary, and c) CaO-SiO$_2$-MgO ternary.

2.3.2. Mineralogical composition

The primary minerals found in slag are defined by the matrix-making compounds of CaO, SiO_2, Fe_XO_Y, MgO, and Al_2O_3. A non-exhaustive mapping of the potential mineral structures developing from these major elements are shown in **Fig. 2-9**. It is important to note that the mineral composition of slag is not purely dictated its elemental composition. The solidification conditions (e.g., solidification rate, oxygen partial pressure, etc.) strongly influence the minerals that emerge from a given molten slag solution. **Figure 2-10** shows the effects of washing and separation on the appearance of a 'homogeneous' batch of desilicating slag; the heterogeneous mineralogical nature of even a single slag batch is indicative of the inherent inhomogeneity. This innate mineralogical complexity in solid slag is quantitatively reinforced by **Fig. 2-11** which plots the range of minerals found is various BOF slags [Gautier, 2015], EAF slags [Mombelli, 2016], and the above-mentioned desilicating slag. A listing of minerals found in XRD analysis of extant BF, BOF, and EAF slags is provided in **Table 2-4**.
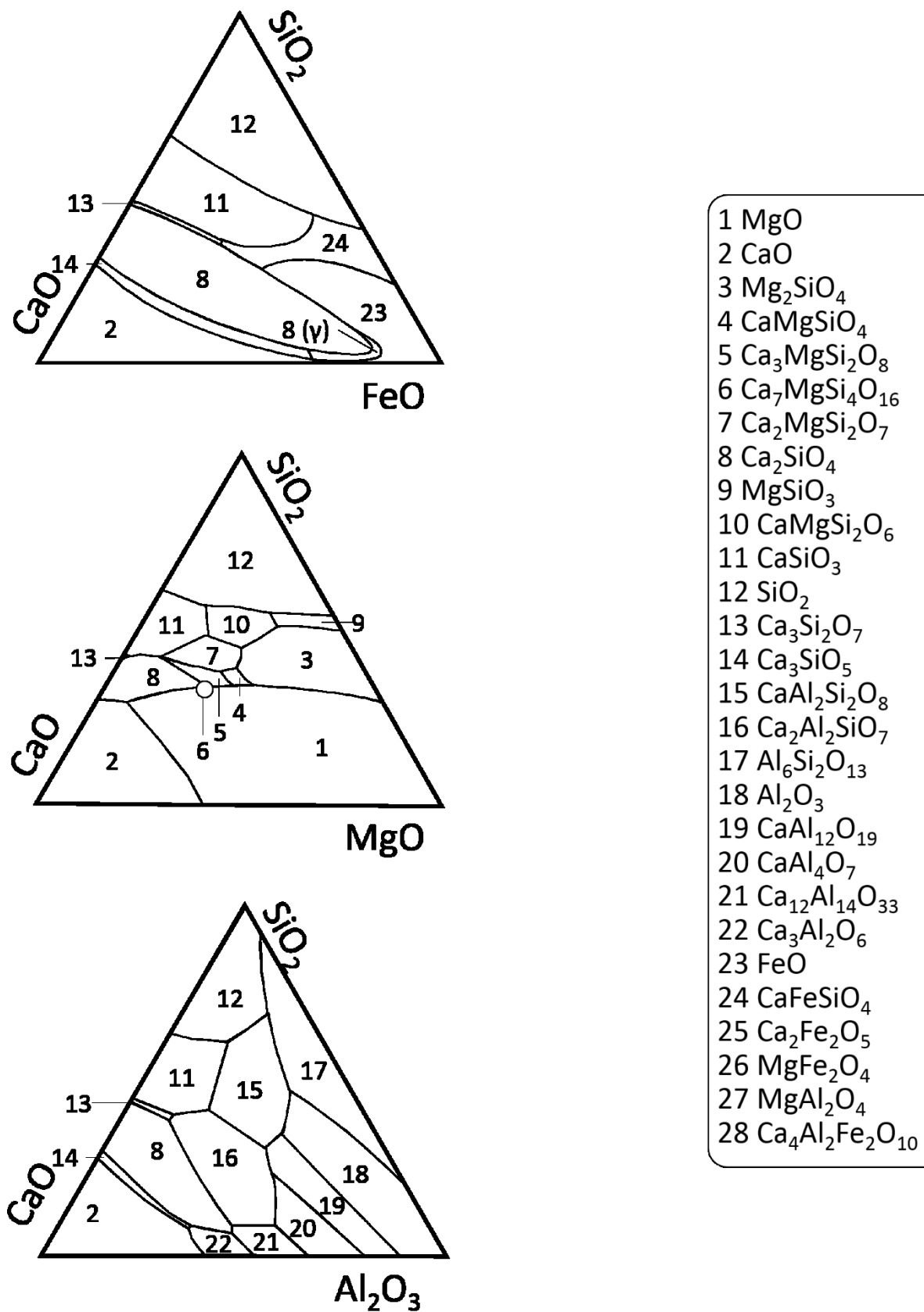
Fig. 2-9. A mapping of the major matrix minerals of solid ISM slag generated from ternary combinations of the primary compounds.

1 MgO
2 CaO
3 Mg_2SiO_4
4 $CaMgSiO_4$
5 $Ca_3MgSi_2O_8$
6 $Ca_7MgSi_4O_{16}$
7 $Ca_2MgSi_2O_7$
8 Ca_2SiO_4
9 $MgSiO_3$
10 $CaMgSi_2O_6$
11 $CaSiO_3$
12 SiO_2
13 $Ca_3Si_2O_7$
14 Ca_3SiO_5
15 $CaAl_2Si_2O_8$
16 $Ca_2Al_2SiO_7$
17 $Al_6Si_2O_{13}$
18 Al_2O_3
19 $CaAl_{12}O_{19}$
20 $CaAl_4O_7$
21 $Ca_{12}Al_{14}O_{33}$
22 $Ca_3Al_2O_6$
23 FeO
24 $CaFeSiO_4$
25 $Ca_2Fe_2O_5$
26 $MgFe_2O_4$
27 $MgAl_2O_4$
28 $Ca_4Al_2Fe_2O_{10}$
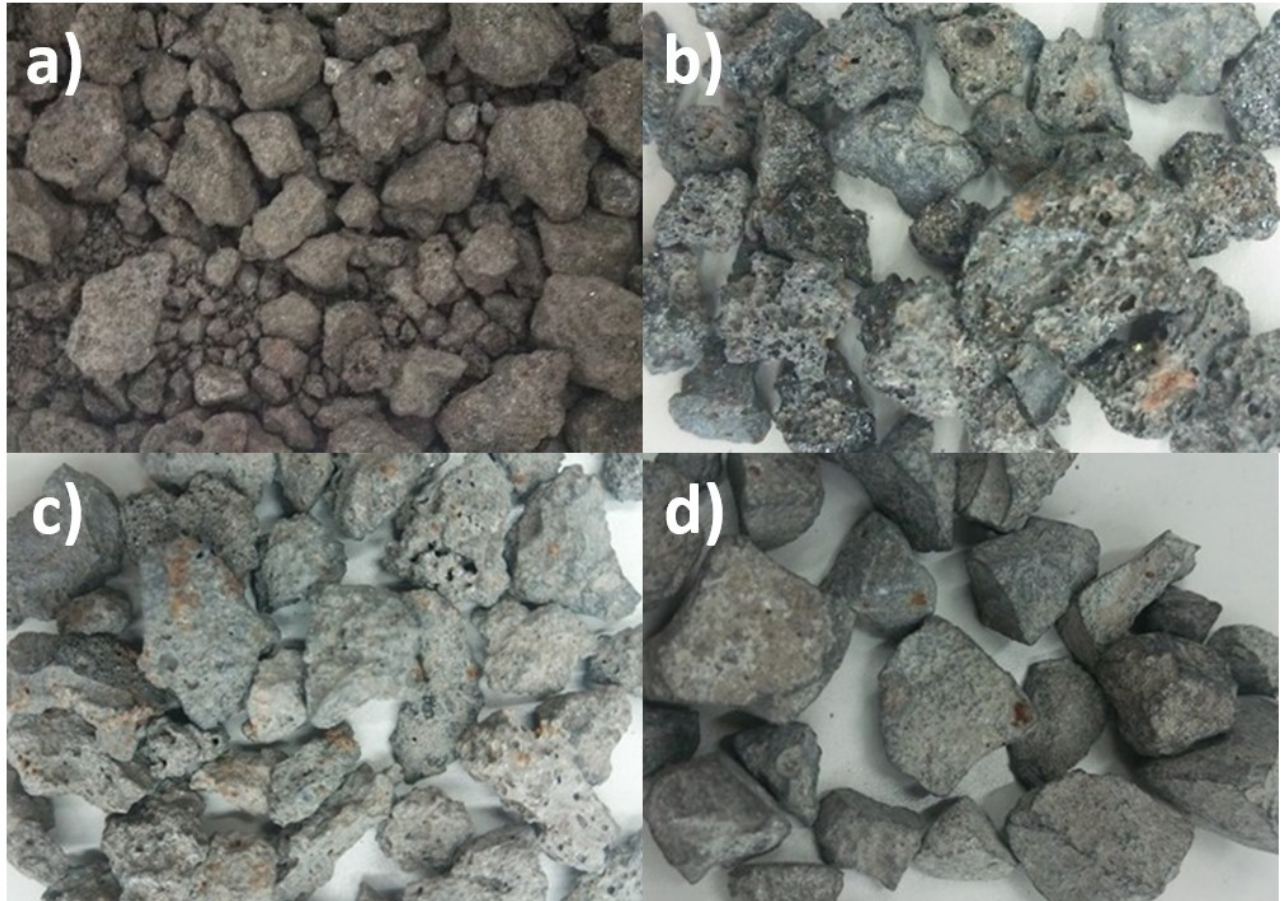
Fig. 2-10. A single batch of commercial desilicating slag a) prior to washing and screening, b) silica matrix slag with metallic iron inclusions after cleaning, c) dicalcium silicate matrix slag with iron oxide inclusions after cleaning, and d) calcium ferrite matrix slag.
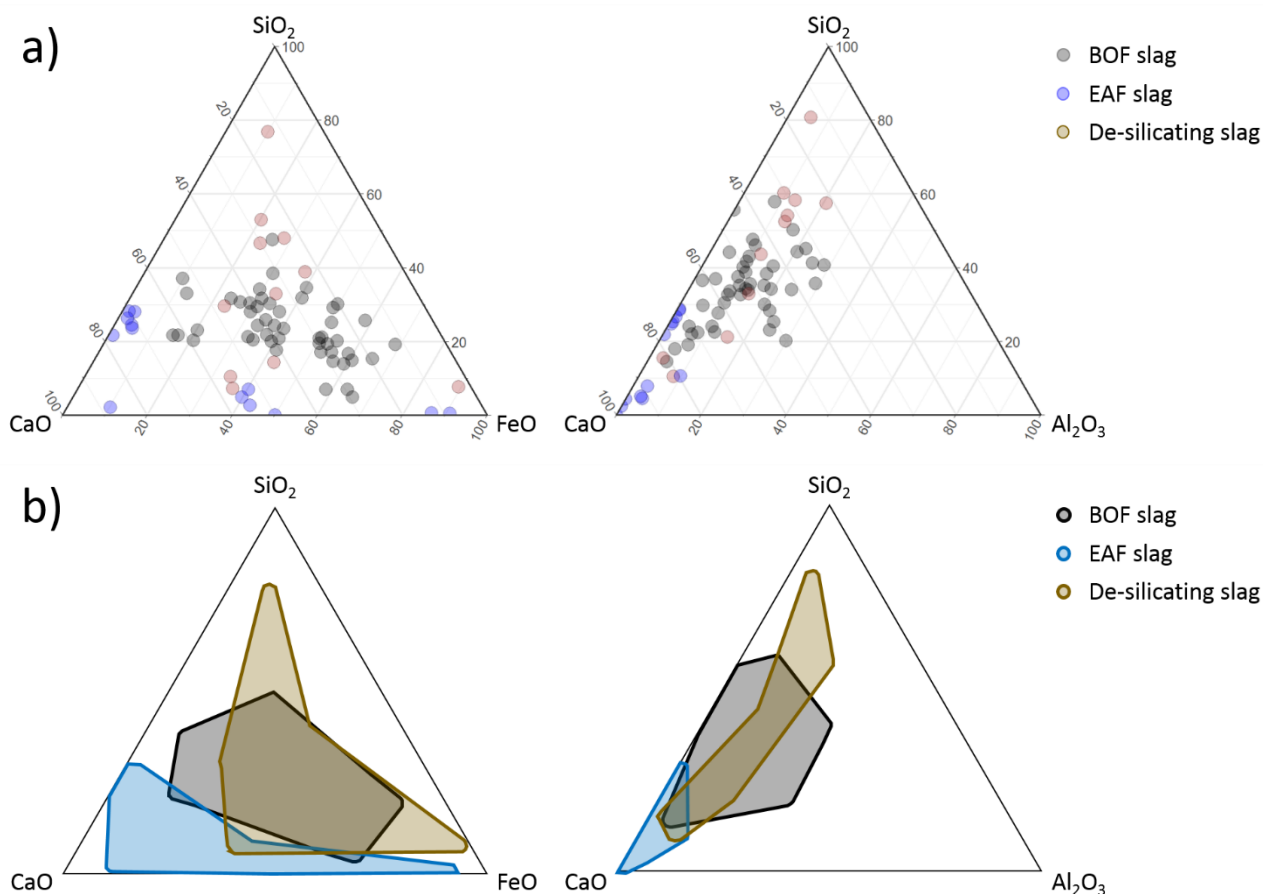
Fig. 2-11. Example ranges of composition found within solid BOF [Gautier et al., 2015], EAF [Mombelli et al., 2016], and De-silicating slag [in house] represented as a) specific sample measurements, and b) as a convex hull of said measurements.

Table 2-4. Minerals found in slag from XRD analysis.

Simple silicates	Mixed silicates	Aluminates	Aluminosilicates	Oxides
SiO_2	$Ca_7MgSi_4O_{16}$	Al_2O_3	Al_2SiO_5	CaO
Ca_3SiO_5	$Ca_3MgSi_2O_8$	$Ca_3Al_2O_6$	$Al_6Si_2O_{13}$	MgO
$CaSiO_3$	$Ca_2MgSi_2O_7$	$Ca_2Al_2O_5$	$Ca_2Al_2SiO_7$	FeO
$Ca_3Si_2O_7$	$Ca_3Fe_2Si_3O_{12}$	$Ca_{12}Al_{14}O_{33}$	$CaAl_2Si_2O_8$	Fe_2O_3
Ca_2SiO_4	$CaMgSiO_4$	$CaAl_{12}O_{19}$	$Ca_3Al_2Si_3O_{12}$	Fe_3O_4
Mg_2SiO_4	$CaMgSi_2O_6$	$MgAl_2O_4$	$Mg_3Al_2Si_3O_{12}$	$Ca_2Fe_2O_5$
$MgSiO_3$	$CaFeSiO_4$	$Ca_4Al_2Fe_2O_{10}$		$MgFe_2O_4$
Fe_2SiO_4				

Other minerals: Phosphorous-containing, sulfur-containing, metallic inclusions, carbonates, replacements with minor cations.

2.3.3. Crystallinity

Slag crystallinity varies from purely amorphous to purely crystalline. Amorphous slag is typically targeted for use as an additive in cement production (so-called 'ground granulated blast furnace slag': GGBS) [Horii et al., 2015]. However, recent work has focused on generating an amorphous structure as part of heat recovery from slag [Kappes and Michels, 2015; Liu et al., 2016; Shigaki et al., 2015]. Regardless of the intended end use, generation of amorphous slag requires rapid cooling from the molten state in order to produce homogeneous nucleation and solidification. Due to the complications of heat transfer, amorphous slag can only be produced at small sizes (typically <2 mm); larger slag will inevitably contain a mixture of crystalline and amorphous phases with the degree of crystallinity increasing with distance from the heat transfer surface (cf. Fig. 6 of Gan et al., 2012). On the other hand, purposefully slow solidification can eliminate the presence of amorphous phases by allowing crystal phases to grow until contacting competing crystals. Additionally, slow solidification implies high temperatures which aids in the expulsion of impurities from the crystal structure and allows for the restructuring of incidentally-generated amorphous slag to crystalline phases.

2.3.4. Grain size distribution

The grain size distribution of slag is dependent on the composition- and undercooling-specific nucleation lag time (τ), liquid phase diffusion, and thermochemical feedbacks (e.g., latent heat of solidification, constitutional supercooling). This complexity makes broadly applicable quantitative estimates of grain size distribution (GSD) difficult. The degree to which slow solidification increases the GSD can be quantified for specific cases where data is available but is difficult to predict for unique compositions and cooling regimes. However, appraisal of the limited data on slag GSD agrees with the general theory and data from other fields [Herlach and Feuerbacher, 1986]; namely, slower solidification produces larger grains. The available data suggests an alteration in GSD of two to three orders of magnitude based on solidification rate (**Fig. 2-12**).
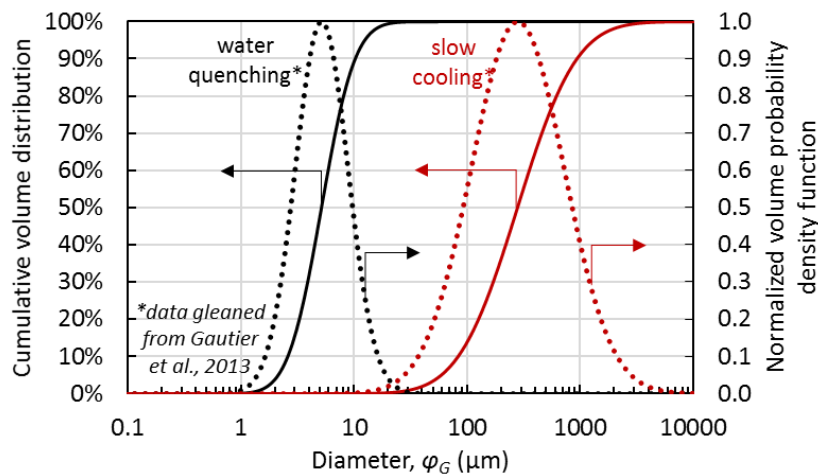
Fig. 2-12. The increase in GSD that accompanies a slower solidification rate.

It is important to note that GSD is compositionally and pathway dependent (i.e., solidification history); therefore, the potential spread in GSD is not necessarily constant across slags. Likewise, equivalent solidification conditions should not be expected to generate equivalent GSD for chemically distinct slags. Example slag GSD gleaned from micrographs in the literature are provided in **Fig. 2-13** [Gautier et al., 2013] and **Fig. 2-14** [Choi and Jung, 2017].
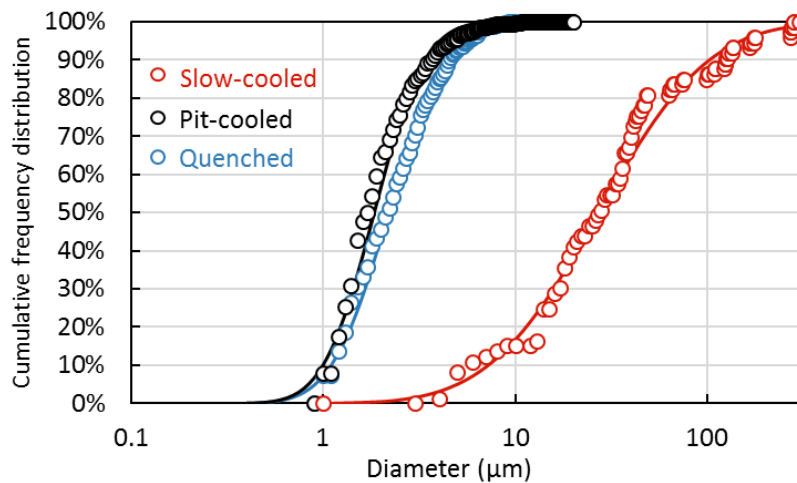
Fig. 2-13. The increase in GSD that accompanies slow solidification and the close matching of empirical GSD data with the lognormal distribution [data gleaned from Gautier et al., 2013].
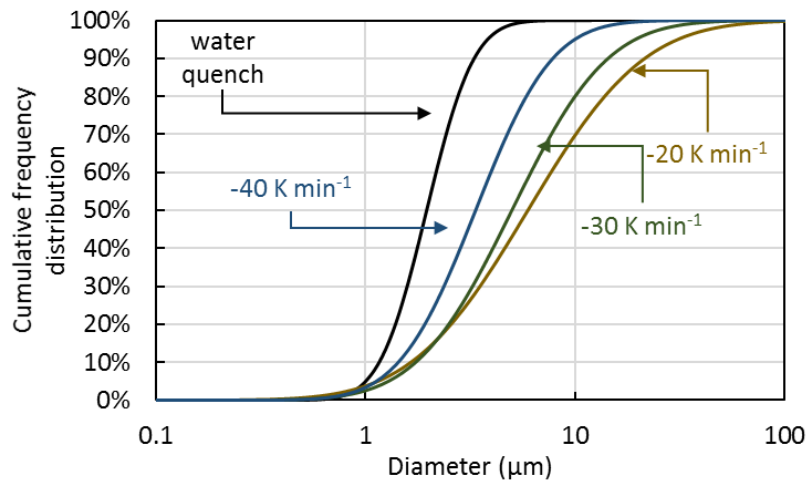
Fig. 2-14. The increasing GSD that accompanies a decrease in solidification rate [data gleaned from Choi and Jung, 2017].

As shown in **Fig. 2-13**, the GSD is well described by the lognormal approximation applied to the mean and standard deviation of the natural logarithm applied to the population of grain diameters [Gegner, 2006; Vaz and Fortes, 1988]. In rapidly solidified slags, the GSD of the dominant phase is often unnoticed due to physical contact with a distinct grain of the same mineralogy; this effect can be overcome by using polarized light in combination with edge detection algorithms [Obara and Kozusnikova, 2007]. Additionally, in slags undergoing intermediate solidification rates, it is necessary to consider intergranular features that result from reaction diffusion phenomenon and constitutional supercooling (cf. Fig. 4(a) of Gautier et al., 2013). Careful examination of 'grains' shows a plethora of minerals distinct from the bulk mineralogy. Therefore, such 'grains' may be regions of distinct mineralogical distributions, not necessarily homogeneous minerals themselves. Precise control of GSD has not yet been demonstrated in the literature.

2.3.5. Particle size distribution

The particle size distribution (PSD) of freshly solidified slag is dependent upon the solidification process employed. Traditional 'pit cooling' generates slag ranging from a few millimeters to 10's of centimeters in diameter. Rapid solidification methods (e.g., water jet impingement, centrifugal cooling) generate slag with a tighter size distribution, usually in the range of hundreds of micrometers to the a few centimeters. Slag processing methods further alter the PSD by impact fractures, abrasion, and thermal fracturing.

Simplification of the PSD into a single distribution is deceptively complicated due to the functionally stochastic nature of particle sizes generated upon fracture [Gilvarry, 1961], the large number of partial and non-fracturing impacts [Morrison and Cleary, 2008], differences in fracturing method [Little et al., 2017], and difficulties surrounding measurement of PSD [Califice et al., 2013]. Despite these complications, PSD in fragmentation can be well approximated by a lognormal distribution applied with the mean and standard deviation of the natural logarithm applied to the population of particle diameters [Åström, 2005; Kolmogorov, 1940]. To generate a synthetic PSD, a connection between the mean and standard deviation of the natural log of the particle diameters is required. A mix of literature data from fresh slag [Huijgen, 2005; Santos et al., 2013] and that generated by ball mills [Kashani et al., 2013; Qi, 2018], and vibrating disk mills [Johnson et al., 2003] was aggregated with in-house fresh slag, ball milled synthetic minerals, and mortar-and-pestle milled synthetic minerals to arrive at the correlation: $\mu = [0.185 \times \sigma] + 0.595$; where μ and σ represent the standard deviation and mean of the natural logarithm of the particle diameters, respectively. Using this correlation, it is possible to generate a hypothetical PSD to match empirical data such as 99% of volume passing a given diameter (X_{V99}) or various population statistics (e.g., volume moment mean diameter: X_{VM}, surface area moment mean diameter: X_{SM}). While an accurate PSD can be determined from direct particle analysis [Vigneau et al., 2000; Đuriš et al., 2016], it is not possible to solve the reverse operation uniquely. In short, calculation of PSD is a trapdoor function. An example of the application of the lognormal method to extant slag and synthetic mineral PSDs is provided in **Fig. 2-15**.
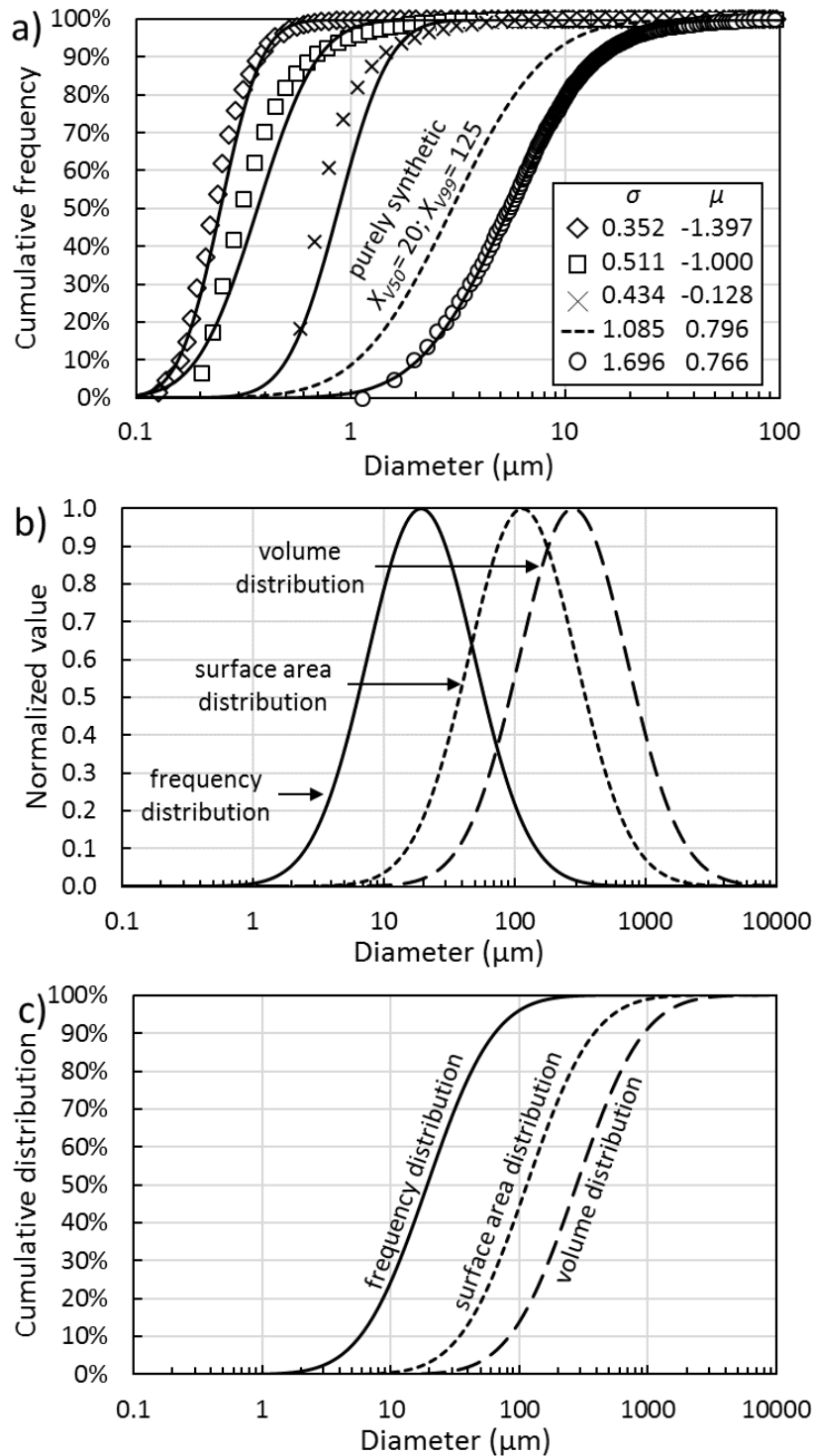
Fig. 2-15. The lognormal approximation of PSD a) compared to empirical data, b) in terms of a normalized probability distribution, and c) in terms of the cumulative distribution.

2.3.6. Porosity

The porosity of slag is affected by the solidification conditions. Rapid solidification methods involving water tend to result in very high porosity slags regardless of the details of the process used [Loncnar et al., 2017], whereas the porosity in air-cooled slags is sensitive to the equipment [Tobo et al., 2014; Kashiwaya et al., 2010]. Porosity is dictated by the exclusion of gas from the solid phase upon phase transition from liquid to solid, followed by nucleation of gas pores, Ostwald ripening of

the pores, and growth along grain boundaries when present. Detailed characterization of slag porosity is not represented in the literature, but porosity development during solidification is well studied in the metal casting industry [Atwood and Lee, 2003]. Broadly speaking, slower solidification leads to larger pore diameters, longer pore networks, lower pore network tortuosity, and less overall porosity [Anovitz and Cole, 2015]. Thus, it may be expected that the surface area associated with porosity is somewhat stable due to negative feedback mechanisms (i.e., high porosity slags with small pore diameters are statistically less connected; highly connected pore networks are typical of lower overall porosity with larger pore diameters). Within the small amount of data reported in the slag literature, slag porosity ranges from nanometers to millimeters [Navarro et al., 2010]. However, most published data is inextricably linked to measurement of total surface area. Because surface area is also dependent on the particle size distribution, and most data is reported from population statistics or laser diffraction measurements, the relative impact of porosity cannot be reliably ascertained.

2.3.7. Embodied CO_2 and reduction potential

The primary CO_2 emissions embodied in slag come from the initial decomposition of (Ca/Mg)-carbonates used as flux. However, there are also emissions due to the heating of flux to its decomposition temperature, the energy input to drive decomposition, mining and transport of flux, and the various pre-charging preparation activities. An additional source of emissions comes from materials that are accidentally entrained in slag; namely ferrous species (**Fig. 2-16**). Ferrous material in slag is generally either metallic iron inclusions in the slag matrix or Fe_XO_Y (possibly in chemical combination with other elements). In either case, the iron in slag has already undergone substantial chemical reduction and thus has a large associated CO_2 intensity.
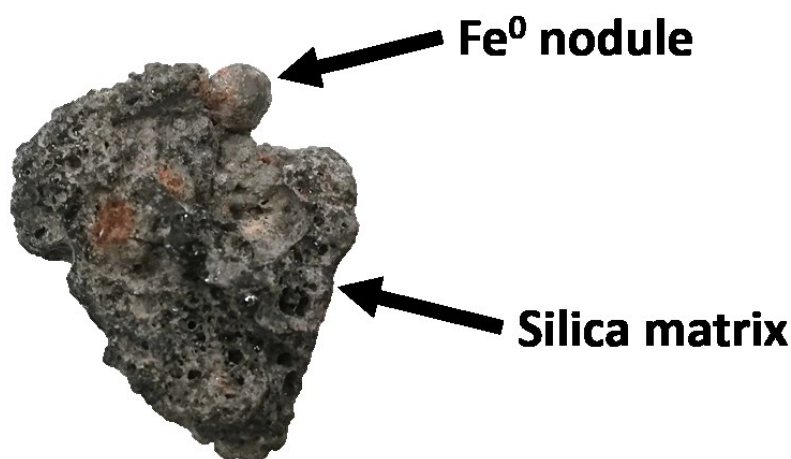
Fig. 2-16. Desilicating slag with and Fe^0 nodule embedded in a silica matrix. Small amounts of iron oxide inclusions are visible as rust.

In most modern ISM operations, effort is taken to recover the metallic iron portion of slag via a series of grinding and magnetic separation steps. As such, the embodied emissions of ironmaking slag are primarily due to the flux material while the Fe_XO_Y portion of steelmaking slag can also carry a substantial amount of embodied CO_2 emissions. Of those emissions, the energy used in heating the flux and ore can potentially be recovered to an extent during the cooling process to ambient temperature. Similarly, the energy required for decomposition of flux can theoretically be somewhat

recovered during the exothermic CO_2 mineralization process. The CO_2 loss from decomposition is obviously undone by the mineralization reaction.

The optimal reuse of freshly generated slag towards CO_2 emissions reductions would clearly recycle both the material and thermal potential of slag to the ISM furnaces. However, trade-offs between heat and material recovery processes makes it prudent to evaluate the relative potential of each towards CO_2 emissions reduction. To provide an unbiased comparison, the CO_2 reduction potential of complete heat recovery and complete material recovery was evaluated.

Slag was simplified to a ternary composition of CaO-SiO_2-Fe^0. Potential heat recovery was determined on a unit mass basis with an assumed initial temperature (T_i) of 1873 K, final temperature (T_f) of 294 K, and heat transfer fluid temperature (T_∞) of 293 K. An estimate of the temperature-dependent specific heat capacity (c_p) of slag was made by separately calculating the c_p of CaO, SiO_2, and Fe^0. The exergy destruction of the heat exchange from the hot slag to the cold air was calculated, ignoring exergy loss to the environment and fluid friction. The recovered energy was converted to CO_2 by way of the CO_2 intensity of the Japanese grid (EI_{CO_2}=0.457 kg CO_2/kWh) [MOE, 2018]. The calculation is summarized by **Eq. (2-5)**.

$$\frac{\text{kg } CO_2 \text{ avoided}}{\text{kg}_{\text{slag}}} = \left\{ \sum_{i}^{SiO_2, CaO, Fe^0} \frac{\text{mol}_i}{\text{kg}_{\text{slag}}} \int_{T_x=T_f}^{T_x=T_i} \left([c_{p,i}T_x - c_{p,i}T_\infty] \left[\frac{T_x - T_\infty}{T_\infty}\right] \right) dT \right\} EI_{CO_2} \qquad (2-5)$$

The CO_2 reduction associated with material recovery was calculated assuming separation into pure CaO, SiO_2, and Fe^0. Calcium oxide was assumed to be used for CO_2 mineralization. No CO_2 reduction was assumed for the recovered SiO_2. Recovered Fe^0 was assumed to be sent to a BOF or an EAF for refining into steel. As this recovered material is offsetting further crude iron production, the CO_2 reduction from FeO recovery was set equivalent to the CO_2 emission from Japanese BF operation (1.61 kg CO_2/ kg crude iron) [Suzuki et al., 2015]. The calculation is summarized by **Eq. (2-6)**.

$$\frac{\text{kg } CO_2 \text{ avoided}}{\text{kg slag}} = \left(\%\text{mass}_{CaO} \left[\frac{\text{molcular weight}_{CO2}}{\text{molecular weight}_{CaO}}\right] \right) + \left(\%\text{mass}_{Fe} \left[\frac{\text{kg}CO_{2,BF}}{\text{kgFe}}\right] \right) \qquad (2-6)$$

Equations (2-5) and **(2-6)** were calculated for every 0.5 mass% variation in composition for the CaO-SiO_2-Fe^0 ternary. The results for heat recovery are displayed in **Fig. 2-17** and the results for material recovery are displayed in **Fig. 2-18.** The ratio of the composition-dependent results indicates whether material or heat recovery is preferable for any composition within the ternary system. This ratio is provided in **Fig. 2-19.** Clearly, heat recovery that eschews material recovery is only advantageous for very high SiO_2 compositions; even then, the relative benefit is small.
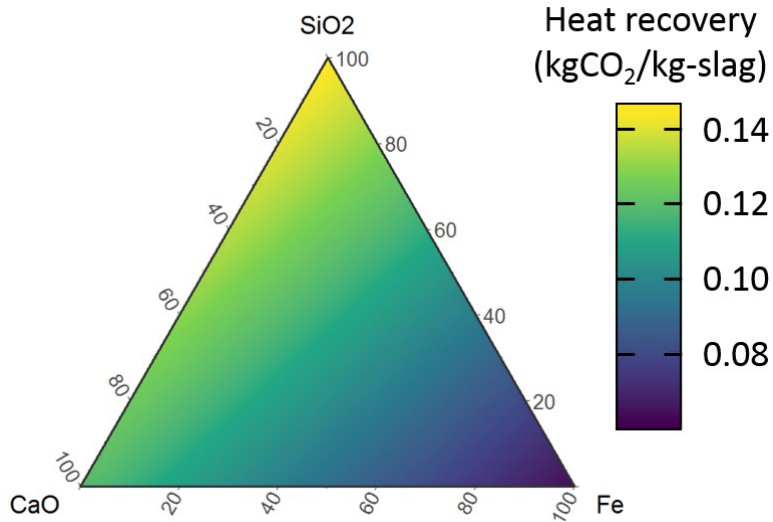
Fig. 2-17. Heat recovery potential from slag in terms of avoided CO₂ emissions.
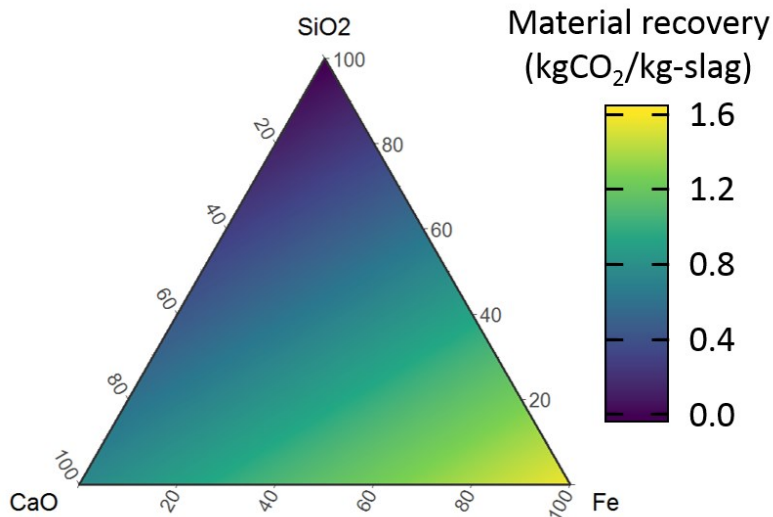
Fig. 2-18. Material recovery potential from slag in terms of avoided CO₂ emissions.
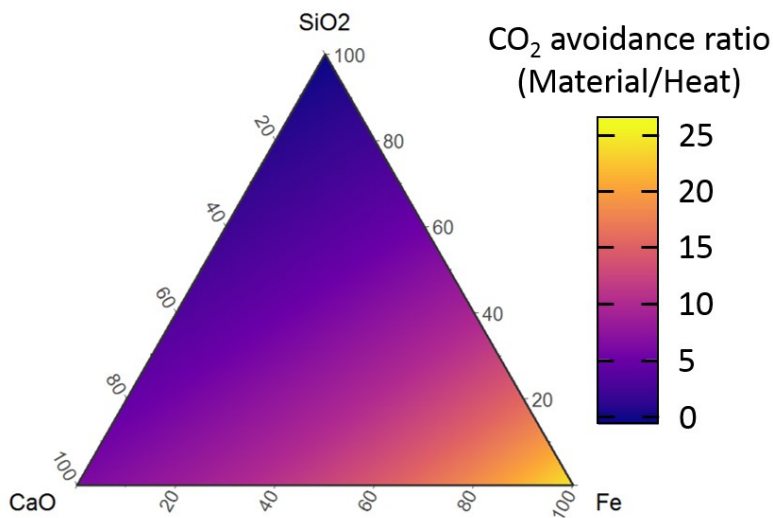
Fig. 2-19. The ratio of CO₂ emissions avoidance of material and heat recovery methods.

When moving from theoretical potential to a realized process, aspects of permanency become prominent. Recovered Fe^0 retains its low oxidation state over periods of years. Recovered CaO, if left in the natural environment, takes up atmospheric CO_2. On the other hand, high quality heat energy is notoriously difficult to store due to the rapid diffusion of heat to the environment. Though this result does not mean there is no role for slag heat recovery methods, the differences in potential impact and temporal stability indicate that material recovery-focused operations are likely preferable to heat recovery-focused methods.

Given that the ISM industry already employs methods for iron recovery from slag, the additional emissions that can be reduced via slag material recovery are due to the mineralization of CO_2 by calcium and magnesium. This potential applies to both legacy slags and those yet to be generated. Carbon dioxide mineralization with future slag represents emissions reductions for the ISM industry. On the other hand, CO_2 mineralization using legacy slag constitutes a negative emission as the embodied CO_2 is already in the atmospheric and oceanic systems. The amount of legacy slag can be estimated by multiplying historical iron and steel production data by the slag generation rate per unit iron and steel [WSA, 2018]. The total CO_2 reduction potential is then determined by multiplying the estimated volume of slag by the range minimum and maximum (Ca+Mg) content in slags of the relevant furnace type. This analysis yields the legacy quantity of slag in **Fig. 2-20a**. This value represents an upper bound of the negative emissions potential as much slag has been reused as an additive in cement production, aggregate in construction, and other such civil works. Nevertheless, the gigatonne scale of the resource means that even partial utilization holds significant potential for CO_2 mineralization. Extending this analysis out to 2100 based on projections of production of iron and steel (Oda et al., 2013; JISF, 2018a; Renforth, 2019) yields the potential CO_2 emissions reduction to the end of the century (**Fig. 2-20b, c**).
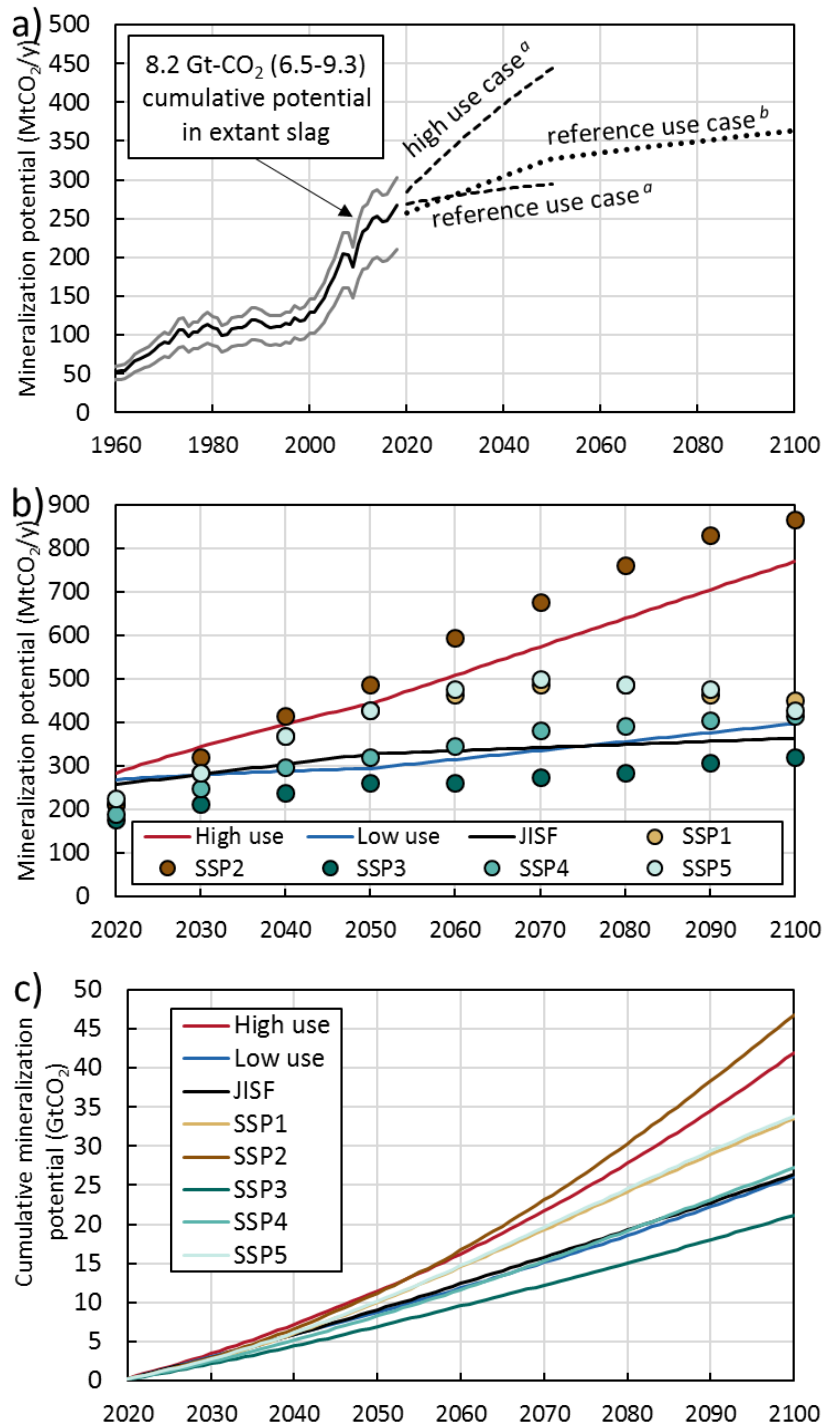
Fig. 2-20. The theoretical a) potential negative emissions from legacy slag (WSA, 2018) and emissions reduction through CO_2 mineralization of legacy and future ISM slag (reference case a: Oda et al., 2013; reference case b: JISF, 2018a), b) the projected emissions reductions based on shared socioeconomic pathways (SSP) from Renforth, 2019, and c) all projections of cumulative emissions reduction to 2100.

The potential moving forward for slag utilization is determined by the quantity of iron and steel produced. Though there are trends of increased scrap utilization, less usage of iron and steel in products and civil works, and replacement of iron and steel by new materials, there is the

counteracting pressure from population increase in developing countries, burgeoning infrastructure in developed countries, and the global need for infrastructure to adapt to climate change. As such, the production of iron and steel is projected to increase 1.6-2.4 times current levels by 2050 [Oda et al., 2013]. Even if novel ISM technologies are realized in that time frame, there are currently no methods proposed that eliminate the need for flux addition. Accordingly, the specific emissions associated with slag production, and the subsequent CO_2 mineralization potential it holds, will not change substantially.

2.4. Slag handling and utilization methods

Even from the start of the 20th century, the potential recovery of valuable materials from slag (i.e., iron) and usage as construction material is evidenced in the literature [Kuehl, 1908; Wood, 1908]. The economic incentive of recovery of entrained iron has led to the common practice of grinding and magnetic separation. Such methods recover upwards of 99% of entrained metallic iron. Concurrently, slag is often repurposed for use as an aggregate or additive in cement production. The preparation process generally involves rapid cooling followed by grinding. However, in the second half of the 20th century, an increasing amount of attention has been paid to the potential for slag to negatively influence the local environment through leaching of heavy metals and alkaline materials into the soil and waterways. Thus, separate from the economic incentive for iron recovery, a necessity to treat slag in such a way to inhibit pollution has become paramount. Whether a regulatory incentive exists is location-dependent, but the avoidance of negative public perception is widely viewed as reason enough to ensure slag is environmentally inert (as evidenced by information provided to the public by ISM companies on their reuse paths of slag). The passivation of slag has been primarily achieved through rapid solidification of slag via various iterations of water- or air-based cooling. Rapid solidification generates an amorphous structure that is less liable to leach alkaline earth and heavy metal species to the environment. Such slag is typically reused as an aggregate in construction. The amorphous (primarily) calcium silicate structure of BF slag is amenable to utilization in cement manufacturing, where it replaces clinker and thereby reduces the overall emissions of cement production. However, only slag of primarily calcium silicate and calcium aluminosilicate composition is suitable for such reuse. In other words, most steelmaking slags cannot be used as a clinker replacement. Moreover, the market for GGBS is smaller than the quantity of ironmaking slag produced, leaving a large portion of slag requiring a different reuse pathway [USGS, 2018]. The current reuse of slag is provided in **Fig. 2-21**.
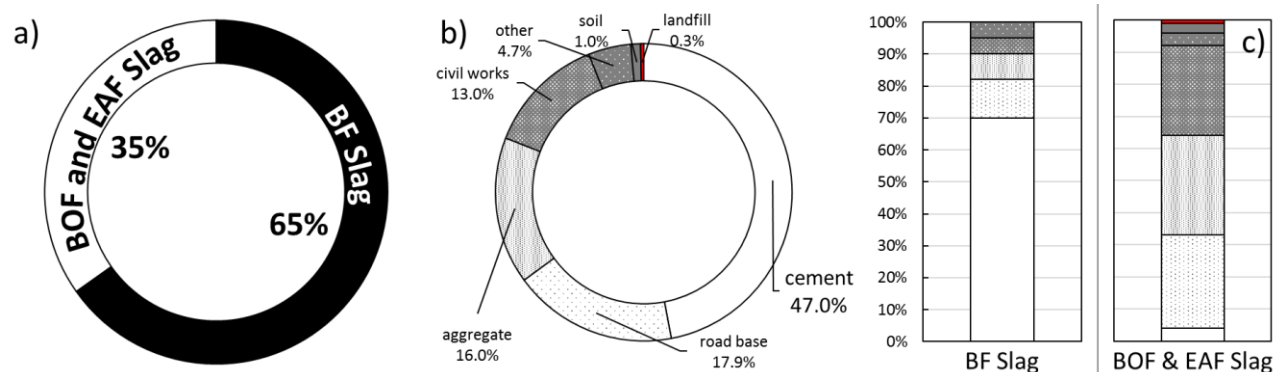
Fig. 2-21. The current distribution of a) slag types, b) usage pathways for all slag, and c) the usage pathways by slag type. All values are in mass percent [Horii et al., 2015].

2.4.1. Thermal recovery pathways

Chapter 2.2.7 quantitatively demonstrated the larger potential of material recovery from slag than heat recovery. Nevertheless, substantial research has gone into heat recovery methods, ostensibly motivated by the desire to retrieve additional value from slags while maintaining extant reuse pathways as aggregate and GGBS. Heat recovery methods can be separated into wet and dry processes. In both instances, slag is converted to a solid phase quickly and the heat is transferred to a working fluid (e.g., air, steam). The low-quality steam generated by wet methods has resulted in the inability to generate power above the needs for the process itself [Zhang et al., 2013]. Dry methods such as a centrifugal solidification and rolled plate solidification have been proven to be able to generate more energy than they consume in operations. Due to operational difficulties, these processes are limited to recovery of sensible from already solidified slag and have additional loses due to production of low temperature air [Nobuyuki et al., 2017]. Moreover, these methods appear to have issues with application to steelmaking slags, which are the primary pathway requiring novel treatment method. A potentially more critical issue is that the optimal slag for heat recovery would be homogeneous with a low thermal conductivity (i.e., an amorphous structure). Generation of homogeneous, amorphous materials inherently results in the loss of potential material recovery. Conversely, material recovery dictates that disparate materials should be generated in large grains to allow for efficient separation (i.e., a heterogeneous, polycrystalline structure). Thus, there is an inherent tradeoff in the slag material properties for material and heat recovery purposes.

2.4.2. Conventional CO_2 mineralization pathways

With the increasing need to implement climate change mitigation methods over the past 30 years, researchers have looked to the mineralization of CO_2 using slag. Thermodynamics indicate that CO_2 reactions with the (Ca,Mg)-silicates of slag are spontaneous and exothermic [Lackner et al., 1995a]. The primary roadblock to implementing such methods are the slow kinetics [Power et al., 2013]. Acceleration of the mineralization kinetics for various solids (e.g., slags, cement kiln dust, flyash, natural silicate minerals) has been investigated through a variety of reaction schemes and equipment [Pan et al., 2012; Romanov et al., 2015; Yuen et al., 2016]. The general process schemes are laid out in **Fig. 2-22**. Many researchers have focused on aqueous leaching of (Ca/Mg) ions from the mother compound prior to conversion to carbonates. To achieve this, some combination of chemicals, mechanical surface activation, high temperatures, high pCO_2, and energy intensive equipment have been employed. However, nearly all studies have failed to perform a full life cycle analysis (LCA) accounting for CO_2 resultant from grinding, chemical production, CO_2 separation, and the like. When

properly analyzed (cf., Zimmermann et al., 2018) the bulk of methods in the literature are net emitters of CO_2 [Ncongwane et al., 2018].
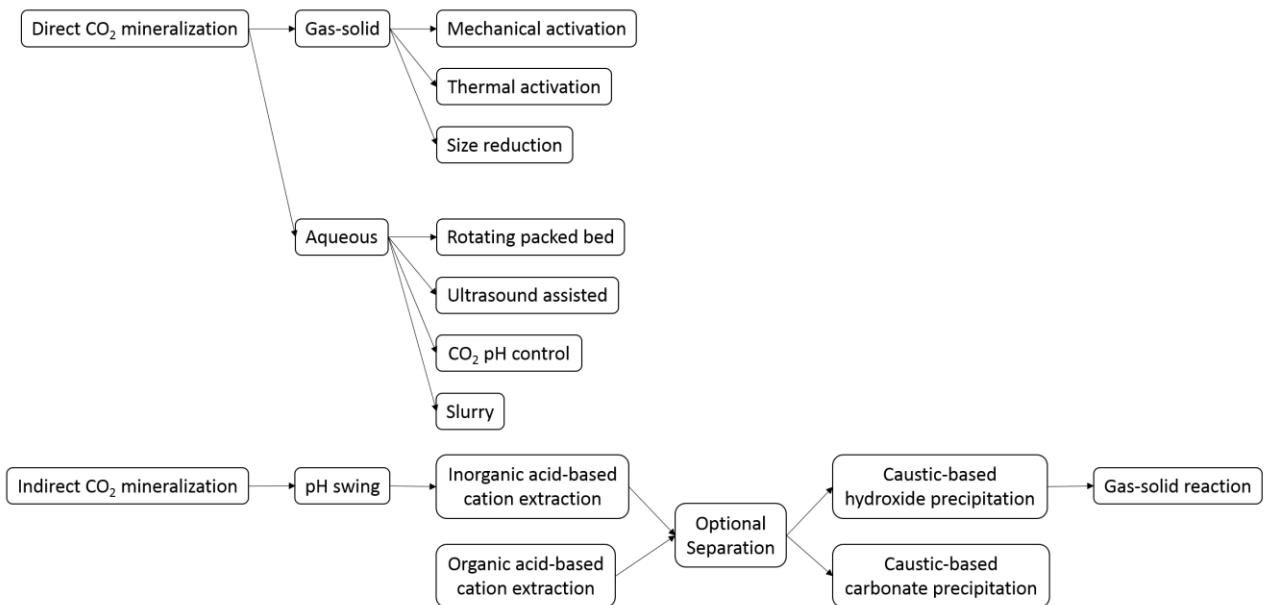
Fig. 2-22. The basic CO_2 mineralization routes from ISM slag in the literature.

As mentioned, gaseous CO_2 mineralization via reaction with solid minerals is not unique ISM slags. In fact, such a method was first proposed in 1990 [Seifritz, 1990], with the first rigorous quantitative assessments of CO_2 mineralization for climate change mitigation emerging from the Los Alamos National Laboratories in the mid 1990's. Researchers initially evaluated direct, gas-solid CO_2 mineralization but found the reaction kinetics to be too slow for industrial application [Butt et al., 1996; Lackner et al., 1995b; Lackner et al., 1997; Kojima et al., 1997]. These initial tests were performed under a pure CO_2 atmosphere, at high temperatures, and in a dry environment. Now it is well established that relative humidity catalyzes gas-solid carbonation reactions of many minerals, including but not limited to: Mg_2SiO_4 [Kwon et al., 2011; Smith et al., 2014; Xie et al., 2017], $Mg_3Si_2O_5(OH)_4$ [Larachi et al., 2010; Veetil et al., 2015], various serpentines [Bhardwaj et al., 2016], MgO and $Mg(OH)_2$ [Fagerlund et al., 2012; Fricker and Park, 2013; Highfield et al., 2016], cementitious materials [Zhang et al., 2017], $CaSiO_3$ [Longo et al., 2015], and CaO and $Ca(OH)_2$ [Nikulshina et al., 2007; Funk and Trettin, 2013]. Moreover, the enhancement from water vapor has been shown to be most prominent at lower temperatures [McKelvy et al., 2001; Manovic and Anthony, 2010]. While this data was being collected, the field of CO_2 mineralization in large part migrated to methods to enhance kinetics via aqueous reactions, thermal/mechanical activation, chemical treatments, and biological enhancement as discussed above.

In addition to the importance of relative humidity, the mineralogy, crystallinity, and geometric effects of slag play a central role in direct gas-solid CO_2 mineralization rate and extent. Gas-solid CO_2 mineralization reactions are well modeled by the Shrinking Core Model (SCM) when the diffusivity of CO_2 through the product layer (D) is known. Along with the previously mentioned papers, there does exist literature on the susceptibility of some common slag minerals to reactions with CO_2 [Ashraf and Olek, 2016; Bodor et al., 2013; Li and Hitch, 2018]. However, explicitly reported D are rare for specific minerals. Consequently, the results from CO_2 mineralization in the literature are difficult to apply

generally. These same deficits are only magnified for amorphous compounds, which are also common to slags. As most mineral feedstocks for CO_2 mineralization (including slag) are heterogeneous, the diffusivity of bulk slag (D_{bulk}) depends on the mineral mélange. An important aspect that has not been quantitatively addressed is the occlusion of reactive minerals from reaction with CO_2 by surrounding unreactive materials ('mineral locking': ML). Neglecting to account for these factors has led the field of CO_2 mineralization to a three-decade malaise with little to show in the way of process improvement. Despite the development of a variety of processing schemes, the only parameter that has generated somewhat consistent positive results is the reduction in the particle size of slag (**Fig. 2-23**) [Bodor et al., 2013; Georgakopoulos et al., 2018; Huijgen, 2005; Rawlins, 2008; Quaghebeur et al., 2015]. Unfortunately, the results displayed in **Fig. 2-23** do not reflect a full life cycle analysis; therefore, the net CO_2 mineralization is undoubtedly less than is reported, though quantitatively unclear.
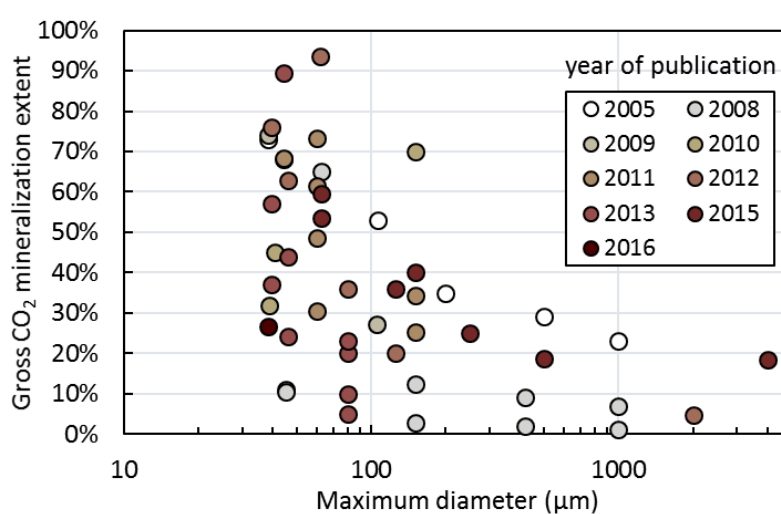
Fig. 2-23. The historical mineralization performance of slag-based direct CO_2 mineralization processes as a function of the maximum particle diameter in the sample.

2.5. Novel slag-based CO₂ mineralization concepts

In contrast to traditional slag-based CO_2 mineralization methods, the methods proposed in this dissertation begin not with solid slag, but with molten slag as it leaves the furnace. By controlling the phase transition from liquid to solid, the mineralogy and micromorphology can be modified to optimize CO_2 mineralization. The molten stage control of slag is divided into two proposed technologies: centrifugal separation and in-container solidification ('MYNA' process: short for Myers-Nakagaki). In-container solidification is followed by solid-state quenching. Both methods end with passive, gas-solid CO_2 mineralization.

In the case of centrifugal separation, slag-based CO_2 mineralization is optional. In place of mineralization, the generated pure (Ca/Mg)O can be returned to the furnace as flux. In such a system, the CO_2 emissions associated with the decomposition of (Ca/Mg)CO_3 are eliminated. Additional CO_2 emissions are avoided by the reduction of fuel needed for heating and decomposition of the flux material. A simplified process flow diagram (PFD) for the centrifugal process is provided in **Fig. 2-24**.
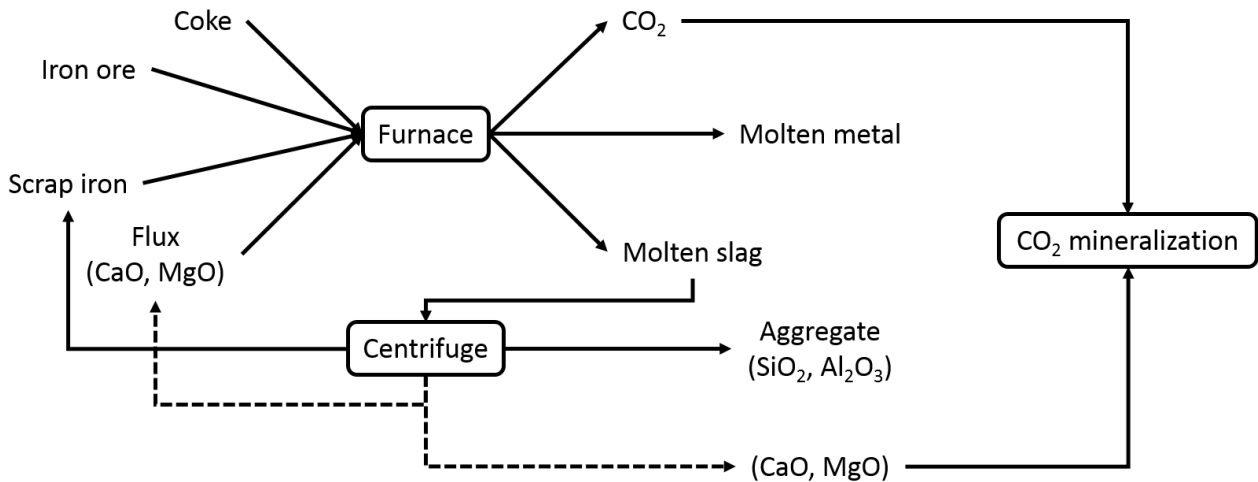
Fig. 2-24. Centrifugal separation process flow diagram.

The PFD for the MYNA process is shown in **Fig. 2-25**. The MYNA process is similar to traditional slag utilization methods in terms of equipment and the timescale of operation. However, the MYNA process differs markedly from traditional methods in the timing and rate of the cooling process. Traditional methods attempt to accelerate the phase transition and decelerate the cooling thereafter. In the MYNA process, the phase transition is decelerated, and the cooling process is accelerated (**Fig. 2-26**). Slow phase transition results in large internal mineral grains while quenching results in efficient mineral fracturing and liberation. These effects combine to enhance the CO_2 mineralization efficiency.
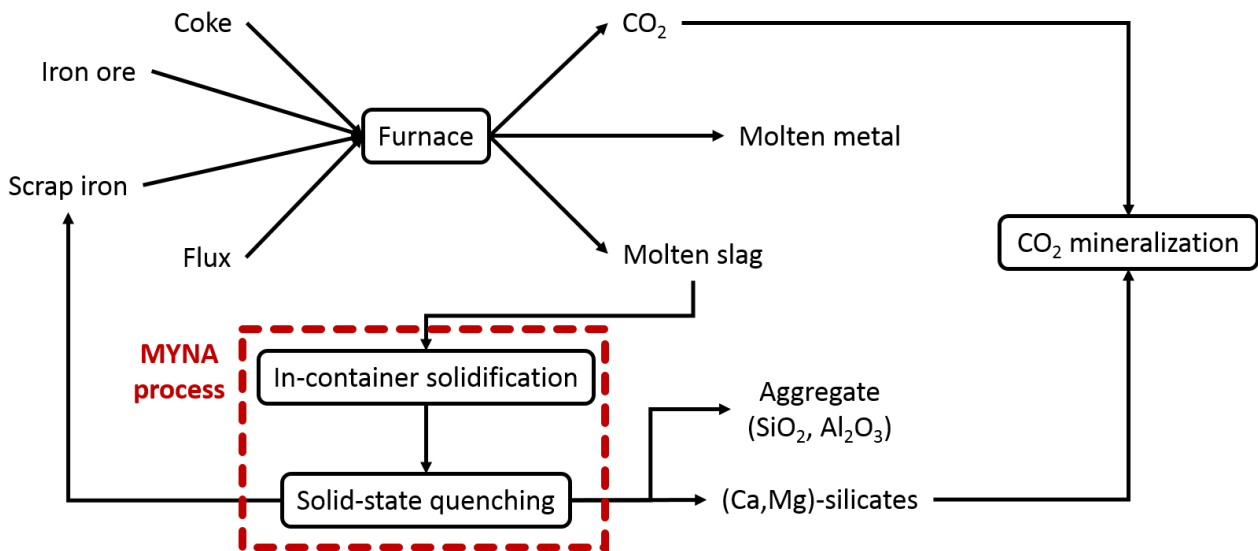
Fig. 2-25. The simplified PFD of the MYNA process.
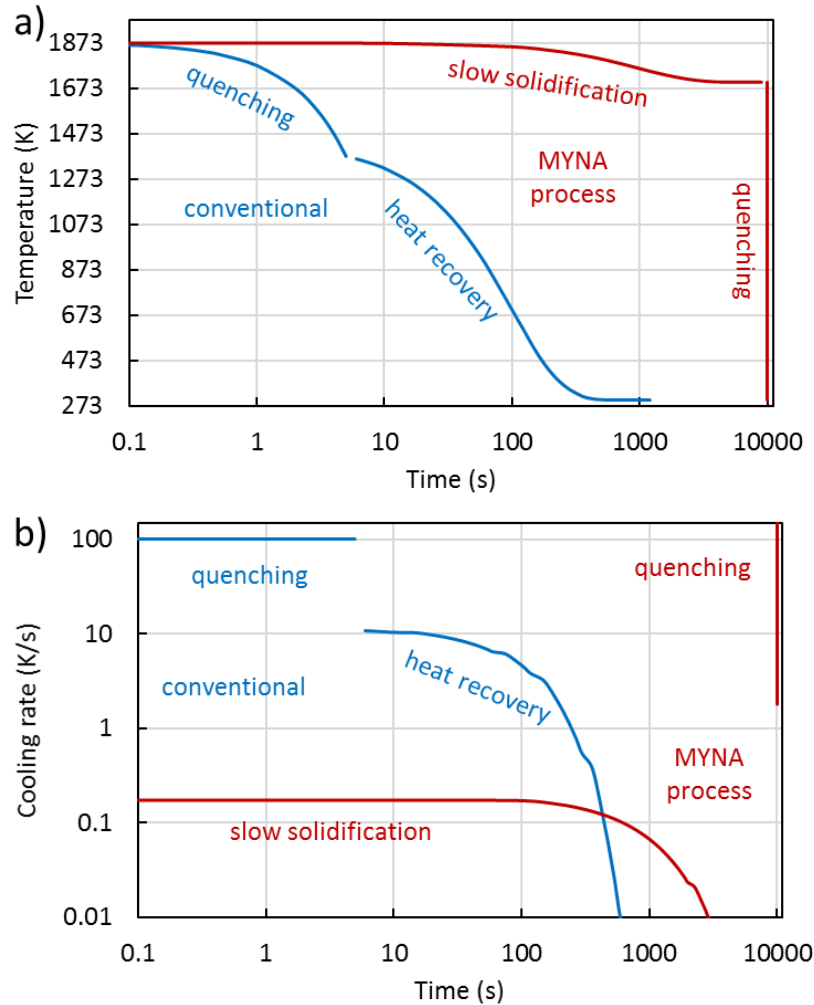
Fig. 2-26. Comparison of the a) timing and b) rate of solidification and cooling in traditional slag treatment methods and the MYNA process.

2.5.1. Solidification control: Centrifuging

Molten slag centrifuging involves the separation of compounds while in the molten state through density differences enhanced by centrifugal force (**Fig. 2-27**). The generated layers of SiO_2, MgO, CaO, Al_2O_3, and Fe_XO_Y (amongst others) undergo solidification due the compositional dependence of the liquidus temperature (T_L). The sharp boundaries between compounds allows for simple, precise separation with CaO, MgO, and Fe_XO_Y being returned to the furnace. Alternatively, CaO and MgO can be used for CO_2 mineralization. Silica, alumina, and other impurities can be sold as aggregates.

The key difficulty in the centrifuge process is obtaining pure phases prior to the solidification of the slag. All slag compositions in ISM are purposefully maintained near low-melting point eutectics for reasons of furnace operation. Separation of slag into its constituent oxides necessarily increases the T_L. Even at the operating temperature of the furnace, pure silica, alumina, calcium oxide and other species will solidify. The only chance to avoid this solidification is to complete separation more quickly than the nucleation lag time (τ).

The overall centrifugal process is displayed in **Fig. 2-28** with the relevant design and calculation methods. Of note is the use of deep neural networks to provide molten slag property estimations

which are used in classical theories and design methods. Extant theories are shown in black text, colored text indicates theories or methods novel to this dissertation.
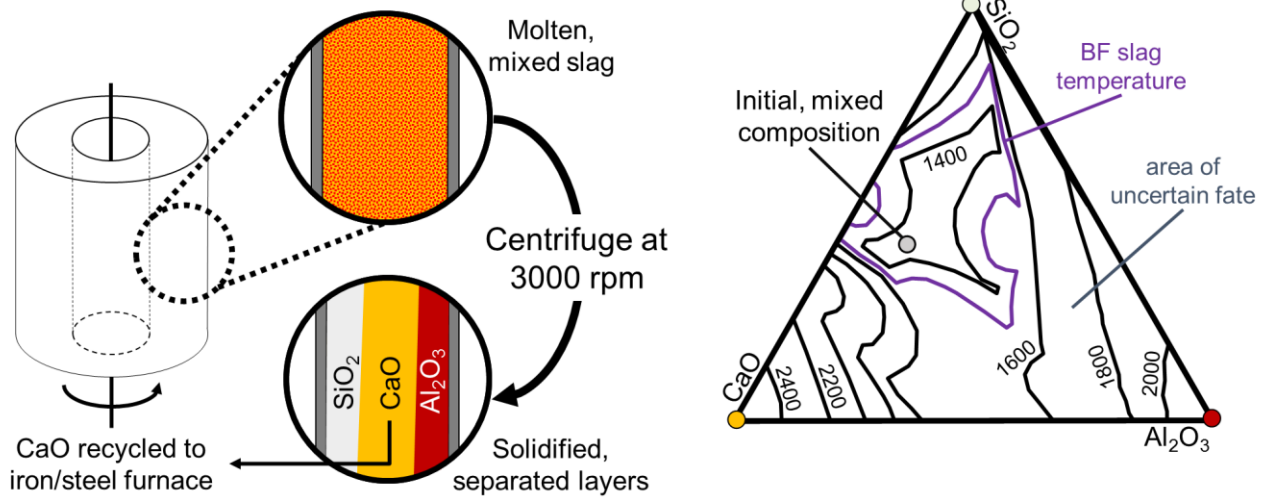
Fig. 2-27. Concept of centrifugal separation of molten slag with the potential for premature solidification as compositionally disparate phases emerge.
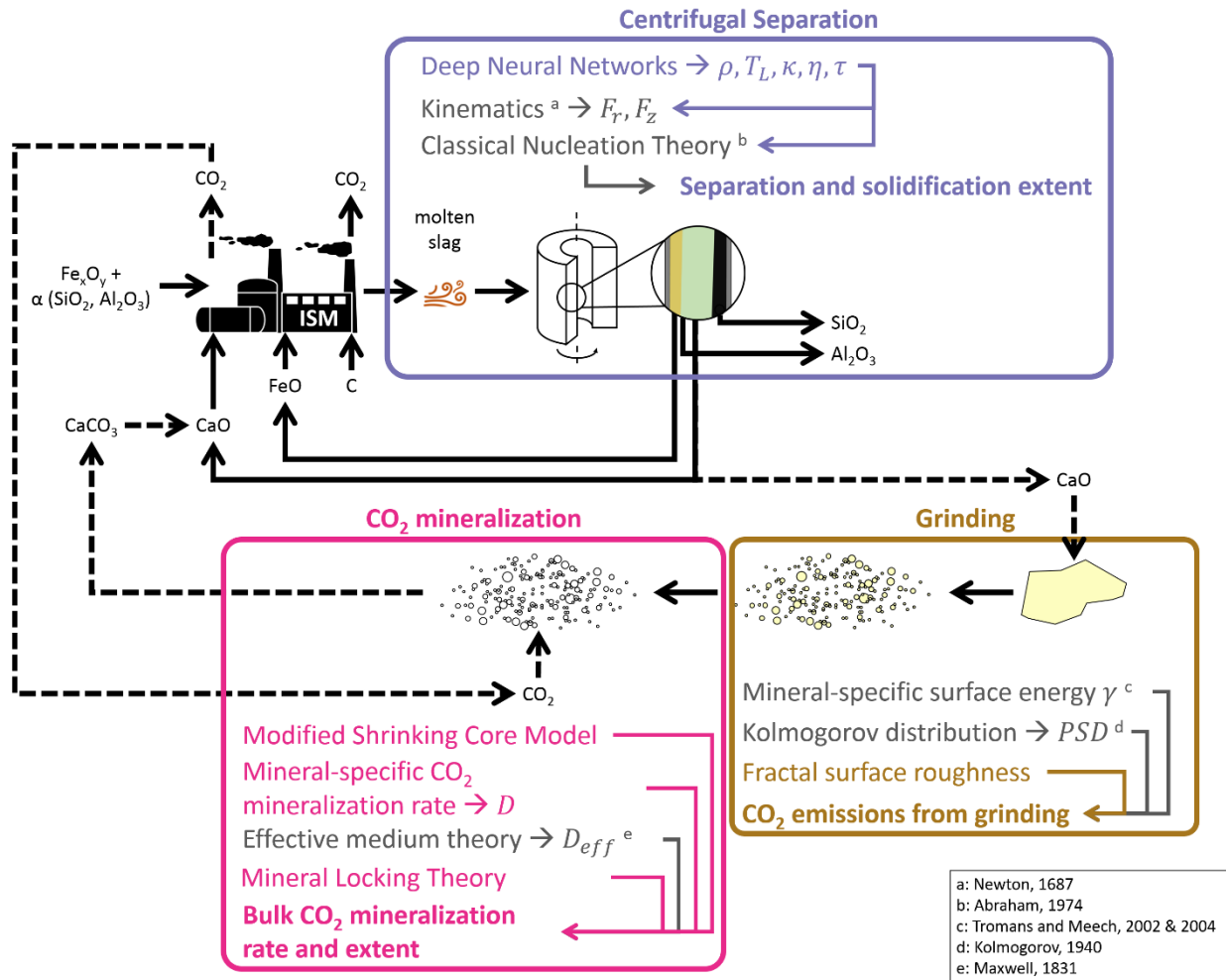
Fig. 2-28. The centrifugal separation and solidification process with the relevant theoretical and methodological constructs for each portion of the process design. Novel methods and theories developed in this dissertation are shown in colored text while black text denotes extant theories.

2.5.2. MYNA process: In-container solidification

The slow solidification regime of the MYNA process is envisioned to occur within a thermally insulated container, similar to the torpedo cars used to transfer molten slags in current ISM facilities. Thermal insulation decelerates the temperature decrease, allowing slag to remain close to its T_L for an extended period. This small undercooling (T_U) reduces concurrent nucleation of disparate species as shown schematically in **Fig. 2-29**. Moreover, the high temperatures promote structural rearrangements and diffusion of compounds in the bulk melt. As a result, the produced slag contains large internal mineral grains of only a few distinct minerals. This relationship between the solidification time, the GSD, and the mineralogical complexity of slag has a strong empirical base (**Fig. 2-30**).
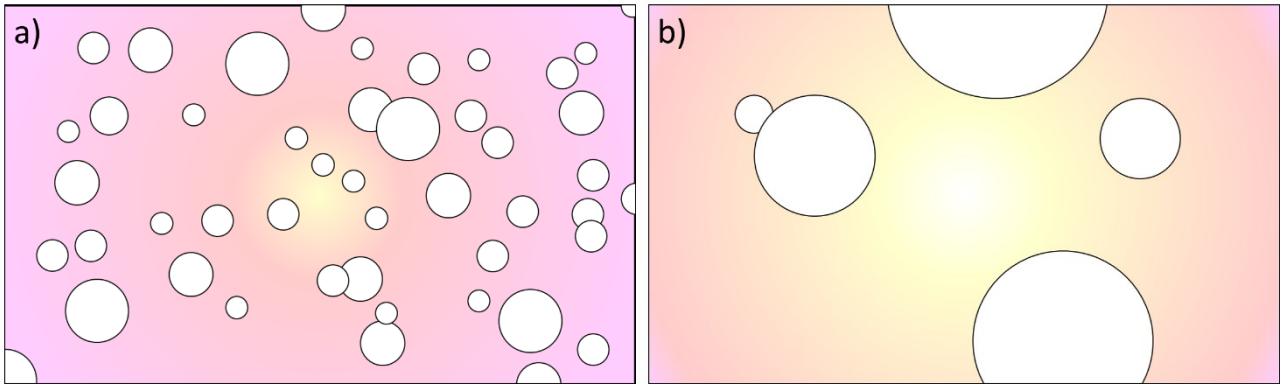
Fig. 2-29. Competition between growing crystal grains that occurs under a) large T_U, resulting in a many concurrent nucleation events (i.e., small GSD), and b) small T_U, resulting in rarer nucleation events and thus more crystal growth prior to interference from other grains (i.e., larger GSD).
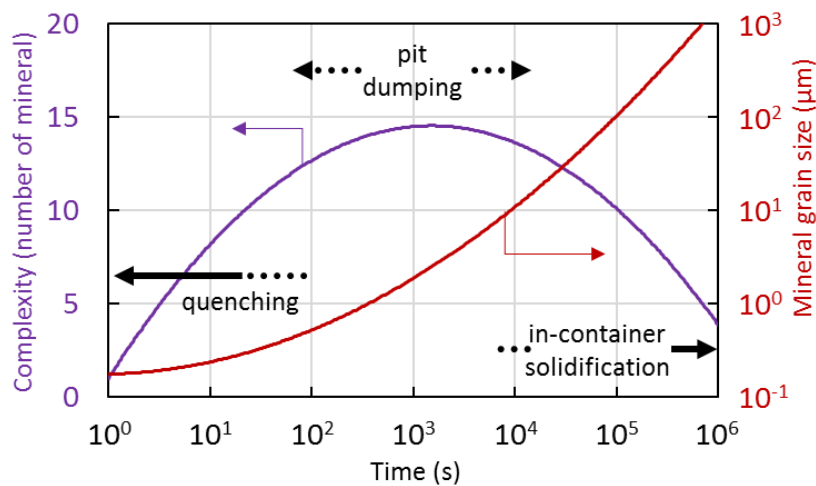
Fig. 2-30. The correlation of mineral variety and GSD with the rate of solidification.

2.5.3. MYNA Process: Solid-state quenching

In the MYNA process, in-container solidification is immediately followed by quenching the solid, hot slag in water. The resultant thermal shock generates internal stresses and microfractures, particularly at grain boundaries between disparate minerals (**Fig. 2-31**). The isotropic nature of thermal stress increases the liberation of disparate compounds compared to traditional grinding processes (**Fig. 2-32**). The liberation of pure compounds from slag allows for Fe^0 and FeO to be returned to the furnace while calcium and magnesium-bearing minerals are used to mineralize CO_2. Full liberation also eliminates the inhibition of CO_2 mineralization by the sequestration of reactive species from the reaction front by neighboring unreactive species (so-called mineral locking: ML).
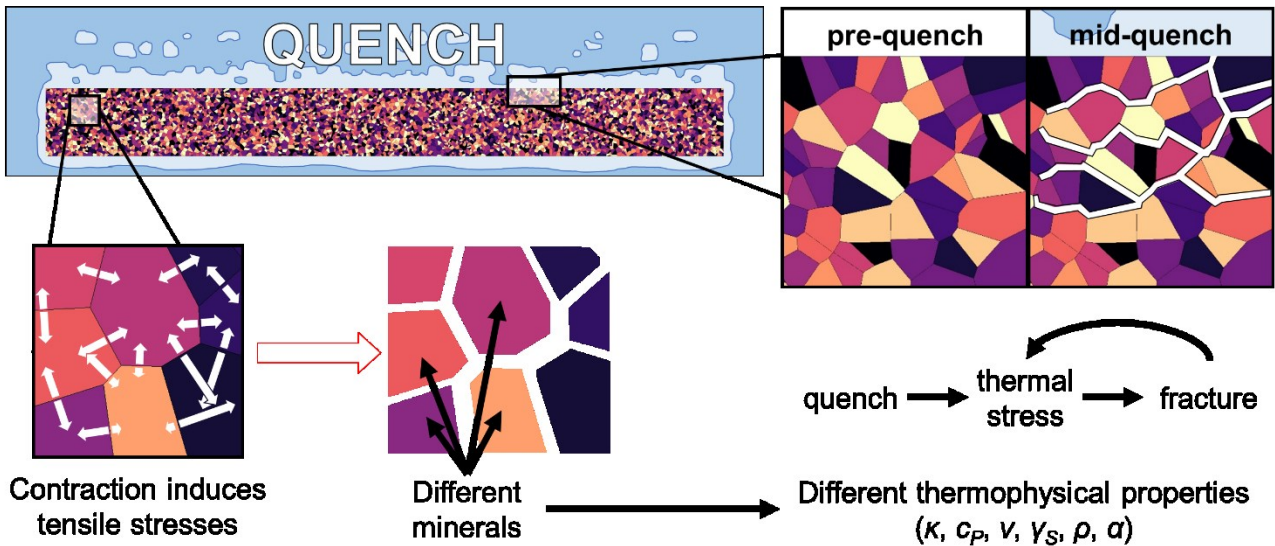
Fig. 2-31. The physical mechanisms underlying mineral liberation via the solid-state quenching process. Thermal stresses are concentrated at grain boundaries, the weakest points in polycrystalline materials, resulting in thermal microfractures at grain boundaries.
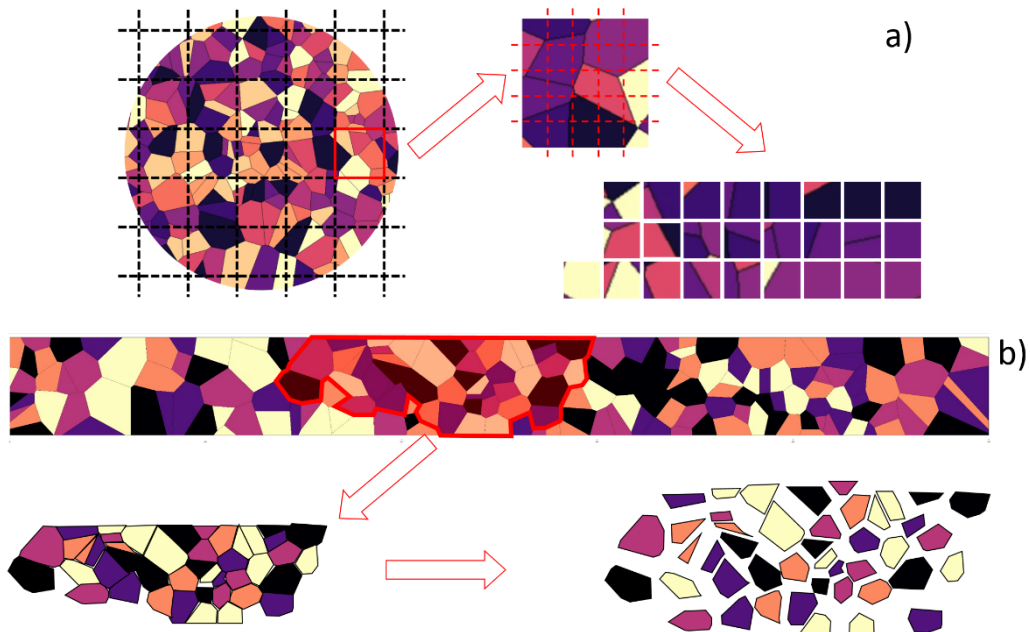
Fig. 2-32. Comparison of the degree of mineral liberation in a) traditional grinding, and b) solid-state quenching. Random fracture planes in traditional grinding results in low liberation compared to the targeted fracturing at grain boundaries that occurs in solid-state quenching.

The overall MYNA process is displayed in **Fig. 2-33** with the relevant design and calculation methods. Of note is the use of deep neural networks to provide molten slag property estimations which are used in classical theories and design methods. Extant theories are shown in black text whole colored text indicates theories or methods novel to this dissertation.
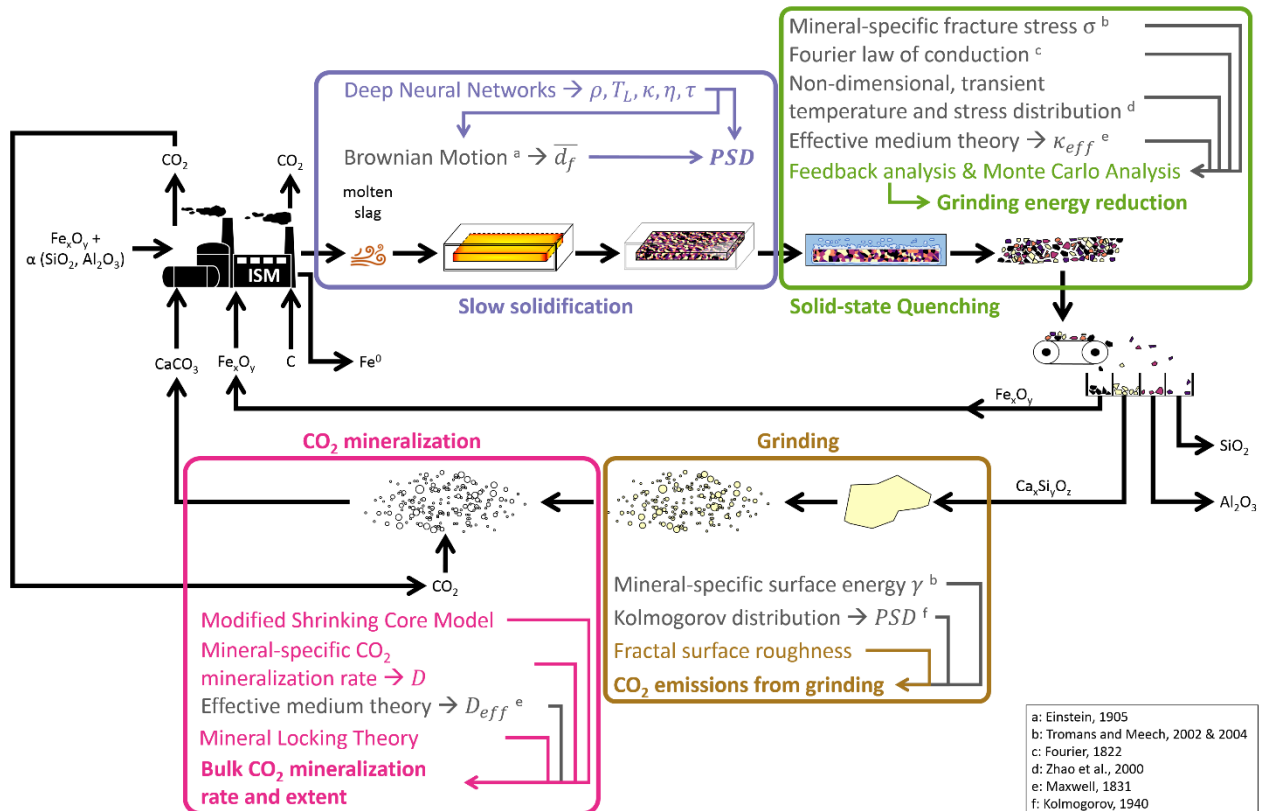
Fig. 2-33. The MYNA process with the relevant theoretical and methodological constructs for each portion of the process design. Methods and theories novel to this dissertation are shown in colored text while black text denotes extant theories.

2.5.4. Passive CO₂ mineralization

Carbon dioxide mineralization using slag is carried out after a prescribed degree of grinding and separation. The amount of grinding is determined by the degree of ML which is a function of mineralogical composition and the GSD. Additionally, some minerals have a very low CO_2 diffusivity through the product layer and thus require grinding to small PSD in order to achieve full CO_2 mineralization on timescales relevant to climate change mitigation. Carbon dioxide mineralization is achieved as a gas-solid reaction without 'enhancement' from chemicals, high temperatures, high pCO₂, or special equipment. The MYNA process is displayed conceptually in **Fig. 2-34**.
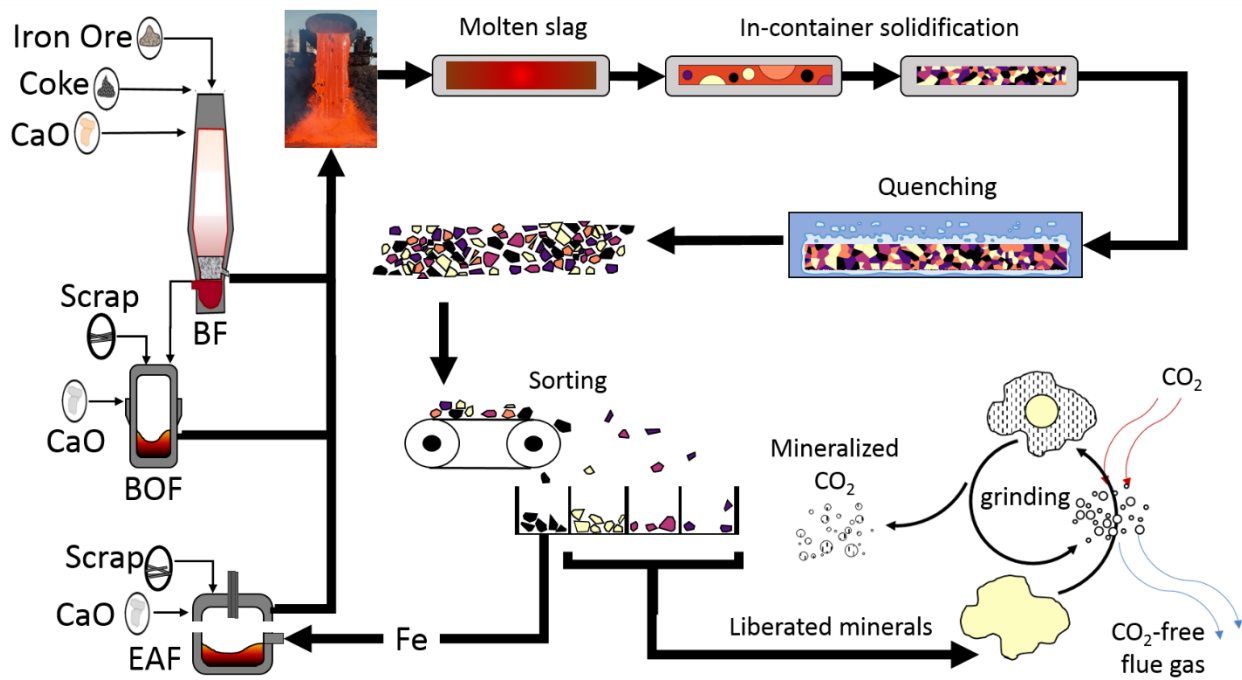
Fig. 2-34. Schematic representation of the MYNA process.

2.5.5. Targeted CO_2 sources

As ISM contains various flue gas streams, and slag can only mineralize ~10% of the total CO_2, determination of optimal gas stream utilization is warranted. Assuming that CCS will eventually be applied to ISM to meet climate change mitigation goals, slag-based CO_2 mineralization should act in a supporting role. In this modality, slag is used to react with the low CO_2 concentration, high volume sinter, reheating furnace, and potentially the lime gas streams. This results in a reduction of the equipment size and operating volume of ~22-26% compared to CCS applied to all ISM off-gases (**Fig. 2-35**) [IEAGHG, 2013]. There is the additional benefit of increasing the concentration of CO_2 in the flue gas streams being sent to CCS which should hypothetically decrease the separation energy penalty.

a) 40%

CO$_2$ concentration (mole%)

24% of CO$_2$:
hot stove

56% of CO$_2$:
power plant

4% of CO$_2$:
lime production

11% of CO$_2$:
coke production

2% of CO$_2$:
sinter production

3% of CO$_2$:
reheating furnace

Share of ISM flue gas volume

b) 30%

CO$_2$ concentration (mole%)

lime, sinter, & reheating CO$_2$
→ mineralization
CCS flue gas:
CO$_2$ conc.=24.3%
91% of CO$_2$
74% of gas volume

all gases merged
CCS flue gas:
CO$_2$ conc.=19.8%
100% of CO$_2$
100% of gas volume

sinter & reheating CO$_2$
→ mineralization
CCS flue gas:
CO$_2$ conc.=24.1%
95% of CO$_2$
78% of gas volume

Share of ISM flue gas volume

Fig. 2-35. The gas volume, CO$_2$ quantity, and CO$_2$ concentration of a) the various flue gases in the ISM process and b) the potential merged gas compositions with and without slag-based CO$_2$ mineralization.

2.6.   Novelty and necessity of this dissertation

This dissertation proposes and develops new methods for reducing CO$_2$ emissions in iron and steelmaking. These new concepts were developed based on a realist's reckoning of the current trajectory of climate change mitigation given historical precedents. Bluntly put, a profitable means for CO$_2$ emissions reduction that requires little-to-no specialized knowledge or equipment is essential for the metallurgical sector. Along those lines, the principles of the proposed technologies are well known since antiquity: centrifugal separation, slow solidification, and gas-solid CO$_2$ mineralization. The novelty of this dissertation is in the merging of available knowledge into new configurations, leveraging of available information in new ways, and generating new data that is of critical importance.

The merger of available knowledge refers to designing a gas-solid CO$_2$ mineralization process from the point at which slag is still molten. The phase transition of molten slag is designed to simplify the separation of solid species, which in turn are ground to optimize the CO$_2$ mineralization reactions, which are conducted at conditions that require the least effort and cost from the ISM operator. In the past, each of these processes has been studied in isolation, resulting in optimized sub-processes, but impractical full-chain methods. What this dissertation provides are low-tech, low cost methods

to operate the full process chain of slag utilization. Though the equipment and processes are simple, the underlying design is made deceptively complex by the complicated composition of molten slag, the solidification-dependence of the mineralogical makeup of solid slag, and the lack of detailed knowledge regarding gas-solid CO_2 mineralization.

To facilitate the design of simple systems, this dissertation leverages deep neural networks to predict molten slag properties. Though property predictions based on thermodynamics are widely used in the metallurgical industry, their accuracy and speed are insufficient for the solution complexity and rapid kinetics of the proposed processes. Deep neural networks were necessary for prediction of molten slag density, viscosity, and nucleation lag time. Access to these property predictions allowed for process design using such classical theories as Newtonian kinematics and Brownian motion.

In the proposed processes, after solidification, the slag undergoes separation, grinding, and reactions with dilute, gaseous CO_2. These processes are well described in isolation by geometrical statistics and the shrinking core model of reaction and diffusion. However, a dearth of mineral-specific data (e.g., critical fracture stress, surface energy, CO_2 diffusivity) and sample-specific data (e.g., particle size distribution, surface roughness) has historically resulted in low reliability estimates of the performance of these sub-processes. This dissertation provides a large portion of the missing mineral-specific data for common slag compounds and establishes modifications to classic theories that accounts for the details of geometric and mineralogical heterogeneity.

The aggregate product of this dissertation are two novel methods that provide a low-cost, low-tech means to reduce CO_2 emissions in ISM. Additionally, the final stage of these methods (i.e., a low-cost, low-tech method of direct gas-solid CO_2 mineralization) is applicable to legacy slag, other solid wastes (e.g., demolition waste), and natural rocks. For the iron and steelmaking industry, these methods can reduce current annual emission by roughly 10% and provide 10's of gigatonnes of CO_2 emissions reduction by the end of the century. Extended to other solid waste streams, these methods may provide an additional 10's of gigatonnes of CO_2 mineralization. If applied to natural rocks, the limit of CO_2 mineralization greatly exceeds the potential CO_2 emissions from the burning of all fossil fuel reserves. Along with the potential scalability of the proposed processes, it is important to note that these processes are profitable and their technical and financial performance increases as the cost of renewable energy and battery technology decreases.

Chapter-specific symbols and abbreviation list

BF: Blast furnace

BOF: Basic oxygen furnace

CAPEX: Capital expense

CCS: CO_2 capture and storage

c_P: Specific heat capacity

DRI: Directly reduced iron

EAF: Electric arc furnace

EOL: End of life

GGBS: Ground granulated blast furnace slag

GSD: Grin size distribution

ISM: Iron and steelmaking

LCA: Life cycle analysis

LiB: Lithium ion battery

ML: Mineral locking

MYNA method: In-container solidification with solid-state quenching

NG: Natural gas

NET: Negative emission technology

OPEX: Operating expense

pCO_2: Partial pressure of CO_2

PCC: Post-combustion capture

PFD: Process flow diagram

PSD: Particle size distribution

RE: Renewable energy

Solar PV: Solar photovoltaic

T_L: Liquidus temperature

T_U: Undercooling

τ: Nucleation lag time

References

Abraham, F., 1974. Homogeneous nucleation theory: the pretransition theory of vapor condensation.

Almemark, M. and Hallberg, L., 2012. Environmental Potential Evaluation The Steel Eco-Cycle Programme Phase 1+2 December 2012. The Swedish Foundation for Scientific Environmental Research.

Alvarez, R.A., Zavala-Araiza, D., Lyon, D.R., Allen, D.T., Barkley, Z.R., Brandt, A.R., Davis, K.J., Herndon, S.C., Jacob, D.J., Karion, A. and Kort, E.A., 2018. Assessment of methane emissions from the US oil and gas supply chain. Science, pp.186-188.

Anovitz, L.M. and Cole, D.R., 2015. Characterization and analysis of porosity and pore structures. Reviews in Mineralogy and geochemistry, 80(1), pp.61-164.

Arens, M., Worrell, E., Eichhammer, W., Hasanbeigi, A. and Zhang, Q., 2017. Pathways to a low-carbon iron and steel industry in the medium-term–the case of Germany. Journal of Cleaner Production, 163, pp.84-98.

Ashraf, W., Olek, J., 2016. Carbonation behavior of hydraulic and non-hydraulic calcium silicates: potential of utilizing low-lime calcium silicates in cement-based materials. J. Mater. Sci. 51, 6173-6191.

Åström, J.A., 2006. Statistical models of brittle fragmentation. Advances in Physics, 55(3-4), pp.247-278.

Atwood, R.C. and Lee, P.D., 2003. Simulation of the three-dimensional morphology of solidification porosity in an aluminium–silicon alloy. Acta materialia, 51(18), pp.5447-5466.

Bale, C.W., Bélisle, E., Chartrand, P., Decterov, S.A., Eriksson, G., Gheribi, A.E., Hack, K., Jung, I.H., Kang, Y.B., Melançon, J., Pelton, A.D., Petersen, S., Robelin, C., Sangster, J., and Van Ende, M-A. 2016. FactSage Thermochemical Software and Databases. Calphad, 54, pp.35-53.

Barca, C., Gérente, C., Meyer, D., Chazarenc, F. and Andrès, Y., 2012. Phosphate removal from synthetic and real wastewater using steel slags produced in Europe. Water research, 46(7), pp.2376-2384.

Barra, M., Ramonich, E.V. and Munoz, M.A., 2001. Stabilization of soils with steel slag and cement for application in rural and low traffic roads. In Beneficial Use of Recycled Materials in Transportation ApplicationsUniversity of New Hampshire, Durham.

Bhardwaj, R., van Ommen, J.R., Nugteren, H.W., Geerlings, H., 2016. Accelerating natural CO2 mineralization in a fluidized bed. Ind. Eng. Chem. Res. 55, 2946-2951.

Bodor, M., Santos, R.M., Kriskova, L., Elsen, J., Vlad, M. and Van Gerven, T., 2013. Susceptibility of mineral phases of steel slags towards carbonation: mineralogical, morphological and chemical assessment. European Journal of Mineralogy, 25(4), pp.533-549.

Butler, B.C.M., 1977. Al-rich pyroxene and melilite in a blast-furnace slag and a comparison with the Allende meteorite. Mineral. Mag, 41, pp.493-499.

Butt, D.P., Lackner, K.S., Wendt, C.H., Conzone, S.D., Kung, H., Lu, Y.C., Bremser, J.K., 1996. Kinetics of thermal dehydroxylation and carbonation of magnesium hydroxide. J. Am. Ceram. Soc. 79, 1892-1898.

Califice, A., Michel, F., Dislaire, G. and Pirard, E., 2013. Influence of particle shape on size distribution measurements by 3D and 2D image analyses and laser diffraction. Powder technology, 237, pp.67-75.

Chaurand, P., Rose, J., Domas, J. and Bottero, J.Y., 2006. Speciation of Cr and V within BOF steel slag reused in road constructions. Journal of Geochemical Exploration, 88(1-3), pp.10-14.

Chaurand, P., Rose, J., Briois, V., Olivi, L., Hazemann, J.L., Proux, O., Domas, J. and Bottero, J.Y., 2007. Environmental impacts of steel slag reused in road construction: A crystallographic and molecular (XANES) approach. Journal of Hazardous Materials, 139(3), pp.537-542.

Choi, M.W. and Jung, S.M., 2017. Crystallization behavior of melted BOF slag during non-isothermal constant cooling process. Journal of Non-Crystalline Solids, 468, pp.105-112.

Daehn, K.E., Cabrera Serrenho, A. and Allwood, J.M., 2017. How will copper contamination constrain future global steel recycling?. Environmental Science & Technology, 51(11), pp.6599-6606.

Das, B., Prakash, S., Reddy, P.S.R. and Misra, V.N., 2007. An overview of utilization of slag and sludge from steel industries. Resources, conservation and recycling, 50(1), pp.40-57.

DeCicco, J.M. and Schlesinger, W.H., 2018. Opinion: Reconsidering bioenergy given the urgency of climate protection. Proceedings of the National Academy of Sciences, 115(39), pp.9642-9645.

De Windt, L., Chaurand, P. and Rose, J., 2011. Kinetics of steel slag leaching: batch tests and modeling. Waste management, 31(2), pp.225-235.

Douglas, G.B., Wendling, L.A. and Coleman, S., 2012. Productive use of steelmaking by-product in environmental applications (I): Mineralogy and major and trace element geochemistry. Minerals Engineering, 35, pp.49-56.

Douglas, E. and Zerbino, R., 1986. Characterization of granulated and pelletized blast furnace slag. Cement and concrete research, 16(5), pp.662-670.

Drizo, A., Comeau, Y., Forget, C. and Chapuis, R.P., 2002. Phosphorus saturation potential: a parameter for estimating the longevity of constructed wetland systems. Environmental science & technology, 36(21), pp.4642-4648.

Drizo, A., Forget, C., Chapuis, R.P. and Comeau, Y., 2006. Phosphorus removal by electric arc furnace steel slag and serpentinite. Water Research, 40(8), pp.1547-1554.

Đuriš, M., Arsenijević, Z., Jaćimovski, D. and Radoičić, T.K., 2016. Optimal pixel resolution for sand particles size and shape analysis. Powder Technology, 302, pp.177-186.

Einstein, A., 1905. Investigations on the Theory of the Brownian Movement. Ann. der Physik.

Emi, T., 2015. Steelmaking technology for the last 100 years: toward highly efficient mass production systems for high quality steels. ISIJ International, 55(1), pp.36-66.

Enkvist, P.A. and Klevnas, P., 2018. The Circular Economy–A Powerful Force for Climate Mitigation: Transformative Innovation for Prosperous and Low-Carbon Industry. Material Economics Sverige AB: Stockholm, Sweden.

Eurostat, 2018. Energy Balance - May 2018 edition. [online] https://ec.europa.eu/eurostat/web/energy/data/energy-balances.

Fagerlund, J., Highfield, J., Zevenhoven, R., 2012. Kinetics studies on wet and dry gas–solid carbonation of MgO and Mg(OH)2 for CO2 sequestration. RSC Adv. 2, 10380-10393.

Fajardy, M. and Mac Dowell, N., 2017. Can BECCS deliver sustainable and resource efficient negative emissions?. Energy & Environmental Science, 10(6), pp.1389-1426.

Fricker, K.J., Park, A.H.A., 2013. Effect of H2O on Mg(OH)2 carbonation pathways for combined CO2 capture and storage. Chem. Eng. Sci. 100, 332-341.

Fourier, J., 1822. Theorie analytique de la chaleur, par M. Fourier. Chez Firmin Didot, père et fils.

Fruehan, R.J., Fortini, O., Paxton, H.W. and Brindle, R., 2000. Theoretical minimum energies to produce steel. Report to the US Department of Energy, Office of Industrial Technologies. Washington, DC.

Funk, A., Trettin, H.R., 2013. DFT Study on the Effect of Water on the Carbonation of Portlandite. Ind. Eng. Chem. Res. 52, 2168-2173.

Gahan, C.S., Cunha, M.L. and Sandström, Å., 2009. Comparative study on different steel slags as neutralising agent in bioleaching. Hydrometallurgy, 95(3-4), pp.190-197.

Gan, L., Zhang, C., Shangguan, F. and Li, X., 2012. A differential scanning calorimetry method for construction of continuous cooling transformation diagram of blast furnace slag. Metallurgical and Materials Transactions B, 43(3), pp.460-467.

Gautier, M., Poirier, J., Bodénan, F., Franceschini, G. and Veron, E., 2013. Basic oxygen furnace (BOF) slag cooling: laboratory characteristics and prediction calculations. International Journal of Mineral Processing, 123, pp.94-101.

Gegner, J., 2006. 2D-3D conversion of object size distributions in quantitative metallography. In Proceedings of the MMT-2006 conference (p. 3).

Georgakopoulos, E., Santos, R.M., Chiang, Y.W. and Manovic, V., 2016. Influence of process parameters on carbonation rate and conversion of steelmaking slags–Introduction of the 'carbonation weathering rate'. Greenhouse Gases: Science and Technology, 6(4), pp.470-491.

Gilvarry, J.J., 1961. Fracture of brittle solids. I. Distribution function for fragment size in single fracture (theoretical). Journal of Applied Physics, 32(3), pp.391-399.

Grubler, A., 1998. Technology and global change. Cambridge: Cambridge University Press.

Hasanbeigi, A., Price, L., Aden, N., Chunxia, Z., Xiuping, L., and Fangqin, S., 2011. A Comparison of Iron and Steel Production Energy Use and Energy Intensity in China and the U.S. Ernest Orlando Lawrence Berkeley National Laboratory.

Heaton, B.S., Down, F.W. and Emery, J.J., 1981. Properties of ground granulated slags in cement blends. In The Second Australian Conference on Engineering Materials, held at Sydney, July 6-8, 1981.

Herlach, D.M. and Feuerbacher, B., 1986. Nucleation and undercooling. In Materials Sciences in Space (pp. 168-190). Springer, Berlin, Heidelberg.

Highfield, J., Chen, J., Haghighatlari, M., Åbacka, J., Zevenhoven, R., 2016. Low-temperature gas-solid carbonation of magnesia and magnesium hydroxide promoted by non-immersive contact with water. RSC Adv. 6, 89655-89664.

Hisashige, S., Katayma, J., and Nakagaki, T., 2019. Quantitative evaluation of SMART steelmaking system by sensitivity analysis of operating conditions on CO2 emissions and exergy. ISIJ International.

Hoekstra, A. and Refa, N., 2017. Characteristics of Dutch EV drivers. EVS30 Symposium, Stuttgart, Germany, October 2017.

Horii, K., Kato, T., Sugahara, K., Tsutsumi, N. and Kitano, Y., 2015. Overview of iron/steel slag application and development of new utilization technologies. Nippon Steel & Sumitomo Technical Report, 109.

Huang, Y., Chen, Y., Castro-Izaguirre, N., Baruffol, M., Brezzi, M., Lang, A., Li, Y., Härdtle, W., von Oheimb, G., Yang, X. and Liu, X., 2018. Impacts of species richness on productivity in a large-scale subtropical forest experiment. Science, 362(6410), pp.80-83.

Huijgen, W.J.J., 2005. Carbon Dioxide Sequestration by Mineral Carbonation (Doctoral dissertation, Wageningen University & Research).

IEAGHG, 2013. Iron and Steel CCS Study: Techno-Economics Integrated Steel Mill. 2013/04.

IEAGHG, 2013b. Overview of the current state and development of CO_2 capture technologies in the ironmaking process. 2013/TR3.

IEAGHG, 2018. Cost of CO_2 capture in the industrial sector: Cement and iron and steel industries. 2018-TR03.

JISF, 2018a. JISF long-term vision for climate change mitigation: A challenge towards zero-carbon steel. The Japan Iron and Steel Federation, November 2018.

JISF, 2018b. Activities of Japanese Steel Industry to Combat Global Warming: Report of "JISF's Commitment to a Low Carbon Society". Presentation. The Japan Iron and Steel Federation, February 2018.

Johnson, D.C., MacLeod, C.L., Carey, P.J. and Hills, C.D., 2003. Solidification of stainless steel slag by accelerated carbonation. Environmental technology, 24(6), pp.671-678.

Junjie, Y., 2018. Progress and Future of Breakthrough Low-carbon Steelmaking Technology (ULCOS) of EU. International Journal of Mineral Processing and Extractive Metallurgy, 3(2), pp.15-22.

Kappes, H. and Michels, D., 2015. Dry slag granulation and energy recovery. In Proceedings of the fourth international slag valorization symposium. Leuven (pp. 39-52).

Kashani, A., Provis, J.L. and van Deventer, J.S., 2013, June. Effect of ground granulated blast furnace slag particle size distribution on paste rheology: a preliminary model. In AIP Conference Proceedings (Vol. 1542, No. 1, pp. 1094-1097). AIP.

Kashiwaya, Y., In-Nami, Y. and Akiyama, T., 2010. Development of a rotary cylinder atomizing method of slag for the production of amorphous slag particles. ISIJ international, 50(9), pp.1245-1251.

Kojima, T., Nagamine, A., Ueno, N., Uemiya, S., 1997. Absorption and fixation of carbon dioxide by rock weathering. Energy Convers. Manag. 38, S461-S466.

Kolmogorov, A.N., 1940. Reprinted by Shiryayev, A.N., 1992. Selected works of A.N. Kolmogorov: Vol. 2, Probability theory and mathematical statistics. Kluwer Academic.

Kourounis, S., Tsivilis, S., Tsakiridis, P.E., Papadimitriou, G.D. and Tsibouki, Z., 2007. Properties and hydration of blended cements with steelmaking slag. Cement and Concrete Research, 37(6), pp.815-822.

Kuehl, H., ATLAS PORTLAND CEMENT Co, 1908. Slag cement and process of making the same. U.S. Patent 900,939.

Kuramochi, T., 2017. Assessment of CO_2 emissions pathways for the Japanese iron and steel industry towards 2030 with consideration of process capacities and operational constraints to flexibly adapt to a range of production levels. Journal of cleaner production, 147, pp.668-680.

Kwon, S., Fan, M., DaCosta, H.F., Russell, A.G., 2011. Factors affecting the direct mineralization of CO_2 with olivine. J. Environ. Sci. 23, 1233-1239.

Lackner, K.S., Wendt, C.H., Butt, D.P., Joyce Jr, E.L., Sharp, D.H., 1995a. Carbon dioxide disposal in carbonate minerals. Energy 20, 1153-1170.

Lackner, K.S., Butt, D.P., Sharp, D.H., Wendt, C.H., 1995b. Carbon dioxide disposal in solid form (No. LA-UR-96-0598; CONF-960322-2). Los Alamos National Lab., NM (United States).

Lackner, K.S., Butt, D.P., Wendt, C.H., 1997. Progress on binding CO_2 in mineral substrates. Energy Convers. Manag. 38, S259-S264.

Larachi, F., Daldoul, I., Beaudoin, G., 2010. Fixation of CO2 by chrysotile in low-pressure dry and moist carbonation: Ex-situ and in-situ characterizations. Geochim. Cosmochim. Acta 74, 3051-3075.

Leeson, D., Mac Dowell, N., Shah, N., Petit, C. and Fennell, P.S., 2017. A Techno-economic analysis and systematic review of carbon capture and storage (CCS) applied to the iron and steel, cement, oil refining and pulp and paper industries, as well as other high purity sources. International Journal of Greenhouse Gas Control, 61, pp.71-84.

Li, J., Hitch, M., 2018. Mechanical activation of magnesium silicates for mineral carbonation, a review. Miner. Eng. 128, 69-83.

Little, L., Mainza, A.N., Becker, M. and Wiese, J., 2017. Fine grinding: How mill type affects particle shape characteristics and mineral liberation. Minerals Engineering, 111, pp.148-157.

Liu, J., Yu, Q., Zuo, Z., Duan, W., Han, Z., Qin, Q. and Yang, F., 2016. Experimental investigation on molten slag granulation for waste heat recovery from various metallurgical slags. Applied Thermal Engineering, 103, pp.1112-1118.

Loncnar, M., Mladenovič, A., Zupančič, M. and Bukovec, P., 2017. Comparison of the mineralogy and microstructure of EAF stainless steel slags with reference to the cooling treatment. Journal of Mining and Metallurgy B: Metallurgy, 53(1), pp.19-29.

Longo, R.C., Cho, K., Brüner, P., Welle, A., Gerdes, A., Thissen, P., 2015. Carbonation of Wollastonite (001) Competing Hydration: Microscopic Insights from Ion Spectroscopy and Density Functional Theory. ACS Appl. Mater. Interfaces 7, 4706-4712.

Luxán, M.P., Sotolongo, R., Dorrego, F. and Herrero, E., 2000. Characteristics of the slags produced in the fusion of scrap steel by electric arc furnace. Cement and Concrete Research, 30(4), pp.517-519.

Mahieux, P.Y., Aubert, J.E. and Escadeillas, G., 2009. Utilization of weathered basic oxygen furnace slag in the production of hydraulic road binders. Construction and Building Materials, 23(2), pp.742-747.

Mandova, H., Leduc, S., Wang, C., Wetterlund, E., Patrizio, P., Gale, W. and Kraxner, F., 2018. Possibilities for CO2 emission reduction using biomass in European integrated steel plants. Biomass and bioenergy, 115, pp.231-243.

Mandova, H., Patrizio, P., Leduc, S., Kjärstad, J., Wang, C., Wetterlund, E., Kraxner, F. and Gale, W., 2019. Achieving carbon-neutral iron and steelmaking in Europe through the deployment of bioenergy with carbon capture and storage. Journal of Cleaner Production.

Manovic, V., Anthony, E.J., 2010. Carbonation of CaO-based sorbents enhanced by steam addition. Ind. Eng. Chem. Res. 49, 9105-9110.

Manso, J.M., Polanco, J.A., Losanez, M. and Gonzalez, J.J., 2006. Durability of concrete made with EAF slag as aggregate. Cement and Concrete Composites, 28(6), pp.528-534.

Maxwell, J.C., 1831. A treatise on electricity and magnetism.

McKelvy, M.J., Chizmeshya, A.V., Bearat, H., Sharma, R., Carpenter, R.W., 2001. Developing Mechanistic Understanding of CO2 Mineral Sequestration Reaction Processes. In the Proceeding of the 26th International Technical Conference on Coal Utilization & Fuel Systems.

MOE, 2018. National Greenhouse Gas Inventory Report of Japan 2018.

Mombelli, D., Mapelli, C., Barella, S., Di Cecca, C., Le Saout, G. and Garcia-Diaz, E., 2016. The effect of chemical composition on the leaching behaviour of electric arc furnace (EAF) carbon steel slag

during a standard leaching test. Journal of environmental chemical engineering, 4(1), pp.1050-1060.

Morrison, R.D. and Cleary, P.W., 2008. Towards a virtual comminution machine. Minerals Engineering, 21(11), pp.770-781.

Mostafa, N.Y., El-Hemaly, S.A.S., Al-Wakeel, E.I., El-Korashy, S.A. and Brown, P.W., 2001. Characterization and evaluation of the hydraulic activity of water-cooled slag and air-cooled slag. Cement and concrete research, 31(6), pp.899-904.

Muhmood, L., Vitta, S. and Venkateswaran, D., 2009. Cementitious and pozzolanic behavior of electric arc furnace steel slags. Cement and Concrete Research, 39(2), pp.102-109.

Müller, D.B., Wang, T. and Duval, B., 2011. Patterns of iron use in societal evolution. Environmental Science and Technology Letters, 45(1), pp.182–188.

Navarro, C., Díaz, M. and Villa-García, M.A., 2010. Physico-chemical characterization of steel slag. Study of its behavior under simulated environmental conditions. Environmental science & technology, 44(14), pp.5383-5388.

Ncongwane, M.S., Broadhurst, J.L. and Petersen, J., 2018. Assessment of the potential carbon footprint of engineered processes for the mineral carbonation of PGM tailings. International Journal of Greenhouse Gas Control, 77, pp.70-81.

Neuhoff, K., Acworth, W., Ancygier, A., Branger, F., Christmas, I., Haussner, M., Ismer, R., van Rooij, A., Sartor, O., Sato, M. and Schopp, A., 2014. Carbon control and competitiveness post 2020: The steel report. London: Climate Strategies.

Newton, I., 1867. The Principia: mathematical principles of natural philosophy.

Nikulshina, V., Galvez, M.E., Steinfeld, A., 2007. Kinetic analysis of the carbonation reactions for the capture of CO_2 from air via the $Ca(OH)_2$–$CaCO_3$–CaO solar thermochemical cycle. Chem. Eng. J. 129, 75-83.

Obara, B. and Kožušníková, A., 2007. Utilisation of the image analysis method for the detection of the morphological anisotropy of calcite grains in marble. Computational Geosciences, 11(4), pp.275-281.

Oda, J., Akimoto, K. and Tomoda, T., 2013. Long-term global availability of steel scrap. Resources, Conservation and Recycling, 81, pp.81-91.

Oh, C., Rhee, S., Oh, M. and Park, J., 2012. Removal characteristics of As (III) and As (V) from acidic aqueous solution by steel making slag. Journal of hazardous materials, 213, pp.147-155.

Ohno, H., Matsubae, K., Nakajima, K., Nakamura, S. and Nagasaka, T., 2014. Unintentional flow of alloying elements in steel during recycling of end‐of‐life vehicles. Journal of Industrial Ecology, 18(2), pp.242-253.

Olivier, J.G.J., Schure, K.M., Peters, J.A.H.W., 2017. Trends in global CO_2 and total greenhouse gas emissions: 2017 Report. PBL Netherlands Environmental Assessment Agency The Hague, 2017.

Pan, S.Y., Chang, E.E. and Chiang, P.C., 2012. CO_2 capture by accelerated carbonation of alkaline wastes: a review on its principles and applications. Aerosol Air Qual Res, 12(5), pp.770-791.

Pauliuk, S., Wang, T. and Müller, D.B., 2013a. Steel all over the world: Estimating in-use stocks of iron for 200 countries. Resources, Conservation and Recycling, 71, pp.22-30.

Pauliuk, S., Milford, R.L., Müller, D.B. and Allwood, J.M., 2013b. The steel scrap age. Environmental science & technology, 47(7), pp.3448-3454.

Persson, M., 2006. Densities and viscosities of slags: modeling and experimental investigations (Doctoral dissertation, KTH).

Philibert, C., 2017. Renewable Energy for Industry: From green energy to green materials and fuels. IEA Insights series 2017.

Poh, H.Y., Ghataora, G.S. and Ghazireh, N., 2006. Soil stabilization using basic oxygen steel slag fines. Journal of materials in Civil Engineering, 18(2), pp.229-240.

Power, I.M., Harrison, A.L., Dipple, G.M., Wilson, S.A., Kelemen, P.B., Hitch, M. and Southam, G., 2013. Carbon mineralization: from natural analogues to engineered systems. Reviews in Mineralogy and Geochemistry, 77(1), pp.305-360.

Price, D., 2009. Yield improvement in the steel industry. Ironmaking & Steelmaking, 36(7), pp.482-486.

Proctor, D.M., Fehling, K.A., Shay, E.C., Wittenborn, J.L., Green, J.J., Avent, C., Bigham, R.D., Connolly, M., Lee, B., Shepker, T.O. and Zak, M.A., 2000. Physical and chemical characteristics of blast furnace, basic oxygen furnace, and electric arc furnace steel industry slags. Environmental science & technology, 34(8), pp.1576-1582.

Quaghebeur, M., Nielsen, P., Horckmans, L. and Van Mechelen, D., 2015. accelerated carbonation of steel slag compacts: Development of high-strength construction Materials. Frontiers in Energy Research, 3, p.52.

Qi, Y., 2018. Metal recovery from steelmaking slag (Doctoral dissertation, University of Toronto).

Rawlins, C.H., 2008. Geological sequestration of carbon dioxide by hydrous carbonate formation in steelmaking slag.

Reck, B.K. and Graedel, T.E., 2012. Challenges in metal recycling. Science, 337(6095), pp.690-695.

Renforth, P., 2019. The negative emission potential of alkaline materials. Nat. Commun. 10, 1401.

RITE, 2018. International Comparisons of Energy Efficiency: Sectors of Electricity Generation, Iron and steel, Cement. Research Institute of Innovative Technologies for the Earth: Systems Analysis Group.

Romanov, V., Soong, Y., Carney, C., Rush, G.E., Nielsen, B. and O'Connor, W., 2015. Mineralization of carbon dioxide: A literature review. ChemBioEng Reviews, 2(4), pp.231-256.

Rubin, E.S., Davison, J.E. and Herzog, H.J., 2015. The cost of CO2 capture and storage. International Journal of Greenhouse Gas Control, 40, pp.378-400.

Santos, R.M., Van Bouwel, J., Vandevelde, E., Mertens, G., Elsen, J. and Van Gerven, T., 2013. Accelerated mineral carbonation of stainless steel slags for CO2 storage and waste valorization: effect of process parameters on geochemical properties. International Journal of Greenhouse Gas Control, 17, pp.32-45.

Scott, P.W., Critchley, S.R. and Wilkinson, F.C.F., 1986. The chemistry and mineralogy of some granulated and pelletized blastfurnace slags. Mineralogical Magazine, 50(355), pp.141-147.

Seifritz, W., 1990. CO2 disposal by means of silicates. Nature, 345(6275), p.486.

Shen, W., Zhou, M., Ma, W., Hu, J. and Cai, Z., 2009. Investigation on the application of steel slag–fly ash–phosphogypsum solidified material as road base material. Journal of hazardous materials, 164(1), pp.99-104.

Shigaki, N., Ta, Y., and Sumi, I., 2017. Development of Heat Recovery System from Steelmaking Slag. JFE technology report No. 40, pp.80-84.

Shigaki, N., Tobo, H., Ozawa, S., Ta, Y. and Hagiwara, K., 2015. Heat recovery process from packed bed of hot slag plates. ISIJ International, 55(10), pp.2258-2265.

Silva, F. and de Carvalho, A., 2016. Evaluating the Financial Health of the Steel Industry'.

Singh, S.P., Tripathy, D.P. and Ranjith, P.G., 2008. Performance evaluation of cement stabilized fly ash–GBFS mixes as a highway construction material. Waste management, 28(8), pp.1331-1337.

Smith, A. and Raven, R., 2012. What is protective space? Reconsidering niches in transitions to sustainability. Research policy, 41(6), pp.1025-1036.

Smith, R.S., Li, Z., Dohnálek, Z., Kay, B.D., 2014. Adsorption, desorption, and displacement kinetics of H_2O and CO_2 on forsterite, Mg_2SiO_4 (011). J. Phys. Chem. C 118, 29091-29100.

Sterman, J.D., Siegel, L. and Rooney-Varga, J.N., 2018. Does replacing coal with wood lower CO_2 emissions? Dynamic lifecycle analysis of wood bioenergy. Environmental Research Letters, 13(1), p.015007.

Suer, P., Lindqvist, J.E., Arm, M. and Frogner-Kockum, P., 2009. Reproducing ten years of road ageing—Accelerated carbonation and leaching of EAF steel slag. Science of the total environment, 407(18), pp.5110-5118.

Suopajärvi, H., Kemppainen, A., Haapakangas, J. and Fabritius, T., 2017. Extensive review of the opportunities to use biomass-based fuels in iron and steelmaking processes. Journal of Cleaner Production, 148, pp.709-734.

Suopajärvi, H., Umeki, K., Mousa, E., Hedayati, A., Romar, H., Kemppainen, A., Wang, C., Phounglamcheik, A., Tuomikoski, S., Norberg, N. and Andefors, A., 2018. Use of biomass in integrated steelmaking–Status quo, future needs and comparison to other low-CO_2 steel production technologies. Applied Energy, 213, pp.384-407.

Suzuki, K., Hayashi, K., Kuribara, K., Nakagaki, T. and Kasahara, S., 2015. Quantitative Evaluation of CO_2 Emission Reduction of Active Carbon Recycling Energy System for Ironmaking by Modeling with Aspen Plus. Isij International, 55(2), pp.340-347.

Tobo, H., Shigaki, N. and Hagio, Y., 2014. Development of heat recovery system from steelmaking slag. JFE Tech. Rep, 19, pp.126-132.

Tossavainen, M., Engstrom, F., Yang, Q., Menad, N., Larsson, M.L. and Bjorkman, B., 2007. Characteristics of steel slag under different cooling conditions. Waste management, 27(10), pp.1335-1344.

Tromans, D. and Meech, J.A., 2002. Fracture toughness and surface energies of minerals: theoretical estimates for oxides, sulphides, silicates and halides. Minerals Engineering, 15(12), pp.1027-1041.

Tromans, D. and Meech, J.A., 2004. Fracture toughness and surface energies of covalent minerals: theoretical estimates. Minerals engineering, 17(1), pp.1-15.

Tsakiridis, P.E., Papadimitriou, G.D., Tsivilis, S. and Koroneos, C., 2008. Utilization of steel slag for Portland cement clinker production. Journal of Hazardous Materials, 152(2), pp.805-811.

UN, 2015. World Population Prospects: The 2015 Revision. United Nations Department of Economic and Social Affairs, Population Division.

USGS, 2018. Mineral commodity summary 2018.

Vaz, M.F. and Fortes, M.A., 1988. Grain size distribution: The lognormal and the gamma distribution functions. Scripta metallurgica, 22(1), pp.35-40.

Veetil, S.P., Pasquier, L.C., Blais, J.F., Cecchi, E., Kentish, S., Mercier, G., 2015. Direct gas–solid carbonation of serpentinite residues in the absence and presence of water vapor: a feasibility study for carbon dioxide sequestration. Environ. Sci. Pollut. R. 22, 13486-13495.

Vigneau, E., Loisel, C., Devaux, M.F. and Cantoni, P., 2000. Number of particles for the determination of size distribution from microscopic images. Powder Technology, 107(3), pp.243-250.

Waligora, J., Bulteel, D., Degrugilliers, P., Damidot, D., Potdevin, J.L. and Measson, M., 2010. Chemical and mineralogical characterizations of LD converter steel slags: A multi-analytical techniques approach. Materials characterization, 61(1), pp.39-48.

Wang, M., Joel, A.S., Ramshaw, C., Eimer, D. and Musa, N.M., 2015. Process intensification for post-combustion CO_2 capture with chemical absorption: a critical review. Applied Energy, 158, pp.275-291.

Wei, R., Zhang, L., Cang, D., Li, J., Li, X. and Xu, C.C., 2017. Current status and potential of biomass utilization in ferrous metallurgical industry. Renewable and Sustainable Energy Reviews, 68, pp.511-524.

Wendling, L., Douglas, G., Coleman, S. and Yuan, Z., 2010. Assessment of the ability of low-cost materials to remove metals and attenuate acidity in contaminated waters.

West, K., 2015. ETP 2015: Iron & steel findings. OECD Steel Committee meeting, May 2015.

Wood, F.W., 1908. Method of treating blast-furnace slag. U.S. Patent 883,770.

World Steel Association, 2018. Steel Statistical Yearbook 2018.

Wyns, T., Khandekar, G., Robson, I., 2018. Industrial Value Chain: A Bridge Towards a Carbon Neutral Europe. The Institute for European Studies.

Xie, J., Wu, S., Zhang, L., Xiao, Y. and Ding, W., 2016. Evaluation the deleterious potential and heating characteristics of basic oxygen furnace slag based on laboratory and in-place investigation during large-scale reutilization. Journal of Cleaner Production, 133, pp.78-87.

Xie, H., Jiang, W., Hou, Z., Xue, Y., Wang, Y., Liu, T., Tang, L., Wu, D., 2017. DFT study of the carbonation on mineral aerosol surface models of olivine: effect of water. Environ. Earth Sci. 76, 732.

Xue, Y., Hou, H. and Zhu, S., 2009. Characteristics and mechanisms of phosphate adsorption onto basic oxygen furnace slag. Journal of Hazardous Materials, 162(2-3), pp.973-980.

Yildirim, I.Z. and Prezzi, M., 2011. Chemical, mineralogical, and morphological properties of steel slag. Advances in Civil Engineering, 2011.

Yuen, Y.T., Sharratt, P.N. and Jie, B., 2016. Carbon dioxide mineralization process design and evaluation: concepts, case studies, and considerations. Environmental Science and Pollution Research, 23(22), pp.22309-22330.

Zhang, H., Wang, H., Zhu, X., Qiu, Y.J., Li, K., Chen, R. and Liao, Q., 2013. A review of waste heat recovery technologies towards molten slag in steel industry. Applied Energy, 112, pp.956-966.

Zhao, J., Wang, D., Yan, P., Zhao, S. and Zhang, D., 2016. Particle characteristics and hydration activity of ground granulated blast furnace slag powder containing industrial crude glycerol-based grinding aids. Construction and Building Materials, 104, pp.134-141.

Zhao, L.G., Lu, T.J. and Fleck, N.A., 2000. Crack channelling and spalling in a plate due to thermal shock loading. Journal of the Mechanics and Physics of Solids, 48(5), pp.867-897.

Zimmermann, A., Wunderlich, J., Buchner, G., Müller, L., Armstrong, K., Michailos, S., Marxen, A., Naims, H., Mason, F., Stokes, G. and Williams, E., 2018. Techno-Economic Assessment & Life-Cycle Assessment Guidelines for CO_2 Utilization.

Chapter 3: Solution property modeling

In order to design processes and equipment that generate solid slag with traits amenable to CO_2 mineralization and material recycling, it is necessary to have knowledge of the properties of molten slag and its transition to the solid phase. The complexity and variability of molten slag compositions overwhelms the capabilities of simple data-fitting methods when extended beyond binary or ternary compositions [Mills et al., 2011]. The iron and steelmaking (ISM) industry has traditionally relied on thermodynamic methods (in particular, 'Calculation by Phase Diagram': CALPHAD) to predict the properties of molten slags. Meanwhile, the phase transition of slag has typically been modeled using 'Classic Nucleation Theory' (CNT). The use of CALPHAD and CNT began with prediction of the behavior of the metallic melt. In this task, CALPHAD and CNT have been extremely successful both in clarifying the physical mechanisms at work and in the engineering design of ISM facilities. However, the extension of these methods to the slag solution has been hindered by the much greater degree of innate complexity. Slag solutions often contain upwards of 10-20 chemical elements which may combine in extremely convoluted structures. Moreover, in contrast to metallic melts, molten slags are a high ionic strength solution, with much more complicated and diverse interactions between component species. This complexity results in a combinatorial explosion within the classic theories which has proven to be a severe challenge to the usefulness of both CALPHAD and CNT. While CALPHAD and CNT remain much more accurate and robust than mere data-fitting, they have several major disadvantages; namely, they:

- are computationally expensive;
- provide no indication of prediction confidence;
- are prone to errors from hidden assumptions;
- perform poorly in interpolation between data sets; and
- perform poorly in extrapolation.

Despite these shortcomings, CALPHAD remains the gold standard for general prediction of thermodynamic properties of molten ISM slag and is commonly exploited in software packages such as Factsage® [Bale et al., 2016]. Lacking other methods, these thermodynamic properties are often used in combination with correlations to prediction non-thermodynamic properties. Likewise, CNT is still widely used for prediction of the kinetics of molten slag solidification despite being shown to provide erroneous predictions at the solidification rates of interest to ISM.

In recent years, the advent of cheap, high-powered computing has allowed for the implementation of simulations based on quantum mechanics (QM) and molecular dynamics (MD). While these methods have been helpful in clarifying the intermolecular physical mechanisms at play, they remain underpowered when it comes to simulation of macro-scale, time-dependent emergent phenomenon. Taking the current rates of increase in computing power, prediction of macro-scale behavior of molten slags from QM or MD remains decades away.

The difficulty in modeling molten slag solutions is evidenced by the considerable time, money, and effort spent on experimental determination of properties despite the availability of cheap, high-powered computers. Unfortunately, the combinatorial explosion inherent in complex slag solutions makes even a global effort of experimental determination of all relevant properties destined to fail.

An alternative to CALPHAD, CNT, QM, MD, and empirical determination is a class of machine learning called 'Deep Neural Networks' (DNN). Simplistically, DNN merely perform high dimensional data fitting. However, in contrast to traditional data fitting, the mechanisms by which DNN obtain a

mapping between inputs and outputs results in predictions with accuracies equivalent to the underlying data set [Funahashi, 1989; Hornik, 1991]. This trait holds true even when there are large gaps in said data (i.e., DNN resist over-fitting) [Mhaskar et al., 2017]. This trait of DNN, combined with the large body of empirical data on molten slags, allows for interpolation between the extant datasets. Deep Neural Networks have the added benefits of:

- low computational load;
- clear indication of prediction accuracy;
- no introduction of assumptions; and
- high skill in interpolation.

On the other hand, usage of DNN requires a large upfront cost of data collection, training, optimization, and the requirement for the human to pose meaningful queries given the available data.

Chapter highlights

- Molten slag property estimation is critical for the design of the centrifugal and MYNA processes.
- Molten slag property estimation using established methods and theories is difficult:
    - empirical correlations cannot match the complex behavior of molten slag;
    - thermodynamic methods struggle with the computational load of complex systems and are challenged by structural and kinetic properties such as viscosity and nucleation lag time;
    - the calculation load of quantum mechanics and molecular dynamics prevents property estimation for properties that emerge at large spatial or temporal scales.
- Deep neural networks are a class of machine learning that can find patterns in high dimensional datasets.
- Properly designed deep neural networks can operate as universal approximators, providing predictions at the inherent error of the dataset.
- Deep neural networks require a large amount of upfront effort through the production of a large, diverse dataset and optimization of the network structure.
- >13,000 data points were gleaned from the literature from 209 sources to produce deep neural networks to estimate molten slag density, liquidus temperature, thermal conductivity, viscosity, and nucleation lag time.
- Deep neural networks produced:
    - estimation of molten slag density and liquidus temperature at accuracies equivalent to or exceeding extant methods.
    - estimation of thermal conductivity and viscosity at a much higher accuracy than any method reported in the literature while also covering a wider compositional space.
    - the first ever prediction of nucleation lag time for unique compositions.
- Deep neural networks were enhanced by feeding the output of deep neural networks of simple properties (e.g., liquidus temperature) as an input into more complex properties (e.g., nucleation lag time), so-called 'bootstrapping'.
- Bootstrapping was used to narrow the field of potential classical theories that explain nucleation lag time by demonstrating that the 'influence' of viscosity is a spurious correlation rather than of mechanistic significance.

Publications relevant to this chapter

- Prediction of nucleation lag time from elemental composition and temperature for iron and steelmaking slags using deep neural networks, ISIJ International Vol. 59 No. 4 p.687-696 (2019), **Corey Adam Myers** and Takao Nakagaki.

3.1. Traditional methods

The metallurgical industry has a long history working with and modeling molten melts including metals and slags. The work of countless academic and industrial researchers has resulted in the maturation of thermodynamic, molecular dynamic, and quantum mechanical simulations of molten systems. This body of work includes both the measurement of ground truth data and the knitting of this data into consistent theoretical frameworks. This herculean effort should not be undervalued. In fact, it is through the work of experimentalists and theorists that the limits of classical theoretical frameworks can be perceived. As will be discussed briefly in Chapter 3.1.1 and 3.1.2, classical theories have reached a level of sophistication and detail where the return on investment on further analysis is greatly diminished. This fact is especially true for prediction of highly complex solutions and for non-thermodynamic properties that emerge at large spatiotemporal scales. Iron and steelmaking slags are particularly complex, with compositions including more than a dozen elements being commonplace. Additionally, the design of the MYNA and centrifugal processes rely upon the emergent, non-thermodynamic properties of viscosity and the nucleation lag time. As such, traditional methods are inherently incapable of supplying the predictions needed for process design.

3.1.1. Calculation by phase diagram

The CALPHAD method operates by calculating the Gibbs energy of phases in a system based on the temperature, composition, and pressure. The Gibbs energy of the system is then minimized by varying the set of stable phases given initial conditions. From this minimization, the phase compositions, phase quantities, and the molar Gibbs energy of the phases and system are predicted. From information of the phase distribution, many other thermodynamic properties can be predicted. However, not all properties of interest have a robust theoretical connection to the outputs of the CALPHAD method (e.g., viscosity). Thus, a correlating function is required to predict non-thermodynamic properties from CALPHAD outputs. As the only empirical data underlying the CALPHAD method is the phase composition, there is no method to quantify the uncertainty of a given prediction without already having equivalent experimental data. Moreover, when calculations occur at compositions with little-to-no data, CALPHAD utilizes data from density functional theory (DFT) databases to fill in the lacking information. Density functional theory is a simplification of quantum field theory and thus has inherent assumptions which may vary from database to database. As such, the choice of DFT database can lead to topological changes in phase diagrams and thus altered predictions from CALPHAD [Sundman et al., 2015]. Due to the combinatorial explosion that occurs in complex systems, and the dearth of empirical data, quaternary and higher interactions are generally ignored in CALPHAD methods [Kattner, 2016]. However, it is well-established that even quaternary interactions significantly modify the molten structure, interactions, and traits of slag [Min and Tsukihashi, 2017].

In the CALPHAD method, the accuracy of a prediction is inextricably linked to the precision at which the calculation of the phase diagram is performed (i.e., the global minimization of the Gibbs energy). Given that slag is a chemically complex solution, the computational load to perform this global minimization is significant [Foundation of Computational Thermodynamics, 2016]. The number of calculations (N) scales as **Eq. (3-1)** where d is the number of dimensions (i.e., number of assumed indivisible compounds under the system conditions), G is the number of grid points in the phase diagram, and O indicates the order of magnitude of the calculation load [Ljungberg et al., 2010]. The increase in calculation load with system complexity is shown graphically in **Fig. 3-1**.

$$N = O(d^2 G^d) \tag{3-1}$$

If errors due to falling into local minima are to be avoided, a sufficiently high-resolution calculation must be adopted (i.e., small grid spacing). The connection between G, d, and prediction precision (q) is provided by **Eq. (3-2)** [Piro and Simunovic, 2016]. This process is described graphically in **Fig. 3-2**.

$$G = \frac{\left(\frac{1}{q} - 1\right)!}{\left(\frac{1}{q} - d\right)!\,(d-1)!} + d \tag{3-2}$$
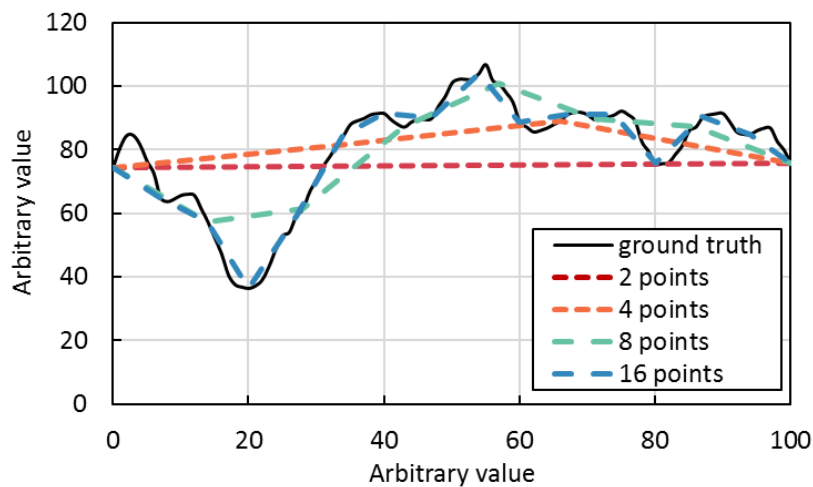
Fig. 3-1. The increase in accuracy accompanying a decrease in grid spacing in the CALPHAD method.
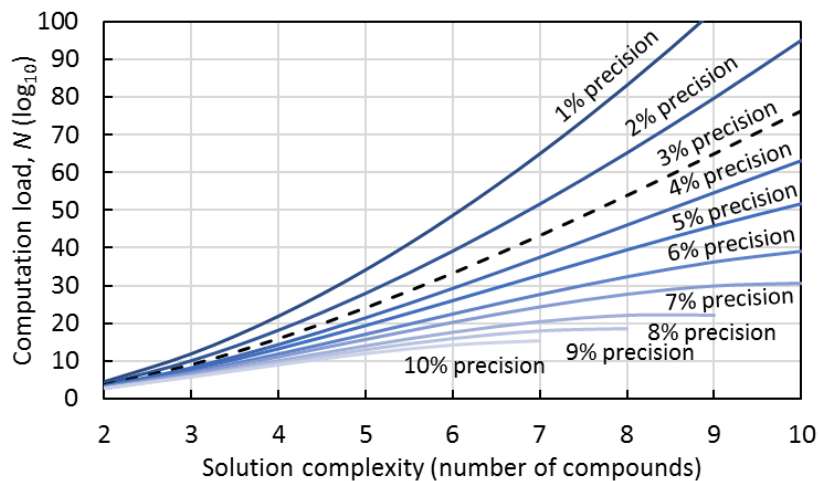
Fig. 3-2. The increase in computational load that accompanies problem dimensionality and desired precision in the CALPHAD method.

3.1.2. Density functional theory and molecular dynamics

The alternative to thermodynamic methods of liquid solution property prediction is calculation of bulk properties from the numerous interactions of individual molecular units. This 'bottom up' method is generally realized using DFT or MD simulations using simplifying assumptions about

particle interactions. In reality, these two methods operate at very different levels of precision. Density functional theory is used primarily for understanding the shape and character of single or a small number of molecules extremely accurately. On the other hand, MD is used to understand emergent behavior from the innumerable interactions of said molecules. Given that the behavior and nature of slag is an important aspect of furnace operation, altering the composition of slag is unlikely to be accepted by the ISM industry. Rather, understanding the macroscale properties and behavior of slag within a narrow chemical composition space but large temperature range is the primary focus of DFT simulations. Therefore, DFT and other QM methods are useful only in so much as they provide insight into why certain characteristics exist; the task of converting that fundamental knowledge into operational changes is the purview of humans or theories that capture emergent behavior (e.g., MD).

The interactions of even a small mass of material at the molecular scale are, from the perspective of humans, functionally infinite. A simple calculation clarifies the conundrum. If each molecule could be completely modeled by a single bit, a cubic centimeter of molten Ca_2SiO_4 (roughly the volume necessary to observe operationally meaningful macroscopic behavior) would require $\sim 1\times10^{22}$ bits to provide a static model. Molecular dynamics simulations require a time step of $\sim 1\times10^{-15}$ s to achieve accurate results [Choe and Kim, 2000]. The current fastest supercomputer in the world, the Sunway TaihuLight supercomputer, performs $\sim 1\times10^{17}$ calculations per second. The nucleation time lag (τ) for slag ranges from $\sim 1\times10^{0}$ - 1×10^{4} seconds. Therefore, to observe the macroscopic behavior of slag using MD would require continuous calculation for $\sim 1\times10^{12}$ - 1×10^{16} years using the world's fastest computer. This issue is well known in the MD field as noted in the review of the state of the art of MD by Sosso et al. (2016) "*…crystal nucleation is a rare event that can occur on time scales of seconds, far beyond the reach of any conventional MD framework... we are almost always forced to base our conclusions on the ancient grounds of classical nucleation theory*".

3.2.   Deep neural networks

In contrast to traditional theories, deep neural networks (DNN) contain no fundamental assumptions about the mechanisms of a phenomenon or an underlying mathematical framework. Deep neural networks instead rely upon mapping input data to an output. As DNN are universal approximators, they are innately able to find extant patterns in high dimensional data. Moreover, the lack of a single theoretical underpinning allows for DNN to be used for prediction of thermodynamic and non-thermodynamic properties. An additional benefit of DNN is they can expose the inherent error of the underlying dataset, thereby providing an appraisal of the state of the art of classical theories. Thus, DNN can be used to focus attention on classical theories or experimental conditions that have the most room for improvement.

3.2.1. Fundamentals of DNN

Neural networks (NN; alternatively, artificial neural networks: ANN) are a subgroup of brain-inspired machine learning architectures loosely based on the architecture of animal central nervous systems. Neural networks are characterized by an interconnected system of simple calculations ('neurons') linking a set of input data (e.g., elemental composition) with some output of interest (e.g., T_L). Deep neural networks contain multiple layers of neurons. The outputs of a layer of neurons act as inputs to the next layer of neurons. Despite DNN recent explosion of use across science and society, ANN are an old technology that have gone through several periods of substantial excitement followed by significant disappointment. Deep and shallow neural networks are in a class of machine learning methods that do not explicitly define rules or patterns. These methods have seen a

significant resurgence compared to user-defined methods in recent years due primarily to the advent of large data sets and high computational power [Cardon et al., 2018]. With sufficient data and computational power, such methods can find patterns that have hitherto avoided detection or classification by humans (e.g., image and speech recognition).

In DNN, the layers of neurons between the input values and output(s) are termed the hidden layers. All outputs and inputs contain a weighting factor which are the primary points of manipulation during calculation optimization ('learning'). In addition to inputs from the previous layer, each neuron also receives a bias function which is modified during optimization. The weighted inputs are summed by a neuron and added to the bias prior to performing some form of rectification (i.e., normalization of outputs) using an 'activation function' (**Fig. 3-3**). The most widely used activation functions are the tanh (**Eq. 3-3**), sigmoid (**Eq. 3-4**), and rectified linear units (ReLU) functions (**Eq. 3-5**), though presumably any function is acceptable. These activation functions are displayed in **Fig. 3-4**.

$$\text{tanh:} \qquad Y(x) = \frac{[1 - \exp(-2x)]}{[1 + \exp(-2x)]} \qquad\qquad (3-3)$$

$$\text{sigmoid:} \qquad Y(x) = \frac{1}{[1 + \exp(-x)]} \qquad\qquad (3-4)$$

$$\text{ReLU:} \qquad Y(x) = \max(0, x) \qquad\qquad (3-5)$$
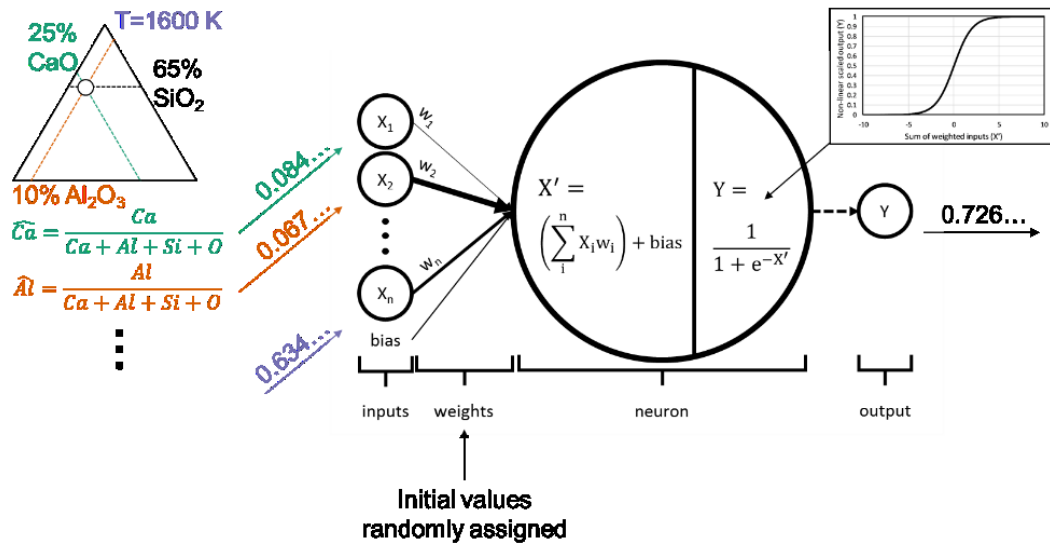
Fig. 3-3. Calculations occurring within a single 'neuron' in a DNN.
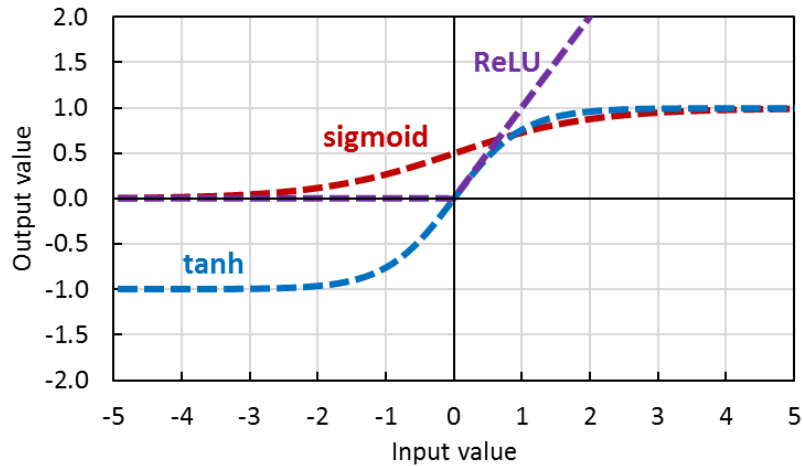
Fig. 3-4. The most widely used activation functions in DNN.

Outputs move through the DNN layers, progressively modifying the initial inputs until reaching the output in a process termed 'forward propagation' as shown in **Fig. 3-5**. The output(s) (o) is (are) compared to the ground truth data (y) to determine the error of the estimate. The performance of the DNN as a whole is calculated by the 'cost function' (C). The C is a function of the network weights, the network biases, the inputs of a single training problem, and the ground truth data being estimated. Due to weighting factors and biases initially being randomly applied, and the large number of weights in the network, it is overwhelming likely that the initial DNN prediction has a large error. The widely utilized C are: sum squared error (SSE) per **Eq. (3-6)**, cross-entropy error (CEE) per **Eq. (3-7)**, exponential cost (EC) per **Eq. (3-8)**, Hellinger distance (H) per **Eq. (3-9)**, Kullback-Leibler divergence (KL) per **Eq. (3-10)**, generalized Kullback-Leibler divergence (gKL) per **Eq. (3-11)**, and the Itakura-Saito distance (IS) per **Eq. (3-12)**. In **Eq. (3-6)** through **Eq. (3-12)**, i indicates a single training example and n is the number of examples in the training set. In **Eq. (3-8)**, ϵ is a constant to be optimized. Though presumably any definition of error could be used, some are inherently more or less well suited to high dimensional data. For example, Euclidean distance is generally a poor error function in high dimensional, noisy data due the accelerating expansion of higher order terms. Data is driven closer to the edges of the hypersphere or hypercube than to other data, smearing out the differences that make data meaningful [Aggarwal et al., 2001].

$$SSE = \sum_{i=1}^{n} (o_i - y_i)^2 \qquad (3-6)$$

$$CCE = \sum_{i=1}^{n} [y_i \log_{10}(o_i)] + [(1 - y_i)\log_{10}(1 - o_i)] \qquad (3-7)$$

$$EC = \epsilon \exp\left[\frac{1}{\epsilon} \sum_{i=1}^{n} (o_i - y_i)^2\right] \qquad (3-8)$$

$$H = \frac{1}{\sqrt{2}} \sum_{i=1}^{n} \left(\sqrt{o_i} - \sqrt{y_i} \right)^2 \qquad (3-9)$$

$$KL = y_i \log_e \left(\frac{y_i}{o_i} \right) \qquad (3-10)$$

$$gKL = \sum_{i=1}^{n} y_i \log_{10} \left(\frac{y_i}{o_i} \right) - \sum_{i=1}^{n} y_i + \sum_{i=1}^{n} o_i \qquad (3-11)$$

$$IS = \sum_{i=1}^{n} \left[\frac{y_i}{o_i} - \log_{10} \left(\frac{y_i}{o_i} \right) - 1 \right] \qquad (3-12)$$
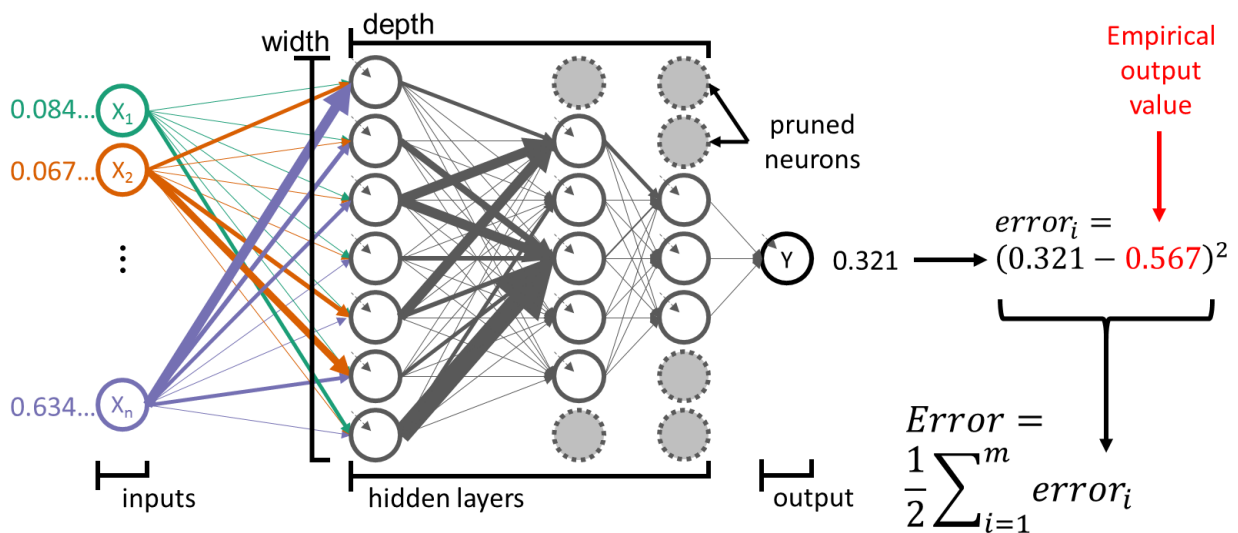
Fig. 3-5. The evolution of input values during forward propagation through hidden layers of neurons leading to a predicted output value.

Once an error has been calculated, the degree to which the error is caused by each weighting function and bias in the DNN is calculated by flowing the error backwards through the DNN in a process called 'backpropagation' (**Fig. 3-6**). Backpropagation is achieved by moving along the negative gradient of the cost function for each weight and bias in the DNN (**Fig. 3-7**).
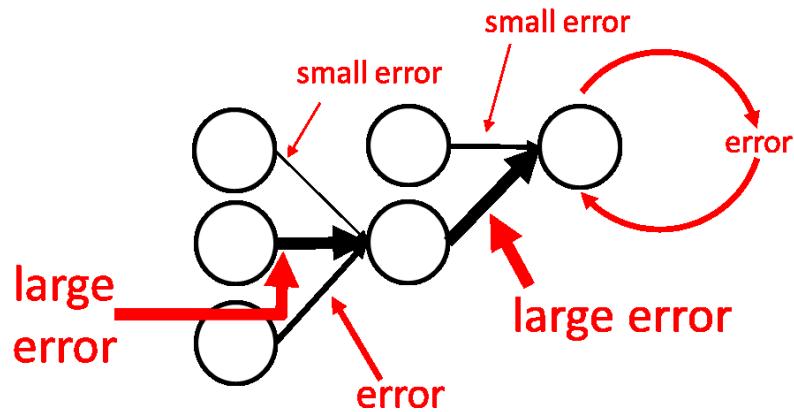
Fig. 3-6. Schematic of error attribution to weights in a DNN through backpropagation. Large weights are indicated by heavy lines and accordingly share more responsibility for the prediction error.
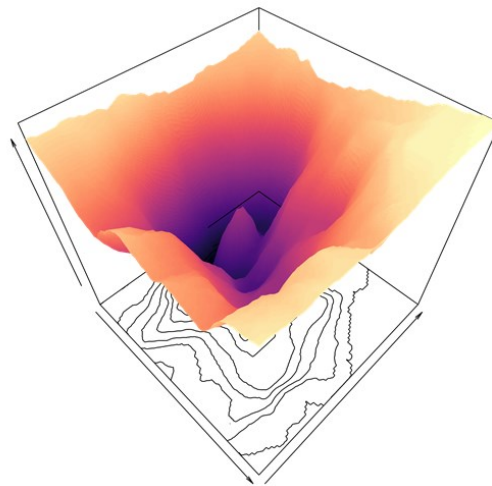
Fig. 3-7. Schematic representation of the error surface (vertical direction) of a DNN. Backpropagation improves the output by moving along the negative gradient of the error surface.

Due to the interconnected nature of the DNN structure and the large number of adjustable parameters, it is infeasible to manually adjust the weighting factors and biases to improve the prediction accuracy. The advent of powerful computers allows for larger and more complicated DNN by automating the backpropagation calculations. To accelerate prediction improvement, a 'learning rate' (Γ) is applied to the updating of the weighting factors. The incremental improvement in the accuracy of the DNN by updating weights such that the overall function moves along the negative gradient of the cost function is termed 'stochastic gradient descent' (SGD). Stochastic gradient descent applied to DNN finds the global minima of the error function [Du et al., 2018]. A large Γ rapidly descends the gradient surface. This quickly finds a minima but has a higher probability of over shooting the global minima. Conversely, a low Γ causes the training time of DNN to increase but is less likely to miss steep gradient minima. Many variations of backpropagation with gradient descent exist. Stochastic gradient descent is the dominant algorithm, but methods that attempt to accelerate

learning by training on a small subset of examples are also common (e.g., 'batch gradient descent', 'mini batch gradient descent') [Ruder, 2017]. A particular version of the gradient descent method termed 'resilient backpropagation' aims to remove the tradeoff between training at a reasonable speed and the potential for overshooting minima [Riedmiller, 1994]. Contrary to traditional backpropagation, each weighting factor (w) has its own learning rate (Γ_w) which is adjusted by the sign of the partial derivative of the error function instead of by its magnitude. The Γ_w is increased when the sign of the partial derivative is consistent across steps and decreased when the sign changes. The update to the weights is given by **Eq. (3-13)** where s is the step. **Figure 3-8** displays the concept of resilient backpropagation.

$$w_i^{s+1} = w_i^s - \Gamma_{w,i}^t \times \text{sign of}\left(\frac{\partial C^s}{\partial w_i^s}\right) \tag{3-13}$$

$$w_i^{(s+1)} = w_i^s - \Gamma_{w,i}^s \times \text{sign of}\left(\frac{\partial C^s}{\partial w_i^s}\right)$$

move towards decreasing error

$$w_i^{(s+2)} = w_i^{(s+1)} - \Gamma_{w,i}^{s+1} \times \text{sign of}\left(\frac{\partial C^{s+1}}{\partial w_i^{s+1}}\right)$$

$$w_i^{(s+3)} = w_i^{(s+2)} - \Gamma_{w,i}^{s+2} \times \text{sign of}\left(\frac{\partial C^{s+2}}{\partial w_i^{s+2}}\right)$$
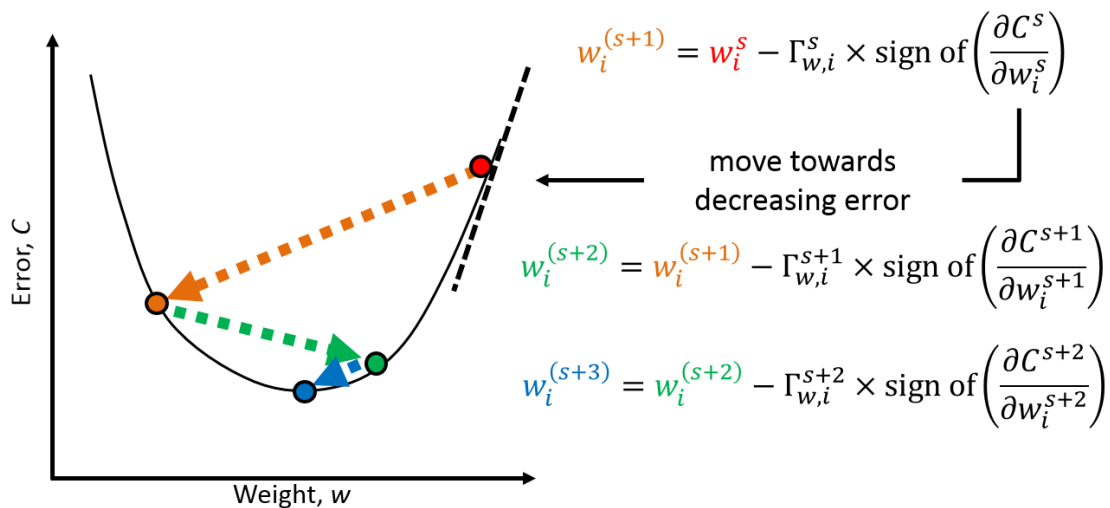
Fig. 3-8. Schematic of the mechanisms of resilient backpropagation.

Once a DNN has been trained to a desired accuracy, its prediction ability on novel data must be tested to ensure that overfitting has not occurred. A trained network simply takes in inputs and provides an output(s); that is, the network performs a single pass of forwards propagation with no backpropagation or updating of weights. Empirically, DNN appear resilient against overfitting when compared to traditional data-fitting methods; nevertheless, overfitting can occur [Arpit et al., 2017; Feng et al., 2018]. Overfitting can be largely suppressed by training a DNN with different combinations of training and testing data and averaging the predictions, so-called 'k-fold cross validation' [Borra and Di Ciaccio, 2010] (**Fig. 3-9**). The 'k-folds' in the process name represent the number of dissections of the training set. It is generally the case that 10-fold cross validation provides the optimal return of overfitting suppression at the minimum computational load. It is also acceptable to run k-fold cross validation where the final estimate uses the median prediction as opposed to the mean prediction; this serves to nullify the effect of extreme outliers on the data [Yu and Clarke, 2015]. An additional countermeasure against overfitting is training a DNN using different initial random weights, so-called 'repetitive weight randomization' (RWR) as shown in **Fig. 3-10**. By

altering the initial weights, local minima in the error surface of a specific dataset are suppressed. The number of potential local minima grows exponentially with the parameter number [Kawaguchi, 2016]. As such, identical architectures trained on identical data will often converge to different solutions if provided different initial weights. Disparate local minima in practice have similar error rates, but the distribution of errors are distinct. This variance is often viewed as a defect, but it can be exploited through wisdom of the crowd methods [Caruana et al., 2004; Ugander et al., 2015] (WoC; termed an 'ensemble' in the machine learning community). Wisdom of the crowd methods are particularly suited to high dimensional combinatorial problems such as those facing molten slag property prediction [Yi et al., 2012]. Ensembling can generate large error reductions as evidenced by its success in machine learning competitions [Deng, 2009].
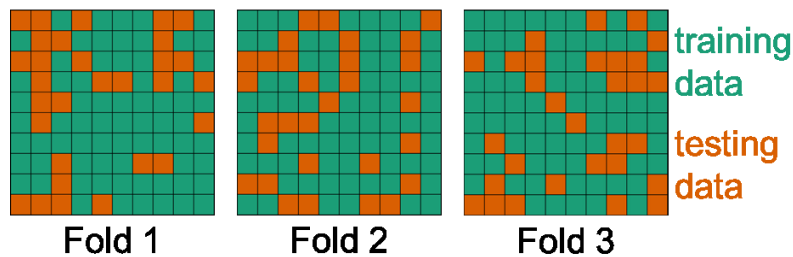
Fig. 3-9. Schematic representation of cross validation using 3 folds of the data.
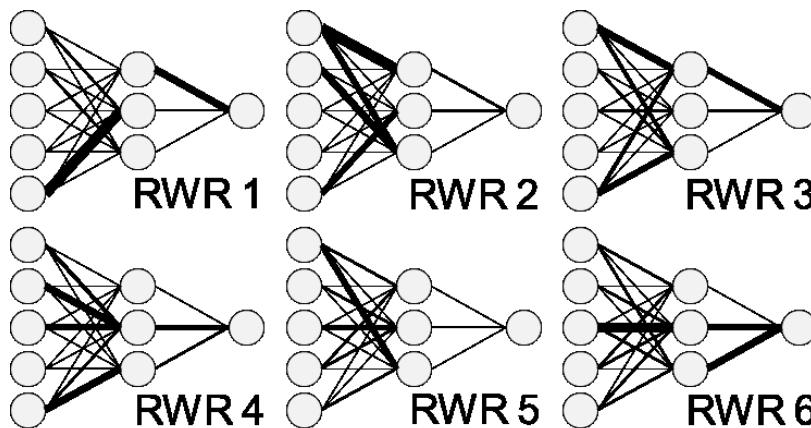
Fig. 3-10. Schematic representation of RWR where the values of the initial weights are represented by the width of the lines.

The order of magnitude of the computation load (O) for a trained DNN with a simple forward pass structure is related to the number of neurons and layers, as shown in **Eq. (3-14)**, where n_L is the number of layers, $n_{N,j}$ is the number of neurons in the current layer (j), and $n_{N,j+1}$ is the number of neurons in the next layer.

$$O\left(\sum_{j=0}^{n_L-1} n_{N,j}[1 + n_{N,j+1}] \right) \tag{3-14}$$

3.2.2.Ancillary tasks

Though the focus of DNN research is squarely on the inner construction and working of the DNN, there are a large number of ancillary tasks required to supply data to, and analyze data from, the DNN. Such tasks include data collection, formatting, input selection, question posing, data extraction and conversion, verification, optimization, and function extension (**Fig. 3-11**). Each of these tasks is touched on lightly below.
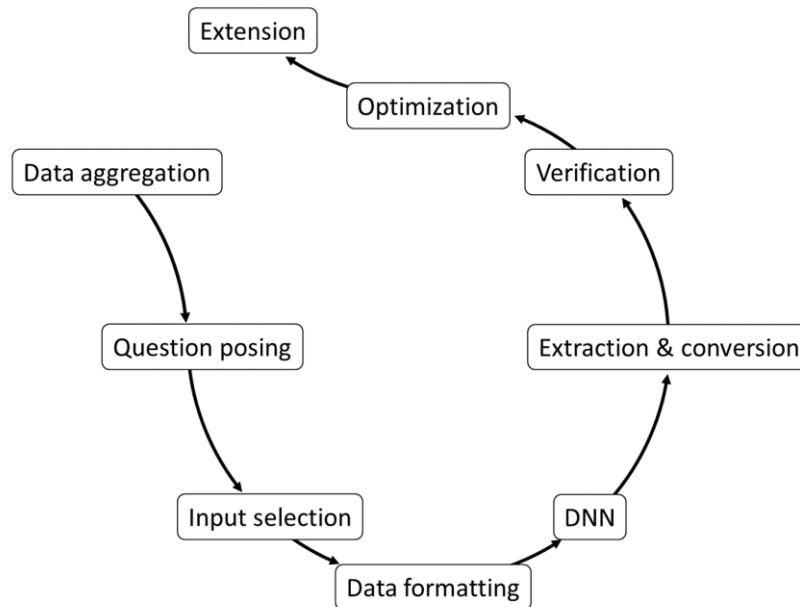
Fig. 3-11. Ancillary tasks in generating DNN predictions.

Data Collection.

Of the tasks necessary to implement DNN, the aggregation of data is the most fundamental. The strength of DNN is to find patterns in high dimensional data that remain cloaked from human intuition. As the dimensionality of a data set increases, so does the minimum amount of data necessary to recognize an innate pattern. This data quantity is further increased by any noise in the data from inherent stochasticity, empirical errors, and imprecise data transfer (e.g., rounding). As the foundation of DNN is data, any biases in the underlying data will transfer to the DNN results unannounced. Therefore, the first principle in data collection for application to DNN is to avoid the instinct to reject data that 'seems' erroneous (cf. Table 2 of Han et al., 2016 for an example of data cleaning). Most critically, the 'cleaning' of data assumes that the human actor knows something of merit about the underlying nature of the problem at hand. However, DNN are employed specifically for problems where humans have failed to find simplifying patterns or mechanistic explanations. As such, even if reliable trends or correlations are known about a given problem, it is improper to impose those patterns on the DNN by preselection of a subset of data. Put another way, it is possible that the seemingly erroneous data actually contains relevant information about the problem that humans have failed to recognize. In short, removal of outliers is tantamount to removal of useful information. There is also a more practical issue at hand. Empirical errors are an inherent facet of human experience and activities. No information can be known with perfect accuracy and precision. The degree of confidence one should have in a prediction is in many cases equally, or more, valuable than

the prediction itself. If outliers are removed from the data, the confidence of the prediction will exceed the ground truth variability of the system of measurement.

Along with the pitfall of 'cleaning' data, a common error is the lack of data to cover the problem one wishes to solve. Even though DNN resist overfitting better than other statistical methods, it is impossible to predict patterns that rely on mechanisms not contained in the information of the input data. Another common error is driving a DNN to predict a pattern accurately at the expense of prediction quality for other patterns; this occurs when the distribution of training data is heavily biased.

In short, a decrease in the signal to noise ratio (S/N) comes with an increase in the quantity of data required to map to the output. Human and range-imposed biases in the data are learned by the DNN as 'truth' and become inextricably mixed with valid data in the process of generating predictions. To avoid such invisible bias propagation, data cleaning should be strictly avoided, and data should be obtained from multiple sources and experimental methods. Though unique data points are inherently more valuable to the performance of a DNN than numerous repetitions of functionally similar systems [Burda et al., 2018], there is undoubtedly much to be gained simply by increasing the amount of data [Dernoncourt et al., 2017]. As demonstrated by Sun et al. (2017), the accuracy of a DNN increases roughly linearly with the order of magnitude of the data quantity. However, currently there is no theoretical underpinning for the quantity of data to bring a DNN to a desired accuracy or generalizability.

Data formatting and problem definition.

The mere collection of a large and diverse data set is not sufficient to generate quality predictions from a DNN. The DNN is simply a statistical tool and has no means to makes accurate predictions if there is not a meaningful connection between the input data and the output. Accordingly, it is the job of the human to determine what is the question to be asked (e.g., what is the viscosity of an 80 mass% Ca_2SiO_4, 10 mass% $Ca_2Fe_2O_5$, 10 mass% Al_2O_3 solution at 1749 K) and what information is worthwhile to provide to the DNN (e.g., the color of the furnace is not useful information while the pO_2 of the atmosphere is useful). Inclusion of input data that is not connected by physical mechanism to the output adds noise to the signal the DNN is attempting to distill. As such, even highly correlated data degrades performance if it is not mechanistically connected. Herein lies a key stumbling block for the use of DNN; deep neural networks are most useful for problems not currently understand by humans, but the computer requires the human to decide what data is important to the problem. This dilemma is particularly challenging for image and voice recognition, where there does not appear to be an inherent fundamental building block from which patterns emerge. For ISM slag, and other systems with strict physical interpretations, the fundamental building blocks are the same as those in classical physical theories (e.g., elements, temperature) [Gabbard et al., 2018; Gilpin, 2018; Ye et al., 2018]. In the case of chemical solutions (e.g., molten slag), interactions occur through electrons. The structure of electron clouds dictates their interactions and so can be captured by the elemental composition. Moreover, the chemical composition can be assumed to be largely homogeneous for molten slags. This means that all information about spatial orientations can be removed, reducing the input data to a simple ratio of chemical species in the melt. Additionally, molten phase molecular interactions are necessarily stochastic and numerous, but the properties of interest are emergent at the macroscale, allowing for the average kinetic energy of the molecules to be described using the absolute temperature without loss of meaningful information. The patterns gleaned from the input

data are then iteratively compiled in each layer of the DNN to generate increasingly complex structures and concepts.

Upon determination of the problem definition and the appropriate input information, the data must be formatted such that a DNN can efficiently utilize it in training. As the fundamental units of molten slag are physical, and the properties of interest contain a relatively low degree of emergent complexity, it is appropriate to provide data in units that have been defined by universal constants (e.g., moles, Kelvin). Usage of more complex parameters (e.g., 'basicity') injects human bias into the DNN analysis. Along with physically meaningful units, it is important to normalize the inputs to the smallest and largest instance in the dataset. This imposes the boundary within which the DNN must find patterns and helps to prevent numerical effects from concealing physical phenomenon. Moreover, this normalization to the underlying data is mathematically necessary in order for the DNN to operate as an universal approximator [Castro et al., 2000]. Inputs scaling orders of magnitude can obscure data at the extremes of the dataset; in such instances it is necessary to logarithmically transform the data such that the differences between datapoints remain discernable.

Data extraction and conversion.

In general, DNN are used to generate predictions of emergent properties from more fundamental properties or traits. Given its emergent character, the optimal form of the output is an open question. The simplest answer is to simply match the standard way the output is reported in the literature. However, this may not have the clearest connection to the underlying physical mechanisms generating the property. It is often beneficial to consider what is the key feature of the output property and then reimagine the output in terms of this trait. This inherently requires a conversion between reported data and this new property. Not all conversions are directionally possible or symmetric, so care must be taken not to inject a systematic error.

Verification. After a DNN has been trained its performance must be tested on unseen data. This serves to determine the true prediction accuracy of the DNN. If there is substantial deviation in the DNN prediction error between the training and verification set, then this is an indication of overfitting to the training data. Overfitting tends to be avoided due to the mechanics of the internal calculations of DNN using SGD. However, this requires that the training data is representative of the verification data. Given that data must be separated prior to use into training and testing data, it is a common issue for overfitting to occur due to improper data coverage in the training set. Training of strictly separate DNN using different subsets of the same underlying data, and then taking some amalgam of their prediction is a powerful method to largely eliminate this issue.

A question that receives little attention, but is of critical importance, is the selection of an error metric. Due to historical reasons, the root mean squared error ($RMSE$) is still the dominant error metric reported in scientific literature (**Eq. (3-15)**). However, error statistics that rely on a squaring of the error (e.g., SSE, RMSE) emphasize large magnitude errors at the expense of clarity on the behavior of the population as a whole. Moreover, they inherently assume that the error distribution is normal and unbiased [Willmott and Matsuura, 2005]. When no privilege is to be given to any data points the mean absolute scaled error ($MASE$) per **Eq. (3-16)**, mean absolute error (MAE) per **Eq. (3-17)**, and mean bias scaled error ($MBSE$) per **Eq. (3-18)** are more appropriate. These error metrics are also preferred when multiple data sources are used and when interpretability is valued. The $MASE$ is an appropriate measure of overall performance, the MAE is useful when the inherent error of a measurement approaches the value of the parameter being measured, and the $MBSE$ is useful in determining if estimates are centered around the data or if there is a fundamental bias present.

$$RMSE = \sqrt{\left(\frac{1}{n}\sum_{i=1}^{n}[o_i - y_i]^2\right)} \qquad (3-15)$$

$$MAE = \frac{1}{n}\sum_{i=1}^{n}|o_i - y_i| \qquad (3-16)$$

$$MASE = \frac{1}{n}\sum_{i=1}^{n}\frac{|o_i - y_i|}{y_i} \qquad (3-17)$$

$$MBSE = \frac{1}{n}\sum_{i=1}^{n}\frac{(o_i - y_i)}{y_i} \qquad (3-18)$$

Optimization.

One of the primary criticisms of DNN is that they constitute a 'black box' from which no insight can be gleaned. However, understanding the mathematical workings that provide DNN with predictive skill has led to method to gain functional insight on the studied problems and how to leverage these methods to further enhance DNN [Shu et al., 2017]. Lin et al. (2017) demonstrated that probability distributions inherent in the universe are particularly compatible with the internal mathematics of DNN. The fact that the universe occupies a small volume in the space of mathematically possible universes radically reduces the potential pattern recognition space of DNN. Moreover, most of the phenomenon of interest at the temporal and spatial scales of interest to humans derive from an emergent hierarchy of interactions; this hierarchical emergent structure is emulated in the calculation architecture of DNN [He et al., 2016]. Ergo, DNN are innately more skillful than shallow neural networks at generating and analyzing complex phenomenon [Baral et al., 2018]. Retrieval of results from the intermediate hidden layers of DNN show the emergence of concepts that are intuitive to humans [Bau et al., 2017]. This seems to support the proposition that the hierarchical structure mirrors the emergent complexity of the output. Given that complexity can theoretically increase with the number of layers of a DNN ('depth'), it is reasonable to expect highly emergent phenomenon to require a deep structure. On the other hand, it has been proven that if the width (i.e., the number of neurons per layer) of the hidden layers never exceeds the width of the input space, then no degree of depth will result in recovery of the universal approximator feature [Johnson, 2018]. While a single hidden layer acts as an universal approximator given an infinite width and infinite accuracy of the activation functions [Barron, 1994; Cybenko, 1989], single layer NN are rarely used in practice because it is exponentially more efficient to train deeper networks than shallow networks [Lin et al., 2017]. Moreover, it has been proven that arbitrary accuracy can be achieved with DNN using a finite number of neurons with a depth that scales only logarithmically with the number of inputs [Rolnik and Tegmark, 2018]. However, as the width dictates the number of combinations of inputs, wider networks are more 'expressive'. In other words, wider networks are

more likely to generate combinations of inputs that relate to underlying physical realities instead of simply fitting the data. The reason for these 'concepts' to emerge is related to the robustness of calculations. Physical laws broadly guide processes, with the noise from functionally stochastic and/or random situational details causing minor deviations from the 'ideal' path. By developing the equivalent of physical laws in the internal calculations, DNN are able to produce more generalizable predictions. This increased generalizability is enhanced by the removal of neurons from deeper layers ('pruning'). Pruning acts as a data compression step, forcing the DNN to remove extraneous data [Huang et al., 2018; Shwartz-Ziv and Tishby, 2017].

There exists a menagerie of variations on the basic DNN structure theme, with various additional connections between neurons being the primary feature [Van Veen, 2016]. However, recent work has shown that the apparent performance increases from novel DNN structures can be achieved simply by careful exploration of the depth-width-pruning space [Shallue et al., 2018]. The main reason for avoiding the optimization problem is a matter of time. With DNN becoming increasingly deep in recent years, the number of potential structures is too numerous to explore in practical time scales. However, for physical systems, the necessary network size is generally small, making structure optimization a tractable problem. Even so, it is prudent to reduce the number of potential networks by setting a general order of priority. As pruning is used to compress data and increase generalizability, it is only useful if a given unpruned structure is skillful. Therefore, the system performance over the possibility space of depth and width is first evaluated. Once the saddle points or asymptotic points become clear, the least complex networks are modified via pruning.

3.3.   Density estimation

The density (ρ) of molten slag is an important operating parameter within ISM furnaces as it partially dictates the speed and degree to which slag and the molten metal separate from one another. In general, the composition-dependent molar volume is calculated commonly with a temperature dependency [Xin et al., 2017]. The primary difference between models is how compositional interdependencies are handled. Though available models provide highly accurate predictions (generally, $MASE$ < 3%), they generally cover relatively limited composition space, with the most recent models covering the quaternary composition space. The increasingly complex potential interdependencies of molar volumes as the dimension of the melt composition is not well accounted for in extant models. Moreover, quantitative information on the temperature dependencies of the plethora of minor inclusions ISM slags remains lacking in the literature. For real slags, with their more complex compositions, in-house data fitting is commonly used to generate ρ estimates.

The ρ of ISM slag was estimated by training a DNN on 776 data points from the literature. Compared to typical DNN, this is an extremely small amount of data. However, the simple nature of the problem and the relative ease with which humans have been able to predict ρ is suggestive that a small dataset may be sufficient. The width and depth of the network were modified until the saddle point of the error was determined. Progressively extreme pruning was applied until the optimal structure was found. To avoid overfitting, 10-fold cross validation was applied; however, due to the highly accurate predictions, no RWR was applied. The optimized structure has an initial width expansion (ϖ) of 4, followed by pruning (ψ) by 50% into 3 hidden layers. The $MASE$ and median absolute squared error $MedASE$ were 0.87% and 0.44%, respectively. The performance, structure, and data composition are provided in **Table 3-1**. The composition space covered by the DNN is shown

in **Fig. 3-12**. The predicted ρ is plotted against empirical ρ in **Fig. 3-13**. In **Fig. 3-14**, the $MASE$ is compared with that from a recent partial molar volume-based method as a function of melt composition and complexity [Xin et al., 2017]. **Figure 3-15** plots the accuracy of the DNN results and those of Xin et al. (2017) against the number of data points; in both model types, increasing data quantity corresponds to an increase in prediction accuracy.
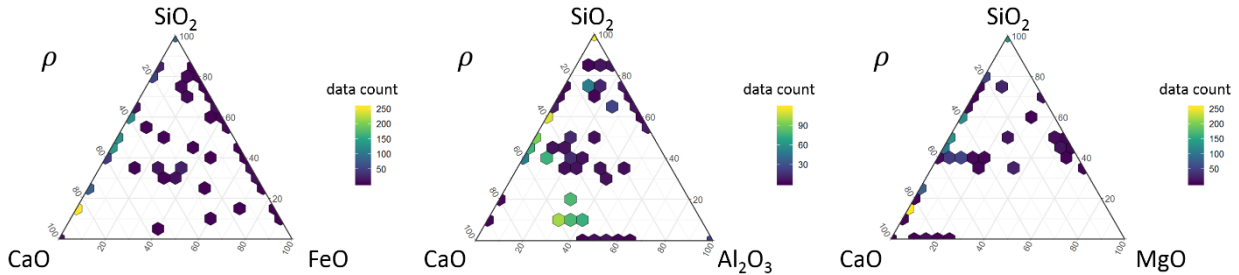
Fig. 3-12. Range of density data used in training DNN plotted on CaO-SiO$_2$-FeO, CaO-SiO$_2$-Al$_2$O$_3$,and CaO-SiO$_2$-MgO ternary diagrams.
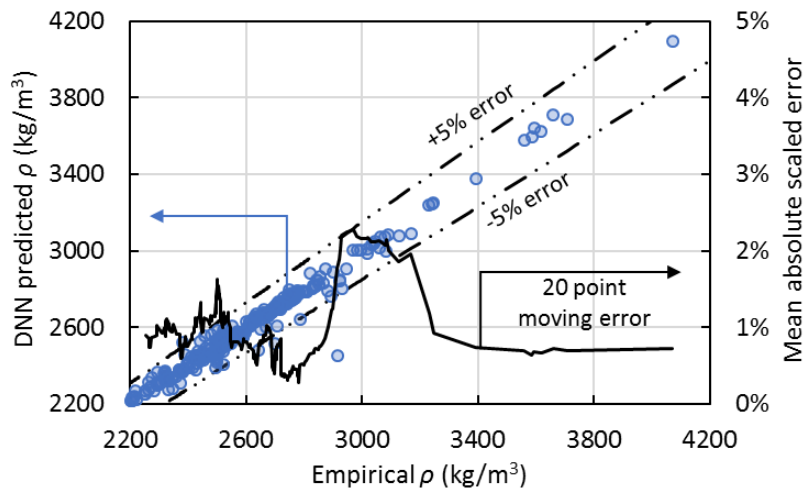
Fig. 3-13. DNN predicted and empirical molten slag density.

Table 3-1. Performance and structure of the DNN predicting molten slag density.

	Property: Density (ρ)	
Performance	$MASE$	0.87%
	$MedASE$	0.44%
	$MBSE$	-0.05%
	R^2	0.97
Structure	Input # (I)	9
	Width ($\varpi = n_{N,1}/I$)	4
	Depth	3
	Pruning rate per layer ($\psi = n_{N,i+1}/n_{N,i}$)	50%
	Structure (in full neuron number)	9 (36-18-9)
Data	Range (kg/m^3)	2131 - 4620
	Range (K)	1002 - 2616
	Range (mol%)	
	Al	(0-40)
	Ca	(0-26)
	Fe	(0-42)
	Mg	(0-26)
	Na	(0-40)
	O	(47-67)
	Si	(0-33)
	Ti	(0-24)
	Training data Testing data	776 332
	Source #	18
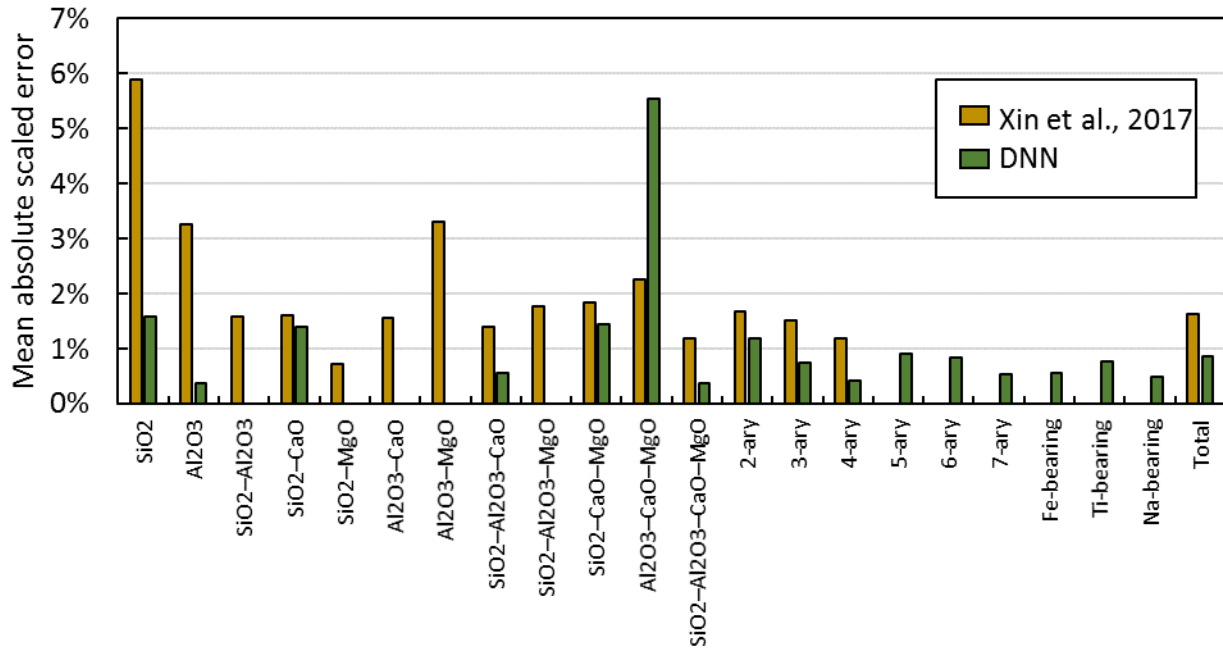
Fig. 3-14. Comparison of DNN and partial molar volume-based predictions of molten slag density.
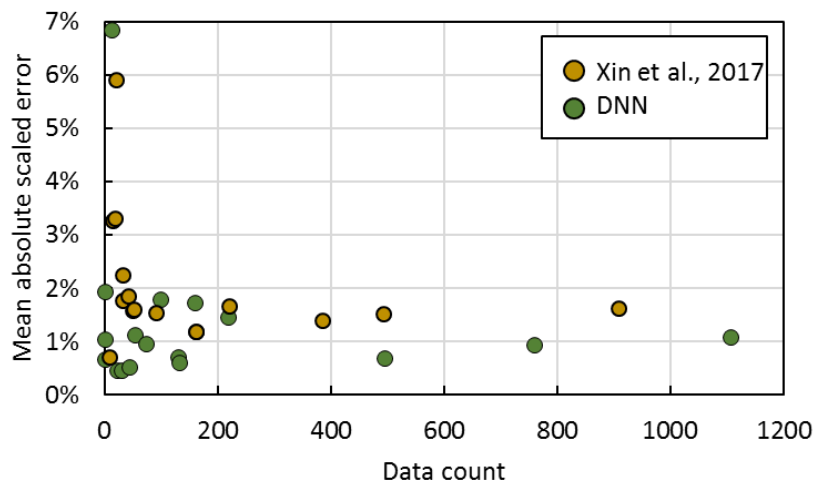
Fig. 3-15. The increased prediction error that coincides with low data quantity for DNN and traditional prediction methods of molten slag density.

3.4. Liquidus temperature estimation

In contrast to ρ, the liquidus temperature (T_L) is a notoriously difficult property to estimate purely from the composition and temperature. This difficulty arises because of the low melting point eutectics between the various constituents of slag. For an isobaric solution, there intrinsically exists a temperature at which liquid and solid phases coexist (T_C). Due to difficulties in experimentally measuring T_c, the ISM industry generally reports the T_L or solidus temperature (T_S), which straddle the T_c at higher and lower temperatures, respectively. In solutions, these temperatures can in general be reduced by the mixing of species. The depression of T_c is roughly linearly proportional to the molal concentration of the solute at low concentrations. The mechanism of this behavior is the increase in entropy that comes with the addition of a dissimilar sized solute [Hitchcock and Hall, 1999;

Koschke et al., 2015]. The increased entropy drives the solution to favor the liquid phase at a given energy content (i.e., T). Ergo, this effect is to a first approximation non-chemical and occurs even between neutral compounds. At a higher solute concentration, the linearity of this phenomenon breaks down due to the increased variety of solute-solute, solvent-solvent, solute-solvent, and multi-component interactions. The slag system is further complicated by the existence of chemical interactions, making the simplifying assumptions of a Lennard-Jones liquid inapplicable. The situation is further obfuscated by the slag composition in the ISM process deliberately being maintained near eutectic points to ensure slag remains molten and low viscosity in the furnace. This complexity makes traditional data-fitting methods completely unsuitable for estimation of T_L as shown in the estimation proposed by Mills et al., (2011) in **Fig. 3-16**. With large datasets, a larger number of fitting parameters, and a smaller compositional space, accurate estimations of T_L can be produced using simple empirical correlations [Dong et al., 2019]. Alternatively, CALPHAD methods can be used to estimate the T_L as they are built atop a mapping of empirical phase diagram data. Unfortunately, these phase diagrams are incomplete in compositional space, with gaps filled by estimates from density functional theory which in turn relies on assumptions that differ between methods and databases [Palumbo et al., 2014]. In fact, there remains no microscopic theory relating the thermodynamics of the first order liquid-solid phase transition to the structure of the solution.
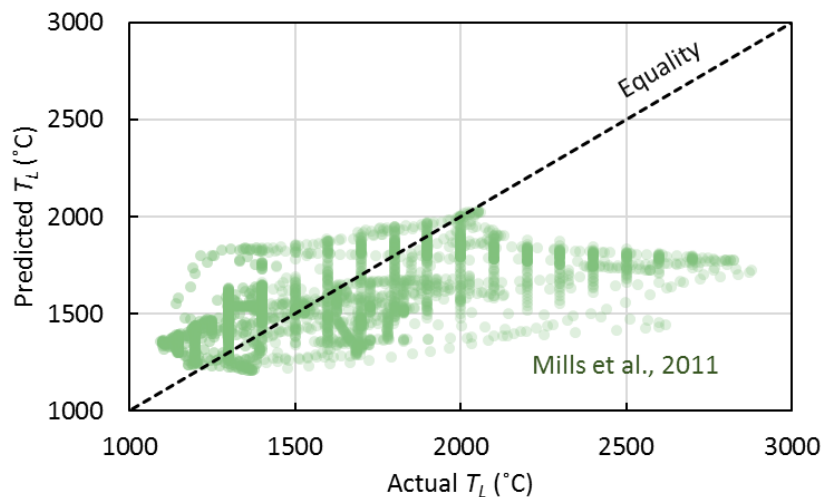
Fig. 3-16. Example of the large errors associated with prediction of liquidus temperature using traditional data fitting.

The T_L of ISM slag was initially estimated using DNN trained on 2222 data points from 38 sources in the literature. The structural optimization method was the same as that used for ρ estimation: namely, the performance as a function of width and depth was first determined, followed by pruning of deeper layers for particularly skillful architectures. To avoid over-fitting, 10-fold cross validation was applied, but no RWR was applied. The optimized structure had an initial $\varpi = 8$ followed by a single hidden layer with $\psi = 50\%$. The $MASE$ and $MedASE$ were 2.44% and 1.37%, respectively. This is indicative of the inherent empirical error in the underlying dataset and not a measure of 'error' by the DNN proper. The results are plotted for a subset of the data (not seen by the DNN during training) in **Fig. 3-17** against predictions from CALPHAD [Hallstedt, 1990]. Recall that CALPHAD also performs data-fitting to predict T_L, therefore the performance is expected to be roughly equivalent between DNN and CALPHAD.
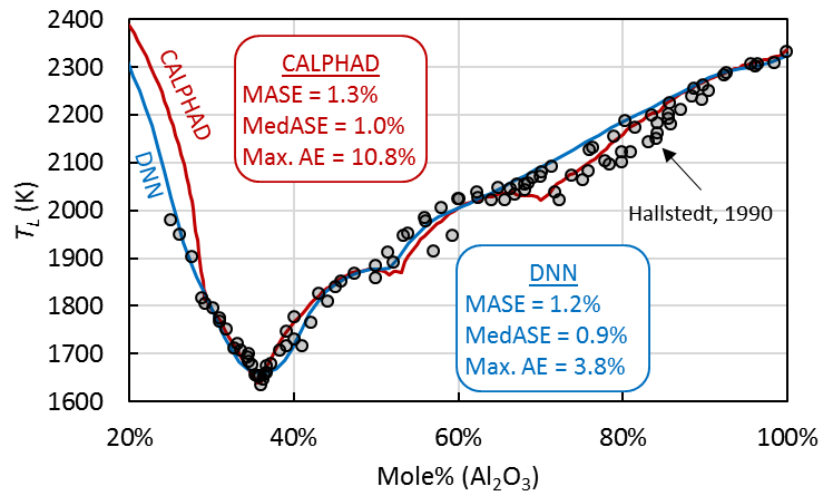
Fig. 3-17. DNN and CALPHAD predictions of T_L plotted against empirical data.

The performance of the initial DNN reflected that of CALPHAD, which is by design close to the inherent empirical error of the dataset. However, the DNN was not trained on solutions containing many of the trace elements common to slag. To rectify this, additional data was gathered, focusing on trace impurities. The total training data count for the 2nd generation DNN was 3490, coming from 76 sources with the dimensionality (i.e., the number of elements) increasing from 9 to 23. It was an open question as to whether the increasing dimensionality of the problem space would overwhelm the inclusion of more data. The structural optimization method was performed on the new data, again with 10-fold cross validation, but without repetitive weight randomization. The resulting optimized structure differed from that of the 1st generation DNN. The initial width increase was only $\varpi = 2$ instead of $\varpi = 8$. The decreased width is believed to be due the additional data providing constraints on relevant emergent parameters. The depth increased from 2 to 3 hidden layers. The increase in depth is hypothesized to be due to the higher complexity of the systems with trace impurities. The 2nd generation DNN performed slightly better than the 1st generation DNN in terms of $MASE$, $MedASE$, and R^2 (**Table 3-2**). The logic behind this seeming paradox is that DNN that receive a wider variety of information must make better models of the world in order to find the underlying physical patterns. **Table 3-2** also provides the DNN structures and input data compositions for both generations of DNN. The composition space covered by each DNN is provided in **Fig. 3-18**. The performance of the 1st and 2nd generation DNN is plotted in **Fig. 3-19** and **Fig. 3-20**, respectively. The general performance of the 2nd generation DNN is compared with that of a recent empirically-fit model and the CALPHAD-based software, FactSage [Dong et al., 2019] in **Fig. 3-21**.

Table 3-2. Performance and structure of the DNN predicting molten slag liquidus temperature.

		1st Generation	2nd Generation
Property: Liquidus temperature (T_L)			
Performance	MASE	2.44%	2.34%
	MedASE	1.37%	0.93%
	MBSE	0.04%	-0.20%
	R^2	0.95	0.97
Structure	Input # (I)	9	23
	Width ($\varpi = n_{N,1}/I$)	8	2
	Depth	2	3
	Pruning rate per layer ($\psi = n_{N,i+1}/n_{N,i}$)	50%	50%
	Structure (in full neuron number)	9 (72-36)	23 (46-23-12)
Data	Range (K)	1093 - 2877	673 - 2877
	Range (mol%)		
	Al	(0-40)	(0-40)
	B	---	(0-40)
	Ba	---	(0-33)
	C	---	(0-11)
	Ca	(0-50)	(0-50)
	Cl	---	(0-67)
	Cr	---	(0-21)
	F	---	(0-67)
	Fe	(0-50)	(0-50)
	K	---	(0-67)
	Li	(0-66)	(0-67)
	Mg	(0-50)	(0-50)
	Mn	---	(0-18)

Na	(0-66)	(0-67)	
O	(33-66)	(0-82)	
P	---	(0-29)	
S	---	(0-17)	
Si	(0-33)	(0-33)	
Sr	---	(0-43)	
Ti	(0-33)	(0-33)	
V	---	(0-29)	
Zn	---	(0-3)	
Zr	---	(0-26)	
Training data Testing data	2222 952	3490 1496	
Source #	38	76	
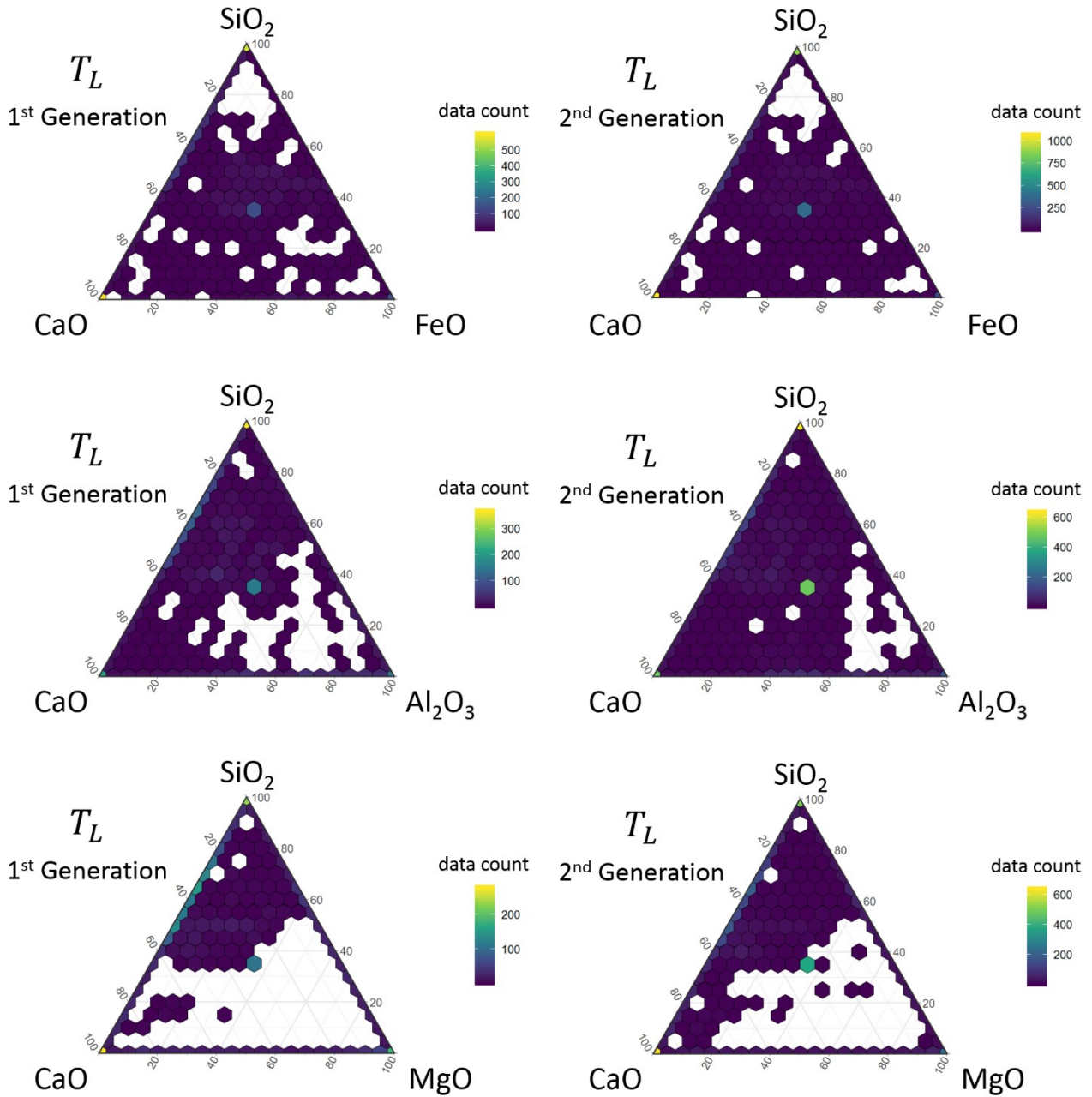
Fig. 3-18. Range of liquidus temperature data used in training DNN plotted on CaO-SiO₂-FeO, CaO-SiO₂-Al₂O₃ ,and CaO-SiO₂-MgO ternary diagrams.
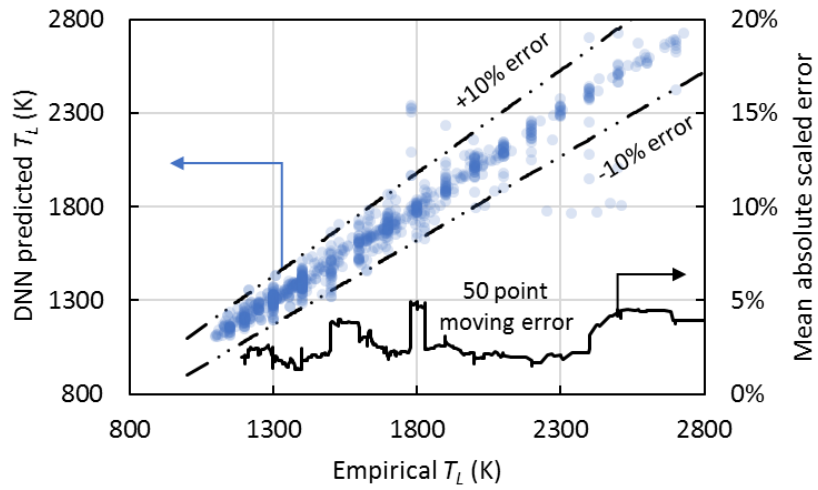
Fig. 3-19. 1st generation DNN prediction vs empirical T_L.
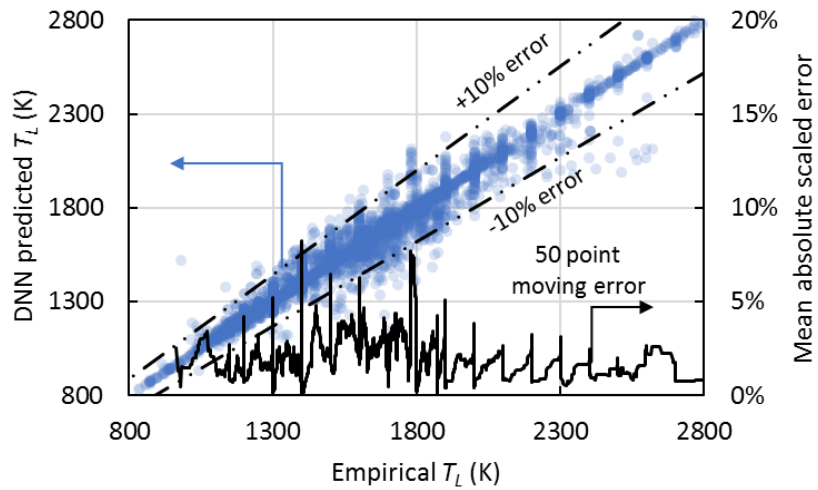
Fig. 3-20. 2nd generation DNN prediction vs empirical T_L.
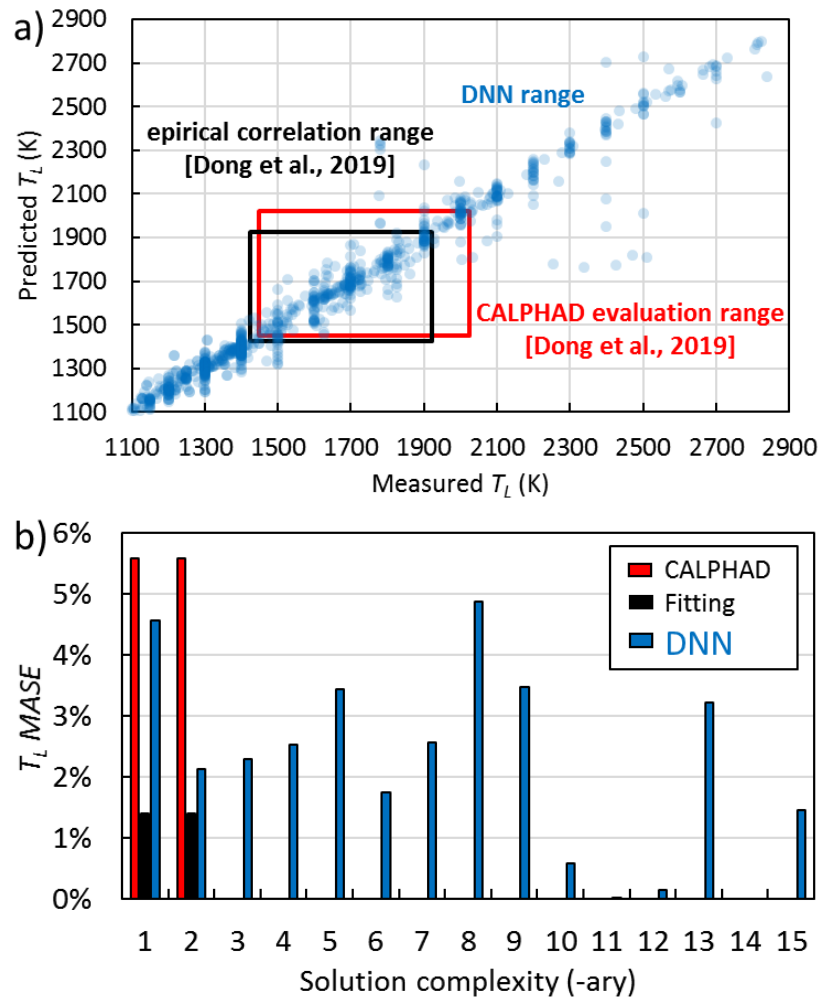
Fig. 3-21. T_L prediction performance for the 2nd generation DNN, a recent empirically-fit model, and CALPHAD a) as a function of temperature and b) for different compositions.

Using the trained 2nd generation DNN, the composition dependence of T_L across the CaO-SiO$_2$-FeO and CaO-SiO$_2$-Al$_2$O$_3$ ternaries was mapped in **Fig. 3-22** and **Fig. 3-23**, respectively. Comparison with CALPHAD generated mappings (**Fig. 3-24** and **Fig. 3-25**, respectively) shows good agreement.

The effect of impurities on T_L for slag compositions relevant to ISM was then analyzed by first determining the T_L of industry average BF, BOF, and EAF slag compositions (**Table 3-3**) and adding in small amounts of various impurities. Impurities were added as compounds, introducing additional elemental components beyond the targeted element. The results for BF, BOF, and EAF slag are provided in **Fig. 3-26**, **Fig. 3-27**, and **Fig. 3-28**, respectively. The T_L is extremely sensitive to the impurity being added as highlighted by **Fig. 3-29**, demonstrating the usefulness of the DNN for the ISM industry.
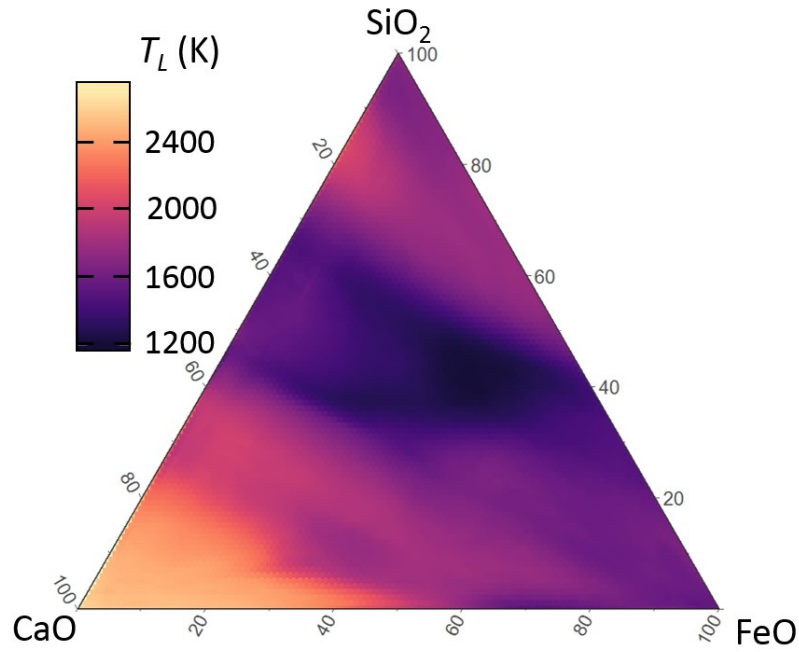
Fig. 3-22. DNN prediction of T_L for the CaO-SiO₂-FeO system.
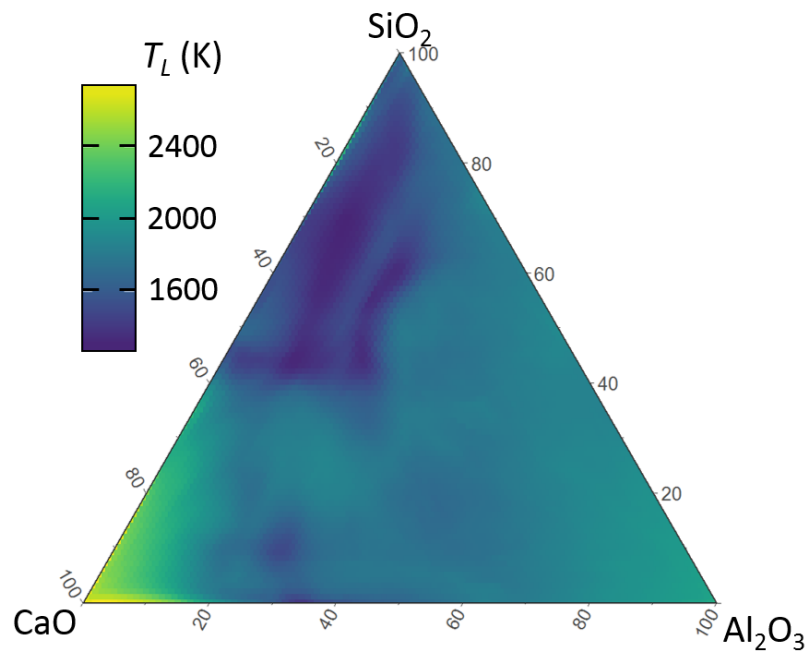
Fig. 3-23. DNN prediction of T_L for the CaO-SiO₂-Al₂O₃ system.
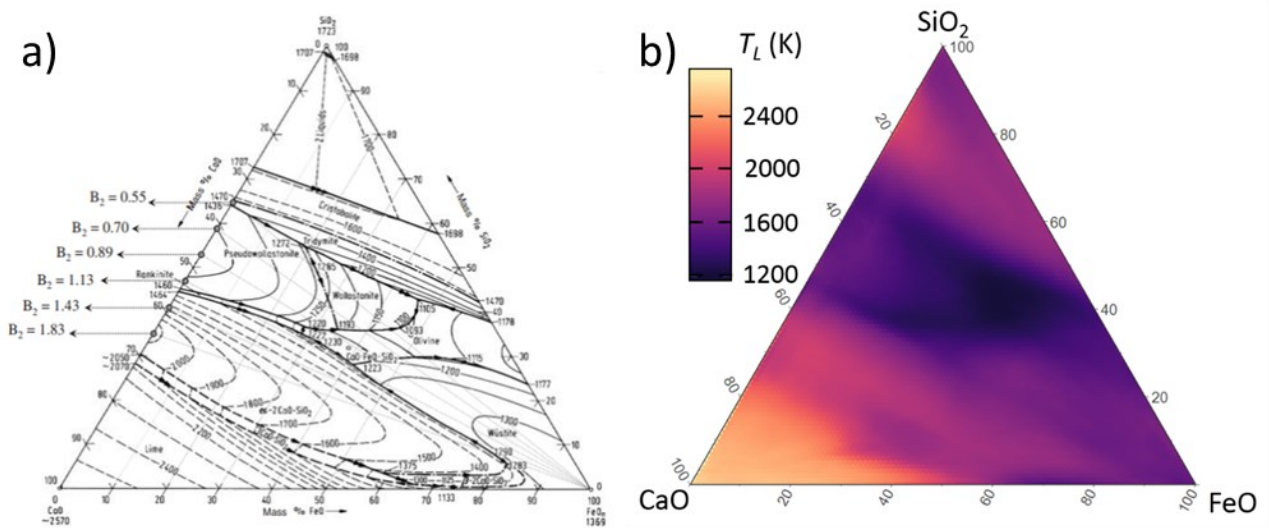
Fig. 3-24. Comparison of the prediction of T_L for the CaO-SiO₂-FeO system from a) CALPHAD [Chuang et al., 2009], b) DNN.
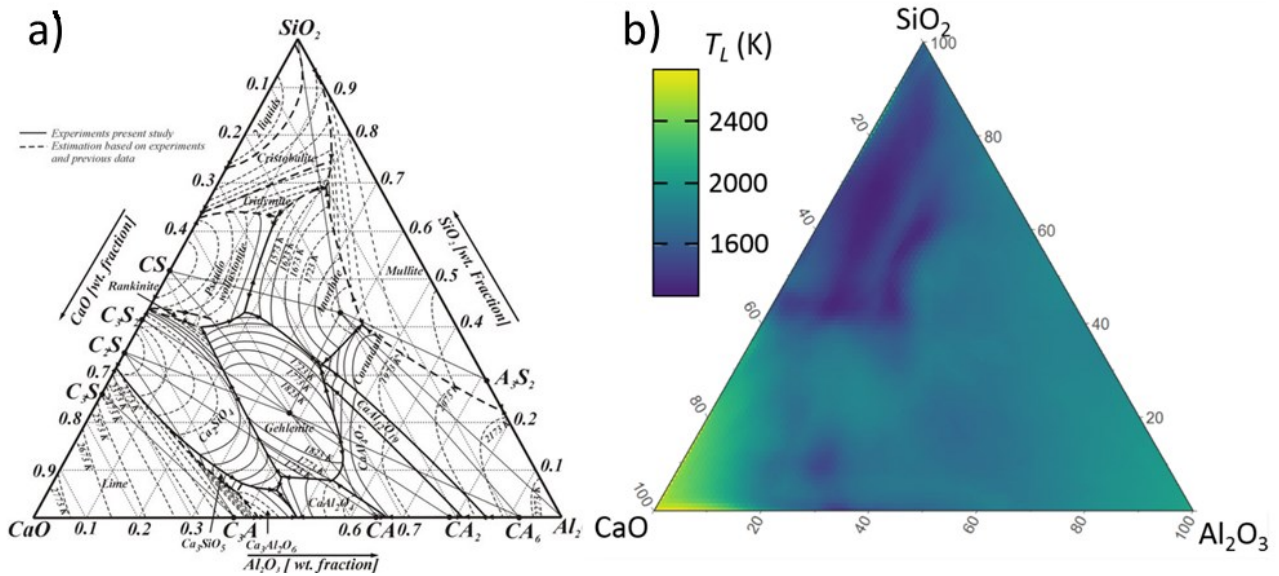
Fig. 3-25. Comparison of the prediction of T_L for the CaO-SiO₂-Al₂O₃ system from a) CALPHAD [Haccuria et al., 2016], b) DNN.

Table 3-3. Industry-average slag compositions in mass percent.

Element	BF slag	BOF slag	EAF slag
Al	6.56%	0.00%	3.40%
Ca	16.36%	24.47%	15.61%
Fe	0.00%	10.06%	12.74%
Mg	4.74%	4.39%	5.25%
Mn	0.00%	1.23%	1.66%
O	58.54%	53.28%	54.35%
Si	13.80%	6.57%	6.99%

Additives: B (as B_2O_3): 1-5%; C (as $CaCO_3$): 1-5%; F (as CaF): 1-5%; K (as K_2O): 1%; Li (as Li_2O): 1-5%; Na (as Na_2O): 1-5%; P (as $Ca_3(PO_4)_2$): 1%; S (as $CaSO_4$): 1-3%; Ti (as TiO_2): 1-5%; V (as V_2O_5): 1-5%; Zr (as ZrO_2): 1%.
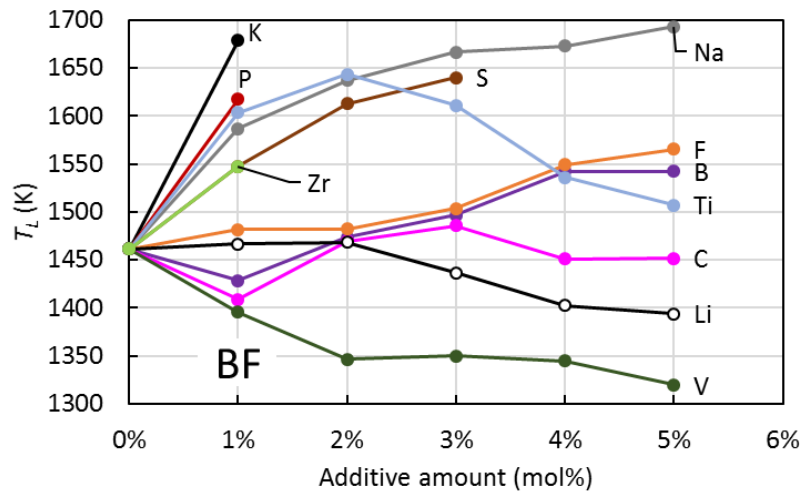
Fig. 3-26. Effect of trace elements on the T_L of industry-average BF slag.
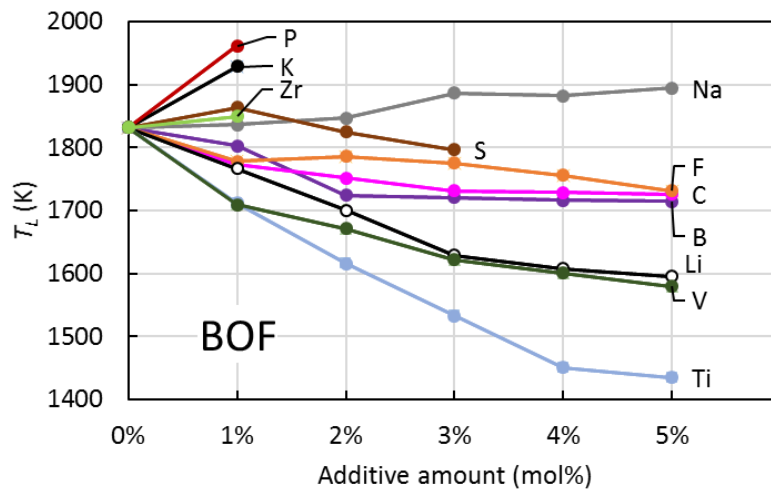
Fig. 3-27. Effect of trace elements on the T_L of industry-average BOF slag.
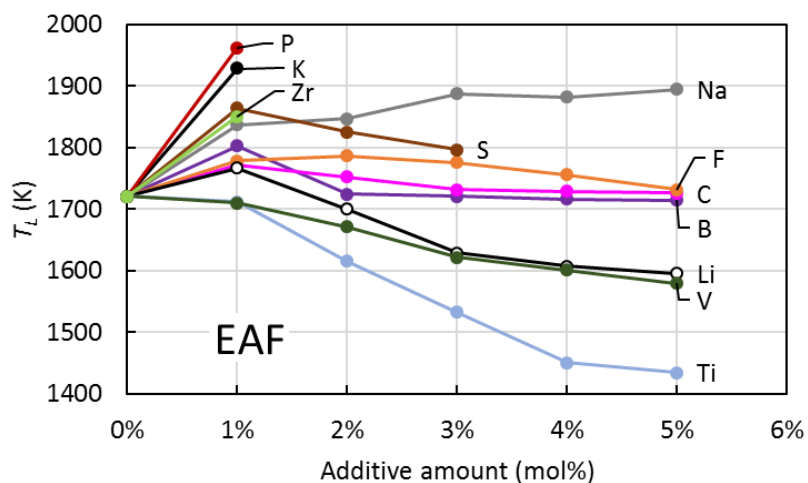
Fig. 3-28. Effect of trace elements on the T_L of industry-average EAF slag.
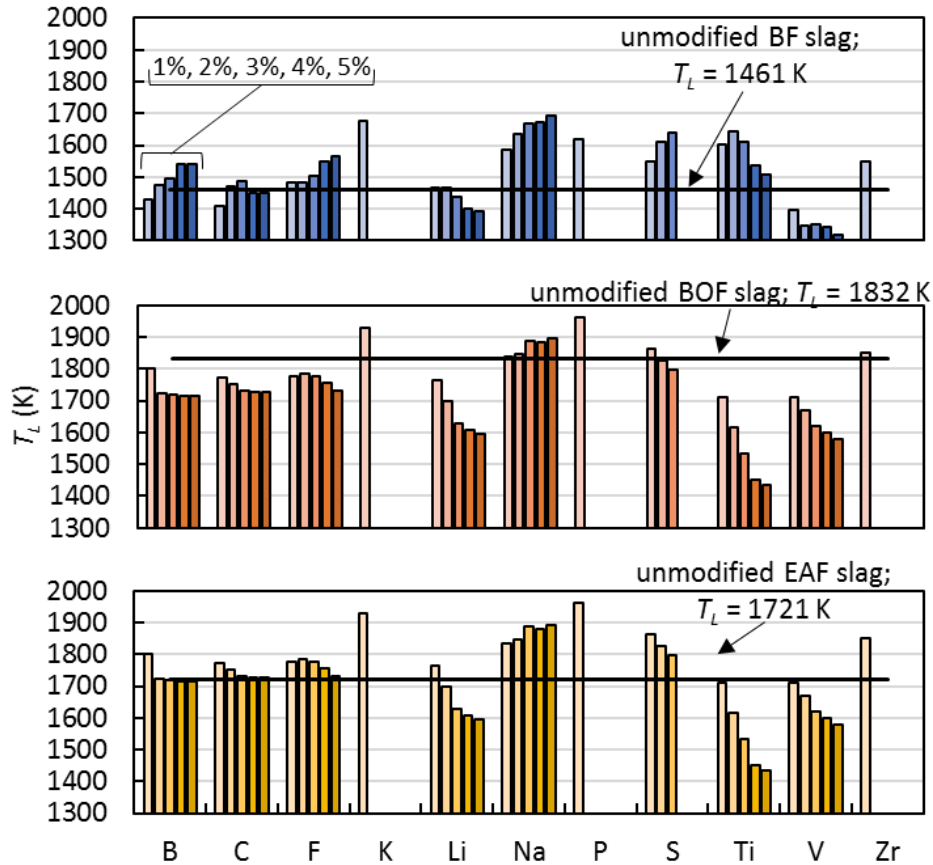
Fig. 3-29. Alteration to ISM slag T_L as a function of impurity type and concentration.

3.5. Thermal conductivity estimation

In the context of ISM, the thermal conductivity (κ) of slag is a critical feature to maintain efficient operations and the fitness of the furnace. The κ of slag largely dictates the degree of heat loss from the metallic melt and the heat transfer to the furnace lining. In addition to ISM operations, the κ is a key factor for designing treatment options for slag as it dictates the rate at which cooling can be applied under given geometric and environmental conditions. Given that the solidification and cooling process are the primary engineering control points determining the mineralogy and micromorphology of solid slag, knowledge of the κ is crucial for slag treatment or reuse schemes. Along with practical interest, κ is an open area of theoretical research. It is widely believed that κ is intimately related to the underlying silicate melt structure. Due to difficulties in high temperature measurement, κ data in the literature contains substantial noise and variation between measurement methods. This low S/N ratio further complicates the already difficult task of producing a theory which captures the emergent behavior of κ across a diverse compositional space.

At the molecular level, quantized thermal energy (phonons) are absorbed through lattice vibrations. This behavior is captured by **Eq. (3-19)** (Debye's equation), where c_V is the specific heat capacity per unit volume, v is the phonon velocity in the medium, and l_{mp} is the mean path length of the phonon.

$$\kappa = \frac{1}{3} c_V v l_{mp} \tag{3-19}$$

In a molten state, the largely disordered structure alters the l_{mp} via scattering of phonons at sites of silicate depolymerization [Kang and Morita, 2006]. The number of scattering sites (n_X) is related to the temperature as **Eq. (3-20)** where R is the gas constant and E_A is the activation energy to break a bond in the silicate structure.

$$\frac{1}{n_X} \propto \frac{1}{\exp(E_A/RT)} \qquad (3-20)$$

Conceptually, higher temperatures break more bonds, resulting in more scattering and thus a shorter mean free path of the phonons. Additionally, phonon-phonon interactions disrupt the free movement of phonons. The l_{mp} is predicted to be $\sim 1/T$. At high temperatures, the quantity of phonons is posited to be proportional T, therefore the phonon-phonon interactions $\propto$ phonon number $\propto T$ [Kittel et al., 1996].

In addition to thermal effects, the composition clearly effects the κ. Starting from a purely silicate network, the addition of any new species results in at least a reconfiguration of the structure, if not necessarily a relative decrease in order. Silicates contain covalent bonds in the basic SiO_4 tetragonal unit (i.e., between silicon and the binding oxygens) and ionic bonds between basic oxide cations and non-bridging oxygens. Basic oxides (e.g., CaO) tend to shorten l_{mp}, both due to their shorter bond lengths and due to the disruption of the silicate network [Ammar et al., 1982]. Even at the level of 3-ary or 4-ary systems, prediction of κ is notoriously inaccurate. Slags encountered in actual ISM operations typically contain >6 major species and two to three times as many trace compounds. This degree of complexity engenders a combinatorial explosion on estimates of structural variation that further reduces the skill of traditional methods.

Several researchers have used general correlations to estimate the κ of molten slag. Most commonly, the relative quantity of 'non-bridging oxygens' (NBO) [Mills, 1993], the viscosity (η) [Hayashi et al., 2001], or the optical basicity [Hayashi et al., 2001] are used in such correlations. The use of NBO attempts to directly indicate the structural aspect of a melt that effects the κ: that is, the relative quantity of covalent and ionic bonds. This strategy is based on the fundamental observation that phonon resistance is lower across covalent bonds than ionic bonds. This method has had relative success for simple systems [Nagata and Goto, 1984], but has been shown to be limited in application [Kang et al., 2014] due to the plethora of potential structures even in simple silicate systems [Freitas et al., 2015], the amphoteric nature of some common slag constituents such as Al [Park et al., 2008], the influence of multivalency [Kang et al., 2012], and the importance of other factors such as cation size [Sukenaga et al., 2006]. The use of η or optical basicity as a correlating factor for κ is based on a strong empirical correlation [Susa et al., 1994] and the theoretical co-dependence on the underlying structure of a melt [Mills et al., 2011]. However, the co-dependence on structure does not mean that the underlying mechanisms are equivalent (in fact, they are most definitely dissimilar), nor does it mean that the structural elements of importance are alike. These facts become increasingly apparent as the complexity of a melt increases, highlighting the spurious nature of these correlations [Matsushita et al., 2011].

The κ of ISM slag was estimated by training a DNN on 694 data points from 14 sources. The typical structural optimization method was employed (modification of width and depth followed by pruning of deeper layers). Over-fitting was suppressed by 10-fold cross validation. No RWR was applied. The

optimized structure required an expansion of the first hidden layer by 16 times the input number with 5 layers of hidden neurons. Each successive hidden layer was pruned 50%. The relatively deep structure and wide initial layer is compatible with the widely held assumption that κ is a result of complex structural interactions within the molten melt.

Despite the small data count and the known difficulty in estimating thermal conductivity, the prediction errors were significantly less than those reported in the literature; $MASE$ and $MedASE$ were 14.97% and 7.97%, respectively. The structure, performance, and composition boundaries are provided in **Table 3-4**. The range of data used in training is provided in **Fig. 3-30** and results of predictions are shown in **Fig. 3-31**. The rolling $MASE$ shows a pronounced increase at low thermal conductivities. However, this effect is due to the limits of empirical measurement accuracy and κ being defined with a lower bound at zero. In **Fig. 3-32** the magnitude of the error is plotted against the κ. The error magnitude decreases monotonically with thermal conductivity, but mathematically will head towards infinity as empirical error is non-zero and the limit of κ is zero. In **Fig. 3-33**, the DNN predictions are compared with those from structural models (e.g., based on NBO or correlated to viscosity) and from composition-specific temperature correlations [Hasegawa et al., 2012; Kang and Morita, 2006; Kim and Morita, 2015; Ozawa and Susa, 2005; Susa et al., 2001]. The DNN outperformed all available methods both in terms of accuracy and application range.
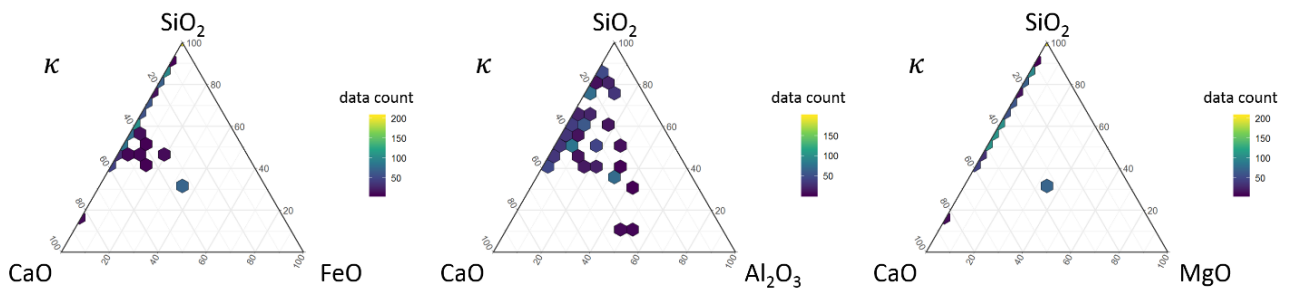
Fig. 3-30. Range of conductivity data used in training DNN plotted on CaO-SiO$_2$-FeO, CaO-SiO$_2$-Al$_2$O$_3$, and CaO-SiO$_2$-MgO ternary diagrams.

Table 3-4. Performance and structure of the DNN predicting molten slag thermal conductivity.

Property: Thermal conductivity (κ)		
Performance	MASE	14.75%
	MedASE	7.66%
	MBSE	-5.23%
	R^2	0.96
Structure	Input # (I)	8
	Width ($\varpi = n_{N,1}/I$)	16
	Depth	5
	Pruning rate per layer ($\psi = n_{N,i+1}/n_{N,i}$)	50%
	Structure (in full neuron number)	8 (128-64-32-16-8)
Data	Range W/(m·K)	0.02 – 7.57
	Range (K)	928 - 1876
	Range (mol%)	
	Al	(0-23)
	B	(0-40)
	Ca	(0-23)
	Fe	(0-7)
	Na	(0-29)
	O	(53-65)
	Si	(0-27)
	Training data Testing data	694 297
	Source #	14
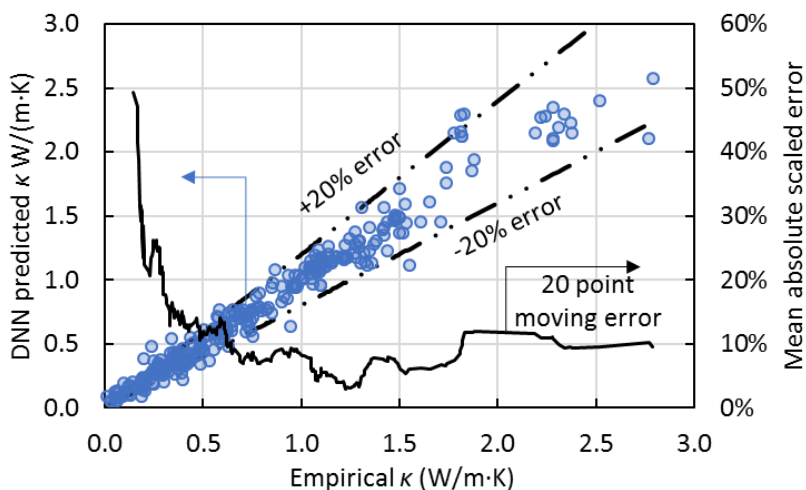
Fig. 3-31. DNN prediction of thermal conductivity compared to empirical data.
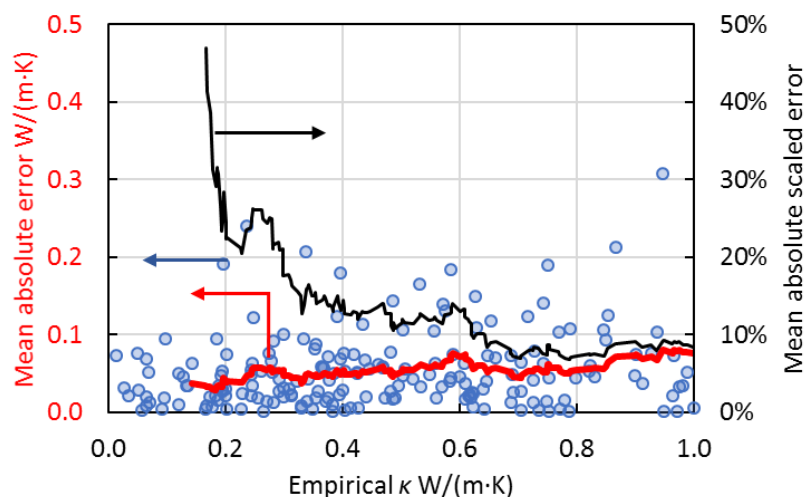
Fig. 3-32. The increase in scaled error that occurs when the ground truth value approaches zero despite a consistent error magnitude.
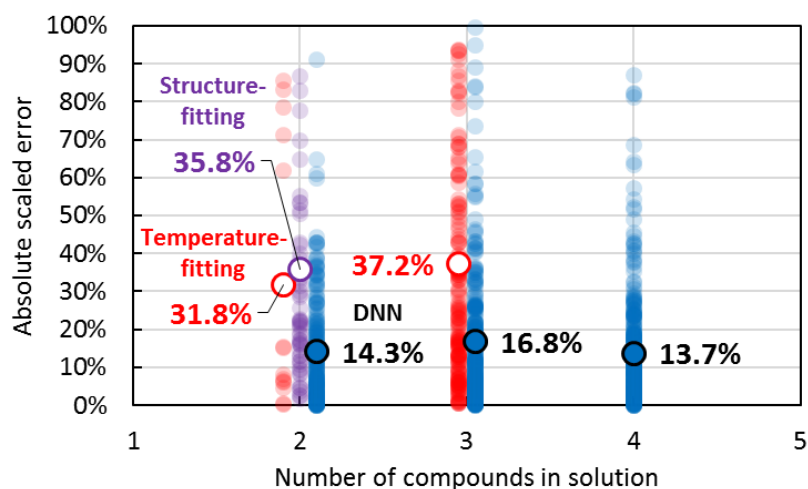
Fig. 3-33. Comparison of DNN prediction of κ with those from composition-specific temperature correlations and structure-based equations.

3.6. Viscosity estimation

Control of the viscosity (η) of ISM slag is important for maintaince of the furnace integrity and smooth operations. The η controls the ability of molten metal to reach the bottom of the furnace, the degree of foaming in EAF operations, the ease with which the slag is poured/tapped, and many other operation-critical factors. Knowledge of η is also essential in the design and operation of slag treatment; all treatment methods require removal from the furnace and some degree of transport (e.g., to a slag pit, to granulation activities, to controlled settling). Like thermal conductivity, η is also of interest to the theoretical community due to its connection to the underlying silicate structure. Due to the shared dependence on molten slag structure, the same complexities that plague κ prediction inhibit the accurate prediction of viscosity. However, the underlying physical mechanism is distinct. Viscosity arises from the dragging of slower moving molecules by faster moving molecules, causing some of the kinetic energy of the faster molecules to be transferred into temporary stretching of bonds. This bond stretching is subsequently converted to vibrational energy and heat. The transfer of energy to surrounding particles by molecule motion results in a density wave and a corresponding rearrangement of a large number of surrounding particles. The extent of influence of this interaction is related to the magnitude of the motion relative to the magnitude of kinetic energy of the surrounding particles (i.e., the temperature). In other words, the signal from a comparatively rapid moving particle is obscured by the noise of the movement of the surrounding particles. As such, the number of particles influenced by the prime mover particle increases as temperature decreases. This increased sphere of influence is one of the mechanisms by which viscosity increases with temperature. It is also proposed that viscosity is thermally activated as given by $\eta = \eta_\infty e^{(E_A/RT)}$, with a temperature-dependent activation energy. The similarity to the general description of κ is readily apparent. Regardless of the base mechanisms assumed, the continued emergence of new models for silicate melt and molten slag η is indicative that current models provide insufficient accuracy and generalizability [Han et. al., 2016].

The η of ISM slag was estimated using a DNN trained on 2058 data points from 37 sources. The depth and width were first optimized, followed by pruning of deeper layers in skillful architectures. Overfitting prevention was realized with 10-fold cross validation but without RWR. The optimized structure expanded the width by 16 times and then had 5 layers of 50% pruning. This structure is equivalent to that found in the κ analysis despite no efforts to generate equivalent structures. Moreover, the data sets are completely independent with large differences in the chemical makeup and temperature range. The matching structures support the findings in the literature of a correlation between κ and η. The equivalent structures also suggest that the DNN is indeed generating a hierarchical representation of the system in order to produce predictions. This result is important as it suggests that analysis of the inner workings of the DNN may lead to insights into the mechanisms underlying the emergence of η and κ. Moreover, the necessity of 5 hidden layers is suggestive that these properties are, to some extent, computationally irreducible. If true, this implies that efforts to generate predictions without the same degree of hierarchical calculation structure are doomed to low accuracy or generalizability.

The $MASE$ and $MedASE$ were 14.70% and 8.22%, respectively. Again, the similarity between the κ results is striking and implies that this level of variability may be inherent to the system. Although measurements are taken of a bulk solution containing innumerable compounds, the stochastic nature of the internal structure may be materializing in the error distribution of the data. The

structure, performance, and composition boundaries are provided in **Table 3-5**. The range of data used in training is graphed in **Fig. 3-34**, the DNN prediction is compared to empirical values in **Fig. 3-35,** and the overall performance is compared with a recent review of η predictions in the literature in **Fig. 3-36**. The DNN provides substantial improvements over all available methods in the literature. It should be noted that this is not a result of data quantity, as Han et al., 2015 and Han et al., 2016 used 2958 and 1780 viscosity data, respectively.
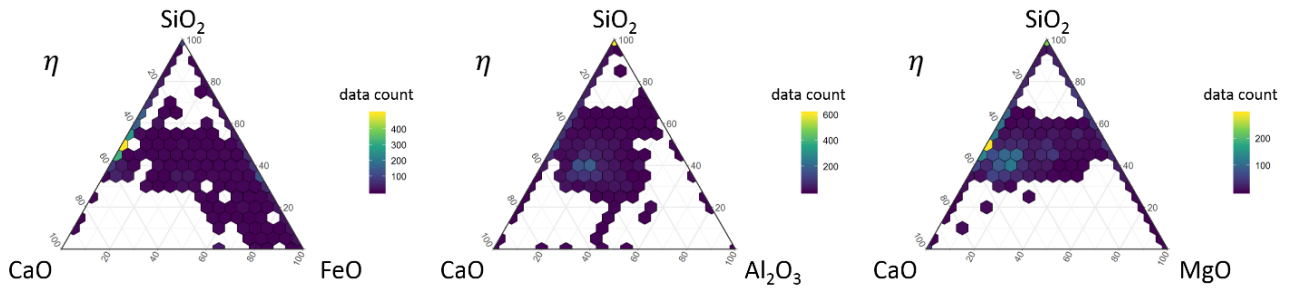
Fig. 3-34. Range of viscosity data used in training DNN plotted on CaO-SiO$_2$-FeO, CaO-SiO$_2$-Al$_2$O$_3$,and CaO-SiO$_2$-MgO ternary diagrams.

Table 3-5. Performance and structure of the DNN predicting molten slag viscosity.

Property: Viscosity (η)		
Performance	MASE	14.70%
	MedASE	8.22%
	MBSE	-2.97%
	R^2	0.97
Structure	Input # (I)	8
	Width ($\varpi = n_{N,1}/I$)	16
	Depth	5
	Pruning rate per layer ($\psi = n_{N,i+1}/n_{N,i}$)	50%
	Structure (in full neuron number)	8 (128-64-32-16-8)
Data	Range (Pas)	$2 \times 10^{-3} - 1 \times 10^{5}$
	Range (K)	1439 − 2477
	Range (mol%)	
	Al	(0-35)
	Ca	(0-32)
	Fe	(0-50)
	Mg	(0-35)
	O	(43-58)
	Si	(0-39)
	Ti	(0-8)
	Training data Testing data	2058 882
	Source #	37
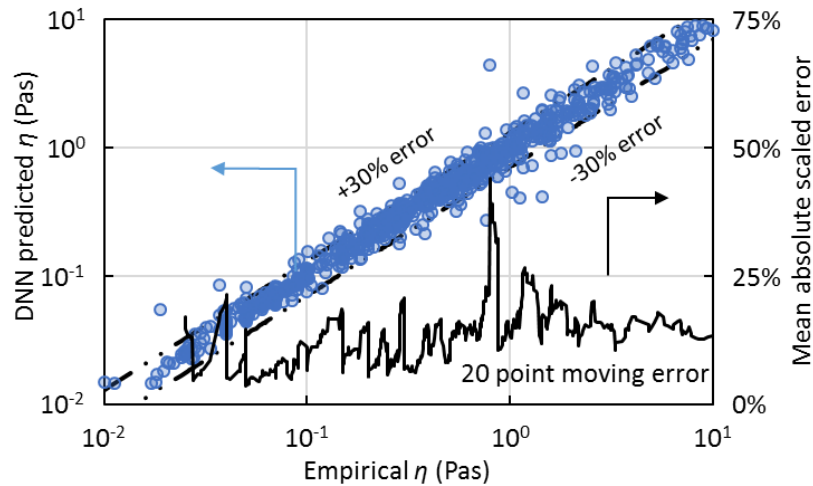
Fig. 3-35. DNN prediction of viscosity plotted against empirical values.
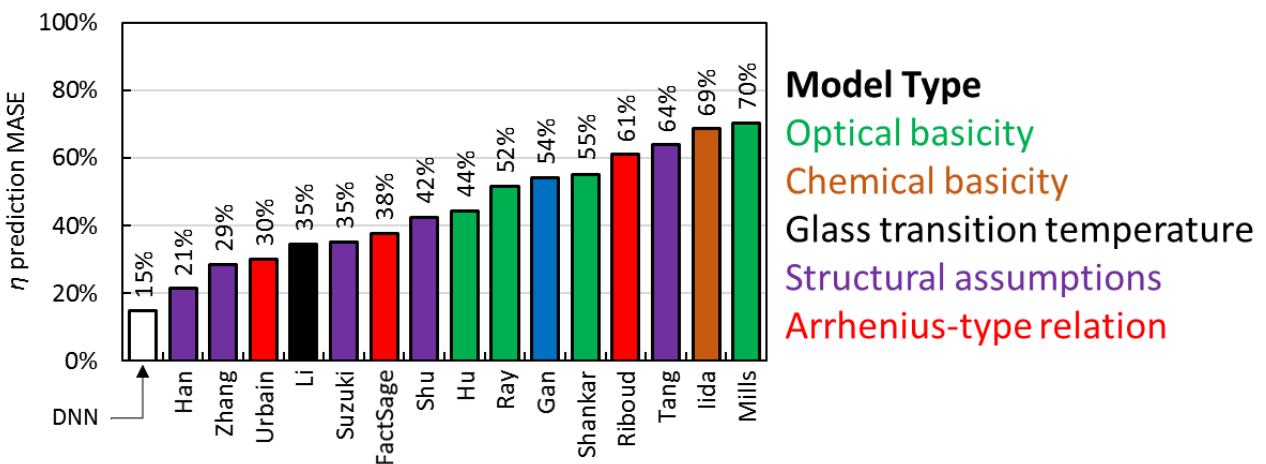
Fig. 3-36. The performance of the DNN viscosity prediction compared to the state-of-the-art prediction methods in the literature.

3.7. Nucleation lag time

Nucleation is the onset of sustained first order phase transition. It is the critical step in controlling the final mineralogy and micromorphology of slag from which return, or modification, becomes energetically expensive. Nucleation of slag is to be avoided in ISM furnaces at all costs. However, once slag has left the furnace, its nucleation is either promoted (in various slag treatment methods) or functionally ignored (i.e., slag dumping). Promotion of nucleation is performed by rapid cooling in order to create a low crystallinity slag. Low crystallinity slag has various environmental benefits and industrial usage pathways, though this dissertation argues that low crystallinity slag is a non-ideal treatment and reuse pathway. In fact, one of the key results of this dissertation is that slag nucleation should be driven to the limiting cases of extremely slow and rare nucleation or, under very particular circumstances (i.e., centrifuging), to extremely rapid, homogeneous nucleation. As such, prediction of the time required for nucleation to begin (nucleation lag time: τ) is of central importance.

Nucleation involves the rearrangement of liquid molecules into a solid structure due to the higher stability provided by the solid form at a given energy density (i.e., temperature). Though the driving forces can be explained with thermodynamics and the concepts are purely classical, the stochastic

nature of fluids makes the kinetics of the process highly probabilistic. Furthermore, ISM slag is in a class of fluids termed high ionic strength solutions (HISS) whose characteristics makes the transition from liquid to solid much more sensitive to kinetics than highly dilute systems. This fact is evidenced by the continued theoretical interest in the kinetics of solidification of slags and similar composition melts. The key feature that continues to defy theoretical understanding is the delay between the proper conditions for solidification and solidification itself (i.e., τ; alternatively termed the induction time but distinct from the relaxation time).

3.7.1. Classical nucleation theory

Classical nucleation theory (CNT) is simply an assignment of the rates of competing phenomenon to determine the timing and speed at which a phase transition occurs. Classical Nucleation Theory starts from the position that, by construction, when a melt drops below its T_L it will solidify. When molecules have high kinetic energy (i.e., high temperature), they naturally remain in the state that provides greater degrees of freedom. When the temperature drops, the molecules no longer have sufficient kinetic energy to resist the bonding force of other molecules, resulting in the formation of a solid. The mechanics of solidification dictate that previously unconstrained elements (i.e., fluids) must form groupings of quasi-permanent arrangements (i.e., solids). This change in local arrangement has two key implications: 1) the entropy of the atoms is lower in the solid state than in the liquid state, and 2) a surface between the liquid and solid states has been created. A surface implies a disruption in bonds which inherently requires energy input to maintain. It is this competition between the need for energy to create new surface area (i.e., to maintain the bond disruption between solid and liquid phases) and the generation of energy by the loss of entropy inherent in the restrictive nature of the solid state. **Figure 3-37** provides the canonical graphical representation of the process.
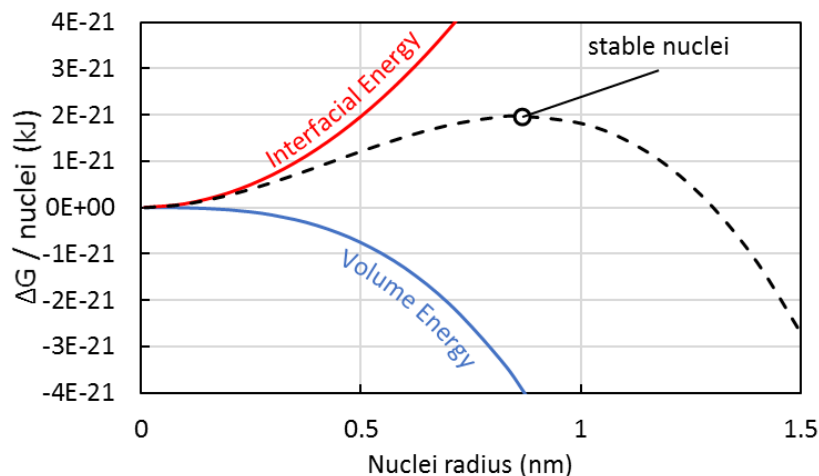
Fig. 3-37. The competition between interfacial and volume energy during nucleation; arbitrary values are used.

The phase transition is initiated by the agglomeration of atoms into a sufficiently large crystalline nucleus (critical diameter: d_0) such that the free energy cost of the newly generated crystal-liquid interface is overcome by the free energy gain of the crystal volume [Karthika et al., 2016]. The clustering and rearrangement of atoms from a molten state to a crystalline state is accomplished through the translation and rotation of atoms along with the stretching, breaking, and forming of

atomic bonds. This physical rearrangement of atoms is a stochastic process that requires a certain amount of time in addition to that needed for aggregation of a sufficient number of particles. The τ is traditionally calculated as **Eq. (3-21)**,

$$\tau = \frac{16}{\pi} \frac{k_B T \gamma}{\Delta G_V^2 d_0^2 D} \qquad (3-21)$$

where k_B is the Boltzmann constant, T is the absolute temperature, γ is the specific free energy of the crystal-liquid interface, ΔG_V is the difference in the Gibbs free energy between an equivalent volume of melt and crystal, and D is the diffusivity through the crystal-liquid interface. The D is typically calculated using **Eq. (3-22)**,

$$D = \frac{d_0^2 k_B T}{h} \exp\left(-\frac{\Delta G_D}{k_B T}\right) \qquad (3-22)$$

where h is the Plank constant and ΔG_D is the kinetic barrier to nucleation. The key divergence in CNT from reality occurs at the transition from the actions of individual molecules (which is purely based on local interactions) to the aggregate behavior of many molecules. Classical Nucleation Theory makes several assumptions that are fitting at the macroscale but are inconsistent with the realities at the microscale [Vekilov, 2010]. This allows CNT to be conceptually and computationally simple, but quantitatively incorrect in important ways for the slag system. A non-exhaustive list of the problematic simplifying assumptions of CNT and their shortcomings are listed below.

Spherical nucleating shape.

Classical Nucleation Theory was initially developed for the prediction of water condensation from the gas phase [Volmer and Weber, 1925]. As the liquid phase does not contain a rigid structure but does contain surface tension, the assumption of sphericity is appropriate. However, in the nucleation of solids from molten slag, there exist no solids with a spherical crystalline structure. When a large enough number of atoms have aggregated, the thermodynamic energy barrier is breached, and the shape does not limit the crystal growth. However, the issue of τ is one of the early stages of atomic aggregation (i.e., a small number of atoms). Therefore, the actual shape of the nucleating solid can have a far larger surface area to volume ratio than the sphere (e.g., SA/V of cube $\approx 1.24\ SA/V$ of sphere) [Wang et al., 2018]. Moreover, for crystalline solids, there is often an energetically preferred direction of growth, further confounding the assumption of sphericity. As such, the size of the nucleating solid (i.e., the number of molecules that have aggregated) must be substantially larger than predicted by CNT and will therefore take significantly longer than expected. Additionally, a non-spherical shape incurs a heterogeneous boundary, altering the local aggregation dynamics.

Sharp boundary between liquid and solid.

Classical Nucleation Theory avoids the complications of two-way molecular movement across the solid-liquid interface by assuming this movement can be aggregated and smoothed over the whole surface. This allows for the further simplification that the interface is sharp and well-defined. From this idealized surface area, the change in Gibbs energy due to surface formation is calculated. However, the non-spherical nature of the nucleating solid and the potential for preferred directions of growth in crystals, means that the flux across the surface will be inhomogeneous [Joswiak et al., 2013]. To account for this disparity requires seeing the 'surface' not as a homogeneous entity but as

the aggregate flux of bi-directional movement of particles. The assumption of a sharp surface can generate prediction errors in both directions.

Constant surface tension.

In CNT, the macroscopic surface tension is assumed to be applicable to the microscale at all temperatures. However, from the perspective of individual molecules, the macroscopic surface tension is that of an infinite flat plane. On the other hand, nucleating solids may contain significant surface curvature. Additionally, as the surface tension is related to intermolecular movement, the available kinetic energy (i.e., temperature) would seem to clearly be of significance. Empirical results indicate that surface tension is dependent on the degree of curvature and temperature [Fokin and Zanotto, 2000].

One dimensional transition.

Phase transition from liquid to solid breaks the translational and orientational symmetries of the slag, a fact that should be accounted for in calculations of Gibbs energy change [Russo and Tanaka, 2016]. The one-dimensional nature of CNT (i.e., based only on the radius of the nucleating particle) makes clear it is a fundamentally flawed simplification of the underlying physical processes.

Diffusivity can be determined from viscosity.

The rate determining phenomenon in nucleation is the diffusion of molecules. However, prediction of diffusivity requires that the kinetic barrier to nucleation be known, which requires knowledge of atomic scale interactions and complicating factors. For this reason, diffusivity is correlated to viscosity under the pretense that the mechanism of viscosity is equally relevant to diffusivity. However, experimental results indicate that this correlation breaks down at high T_U; whether this is due to the correlation being spurious or due to the appearance of some new -or the suppression of some existent- mechanism at high undercoolings remains unclear [Krüger and Deubener, 2015]. Regardless of this result, calculating diffusivity from viscosity merely pushes the responsibility of property prediction to viscosity. As noted in Chapter 3.6, the viscosity is also not amenable to accurate prediction using current theories.

Compositional homogeneity.

For historical reasons, and reasons of calculation simplicity, CNT treats the melt and solidifying species as homogeneous. While solutions are certainly homogeneous at the macroscale, the solidification of compounds distinct from the bulk composition provides explicit proof that at the microscopic scale there exists heterogeneity in the slag solution. This feature has been shown empirically in molten solutions with density fluctuations in the melt being attributed to compositional differences [Gebauer et al., 2014; Gupta et al., 2016; Zhang et al., 2018]. Simulations using the simplified Lennard-Jones liquids also indicate the natural de-mixing of compounds based purely on differences in size, diffusion rate, and shape [Digregorio et al., 2018; Kumari et al., 2017; Nunes et al., 2018; Weber and Frey, 2016]. Compositional heterogeneity implies that the statistics for nucleation under CNT may be conservatively skewed. Moreover, the nucleation of a compound with composition distinct from the bulk melt induces changes in the melt composition. The changes in Gibbs energy for the volume and the surface must then account for the compositional difference between the solid and liquid phase.

Homogeneous diffusion rates.

Along with compositional homogeneity, CNT inherently assumes that diffusivity is homogeneous and constant. However, at a given temperature the Stokes-Einstein relation ($D = (k_B T)/(6\pi\eta r)$

where r is the particle radius) indicates that the diffusivity is related to the particle size. It is therefore expected that diffusion rates are different for the disparate components of slag.

In addition to the above issues, there remains open debate on many issues related to CNT (e.g., the time scale of structure fluctuations is less than the relaxation time scale of the melt [Royall, 2018]; internal elastic stresses due to the density misfit between the crystal and liquid are unaccounted for [Abyzov et al., 2016], etc.).

To address the issues stated above, a substantial portion of the field has turned to Monte Carlo Molecular Dynamics (MCMD) simulations. However, the practical conundrums raised in Chapter 3.1.2 are valid for prediction of τ.

As there are no suitable purely theoretical methods to predict the τ, the ISM field has depended on experimentally determined values. Experiments take one of the following forms: differential thermal analysis (DTA), single hot thermocouple technique (SHTT), or double hot thermocouple technique (DHTT). Differences in the scale and geometries of these methods (i.e., parameters related to heat transfer rates) lead to substantial variation in results. The stochastic nature of nucleation makes a range nucleation lag times an unavoidable result of testing [Krüger and Deubener, 2014; Krüger and Deubener, 2016]. By running a sufficiently large number of tests, the likely nucleation lag time for a given composition as a function of undercooling can be graphed. One of the key issues for ISM is that slags are designed to sit at eutectic points in the compositional space for operational purposes. This means that the nucleation lag time derived from experiments will vary substantially for slight changes in the chemical composition. These experimental issues emphasize the need for a theoretical handling of nucleation lag time.

3.7.2. DNN method

The τ of ISM slag was estimated using a DNN trained on 1103 data points from 32 sources plotted in **Fig. 3-38**. The depth and width were first optimized, followed by pruning of deep layers of skillful architectures. Overfitting prevention was realized with 10-fold cross validation but without RWR. The optimized structure expanded the width by 2 and only had two layers, with a 50% compression. The $MASE$ and $MedASE$ were 71.21% and 35.91%, respectively (**Fig. 3-39**). The low accuracy is not particularly surprising given the difficulty in measuring τ and the fact that values range many orders of magnitude with small changes in temperature. The ability of the DNN to produce realistic predictions of τ of compositions not in the data set is provided in **Fig. 3-40**. It is worth noting that **Fig. 3-40(d)** includes elements that were completely absent from the training set; even so, the prediction is qualitatively similar to the empirical results. Unfortunately, the qualitative similarity does not translate to a quantitative accuracy sufficient for most processes needing to predict or control the τ. A more troublesome result is the fact that the optimized DNN structure shows much less complexity than that of the DNN for T_L. It was expected that the DNN should need to calculate the T_L in order to determine the τ. This low structural complexity indicates that the DNN may have simply fit the patterns in the data without taking the further step of finding representations within the data of physically relevant meaning. It was unclear if this state of affairs was due to a lack of data quantity, the high degree of noise in the empirical data, the highly sensitive nature of τ, the inherent stochasticity, or do to issues with the scale of measurement.
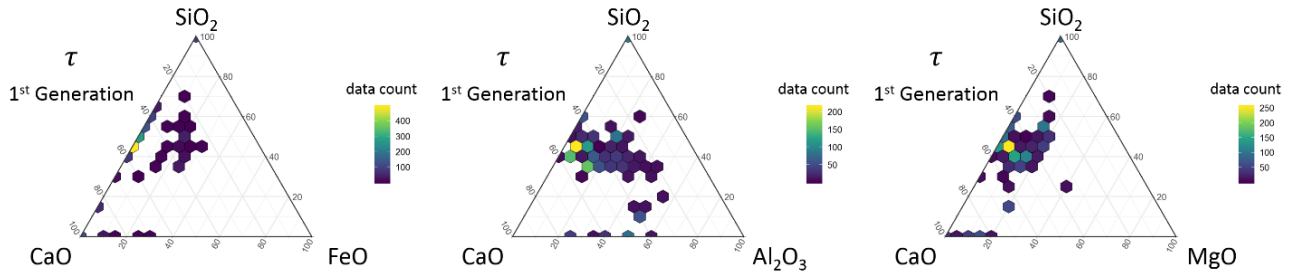
Fig. 3-38. Range of nucleation lag time data used in training DNN plotted on CaO-SiO₂-FeO, CaO-SiO₂-Al₂O₃, and CaO-SiO₂-MgO ternary diagrams.
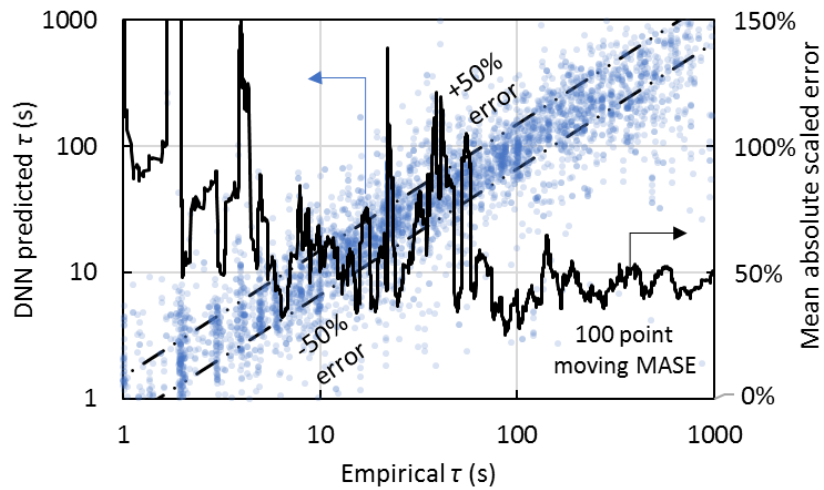
Fig. 3-39. The 1ˢᵗ generation DNN prediction of nucleation lag time compared to empirical data.
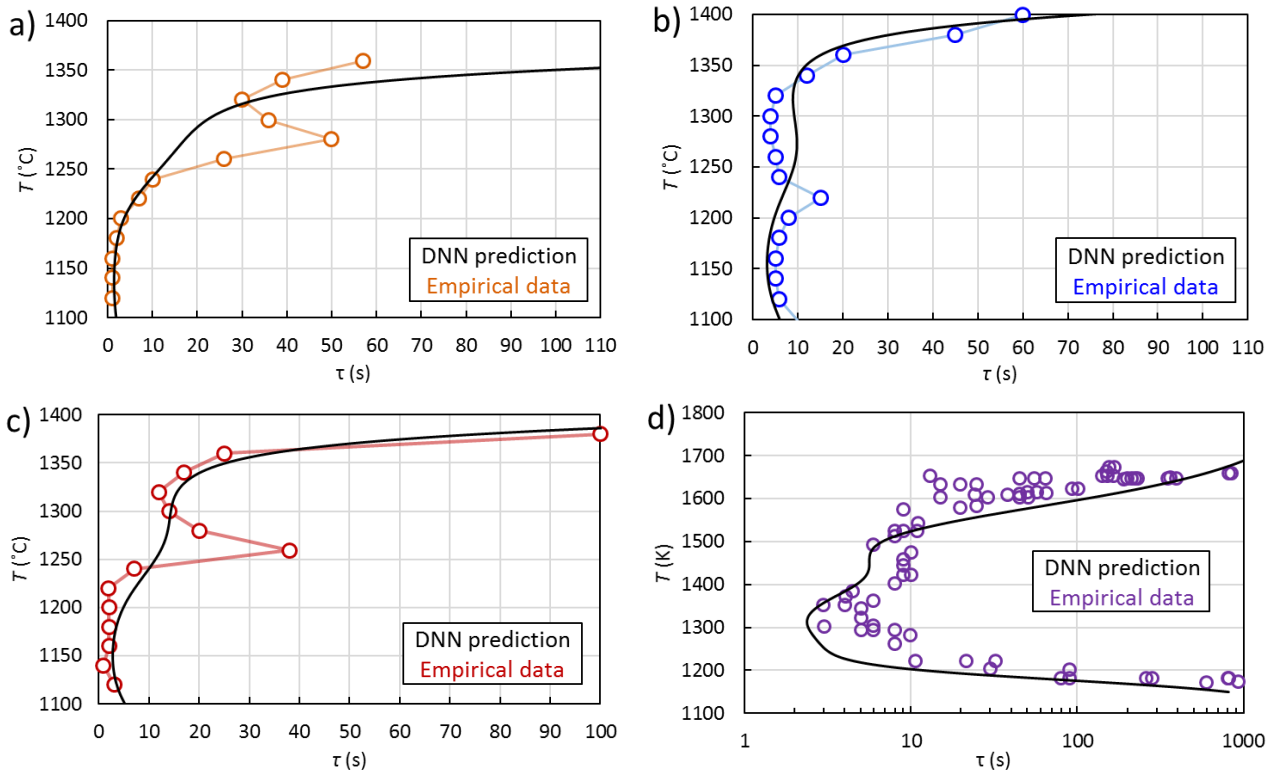
Fig. 3-40. The DNN prediction of nucleation lag time compared to empirical results from Sun et al., 2014 (a-c) and Kashiwaya et al., 2007 (d). The molar compositions are a) 9% MgO, 11% Al_2O_3, CaO=SiO_2; b) 9% MgO, 23% Al_2O_3, CaO=SiO_2; c) 9% MgO, 20% Al_2O_3, CaO=SiO_2; and d) 43% CaO, 34% SiO_2, 14% Al_2O_3, 6% MgO, with trace FeO and MnO.

Given the experience of increased skill with increased data quantity and variety (see Chapter 3.4), a 2nd generation DNN based on additional data from the literature was generated. The quantity of training data was increased from 1123 to 2244 and the number of sources increased from 32 to 64. In addition to wider compositional ranges for many of the elements in the dataset, 12 additional elements were added (**Fig. 3-41 and Fig. 3-42**). Another round of structural optimization resulted in a structure with an initial increase in width of 4, again with 2 layers of depth, pruned at 50%. Along with 10-fold cross validation, 10 repetition weight randomization was employed (i.e., 10 variations for each fold of the data) (**Fig. 3-43** and **Fig. 3-44**). Combined, these changes reduced the $MASE$ to 39.89% and the $MedASE$ to 28.50% (**Fig. 3-45**). The details of the DNN structures and performance are provided in **Table 3-6**.
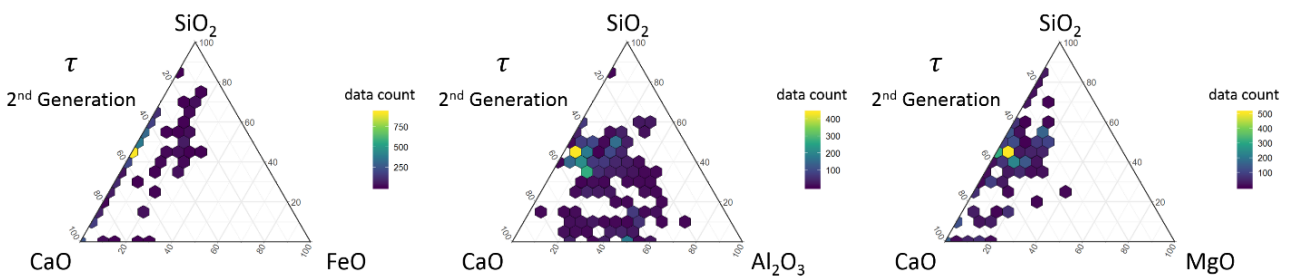
Fig. 3-41. Range of nucleation lag time data used in training 2nd generation DNN plotted on CaO-SiO_2-FeO, CaO-SiO_2-Al_2O_3 ,and CaO-SiO_2-MgO ternary diagrams.
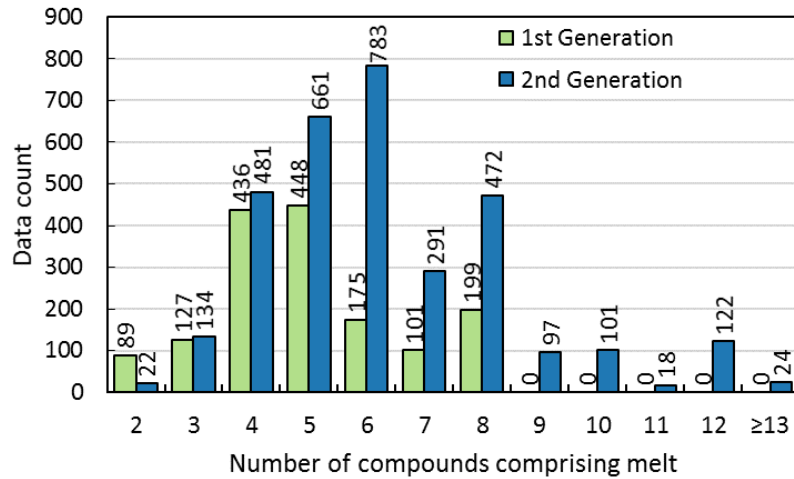
Fig. 3-42. The increase in data quantity and variety from the 1st to 2nd nucleation lag time DNN.
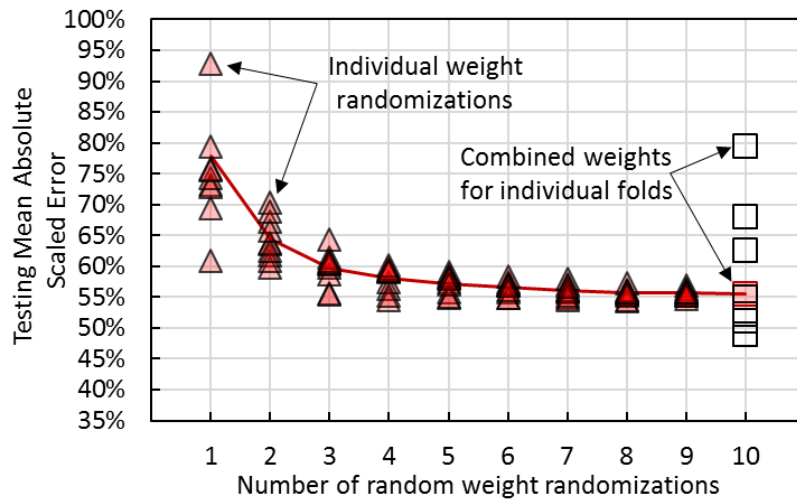
Fig. 3-43. The improved accuracy that comes with repetitive weight randomization.
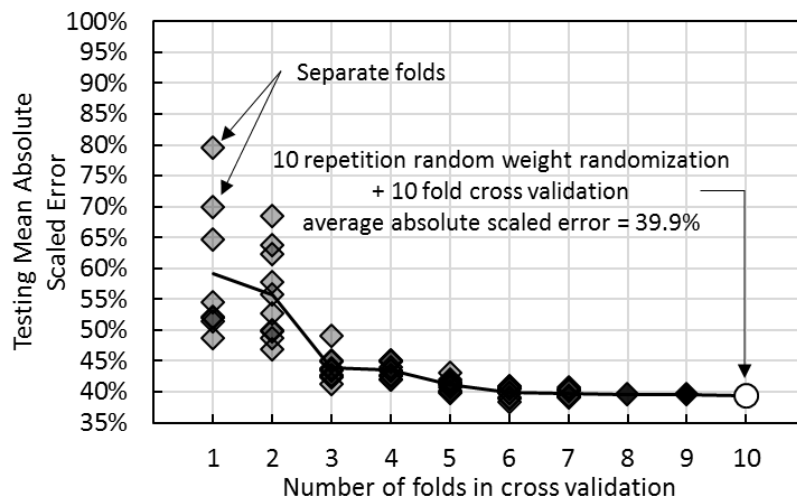
Fig. 3-44. The improved accuracy that comes with cross validation and random weight repetition.
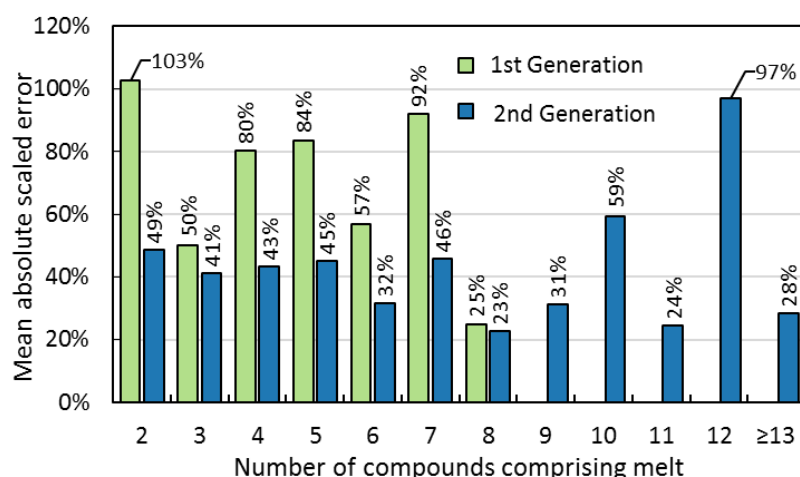
Fig. 3-45. Comparison of the complexity-dependent accuracy between the 1st and 2nd generation DNN predictions of nucleation lag time.

Table 3-6. Performance and structural parameters of the 1st and 2nd generation DNN predicting nucleation lag time.

Property: Nucleation lag time (τ)			
		1st Generation	2nd Generation
Performance	MASE	71.21%	39.89%
	MedASE	35.91%	28.50%
	MBSE	-35.72%	-34.48%
	R^2	0.80	0.94
Structure	Input # (I)	12	24
	Width $(\varpi = n_{N,1}/I)$	2	4
	Depth	2	2
	Pruning rate per layer $(\psi = n_{N,i+1}/n_{N,i})$	50%	50%
	Structure (in full neuron number)	12 (24-12)	24 (96-48)
Data	Range (s)	0.2 - 3572	0.06 – 50181
	Range (K)	700 - 1753	864 – 1997
	Range (mol%)		
	Al	(0.5-23.8)	(0.5-23.8)
	B	(1.9-6.4)	(0.07-11.7)

Ba	---	0.01
C	---	(0.06-11.1)
Ca	(5.2-29.2)	(2.7–29.2)
Cl	---	0.01
Cr	---	(0.01–0.07)
F	(6.7-36.7)	(3.4-36.7)
Fe	(0.1-10.9)	(0.01-10.9)
K	---	(0.005-1.3)
Li	(0.8-22.2)	(0.7-11.4)
Mg	(1.1-8.5)	(0.2-8.8)
Mn	---	(0.003-2.1)
Na	(1.6-12.5)	(0.1-9.3)
O	(25.4-62.2)	(24.4-65.8)
P	---	(0.01-1.1)
S	---	(0.07-3.4)
Si	(2.1-22.2)	(1.7-26.1)
Sr	---	(0.03-0.9)
Ti	(0.8-7.2)	(0.03-8.2)
V	---	(0.1-12.3)
Zn	---	0.01
Zr	---	(0.01-0.9)
Training data Testing data	1103 473	2244 962
Source #	32	64

Despite the improved performance, the continued structural simplicity was a troubling feature of the 2nd generation nucleation lag time DNN. To facilitate the DNN learning more complex features, the DNN was feed the T_L, the η, or both as inputs along with the chemical composition and temperature (**Fig. 3-46**). These estimates were generated by the DNN described in Chapters 3.4 and 3.6. This methodology is termed 'bootstrapping'. The T_L is by construction useful information to the problem at hand; therefore, it acted as a proof of concept to show that accuracy or robustness could be improved via bootstrapping. The choice to add η as an input emerged from the open debate in the community about the role of η in determining τ.

All bootstrapped DNN outperformed the non-bootstrapped DNN. However, the T_L-bootstrapped DNN performed better than the η-bootstrapped DNN and better than the DNN bootstrapped with both values (**Table 3-7**). A few key points can be gleaned from these results. Firstly, the bootstrapping concept has been shown to have merit. By leveraging DNN and humanity's accumulated knowledge, it may be possible to apply DNN to answer hitherto intractable problems which can then be connected in a cascading fashion to other problems of interest. Secondly, these results support the position that the connection between τ and η is a spurious correlation; that is, the behavior of τ and η may be similarly altered by changes to the underlying environment, but η does not appear to be mechanistically connected to τ. Not only did bootstrapping with η not perform as well as bootstrapping with T_L, but also the combined bootstrapping reduced the prediction performance. This means that the η added more noise than signal to the τ data. The T_L-bootstrapped DNN is compared with the 2nd generation DNN in **Fig. 3-47**.
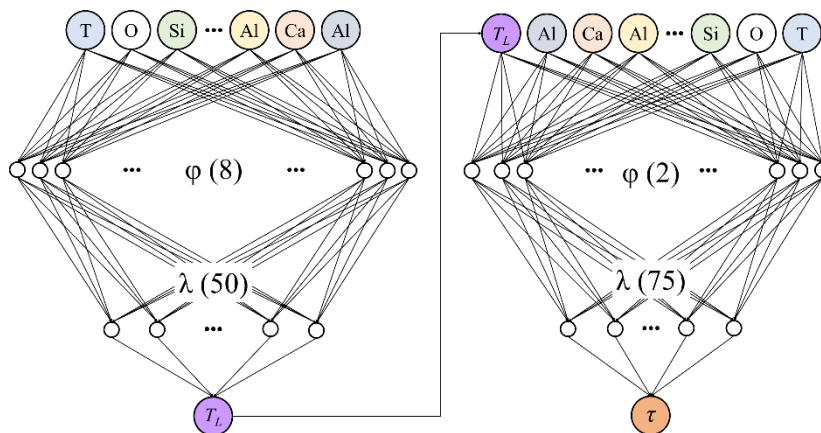
Fig. 3-46. Schematic of the bootstrapping concept.

Table 3-7. The performance of the bootstrapped nucleation lag time DNNs.

Bootstrap	Structure			$MASE$	$\Delta MASE$
	ϖ	n_L	ψ		
None	4	2	50	39.9%	5.8%
$\boldsymbol{\eta}$	1	3	0	39.1%	6.9%
$\boldsymbol{T_L}$	1	3	0	35.1%	6.2%
	2	2	75	33.4%	3.9%
$\boldsymbol{T_L}\,\&\,\boldsymbol{\eta}$	3	2	0	38.3%	5.8%
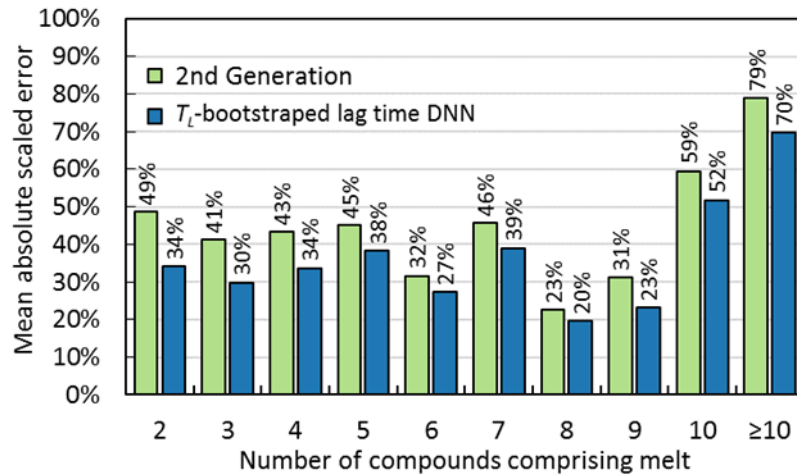
Fig. 3-47. Comparison of the complexity-dependent prediction accuracy for the 2nd generation and T_L-bootstrapped DNN.

Analysis of the T_L-bootstrapped DNN results also yields some interesting insights. It is notable that a large number of data coalesce around the values of 1, 2, 3, 4, and 5 seconds and that the absolute scaled error spikes at these points (**Fig. 3-48**). This is suggestive of values being rounded either during measurement or reporting. It is also interesting to note that the degree of spread in the data agrees with reports of the inherent stochasticity of molten silicate melt systems undergoing nucleation (**Fig. 3-49**). This suggests that further improvements in prediction accuracy should not be expected and may actually indicate over-fitting. Another point of note is that the empirical stochasticity seems to increase with nucleation lag time more than was predicted from other researchers.
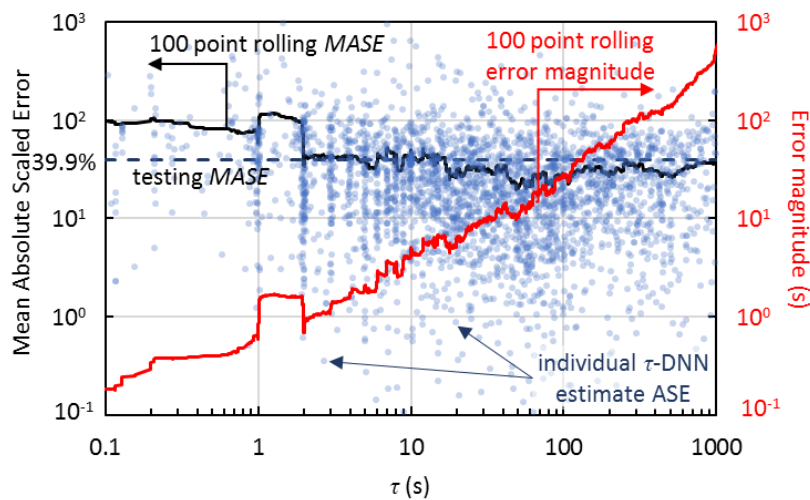
Fig. 3-48. The 2nd generation DNN prediction of nucleation lag time plotted against empirical data.
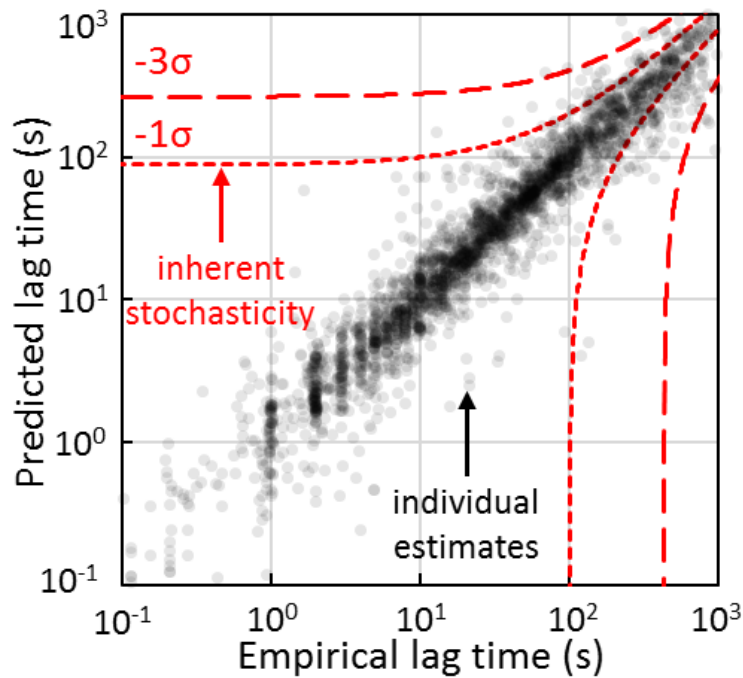
Fig. 3-49. Comparison of the DNN nucleation lag time predictions with the inherent stochasticity of crystal nucleation [Krüger and Deubener, 2014; Krüger and Deubener, 2016].

The ability of the T_L-bootstrapped DNN to provide qualitatively and quantitatively accurate predictions is shown in **Fig. 3-50**. The results from Kashiwaya et al., 2007 are now largely within 3 standard deviations of the DNN estimate.
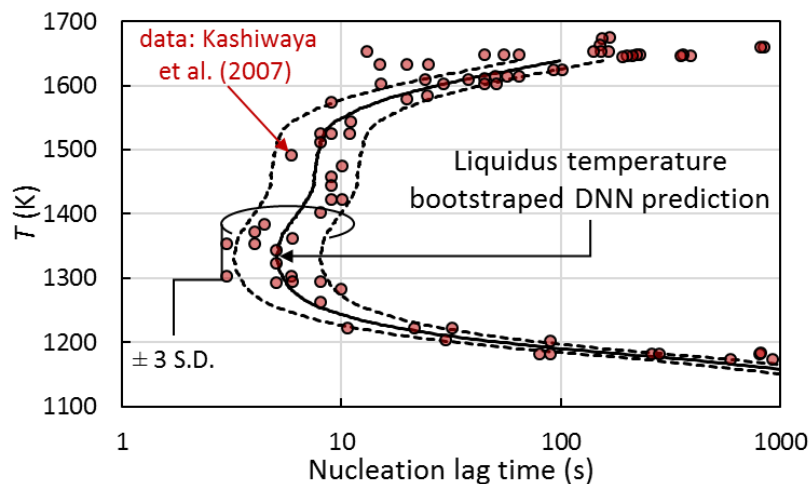
Fig. 3-50. Prediction of the nucleation lag time using the T_L-bootstrapped DNN compared with the empirical data of Kashiwaya et al., 2007.

An example application of the τ and T_L is the determination of the critical cooling rate (CCR). The CCR is the rate at which a solution must be cooled in order to avoid crystal formation. The calculation method is illustrated in **Fig. 3-51**. Assuming a constant cooling rate can be achieved, the CCR is equivalent to the slope of the line connecting the minimum τ on the TTT curve and the T_L at time 0. If the minimum τ is invariant for several temperatures then the lowest temperature instance is chosen. **Figure 3-52** performs the calculation on the Kashiwaya et al., 2007 dataset. In **Fig. 3-53** and

Fig. 3-54, the calculation is performed across the whole CaO-SiO₂-FeO and CaO-SiO₂-Al₂O₃ systems, respectively. Similar to τ, the CCR covers several orders of magnitude; therefore, it was logarithmically transformed (base 10) prior to mapping to the ternary system. The compositions are molar. From the ternary diagram, it is evident that production of amorphous slags from steelmaking slag is difficult due to the extremely large CCR required. Post calculation analysis shows that there is no simple mathematical expression linking the T_L and the τ despite the qualitative similarity seen in the ternary diagrams.
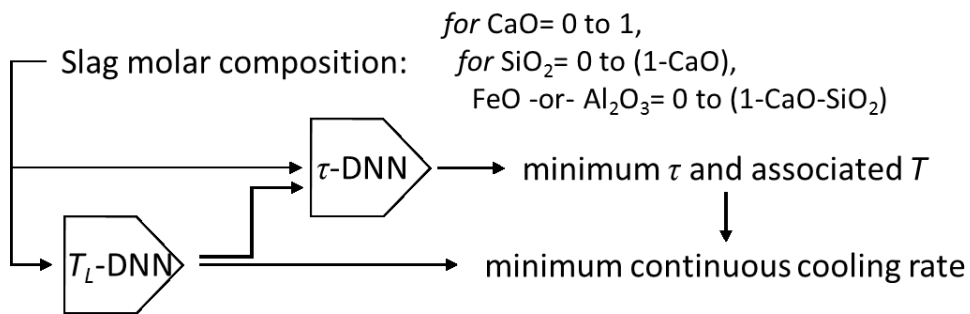
Fig. 3-51. The calculation method to determine the critical cooling rate.
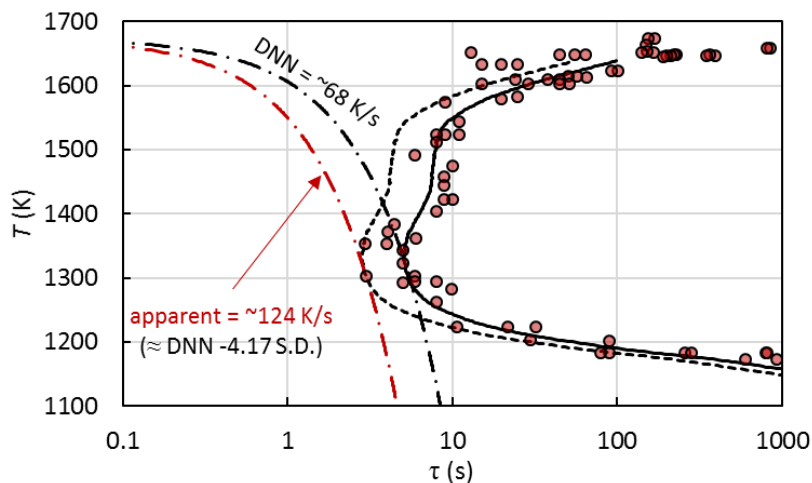
Fig. 3-52. The calculated critical cooling rate for the data of Kashiwaya et al., 2007.
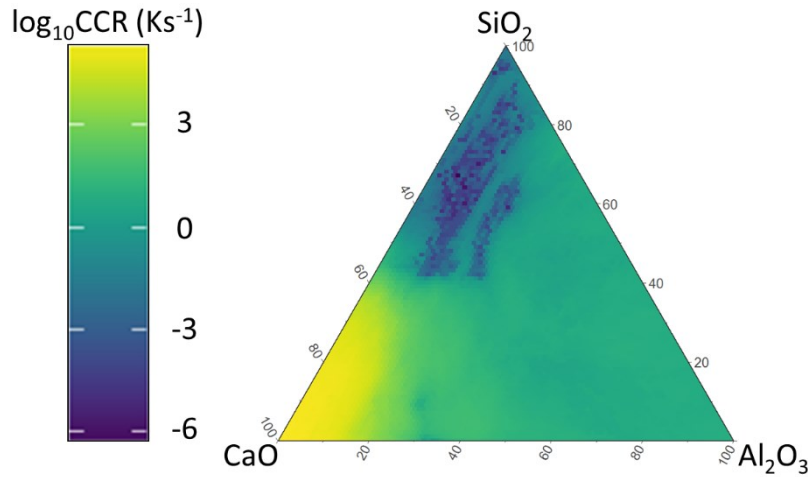
Fig. 3-53. The calculated critical cooling rate for the system CaO-SiO$_2$-FeO.
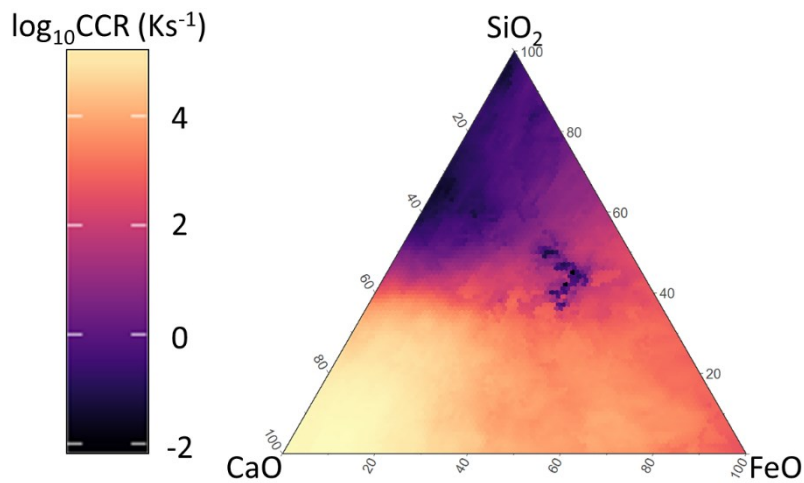
Fig. 3-54. The calculated critical cooling rate for the system CaO-SiO$_2$-Al$_2$O$_3$.

As has been noted throughout this dissertation, the composition of slag contains numerous impurities. There are proposals in the literature for chemical addition to slag after removal from the furnace in order to generate useful features or properties. In either case, impurities are a part of ISM slag, and their impact deserves scrutiny. Analysis of the impact of additives on the CCR of prototypical BF, BOF, and EAF slag were modeled as shown in **Table 3-8**. **Figure 3-55** provides the resultant change in CCR for BF, BOF, and EAF slags. The clearest result from this analysis is that simple correlations do not adequately reflect the behavior of complex systems such as molten slag. These systems may have some degree of irreducible complexity, acting as a barrier to implementation of simplistic correlations. Put simply, the utility of the DNN method likely increases as problems become more complex and emergent.

Table 3-8. Compositions used in the prediction of impurity effect on critical cooling rate of slags.

Element	BF slag	BOF slag	EAF slag
Al	6.56%	0.00%	3.40%
Ca	16.36%	24.47%	15.61%
Fe	0.00%	10.06%	12.74%
Mg	4.74%	4.39%	5.25%
Mn	0.00%	1.23%	1.66%
O	58.54%	53.28%	54.35%
Si	13.80%	6.57%	6.99%

Additives

B (as B_2O_3): 1-5%; C (as $CaCO_3$): 1-5%; F (as CaF): 1-5%; K (as K_2O): 1%; Li (as Li_2O): 1-5%; Na (as Na_2O): 1-5%; P (as $Ca_3(PO_4)_2$): 1%; S (as $CaSO_4$): 1-3%; Ti (as TiO_2): 1-5%; V (as V_2O_5): 1-5%; Zr (as ZrO_2): 1%.
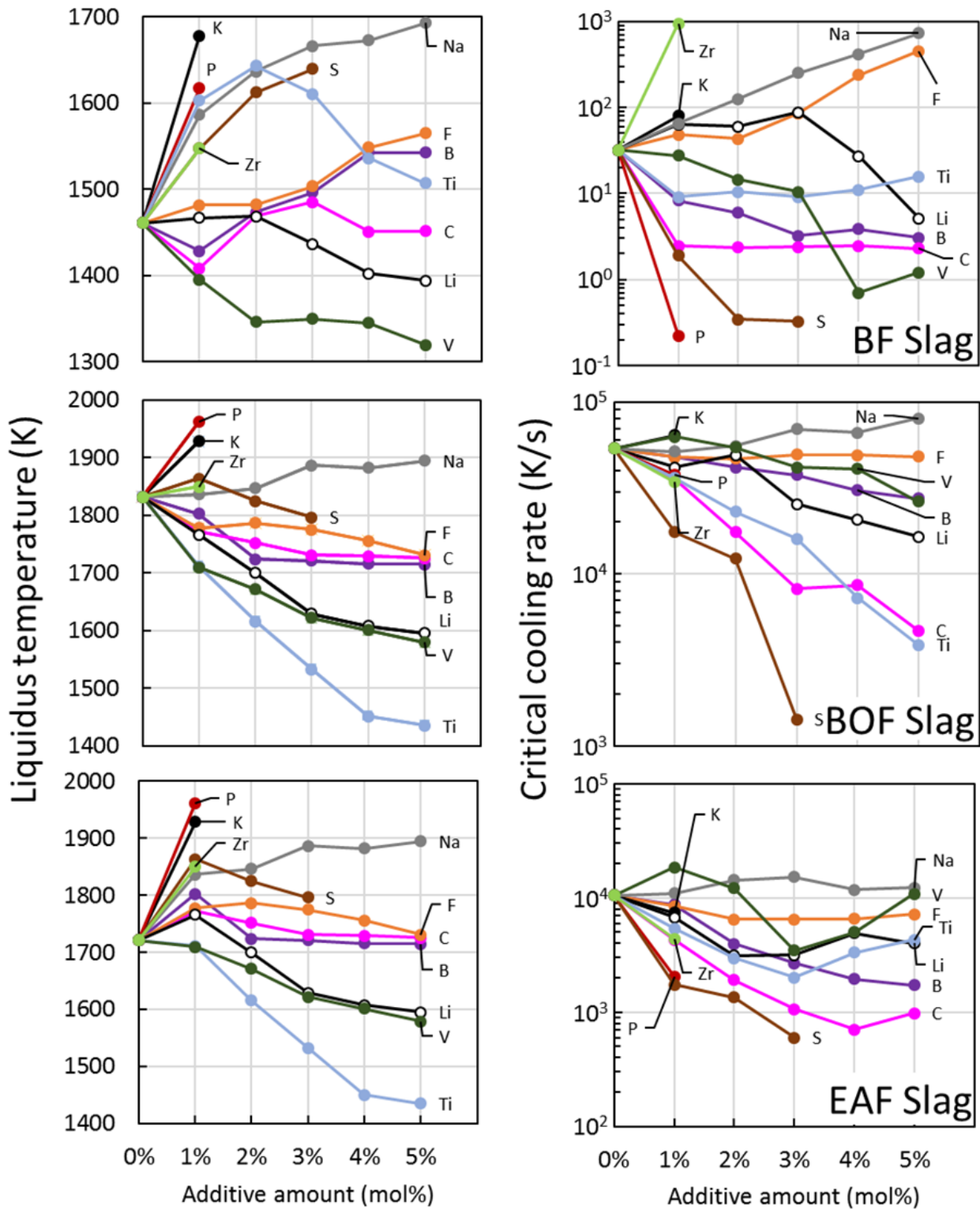
Fig. 3-55. The effect of impurities on critical cooling rate for BF, BOF, and EAF slags. The alteration to the liquidus temperature is including for easy reference.

Chapter-specific symbols and abbreviation list

ANN: Artificial neural network
BF: Blast furnace
BOF: Basic oxygen furnace
CALPHAD: Calculation by phase diagram
CCR: Critical cooling rate
CEE: Cross entropy error
CNT: Classical nucleation theory
c_V: Specific heat capacity per unit volume
d: Dimension of the solution, used in CALPHAD
d_0: Critical diameter
D: Diffusivity through the crystal-liquid interface
DFT: Density functional theory
DHTT: Double hot thermocouple technique
DNN: Deep neural networks
DTA: Differential thermal analysis
E_A: Activation energy
EAF: Electric arc furnace
EC: Exponential cost
G: Number of grid points in phase diagram, used in CALPHAD
gKL: Generalized Kullback-Leibler divergence
h: Plank constant
H: Hellinger distance
HISS: High ionic strength solution
i: Training example
IS: Itakura-Saito distance
ISM: Iron and steelmaking
j: Layer
k_B: Boltzmann constant
KL: Kullback-Leibler divergence
l_{mp}: Phonon mean path length
MAE: Mean absolute error
$MASE$: Mean absolute scaled error
$MBSE$: Mean bias scaled error
$MedASE$: Median absolute scaled error
MD: Molecular dynamics
n: Number of examples in a training set
N: Number of calculations required in global minimization of Gibbs energy, used in CALPHAD
n_L: Number of layers
n_N: Number of neurons
n_X: Number of scattering sites
NN: Neural network
o_i: Prediction for example i

q: Precision

QM: Quantum mechanics

R: Gas constant

ReLU: Rectified linear units

$RMSE$: Root mean squared error

RWR: Repetitive weight randomization

s: Step in backpropagation

SGD: Stochastic gradient descent

SHTT: Single hot thermocouple technique

SSE: Sum squared error

S/n: Signal-to-noise ratio

T: Temperature

T_C: Solid-liquid coexistence temperature

T_L: Liquidus temperature

T_S: Solidus temperature

w: Weight function

WoC: Wisdom of the crowd

y_i: Ground truth for example i

Γ: Learning rate in backpropagation

O: Order of magnitude

ΔG_D: Kinetic barrier to nucleation

ΔG_V: Gibbs free energy difference between an equivalent volume of liquid and crystal

ϵ: Constant in EC function

κ: Thermal conductivity

v: Phonon velocity

ϖ: Neuron expansion ratio from inputs to first hidden layer

ρ: Density

τ: Nucleation lag time

η: Viscosity

ψ: Compression percent between hidden layers

γ: Interfacial energy

References

Abyzov, A.S., Fokin, V.M., Rodrigues, A.M., Zanotto, E.D. and Schmelzer, J.W., 2016. The effect of elastic stresses on the thermodynamic barrier for crystal nucleation. Journal of Non-Crystalline Solids, 432, pp.325-333.

Aggarwal, C.C., Hinneburg, A. and Keim, D.A., 2001, January. On the surprising behavior of distance metrics in high dimensional space. In International conference on database theory (pp. 420-434). Springer, Berlin, Heidelberg.

Ammar, M.M., Gharib, S., Halawa, M.M., El Badry, K., Ghoneim, N.A. and El Batal, H.A., 1982. Thermal conductivity of some silicate glasses in relation to composition and structure. Journal of Non-Crystalline Solids, 53(1-2), pp.165-172.

Arpit, D., Jastrzębski, S., Ballas, N., Krueger, D., Bengio, E., Kanwal, M.S., Maharaj, T., Fischer, A., Courville, A., Bengio, Y. and Lacoste-Julien, S., 2017. A closer look at memorization in deep networks. arXiv preprint arXiv:1706.05394.

Bale, C.W., Bélisle, E., Chartrand, P., Decterov, S.A., Eriksson, G., Gheribi, A.E., Hack, K., Jung, I.H., Kang, Y.B., Melançon, J. and Pelton, A.D., 2016. FactSage thermochemical software and databases, 2010–2016. Calphad, 54, pp.35-53.

Baral, C., Fuentes, O. and Kreinovich, V., 2018. Why deep neural networks: a possible theoretical explanation. In Constraint Programming and Decision Making: Theory and Applications (pp. 1-5). Springer, Cham.

Barron, A.R., 1994. Approximation and estimation bounds for artificial neural networks. Machine learning, 14(1), pp.115-133.

Bau, D., Zhou, B., Khosla, A., Oliva, A. and Torralba, A., 2017. Network dissection: Quantifying interpretability of deep visual representations. arXiv preprint arXiv:1704.05796.

Borra, S. and Di Ciaccio, A., 2010. Measuring the prediction error. A comparison of cross-validation, bootstrap and covariance penalty methods. Computational statistics & data analysis, 54(12), pp.2976-2989.

Burda, Y., Edwards, H., Storkey, A. and Klimov, O., 2018. Exploration by random network distillation. arXiv preprint arXiv:1810.12894.

Cardon, D., Cointet, J.P. and Mazières, A., 2018. La revanche des neurones. Réseaux, (5), pp.173-220.

Caruana, R., Niculescu-Mizil, A., Crew, G. and Ksikes, A., 2004, July. Ensemble selection from libraries of models. In Proceedings of the twenty-first international conference on Machine learning (p. 18). ACM.

Castro, J.L., Mantas, C.J. and Benıtez, J.M., 2000. Neural networks with a continuous squashing function in the output are universal approximators. Neural Networks, 13(6), pp.561-563.

Choe, J.I. and Kim, B.C., 2000. Determination of proper time step for molecular dynamics simulation. Bulletin of the Korean Chemical Society, 21(4), pp.419-424.

Chuang, H.C., Hwang, W.S. and Liu, S.H., 2009. Effects of basicity and FeO content on the softening and melting temperatures of the CaO-SiO2-MgO-Al2O3 slag system. Materials transactions, 50(6), pp.1448-1456.

Cybenko, G., 1989. Approximation by superpositions of a sigmoidal function. Mathematics of control, signals and systems, 2(4), pp.303-314.

Deng, J., 2009. A large-scale hierarchical image database. Proc. of IEEE Computer Vision and Pattern Recognition, 2009.

Dernoncourt, F., Lee, J.Y., Uzuner, O. and Szolovits, P., 2017. De-identification of patient notes with recurrent neural networks. Journal of the American Medical Informatics Association, 24(3), pp.596-606.

Digregorio, P., Levis, D., Suma, A., Cugliandolo, L.F., Gonnella, G. and Pagonabarraga, I., 2018. Full phase diagram of active Brownian disks: from melting to motility-induced phase separation. arXiv preprint arXiv:1805.12484.

Dong, J., Zhang, D. and Gan, L., 2019. An empirical formula for accurate calculation of liquidus temperature of blast furnace slags in SiO2–Al2O3–CaO–MgO system. Ironmaking & Steelmaking, 46(1), pp.71-74.

Du, S.S., Lee, J.D., Li, H., Wang, L. and Zhai, X., 2018. Gradient descent finds global minima of deep neural networks. arXiv preprint arXiv:1811.03804.

Feng, S., Wallace, E., Grissom II, A., Iyyer, M., Rodriguez, P. and Boyd-Graber, J., 2018. Pathologies of neural models make interpretations difficult. In Proceedings of the 2018 Conference on Empirical Methods in Natural Language Processing (pp. 3719-3728).

Fokin, V.M. and Zanotto, E.D., 2000. Crystal nucleation in silicate glasses: the temperature and size dependence of crystal/liquid surface energy. Journal of non-crystalline solids, 265(1-2), pp.105-112.

Foundation of Computational Thermodynamics, 2016. Thermo-Calc software: Console mode examples guide, Thermo-Calc version 2016b.

Freitas, A.A., Santos, R.L., Colaço, R., Horta, R.B. and Lopes, J.C., 2015. From lime to silica and alumina: systematic modeling of cement clinkers using a general force-field. Physical Chemistry Chemical Physics, 17(28), pp.18477-18494.

Funahashi, K.I., 1989. On the approximate realization of continuous mappings by neural networks. Neural networks, 2(3), pp.183-192.

Gabbard, H., Williams, M., Hayes, F. and Messenger, C., 2018. Matching matched filtering with deep networks for gravitational-wave astronomy. Physical review letters, 120(14), p.141103.

Gebauer, D., Kellermeier, M., Gale, J.D., Bergström, L. and Cölfen, H., 2014. Pre-nucleation clusters as solute precursors in crystallisation. Chemical Society Reviews, 43(7), pp.2348-2371.

Gilpin, W., 2018. Cellular automata as convolutional neural networks. arXiv preprint arXiv:1809.02942.

Gupta, P.K., Cassar, D.R. and Zanotto, E.D., 2016. Role of dynamic heterogeneities in crystal nucleation kinetics in an oxide supercooled liquid. The Journal of Chemical Physics, 145(21), p.211920.

Haccuria, E., Crivits, T., Hayes, P.C. and Jak, E., 2016. Selected Phase Equilibria Studies in the Al2O3–CaO–SiO2 System. Journal of the American Ceramic Society, 99(2), pp.691-704.

Hallstedt, B., 1990. System CaO– Al2O3. J. Am. Ceram. Soc, 73(1), pp.15-23.

Han, C., Chen, M., Zhang, W., Zhao, Z., Evans, T., Nguyen, A.V. and Zhao, B., 2015. Viscosity Model for Iron Blast Furnace Slags in SiO2–Al2O3–CaO–MgO System. steel research international, 86(6), pp.678-685.

Han, C., Chen, M., Zhang, W., Zhao, Z., Evans, T. and Zhao, B., 2016. Evaluation of Existing Viscosity Data and Models and Developments of New Viscosity Model for Fully Liquid Slag in the SiO2-Al2O3-CaO-MgO System. Metallurgical and Materials Transactions B, 47(5), pp.2861-2874.

Hasegawa, H., Hoshino, Y., Kasamoto, T., Akaida, Y., Kowatari, T., Shiroki, Y., Shibata, H., Ohta, H. and Waseda, Y., 2012. Thermal conductivity measurements of some synthetic Al2O3-CaO-SiO2 slags by means of a front-heating and front-detection laser-flash method. Metallurgical and Materials Transactions B, 43(6), pp.1405-1412.

Hayashi, M., Ishii, H., Susa, M., Fukuyama, H. and Nagata, K., 2001. Effect of ionicity of nonbridging oxygen ions on thermal conductivity of molten alkali silicates. Physics and chemistry of glasses, 42(1), pp.6-11.

He, K., Wang, Y. and Hopcroft, J., 2016. A powerful generative model using random weights for the deep image representation. In Advances in Neural Information Processing Systems (pp. 631-639).

Hitchcock, M.R. and Hall, C.K., 1999. Solid–liquid phase equilibrium for binary Lennard-Jones mixtures. The Journal of chemical physics, 110(23), pp.11433-11444.

Hornik, K., 1991. Approximation capabilities of multilayer feedforward networks. Neural networks, 4(2), pp.251-257.

Huang, Q., Zhou, K., You, S. and Neumann, U., 2018. Learning to prune filters in convolutional neural networks. arXiv preprint arXiv:1801.07365.

Johnson, J., 2018. Deep, Skinny Neural Networks are not Universal Approximators. arXiv preprint arXiv:1810.00393.

Joswiak, M.N., Duff, N., Doherty, M.F. and Peters, B., 2013. Size-dependent surface free energy and Tolman-corrected droplet nucleation of TIP4P/2005 water. The journal of physical chemistry letters, 4(24), pp.4267-4272.

Kang, Y. and Morita, K., 2006. Thermal conductivity of the CaO–Al2O3–SiO2 system. ISIJ international, 46(3), pp.420-426.

Kang, Y., Nomura, K., Tokumitsu, K., Tobo, H. and Morita, K., 2012. Thermal Conductivity of the Molten CaO-SiO 2-FeO x System. Metallurgical and Materials Transactions B, 43(6), pp.1420-1426.

Kang, Y., Lee, J. and Morita, K., 2014. Thermal conductivity of molten slags: a review of measurement techniques and discussion based on microstructural analysis. ISIJ International, 54(9), pp.2008-2016.

Karthika, S., Radhakrishnan, T.K. and Kalaichelvi, P., 2016. A review of classical and nonclassical nucleation theories. Crystal Growth & Design, 16(11), pp.6663-6681.

Kashiwaya, Y., Nakauchi, T., Pham, K.S., Akiyama, S. and Ishii, K., 2007. Crystallization behaviors concerned with TTT and CCT diagrams of blast furnace slag using hot thermocouple technique. ISIJ international, 47(1), pp.44-52.

Kattner, U.R., 2016. The CALPHAD method and its role in material and process development. Tecnologia em metalurgia, materiais e mineracao, 13(1), p.3.

Kawaguchi, K., 2016. Deep learning without poor local minima. In Advances in Neural Information Processing Systems (pp. 586-594).

Kim, Y. and Morita, K., 2015. Thermal conductivity of molten B2O3, B2O3–SiO2, Na2O–B2O3, and Na2O–SiO2 systems. Journal of the American Ceramic Society, 98(5), pp.1588-1595.

Kittel, C., McEuen, P. and McEuen, P., 1996. Introduction to solid state physics (Vol. 8, pp. 323-324). New York: Wiley.

Koschke, K., Limbach, H.J., Kremer, K. and Donadio, D., 2015. Freezing point depression in model Lennard-Jones solutions. Molecular Physics, 113(17-18), pp.2725-2734.

Krüger, S. and Deubener, J., 2014. Stochastic nature of the liquid-to-crystal heterogeneous nucleation of supercooled lithium disilicate liquid. Journal of Non-Crystalline Solids, 388, pp.6-9.

Krüger, S. and Deubener, J., 2015. Lag time to crystal nucleation of supercooled lithium disilicate melts: A test of the classical nucleation theory. Journal of Non-Crystalline Solids, 426, pp.1-6.

Krüger, S. and Deubener, J., 2016. The TTT curves of the heterogeneous and homogeneous crystallization of lithium disilicate–a stochastic approach to crystal nucleation. Frontiers in Materials, 3, p.42.

Kumari, S., Nunes, A.S., Araújo, N.A. and Telo da Gama, M.M., 2017. Demixing of active particles in the presence of external fields. The Journal of Chemical Physics, 147(17), p.174702.

Lin, H.W., Tegmark, M. and Rolnick, D., 2017. Why does deep and cheap learning work so well?. Journal of Statistical Physics, 168(6), pp.1223-1247.

Ljungberg, K., Mishchenko, K. and Holmgren, S., 2010. Efficient algorithms for multidimensional global optimization in genetic mapping of complex traits. Advances and applications in bioinformatics and chemistry: AABC, 3, p.75.

Matsushita, T., Watanabe, T., Hayashi, M. and Mukai, K., 2011. Thermal, optical and surface/interfacial properties of molten slag systems. International Materials Reviews, 56(5-6), pp.287-323.

Mhaskar, H., Liao, Q. and Poggio, T.A., 2017, February. When and why are deep networks better than shallow ones?. In AAAI (pp. 2343-2349).

Mills, K.C., 1993. The influence of structure on the physico-chemical properties of slags. ISIJ International, 33(1), pp.148-155.

Mills, K.C., Yuan, L. and Jones, R.T., 2011. Estimating the physical properties of slags. Journal of the Southern African Institute of Mining and Metallurgy, 111(10), pp.649-658.

Min, D.J. and Tsukihashi, F., 2017. Recent advances in understanding physical properties of metallurgical slags. Metals and Materials International, 23(1), pp.1-19.

Nagata, K., and Goto, K.S., 1984. In Proc. of 2nd Int. Symp. on Metallurgical Slags and Fluxes. Ed. By Fine, H.A., and Gaskell, D.R., Metall. Soc. AIME, pp.875.

Nunes, A.S., Gupta, A., Araújo, N.A. and da Gama, M.M.T., 2018. Field-driven dynamical demixing of binary mixtures. arXiv preprint arXiv:1801.10205.

Ozawa, S. and Susa, M., 2005. Effect of Na2O additions on thermal conductivities of CaO–SiO2 slags. Ironmaking & steelmaking, 32(6), pp.487-493.

Palumbo, M., Fries, S.G., Hammerschmidt, T., Abe, T., Crivello, J.C., Breidi, A.A.H., Joubert, J.M. and Drautz, R., 2014. First-principles-based phase diagrams and thermodynamic properties of TCP phases in Re–X systems (X= Ta, V, W). Computational Materials Science, 81, pp.433-445.

Park, J.H., Kim, H. and Min, D.J., 2008. Novel approach to link between viscosity and structure of silicate melts via Darken's excess stability function: focus on the amphoteric behavior of alumina. Metallurgical and Materials Transactions B, 39(1), pp.150-153.

Piro, M.H.A. and Simunovic, S., 2016. Global optimization algorithms to compute thermodynamic equilibria in large complex systems with performance considerations. Computational Materials Science, 118, pp.87-96.

Riedmiller, M., 1994. Advanced supervised learning in multi-layer perceptrons-from backpropagation to adaptive learning algorithms. Computer standards and interfaces, 16(3), pp.265-278.

Rolnik, D., Tegmark, M., 2018. The power of deeper networks for expressing natural functions. The Sixth International Conference on Learning Representations, Vancouver, Canada.

Royall, C.P., 2018. Kinetic Crystallisation Instability in Liquids with Short-Ranged Attractions. arXiv preprint arXiv:1806.05469.

Ruder, S., 2016. An overview of gradient descent optimization algorithms. arXiv preprint arXiv:1609.04747.

Russo, J. and Tanaka, H., 2016. Crystal nucleation as the ordering of multiple order parameters. The Journal of Chemical Physics, 145(21), p.211801.

Shallue, C.J., Lee, J., Antognini, J., Sohl-Dickstein, J., Frostig, R. and Dahl, G.E., 2018. Measuring the effects of data parallelism on neural network training. arXiv preprint arXiv:1811.03600.

Shu, Y., Zhu, M., He, K., Hopcroft, J.E. and Zhou, P., 2017. Understanding deep representations through random weights. arXiv preprint arXiv, 1704.

Shwartz-Ziv, R. and Tishby, N., 2017. Opening the black box of deep neural networks via information. arXiv preprint arXiv:1703.00810.

Sosso, G.C., Chen, J., Cox, S.J., Fitzner, M., Pedevilla, P., Zen, A. and Michaelides, A., 2016. Crystal nucleation in liquids: Open questions and future challenges in molecular dynamics simulations. Chemical reviews, 116(12), pp.7078-7116.

Sukenaga, S., Saito, N., Kawakami, K. and Nakashima, K., 2006. Viscosities of CaO–SiO2–Al2O3–(R2O or RO) melts. ISIJ international, 46(3), pp.352-358.

Sun, C., Shrivastava, A., Singh, S. and Gupta, A., 2017, October. Revisiting unreasonable effectiveness of data in deep learning era. In Computer Vision (ICCV), 2017 IEEE International Conference on (pp. 843-852). IEEE.

Sun, Y., Zhang, Z., Liu, L. and Wang, X., 2014. Multi-Stage control of waste heat recovery from high temperature slags based on time temperature transformation curves. Energies, 7(3), pp.1673-1684.

Sundman, B., Kattner, U.R., Palumbo, M. and Fries, S.G., 2015. OpenCalphad-a free thermodynamic software. Integrating Materials and Manufacturing Innovation, 4(1), p.1.

Susa, M., Kubota, S., Hayashi, M. and Mills, K.C., 2001. Thermal conductivity and structure of alkali silicate melts containing fluorides. Ironmaking & steelmaking, 28(5), pp.390-395.

Susa, M., Mills, K.C., Richardson, M.J., Taylor, R. and Stewart, D., 1994. Thermal properties of slag films taken from continuous casting mould. Ironmaking & steelmaking, 21(4), pp.279-286.

Ugander, J., Drapeau, R. and Guestrin, C., 2015, June. The wisdom of multiple guesses. In Proceedings of the Sixteenth ACM Conference on Economics and Computation (pp. 643-660). ACM.

Van Veen, F., 2016. The Neural Netowrk Zoo. The Asimov Institute. Retrieved January 11, 2019.

Vekilov, P.G., 2010. Nucleation. Crystal growth & design, 10(12), pp.5007-5019.

Volmer, M. and Weber, A., 1926. Keimbildung in übersättigten Gebilden. Zeitschrift für physikalische Chemie, 119(1), pp.277-301.

Wang, J., Mbah, C.F., Przybilla, T., Zubiri, B.A., Spiecker, E., Engel, M. and Vogel, N., 2018. Magic number colloidal clusters as minimum free energy structures. Nature communications, 9(1), p.5259.

Weber, S.N., Weber, C.A. and Frey, E., 2016. Binary mixtures of particles with different diffusivities demix. Physical review letters, 116(5), p.058301.

Willmott, C.J. and Matsuura, K., 2005. Advantages of the mean absolute error (MAE) over the root mean square error (RMSE) in assessing average model performance. Climate research, 30(1), pp.79-82.

Xin, J., Gan, L., Jiao, L. and Lai, C., 2017. Accurate Density Calculation for Molten Slags in SiO2–Al2O3–CaO–MgO Systems. ISIJ International, pp.1340-1349.

Ye, W., Chen, C., Wang, Z., Chu, I.H. and Ong, S.P., 2018. Deep neural networks for accurate predictions of crystal stability. Nature communications, 9(1), p.3800.

Yi, S.K.M., Steyvers, M., Lee, M.D. and Dry, M.J., 2012. The wisdom of the crowd in combinatorial problems. Cognitive science, 36(3), pp.452-470.

Yu, C.W. and Clarke, B., 2015. Regular, median and Huber cross‐validation: A computational comparison. Statistical Analysis and Data Mining: The ASA Data Science Journal, 8(1), pp.14-33.

Zhang, P., Maldonis, J.J., Liu, Z., Schroers, J. and Voyles, P.M., 2018. Spatially heterogeneous dynamics in a metallic glass forming liquid imaged by electron correlation microscopy. Nature communications, 9(1), p.1129.

Chapter 4: Solidification control

In Chapter 2, it was shown that the potential CO_2 reductions from utilization of slag are significantly higher for the recovery of material than for the recovery of heat. Therefore, optimal slag utilization is fundamentally a problem of separation. Review of the literature shows that almost all slag processes either deliberately or unknowingly depend on comminution to achieve separation. Due to the energetic inefficiency of grinding and the associated CO_2 emissions, methods that can reduce the need for comminution are of importance. Separation of components in slag can occur when slag is molten or after solidification. When separation occurs after solidification, the key facet determining the comminution energy required to achieve a given separation extent and product purity is the grain size distribution (GSD) of the internal minerals. The GSD is determined primarily by the slag chemical composition and the rate of solidification. Therefore, regardless of whether separation is realized from molten or solid slag, engineered handling of molten slag is necessary.

An unspoken assumption of the slag treatment field is that the mineralogical makeup of slag cannot be modified without addition of materials after removal from the furnace. One of the key positions that this dissertation takes is that control of the solidification of molten ISM slag can alter the mineralogical makeup. This fact reinforces the position that the design of any process to mineralize CO_2 using slag should begin with the slag immediately after exiting the furnace (i.e., in the molten state).

Upon exiting the furnace, two phase transition pathways are envisioned for molten slag: 1) centrifugal separation and 2) in-container, slow solidification. In the centrifugal separation scheme, molten slag is poured into a solid, sedimentation style centrifuge. Rapid rotation separates the internal heterogeneities into layers of pure compounds by liquid-phase demixing. As layers form, the liquidus temperature (T_L), nucleation time lag (τ), and other molten phase properties become spatially distinct due to the change in the local chemical composition. In general, separation of compounds increases the T_L for all layers relative to the initial mixture. However, due to the complex nature of nucleation, the alteration of τ is not uniform or obvious across disparate compositions. The τ allows for continued separation of species even after the T_L exceeds the local temperature (T). Eventually, solidification occurs as homogeneous solidification when the chemically disparate layers have become relatively pure and chemically stable. Growth of prematurely nucleating sites is suppressed by the anisotropic nature of diffusion due to the large centrifugal force and the continuously changing composition of the surrounding bulk melt. By leveraging knowledge of the τ, the angular frequency can be controlled to completely avoid nucleation and growth until chemically pure layers have been formed. The pure layers of calcium and magnesium oxide can be recycled to the furnace, sintering, or pelletizing process as flux. Alternatively, the calcium and magnesium oxide can be used to capture CO_2 from the ISM flue gas or directly from the atmosphere. This creates a closed loop in ISM of CO_2 emissions associated with $CaCO_3$ decomposition which accounts for ~10% of current ISM emissions. Recovered Fe^0 and FeO (oxidation state is slag-dependent) can be recycled to the steelmaking and ironmaking process, respectively. Likewise, trace metals such as titanium and manganese can be recovered and used for alloying purposes. Most metallic iron is already recovered from slags by grinding and magnetic separation. However, a large portion of charged iron is locked up in non-magnetic compounds with silica (for ironmaking slag) and calcium (for steelmaking slag). Recovery of these iron resources means the embodied CO_2 emissions of reducing iron ore to low oxidation states are recovered. Silica and alumina layers can be sold as an aggregate; it may be

possible to upcycle these materials to high-end applications depending on the purity and microstructure. In the ideal case, centrifugal separation acts to shuttle silica, alumina, and other impurities from the charge material to a solid waste while maintaining an internal loop of CaO and increasing the conversion efficiency of iron ore to crude iron and steel. In addition to material recovery, heat can be recovered from the distinct compound layers prior to reuse. The total heat available may be higher than traditional heat recovery methods due to the lack of a cooling step; though the mineralogy and geometry may be non-ideal for heat recovery purposes.

The alternative proposed phase transition pathway is to slowly solidify slag in an insulated container (termed 'MYNA' after the process originators, Myers-Nakagaki). Retaining molten slag in an insulated container slows its cooling; decelerated cooling has four important physical consequences: 1) enhanced liquid-liquid segregation, 2) reduced nucleation rate, 3) reduced driving force for growth, and 4) reduced variety of nucleating species. By remaining above its T_L, the various elemental constituents of molten slag have the time and energy required to locally de-mix based on differences such as diffusivity, size, and shape. These local heterogeneities may avoid both solidification and disintegration over long time periods due to factors that are not accounted for in Classical Nucleation Theory (CNT). Moreover, these heterogeneities are generated due to kinetic and geometric effects as opposed to equilibrium thermodynamic effects; thus, the composition of the heterogeneities may be dissimilar from those predicted by CNT. Once nucleation and growth begin, the maintenance of the slag near its T_L means that the τ is greatly increased and the number density of nuclei is greatly reduced. By minimizing the number of nuclei, the competition between crystals for space is reduced, and the size of the generated crystals is increased. Likewise, the high temperatures mean that diffusion remains rapid and rejection of inclusions is not energy-constrained; therefore, chemically pure crystals are formed without the arresting effects of material insufficiency. Moreover, the low undercooling (T_U) of a melt held in an insulated container means that only the most kinetically favorable minerals will nucleate and grow; other minerals will be prevented from developing due to a loss of material to the more rapidly solidified minerals. The combined effect these phenomena is the generation of a relatively simple mixture of large mineral grains which can be separated at low energy expenditure in downstream processes.

In this Chapter discussing the phase transition of molten slag, and this dissertation more broadly, the term solidification includes true, crystalline solids and amorphous compounds whose viscosity at standard temperature and pressure is such that they can be handled and modeled as a solid. Likewise, when the term solidification is used in the description of processes and phenomenon, it connotes any material with very high viscosity, such that at the time scales of interest, there is negligibly small relative movement or rearrangement of molecules.

Chapter highlights

- Two processes are proposed to alter the mineralogy and grain size distribution of slag by controlling its phase transition: centrifugal separation and slow solidification. Both methods rely on property data supplied by deep neural networks.
- Centrifugal separation was modeled using kinematics with the local fluid properties (e.g., viscosity, density, nucleation lag time) being estimated by deep neural networks. Centrifugal separation produces homogeneous solidification as the composition of the slag changes within the centrifuge. Homogeneous solidification is suppressed during separation by the sudden changes in composition leading to long nucleation lag times.
- Centrifugal separation of ironmaking slags generates primarily Ca-silicate, (Ca,Mg)O, and alumina layers. A very small amount of silica is produced on the inner wall of the centrifuge and a small amount of metallic iron is concentrated to the outer wall of the centrifuge.
- Centrifugal separation of steelmaking slags generates primarily a (Ca,Mg)O and FeO layers. The small amount of SiO_2 is retained in a Ca-silicate layer. Most Al_2O_3 is lost to thin layers of mixed compounds without any significant financial or CO_2 mitigating value.
- Slow solidification was modeled as an isothermal process occurring just below the liquidus temperature as determined by deep neural network.
- The limiting size of mineral grains produced by slow solidification was calculated based on the compositional alteration to the bulk melt caused by solidification and the resultant nucleation lag time and limits of ionic diffusion.
- Slow solidification is predicted to increase the average grain diameter by ~2 orders of magnitude compared to rapid solidification methods.
- Slow solidification will likely result in the expulsion of small cations (e.g., Mg, Fe, Al) from the Ca-silicate structure, thereby altering not just the mineral grain size, but also the mineralogy.

Publications relevant to this chapter

- Quantification of the CO_2 mineralization potential of ironmaking and steelmaking slags under direct gas-solid reactions in flue gas, International Journal of Greenhouse Gas Control Vol. 87C p.100-111 (2019), **Corey A. Myers**, Takao Nakagaki, and Kosei Akutsu.
- Effect of Solidification and Cooling Methods on the Efficacy of Slag as a Feedstock for CO_2 Mineralization, ISIJ International Vol. 58 No. 2 p.211-219 (2018), **Corey Adam Myers** and Takao Nakagaki.

4.1. Centrifugal process

Centrifugal separation of homogeneous slag into chemically disparate species has already been experimentally demonstrated for many slag compositions [Gao et al., 2015; Gao et al., 2017; Li et al., 2018; Lu et al., 2017; Wang et al., 2018]. Both sedimentation-type and filtration-type centrifuges have been validated in the literature (**Fig. 4-1**). Among the established abilities of centrifugal separation are: concentration and separation of metallic species from the melt, preferential separation of metals from a metallic melt, concentration of phosphorous into a distinct mineral layer, enhanced growth of a specific mineral, and generation of layers with sharp changes in chemical composition. While these results are impressive, they all depend upon the principle of separating a nucleating solid from the mother solution. The dependence on nucleation limits the potential chemical composition of the generated layers to those compounds which naturally precipitate from slag. In order to expand the space of minerals that can be recovered from slag, centrifugal separation from a completely molten state is necessary. Achieving this would open up the possibility for recovery of pure, simple oxides from molten slag, in turn greatly reducing the CO_2 intensity and increasing the production efficiency of ISM. An additional area lacking in the current research is a theoretical framework from which to evaluate and optimize the process. Though centrifugal separation is understood for solid-liquid and immiscible liquid-liquid systems, a theory that includes solid nucleation and growth and the level of solution complexity seen in ISM slags is lacking. Lastly, the empirical evidence for centrifugal separation relies on systems of a few cubic centimeters, it is unclear if such systems would remain functional or practical at the scale of industrial ISM.

A numerical simulation of centrifugal separation of molten ISM slag was built to establish the limits of distinct material generation and operation efficiency. The centrifugal simulation was run on three slag compositions representative of the industry wide averages for BF, BOF, and EAF slags. The slag compositions used in the simulation are provided in **Table 4-1**.
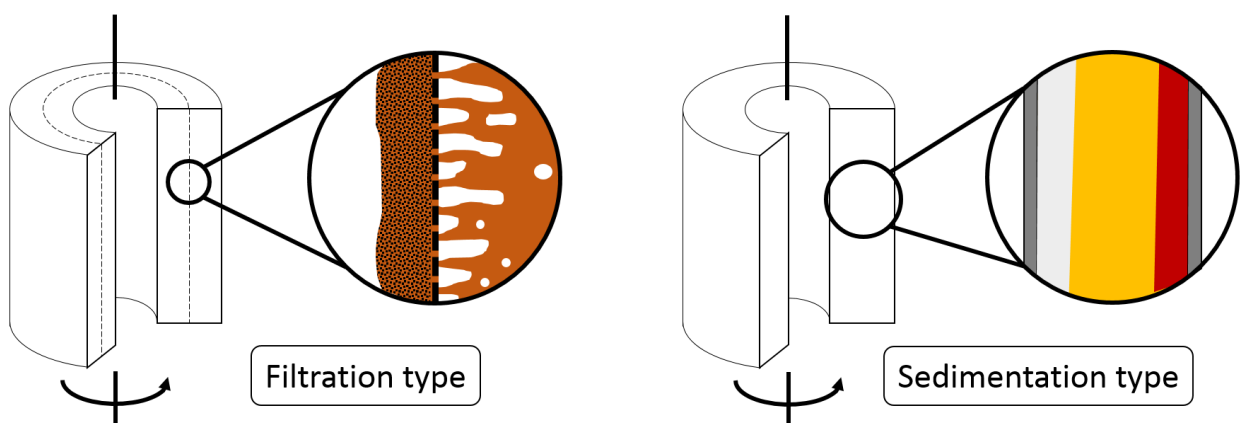
Fig. 4.1. Sedimentation-type and filtration-type centrifuges.

Table 4-1. The industry average compositions for BF, BOF, and EAF slag used in the centrifugal separation simulation.

Compound (mass%)	BF	BOF	EAF
Al_2O_3	14.6%	3.0%	6.6%
CaO	39.9%	49.8%	33.5%
Fe/O	0.6%	26.2%	35.1%
MgO	8.3%	6.4%	8.1%
SiO_2	36.1%	14.3%	16.1%
TiO_2	0.5%	0.3%	0.6%

The internal volume of the centrifuge was divided into a grid structure with each cell being modeled as a non-deformable cluster of a single component oxide (**Fig. 4-2**). The oxides were randomly distributed across the grid to represent a fully mixed solution.
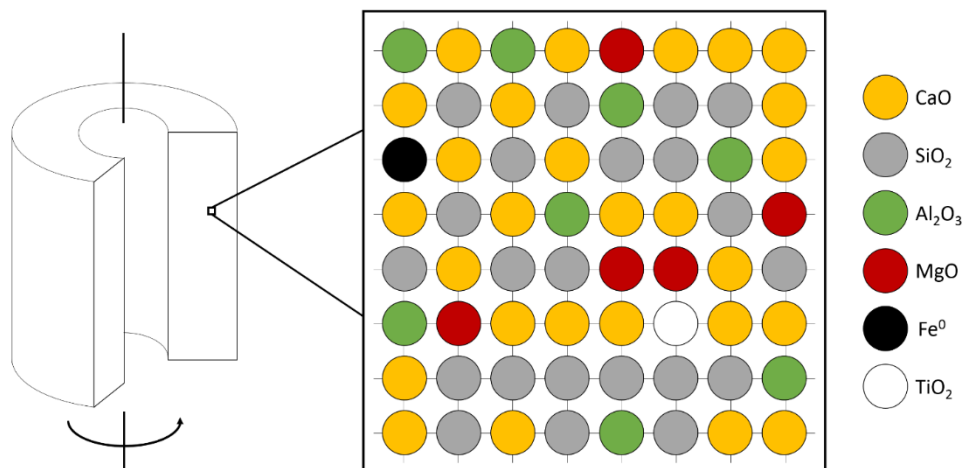
Fig. 4-2. Initial distribution of compounds in the molten slag within a cross-section of the centrifuge.

The centrifugal separation of materials was simulated by tracking the movement of clusters through balancing the local gravitational, centrifugal, buoyancy, and drag forces. The composition of the melt surrounding a cluster was computed as the average of the elements within the maximal distance the cluster could travel within a single time step (**Fig. 4-3**). This length scale is the functional limit of chemical communication the cluster could achieve within a timestep.
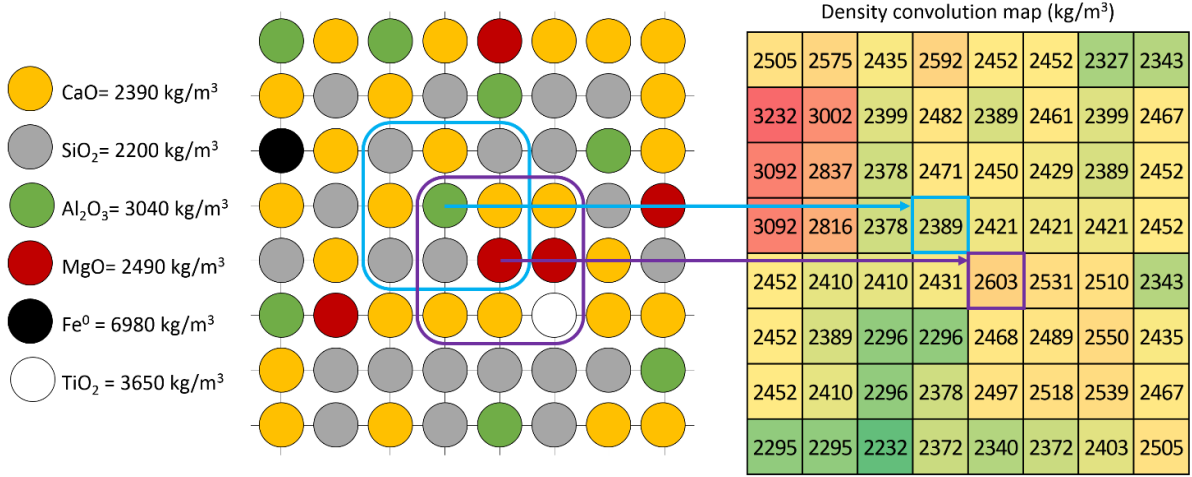
Fig. 4.3. Calculation of the local composition and properties (density shown as an example).

The instantaneous acceleration on a cluster was calculated by balancing the gravitational force (F_g) **Eq. (4-1)**, buoyancy force (F_b) **Eq. (4-2)**, centrifugal force (F_c) **Eq. (4-3)**, and drag force (F_d) **Eq. (4-4)** in the vertical direction (F_z) **Eq. (4-5)** and radial direction (F_r) **Eq. (4-6)**. The acceleration period of the centrifuge was not evaluated in the simulation as the low centrifugal force period was assumed to have minimal impact on results.

$$F_g = \rho_{cl} \left(\frac{4}{3}\right) \pi r_{cl}^3 g \tag{4-1}$$

$$F_b = \rho_f \left(\frac{4}{3}\right) \pi r_{cl}^3 g \tag{4-2}$$

$$F_c = \rho_{cl} \left(\frac{4}{3}\right) \pi r_{cl}^3 \omega^2 R \tag{4-3}$$

$$F_d = 6\pi\eta r_{cl} V \tag{4-4}$$

$$F_z = \left[(\rho_{cl} - \rho_f) \frac{4}{3} \pi r_{cl}^3 g \right] - (6\pi\eta r_{cl} V_z) \tag{4-5}$$

$$F_r = \left[(\rho_{cl} - \rho_f) \frac{4}{3} \pi r_{cl}^3 \omega^2 R \right] - (6\pi\eta r_{cl} V_r) \tag{4-6}$$

In **Eq. (4-1)-(4-6)** the density of the cluster is given by ρ_{cl}, the density of the local melt is given by ρ_m, the radius of the cluster is given by r_{cl}, gravity is given by g, the radial frequency of the centrifuge is given by ω, the radial distance of a cluster is given by R, the melt viscosity is given by η, the radial velocity of a cluster is given by V_r, and the vertical velocity of a cluster is given by V_z. The local composition was used to predict the composition- and temperature-dependent ρ_f and η using the DNN described in Chapter 3. Clusters were treated independently except when surfaces overlapped.

When clusters of the same material overlapped, they were assumed to instantaneously merge into a new spherical cluster with the position updated to the center of mass of the clusters prior to merger (**Fig. 4-4**). Though instantaneous merger is unrealistic, rapid merger of similar clusters is expected due to entropic forces and minimization of the surface energy.
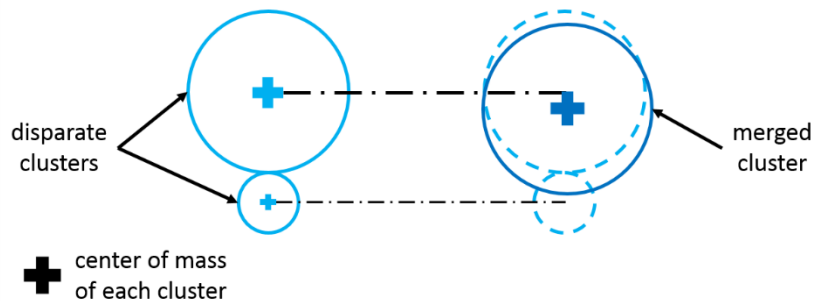
Fig. 4-4. The merger of clusters.

Dissimilar clusters were assumed to cross paths without interacting. This assumption is supported by the large energy barrier of any merger pathways. Merger while maintaining distinct compositional regions would induce a large additional surface energy between the regions. Merger with complete mixing would require substantial rearrangement of all the internal molecules. In comparison, the relative translation of a cluster around another cluster is a low energy process which is driven by the centrifugal force (**Fig. 4-5**). After each time step, the position of each cluster was used to reorder the clusters in the radial and then the vertical grids (**Fig. 4-6**). The reset clusters were then evaluated for another time step.
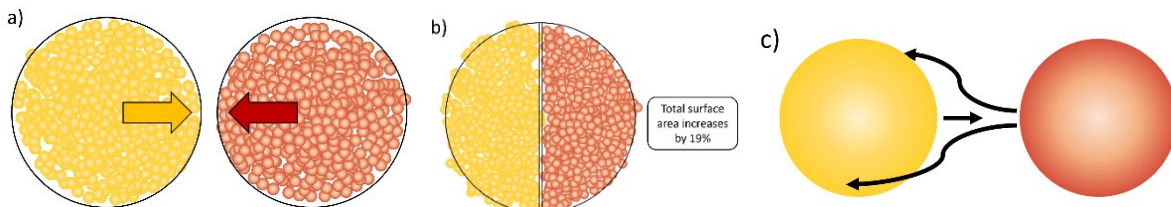
Fig. 4-5. Schematic displaying the logic of dissimilar cluster interaction with a) clusters approaching one another, b) the increase surface area of a 'merged cluster', and c) the low energy option of cluster bypass.
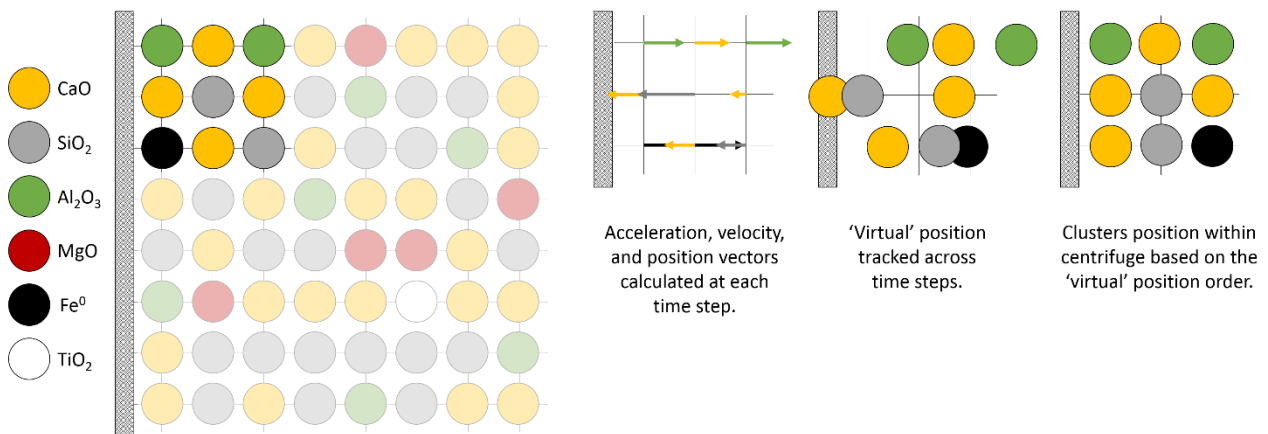
Fig. 4-6. The reordering clusters after each time step.

Concretely, the clusters are prenucleation clusters which exist in any molten system near its T_L [Gebauer et al., 2014; Radu and Kremer, 2017; Tanaka et al., 2010; Zhang et al., 2017]. Importantly, these clusters are not nucleation sites in the traditional sense of CNT (though they can become nucleation sites). Rather, these are sites of local demixing which occur for purely geometric and statistical reasons. As these clusters are distinct from the nucleation sites of CNT, they require an alternative (theoretical or empirical) basis to determine their composition, size, and structure. Though CNT does not provide quantitative information about these local heterogeneities, it does inherently assume their existence. In CNT, the individual atoms undergoing nucleation have no knowledge of the aggregate set of events that lead to stable growth; therefore, the action of aggregation -and dissipation- are a continuous process.

Molecular dynamics (MD) simulation of simplified liquid solutions (e.g., Hard Sphere Model, Lennard-Jones liquid) have demonstrated that separation occurs in otherwise homogeneous liquids due to differences in size [Louis et al., 2002], density [Rivas et al., 2011], shape [McCandlish et al., 2012], rotation [Scholz et al., 2018], and diffusivity [Stenhammar et al., 2015]. It has further been demonstrated that application of a body force enhances such demixing [Kumari et al., 2017; Nunes et al., 2018]. These theoretical results have been confirmed by analogous experimental results [Buttinoni et al., 2013] and testing on molten silicate melts [Hammer, 2008]. The trend of demixing in binary Lennard-Jones liquids of equivalent number is that larger, denser, slower, and less energetic particles tend to aggregate together due purely to entropic effects (**Fig. 4-7**). In greater complexity systems with non-uniform particle numbers, the probability of particle-particle interactions become increasingly important. For example, the entropic pressure that causes slow particles to aggregate in a bath of fast particles can reverse if the fast particles are rare enough in number [Tanaka et al., 2017]. Given the complexity of even purely geometric systems, the most that can be said is that local demixing occurs and roughly scales with the degree of differences between particles.
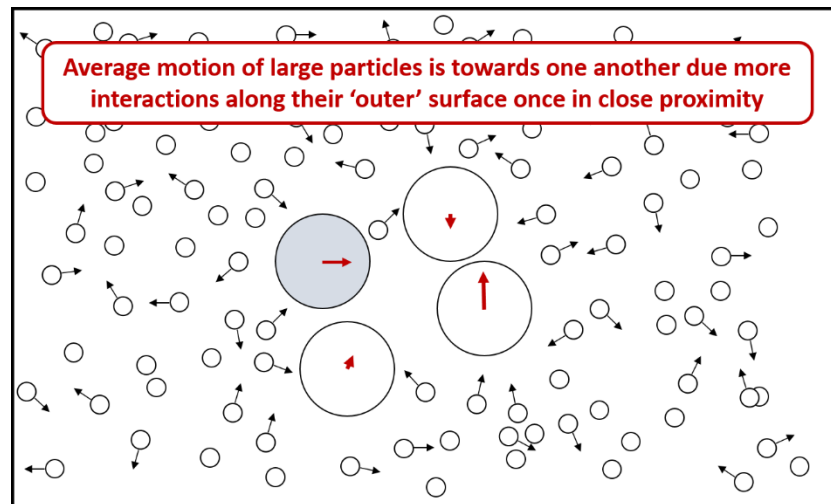
Fig. 4-7. Entropic pressure on large particles to cluster in a liquid of small particles.

In addition to pure geometric effects, it is important to consider the bonding strength of clustering particles. As the particles constituting the liquid cluster are, by definition, not in a crystalline form, the bond strength can be approximated by the cation-anion distance while neglecting the crystalline structure. Therefore, compounds composed of small ionic radii with simple geometries are expected to contain the strongest intracluster bonds. More strongly bound clusters should be more resilient to dissolution by impacts from the surrounding fluid (i.e., more stable once formed).

Despite the abundance of theoretical and empirical evidence of demixing and local heterogeneities in liquid systems, there remains little theoretical guidance on estimating the size and composition of heterogeneous regions in complex solutions. To guide the determination of clusters in centrifugal separation simulation, empirical evidence from rapidly solidified slag was used to set the innate size of clusters in molten slag. The size of innate clusters is inherently dependent on the chemical composition. However, review of micrographs from the literature found a consistent minimum diameter for crystals grains formed in rapidly solidified slag of 400-1000 nm [Choi and Jung, 2017; Gautier et al., 2013; Reddy et al., 2016; Wang et al., 2012]. Note that theoretical [Dargaud et al., 2012] and empirical [Cogswell and Carter, 2011] evidence sets that absolute limit on stable cluster diameter to 8-15 nm. The 2D nature of micrographs means that some portion of the smaller size fraction are off-center cuts across grains (so-called: 'cut-section effect') [Higgins, 2000; Sahagian and Proussevitch, 1998]. Therefore, even in a monodisperse sample of perfectly spherical grains, there will be an apparent distribution of sizes given be **Eq. (4-7)** and graphed in **Fig. 4-8** [Royet, 1991]. In **Fig. 4-8**, the probability of observing a grain with diameter in the range of d_x to d_y is given by $P(x,y)$, where d_y ranges from ~0 to unity and d_x is normalized to d_y.

$$P(x,y) = \sqrt{1 - d_x^2} - \sqrt{1 - d_y^2} \qquad\qquad (4-7)$$
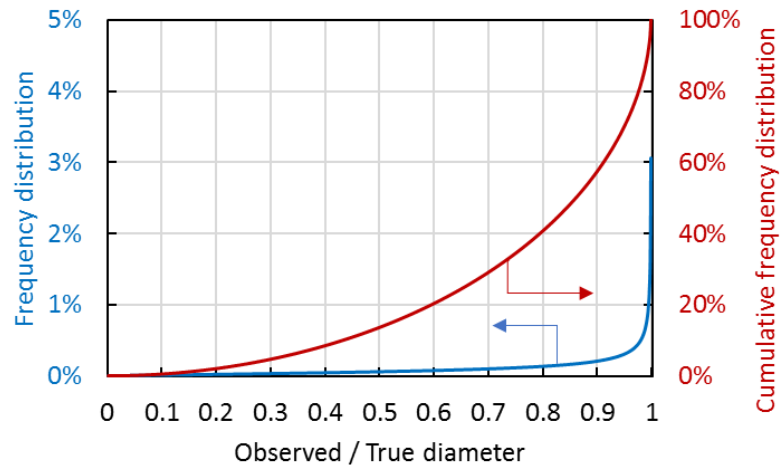
Fig. 4-8. The erroneous measurement of undersized grains from a monodisperse sample.

Accounting for the inclusion of erroneously small particles in 2D cut section micrographs, the inherent diameter of heterogeneity was set to 7000 nm in diameter, equivalent to the frequency peak of minimal size crystal grains. The cluster size distribution was initially set as uniform, though mergers result in an evolving size distribution.

In addition to simple separation via the equations of motion, the potential for nucleating solids was analyzed. Using the local chemical composition, the T_L and τ were calculated at each time step. The T_L and τ were not connected to distinct clusters, but rather to set points within the centrifuge corresponding to the initial spatial discretization. The region used to calculate the local chemical composition was set to a diameter of 5 mm (roughly consistent with the size of samples used in empirical determination of τ). The substantial overlap of 'local regions' for neighboring points results in a spatially smooth prediction of T_L and τ through the centrifuge.

As the τ is composition-dependent, it is expected to change for a given location over the course of centrifuging. The physical mechanism of τ is the time it takes for a stochastic aggregation of a sufficient number of particles into a discrete region and the reconfiguration of those particles into the proper crystal structure. In other words, τ is a simplification of the history of the detailed intermolecular interactions. The instantaneous τ cannot simply be compared to the elapsed time (t_e). Substantial alteration of the composition 'resets the clock' of nucleation lag time (i.e., $t_e = 0$) (**Fig. 4-9**).
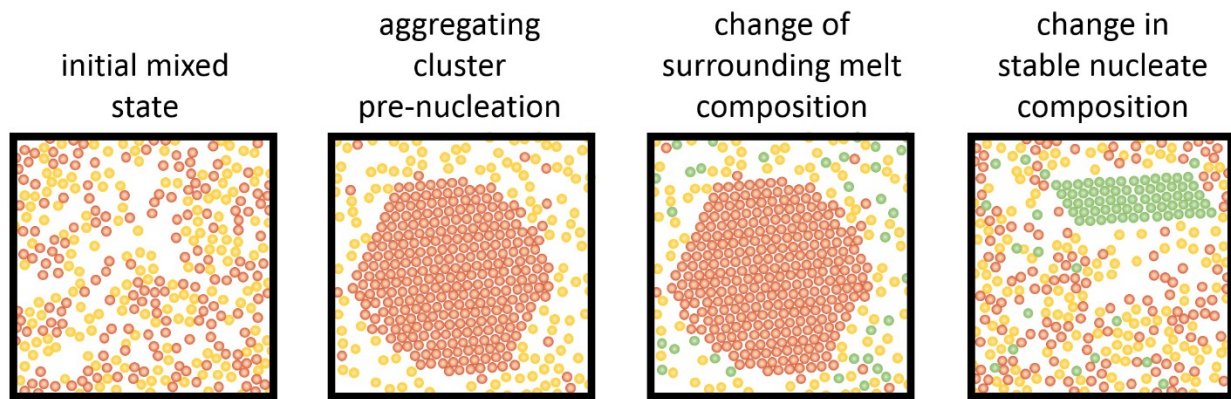
Fig. 4-9. Schematic explaining the non-additive nature of elapsed time.

The degree of compositional change that is functionally meaningful is an open theoretical question as the specifics of the aggregating cluster composition and structure are of singular importance. It is expected that the sensitivity of the t_e to composition is higher in areas of the compositional space where multiple compounds exist in close proximity. However, even when a given structure is ostensibly stable over a wide compositional space, the inclusion of impurities in the structure results in a fundamentally different structure evidenced by changes in the T_L and τ (**Fig. 4-10**). Moreover, the simple ternary diagrams common to the ISM slag literature are not representative of the solution complexity common to ISM. As the number of chemical species increases, the segregation of the compositional space into distinct structures becomes increasingly complex. Given these considerations, the compositional distance relating to structural change in the CaO-SiO_2-Al_2O_3 and CaO-SiO_2-FeO eutectic used in BF operation was used to determine the compositional change that leads to resetting t_e to 0 (**Fig. 4-11**). If the local molar chemical composition remained ±1% for all the elements present in the melt then t_e was increased by the time step. Otherwise t_e was reset to 0 due to the new chemical environment.

An additional phenomenon that may suppress nucleation and growth during centrifugal separation is the disruption of the interfacial boundary due to shear forces. Empirical evidence suggests that active movement of a nuclei relative to the melt inhibits crystal growth [Bartels and Furman, 2002]. The bulk motion of the nuclei acts to strip away molecules from the trailing surface of the cluster, inhibiting its growth. Additionally, the shear converts the stable geometry from spherical to oblong in CNT [Mokshin et al., 2013]. Due to the nascent theoretical understanding of this phenomenon, it was not included in the simulation.
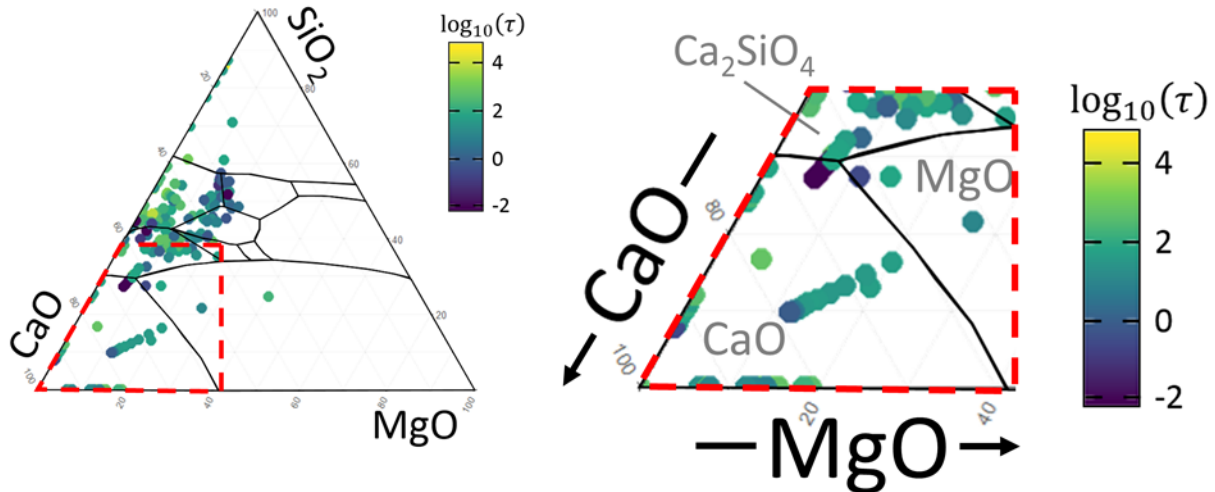
Fig. 4-10. Empirical data showing changes to the 'stable' crystal structure as evidenced by alteration of the nucleation lag time within compositions conventionally regarded as having a continuous structure.
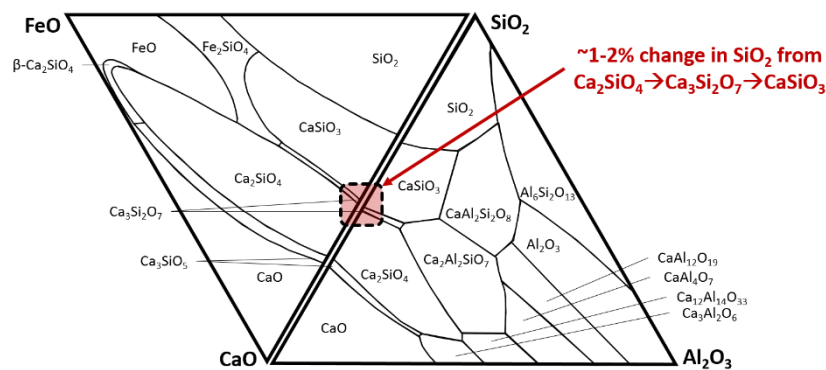
Fig. 4-11. Sensitivity of stable crystal structure to composition in the simple CaO-SiO₂-FeO and CaO-SiO₂-Al₂O₃ ternaries.

Though the τ was calculated by DNN, Classical Nucleation Theory (CNT) was used to calculate the nucleation and growth process once τ was exceeded. Note that cluster size is not equivalent to the size of a nucleating compound. Clusters are inherently random in internal structure whereas a nucleating compound has a defined crystal structure; therefore, clusters can become much larger than the critical radius of nucleation (r^*) and should not be expected to crystalize instantaneous once the τ has been exceeded. For a spherical nucleus of radius equal to r, the Gibbs free energy of formation (ΔG) is given by **Eq. (4-8)**.

$$\Delta G = 4\pi r^2 \gamma_S - \frac{4\pi r^3}{3} \Delta G_V \qquad\qquad (4-8)$$

In **Eq. (4-8)**, γ_S is the interfacial energy and ΔG_V is the difference in volumetric Gibbs free energy of the melt and the solid. The left-hand term indicates the energetic burden of creating a new surface area, while the right-hand term indicates the reduced energy of the solid phase. Differentiating **Eq. (4-8)** yields the critical radius (r^*) at which the volumetric driving force overcomes the increased

surface energy, resulting in growth being thermodynamically favored. The r^* can be calculated for a given composition based on the liquidus temperature (T_L), latent heat of fusion (L), and degree of undercooling (T_U), per **Eq. (4-9)**.

$$r^* = \left(\frac{2\gamma_S T_L}{L}\right)\left(\frac{1}{T_U}\right) \qquad\qquad (4-9)$$

According to CNT, the nucleation rate per unit volume (I) for the critical radius is calculated per **Eq. (4-10)**, where f_0 is the frequency of an atom attachment, C_0 is the number of atoms per unit volume calculated per **Eq. (4-11)**, k_B is the Boltzmann constant, ΔG is the excess Gibbs energy between the liquid and solid as defined by **Eq. (4-12)**, N_A is Avogadro's number, and the molecular weight is denoted by MW. Literature values were used for L and γ_S.

$$I = f_0 C_0 \exp\left(\frac{-\Delta G}{k_B T}\right) \qquad\qquad (4-10)$$

$$C_0 = \frac{\rho N_A}{MW} \qquad\qquad (4-11)$$

$$\Delta G = \left(\frac{16\pi\gamma_S^3 T_L^2}{3L^2}\right)\left(\frac{1}{T_U^2}\right) \qquad\qquad (4-12)$$

The calculations were performed for the average composition over the local region, but nucleating crystals were only applied to the stationary central point. No melting of the nucleated solids was considered. If the local chemical composition remained constant over the next time step, additional solids were nucleated and the already nucleated crystals were assumed to have grown at a continuous rate (Ω), calculated per **Eq. (4-13)** [Ainslie et al., 1962; Wagstaff, 1969]. In **Eq. (4-13)**, α is the atomic jump distance which was set to the molecular diameter.

$$\Omega = \frac{L T_U}{3\pi\alpha^2\eta T_L} \qquad\qquad (4-13)$$

Agglomeration of solids was not explicitly considered. Rather, as the number of solid nuclei and their size increases the volume of molten slag decreases. The geometric frustration of the solid-melt structure was not modeled, nor was its influence on the solidification process (i.e., agglomeration) modeled.

When solids begin to nucleate and grow, they effect the viscosity of the melt as described by the Einstein-Roscoe equation given in **Eq. (4-14)** [Wu et al., 2011]. The adjusted viscosity is given by η^* and the volume fraction of solid particles is given by f. Assuming spherical particles of uniform size, the constants a and n in **Eq. (4-14)** become 1.35 and 2.5, respectively [Roscoe, 1952].

$$\eta^* = \frac{\eta}{(1-af)^n} \qquad\qquad (4-14)$$

The heat generation from solidification (latent heat) and heat loss to the environment were set to zero. In other words, the simulation remained isothermal without accounting for thermal energy. The primary rational for this simplification was to more clearly discern the effects of compositional alteration to the T_U and τ. The overall calculation scheme is provided in **Fig. 4-12** and shown schematically in **Fig. 4-13**. Additional details of the calculation method are aggregated in **Table 4-2**.
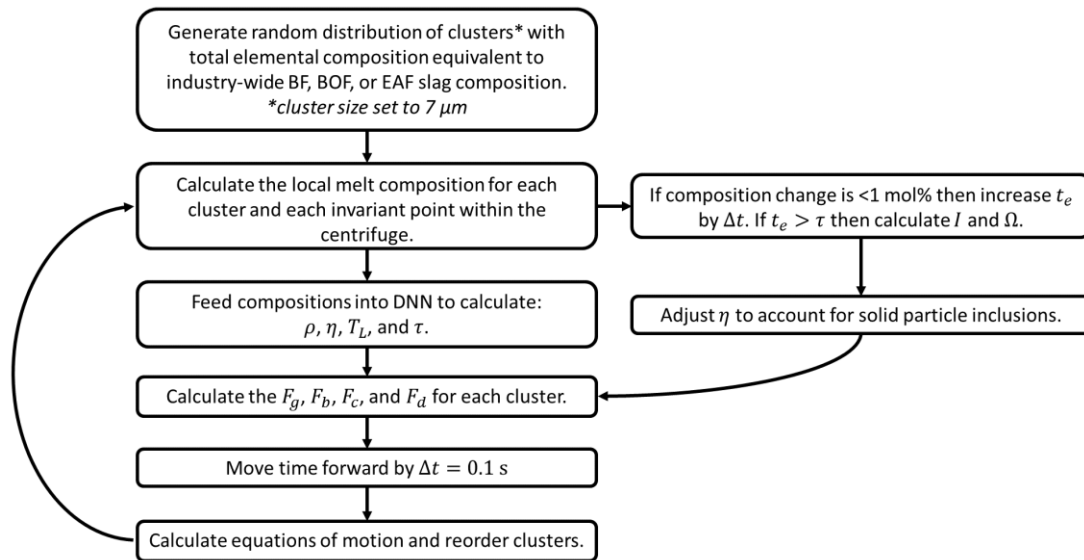
Fig. 4-12. Calculation scheme of the centrifugal separation and solidification simulation.
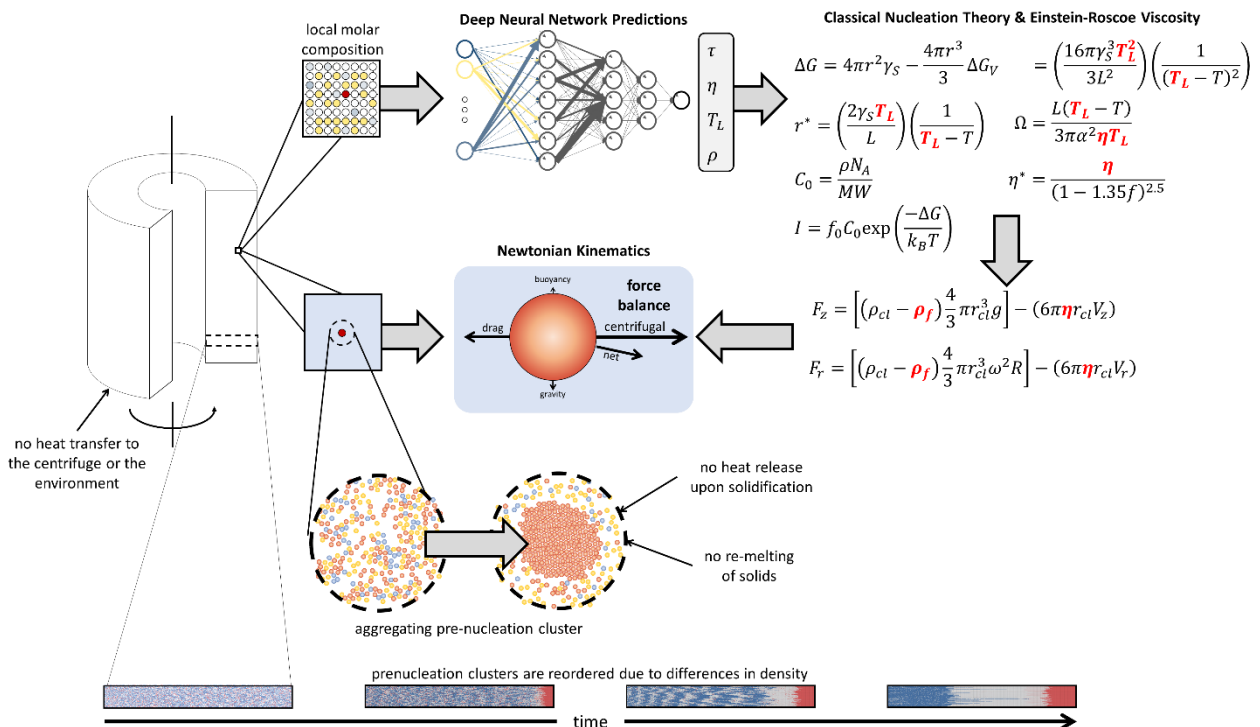
Fig. 4-13. Calculation scheme of the centrifugal separation and solidification simulation.

Table 4-2. Calculation details of the centrifugal separation and solidification simulation.

Feature	Value	Notes
Cluster diameter (nm)	7000	Based on examination of micrographs of quenched, molten slag from the literature and Royet (1991) to determine maximal randomly assembled cluster size in melt.
Time step (s)	0.1	Selected to limit calculation load while providing sufficiently detailed determination of kinematics and nucleation lag time.
Temperature (K)	1773	Set uniform across slag types; in reality, BF, BOF, and EAF furnaces operate at different temperatures, with additional variation within furnace types.
Calculation Method		
Density (ρ)	DNN	Average composition from a 5 mm diameter around each cluster.
Viscosity (η)	DNN + Einstein-Roscoe	Average composition from a 5 mm diameter around each cluster. If solid nuclei are present, their effect is calculated in addition to the melt viscosity predicted by DNN.
Liquidus temperature (T_L)	DNN	Average composition from a 5 mm diameter around each cluster.
Nucleation lag time (τ)	T_L-bootstrapped DNN	Average composition from a 5 mm diameter. Nucleation lag time is reset to 0 when molar composition alters by >1% from previous time step. A gradual transition of composition over multiple time steps does not restart the nucleation lag time so long as the change per time step is ≤1 mol%. Nucleation lag time is calculated at fixed positions within the centrifuge (i.e., not associated with clusters).
Solidification and growth	Classical nucleation theory	If the nucleation lag time is exceeded, then the number of nuclei is calculated based on the local conditions. Re-melting of solids is not considered. If the local composition changes ≤1 mol% between time steps, then the growth of nuclei is calculated. If the molar composition of the surrounding melt changes >1% then nucleated solids do not grow and are not considered for growth in future calculations. Intergrowth of solids and trapping of interspatial liquids (agglomeration) is not considered. Alteration to density due to solidification is not considered. The influence of pressure and gas phase composition are not included in the calculation of the Gibbs free energy. The Gibbs energy of the solid phases are based on crystalline solids; when phases solidify for which there is not Gibbs data, the closest crystalline compound by molar composition is used.
Segregation	Newtonian kinematics	During the time step clusters move under the assumption of constant local density, body forces, and drag forces. No limitation on cluster movement (e.g., centrifuge walls) is made during the time step. After each time step, clusters are reordered within the centrifuge.

		The centrifuge is considered adiabatic. No heat transfer from the slag to the centrifuge is considered. Heat generation from solidification is ignored. Heat loss from drag is ignored.
Heat balance	---	
Centrifuge Configuration		
Type	vertical axis	Sedimentation type.
Internal slag volume (m^3)	2	---
Offset from rotational axis (m)	0.3	A lack of offset results in very small centrifugal forces at the center of the centrifuge and accordingly, loss of Ca, Mg, and Fe to mixed phases. This value has not been optimized.
Centrifuge external radius (m)	0.639	Larger offsets increase the separating power of the centrifuge and decrease the relative separation distance. However, larger offsets also increase the surface area per unit slag volume, making consideration of heat loss more pressing. This value has not been optimized.
Angular velocity (rpm)	3,000	Limited by the 50 Hz utility electricity.

Sizing of the centrifuge involves trade-offs between several factors cutting across operational ease, risk, scale-up, and the physical mechanisms of separation. Maintaining separation ability was considered a fundamental constraint, thereby dictating most of the sizing process. Maintaining separation functionally means a design with high centrifugal forces, a small radial travel distance for separating slag, and the prevention of excessive heat loss to the centrifuge body and surrounding environment. Heat loss occurs due to long filling times, a large centrifuge-slag surface area, and a large centrifuge mass. From a perspective of risk avoidance and adoption rate, it was considered more viable to introduce small centrifuges into extant ISM facilities, slowly replacing current slag treatment processes as know-how and capital permits. Moreover, as a shut-down of slag treatment would cause a shut-down of the overall ISM process, it was deemed preferable to have several small centrifuges which could be more easily replaced and maintained than a single large centrifuge. These considerations led to the selection of a centrifuge with 2 m^3 slag capacity (**Fig. 4-14**).
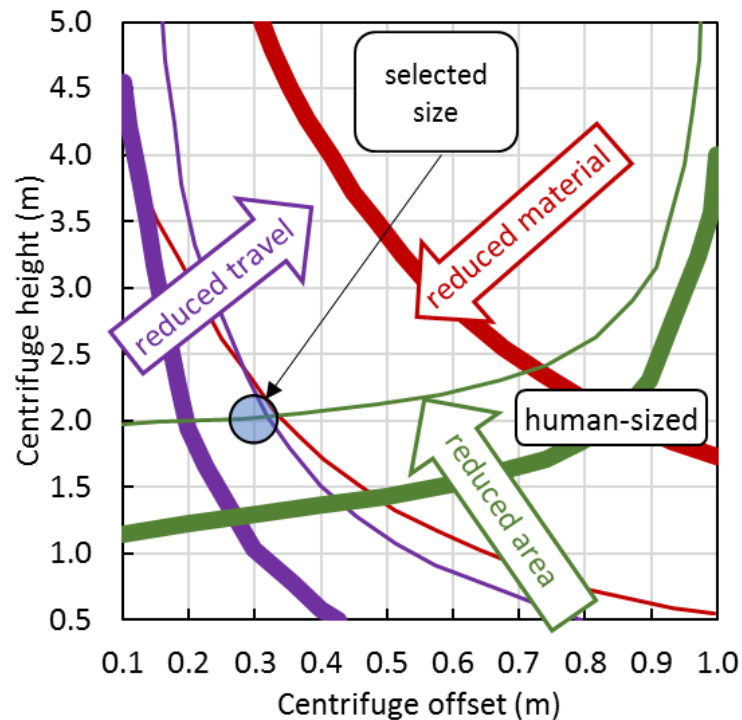
Fig. 4-14. The factors influencing sizing for a centrifuge with an internal volume of 2 m^3.

4.1.1. Simulation results

The centrifugal separation and solidification simulation indicated that solid nucleation is delayed by the kinetic energy barrier (due to large T_U) imposed by the excursion of slag from the steep and deep eutectics of the mixed slag systems. General trends were: 1) high SiO_2 content layers become effectively solid prior to formation of a pure silica layer due to the high η, small centrifugal acceleration, and minor T_U of those melts, 2) Fe^0 and FeO content is recovered at high purity due to the rapid separation of dense phases and the low T_L of iron-laden melts, 3) a significant portion of CaO and MgO is recovered as high purity (Ca,Mg)O, and 4) (Ca,Mg)-silicate layers are recovered primarily as $(Ca,Mg)SiO_3$, $(Ca,Mg)_3SiO_5$, and $(Ca,Mg)_2SiO_4$ in BF, BOF, and EAF slags, respectively.

Blast Furnace slag

Blast furnace slag has minimal iron content, so the focus of centrifugal separation is the recovery of (Ca,Mg)O for recycling to the blast furnace or capture of CO_2. **Figure 4-15** provides snapshots of the radially dependent ρ, η, and T_U of molten BF slag under centrifugal separation after 1, 2, 3, and 4 minutes.
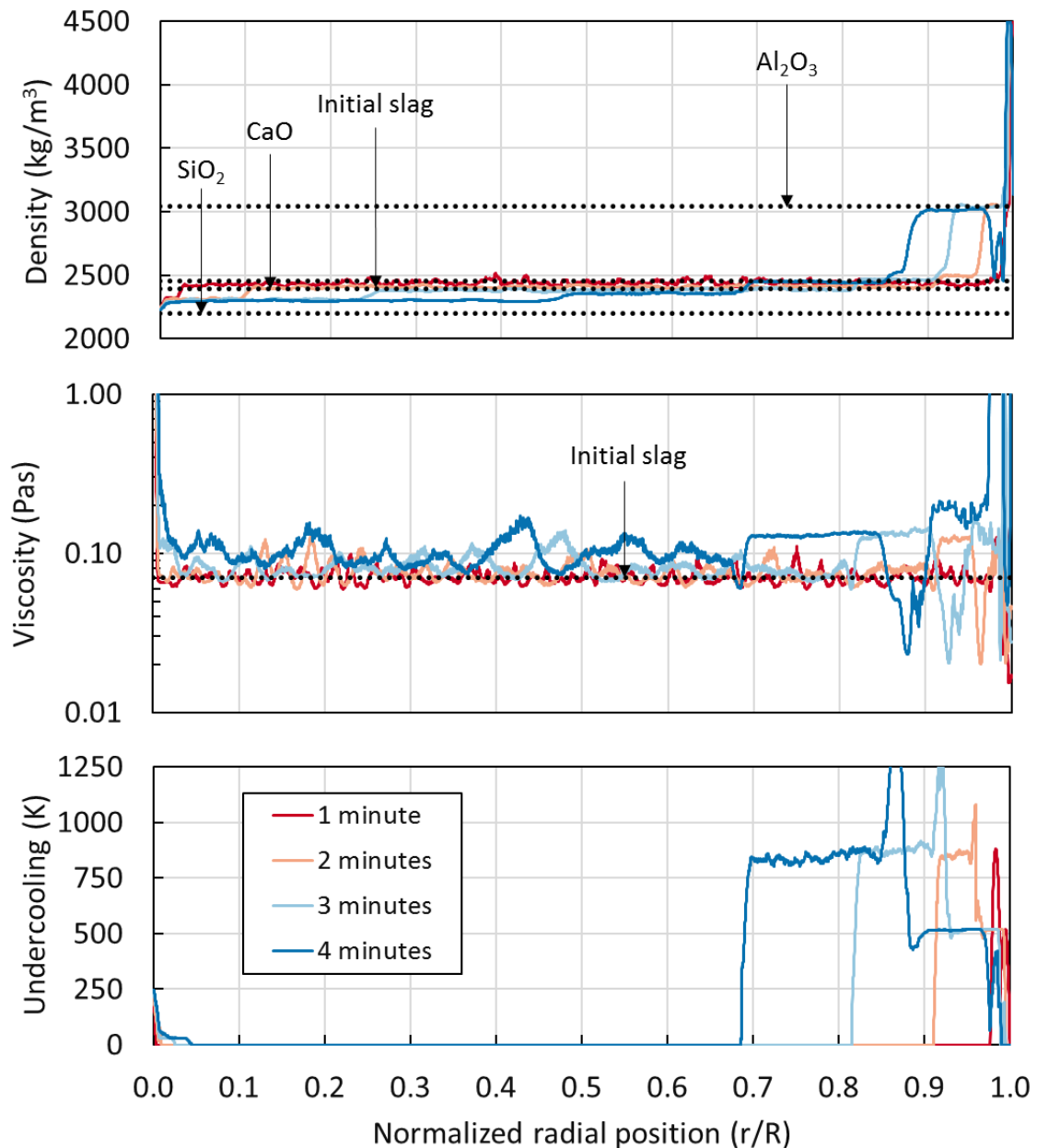
Fig. 4-15. Snapshots of the evolution of the BF slag during centrifugal separation.

In BF slag, the separation of Al_2O_3 from the melt leaves the remaining slag in a low T_L eutectic, thereby delaying solids nucleation. There was a sharp compositional transition within the centrifuge between the (Ca,Mg)-silicate melt and the high purity CaO-MgO melt. The T_L of the CaO-MgO melt was much higher than the slag temperature causing the nucleation of CaO-MgO to be suppressed via the kinetic barrier. The transition from low T_L eutectic to large T_U allowed for both the (Ca,Mg)SiO$_3$ and (Ca,Mg)O layers to form prior to phase change. Small amounts of solids nucleation occurred due to transient compositions with minor T_U, but the arrested growth of nuclei due to compositional change limited the volume fraction of solids and the η^* was only marginally larger than η. The bulk of prematurely nucleated solids were concentrated in the outer portion of the centrifuge.

After 4 minutes of centrifuging, separation was functionally complete though substantial solids nucleation had not yet occurred. Continued centrifuging would allow t_e to exceed τ resulting in

homogeneous nucleation due to the magnitude of T_U. Of the Ca/Mg content, 42.2% was converted to >95% purity CaO-MgO, 8.9% to lower purity CaO-MgO, 44.3% to ambiguously crystalline (Ca,Mg)-silicates, 2.8% was trapped in a silicate matrix, and 1.8% was converted to compounds with other elements. The final composition of the centrifuged BF slag is shown in **Fig. 4-16**.
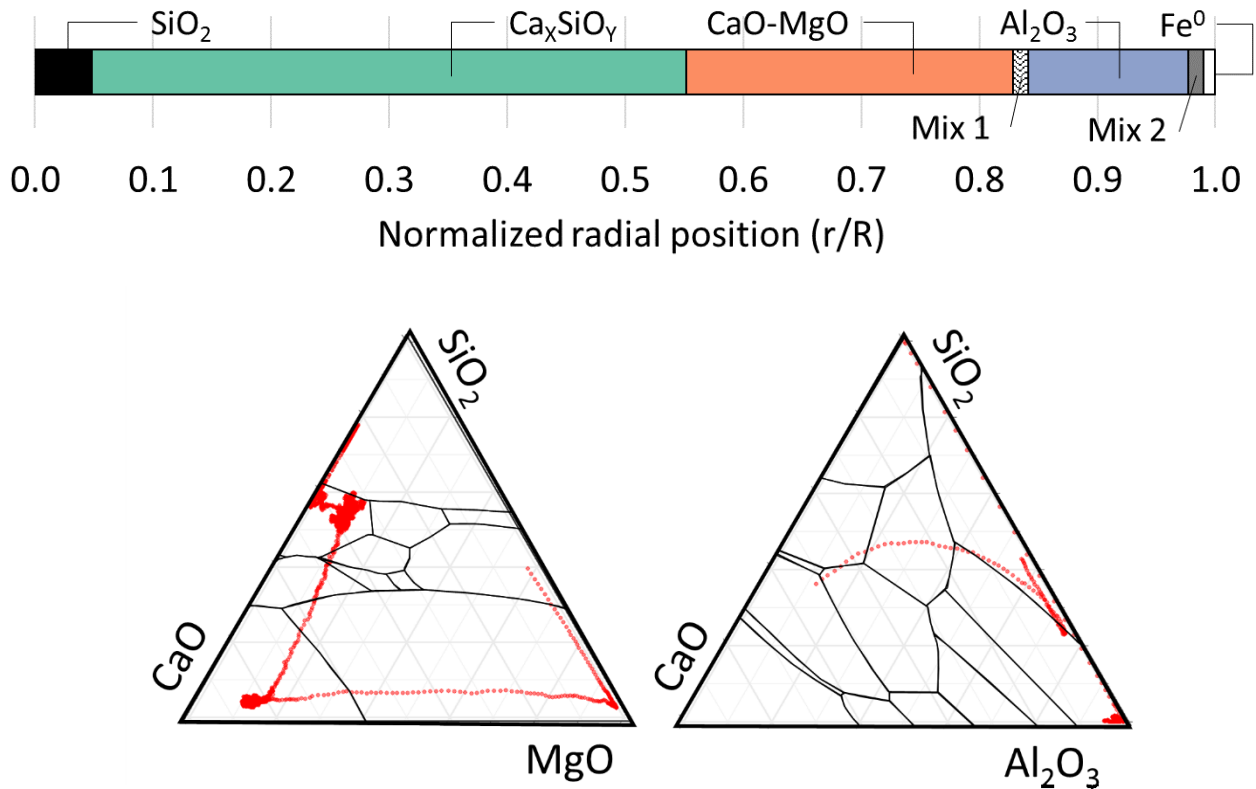
Fig. 4-16. The composition of materials derived from BF slag after centrifuging for 5 minutes.

Basic Oxygen Furnace slag

   Basic Oxygen Furnace (BOF) slag is high in FeO, CaO, and MgO content. The reduction of iron ore is the largest CO_2 source in ISM; thus, along with recovery of calcium and magnesium, FeO is the main target of centrifugal treatment of BOF slag. Snapshots at 1, 2, 3, and 4 minutes of the centrifugal separation of BOF slag are provided **Fig. 4-17**.
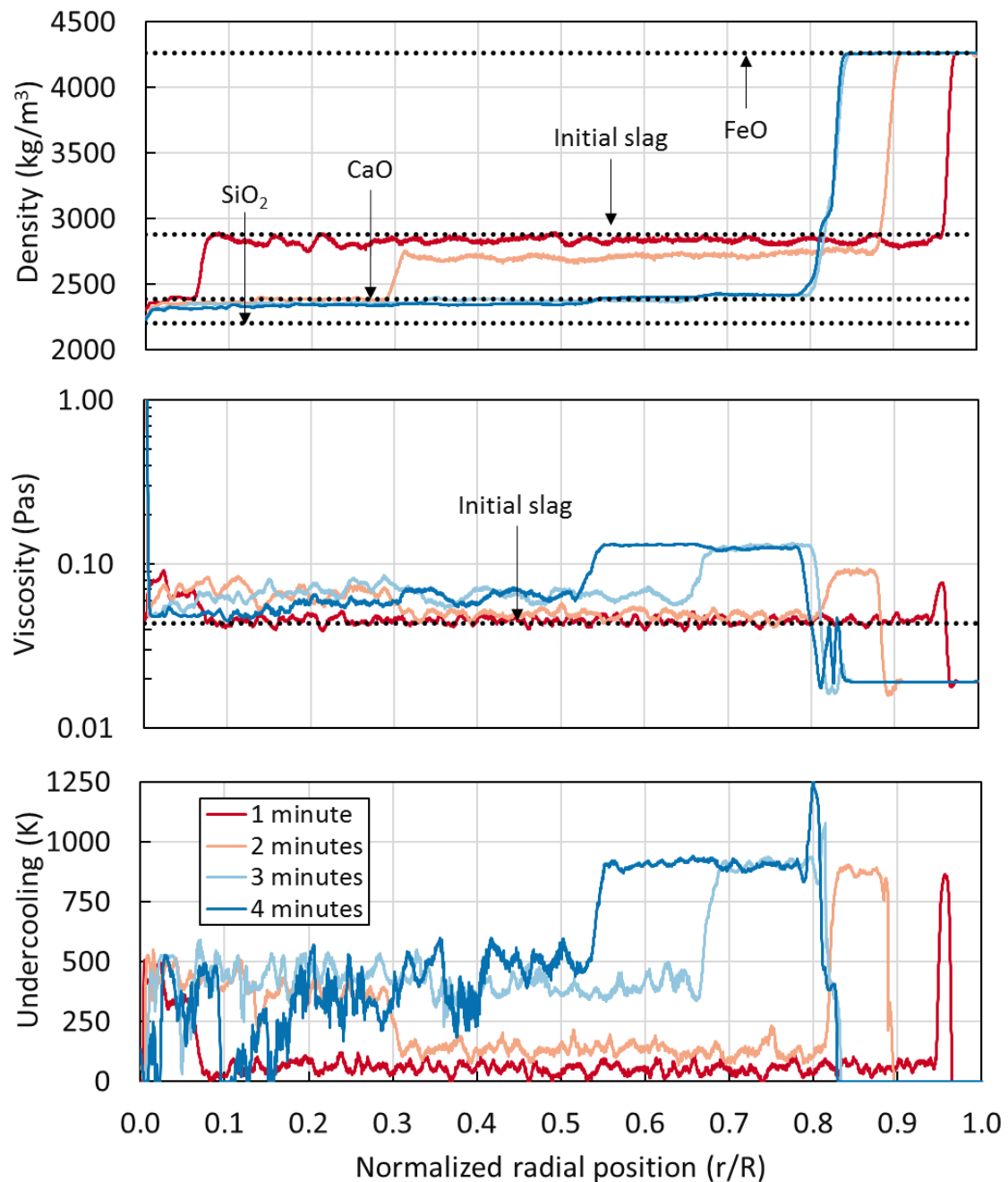
Fig. 4-17. Snapshots of the evolution of the BOF slag during centrifugal separation.

In the BOF slag, solids nucleation proceeded from the center of the centrifuge as FeO was drawn to the periphery of the centrifuge. By 180 seconds, all of the FeO had separated from the bulk melt into a pure, outer layer. Even after FeO separation, Al_2O_3 continued to separate from the bulk melt, but typically underwent solids nucleation and growth when it reached high (Ca,Mg)O- low SiO_2- content compositions. A layer of high purity CaO-MgO remained molten radially internal to the solid, mixed aluminates. After 5 minutes, all materials had undergone solids nucleation and growth. An inner core of (Ca,Mg)-silicate was surrounded by a high purity CaO-MgO shell, a thin shell of mixed aluminates, and an out layer of FeO. Of the iron content, 92.2% was converted to >95% purity FeO, 3.5% to lower purity FeO, and 4.3% was lost to compounds with other elements. In the case of calcium and magnesium, 28% was converted to >95% purity CaO-MgO, 66.6% to lower purity CaO-

MgO (average SiO_2 content of 20.9%), 2.9% to amorphous $(Ca,Mg)_3SiO_5$, and 2.5% was lost to compounds with other elements. The final composition of the centrifuged BOF slag is shown in **Fig. 4-18**.
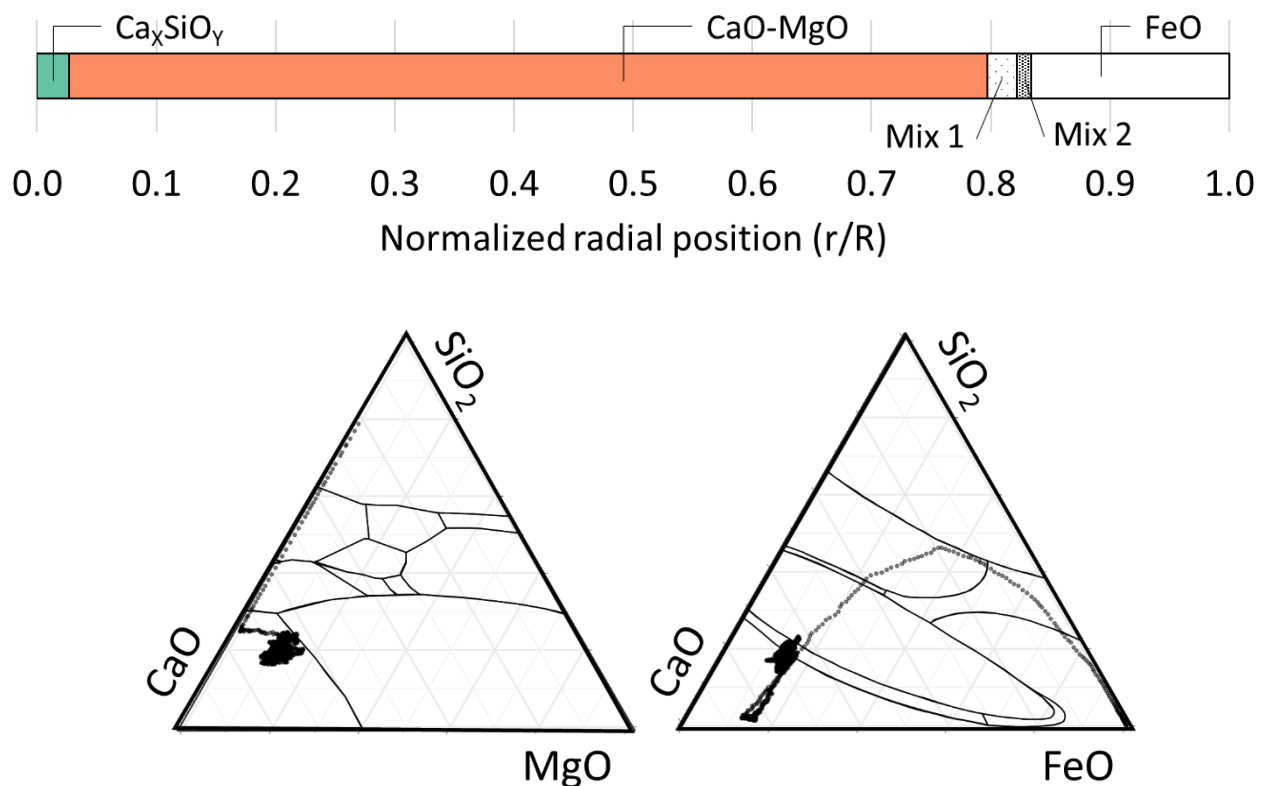
Fig. 4-18. The composition of materials derived from BOF slag after centrifuging for 5 minutes.

Electric Arc Furnace slag

Electric Arc Furnace (EAF) slag is compositionally similar to BOF slag and thus behaves similarly when centrifuged. However, EAF slag has higher Al_2O_3 and FeO content and a lower $(Ca,Mg)O$ to SiO_2 ratio than BOF slag. This resulted in larger FeO and Al_2O_3 layers which decreased the separation power of $(Ca,Mg)O$ from the $CaO-MgO-SiO_2$ melt due to radial position. As a result, the compositional transition from the low T_L eutectic of the $CaO-MgO-SiO_2$ system to the high T_L of $CaO-MgO$ melts was more gradual and accordingly more solids nucleation and growth occurred at the intermediate compositions. However, the increased FeO-content also extended the period over which T_L-suppressing FeO was present in the $CaO-MgO-SiO_2$ melt; resulting in a larger portion of the recovered $(Ca,Mg)O$ to be of high purity. As was the case for (Ca,Mg)-silicates in the BOF slag, the $(Ca,Mg)_2SiO_4$ formed through repeated nucleation, but not growth. In EAF slag, 90.2% of the iron content was converted to >95% purity FeO, 6.2% to lower purity FeO, and 3.6% was converted to compounds with other elements. Of the calcium and magnesium content, 57.7% was converted to >95% purity CaO-MgO, 19% to lower purity CaO-MgO (average SiO_2 content of 16.6%), 19.3% to amorphous $(Ca,Mg)_2SiO_4$, 0.2% was trapped in silica, and 3.8% reacted with other elements. **Figure 4-19** provides the molar composition of centrifuged EAF slag at 1, 2, 3, and 4 minutes. **Figure 4-20** is the final composition of centrifuged EAF slag.
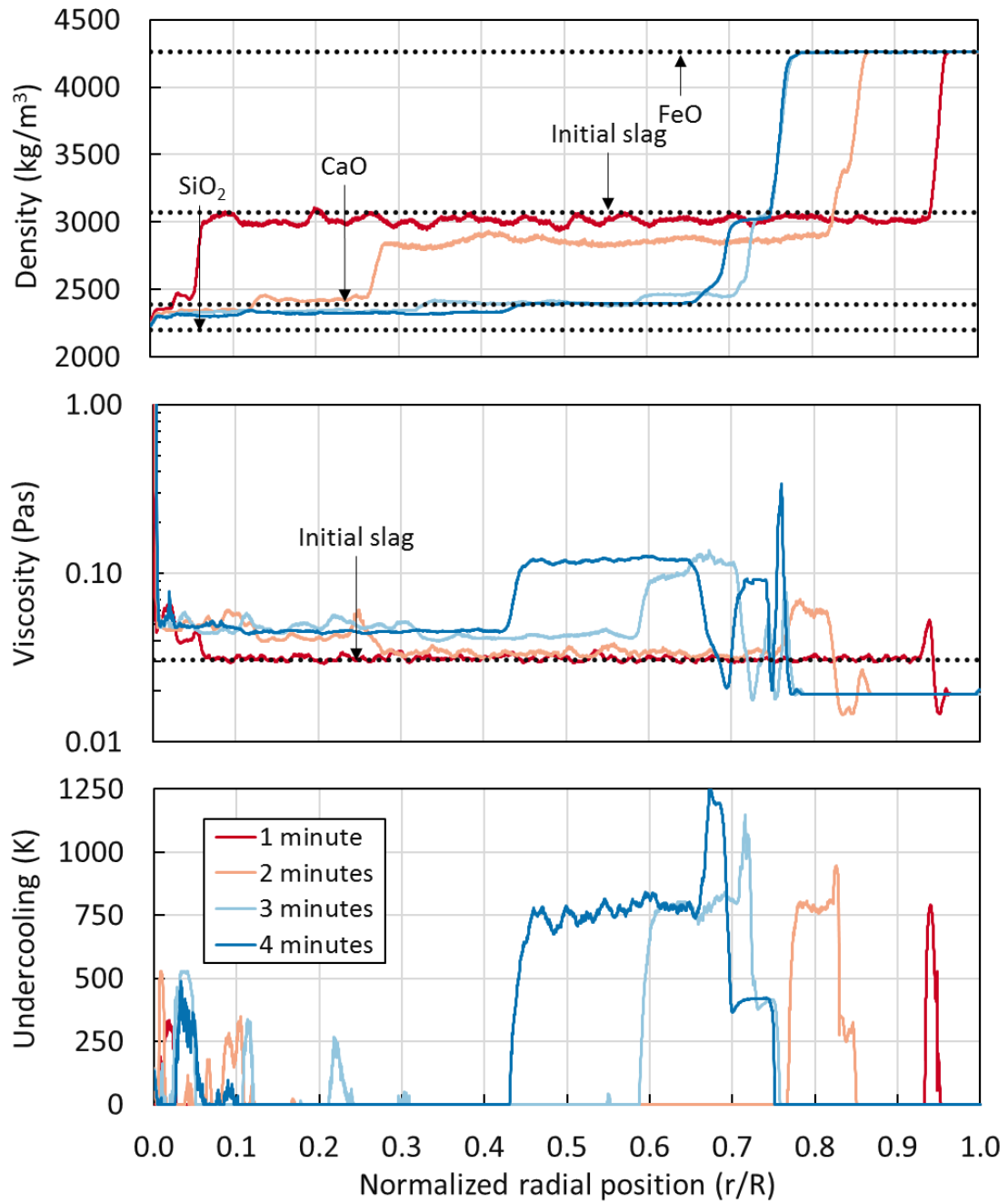
Fig. 4-19. Snapshots of the evolution of the EAF slag during centrifugal separation.
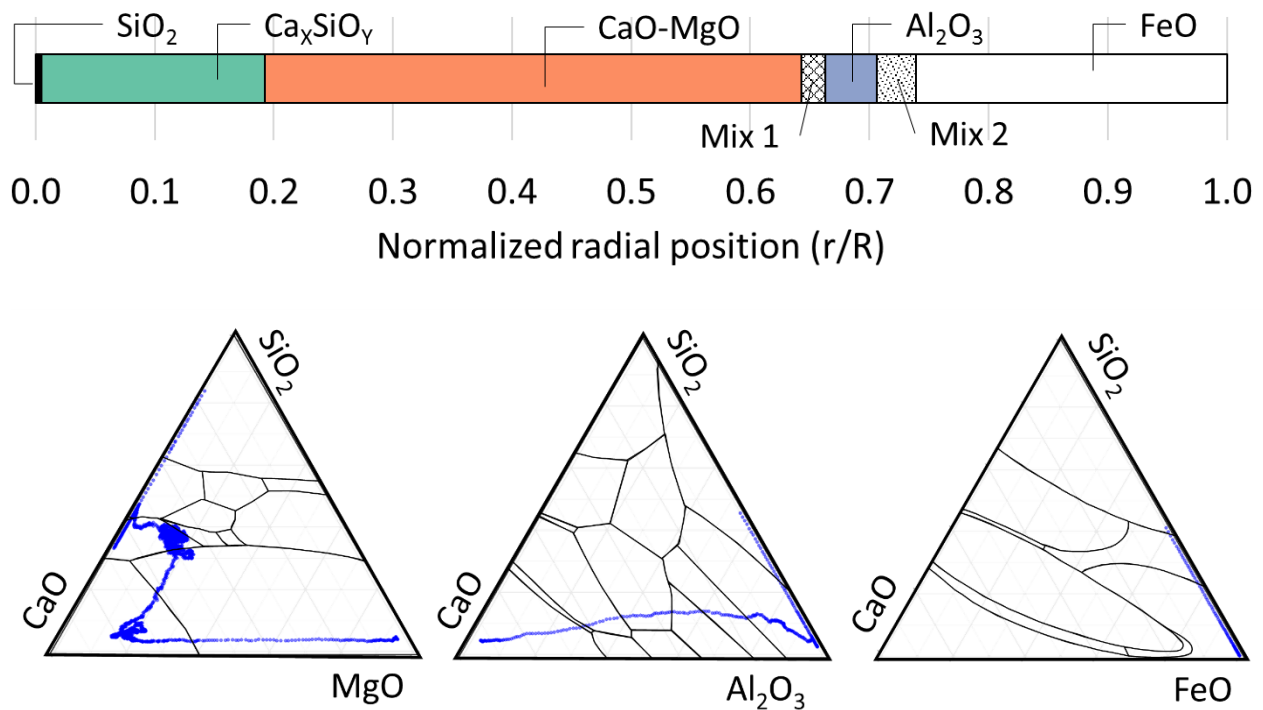
Fig. 4-20. The composition of materials derived from EAF slag after centrifuging for 5 minutes.

Undercooling and suppressed growth

The transient, radially-dependent T_U predicted by the simulation (see **Fig. 4-15, 4-17, 4-19**) exceeds 750 K in areas of particularly high CaO, MgO, or Al₂O₃ content. On the other hand, real world applications of homogeneous solidification typical observe T_U on the order of a few hundred Kelvin. In most industrial processes, the ratio of the undercooling to the liquidus temperature is greater than 0.8 (i.e., $T_U/T_L > 0.8$). In laboratory settings, $T_U/T_L \sim 0.4$ has been reported with theoretical analysis indicating a minimum T_U/T_L for any substance of ~0.33 [Luo et al., 2003]. The discrepancy between the theoretical minimum T_U/T_L and what is observed experimentally and in industrial operations is related to the time scale of heat transfer in large volumes and the difficulty in elimination of nucleation sites in industrial settings. In thermally generated T_U, the loss of heat at the surface creates a small T_U in the local melt. This T_U is dampened by the newly generated ΔT between the undercooled melt and adjacent melt still at the initial temperature. A small T_U reduces the τ for homogeneous nucleation, which in turn acts as seeds for heterogeneous nucleation [Gránásy et al., 2014]. These effects are minimized by reducing the volume of the melt, in effect increasing the maximum potential cooling rate of the melt volume [Perepezko and Wilde, 2016]. However, there does not appear to be a practical method to achieve similar (T_U/T_L) on the large volumes seen in industrial settings. A method to circumvent this phenomenon is to utilize constitutional supercooling [StJohn et al., 2015]. In the proposed centrifugal method, the radially dependent change in composition is abrupt, leading to sudden and significant changes in slag properties. The abrupt composition change is due to the separation mechanics of the centrifuge. As separation between elements occurs, the melt density increases with radial distance from the rotational axis. This acts to accelerate compounds to areas of equivalent composition and suppress the occurrence of gradual transition zones. The compositional jumps (e.g., from (Ca,Mg)-silicates to CaO-MgO) explains the sudden increase in T_U to >750 K. The particularly high T_L of calcium and magnesium oxides means

the undercooling of 750 K is equivalent to a (T_U/T_L) ~0.70 and ~0.71 in BF (T=1773 K) and BOF/EAF (T=1873 K) slags, respectively. Equivalently, an undercooling of 1250 K corresponds to a (T_U/T_L) ~0.59 and ~0.60 in BF and BOF/EAF slags, respectively. In other words, the predicted level of T_U is not restricted by physical laws and may be possible even in industrial settings due to the mechanism being compositionally based, as opposed to thermally based.

An additional phenomenon not seen in thermal undercooling processes that was predicted by the centrifugal simulation was the repeated nucleation but lack of growth within the melt. A similar effect is seen in constitutional supercooling of alloys, where a so-called 'nucleation free zone' develops ahead of solidifying dendrites. Due to the speed of separation in the current simulation, the nucleation time lag inhibits solidification to areas where the undercooling is only a few hundred Kelvin. As discussed above, this level of undercooling is primarily limited to the spatially small transition regions. As such, solid nuclei rapidly lose the chemical resources necessary for growth. Recall that the growth-suppressing effects of interfacial disruption were not included in the simulation, so the predicted nucleation and growth may be conservatively large. The overall solidification extent over the course of centrifuging is graphed in **Fig. 4-21**. Premature solidification is arrested by the consistent compositional change which prevents the rapid growth in η which might otherwise halt separation. The increasing solidification rate near the end of centrifuging is due to the stabilization of the melt composition. Beginning at 5 minutes, rapid transitions to complete solidification (not graphed for clarity) occur as compositions remained relatively stable.
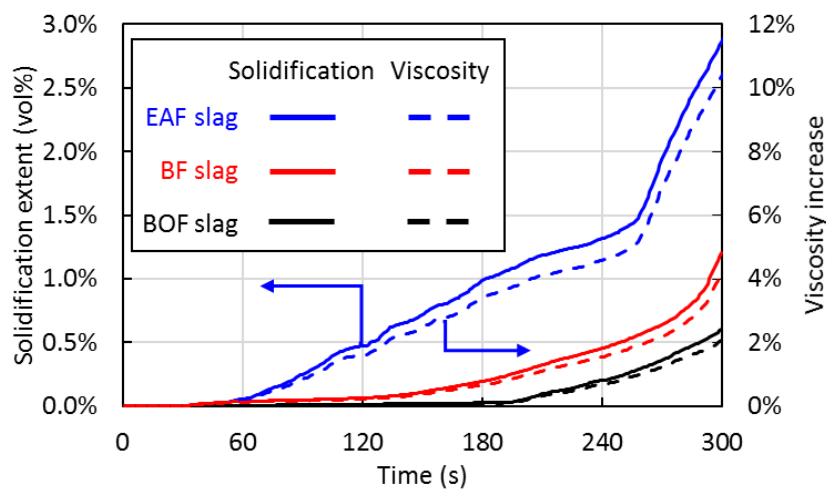
Fig. 4-21. The total solidification extent over the course of centrifugal separation.

Application to other slags

The simulation demonstrated the potential for substantial separation of the constituent elements in slag via centrifuging. However, the qualitatively different behaviors of the three slag compositions analyzed indicates that the process cannot be applied carelessly. Nevertheless, a reasonable first approximation of the behavior of different molten slags can be made. **Figure 4-22** provides a graphical example of the method using the average BF, BOF, and EAF compositions for reference. First, the chemical composition of a slag is mapped on a ternary diagram as SiO_2-(CaO+MgO)-(Al_2O_3+FeO+Fe^0). This segregation of compounds allows for the estimation of undercooling at the interface of SiO_2 and (Ca,Mg)O. A line should be drawn from the (Al_2O_3+FeO+Fe^0) vertex through the slag composition to the opposite face of the ternary diagram. This location indicates the average

composition of the slag after the segregation of the denser, T_L-reducing species. The separation time of these heavier species increases as their initial concentration increases. Thus, an $(Al_2O_3+FeO+Fe^0)$-lean slag melt will reach this composition quickly, with minimal initial deviation (i.e., minimal separation of $(Ca,Mg)O$ from the (Ca,Mg)-silicate melt). Melts with higher $(Al_2O_3+FeO+Fe^0)$ concentrations will incur a wider distribution of (Ca,Mg)-silicates by the time the heavier compounds have segregated (compare **Fig. 4-18** and **Fig. 4-20**). Unfortunately, the separation time of heavier elements, and the degree of (Ca,Mg)-silicate variation cannot be estimated simply. The degree of $(Ca,Mg)O$ separation from the $(Al_2O_3+FeO+Fe^0)$-free melt will depend on the degree of T_U. This can be estimated by comparing the initial slag temperature with the T_L based on widely available CaO-MgO-SiO$_2$ phase diagrams. Based on the simulations in this work, when the slag temperature is $< 0.7\,T_L$, nucleation is avoided, and further purification of the compounds occurs. At slag temperatures in the range of $0.7 - 0.8\,T_L$ some degree of nucleation occurs but growth is suppressed, resulting in a variety of compounds in this composition range. This phenomenon manifests as the spread in the CaO to MgO ratio at low SiO$_2$ contents. At compositions where the slag temperature and T_L are similar (e.g., high SiO$_2$ melts), rapid conversion to crystalline or amorphous solids is expected. This can be seen by the lack of pure SiO$_2$ in the results. If the slag temperature is higher than the T_L, then separation should continue within the melt. For example, the BF slag remains above its T_L, allowing for further separation of compounds.
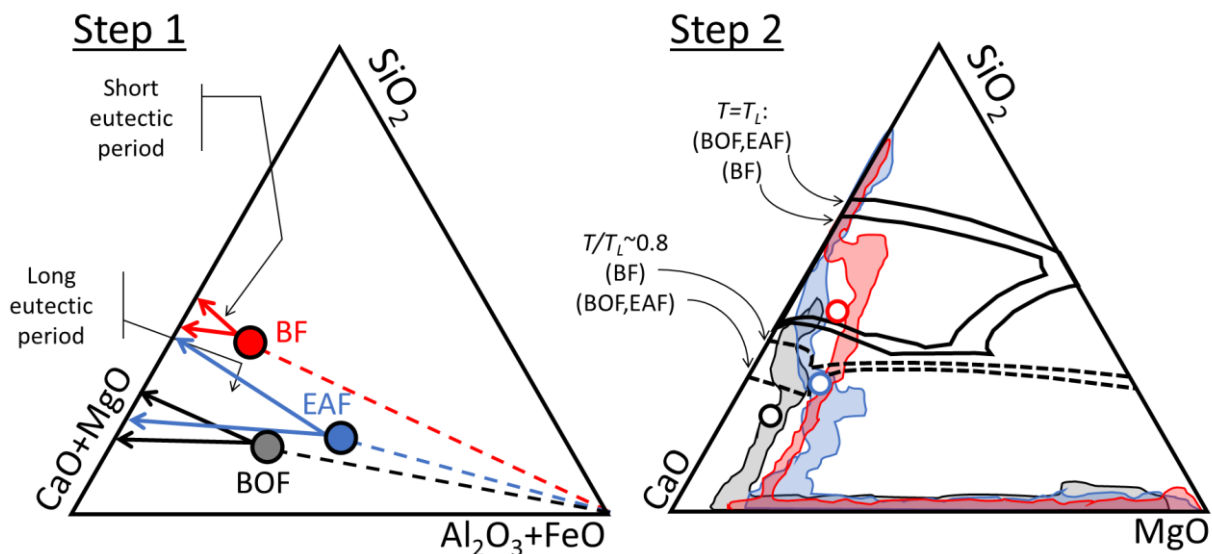
Fig. 4-22. Schematic of the method to determine to a first approximation the suitability of a given slag composition for centrifugal separation and solidification.

Open issues

Of the simplifying assumptions made, discounting the cooling effect of the centrifuge on the molten slag is the most likely to result in qualitative changes to the results. However, practical engineering solutions to this problem seem likely. For example, running the centrifuge in a semi-continuous batch method would reduce the heat loss from the melt to the centrifuge body. Additionally, the heat generated from solidification is non-trivial and is applied towards the end of the centrifuging regime, thereby helping to maintain a high temperature for the centrifuge body.

Additional measures such as operating the centrifuge within a low-pressure area and engineering the emissivity of the centrifuge body and surroundings would further cut down on heat loss.

An additional point that may require further investigation is the internal pressure and shear within the molten melt. The high centrifugal forces of the centrifuge generate large internal pressures to the slag melt which may meaningfully alter the molten properties. To account for such pressure effects, DNN would need to be retrained on datasets including the high-pressure data and CNT would need to be modified to account for the evolution of the preferential nucleation shape with shear.

4.1.2. Matching slag production rate

The need to operate the centrifuge rapidly and in small batches, means that a molten slag storage tank to facilitate matching the slag production and treatment rates is not possible. Rather, the centrifuges must be able to receive the slag as it is tapped from the furnace and be able to complete separation, solidification, and removal of slag by the time the next slag tapping occurs. Matching the furnace operations is therefore a case-by-case basis, as each furnace and operator works on a unique tapping schedule, with some performing continuous slag removal and others performing tapping operations on the order of minutes to hours [Agrawal et al., 2016; Agrawal et al., 2018; Roche et al., 2018a,b; Upadhyay and Kundu, 2013].

A rough order of magnitude calculation was performed to determine the number of centrifuges required to meet BF slag production rates for a 4 Mtonne-steel/y facility [IEAGHG, 2013]. The BF slag production is 1.111 Mtonne/y; assuming a standard BF slag density, this comes to 0.682 m^3 of slag per minute. For a 2 m^3 centrifuge, the filling rate is limited by the production rate, and takes 2 minutes 56 seconds. Though complete centrifugal separation is expected within 5 minutes, with rapid solidification thereafter, operation time was set to 10 minutes to ensure ample time for slag with long τ to nucleate and grow. Removal of solid slag from the centrifuge has not been researched, but the simple centrifuge design is expected to allow slag removal and preparing the centrifuge for the next slag batch in 5 minutes. The total turnover time of a single centrifugal batch is thus ~18 minutes, 15 minutes of which the centrifuge cannot take on new slag. To fully handle the slag from such a facility requires at least 6 centrifuges to cover operational and unloading time. Given that the steel volume of each centrifuge is ~0.227 m^3, the CO_2 intensity of steel is 1.636 kgCO_2/kg-steel, and the CO_2 reduction potential of BF slag is ~0.434 kgCO_2/kg-slag, each centrifuge 'pays off' its CO_2 debt after 1.11 loads. Assuming an operational life of 1 year for each centrifuge body reduces the net CO_2 mineralization efficiency by 0.004%.

For a repetitive tapping schedule, the number of centrifuges required is the greater of **Eq. (4-15)** and **Eq. (4-16)**, where t_D is the 'dead time' of the centrifuge (i.e., the time during which it cannot receive slag), t_B is the 'build-up time' of slag in the furnace (i.e., between tapping cycles), t_F is the 'fill time' (i.e., the time during which the centrifuge can receive slag), V_c is the slag volumetric capacity of the centrifuge, V_T is the volume of slag over a complete tapping cycle, and N is the number of centrifuges required to match operations. The fill time is a function of centrifuge volume and tapping schedule. It was assumed that manpower limits the reuse of centrifuges over a single tapping cycle.

$$N = \left(\frac{t_D - t_B}{t_F} \right) + 1 \qquad (4-15)$$

$$N = \frac{V_T}{V_c} \qquad (4-16)$$

The number of centrifuges required as a function of tapping interval is provided in **Fig. 4-23**, assuming each centrifuge has an internal volume of 2 m³. More rapid slag tapping schedules require more centrifuges. However, due to the constraint of not allowing centrifuge reuse during a single tapping cycle, the number of centrifuges increases for tapping cycles longer than 20 minutes. Automation of the process would allow for rapid centrifuge reuse, eliminating the dramatic increase in centrifuge number.
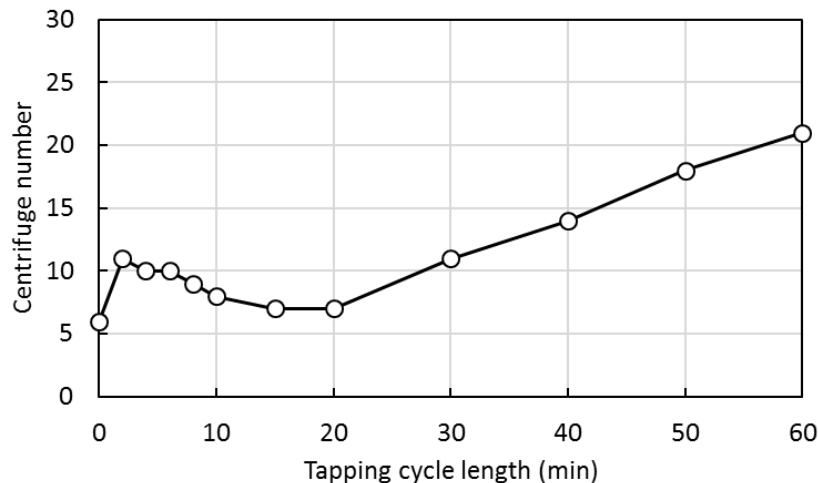
Fig. 4-23. The influence of tapping cycle length on the number of centrifuges required. Calculated for 2 m³ centrifuge treating 1.111 Mtonne/y BF slag.

4.2.   MYNA process: In-container solidification

Slow solidification is completely distinct from centrifuging both in the manifest phenomenon and in the means of lowering CO_2 emissions. The goal of slow solidification is not to create CaO which can be returned to the furnace, but rather to generate Ca-bearing species that readily react with CO_2 and can be separated from other materials at low energetic input. To do so, the slow solidification process takes advantage of the dynamics of nucleation and growth to produce large mineral grains of compositionally distinct species. Nucleation is a stochastic process whose build-up is hidden by the small length scales and rapid timescales of the phenomenon. In reality, clusters of molecules are agglomerating and dissipating continuously in a molten solution, even above its melting point. As the temperature decreases, the size and lifetime of the transient clusters increases. Below the melting point the nucleating clusters are energetically favored to grow, causing the phase change to appear sudden and distinct. However, the true nature of nucleation being gradual means that the rate of nucleation is related to the degree of temperature depression below the liquidus temperature (T_L), known as undercooling ($T_U = T_L - T$). Increasing the undercooling hastens the onset of nucleation and increases the number density of nuclei in a given volume. This process continues until further reduction in temperature causes the concurrent increase in viscosity and decrease in kinetic energy to increase the nucleation lag time (τ) and a decrease the number of nucleation sites. The slow solidification method looks to operate as close to the T_L for as long as possible in order to reduce the nucleation rate and increase the diffusion of species in the melt. By doing so, there is less competition between nucleation sites for resources (i.e., atoms and space), more chance for mergers between similar compounds, and more opportunity for expulsion of impurities from solids. By extending the period near solidification conditions, the degree of entropic demixing from geometric and diffusional

effects increases. The molten slag becomes more and more heterogeneous, eventually producing a solid with large-scale heterogeneity which can be easily separated. The end result is the generation of large, extremely pure mineral grains.

From an exergetic standpoint, the available exergy of the high temperature molten melt is used to 'pre-separate' the slag into larger mineral grains. As a result, the exergy required for demixing solid slag is substantially reduced.

The demixing process in molten slag is facilitated by differences in molecular radius and mass, but fundamentally can operate purely on the diffusion that occurs during solidification as illustrated in **Fig. 4-24**. At temperatures well above T_L the kinetic energy prevents aggregation of molecules and washes out the effects of minor differences in molecular radius and mass (**Fig. 4-24a**). As the temperature decreases, the stochastic clustering of molecules becomes prevalent, with differences in molecular characteristics providing entropic pressure to de-mix (**Fig. 4-24b**). The aggregation of a given molecule results in a disequilibrium in the particle flux: particles diffuse via Brownian motion towards the aggregation site but are not able leave the cluster (**Fig. 4-24c**). This one-way flux produces a low concentration gradient moving radially outward from the cluster. Due to geometric effects, and the fact that diffusion time is proportional to the square of the mean distance, a shell depleted in the aggregating molecule develops around the growing aggregate. This diffusion-based alteration of composition changes the local dynamics of nucleation (i.e., constitutional supercooling) (**Fig. 4-24d**). As a result, in the limiting case of a single nucleating particle, the solidification-diffusion interdependencies will produce a secondary solid phase present as shell around the initial nuclei (**Fig. 4-24e** and **Fig. 4-24f**). The key challenge in developing the in-container solidification process is to design a process that robustly generates large grain sizes despite the chemical variability across slags.
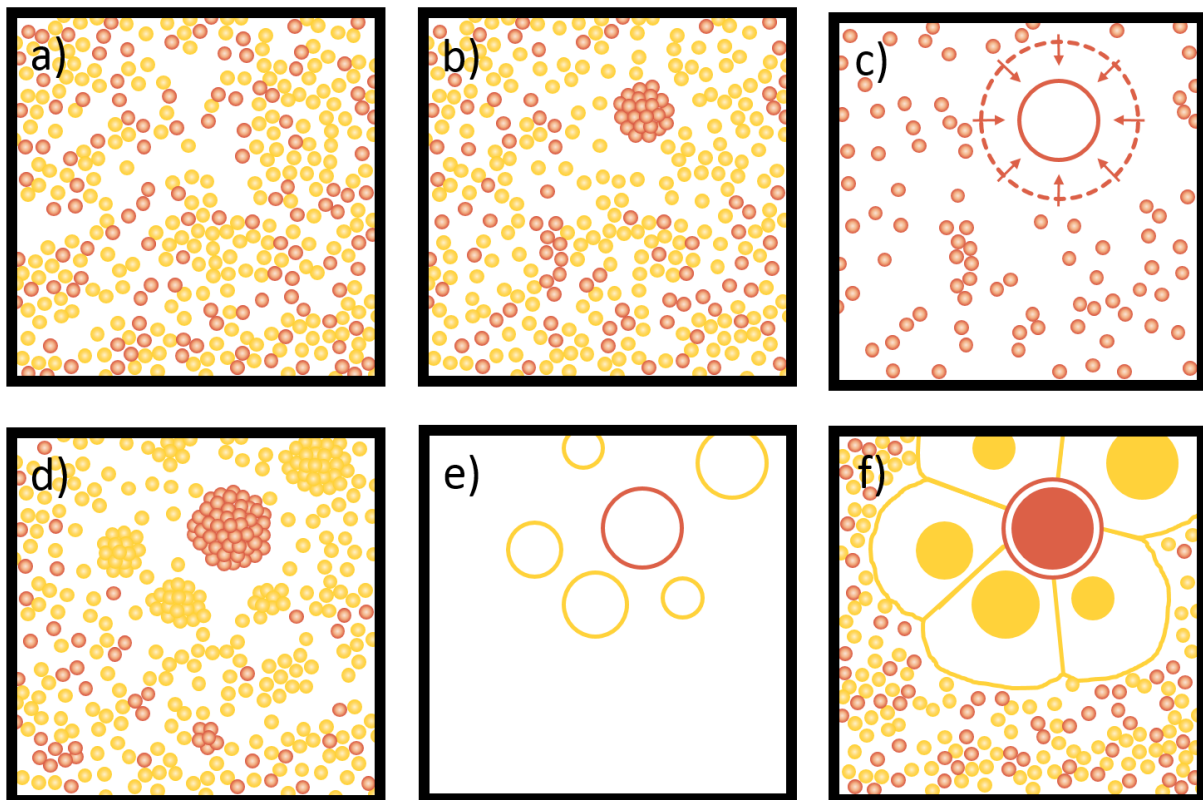
Fig. 4-24. The alteration to the local solution from a) an initially mixed solution, b) a local cluster development with c) the one-way flow of solutes, d) the development of a two-tiered structure, e) the onset of nucleation, and f) growth.

4.2.1. Empirical limits

The GSD that develops under slow solidification is inherently dependent upon the specific solution chemistry and the spatiotemporal temperature history. Moreover, the specific properties of the melt and nucleating species (e.g., the energy barrier to diffusion across the nucleate-melt interface) is necessary information to make quantitative predictions. However, even in instances when all necessary information is available, the results are only relevant to the specific conditions. While example cases can be instructive, the useful information is what are the limits to the growth of nucleating solids under the range of industrially practical conditions. To gain perspective on the scale of GSD that can be expected, a literature review of micrographs of slowly solidified silicate melts was performed. A fairly large amount of data exists in the field of petrology; unfortunately, the majority of this data represents high pressure conditions, which fundamentally alter the solidification kinetics. With the notable exception of Gautier et al., 2013 and Du et al., 2017, very little work has looked at the behavior of ISM slag under very slow solidification conditions. Nevertheless, from this data, work on coal slag solidification [Shen et al., 2017a; Shen et al., 2017b], and petrological studies at atmospheric pressure [Bartels and Furman, 2002; Dunbar et al., 1995], a maximum observed GSD can be determined for equant (roughly spherical) and acicular (needle-like) crystals. The differing geometry of growth means that acicular crystals inherently have a larger propensity for intergrowth and are less prone to the diffusional constraints of equant solids (**Fig. 4-25**). Additionally, in-house testing of commercial desilicating slag was performed. The slag T_L was determined empirically to be

1260 ˚C. The slag was then heated to 1300 ˚C under N$_2$ atmosphere and held for 12 hours, followed by cooling at 10 ˚C/min. Example micrographs are provided in **Fig. 4-26**. Note that, unlike the determination of the minimum grain size, 2D micrographs can be used to accurately determine the maximum grain size as the 'cut-section effect' and 'intersection-probability effect' relate to erroneous estimates of non-maximal particle size. The empirical maximum for GSD of equant crystals appears to be on the order of 1 millimeter. For acicular crystals, experiments indicate the maximum length to be on the order of millimeters while the width likely has a maximum of a couple hundred micrometers. The various empirical maximums are provided in **Fig. 4-27**.
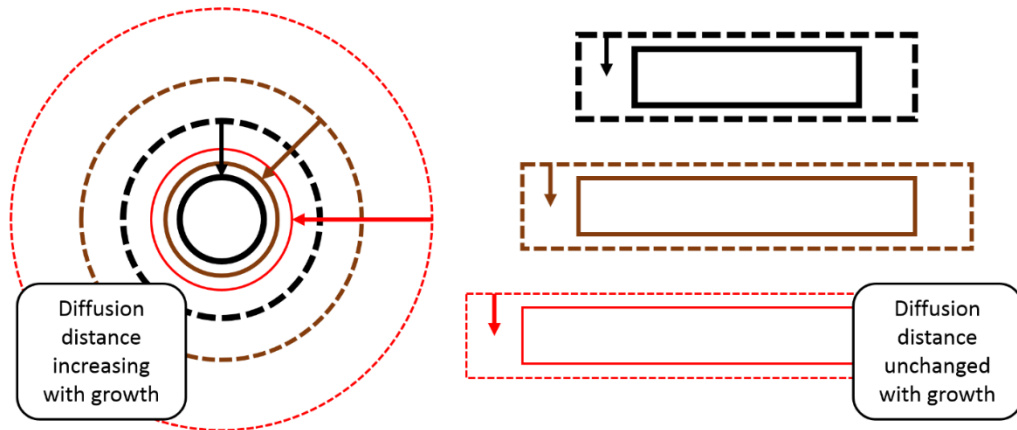
Fig. 4-25. The reduced diffusional growth constraint on acicular compared to equant crystals.
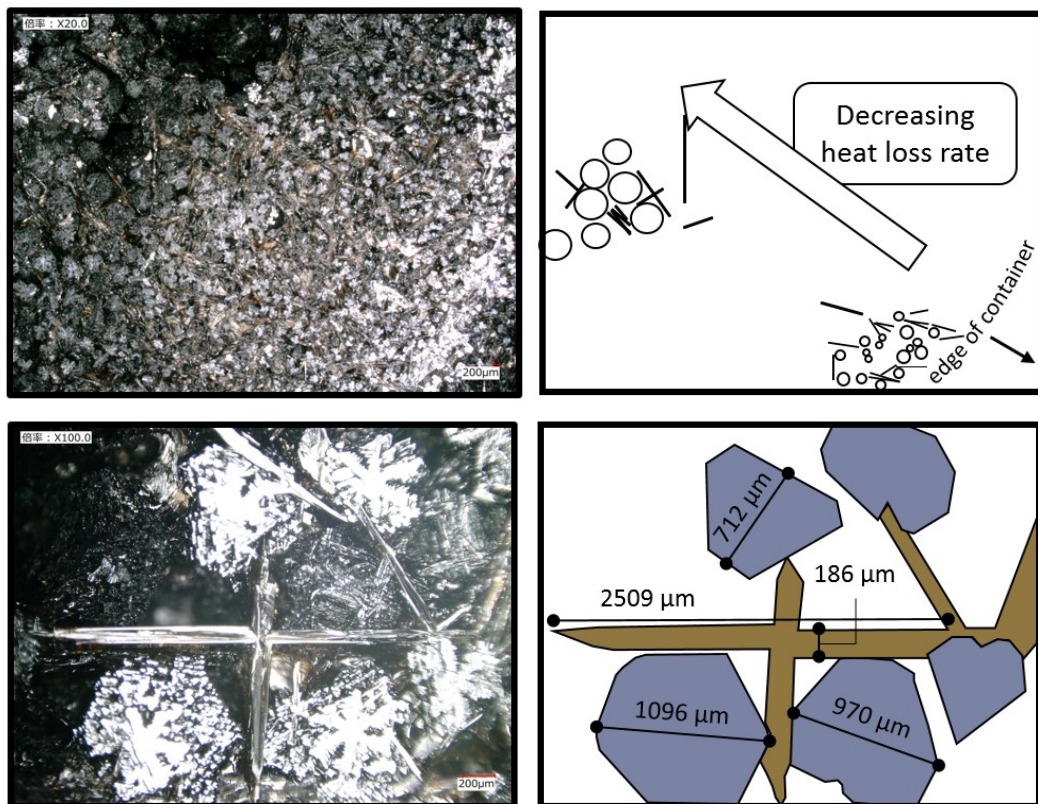
Fig. 4-26. Example micrographs of the disparate mineral grains produced from an extended temperature hold above the T_L of a commercial desilicating slag.
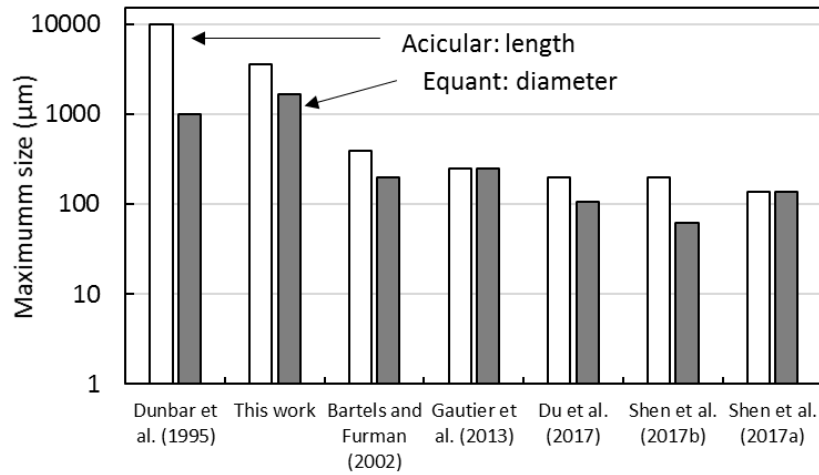
Fig. 4-27. The range of maximal crystal sizes from the literature on slow solidification.

4.2.2. Theoretical limits

The maximal grain size observed empirically is useful information but does not necessarily represent the fundamental limit to grain size growth, even under practical solidification regimes. A case-by-case analysis of the likely GSD is technically possible but does not inform about the case-independent limits. The first step in determining such fundamental limits is determining what physical mechanism constrains growth. In an unmixed molten system, the diffusion of molecules to a solidification front can be simplified as a random walk (i.e., Brownian motion). However, the solidification front acts as a one-way gate, allowing influx of new molecules while preventing the efflux of attached molecules. Assuming the solid is of a different composition (C_A^s) than the bulk melt (C_A^m), then solidification results in a concentration of some subset of the melt, with a concurrent depletion of that molecule from the immediate vicinity of the solid. The degree of concentration occurring through solidification dictates the volume of surrounding melt needed to 'feed' the solidification of a spherical solid (V_{feed}) from an initial radius (r_i) to a larger radius (r_f) per **Eq. (4-17)**. The V_{feed} can be converted into a distance from the solidification front (d_f) via **Eq. (4-18).** Merging **Eq. (4-17)** and **Eq. (4-18)** yields the distance that a molecule must diffuse to reach the solidification front as shown in **Eq. (4-19)**.

$$V_{feed} = \frac{C_A^s}{C_A^m}\left[\frac{4}{3}\pi\left(r_f^3 - r_i^3\right)\right] \qquad (4-17)$$

$$V_{feed} = \frac{4}{3}\pi\left[\left(d_f + r_i\right)^3 - r_i^3\right] \qquad (4-18)$$

$$d_f = \left\{\left[\frac{C_A^s}{C_A^m}\left(r_f^3 - r_i^3\right)\right] + r_i^3\right\}^{1/3} + r_i \qquad (4-19)$$

The basic relation put forth by Einstein (1905) states that the expected distance traveled by a particle (i.e., radial distance from an initial position after an arbitrary time averaged over many

instances or particles: $\overline{d_f}$) is proportional to the square root of the time (t) as indicated by **Eq. (4-20)**, where D is the diffusivity.

$$\overline{d_f} = \sqrt{2Dt} \qquad\qquad (4-20)$$

The D can be estimated via **Eq. (4-21)** where R is the gas constant, r_{ion} is the ionic radius of the diffusing component.

$$D = \frac{RT}{6\pi\eta r_{ion} N_A} \qquad\qquad (4-21)$$

Inserting **Eq. (4-21)** into **Eq. (4-20)** provides the diffusion distance as a function of the diffusing ion, the slag temperature (T), the slag viscosity (η), and the time (t). The key step is to replace t with the nucleation lag time (τ), leading to **Eq. (4-22)**. Once solidification occurs, the diffusion of the solidifying species is functionally halted, leading to a maximum grain size. Therefore, τ represents the time available for diffusion to occur for a given composition and temperature. By way of examining the literature data, the range of reasonable values for τ can be determined (cf. Chapter 3.7).

$$\overline{d_f} = \left(\frac{\tau RT}{3\pi\eta r_{ion} N_A} \right)^{1/2} \qquad\qquad (4-22)$$

Equation 4-21 makes clear that a smaller ionic species will diffuse faster; thus, the maximum $\overline{d_f}$ can be estimated by assuming a small ionic radius species (e.g., MgO$\approx$165 pm). Though η is T-dependent, it is also composition-dependent. Therefore, the literature data can inform the range of reasonable values (cf. Chapter 3.6). The calculation assumptions, methods, and container configuration are provided in **Table 4-3**, a schematic is provided in **Fig. 4-28**.

diffusing ion moves towards an expanding solidification surface

average diffusion distance in a given time

the solidification front grow radially outward, towards the diffusing molecule

Deep Neural Network Predictions

T_L

η

τ

Geometric relations

$$V_{feed} = \frac{C_A^s}{C_A^m}\left[\frac{4}{3}\pi(r_f^3 - r_i^3)\right]$$

$$V_{feed} = \frac{4}{3}\pi\left[(d_f + r_i)^3 - r_i^3\right]$$

$$d_f = \left\{\left[\frac{C_A^s}{C_A^m}(r_f^3 - r_i^3)\right] + r_i^3\right\}^{1/3} + r_i$$

Diffusion equations

$$\overline{d_f} = \sqrt{2Dt} \qquad D = \frac{RT}{6\pi\eta r_{ion}N_A} \qquad \overline{d_f} = \sqrt{\left(\frac{\tau RT}{3\pi\eta r_{ion}N_A}\right)}$$

solidification front growth depends on molten properties and concentration

if the transit time is longer than the nucleation lag time, the molecular does not reach the solidification front

if the transit time is shorter than the nucleation lag time, the molecular joins the solidification front

Fig. 4-28. Scheme used in the calculation of the limits of grain size in slow solidification.

Table 4-3. Calculation details of the slow solidification calculation.

Feature	Value	Notes
Composition	---	Based on industry average chemical composition in the phase space of CaO-MgO-Fe_XO_Y-Al_2O_3-SiO_2.
Temperature	---	Set equal to the highest temperature at which the τ-DNN provide an estimate of nucleation lag time.
Viscosity	---	Based on composition and temperature.
Nucleation lag time	---	Based on composition and temperature.
Ionic radius (pm)	72	Based on ionic radius of Mg.
Calculation Method		
Viscosity (η)	DNN	Based on average composition of the melt and temperature.
Liquidus temperature (T_L)	DNN	Based on average composition of the melt.
Nucleation lag time (τ)	T_L-bootstrapped DNN	Based on average composition of the melt and temperature.
Geometric evolution of particles	---	Based on spherical particles. All other geometries not considered.
Heat balance	---	Adiabatic. No heat loss and no heat release from solidification.
Container Configuration		
Dimensions (m)	$7.64 \times 7.64 \times 0.74$	Rectangular.
Internal slag volume (m^3)	4.9	10 cm thickness.
Refractory (mm)	300	MgO. Alumina and silica-based refractories are avoided because the dissolution of these compounds would result in slag with lower CO_2 diffusivities.
Casing (mm)	20	Carbon steel.

Using the range of values from the literature on τ and η, the expected maximal $\overline{d_f}$ was calculated and plotted in **Fig. 4-29**. The interdependencies of nucleation lag time, viscosity, and temperature mean that **Fig. 4-29** provide an estimate of the order of magnitude of grain size, as opposed to highly accurate predictions. Even so, **Fig. 4-29** provides valuable insight. Firstly, the direct effect of temperature on the diffusion distance is small over the range of likely temperatures (**Fig. 4-29b**). However, the significant impact of viscosity and the nucleation lag time means that temperature needs to be considered as it relates to these properties. Increased temperature reduces viscosity and increases the nucleation lag time. An increase in temperature coincides with movement towards the upper left portion of the graphs (**Fig. 4-29c**), in agreement with the empirical findings of Shen et al. (2017b). Note that the value $\overline{d_f}$ is the distance from the solidification front, and so is related to the

diameter of the grains that make up the solid shell around nuclei that first solidified. It is therefore possible to have two very different grains sizes within a signal sample (i.e., $r_f \neq \overline{d_f}$). However, rearrangement of **Eq. (4-17)** allows for determination of r_i as a function of C_A^s/C_A^m and $\overline{d_f}$. Doing so leads to **Fig. 4-29d**, where C_A^s was set to 1. This indicates that the size difference will not exceed a factor of 4, meaning the degree of separation effort should be of similar scale regardless of the relative size of core and shell solids.
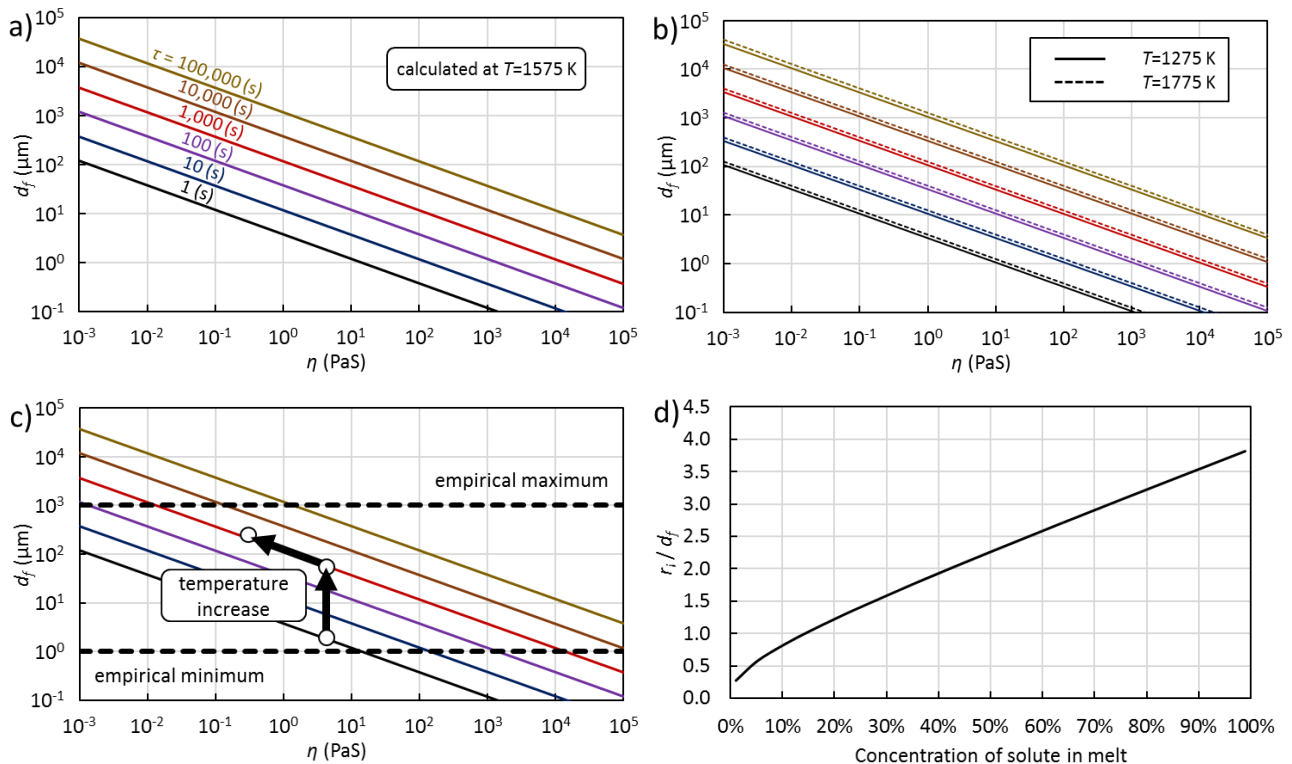
Fig. 4-29. The diffusion-based calculation of grain size in slowly solidified slag showing a) the basic graph construction, b) the weak direct dependence on temperature, c) the strong indirect dependence on temperature with empirical limits indicated, and d) the ratio of the larger to smaller grains that can develop due to ratios of the solutes in the melt.

Whether grain sizes larger than those found empirically can be produced reliably across a range of compositions remains an open question. Larger grains sizes are theoretically possible. However, practical engineering constraints such as timing, space, cost, and the need to operate with no or minimal energy input will likely limit the grain size more than constraints from physics.

4.2.3. Matching slag production rate

For the MYNA process to be realizable in extant ISM facilities, the rate of solidification needs to match the rate of slag production. In the modern integrated steel mill, the BF and BOF processes coexist and are the primary sources of slag. De-silicating (DeS) and refining (Ladle) activities also produce slag. However, the disparate chemical composition, temperature, and production schedule of these slags means that mixing is likely unadvisable. Rather, each subprocess will require its own slag treatment equipment. However, space concerns and potential benefits of space sharing (e.g., temperature management), mean that different slags will have different containers, but the in-container solidification may occur in the same general location.

Though the various slags are chemically distinct, their solidification process will be roughly similar given the time scale of solidification is on the order of hours. Likewise, the container used for solidification may very in length and width but will be subject to a relatively consistent depth based on the competing needs of thermal isotropy and low heat loss. Based on these parameters, the depth of the molten slag was set to 10 cm, while the length, width, and number of containers are varied to match slag production rates. For a BF-BOF facility production 4 Mtonne/y of steel generates on the order of 1.11 Mtonne/y of BF slag, 0.89 Mtonne/y of BOF slag, 0.08 Mtonne/y of DeS slag, and 0.03 Mtonne/y of Ladle slag [IEAGHG, 2013]. Due to their comparatively small volume, DeS and Ladle slag were not considered in calculations.

Using the DNN prediction of molten ρ for industry average BF and BOF slag, the volumetric rate of slag production was determined. Assuming continuous tapping of the slag furnace, the number and size of containers needed to match the production of slag was calculated. The calculation depends on the assumed time for solidification. The T_L for the BF and BOF slag were predicted by DNN, along with the τ and η. From these values the scale of GSD was determined. In both cases the GSD was considered sufficiently large such that no effort is needed to extend the time near the T_L. Even so, slow cooling of the molten slag has been shown to promote larger grain sizes, therefore the time to the T_L was considered a design parameter, open to further research. The total cooling time was set to 1, 6, and 12 hours. Containers were envisioned to be stacked atop one another to limit the footprint of the MYNA process, and to reduce heat loss. Containers were stacked no higher than their side length, which includes 300 mm envelope of insulating bricks and a 20 mm steel shell. The number of such columns was increased until all containers were stacked. Assuming the solidification process takes 12 hours, the number of container and the overall footprint as a function of internal slag volume is shown in **Fig. 4-30a** and **4-30b,** respectively. Equivalent graphs are given for a 6-hour solidification (**Fig. 4-30c** and **4-30d**) and a 1-hour solidification (**Fig. 4-30e** and **4-30f**). The results from Chapter 4.2.2 suggest 1 hour should be sufficient to realize the large grain sizes targeted by in-container solidification. The small container size region of the 1-hour solidification process is highlighted in **Fig. 4-30g**. The embodied CO_2 emissions for container construction (i.e., the emissions from production of steel and MgO) for the prototypical 1.111 Mtonne/y of slag generation are plotted in **Fig. 4-30h**. Minimization of footprint, container number, and embodied CO_2 emissions suggests a container with a molten slag holding capacity of 4.9 m^3 is optimal.
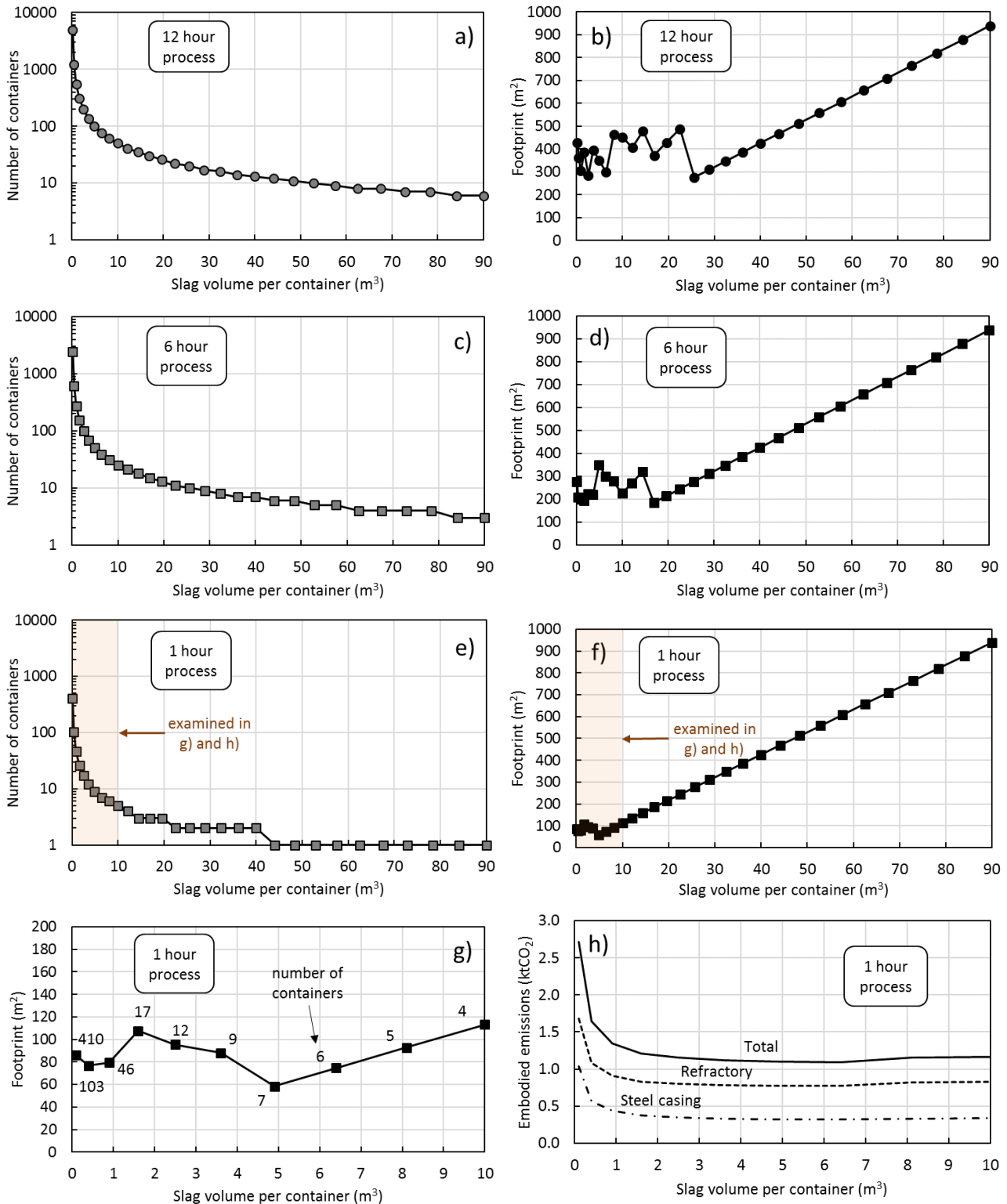
Fig. 4-30. The optimization of container size, footprint, and number for a), b) a 12-hour solidification period, c), d) a 6-hour solidification period, e), f) a 1-hour solidification period, with g) the optimal range for 1 hour highlighted, and h) the embodied CO_2 emissions of container construction in the optimal range.

Chapter-specific symbols and abbreviation list

a: Constant in Einstein-Roscoe equation
BF: Blast furnace
BOF: Basic oxygen furnace
C_A^s: Composition of solid
C_A^m: Composition of melt
C_0: Atom number per unit volume
CNT: Classical nucleation theory
D: Diffusivity
d_f: Distance from the solidification front
$\overline{d_f}$: Mean diffusion distance
d_x: Observed grain of diameter x
EAF: Electric arc furnace
f: Volume fraction of solids in the melt
f_0: Frequency of atom attachment
GSD: Grain size distribution
I: Nucleation rate
ISM: Iron and steelmaking
k_B: Boltzmann constant
L: Latent heat of fusion
MD: Molecular dynamics
MW: Molecular weight
n: Constant in Einstein-Roscoe equation
N: Number of centrifuges
N_A: Avogadro's number
$P(x, y)$: Probability of grain diameter between d_x and d_y
R: Gas constant
r^*: Critical radius
r_c: Cluster radius
r_f: Final solid radius
r_i: Initial solid radius
r_{ion}: Ionic radius
t: Time
t_B: Build-up time
t_D: Dead time
t_e: Elapsed time
t_F: Fill time
T: Temperature
T_L: Liquidus temperature
T_U: Undercooling
V_c: Volume of centrifuge
V_{feed}: Volume around a solid need to supply material to the solid
V_T: Total volume of slag during a tapping cycle

ΔG: Excess Gibbs energy

Ω: Continuous crystal growth rate

σ: Mean

ρ: Density

τ: Nucleation lag time

μ: Standard deviation

η: Viscosity

η^*: Solids-bearing viscosity

γ_S: Interfacial energy

References

Agrawal, A., Kor, S.C., Nandy, U., Choudhary, A.R. and Tripathi, V.R., 2016. Real-time blast furnace hearth liquid level monitoring system. Ironmaking & Steelmaking, 43(7), pp.550-558.

Agrawal, A., Tiwari, M., Agarwal, M.K. and Kothari, A.K., 2018. Drainage rate and hearth liquid level estimation in absence of direct measurements in blast furnace. Ironmaking & Steelmaking, pp.1-9.

Ainslie, N.G., Morelock, C.R., and Turnbull, D., 1962. In Symposium on Nucleation and Crystallization in Glasses and Melts. The American Ceramic Society, Inc., Columbus, Ohio. pp. 97-107.

Bartels, K.S. and Furman, T., 2002. Effect of sonic and ultrasonic frequencies on the crystallization of basalt. American Mineralogist, 87(2-3), pp.217-226.

Buttinoni, I., Bialké, J., Kümmel, F., Löwen, H., Bechinger, C. and Speck, T., 2013. Dynamical clustering and phase separation in suspensions of self-propelled colloidal particles. Physical review letters, 110(23), p.238301.

Choi, M.W. and Jung, S.M., 2017. Crystallization behavior of melted BOF slag during non-isothermal constant cooling process. Journal of Non-Crystalline Solids, 468, pp.105-112.

Cogswell, D.A., and Carter, W.C., 2011. Thermodynamic phase-field model for microstructure with multiple components and phases: The possibility of metastable phases. Physical Review E, 83, pp.061602-1-061602-13.

Dargaud, O., Cormier, L., Menguy, N. and Patriarche, G., 2012. Multi-scale structuration of glasses: Observations of phase separation and nanoscale heterogeneities in glasses by Z-contrast scanning electron transmission microscopy. Journal of Non-Crystalline Solids, 358(10), pp.1257-1262.

Du, C.M., Gao, X., Ueda, S. and Kitamura, S.Y., 2017. Effects of cooling rate and acid on extracting soluble phosphorus from slag with high P2O5 content by selective leaching. ISIJ International, 57(3), pp.487-496.

Dunbar, N.W., Jacobs, G.K. and Naney, M.T., 1995. Crystallization processes in an artificial magma: variations in crystal shape, growth rate and composition with melt cooling history. Contributions to Mineralogy and Petrology, 120(3-4), pp.412-425.

Einstein, A., 1905. Investigations on the Theory of the Brownian Movement. Ann. der Physik.

Gao, J., Guo, L. and Guo, Z., 2015. Concentrating of iron, slag and apatite phases from high phosphorous iron ore gaseous reduction product at 1473 K by super gravity. ISIJ International, 55(12), pp.2535-2542.

Gao, J., Lu, Y., Wang, F. and Guo, Z., 2017. Effects of super-gravity field on precipitation and growth kinetics of perovskite crystals in CaO–TiO2–SiO2–Al2O3–MgO melt. Ironmaking & Steelmaking, 44(9), pp.692-698.

Gautier, M., Poirier, J., Bodénan, F., Franceschini, G. and Veron, E., 2013. Basic oxygen furnace (BOF) slag cooling: laboratory characteristics and prediction calculations. International Journal of Mineral Processing, 123, pp.94-101.

Gebauer, D., Kellermeier, M., Gale, J.D., Bergström, L. and Cölfen, H., 2014. Pre-nucleation clusters as solute precursors in crystallisation. Chemical Society Reviews, 43(7), pp.2348-2371.

Gránásy, L., Podmaniczky, F., Tóth, G.I., Tegze, G. and Pusztai, T., 2014. Heterogeneous nucleation of/on nanoparticles: a density functional study using the phase-field crystal model. Chemical Society Reviews, 43(7), pp.2159-2173.

Hammer, J.E., 2008. Experimental studies of the kinetics and energetics of magma crystallization. Reviews in mineralogy and geochemistry, 69(1), pp.9-59.

Higgins, M.D., 2000. Measurement of crystal size distributions. American Mineralogist, 85(9), pp.1105-1116.

IEAGHG, 2013. Iron and Steel CCS Study: Techno-Economics Integrated Steel Mill. 2013/04.

Kumari, S., Nunes, A.S., Araújo, N.A. and Telo da Gama, M.M., 2017. Demixing of active particles in the presence of external fields. The Journal of Chemical Physics, 147(17), p.174702.

Li, C., Gao, J.T., Wang, F.Q. and Guo, Z.C., 2018. Enriching Fe-bearing and P-bearing phases from steelmaking slag melt by super gravity. Ironmaking & Steelmaking, 45(1), pp.44-49.

Louis, A.A., Allahyarov, E., Löwen, H. and Roth, R., 2002. Effective forces in colloidal mixtures: From depletion attraction to accumulation repulsion. Physical Review E, 65(6), p.061407.

Lu, Y., Gao, J., Wang, F. and Guo, Z., 2017. Separation of Anosovite from Modified Titanium-Bearing Slag Melt in a Reducing Atmosphere by Supergravity. Metallurgical and Materials Transactions B, 48(2), pp.749-753.

Luo, S.N., Ahrens, T.J., Çağın, T., Strachan, A., Goddard III, W.A. and Swift, D.C., 2003. Maximum superheating and undercooling: Systematics, molecular dynamics simulations, and dynamic experiments. Physical Review B, 68(13), p.134206.

McCandlish, S.R., Baskaran, A. and Hagan, M.F., 2012. Spontaneous segregation of self-propelled particles with different motilities. Soft Matter, 8(8), pp.2527-2534.

Mokshin, A.V., Galimzyanov, B.N. and Barrat, J.L., 2013. Extension of classical nucleation theory for uniformly sheared systems. Physical Review E, 87(6), p.062307.

Nunes, A.S., Gupta, A., Araújo, N.A. and da Gama, M.M.T., 2018. Field-driven dynamical demixing of binary mixtures. arXiv preprint arXiv:1801.10205.

Perepezko, J.H. and Wilde, G., 2016. Melt undercooling and nucleation kinetics. Current Opinion in Solid State and Materials Science, 20(1), pp.3-12.

Radu, M. and Kremer, K., 2017. Enhanced crystal growth in binary Lennard-Jones mixtures. Physical review letters, 118(5), p.055702.

Reddy, R.J., Chaubal, P., Pistorius, P.C., and Pal, U., 2016. Proceedings of the 10th International Conference on Molten Slags, Fluxes and Salts. Seattle, USA.

Rivas, N., Cordero, P., Risso, D. and Soto, R., 2011. Segregation in quasi-two-dimensional granular systems. New journal of physics, 13(5), p.055018.

Roche, M., Helle, M., van der Stel, J., Louwerse, G., Shao, L. and Saxén, H., 2018a. Off-line Model of Blast Furnace Liquid Levels. ISIJ International, pp.ISIJINT-2018.

Roche, M., Helle, M., van der Stel, J., Louwerse, G., Shao, L. and Saxén, H., 2018b. On-Line Estimation of Liquid Levels in the Blast Furnace Hearth. Steel Research International, p.1800240.

Roscoe, R., 1952. The viscosity of suspensions of rigid spheres. British Journal of Applied Physics, 3(8), p.267.

Royet, J.P., 1991. Stereology: a method for analyzing images. Progress in neurobiology, 37(5), pp.433-474.

Sahagian, D.L. and Proussevitch, A.A., 1998. 3D particle size distributions from 2D observations: stereology for natural applications. Journal of Volcanology and Geothermal Research, 84(3-4), pp.173-196.

Scholz, C., Engel, M. and Pöschel, T., 2018. Rotating robots move collectively and self-organize. Nature communications, 9(1), p.931.

Shen, Z., Hua, X., Liang, Q., Xu, J., Han, D. and Liu, H., 2017a. Reaction, crystallization and element migration in coal slag melt during isothermal molten process. Fuel, 191, pp.221-229.

Shen, Z., Liang, Q., Xu, J., Dai, Z. and Liu, H., 2017b. Study on the two-dimensional micro-scale crystal growth of a coal slag. Fuel, 205, pp.24-33.

Stenhammar, J., Wittkowski, R., Marenduzzo, D. and Cates, M.E., 2015. Activity-induced phase separation and self-assembly in mixtures of active and passive particles. Physical review letters, 114(1), p.018301.

StJohn, D.H., Prasad, A., Easton, M.A. and Qian, M., 2015. The contribution of constitutional supercooling to nucleation and grain formation. Metallurgical and Materials Transactions A, 46(11), pp.4868-4885.

Tanaka, H. and Brenner, M.P., 2017. Hot particles attract in a cold bath. Physical Review Fluids, 2(4), p.043103.

Tanaka, H., Kawasaki, T., Shintani, H. and Watanabe, K., 2010. Critical-like behaviour of glass-forming liquids. Nature materials, 9(4), p.324.

Upadhyay, H. and Kundu, T.K., 2013. Drain rate and liquid level simulation in blast furnace hearth using plant Data. ISRN Metallurgy, 2013.

Wagstaff, F.E., 1969. Crystallization and melting kinetics of cristobalite. Journal of the American Ceramic Society, 52(12), pp.650-654.

Wang, D., Jiang, M., Liu, C., Min, Y., Cui, Y., Liu, J. and Zhang, Y., 2012. Enrichment of Fe‐Containing Phases and Recovery of Iron and Its Oxides by Magnetic Separation from BOF Slags. steel research international, 83(2), pp.189-196.

Wang, Z., Gao, J., Meng, L., Shi, A. and Guo, Z., 2018. Recovery of Zinc from Zn–Al–Fe Melt by Super-gravity Separation. ISIJ International, 58(6), pp.1175-1177.

Wu, L., Ek, M., Song, M. and Sichen, D., 2011. The effect of solid particles on liquid viscosity. steel research international, 82(4), pp.388-397.

Zhang, P., Maldonis, J.J., Liu, Z., Schroers, J. and Voyles, P.M., 2018. Spatially heterogeneous dynamics in a metallic glass forming liquid imaged by electron correlation microscopy. Nature communications, 9(1), p.1129.

Chapter 5: Comminution

In the processes proposed in this dissertation, the method of CO_2 emissions reduction is two-fold: 1) recovery of flux and low oxidation state iron (i.e., Fe^0 or FeO) for recycling to the furnace and 2) mineralization of CO_2 using the (Ca/Mg)-bearing compounds of slag. The CO_2 emissions reduction from the former is well understood and is simply a matter of quantifying the amount recovered material. The latter mechanism requires calculation of the rate of CO_2 mineralization, which is fundamentally linked to the reactive surface area (SA). Carbon dioxide mineralization using calcium- and magnesium-containing solids (e.g., slag, natural rocks) is a kinetically slow process. To expedite the reaction, increasing the SA is a common and mature technique. However, from the perspective of industrial-scale CO_2 mineralization, it is critical to consider the rate of CO_2 mineralization, the net CO_2 mineralization extent (i.e., over the full process chain and life cycle), and the cost per unit CO_2 reduction. A highly efficient process that operates at the timescale of millennia and a rapidly operating process with a low net CO_2 mineralization extent are both of little value. Likewise, a process that makes an emitter economically uncompetitive will not be adopted. As such, the mineral-specific comminution energy was calculated and applied to grinding extents commonly reported in the CO_2 mineralization literature. Additionally, a novel comminution process (solid-state quenching) was developed to reduce grinding energy and increase the liberation efficiency of the MYNA process.

Chapter highlights

- Comminution is an integral part of all CO_2 mineralization schemes as it increases the reactive surface area, decreases the diffusion depth, and promotes separation of distinct materials.
- Comminution energy is poorly quantified in the literature.
- The mineral-specific surface energy and critical fracture stress for most minerals found in iron and steelmaking slags was calculated based on the crystal structure.
- Aluminates, aluminosilicates, and oxides have higher surface energies and critical fracture stresses than silicates.
- Larger grain sizes have lower fracture stresses because the grain faces act as fracture nucleation sites, with the critical stress scaling inversely with the scale of nucleation site.
- The total energy of grinding was calculated based on the mineral-specific surface energy and the full particle size distribution as determined by the Kolmogorov approximation.
- Grinding of materials can release more CO_2 (through emissions from energy production) than are mineralized by the material.
- Solid, high temperature slag can be fractured by quenching in water, generating thermal stresses which are amplified at boundaries between disparate minerals.
- Solid-state quenching of slag is stress-limited, not energy-limited.
- Quenching of slag induces spalling fractures which reduce heat transfer deeper into the slag, thereby concentrating heat loss and thermal stress at the surface of slag.
- Larger mineral grains reduce the negative feedback of spalling fractures due to fewer fractures and a lower critical stress intensity.
- Up to 40% of minerals can be fractured and liberated from a slag plate by thermal quenching. Higher levels of liberation become increasing difficult to realize due to the requirement for stress conservation in slag.

Publications relevant to this chapter

- Quantification of the CO_2 mineralization potential of ironmaking and steelmaking slags under direct gas-solid reactions in flue gas, International Journal of Greenhouse Gas Control Vol. 87C p.100-111 (2019), **Corey A. Myers**, Takao Nakagaki, and Kosei Akutsu.
- Application of quenching to polycrystalline metallurgical slags to reduce comminution energy and increase mineral liberation, In Proceedings of the 16th International Heat Transfer Conference Beijing China, IHTC Digital Library, p. IHTC-22437 (2018), **Corey A. Myers** and Takao Nakagaki.
- Enhanced recovery process of calcium oxide and metals from steelmaking slag with net carbon sequestration, Energy Procedia Vol. 114 p.6246-6255 (2017), **Corey Myers**, Takao Nakagaki, and Takuya Mitamura.

5.1. Surface energy and critical stress

Prior to reaction with CO_2, solid phase ISM slag minerals will undergo some degree of size reduction (comminution). In the literature on slag-based and rock-based CO_2 mineralization, there is surprisingly little information on the specific grinding energy for the plethora of minerals present. The majority of information available is simply empirical correlations from grinding of compositionally complex slags and rocks (e.g., the Bond Mill Work Index). Such unsophisticated correlations are well-known to be inaccurate and are inherently incapable of providing information on mineral-specific grinding energy. To alleviate this data insufficiency, the mineral-specific grinding energy for the 38 major compounds found in ISM slag was calculated. Using the Born model of bonding and a mixture of structural data from experiments, quantum mechanics (QM) simulations, and thermodynamics, the mineral-specific surface energy (γ_S) and critical tensile stress for crack propagation (K_{IC}) in Mode 1 fracture was calculated [Tromans and Meech, 2002; Tromans and Meech, 2004]. The Born model posits that the energy of a crystalline structure emerges from the electrostatic interaction between functional anions and cations with an additional repulsive interaction at shorter length scales. The internal energy per molecule (U_m) can then be approximated as **Eq. (5-1)**,

$$U_m = \frac{N n_{Va}^2 M}{a_n} \left(\frac{e^2}{4\pi\varepsilon_0} \right) \left(\frac{R_0^{n-1}}{nR^n} - \frac{1}{R} \right) \qquad (5-1)$$

where N is the number of atoms per cubic meter, n_{va} is the largest common valence number between the ions, M is the Madelung constant, a_n is the stoichiometric number of atoms per molecule, e is the elementary charge (1.602177×10^{-19} C), ε_0 is the vacuum permittivity (8.854188×10^{-12} C/Vm), R_0 is the equilibrium interatomic distance of an unstrained crystal, L is the stretched length, and n is a mineral specific constant necessarily >1 that is conceptually related to the compressibility. The number of atoms per cubic meter is calculated per **Eq. (5-2)**,

$$N = a_n \left(\frac{N_A}{M_V} \right) \qquad (5-2)$$

where N_A is Avogadro's constant and M_V is the molar volume obtained by dividing the molecular weight by the crystal density. When the crystal is unstrained the energy per molecule reaches its minimum energy (U_C) given by **Eq. (5-3)**,

$$U_C = \frac{N n_{Va} M}{R_0 a_n} \left(\frac{e^2}{4\pi\varepsilon_0} \right) \left(\frac{1}{n} - 1 \right) \qquad (5-3)$$

where $R_0 = N^{-1/3}$. Likewise, the U_C is equal to the molar enthalpy of the crystal generated from gaseous ions divided by the molar volume ($= \Delta H_f / M_V$). The constant n from is calculated by **Eq. (5-4)**. In **Eq. (5-4)**, E is the isotropic tensile elastic modulus and ν is Poisson's ratio. The isotopic tensile elastic modulus is obtained from **Eq. (5-5)**, where G is the shear modulus, and K is the bulk modulus, both obtained from QM [Jain and Ong, 2013]. The ν is obtained via **Eq. (5-6)**.

$$n = 1 + \left(\frac{3E a_n R_0^4}{[1 - 2v]n_{Va}M}\right)\left(\frac{4\pi\varepsilon_0}{e^2}\right) \tag{5-4}$$

$$E = \frac{([2G\{1 + v\}] + [3K\{1 - 2v\}])}{2} \tag{5-5}$$

$$v = \left(\frac{3K + 2G}{2G + 6K}\right) \tag{5-6}$$

All values in **Eq. (5-1)** through **Eq. (5-6)** are in terms of constants available from the literature, M, and n. Thus, by iteratively solving **Eq. (5-3)** and **Eq. (5-4)**, the values of M and n are obtained and the strained crystal energy is determined. The crystal energy as a function of strain in the bonds is displayed graphically in **Fig. 5-1**.
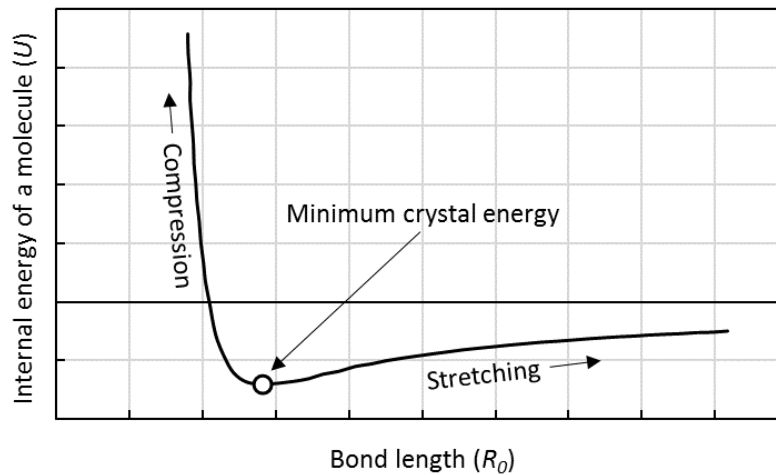
Fig. 5-1. The effect of the average bond length on the specific internal energy of the crystal.

With the stretch-related crystal energy calculatable, the tensile stress (σ_x) can be determined by the straightforward application of **Eq. (5-7)**. By integrating **Eq. (5-7)** from the unstrained state (R_0) to the fracture distance (R_{limit}), the minimum total energy of brittle fracture (i.e., no plastic deformation) can be obtained according to **Eq. (5-8)**.

$$\sigma_x = \left(\frac{1 - 2v}{3}\right)\left(\frac{N^{1/3}n_{Va}^2 M}{a_n}\right)\left(\frac{e^2}{4\pi\varepsilon_0}\right)\left(\frac{1}{R_x^2} - \frac{R_0^{n-1}}{R_x^{n-1}}\right) \tag{5-7}$$

$$G_C = \int_{R_x=R_0}^{R_x=R_{limit}} \sigma_x \partial R_x \tag{5-8}$$

The magnitude of stretching required to induce fracture (R_{limit}) is equal to the inherent separation distance plus 2 nanometers ($R_{limit} = R_0 + (2 \times 10^{-9}$ m)); this value is obtained from

plotting σ_x against R_x to the point of $\sigma_x = 0$. Input of **Eq. (5-7)** into **Eq. (5-8)** and integration yields the critical crack energy release (G_C) per **Eq. (5-9)**.

$$G_C = \left[\left(\frac{1-2v}{3}\right)\left(\frac{N^{2/3}n_{Va}M}{a_n}\right)\left(\frac{e^2}{4\pi\varepsilon_0}\right)\left(\frac{R_0^{\,n-1}}{nR_x^n} - \frac{1}{R_x}\right)\right]_{R_x=R_0}^{R_x=R_{limit}} \tag{5-9}$$

Equation (5-9) represents half of the mineral-specific surface energy (γ_S). The G_C and γ_S represent average values of bond breakage over a randomly oriented polycrystalline structure. In other words, the anisotropy innate in the fracture planes of many crystals is aggregated and averaged by the isotropic treatment of the crystal volume. Given that comminution of slag for CO_2 mineralization inherently occurs at the macroscale with randomly oriented slag particles and randomly oriented internal grain structures, this assumption is not only appropriate, it is necessary. Nevertheless, the degree of crystallinity and the quantity of grain boundaries in ISM slag varies between solidification methods. The grinding energy of intragranular fracture (intragranular: IG), fracture at grain boundaries of the same material (grain boundary: GB), fractures at grain boundaries between disparate minerals (inter-mineral: IM), and fractures through an amorphous phase (intra-amorphous: IA) are of innately different energies due to the different degrees of bonding extent and bond length (**Fig. 5-2**).

Extended bond lengths and incomplete bonding weaken grain boundaries
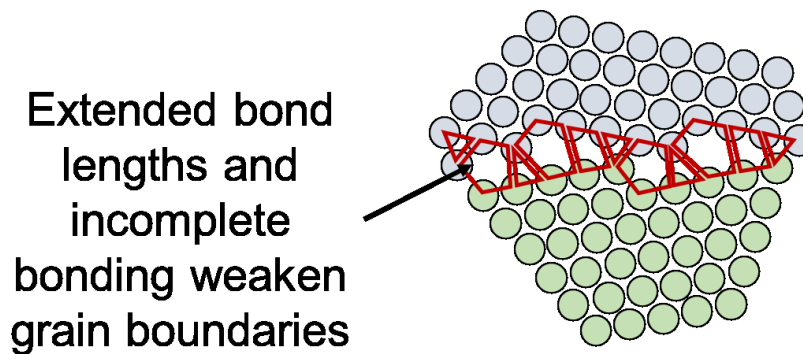
Fig. 5-2. The bond lengths at grain boundaries are inherently more stretched than those within a single crystal structure.

The intragranular surface energy (γ_{IG}) is equivalent to the ideal case described above and is given by **Eq. (5-10)**.

$$\gamma_{IG} = \frac{1}{2}\left[\left(\frac{1-2v}{3}\right)\left(\frac{N^{2/3}n_{Va}M}{a_n}\right)\left(\frac{e^2}{4\pi\varepsilon_0}\right)\left(\frac{R_0^{\,n-1}}{nR_x^n} - \frac{1}{R_x}\right)\right]_{R_x=R_0}^{R_x=R_{limit}} \tag{5-10}$$

From geometric studies it is seen that in single mineral polycrystalline materials there are a subset of potential binding sites (f) whose innate 'bond' length is $\sim 1.5R_0$ [Bragg and Nye, 1947]. The remaining sites ($1-f$) show an R_x equivalent to R_0 (i.e., no inherent strain). By applying a multiplying factor to the innate atomic distance ($m = 1.5$) of the stretched sites in polycrystalline

compounds and calculating the surface energy for unstrained and strained portions separately, the surface energy in grain boundary fracture (γ_{GB}) is given by **Eq. (5-11)**.

$$\gamma_{GB} = \frac{1}{2}\left[\left(\frac{1-2v}{3}\right)\left(\frac{N^{2/3}n_{Va}M}{a_n}\right)\left(\frac{e^2}{4\pi\varepsilon_0}\right)\right]$$
$$\times\left\{\left[f\left(\frac{R_0^{n-1}}{nR_x^n} - \frac{1}{R_x}\right)\right]_{R_x=R_0}^{R_x=R_{limit}} + \left[(1-f)\left(\frac{R_0^{n-1}}{nR_x^n} - \frac{1}{R_x}\right)\right]_{R_x=mR_0}^{R_x=R_{limit}}\right\} \qquad (5-11)$$

Tromans and Meech recommend using $f = 0.5$ in **Eq. (5-11)** based on results of geometric studies and the overwhelming number of potential grain boundary arrangements. The calculation of fracture energy through and amorphous phase is achieved by altering the correction factors f to 0 and m to 1.5. Concretely, this means all bonds are stretched relative to the crystalline structure, and the atomic distance is on average 1.5 times that of the crystalline state. This yields **Eq. (5-12)** for surface energy of amorphous fracture (γ_{IA}).

$$\gamma_{IA} = \frac{1}{2}\left[\left(\frac{1-2v}{3}\right)\left(\frac{N^{2/3}n_{Va}M}{a_n}\right)\left(\frac{e^2}{4\pi\varepsilon_0}\right)\left(\frac{R_0^{n-1}}{nR_x^n} - \frac{1}{R_x}\right)\right]_{R_x=1.5R_0}^{R_x=R_{limit}} \qquad (5-12)$$

Calculation of fracture energy between disparate minerals is accomplished by alteration of f and m; however, Tromans and Meech provide only qualitative guidance on how to decide these values. Disparate phases are generated by the competitive interaction between growing mineral phases during solidification. Grain boundaries between disparate minerals can neither be classified as crystalline or amorphous as the process of generation is distinct. For mono-mineral grain boundaries, the misalignment from random orientation, and the constrictive nature of solidification results in ~50% of the bonds being stretched to ~1.5 times their R_0. In amorphous structures, the bond lengths are varied (with some portion likely $\leq R_0$); but, taken in aggregate, it is equivalent to all bonds being stretched by the same $1.5R_0$. Given that the average bond length in amorphous structures is longer than in crystalline structures, the inter-mineral correction factors were set to $f = 0.25$ and $m = 1.5$, yielding **Eq. (5-13)**.

$$\gamma_{IM} = \frac{1}{2}\left[\left(\frac{1-2v}{3}\right)\left(\frac{N^{2/3}n_{Va}M}{a_n}\right)\left(\frac{e^2}{4\pi\varepsilon_0}\right)\right]$$
$$\times\left\{\left[0.25\left(\frac{R_0^{n-1}}{nR_x^n} - \frac{1}{R_x}\right)\right]_{R_x=R_0}^{R_x=R_{limit}} + \left[0.75\left(\frac{R_0^{n-1}}{nR_x^n} - \frac{1}{R_x}\right)\right]_{R_x=1.5R_0}^{R_x=R_{limit}}\right\} \qquad (5-13)$$

Comparing these estimates with empirical results indicates the efficiency of grinding equipment (e.g., due to losses to heat, sound, and structural distortion) is consistently ~1%. The extremely low efficiency of grinding is due to the large number of impacts that cause no fractures, instead generating sound, heat, and structural strain [Morrison and Cleary, 2008; Cleary and Morrison, 2016].

Only in the case of amorphous slags does the method of Tromans and Meech require significant adjustment. This adjustment is necessary because amorphous structures inherently contain some amount of ductility and will display plastic deformation to a larger degree than crystalline structures. Evaluating the results of Wang et. al. (2015) with Tromans and Meech shows γ_{IA} is $\sim 1.63\gamma_{IG}$, $\sim 1.78\gamma_{GB}$, and $\sim 1.96\gamma_{IM}$. This result is consistent across silica, sodium silicate, and calcium aluminosilicate glasses (i.e., the entire structural landscape of silicate glasses). Similar empirical results were found in the fracture testing of truly amorphous and polycrystalline slag; amorphous slag required ~1.82 times more energy than the polycrystalline slag, which is ostensibly a mixture of intragranular, grain boundary, and intra-mineral fractures [Purwanto et al., 2004].

From the fracture energy of each fracture type (i.e., $G_X = 2\gamma_X$; where X is a stand-in for IG, GB, IM, or IA) the stress intensity factor for Mode 1 fracture propagation (K_x) can be determined per **Eq. (5-14)**,

$$K_X = \frac{\sqrt{EG_X}}{\sqrt{1-\nu^2}}$$

$$(5-14)$$

which is related to the critical tensile stress for crack propagation (σ_C), the inherent flaw size (w), and the shape factor (Y) by **Eq. (5-15)**.

$$\sigma_{C,X} = \frac{K_X}{Y\sqrt{w}}$$

$$(5-15)$$

The Y is equal to $\sqrt{\pi}$ for straight through internal fractures with length $2a$, and $2/\sqrt{\pi}$ for internal disk-shaped fractures of radius a. Given the preponderance of fractures occur at grain boundaries and triple-point boundaries, the internal disk-shaped fracture is assumed to be the dominant fracture type. The values used in calculations of surface energy and critical tensile stress are provided in **Table 5-1** (ΔH_f, MW, ρ, E, ν, K, G,) and **Table 5-2** (R_0, M, and n).

Table 5-1. The values used in calculation of mineral-specific fracture properties.

Mineral	ΔH_f (kJ/mol)	MW (g/mol)	ρ (kg/m³)	E (GPa)	ν	K (GPa)	G (GPa)
Al_2O_3	-1675.190	101.964	3985	348.587	0.210	214.835	133.620
Al_2SiO_5	-2590.314	162.044	3247	220.588	0.239	141.000	89.000
$Al_6Si_2O_{13}$	-6819.209	426.049	3168	227.576	0.280	172.400	88.900
Ca_2SiO_4 (β)	-2306.045	172.237	3280	189.638	0.223	114.070	77.535
Ca_2SiO_4 (γ)	-2304.800	172.237	2970	160.842	0.226	97.914	65.584
$Ca_{12}Al_{14}O_{33}$	-19429.998	1386.651	2610	146.540	0.228	89.665	59.685
$Ca_2Al_2SiO_7$	-3978.980	274.198	2850	169.814	0.231	105.275	68.965
$Ca_2Fe_2O_5$	-2133.756	271.841	4040	128.653	0.294	103.933	49.723
$Ca_2MgSi_2O_7$	-3877.192	272.624	2953	176.457	0.231	109.320	71.673
$Ca_3Al_2O_6$	-3587.801	270.192	2965	149.398	0.235	94.105	60.465
$Ca_3Al_2Si_3O_{12}$	-6632.862	450.441	3570	295.043	0.009	100.130	146.220
$Ca_3MgSi_2O_8$	-4564.326	328.701	3145	183.664	0.227	112.045	74.855
$Ca_3Si_2O_7$	-3956.310	288.397	2895	166.598	0.223	100.275	68.105
Ca_3SiO_5	-2929.202	228.314	3012	156.097	0.227	95.226	63.620
$Ca_4Al_2Fe_2O_{10}$	-5096.112	485.956	3610	162.353	0.255	110.640	64.660
$Ca_7MgSi_4O_{16}$	-2306.045	673.175	3096	171.314	0.225	103.789	69.930
$CaAl_2Si_2O_8$	-4242.999	278.204	2730	183.905	0.235	115.775	74.440
$CaCO_3$ (A)	-1207.126	84.087	2930	50.400	0.370	66.000	18.000
$CaCO_3$ (C)	-1206.900	84.087	2710	85.240	0.310	76.000	32.000
$CaCO_3$ (V)	-1202.482	84.087	2540	85.240	0.310	76.000	32.000
$CaFeSiO_4$	-1938.760	188.004	3560	166.313	0.274	122.460	65.290
$CaMgSiO_4$	-2250.030	156.464	3200	179.450	0.231	111.170	72.890
CaO	-635.089	56.077	3350	196.960	0.215	105.000	74.000
$CaSiO_3$	-1634.940	116.16	2804	170.928	0.225	103.570	69.770
$CaSiO_3$ (P)	-1621.660	116.16	2905	173.081	0.225	104.918	70.642
Fe_2SiO_4	-1480.200	203.771	4480	178.835	0.305	152.640	68.533
Fe_3O_4	-1115.500	231.531	5170	170.240	0.340	176.000	64.000
FeO	-272.040	71.844	5745	112.692	0.364	137.800	41.400
Mg_2SiO_4	-2176.935	140.691	3270	184.580	0.240	119.000	74.000
$Mg_3Al_2Si_3O_{12}$	-6280.188	403.122	3740	263.909	0.245	172.310	106.010
$MgSiO_3$	-1548.498	200.774	3190	184.580	0.240	119.000	74.000

MgAl$_2$O$_4$	-2299.108	142.265	3600	273.830	0.266	-	-
MgCO$_3$	-1111.396	68.314	3010	115.633	0.299	96.000	44.500
MgFe$_2$O$_4$	-1434.495	199.991	3603	104.529	0.333	104.213	39.213
MgO	-601.241	40.304	3560	307.180	0.179	119.000	151.000
SiO$_2$ (C)	-906.903	60.083	2334	65.181	-0.166	16.300	39.100
SiO$_2$ (T)	-907.533	60.083	2265	58.091	0.009	19.700	28.800
SiO$_2$ (α)	-910.957	60.083	2649	190.594	0.247	125.383	76.443

Table 5-2. The calculated values used to determine the mineral-specific fracture properties.

Mineral	R_0 (m)	M	n
Al$_2$O$_3$	2.041×10^{-10}	6.888	2.968
Al$_2$SiO$_5$	2.180×10^{-10}	5.259	3.364
Al$_6$Si$_2$O$_{13}$	2.199×10^{-10}	4.633	4.399
Ca$_2$SiO$_4$ (β)	2.318×10^{-10}	2.116	7.083
Ca$_2$SiO$_4$ (γ)	2.396×10^{-10}	2.206	6.713
Ca$_{12}$Al$_{14}$O$_{33}$	2.464×10^{-10}	7.019	2.838
Ca$_2$Al$_2$SiO$_7$	2.370×10^{-10}	4.414	3.939
Ca$_2$Fe$_2$O$_5$	2.316×10^{-10}	6.376	2.826
Ca$_2$MgSi$_2$O$_7$	2.338×10^{-10}	2.496	6.111
Ca$_3$Al$_2$O$_6$	2.396×10^{-10}	6.193	2.956
Ca$_3$Al$_2$Si$_3$O$_{12}$	2.188×10^{-10}	2.895	4.090
Ca$_3$MgSi$_2$O$_8$	2.314×10^{-10}	2.181	6.758
Ca$_3$Si$_2$O$_7$	2.398×10^{-10}	3.102	5.172
Ca$_3$SiO$_5$	2.409×10^{-10}	3.436	4.640
Ca$_4$Al$_2$Fe$_2$O$_{10}$	2.316×10^{-10}	6.242	2.991
Ca$_7$MgSi$_4$O$_{16}$	2.345×10^{-10}	1.640	8.448
CaAl$_2$Si$_2$O$_8$	2.352×10^{-10}	3.222	5.297
CaCO$_3$ (A)	2.120×10^{-10}	2.205	3.315
CaCO$_3$ (C)	2.176×10^{-10}	2.083	4.145
CaCO$_3$ (V)	2.224×10^{-10}	2.084	4.425
CaFeSiO$_4$	2.323×10^{-10}	2.242	7.184
CaMgSiO$_4$	2.264×10^{-10}	2.223	6.113
CaO	2.404×10^{-10}	3.833	4.911

CaSiO$_3$	2.396×10^{-10}	2.903	5.594
CaSiO$_3$ (P)	2.368×10^{-10}	2.876	5.480
Fe$_2$SiO$_4$	2.210×10^{-10}	2.220	7.382
Fe$_3$O$_4$	2.198×10^{-10}	3.673	5.392
FeO	2.182×10^{-10}	4.215	3.896
Mg$_2$SiO$_4$	2.169×10^{-10}	2.272	5.503
Mg$_3$Al$_2$Si$_3$O$_{12}$	2.076×10^{-10}	2.588	5.821
MgSiO$_3$	2.186×10^{-10}	1.772	6.963
MgAl$_2$O$_4$	2.109×10^{-10}	5.872	3.564
MgCO$_3$	1.961×10^{-10}	2.087	3.655
MgFe$_2$O$_4$	2.361×10^{-10}	7.909	2.600
MgO	2.110×10^{-10}	3.916	4.156
SiO$_2$ (C)	2.424×10^{-10}	14.701	1.150
SiO$_2$ (T)	2.449×10^{-10}	6.419	1.431
SiO$_2$ (α)	2.324×10^{-10}	2.107	7.785

5.1.1. Results

The results of the calculation of intragranular, grain boundary, inter-mineral, and intra-amorphous surface energy, critical stress factor, and critical stress intensity are provided graphically in **Fig. 5.3-5.5**. The values are listed in **Table 5-3**. The results show a clear increase in γ_S for aluminum-bearing minerals. Minerals with small ionic radii (e.g., MgO and SiO$_2$) are also prone to higher surface energies due to the inherently shorter bond lengths and geometrically simple structure leading to relatively tighter packing. Of relevance to grinding operations, carbonates are consistently of lower surface energy than their source minerals in ISM. Thus, delaying grinding until after a degree of CO$_2$ mineralization has occurred may provide meaningful reductions in energy consumption. There is a consistent behavior between the fracture types; concretely, $\gamma_{GB} \approx (0.892 \pm 0.021)\gamma_{IG}$ and $\gamma_{IM} \approx (0.878 \pm 0.026)\gamma_{GB}$.
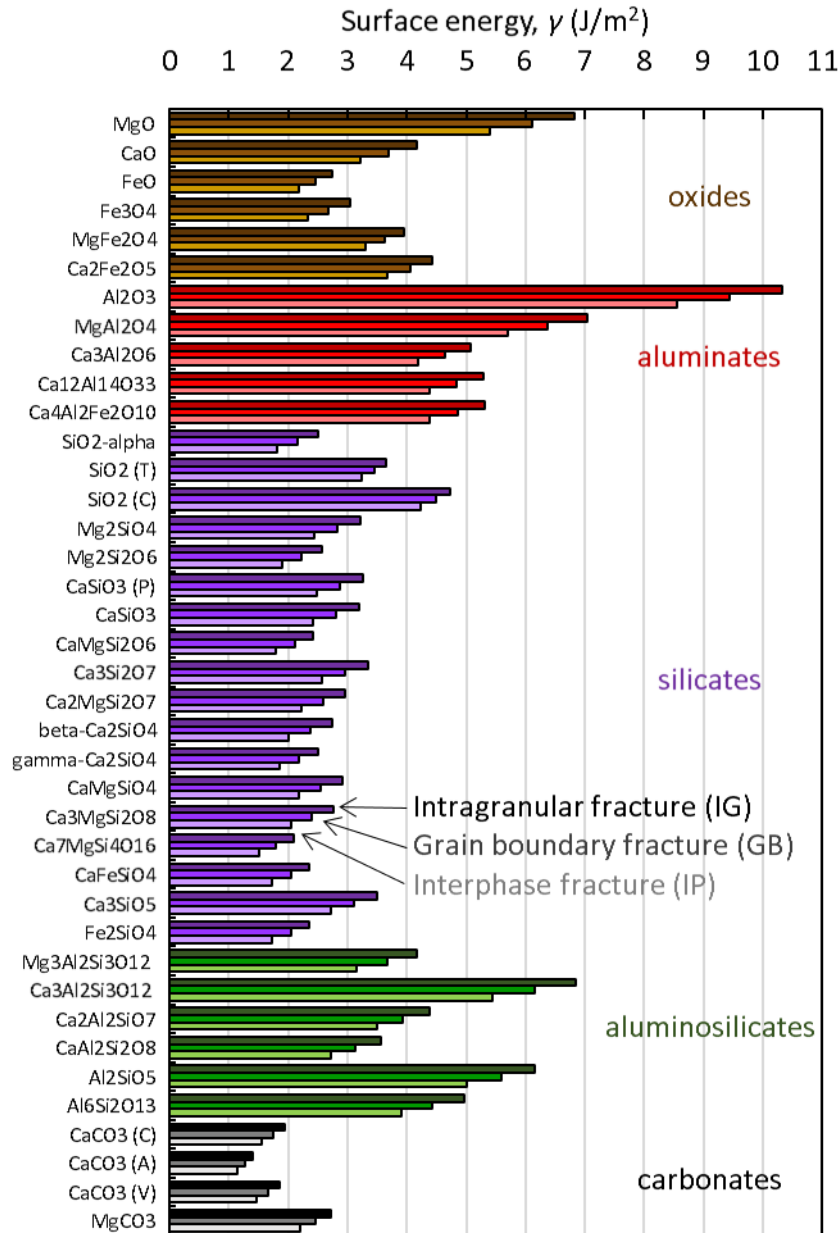
Fig. 5-3. Surface energy for 38 minerals common to slag under three different fracturing mechanisms.
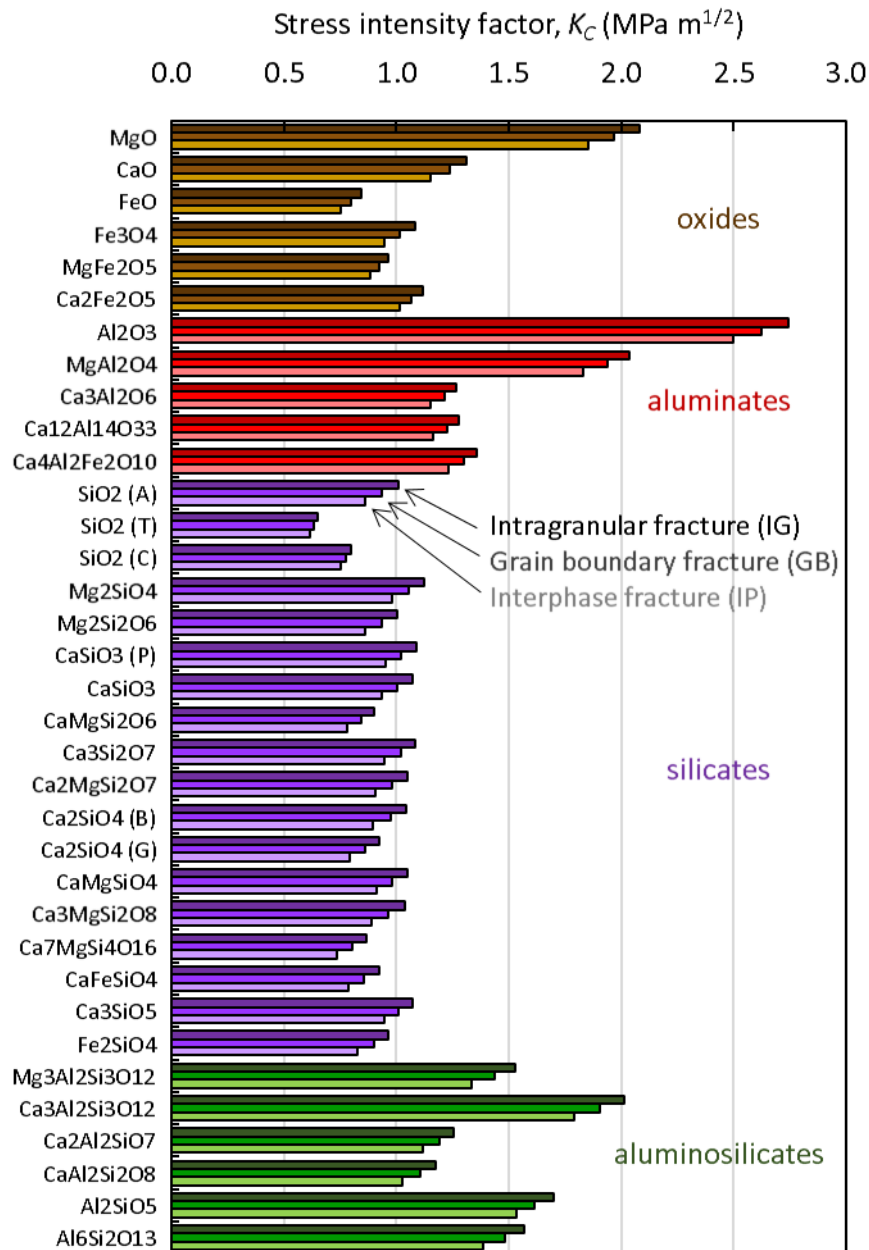
Fig. 5-4. Mode 1stress intensity factor for 38 minerals common to slag under three different fracturing mechanisms.
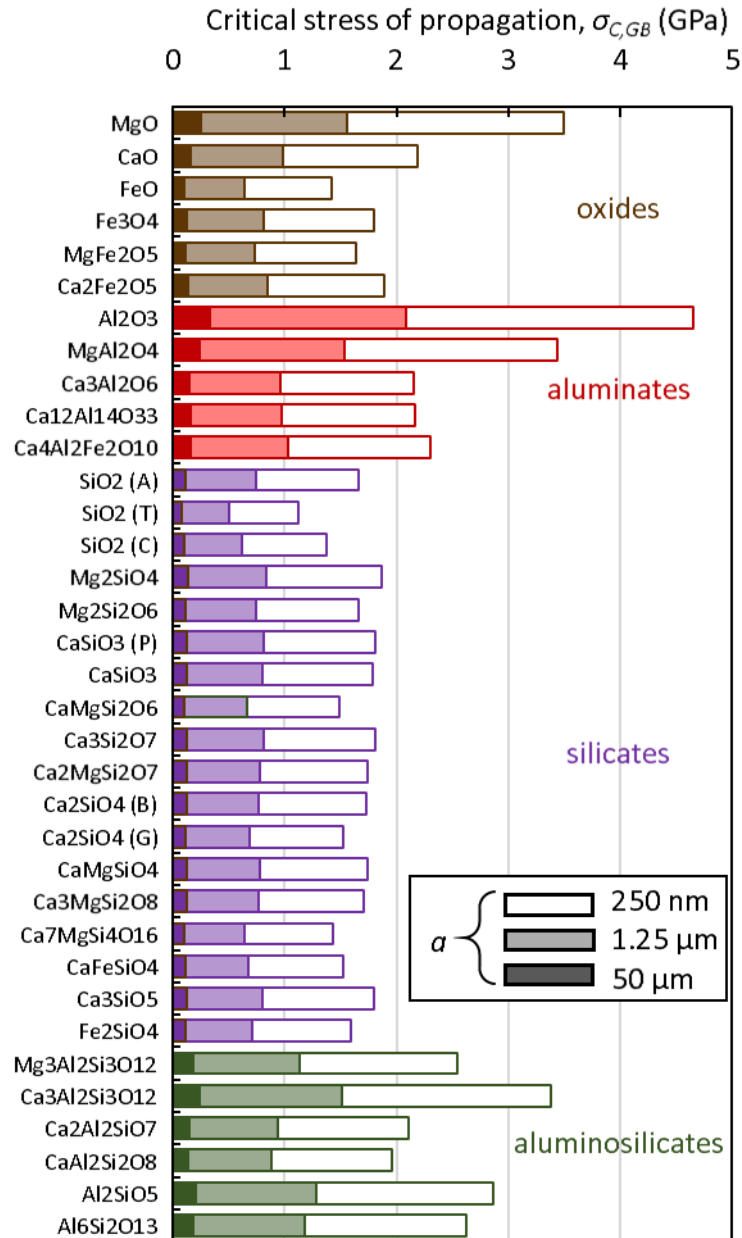
Fig. 5-5. Critical stress intensity of crack propagation for a grain boundary fracture under different inherent flaw sizes.

Table 5-3. The mineral- and fracture-dependent surface energy.

Mineral	γ_{IG} (J/m^2)	γ_{GB} (J/m^2)	γ_{IM} (J/m^2)
MgO	6.820	6.115	5.410
CaO	4.172	3.695	3.218
FeO	2.738	2.463	2.188
Fe$_3$O$_4$	3.044	2.685	2.326
MgFe$_2$O$_5$	3.945	3.626	3.306
Ca$_2$Fe$_2$O$_5$	4.424	4.050	3.675
Al$_2$O$_3$	10.317	9.436	8.554
MgAl$_2$O$_4$	7.035	6.365	5.695
Ca$_3$Al$_2$O$_6$	5.085	4.641	4.196
Ca$_{12}$Al$_{14}$O$_{33}$	5.296	4.841	4.387
Ca$_4$Al$_2$Fe$_2$O$_{10}$	5.315	4.850	4.385
α-SiO$_2$ (α)	2.510	2.166	1.822
SiO$_2$ (T)	3.659	3.446	3.234
SiO$_2$ (C)	4.731	4.486	4.242
Mg$_2$SiO$_4$	3.207	2.826	2.445
MgSiO$_3$	2.569	2.233	1.897
CaSiO$_3$ (P)	3.259	2.868	2.477
CaSiO$_3$	3.187	2.801	2.415
Ca$_3$Si$_2$O$_7$	3.353	2.960	2.568
Ca$_2$MgSi$_2$O$_7$	2.958	2.588	2.217
Ca$_2$SiO$_4$ (β)	2.732	2.370	2.008
Ca$_2$SiO$_4$ (γ)	2.512	2.185	1.857
CaMgSiO$_4$	2.913	2.550	2.186
Ca$_3$MgSi$_2$O$_8$	2.766	2.406	2.046
Ca$_7$MgSi$_4$O$_{16}$	2.091	1.796	1.502
CaFeSiO$_4$	2.357	2.043	1.729
CaMgSi$_2$O$_6$	2.415	2.108	1.801
Ca$_3$SiO$_5$	3.495	3.106	2.717
Fe$_2$SiO$_4$	2.364	2.048	1.732
Mg$_3$Al$_2$Si$_3$O$_{12}$	4.168	3.664	3.159
Ca$_3$Al$_2$Si$_3$O$_{12}$	6.856	6.150	5.443
Ca$_2$Al$_2$SiO$_7$	4.388	3.940	3.491
CaAl$_2$Si$_2$O$_8$	3.558	3.138	2.718
Al$_2$SiO$_5$	6.155	5.585	5.014
Al$_6$Si$_2$O$_{13}$	4.965	4.434	3.902
CaCO$_3$ (C)	1.951	1.748	1.546
CaCO$_3$ (A)	1.394	1.266	1.138
CaCO$_3$ (V)	1.867	1.666	1.465
MgCO$_3$	2.723	2.463	2.202

α: alpha quartz; T: Tridymite; C: Cristobalite for SiO$_2$, Calcite for CaCO$_3$; P: Pseudowollastonite; β: beta dicalcium silicate; γ: gamma dicalcium silicate; A: Aragonite; V: Vaterite

5.2. Comminution energy

The total energy of grinding a mineral is dependent on the crystal structure of the material and the fracture type. Fracture type has a relatively minor but consistent effect on grinding energy with $\gamma_{GB} \approx 0.89\gamma_{IG}$ and $\gamma_{IM} \approx 0.88\gamma_{GB}$. However, these numbers represent the ideal differences; in actual slag, the grain boundaries will be randomly oriented relative to the applied tensile stress. As such, GB and IM fractures will require additional energy expenditure per distance traveled along the line of application of tensile stress (**Fig. 5-6**) [Mousavi et al., 2015].
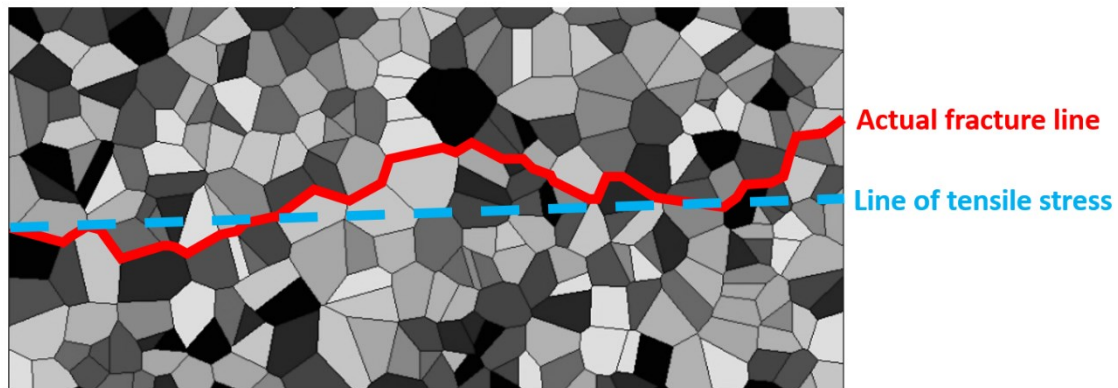
Fig. 5-6. Deviations from straight-line fracture that accompany fracturing along grain boundaries in polycrystalline materials.

Given these competing effects, naïve usage of γ_{IG} is permissible. The grinding energy (E_G) required to generate a given PSD can be calculated via **Eq. (5-16)**. In **Eq. (5-16)**, the term ε_G is the efficiency of grinding (~1% for most minerals and equipment) [Tromans, 2008] and ΔSA is the change in surface area that accompanies grinding. Naturally, ΔSA must be determined by the complete PSD as shown in **Eq. (5-17)**.

$$E_G = \gamma_{IG}\Delta SA\varepsilon_G \qquad (5-16)$$

$$\Delta SA = \sum_{i,1} 4\pi r_{i,1}^2 - \sum_{i,0} 4\pi r_{i,0}^2 \qquad (5-17)$$

In **Eq. (5-17)**, i represents every particle in the sample, the total sample mass must be constant, and the subscripts '0' and '1' indicate the sample before and after grinding, respectively. Note that the value of i changes with the degree of grinding. Accurately determination of ΔSA then requires the full PSD as opposed to statistical metrics such as X_{SM} or X_{VM}. Representation of PSD via the lognormal distribution was discussed in Chapter 2. The physical basis for the generation of a distribution of particle sizes is provided in **Fig. 5-7**.
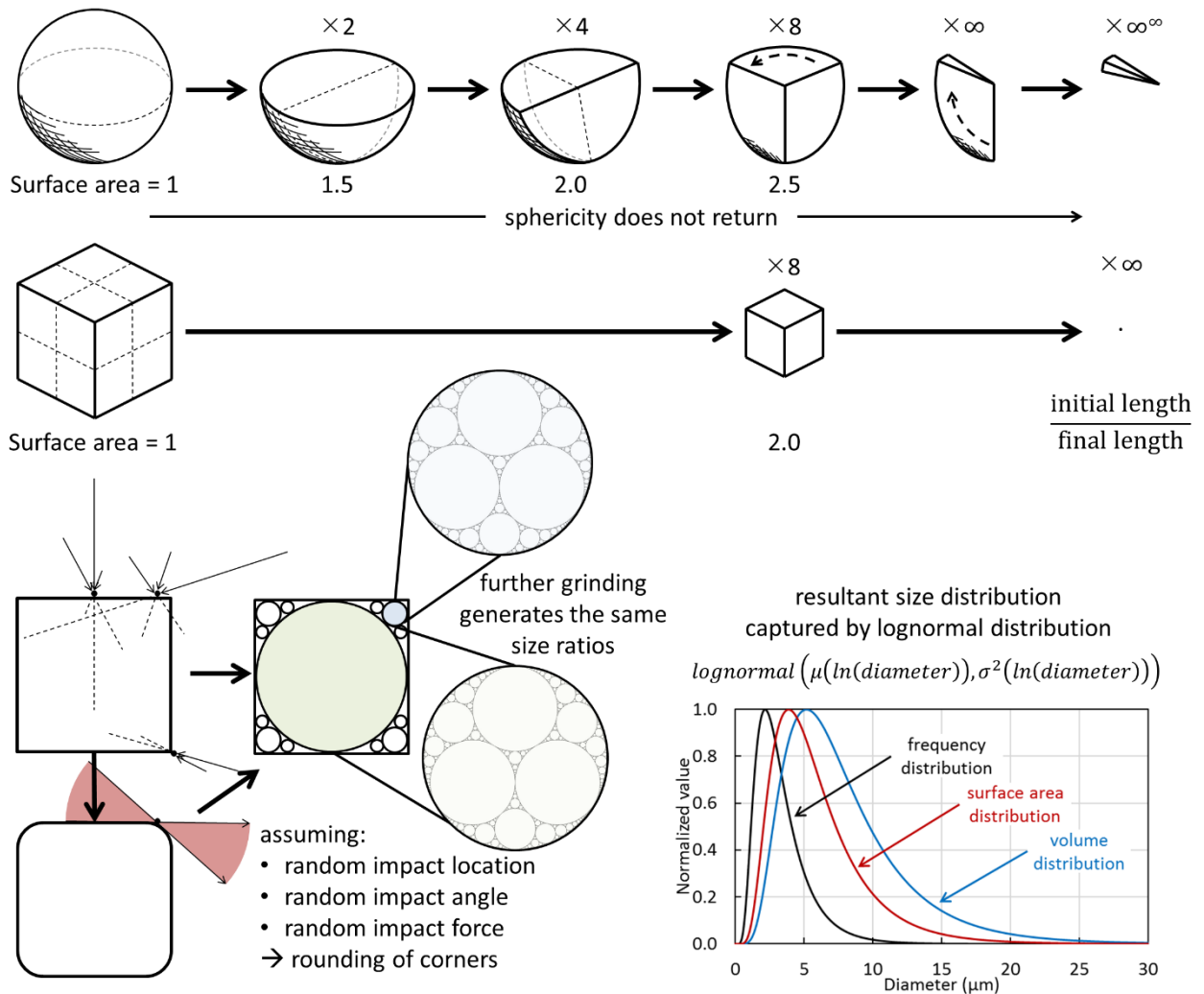
Fig. 5-7. Geometric relationships producing a particle size distribution from random comminution.

Applying G_E in conjunction with power supply CO_2 intensity (**Table 5-4**) determines the net CO_2 mineralization potential of a mineral as a function of grinding extent as demonstrated in **Fig. 5-8(a)** assuming a natural gas power supply [IEA, 2016; Pehl et al., 2017]. **Figures 5-8(b) and 5-8(c)** only display the CO_2 potential lines for the limiting case minerals. In **Fig. 5-8(b)**, the impact of accounting for the complete PSD when determining the comminution energy consumption is highlighted; the population statistic used for comparison is the volume moment mean diameter. The volume moment mean diameter is widely reported as it is the output of laser diffraction-based particle size analyses. The error source of such methods derives from the fact that the majority of surface area produced during grinding is conveyed to the finest particles in a distribution. As such, the G_E is underestimated in monodisperse simplifications of polydisperse samples. In **Fig. 5-8(c)** and **Table 5-5**, the X_{V99} curves for 90%, 50%, and break-even (i.e., 0%) CO_2 mineralization are plotted as a function of the CO_2 intensity of the source energy.

Table 5-4. CO_2 intensities of various energy sources and national grids.

Energy source	CO_2 intensity (gCO_2/kWh)
Natural gas	405
Diesel	715
Solar PV	5.2
Onshore wind	4.2
OECD	421
China	681

Table 5-5. The X_{V99} at which different net CO_2 mineralization are achieved assuming power supplied by natural gas (**Table 5-4**).

|	X_{V99} (µm) at which net CO_2 mineralization is:		
Mineral	0%	50%	90%
CaO	0.62	1.66	14.50
MgO	0.60	1.61	14.00
$Ca_2Fe_2O_5$	1.67	4.08	35.88
$MgFe_2O_4$	2.68	7.06	60.63
Ca_3SiO_5	0.71	1.90	17.00
Ca_2SiO_4	0.53	1.41	12.25
$Ca_3Si_2O_7$	1.00	2.47	22.25
$CaSiO_3$	1.29	3.23	28.38
$Ca_7MgSi_4O_{16}$	0.39	0.99	8.75
$Ca_3MgSi_2O_8$	0.53	1.43	12.38
$Ca_2MgSi_2O_7$	0.74	1.96	17.50
$CaMgSiO_4$	0.52	1.40	12.13
$MgSiO_3$	0.65	1.75	15.50
Mg_2SiO_4	0.50	1.35	11.50
$Ca_3Al_2O_6$	1.75	4.29	38.00
$Ca_{12}Al_{14}O_{33}$	2.99	7.70	66.25
$MgAl_2O_4$	3.71	9.61	83.50
$Mg_3Al_2Si_3O_{12}$	1.59	3.87	34.00
$Ca_3Al_2Si_3O_{12}$	3.68	9.53	82.75
$Ca_2Al_2SiO_7$	2.37	6.37	55.00
$CaAl_2Si_2O_8$	5.13	13.27	111.00
$Ca_4Al_2Fe_2O_{10}$	2.06	5.37	47.00
$CaFeSiO_4$	1.14	2.87	25.25
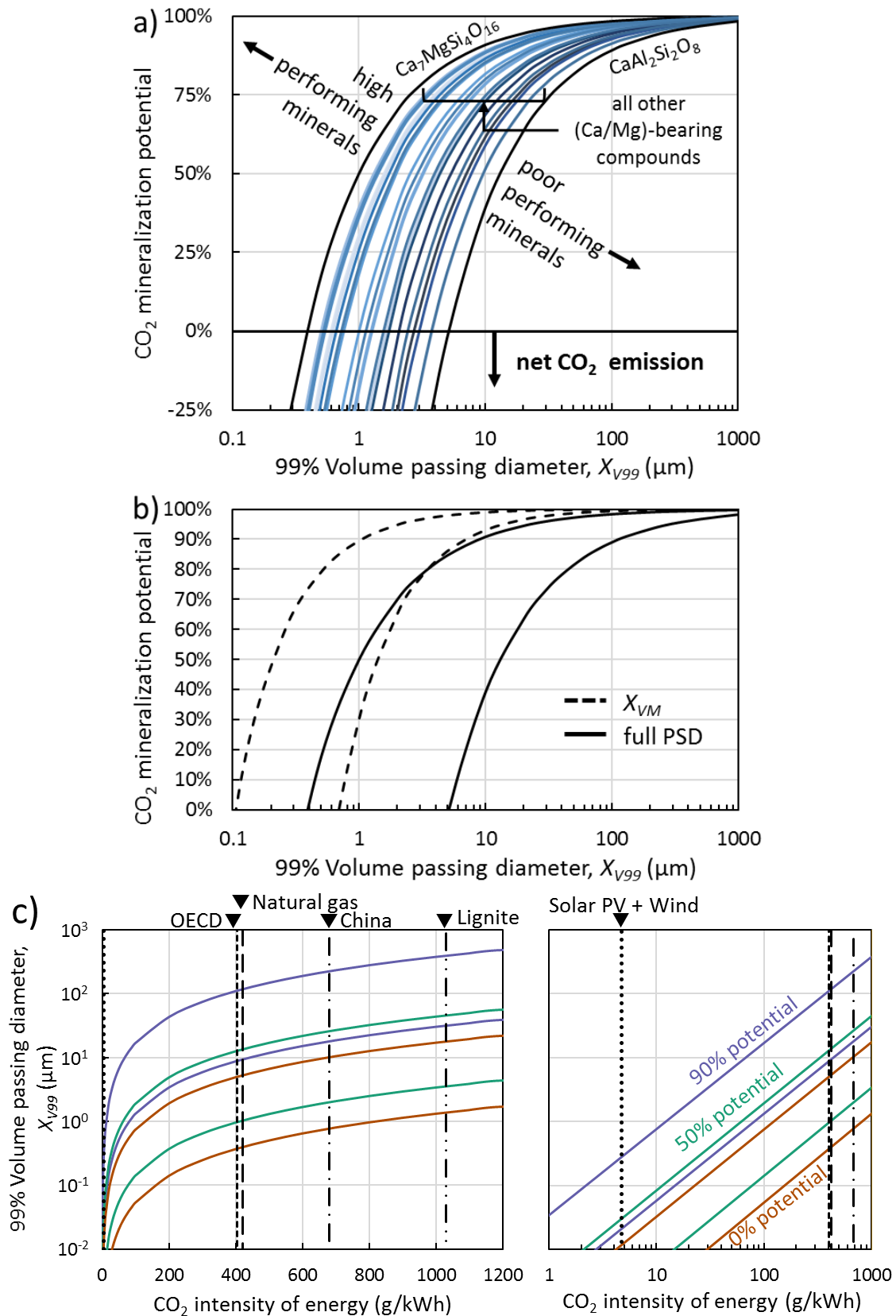
Fig. 5-8. The effect of grinding energy consumption on the net CO_2 mineralization potential of the minerals common to ISM slag when a) power is supplied by natural gas, b) the full PSD is accounted for in the calculation, and c) the source energy CO_2 intensity is changed.

In **Fig. 5-9**, the additional energy expenditure for the grinding of gangue materials is provided. The break-even X_{V99} (i.e., CO_2 mineralization potential=0) is plotted assuming grinding is powered by natural gas. Minerals with an inherently low CO_2 mineralization potential are more severely affected by the inclusion of gangue; in particular, high γ_{IG} gangue such as aluminates depresses performance.
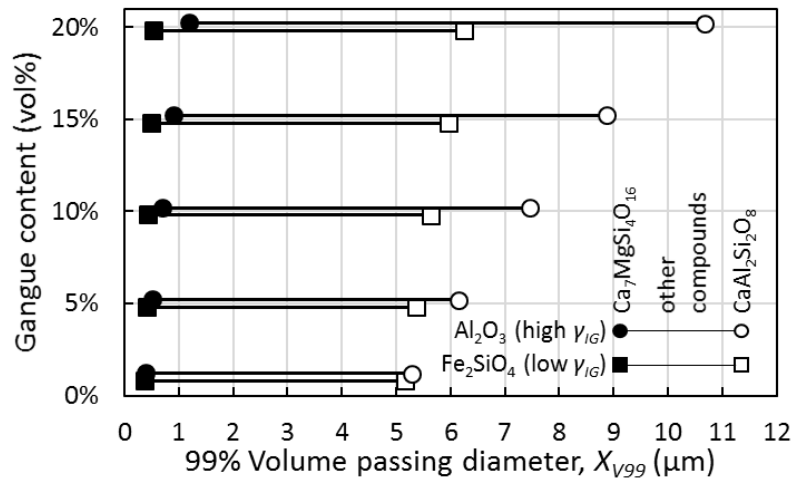

Fig. 5-9. Gangue mineral effect on the point at which grinding becomes a CO_2 emitting process.

5.3.   Thermal fracturing and liberation

In traditional ISM slag treatment methods, slag is rapidly solidified to generate an amorphous structure; rapid solidification is often slowly followed by some form of slow cooling that provides heat recovery. The timing of cooling in the MYNA process is opposite of traditional methods (cf. **Fig.2-25**). Namely, slag is slowly solidified in order to generate large mineral grains and then rapidly quenched in order to facilitate separation of said disparate minerals through thermal fracturing. Though the T_L of ISM slags varies with the chemical composition, it can be expected that all slags are completely solid by 1000 ˚C (cf. **Fig.3-22** and **Fig. 3-23**). Quenching of the solid slag in water as opposed to air or other cooling fluids is advantageous for its high cooling rate (due to high c_P of water), simplicity, and passive nature (heat loss from pool to the environment). Moreover, water-based quenching in one form or another is already common at ISM facilities, reducing potential knowledge gaps or operator reticence about new technology. The merit of quenching a solid, polycrystalline material is that disparate minerals have different thermomechanical properties and thus have unique responses to the thermal shock. As thermal stress (σ_T) is isotropic, the result of these differences causes the σ_T to be concentrated at the grain boundaries and triple points, particularly of disparate minerals (cf. **Fig.2-31**) [Moore and Lockner, 1995; Frøseth et al., 2005]. In addition to directly reducing the amount of energy that is required for grinding, the formation of GB fractures produces higher liberation efficiency than conventional grinding (cf. **Fig.2-32**).

In determining the overall efficacy of solid-state quenching, the first question to be addressed is whether the process is σ-limited or energy-limited. An energy-limited process would have sufficient σ_T to induce and propagate fractures, but insufficient energy to propagate fractures to fully liberate disparate minerals (i.e., the energy of the new SA is greater than the available thermal energy). A σ-limited situation denotes an insufficient σ_T to propagate fractures despite the available thermal energy exceeding the new surface energy of the fracture planes. As fractures propagate through the slag, the heat transfer environment will be modified due to the void spaces between the fracture

surfaces. These void spaces imbue a significant heat transfer resistance. This resultant change in the transient temperature field in turn alters the σ_T field. The alteration in σ_T then dictates whether fracturing can progress further.

Fracture production through thermal shock was demonstrated by Hasselman to begin at a critical temperature difference denoted ΔT_C [Hasselman, 1969]. The topology of thermally induced microfractures was first linked to the intensity of the thermal shock by Bahr et al. (1986) who demonstrated that the structure of microfractures is linked to the intensity of the thermal shock ($=\Delta T / \Delta T_C$ where $\Delta T > \Delta T_C$). A low shock intensity induces evenly spaced plane strain fractures. As the intensity increases, more and more fractures along the external surface intersect into an increasingly fracture-dense structure. Those fractures that move across the heat transfer surface are termed 'channeling'. Concurrent with a decreasing temperature and stress gradient, the density of cellular network created by intersecting and dendritic fractures decreases with distance from the heat transfer surface [Bourdin et al., 2014]. At sufficiently intense thermal stresses, fractures propagating orthogonal to the temperature gradient appear ('spalling') [Bahr et al., 2010]. Spalling fractures develop due to inherent imperfections along the plane strain or channeling surface and due to microbranching that occurs from fracture tip instability at rapid propagation velocities such as are seen in thermal fracturing (i.e., 40% of the sonic limiting velocity) [Chen et al., 2017]. Irrespective of fracture mechanism, in thermal shock systems the propagation of spalling-type fractures is typically the energetically preferred pathway. However, the initiation of spalling fractures can be difficult [Zavattieri and Espinosa, 2001].

Figure 5-10 provides a schematic of the calculation set-up, simplifications, and flow used in the simulation of solid-state quenching of a polycrystalline slag plate.
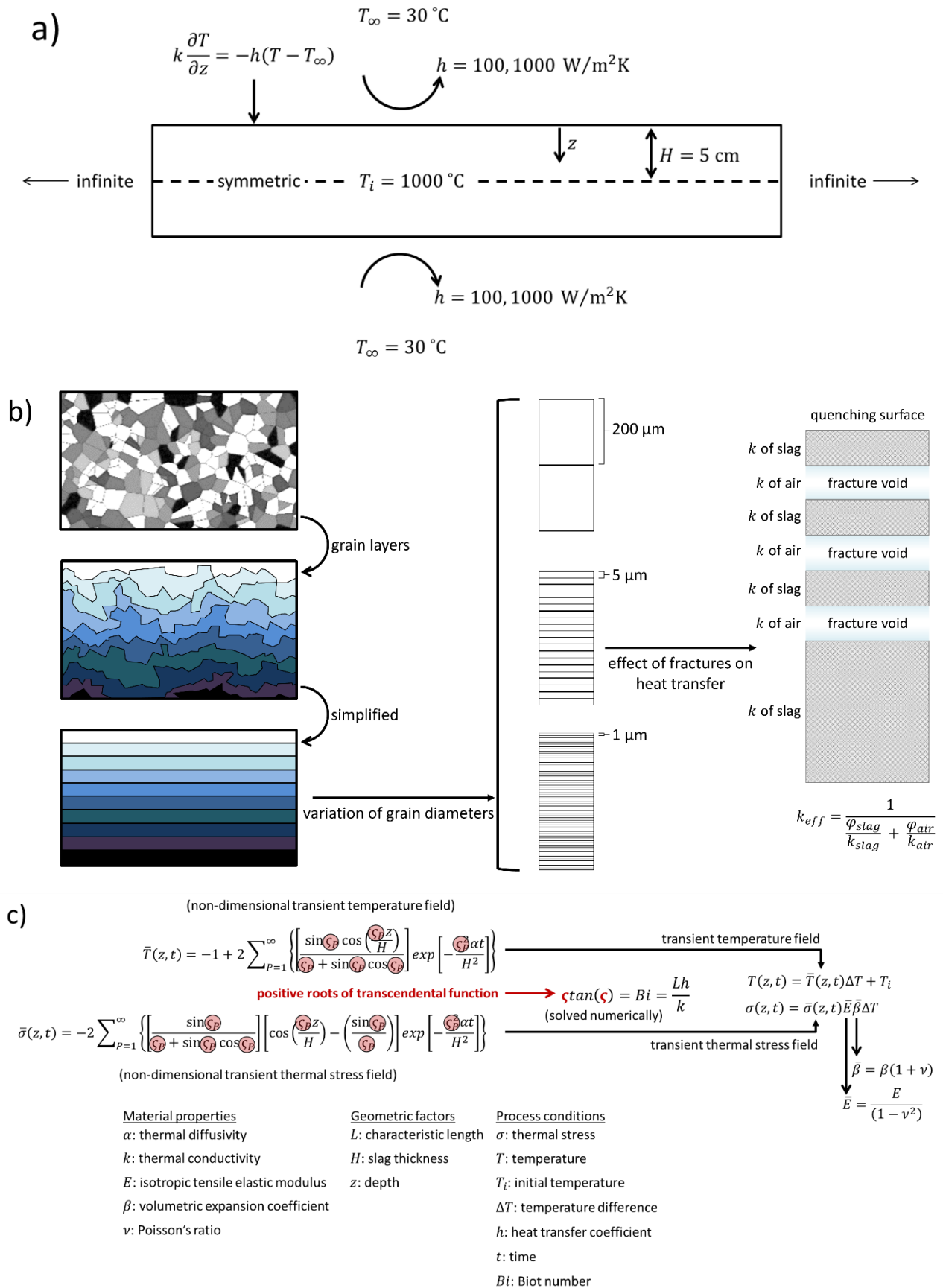
a)

$T_\infty = 30\ °\mathrm{C}$

$k\dfrac{\partial T}{\partial z} = -h(T - T_\infty)$

$h = 100, 1000\ \mathrm{W/m^2K}$

z

$H = 5\ \mathrm{cm}$

infinite ⟵ - - - symmetric - - - $T_i = 1000\ °\mathrm{C}$ - - - - - - - - - - infinite ⟶

$h = 100, 1000\ \mathrm{W/m^2K}$

$T_\infty = 30\ °\mathrm{C}$

b)

200 μm

grain layers

5 μm

effect of fractures on heat transfer

simplified

1 μm

variation of grain diameters

quenching surface

k of slag

k of air   fracture void

k of slag

k of air   fracture void

k of slag

k of air   fracture void

k of slag

$$k_{eff} = \dfrac{1}{\dfrac{\varphi_{slag}}{k_{slag}} + \dfrac{\varphi_{air}}{k_{air}}}$$

c)

(non-dimensional transient temperature field)

$$\bar{T}(z,t) = -1 + 2\sum_{P=1}^{\infty}\left\{\left[\frac{\sin\varsigma_P \cos\left(\frac{\varsigma_P z}{H}\right)}{\varsigma_P + \sin\varsigma_P \cos\varsigma_P}\right]exp\left[-\frac{\varsigma_P^2 \alpha t}{H^2}\right]\right\}$$

transient temperature field

positive roots of transcendental function ⟶ $\varsigma tan(\varsigma) = Bi = \dfrac{Lh}{k}$

(solved numerically)

$T(z,t) = \bar{T}(z,t)\Delta T + T_i$

$\sigma(z,t) = \bar{\sigma}(z,t)\bar{E}\bar{\beta}\Delta T$

$$\bar{\sigma}(z,t) = -2\sum_{P=1}^{\infty}\left\{\left[\frac{\sin\varsigma_P}{\varsigma_P + \sin\varsigma_P \cos\varsigma_P}\right]\left[\cos\left(\frac{\varsigma_P z}{H}\right) - \left(\frac{\sin\varsigma_P}{\varsigma_P}\right)\right]exp\left[-\frac{\varsigma_P^2 \alpha t}{H^2}\right]\right\}$$

transient thermal stress field

(non-dimensional transient thermal stress field)

$\bar{\beta} = \beta(1 + \nu)$

$\bar{E} = \dfrac{E}{(1 - \nu^2)}$

Material properties
α: thermal diffusivity
k: thermal conductivity
E: isotropic tensile elastic modulus
β: volumetric expansion coefficient
ν: Poisson's ratio

Geometric factors
L: characteristic length
H: slag thickness
z: depth

Process conditions
σ: thermal stress
T: temperature
T_i: initial temperature
ΔT: temperature difference
h: heat transfer coefficient
t: time
Bi: Biot number

Fig. 5-10. The solid-state quenching a) calculation set-up, b) conceptual simplification of grains and spalling fractures, and c) the calculation flow for the transient temperature and thermal stress fields.

5.3.1. Energy-limited versus stress-limited

Determination of whether energy or σ constrains the thermal shock fracturing process, the available σ_T was compared with the necessary stress for fracture propagation ($\sigma_{C,x}$); likewise, the available thermal energy (E_T) was compared with the energy of newly-generated SA. The mineral-specific surface energies aggregated in **Table 5-3** and the Mode 1 critical stress intensity (K_C) were calculated per **Eq. (5-18)** and related to $\sigma_{C,x}$ by **Eq. (5-19)**. By setting the σ_T equal to $\sigma_{C,x}$, the critical thermal shock for fracture instigation was acquired as **Eq. (5-20)**.

$$K_{C,x} = \frac{\sqrt{2E\gamma_{S,x}}}{\sqrt{1-v^2}} \qquad\qquad (5-18)$$

$$\sigma_{C,x} = \frac{K_{C,x}}{Y\sqrt{w}} \qquad\qquad (5-19)$$

$$\Delta T_{C,x} = \frac{K_{C,x}}{E\beta Y\sqrt{w}} \qquad\qquad (5-20)$$

The material-specific volumetric expansion coefficient is given by β and x is a placeholder for the potential fracture types. The sensitivity of ΔT_C to flaw size (w) is exacerbated by its typical scale of nanometers to micrometers. Flaws within ISM slag are dominated by grain boundaries and triple points. The low degree of quantitative knowledge about pores and pore structures in slag is ameliorated in this instance by the fact that pores are predominantly located along grain boundaries and at triple points; as such, pores can be assumed to be accounted for when utilizing grain boundaries to determine the flaw size. Moreover, purely geometric arguments demonstrate that for a class of flaws to be of quantitative relevance to overall fracturing extent, they can be no larger than the average edge length of the mineral grains ($w \approx GSD/4$). Rearrangement of **Eq. (5-20)** allows for the determination of the w and therefore the GSD that can be fractured as a function of ΔT_C (**Eq. (5-21)**). The $\Delta T_{C,x}$ was set to the liquidus temperature (T_L) and the inherent grain size limit to which quenching is viable was determined. The results are plotted in **Fig. 5-11** with each line representing a different mineral and ending at its T_L. The typical range of T_L in ISM slags is also plotted to demonstrate that the maximum practical thermal stress intensity is consistently less than the limit set by the mineral-specific liquidus temperature.

$$w = \left(\frac{K_{C,x}}{E\beta Y\Delta T_{C,x}}\right)^2 \qquad\qquad (5-21)$$
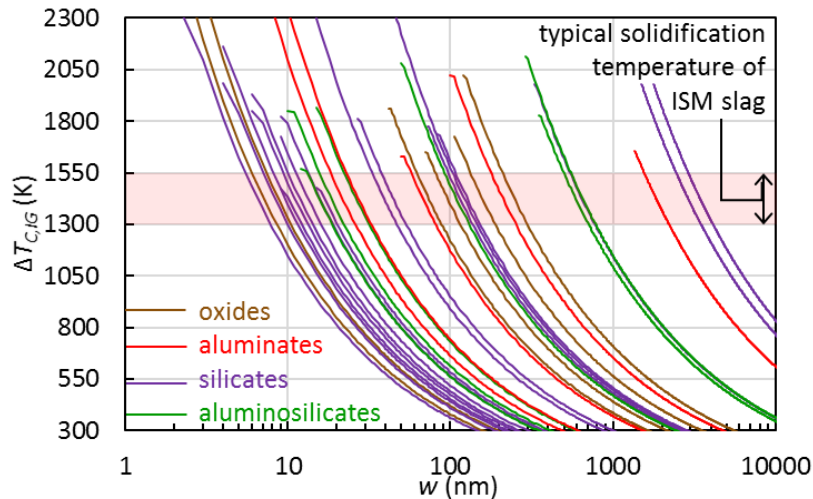
Fig. 5-11. The dependence of ΔT_C on the inherent flaw size; calculated for IG fractures.

To determine the extent to which energy limits the propagation of fractures, all thermal energy contained within the slag over a given temperature range was assumed to be applied to the generation of the new surface area. The maximum potential fracturing extent was defined in terms of the radius (r) of particles generated by fracturing. This radius is identical to the internal mineral grain size. Though the GSD has an inherent distribution of sizes, for the purpose of calculations, it was assumed consistent throughout. The energetically limited radius (r_{limit}) is given in **Eq. (5-22)**.

$$r_{limit} = \frac{3 \times 1.15 \times \zeta \times BET}{\frac{\rho}{\gamma_{GB}} \int_{T_\infty}^{T_i} c_p(T)\, dT} \qquad\qquad (5-22)$$

Equation (5-22) contains several constants due to geometric features. The constant 3 comes from rearrangement of equations. The constant of 1.15 is due to the fact that spheres are not a space-filling solid and thus are rarely found in extant solids; irregular shapes, closely approximated by voronoi cells, are typically encountered in slag. The constant of 1.15 is the average additional surface area increase for a given volume that occurs when converting from a sphere to a voronoi cell [Tanemura, 2003]. In **Eq. (5-22)**, ζ represents the mesoscale roughness factor that depends on the stress loading rate; an empirically determined mesoscale roughness factor of 3.877 was used as thermal fracturing is an inherently high loading rate process [Sadrai et al., 2006]. High-loading rate fractures result in a rougher mesoscale structure due to instability in the crack tip progression and the lack of time for strain-relaxation to control the fracture progression to the 'optimal' (i.e., lowest fracture energy) route. In **Eq. (5-22)**, *BET* is the empirically determined mineral-dependent nanoscale surface roughness which can be found for the various minerals in **Table 5-1**. The nanoscale surface roughness is dependent on the crystal face being examined; to account for this, the *BET* assumes an equal surface area for each crystal facet. The initial temperature of the slag (i.e., prior to quenching) is given by T_i. The temperature of the water bath prior to slag quenching is given by T_∞. The heat capacity for each mineral (c_p) was calculated across the temperature range from 0 to T_L using the method of Waples and Waples (2004). Flaw size was connected to the radius of grains as $2w = r$. Thus, comparison of **Eq. (5-21)** and **Eq. (5-22)** demonstrates that if $r_{limit} > 2w$ then full liberation cannot be achieved due to insufficient thermal energy. The above

equations represent the absolute limit of fracturing potential as they are set to 0 K and do not consider feedbacks from the fracturing process. The results are plotted in **Fig. 5-12** as $2w/r$ against ΔT for the primary minerals of ISM slag. All of the evaluated minerals are σ-limited in the thermal fracturing process. Concretely, if sufficient σ_T is present, all of the grain boundaries will be fractured and complete mineral liberation will be achieved. In **Fig. 5-13**, the GSD that is liberated for a given ΔT is plotted. Notable in **Fig. 5-13** is the three orders of magnitude difference in the GSD of liberated particles as a function of the mineral.
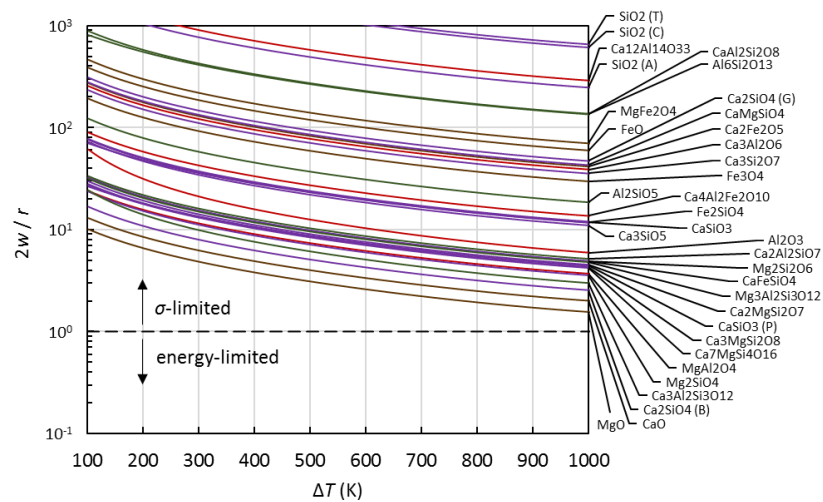

Fig. 5-12. Thermally induced fracturing of the minerals constituting ISM slag is limited by the availability of thermal stress rather than energetic limitations.
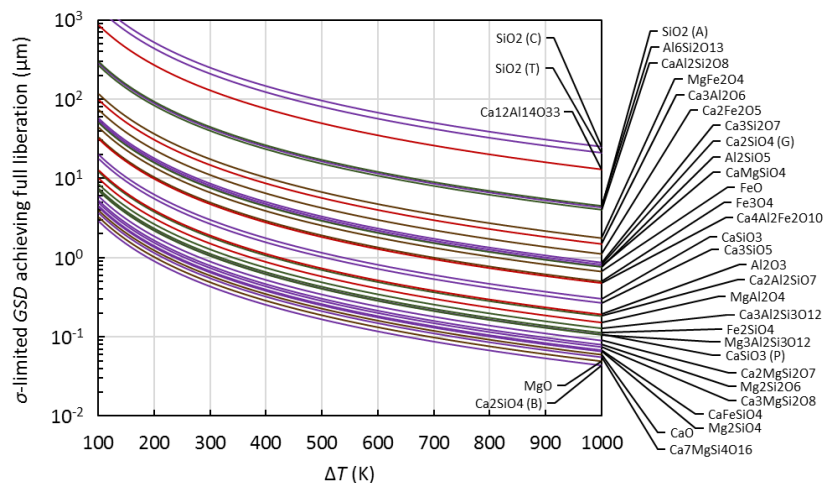

Fig. 5-13. The grain size of each mineral that undergoes complete liberation for a given thermal shock.

5.3.2. Material properties and feedbacks

Material properties

Consideration of feedbacks from fracturing during quenching of slag is complicated by the large variety of slag mineralogies, micromorphologies, macro geometry, and quenching conditions. In order to account for this complexity while also generating widely applicable results, a dimensionless analysis over a range of mineral compositions representative of extant ISM slag was performed. To minimize the

effects of macroscale geometry, the calculation was performed on a slag plate of infinite length and width with a thickness of $2H$. The calculation was performed on only one half of the slag plate (i.e., upper or lower half); this inherently assumes that the heat transfer is equivalent at the lower and upper slag plate surfaces. In reality, the buoyancy of generated steam will generate different heat transfer profiles at the upper and lower surface. This differences in heat transfer at the surfaces will also produce a difference in the thermal stress within the plate, and therefore produce a bending moment within in the plate. However, as the purpose of the calculation is to generate a first-order approximation of the effects of feedbacks, the above-noted details were considered superfluous. The slag plate was given a uniform initial temperature $T_i = 1300\ K$. This temperature was chosen because it represents a temperature at which any ISM should be completely solid; in other words, it removes complications of considering composition dependent T_L and the kinetics of solidification. The slag plate was subjected to a uniform ΔT ($T_i - T_\infty = 1000\ K$) on the upper and lower faces (i.e., $z = \pm H$) at time (t) = 0. **Equation (5-23)** and **(5-24)** provide the transient temperature of the slag plate. In **Eq. (5-23)**, the thermal conductivity of the slag is given by k and heat transfer coefficient is given by h; in **Eq. (5-24)**, the thermal diffusivity is given by α.

$$k\frac{\partial T(z,t)}{\partial z} = -h(T - T_\infty), at\ z = H \tag{5-23}$$

$$\frac{\partial^2 T(z,t)}{\partial z^2} = \frac{1}{\alpha}\frac{\partial T(z,t)}{\partial t} \tag{5-24}$$

Unlike many natural rock formations, the grains within ISM slag are randomly oriented. This characteristic, along with the fact that the grains are much smaller than H, means that k and α can be assumed to be homogeneous and isotropic. Thermal conductivity and thermal diffusivity were determined based on the slag composition. Thermal conductivity was calculated for 15 extant slags based on literature data (8 ironmaking slags, 7 steelmaking slags) [Gautier et al., 2013; Bodor et al., 2013; Liu et al., 2016]. An additional synthetic slag containing equally proportioned by mass (Ca,Mg,Fe)-silicates and one containing equal amounts of (Ca,Mg,Fe)-aluminosilicates were also evaluated to highlight any differences between the primary mineral classes found within ISM slags. When determining the thermal conductivity of polycrystalline materials, the grain size distribution was set as 1 µm, 5 µm, and 200 µm diameters to reflect the likely size distribution for different solidification methods. Effective Medium Theory in three dimensions was used to calculate the bulk conductivity (k_{bulk}). Spherical grains were assumed for the sake of calculation simplicity. **Equation 5-25** was solved numerically to determine k_{bulk}.

$$\sum_m \left[\varphi_m \frac{k_m - k_{bulk}}{k_m + 2k_{bulk}} \right] = 0 \tag{5-25}$$

In **Eq. (5-25)**, each mineral compound is designated by m; this includes void spaces. The volume fraction of each compound was designated by φ_m. As there exists no industry-wide analysis of void space in slags and the available information is insufficient to come to general conclusions, the total

porosity of slag was set to 0, 1, 10, and 25%. Pores were considered to be isolated from one another with no internal air circulation; the thermal conductivity within pores was set to the conductivity of air at the pre-quenched temperature. In reality, it is highly unlikely that the gas composition within pore spaces is equivalent to atmospheric composition, as the gas is derived from off-gassing from the molten slag during solidification. Moreover, the temperature of the gas in the void spaces should decrease concurrently with the slag given its low specific heat. As such, the assumed thermal conductivity is believed to be conservatively high. The increased thermal resistance caused by grain boundaries (i.e., Kapitza resistance: R_λ) was applied to the bulk conductivity to determine the polycrystalline conductivity (k_{poly}) via **Eq. (5-26)**.

$$k_{poly} = \frac{1}{\left(\frac{1}{k_{bulk}} + \frac{n_B}{H} R_\lambda \right)} \qquad (5-26)$$

In **Eq. (5-26)**, the number of grain boundaries is given by n_B (defined as $n_B = (H/GSD) - 1$). The Kapitza resistance is dependent on the material and on the orientation of the grain boundary relative to the heat flux. Currently there exists no method to estimate the Kapitza resistance based on the material. Likewise, the dearth of empirical data relevant to slag makes correlations impossible. As such, the Kapitza resistance was set as a constant that is generally applicable to polycrystalline ceramics ($R_\lambda = 1 \times 10^{-8}$ m²K/W) [Smith et al., 2003]. The calculated and reported thermophysical properties of the slags used in this evaluation are given in **Table 5-6**.

Table 5-6. Calculated thermophysical properties of slags.

	I1	I2	I3	I4	I5	I6	I7	I8	CAS	CS
ρ kg/m³	2834	2845	2877	2944	2835	2840	2825	2914	2864	3406
c_p J/(kgK)	1154	1154	1163	1177	1156	1154	1159	1170	1161	1226
$E(\times 10^{11} \text{Pa})$	1.715	1.702	1.699	1.744	1.710	1.732	1.717	1.754	1.722	1.696
$\beta(\times 10^{-5}\,1/\text{K})$	2.512	2.731	2.855	2.986	2.532	2.478	2.318	2.870	2.660	2.838
k W/(mK)	0.868	0.840	0.810	0.824	0.916	0.904	1.002	1.090	0.907	2.402
ν	0.231	0.231	0.230	0.230	0.231	0.232	0.230	0.233	0.231	0.244
	S1	S2	S3	S4	S5	S6	S7	**Fixed values:**		
ρ kg/m³	3708	3541	3124	3229	3325	3463	3448	R_λ: 1×10⁻⁸ (m²K/W)		
c_p J/(kgK)	1209	1218	1243	1229	1227	1239	1217	ε: 0.9 (-)		
$E(\times 10^{11} \text{Pa})$	1.606	1.648	1.825	1.823	1.423	1.906	1.643	H: 5 (mm)		
$\beta(\times 10^{-5}\,1/\text{K})$	2.580	3.012	2.803	2.735	1.909	3.763	3.063	δ: 400 (nm)		
k W/(mK)	2.182	2.574	1.521	2.136	2.557	3.395	2.453	Porosity: 0,1,10,25%		
ν	0.265	0.252	0.224	0.230	0.255	0.232	0.248	GSD: 1, 5, 200 (µm)		
I: ironmaking slag; S: steelmaking slag; CAS: average of aluminosilicates; CS: average of silicates; values reported before application of R_λ or porosity.										

The heat transfer coefficient is inherently a function of the design of the quenching process and varies during the quenching process itself. At the onset of quenching, the large ΔT results in so-called film boiling at the slag surface (i.e., a layer of steam exists between the slag and the water). As the

slag temperature decreases the boiling regime changes; upon crossing the Leidenfrost point the regime becomes nucleate boiling (i.e., boiling occurs at points across the slag surface, with other areas in direct contact with the water). The heat transfer coefficient changes with the boiling regime as shown in **Fig. 5-14** for the prototypical slag compound Ca_2SiO_4. To cover the range of heat transfer conditions that are likely to occur during slag quenching, the calculation was run at h equal to 100 and 1000 (W/m²K).
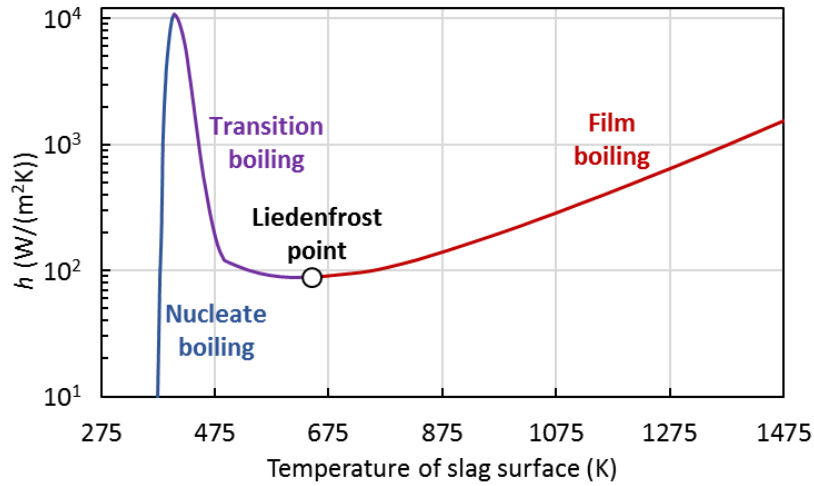
Fig. 5-14. The alteration of the heat transfer coefficient with the boiling regime.

The transient temperature distribution as a function of depth within the slag was determined using **Eq. (5-27)** using the separation of variables technique. The numerically determined positive roots of the transcendental equation are given by ς_P. The transcendental equation is provided in **Eq. (5-28)**, where Bi is the Biot number. **Equation (5-27)** was converted to a temperature by **Eq. (5-29)**.

$$\bar{T}(z,t) = -1 + 2\sum_{P=1}^{\infty} \left\{ \left[\frac{\sin \varsigma_P \cos\left(\frac{\varsigma_P z}{H}\right)}{\varsigma_P + \sin \varsigma_P \cos \varsigma_P} \right] exp\left[-\frac{\varsigma_P^2 \alpha t}{H^2} \right] \right\} \tag{5-27}$$

$$\varsigma tan(\varsigma) = Bi \tag{5-28}$$

$$T(z,t) = \bar{T}(z,t)\Delta T + T_i \tag{5-29}$$

As the bending moment was ignored and the slag was assumed to by unconstrained, the transient stress distribution $\bar{\sigma}(z,t)$ was calculated from the transient temperature distribution via **Eq. (5-30)**. **Equation (5-30)** was converted to stress by **Eq. (5-31)** through **(5-33)**.

$$\bar{\sigma}(z,t) = -2\sum_{P=1}^{\infty} \left\{ \left[\frac{\sin \varsigma_P}{\varsigma_P + \sin \varsigma_P \cos \varsigma_P} \right] \left[\cos\left(\frac{\varsigma_P z}{H}\right) - \left(\frac{\sin \varsigma_P}{\varsigma_P}\right) \right] exp\left[-\frac{\varsigma_P^2 \alpha t}{H^2} \right] \right\} \tag{5-30}$$

$$\sigma(z,t) = \bar{\sigma}(z,t)\bar{E}\bar{\beta}\Delta T \tag{5-31}$$

$$\bar{E} = \frac{E}{(1 - v^2)} \qquad\qquad (5-32)$$

$$\bar{\beta} = \beta(1 + v) \qquad\qquad (5-33)$$

Fracturing

Fracturing of slag alters the k through the introduction of additional void spaces. As previously noted, three types of fracturing exist in slag; plane strain fractures and channelling fractures run parallel to the heat flux, while spalling fractures run normal to the heat flux. A result of these distinct geometries relative to the heat flux is that spalling fractures have an outsized impact on the thermal conductivity of slag (**Fig. 5-15**).
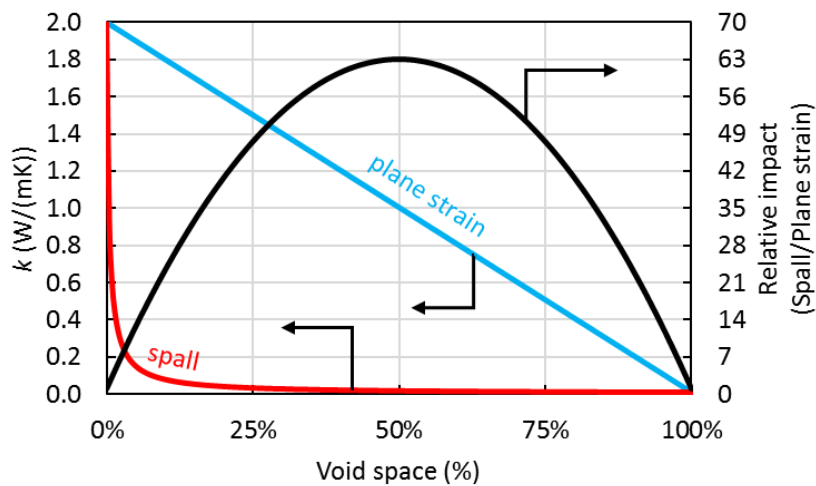

Fig. 5-15. The effect of fracture type on alteration to the conductivity of slag.

Figure 5-15 was calculated by determining the effective conductivity adjusted for the geometry of fracturing (**Fig. 5-16**). The large impact of spalling occurs because there are is no connectivity of slag that allows for high thermal flux. In the case of plane strain and channelling fractures, there exist pathways for heat to reroute itself around the low conductivity void space.
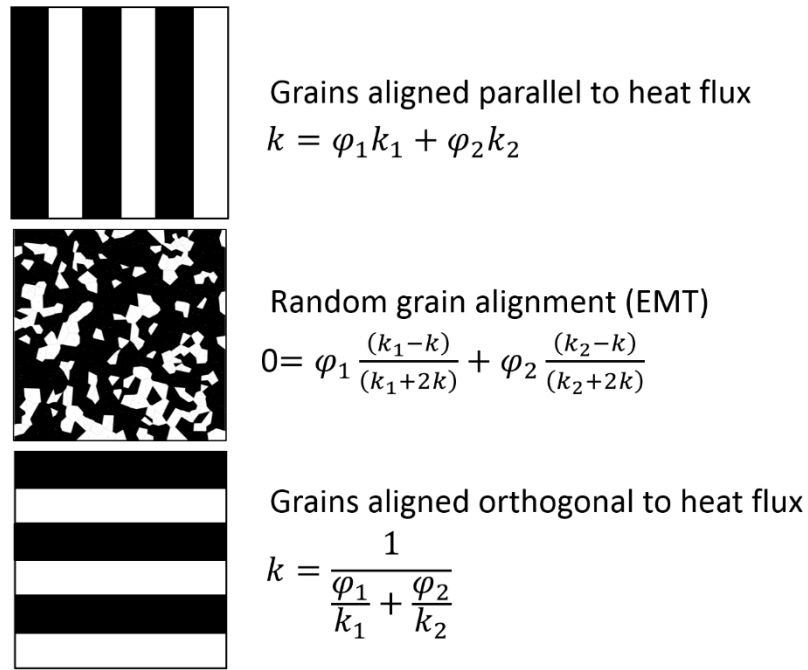
Grains aligned parallel to heat flux

$k = \varphi_1 k_1 + \varphi_2 k_2$

Random grain alignment (EMT)

$0 = \varphi_1 \dfrac{(k_1 - k)}{(k_1 + 2k)} + \varphi_2 \dfrac{(k_2 - k)}{(k_2 + 2k)}$

Grains aligned orthogonal to heat flux

$k = \dfrac{1}{\dfrac{\varphi_1}{k_1} + \dfrac{\varphi_2}{k_2}}$

Fig. 5-16. The impact of grain alignment on thermal conductivity.

Per **Fig. 5-16**, the effective conductivity of spalling fracturing in heterogeneous, polycrystalline ISM slag (k_{eff}) is given by **Eq. (5-34)**. The average thermal conductivity within the spalling fractures (k_{spall}) was calculated to account for both conduction and radiation due to the high temperatures involved. Given sufficient time, the voids created by spalling may become filled with water due to interconnections with plane strain fractures. As the time scale of thermal fracturing is on the order of milliseconds, it was assumed that there was insufficient time for water ingress. On the other hand, it was assumed that the low pressures generated by void spaces created by fractures would cause rapid infilling from gases. These gases would likely be primarily superheated steam from the quenching process. Given the degree of uncertainty in regard to gas composition, the void space was assumed to be filled with air at the initial slag temperature as a reasonable approximation.

$$k_{eff} = \frac{1}{\dfrac{\varphi_{poly}}{k_{poly}} + \dfrac{\varphi_{spall}}{k_{spall}}} \qquad (5-34)$$

The parallel thermal resistance of conduction through the air-filled void space and radiative resistance is given by **Eq. (5-35)**. The width of the void space is given by δ_V, the Stefan-Boltzmann constant is given by k_B, and the emissivity (ε) was set constant to 0.9 for all slag at all temperatures. As the radiative resistance is dependent on the temperature difference between the surfaces of the void, it was calculated for the limiting conditions of $T_z = T_{z+\delta}$ and $T_z = T_i$ where $T_{z+\delta}$ was set equal to T_∞.

$$k_{spall} = \delta_V \left(\frac{k_{air\ @\ T_i}}{\delta_V} + \varepsilon k_B (T_z + T_{z+\delta})(T_z^2 + T_{z+\delta_V}^2) \right) \qquad (5-35)$$

The amount of void space (i.e., volume fraction: φ_{spall}) was calculated per **Eq. (5-36)** based on the number of grain boundaries under tension (n_B^*) from **Eq. (5-37)**. The value $z_{\sigma=0}$ was calculated from the dimensionless analysis sans fracturing feedbacks. The average spalling thickness was set to 400 nm based on analysis of micrographs available in the literature [Marschall et al., 2013]. The conditions and assumptions of the solid-state quenching analysis are aggregated for simple lookup and reproducibility in **Table 5-7**.

$$\varphi_{spall} = \frac{(n_B^* \delta_V)}{(n_B^* \delta_V) + H} \tag{5 - 36}$$

$$n_B^* = \frac{z_{\sigma=0}}{GSD} - 1 \tag{5 - 37}$$

Table 5-7. Calculation details of the solid-state quenching simulation

Feature	Value	Notes
Grain diameter (µm)	1 5 200	Roughly representative of rapid cooling (1 µm), pit-cooling (5 µm), and slow solidification (200 µm).
Slag thickness (mm)	10	Simulation occurs across ½ of the slag thickness (5 mm).
Fracture thickness (nm)	400	Average based on micrographs from various slag compositions and thermal fracturing regimes. Insufficient variation based on slag properties or quenching conditions to vary this property.
Time step (s)	NA	Non-dimensional time allows for calculation at specific instances. Calculations performed at 0.1, 0.5, 1, 2, 3, 4, 5, 10, 30, 60, and 120 seconds. Calculations also performed at the time of largest tensile stress at the slag surface ($= 0.21/[1 + 0.88Bi]$).
Slag temperature (K)	1300	Assumed temperature to ensure complete solidification regardless of slag composition. Set uniform through the slag plate.
Water temperature (K)	30	Not varied during the simulation.
Air temperature (K)	30	Not varied during the simulation.
Kapitza resistance (m^{2}K/W)	1×10^{-8}	Occurring between mineral grains. Removed upon fracture.
Emissivity	0.9	---
Other properties	from literature	Isotropic tensile elastic modulus (E), thermal diffusivity (α), volumetric expansion coefficient (β), conductivity (k), density (ρ), specific heat (c_p), Poisson's ratio (ν). Properties calculated from mineralogical composition based on volumetric averages.

Calculation Method	
Thermal conductivity	Effective medium theory in 3 dimensions was used to calculate the unfractured, polycrystalline slag conductivity. This conductivity was used with the conductivity of air to calculate the thermal conductivity in fractured slag. Air and slag were layered perpendicular to the stress gradient. Additional condition including radiative transfer through void spaces generated by fracturing.
Transient temperature field	1 dimensional, infinite plate with symmetric heat flux from the top and bottom surfaces. Vertical grid spacing set to ¼ of the grain diameter in order to ensure sufficient resolution. Calculated by conversion to a non-dimensional form with integral solved by separation of variables. Positive roots of transcendental equation based on Biot number utilized.
Transient thermal stress field	1 dimensional, infinite plate with symmetric heat flux from the top and bottom surfaces. Vertical grid spacing set to ¼ of the grain diameter in order to ensure sufficient resolution. Calculated by conversion to a non-dimensional form with integral solved by separation of variables. Positive roots of transcendental equation based on Biot number utilized.
Positive roots of transcendental function	$\varsigma \tan \varsigma = Bi$ used to solve transient, non-dimensional temperature and thermal stress fields. Transcendental equation solved numerically to the first 50 positive roots.

5.3.3. Comminution reduction potential

An example of the transient temperature field without consideration of feedbacks from fracturing is provided in **Fig. 5-17**. Due to the relative similarity in results, the highest and lowest k slags are used for displaying the range of results (code S6 and I3 from **Table 5-6**, respectively). **Figures 5-18** and **5-19** demonstrate the temperature evolution in slag S6 at a heat transfer coefficient of 100 and 1000 W/(m²K), respectively. **Figures 5-20** and **5-21** demonstrate the temperature evolution in slag I3 at a heat transfer coefficient of 100 and 1000 W/(m²K), respectively. Unsurprisingly, the higher conductivity slag maintains a more uniform temperature across the depth of the slag and cools off more rapidly.
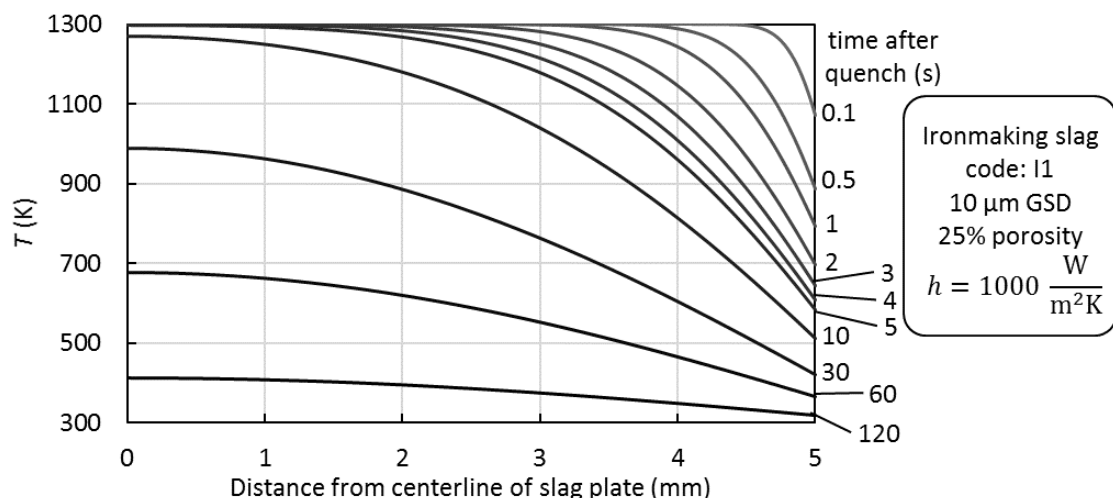

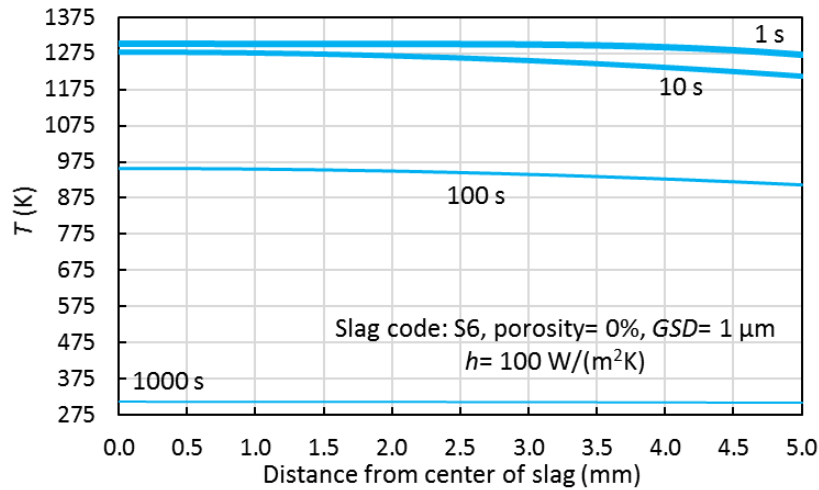**Fig. 5-17.** Example transient temperature distribution graph.

Fig. 5-18. The evolution of temperature along the depth of the slag plate over the course of quenching for a high conductivity slag under mild heat transfer conditions.
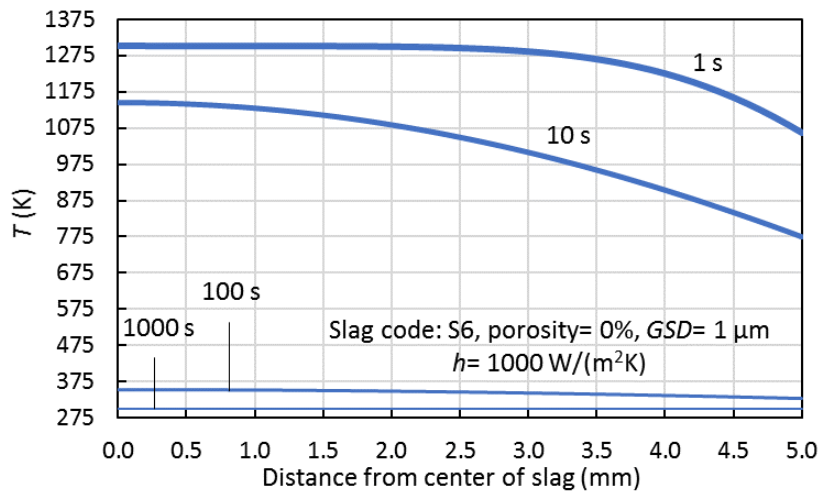

Fig. 5-19. The evolution of temperature along the depth of the slag plate over the course of quenching for a high conductivity slag under intense heat transfer conditions.
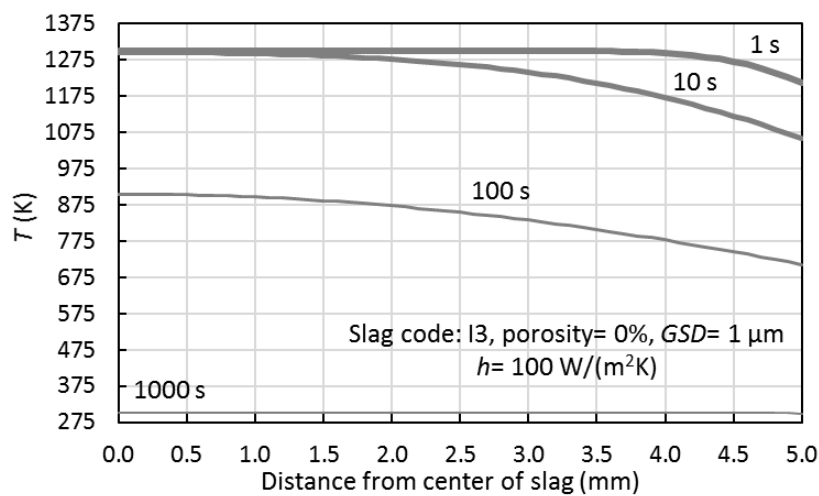

Fig. 5-20. The evolution of temperature along the depth of the slag plate over the course of quenching for a low conductivity slag under mild heat transfer conditions.
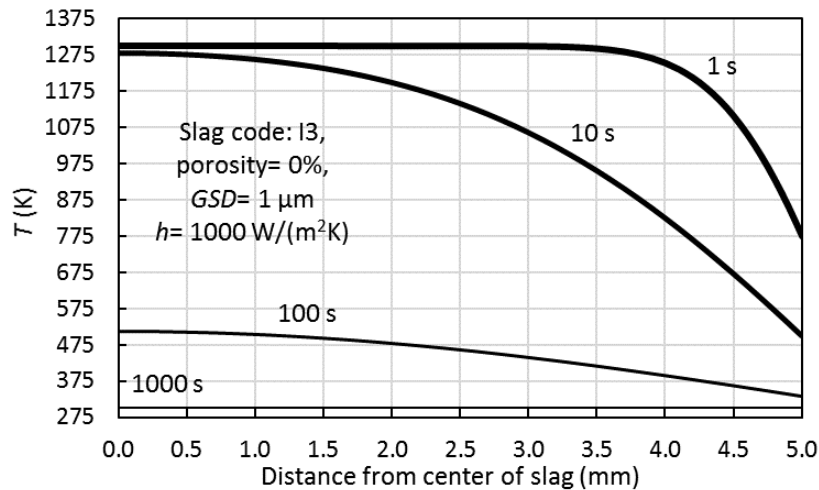
Fig. 5-21. The evolution of temperature along the depth of the slag plate over the course of quenching for a low conductivity slag under intense heat transfer conditions.

Analysis of the effects of GSD and porosity show little effect on the transient temperature distribution. This can be understood by the negligible magnitude of the Kapitza resistance and the random distribution of pore spaces allowing for thermal bypassing in 3 dimensions, respectively.

An example of the transient stress field without consideration of feedbacks from fracturing is provided in **Fig. 5-22**. An initial rapid rise along the outer edge of the slag plate is followed by a gradual decline and inward diffusion of stress as the temperature equilibrates. An alternative method of displaying the results which demonstrates the symmetric nature of the thermal stress and the concurrent generation of internal compressive stresses is given in **Fig. 5-23**. To remain consistent with the temperature field analysis, slags I3 and S6 at h of 100 and 1000 W/(m^{2}K) are used for comparative purposes in **Fig. 5-24**. Naturally, higher heat transfer rates generate larger thermal stresses at the heat transfer surface of slag. The graphs of thermal stress indicate a consistent trend of tensile stress being limited to a given depth within the slag, with deeper layers experiencing compressive stress. Once again, only minor differences are seen between the different ironmaking slags or steelmaking slags, but significant differences exist between slag types. Porosity and grain size distribution effects on the stress distribution are minor compared to the mineral composition of slag.
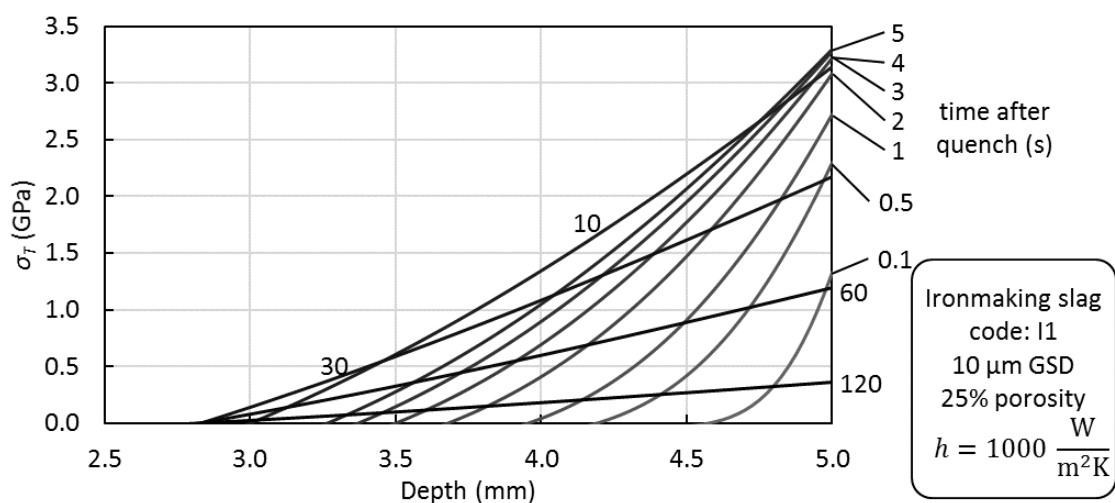

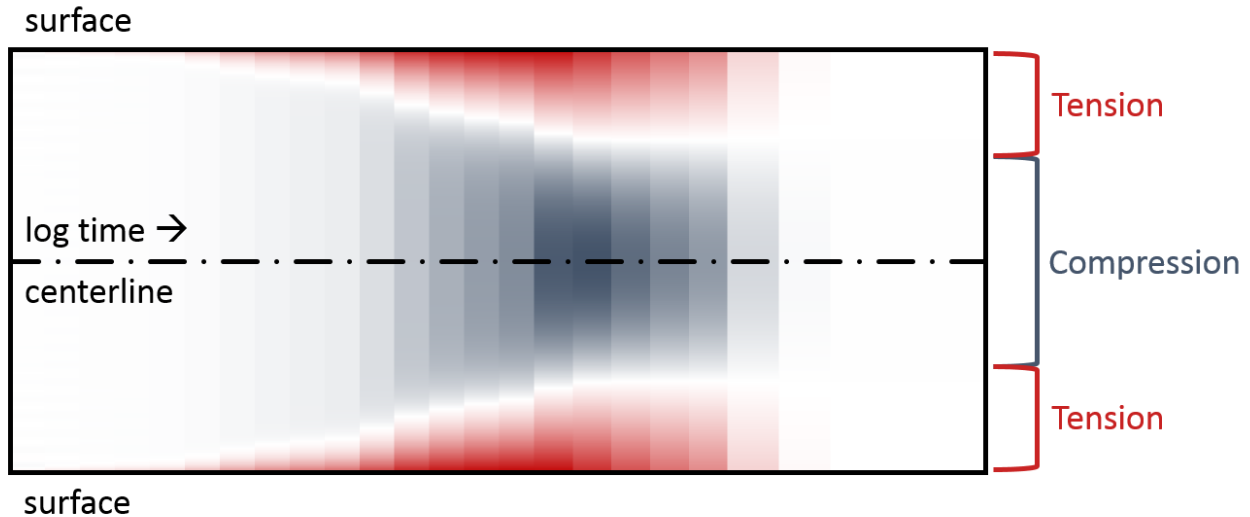**Fig. 5-22.** An example of the transient stress distribution within slag.

surface

Tension

log time →

centerline

Compression

surface

Tension

Fig. 5-23. An alternative visualization of the transient stress distribution within slag.

slag: I3, *h*=1000 W/(m²K)
Bi=8.949, *t*= 4.081 s

slag: S6, *h*=1000 W/(m²K)
Bi=1.473, *t*=4.847 s

slag: I3, *h*=100 W/(m²K)
Bi=0.895, *t*=22.946 s

slag: S6, *h*=100 W/(m²K)
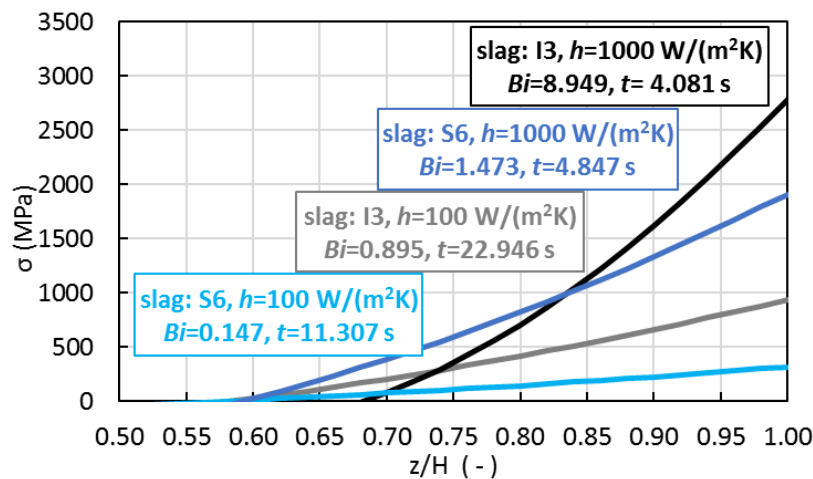*Bi*=0.147, *t*=11.307 s

Fig. 5-24. The maximal stress extent for slags I3 and S6 at high and low quenching intensities.

The effects of fracturing on the transient temperature distribution in slag S6 and I3 are provided in **Fig. 5-25** and **Fig. 5-26**, respectively. Spalling fractures insulate the interior portions of the slag, reducing heat loss. This insulation also serves to increase the heat loss from the outer portions of the slag. The effect is clearly larger on the high k steelmaking slag (S6) than on the low k iron making slag (I3). The feedback effects from spalling appears to have a larger impact on the thermal shock behaviour than any specific material property. In reality, the temperature and stress distributions in slag will lay somewhere between the unfractured and fractured simulation results (fracture results assume that all the fractures have occurred from the onset of the process instead of as the heat transfer occurs).
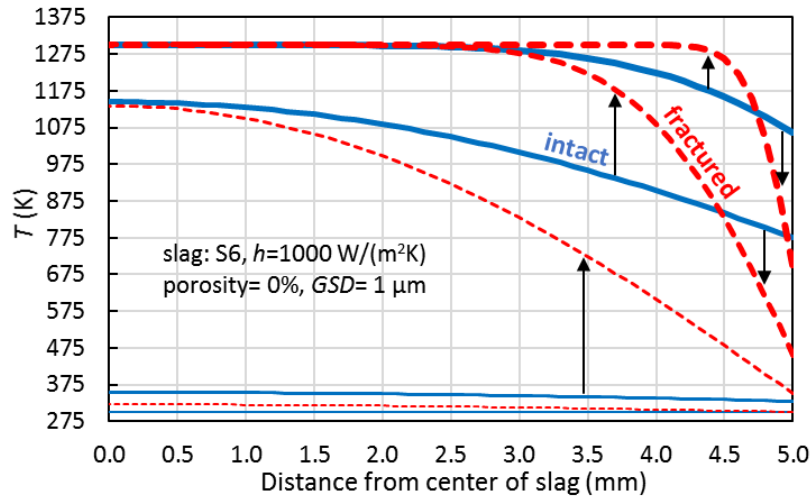
Fig. 5-25. The thermal segregation of the slag surface and interior by the insulating effect of fractures in high k steelmaking slag under intense quenching.
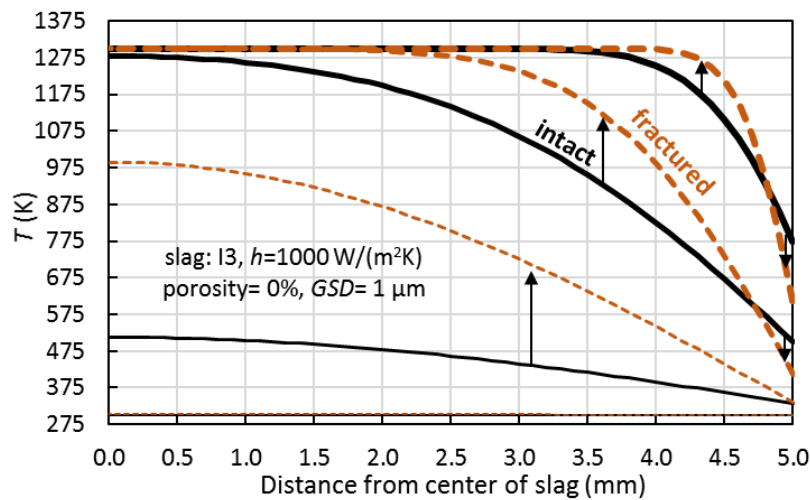

Fig. 5-26. The thermal segregation of the slag surface and interior by the insulating effect of fractures in comparatively low k ironmaking slag under intense quenching.

The effect of fracturing on the thermal stress field is displayed in **Fig. 5-27** and **Fig. 5-28** for slag S6 and I3, respectively. The increased heat transfer at the surface and decreased heat transfer in the deeper layers increases the temperature gradient and thus the thermal stress in the outer layers of the slag. This intensified surface stress comes at the expense of stress in deeper portions of the slag. As such, there may be more extensive fracturing in the outer layers (due to higher magnitude stress), but less overall mineral liberation. **Figure 5-29** summarizes the range of stresses experienced across all studied slags and the synthetic silicate and aluminosilicate slags. Steelmaking slag generally experiences larger stresses, but substantial overlap with ironmaking slag is present throughout.
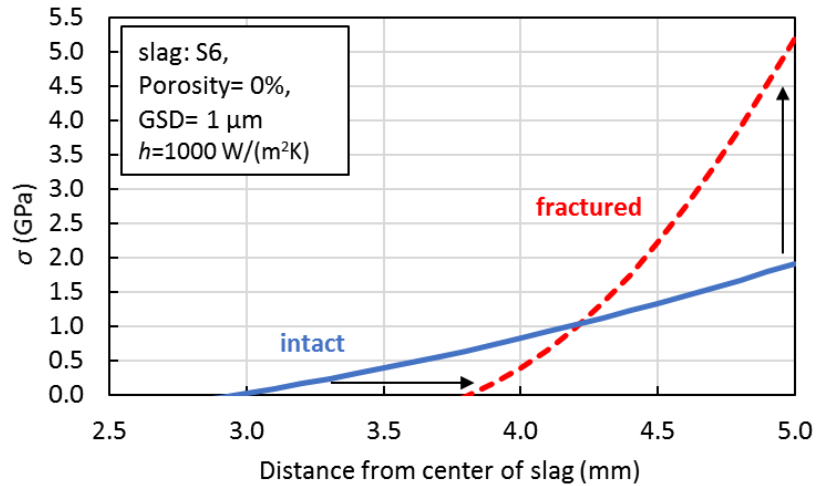
Fig. 5-27. The alteration of the maximal stress line that comes with the insulating feedbacks of fractures in steelmaking slag.
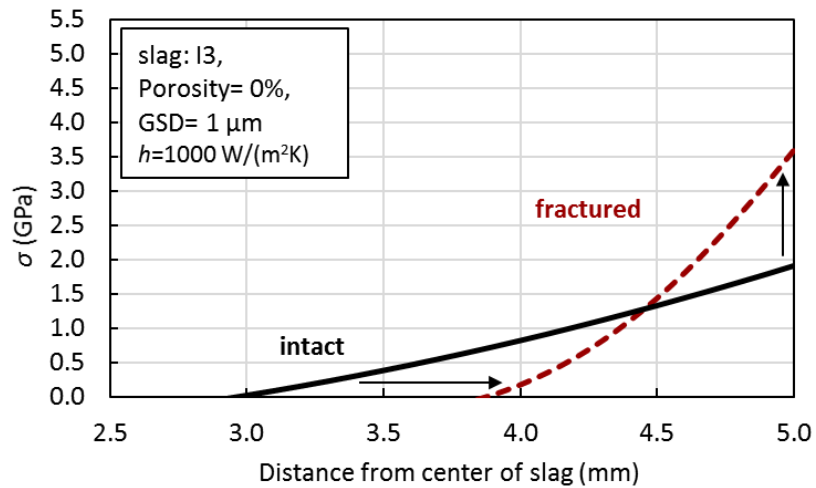

Fig. 5-28. The alteration of the maximal stress line that comes with the insulating feedbacks of fractures in ironmaking slag.
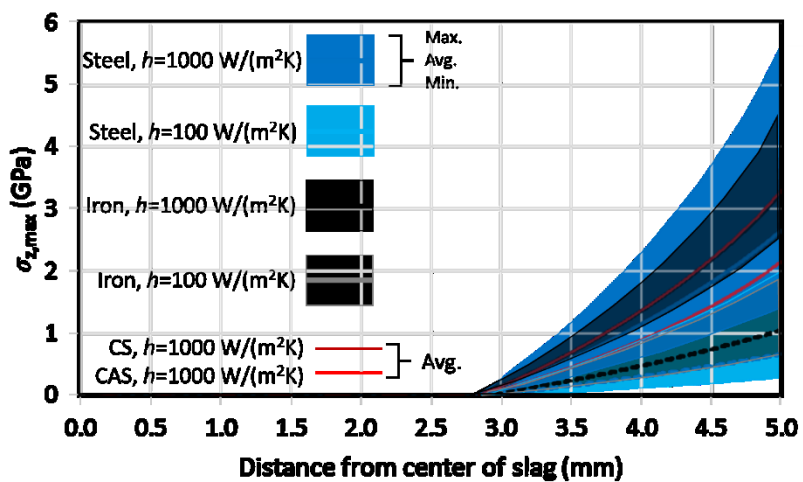

Fig. 5-29. The depth-dependent maximal stress ranges for ironmaking and steelmaking slags at heat transfer rates of 100 and 1000 W/(m²K).

Given that the purpose of quenching is to reduce grinding energy and increase liberation, the grinding energy reduction was quantified. As thermal stress-based fracturing of ISM slag is a σ-limited process, the fractures generate completely liberated materials and the grinding energy reduction is equivalent to the energy content of the generated surface area. To convert this into a percent reduction in grinding energy, the volume percent of liberated material was calculated using **Eq. (5-38)**.

$$\int_0^H \sum_m \begin{cases} \sigma_{z,max} > \sigma_{C,GB} & \varphi_m \\ else & 0 \end{cases} dz \qquad (5-38)$$

The maximum stress at each location (step size of the lesser of 1 m µor ¼ the GSD) does not occur at the same instant, therefore the maximum stress ($\sigma_{z,max}$) over the first 100 seconds, calculated at a timestep of 1 millisecond was determined. The location-dependent maximum stress was converted to a fracture extent in **Fig. 5-30** for all 17 slags under the conditions listed in **Table 5-6** (i.e., GSD, porosity, and h). **Figure 5-30** indicates the importance of intense quenching conditions in order to generate a meaningful quantity of fractures. However, the significant degree of scatter in the data indicates that other factors also meaningfully influence fracturing.
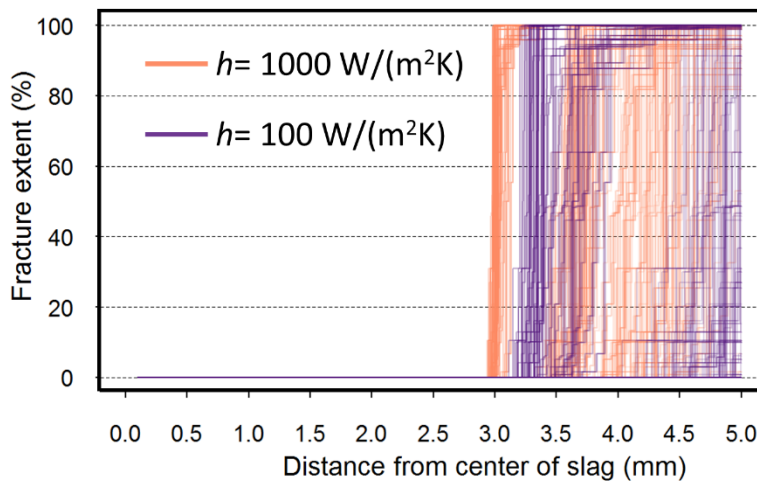

Fig. 5-30. Fracture extent after 100 seconds as a function of depth from the slag surface for all the conditions listed in **Table 5-6**.

The total fracture extent (i.e., area under the curve) for each line in **Fig. 5-30** was calculated to represent the reduction in grinding energy. This value was then segregated and aggregated based on slag type (ironmaking, steelmaking, or synthetic), grain size distribution (1, 5, 200 µm), and quenching intensity (100 or 1000 W/(m²K)). The results are summarized in **Fig. 5-31**. **Figure 5-31** indicates that a maximal fracturing extent exists for the given geometry of ~40%; this is due for the need for a balance between tensile and compressive stresses. Higher quenching intensity and larger grain sizes are the strongest drivers of enhanced fracturing. This result is due to the higher thermal stresses that coincide with higher h and the lower σ_c that accompanies larger grain sizes. Moreover, larger grain sizes result in fewer voids for a given volume of slag; therefore, the suppressive effects from fracturing on thermal stress deep within the slag are reduced. As the h is limited by the liquidus temperature of slag and the temperature of the cold bath, the primary method to increase thermal

fracturing appears to be increasing the GSD via modification of the solidification process. Ironmaking slag is generally more amenable to fracturing than the steelmaking slag; this result is mirrored by the results from the synthetic slags where the silicates are generally more responsive to fracturing than the aluminosilicates. As grain size increases, the effects of quenching intensity and slag composition become less and less important to the overall fracture extent. At grain sizes common to conventional cooling conditions, the quenching intensity is of primary importance to the fracturing extent.
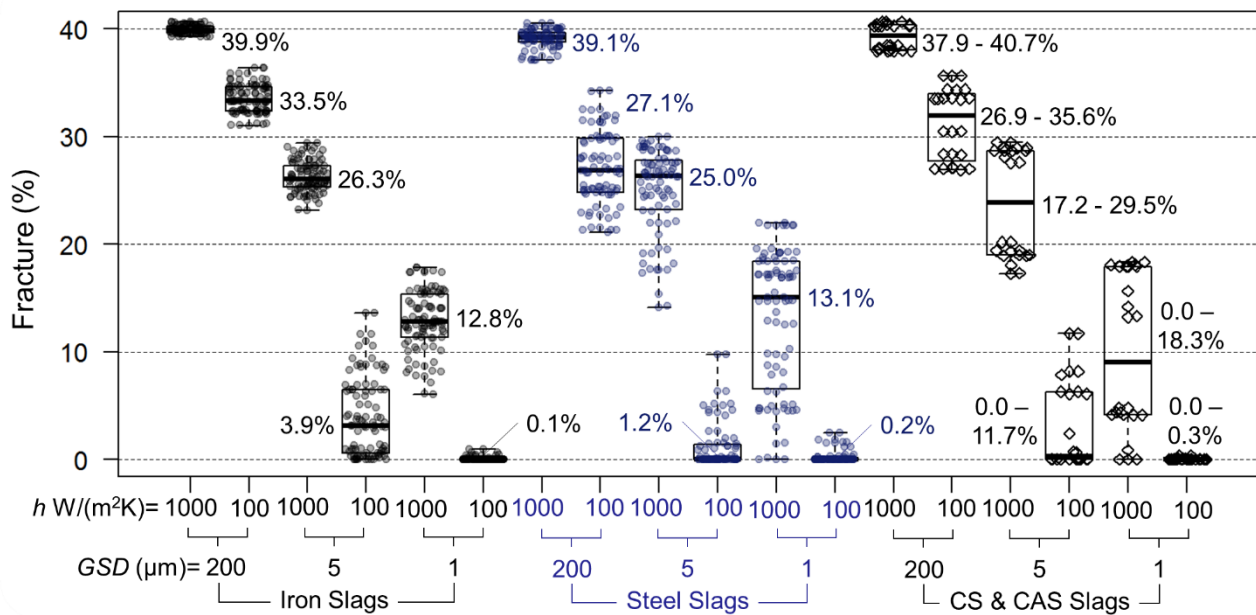

Fig. 5-31. The overall comminution energy reduction for the slags and conditions listed in **Table 5-6**.

The spread of data within each subgroup is due to differences in slag properties (e.g., porosity, mineral composition) and the inclusion of feedback mechanisms (**Fig. 5-32**). For example, fracturing extent tends to increase with the inclusion of the feedbacks from fracturing; on the other hand, including the effects of radiation when calculating feedbacks has essentially no impact (see **Fig. 5-32a**). Porosity tends to increase the degree of fracturing, though this is more pronounced when not including the feedback effects of fracturing (see **Fig. 5-32b-e**).
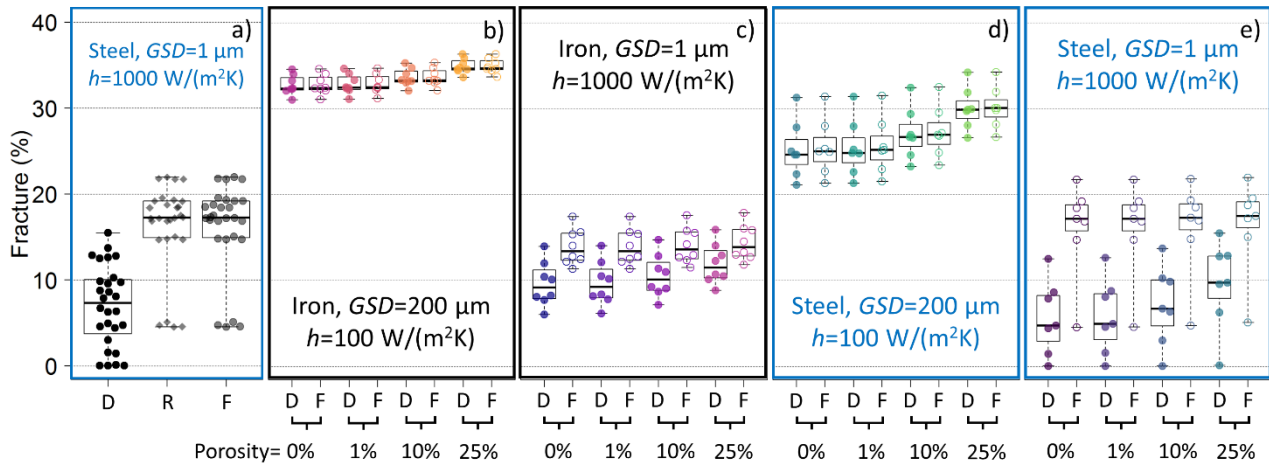
Fig. 5-32. Secondary drivers of fracturing extent of quenched slags. D: diffusion only; F: diffusion and fracturing; R: diffusion, fracturing, and radiation feedbacks.

Though the analysis indicates that comminution energy reduction can only be reduced by 40%, further reductions are possible through multiple quenching sessions. The maximal stress intensity occurs within a few seconds for all conditions. At this time scale, the slag internal to the ~40% fracture plane remains close to the initial temperature. Conceptually, slag quenching could be designed for immediate slag recovery followed by removal of the external, fractured layers. The remaining hot slag plate could then be re-quenched, again generating thermal fractures (**Fig. 5-33**). Large mineral grains are a requirement for consistent, high fracture extent; therefore, multiple quenching may reach a physical limit based on the structural integrity of a slag plate as highlighted by the number of mineral grains with associated grinding energy reduction (purple in **Fig. 5-33**).
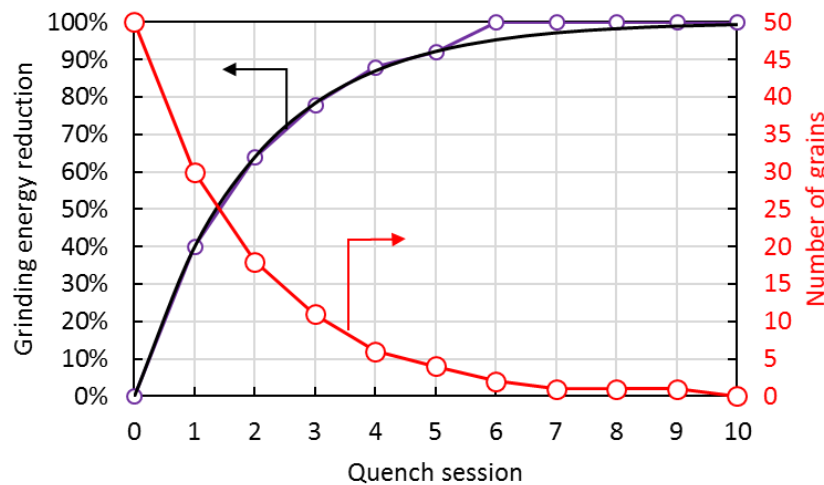
Fig. 5-33. The total energy reduction (black) over several sessions of quenching. The change in the number of internal mineral grains across the depth of the slag indicates that quenching may achieve 100% liberation by the 6th session.

5.3.4. Application to amorphous slags

A separate analysis of solid-state quenching applied to amorphous, spherical slag was undertaken. The motivation for such an analysis is primarily to verify the theoretical findings with a separate

calculation method and empirical testing. Testing was performed on desilicating slag provided by a commercial ISM company. X-ray fluorescence and XRD testing indicated the slag was typical of the industry; that is, a mixture of amorphous calcium silicates with iron oxide inclusions, silica with metallic iron inclusions, and homogeneous calcium ferrites. Quenching was performed on the calcium silicates and silicates by heating the slag to 900 ˚C, followed by quenching in water at 30 ˚C. Two control samples were also tested, one with heating to 900 ˚C followed by cooling in air, and another with no thermal treatment. Control and quenched samples were crushed in a hydraulic press to determine any change in comminution energy. Each group was tested on 40 individual slag particles. The experimental conditions were modeled as described **Table 5-8** in a 2D transient heat and stress analysis in COMSOL Multiphysics®. The aggregated results are provided in **Fig. 5-34**.
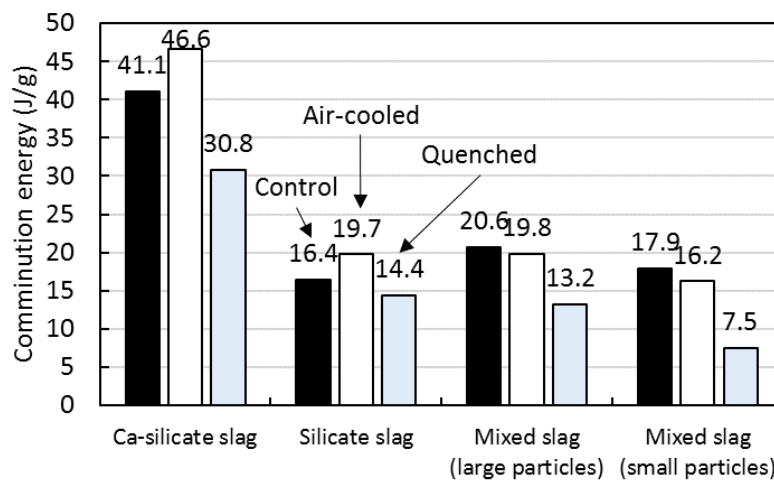

Fig. 5-34. Empirical reduction in comminution energy of desilicating slag via solid state quenching.

Table 5-8. Parameters of 2D transient heat and stress analysis of slag quenching.

Literature values	$c_p, E, K, \alpha_L, \gamma, k, \nu, \rho$
Slag diameter	3.6 mm (spherical) 7.8 mm (spherical) 13.5 mm (spherical)
Slag porosity	no voids foam with void diameter = 0.45 ± 0.28 mm
Slag matrix material	SiO_2 (amorphous) Ca_2SiO_4 (amorphous)
Inclusion material	Fe^0 (SiO_2 matrix) Fe_2O_3 (Ca_2SiO_4 matrix)
Inclusion diameter	Spherical inclusions, gaussian distribution 711 ± 563 µm
Slag temperature	900 ˚C → T_∞
Water temperature	$T_\infty = 22\ °C$
	Heat transfer by temperature-dependent boiling mechanism
Air temperature	$T_\infty = 22\ °C$
	Heat transfer by natural convection

The governing equation of the transient 2-dimensional temperature field is given in **Eq. (5-39)**. The inherent heterogeneity of the slag required that Fe^0 and Fe_2O_3 inclusions be included in the model. The matrix material was populated with inclusions to match the empirical measured inclusion distribution and located in the slag matrix by a random number generator applied to the radial (r) and angular (θ) axes. The initial T was set as uniform throughout the slag. Internal voids were filled with air in the simulation. Internal convection within the voids was ignored, but radiative and conductive heat transfer were included in the calculation. Surface heat transfer (**Eq. (5-40)**) was balanced between convective transfer to the fluid and conductive transfer from the slag interior (T_R). Slag-air heat transfer was modeled as natural convection. The large initial temperature difference between the slag and water resulted in film boiling, followed by nucleate boiling as temperatures converge. The effective of boiling condition on h is provided in **Eq. (5-41)** through **Eq. (5-44)** [Incropera and DeWitt, 2002]. The bubble diameter in **Eq. (5-43)** was the largest diameter bubble that can be generated at the interface of the slag and water. The physical meaning of the equations used in the COMSOL simulation is provided in **Fig. 5-35**.

$$\frac{\partial T}{\partial t}(r, \theta, t) = \left(\frac{1}{\rho c_p}\right)\left(\frac{1}{r}\frac{\partial}{\partial r}\left(rk\frac{\partial T}{\partial r}\right) + \frac{1}{r^2}\frac{\partial T}{\partial \theta}\left(k\frac{\partial T}{\partial \theta}\right)\right) \qquad (5-39)$$

$$h[T(R, \theta, t) - T_\infty] = -k\nabla T_R \qquad (5-40)$$

$$h = \frac{k}{\phi} Nu \tag{5-41}$$

$$Nu_{film\ boiling} = 0.67 \left[\frac{g(\rho_l - \rho_v)\left(h_{fg} + 0.8 c_{p,v}(T_R - T_{sat})\right)\phi^3}{v_v k_v (T_R - T_{sat})} \right]^{0.25} \tag{5-42}$$

$$Nu_{nucleate\ boiling} = \frac{(^q/_A)\phi_{bubble}}{(T_R - T_{sat})k_l} \tag{5-43}$$

$$\phi_{bubble} = \left[\frac{\gamma_{sur}}{g(\rho_l - \rho_v)} \right]^{0.5} \tag{5-44}$$

$$\sigma_T = \Delta T \alpha_L E e^{\left(\frac{-\tau_R E}{K_R} \right)} \tag{5-45}$$
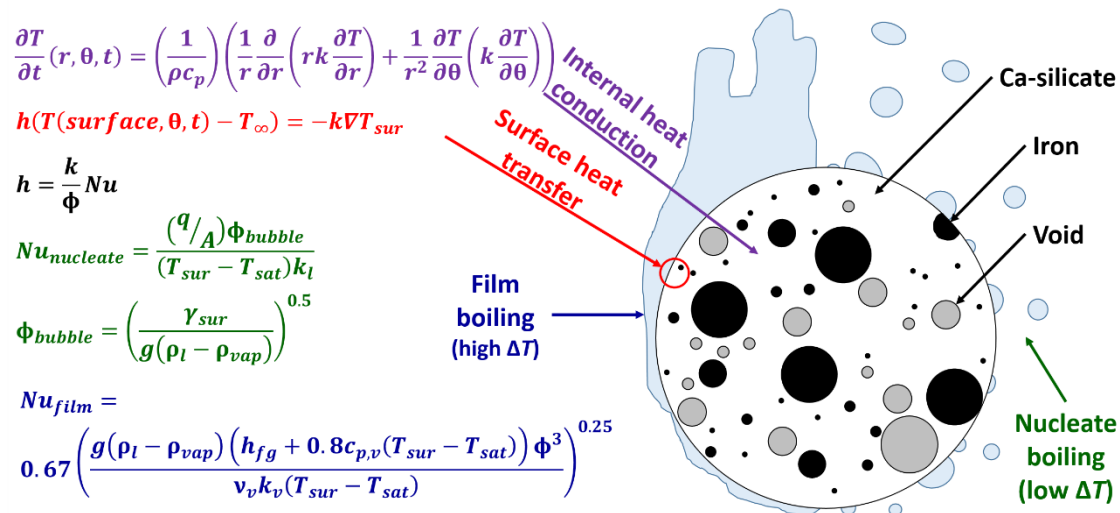

Fig. 5-35. Schematic of the COMSOL model of solid-state slag quenching.

The temperature field within slag was converted to thermal stress in the COMSOL program. The radially dependent stress was measured at 10 equally spaced locations around the central axis of the slag and averaged to determine the stress as a function of depth (care was taken to avoid locations on a void or iron inclusion). When the bulk stress exceeded the fracture stress of the material, it was assumed fractures occurred to the extent available from the thermal energy. Grain boundary fractures between the amorphous matrix and the iron or iron oxide inclusions were calculated as the stress radiating from such inclusions. The size and depth of the inclusions was altered to determine the degree of fracturing of the matrix material around such inclusions. An example of the transient bulk stress distribution is given in **Fig. 5-36**. The predicted bulk and grain boundary fractures are

provided in **Fig. 5-37**, along with the empirical results for comparison. The results make clear the importance of grain boundary fracture mechanism even in amorphous slags, due to inclusion of metallic iron and iron oxide species. The analysis results mirror those of quenching a plate-shaped slag in terms of a maximum depth at which tensile stresses exist.
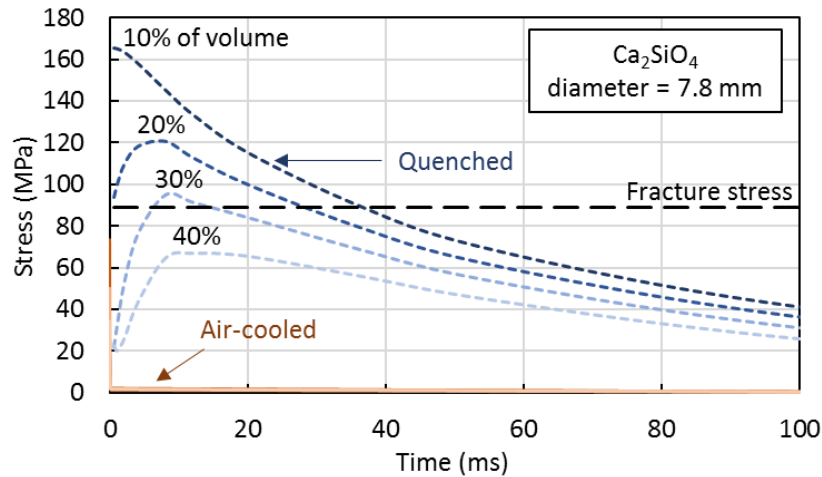

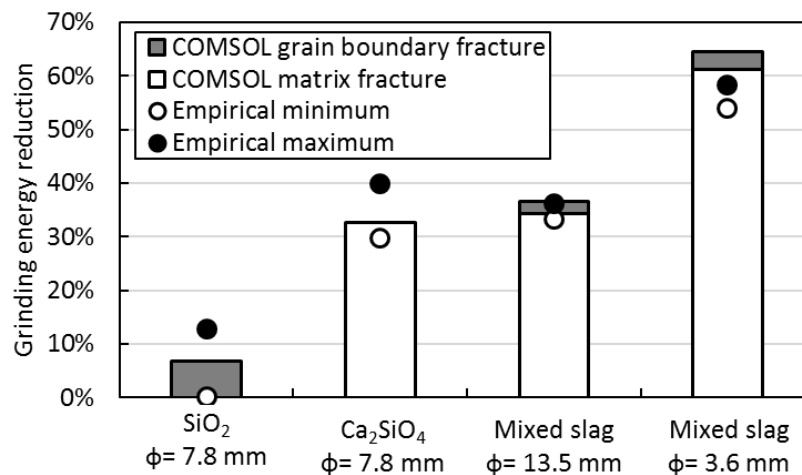**Fig. 5-36.** Example COMSOL simulation of transient stress profile in a water-quenched and air-cooled slag particle.

Fig. 5-37. Comparison between COMSOL simulation of fracture extent and empirical results.

Chapter-specific symbols and abbreviation list

A: Projected area

a: Fracture radius

a_n: Stoichiometric number of atoms per molecule

AR: Aspect ratio

D: CO_2 diffusivity through the product layer

E: Isotropic tensile elastic modulus

E_G: Grinding energy

E_T: Thermal energy

e: Elementary charge

f: Percentage of stretched binding sites

f_D: Fractal dimension

G: Shear modulus

GB: Grain boundary fracture

G_C: Critical crack energy release

g: gravity

h: Heat transfer coefficient

H: ½ slag plate thickness

ΔH_f: Molar enthalpy of formation

IA: Intra-amorphous fracture

IG: Intragranular fracture

IM: Inter-mineral fracture

ISM: Iron and steelmaking

k: Thermal conductivity

k_B: Stefan-Boltzmann constant

k_{bulk}: Bulk thermal conductivity

k_{eff}: Effective bulk thermal conductivity

k_{poly}: Polycrystalline conductivity

k_{spall}: Conductivity within voids created by spalling facture

K: Bulk modulus

K_R: Relaxation parameter

K_C: Critical stress intensity factor for fracture propagation

L: Bond stretch length

LCA: Life cycle assessment

m: Generic mineral

M: Madelung constant

M_V: Molar volume

MYNA process: In-container solidification with solid-state quenching

N: Number of atoms per m³

n: Mineral-specific constant related to compressibility

N_A: Avogadro's constant

n_B: Number of grain boundaries

n_B^*: Number of grain boundaries under tension

n_i: Number of particles in a distribution

n_V: Largest common valence number in a molecule

P: Perimeter

QM: Quantum mechanics

PSD: Particle size distribution

q/A: Heat flux

RF: Surface roughness factor

r: Radius

r_i: Radius of an individual particle in a distribution

r_{limit}: Energetically-limited radius of particles after thermal fracturing

r^L: Major radius of equivalent area ellipse

r^S: Minor radius of equivalent area ellipse

r': Radius of equivalent area circle

R_0: Equilibrium interatomic distance of an unstrained crystal

R_λ: Kapitza resistance

SA: Surface area

SCM: Shrinking core model

T: Temperature

T_L: Liquidus temperature

ΔT: Temperature difference

ΔT_C: Critical temperature difference for thermal fracturing

U_C: Minimum crystal energy

U_m: Internal energy of a molecule

V_e: Ellipse volume

w: Inherent flaw size

x: Generic fracture type

X: Particle diameter

X_{SM}: Surface area-moment mean diameter

X_{VM}: Volume-moment mean diameter

X_{99}: 99% volume passing diameter

Y: Shape factor

α: Thermal diffusivity

α_L: Linear coefficient of thermal expansion

β: Volumetric expansion coefficient

$\partial\xi/\partial t$: Reaction rate

δ: Reaction depth

δ_V: Void depth

ε: Emissivity

ε_0: Vacuum permittivity

ε_G: Efficiency of grinding

ζ: Loading rate dependent mesoscale roughness factor

ρ: Density

ρ_l: Density of liquid phase

ρ_v: Density of vapor phase

$\sigma_{c,x}$: Critical tensile stress for fracture propagation

σ_x: Tensile stress

σ_T: Thermal stress

v: Poisson's ratio

τ_R: Relaxation time

φ_m: Volume fraction of component m

φ_{spall}: Volume fraction of void space from spalling

ϕ: Diameter

γ_{GB}: Interfacial energy at grain boundary fracture

γ_{IA}: Interfacial energy at intra-amorphous fracture

γ_{IG}: Interfacial energy at intragranular fracture

γ_{IM}: Interfacial energy at inter-mineral fracture

γ_S: Interfacial energy

γ_{sur}: Surface tension

ξ: Reaction extent

References

Bahr, H.A., Fischer, G. and Weiss, H.J., 1986. Thermal-shock crack patterns explained by single and multiple crack propagation. Journal of Materials Science, 21(8), pp.2716-2720.

Bahr, H.A., Weiss, H.J., Bahr, U., Hofmann, M., Fischer, G., Lampenscherf, S. and Balke, H., 2010. Scaling behavior of thermal shock crack patterns and tunneling cracks driven by cooling or drying. Journal of the Mechanics and Physics of Solids, 58(9), pp.1411-1421.

Bodor, M., Santos, R.M., Kriskova, L., Elsen, J., Vlad, M. and Van Gerven, T., 2013. Susceptibility of mineral phases of steel slags towards carbonation: mineralogical, morphological and chemical assessment. European Journal of Mineralogy, 25(4), pp.533-549.

Bourdin, B., Marigo, J.J., Maurini, C. and Sicsic, P., 2014. Morphogenesis and propagation of complex cracks induced by thermal shocks. Physical review letters, 112(1), p.014301.

Bragg, W.L. and Nye, J.F., 1947. A dynamical model of a crystal structure. Proc. R. Soc. Lond. A, 190(1023), pp.474-481.

Chen, C.H., Bouchbinder, E. and Karma, A., 2017. Instability in dynamic fracture and the failure of the classical theory of cracks. Nature Physics, 13(12), p.1186.

Cleary, P.W. and Morrison, R.D., 2016. Comminution mechanisms, particle shape evolution and collision energy partitioning in tumbling mills. Minerals Engineering, 86, pp.75-95.

Frøseth, A.G., Van Swygenhoven, H. and Derlet, P.M., 2005. Developing realistic grain boundary networks for use in molecular dynamics simulations. Acta materialia, 53(18), pp.4847-4856.

Gautier, M., Poirier, J., Bodénan, F., Franceschini, G. and Veron, E., 2013. Basic oxygen furnace (BOF) slag cooling: laboratory characteristics and prediction calculations. International Journal of Mineral Processing, 123, pp.94-101.

Hasselman, D.P.H., 1969. Unified theory of thermal shock fracture initiation and crack propagation in brittle ceramics. Journal of the American Ceramic society, 52(11), pp.600-604.

Incropera, F.P. and DeWitt, D.P., 2002. Fundamentals of heat and mass transfer 5th edition. Hoboken: John Willey & Sons, Inc.

International Energy Agency Staff, 2008. CO2 Emissions from Fuel Combustion: 1972. Organization for Economic.

Jain, A. and Ong, S.P., 2013. A. Jain, SP Ong, G. Hautier, W. Chen, WD Richards, S. Dacek, S. Cholia, D. Gunter, D. Skinner, G. Ceder, and KA Persson, APL Mater. 1, 011002 (2013). APL Mater., 1, p.011002.

Liu, C., Zhang, Y.Z., Li, J., Li, J.G. and Kang, Y., 2016. Thermodynamic simulation on mineralogical composition of CaO–SiO 2–Al 2 O 3–MgO quaternary slag system. SpringerPlus, 5(1), p.1028.

Marschall, I., Kölbl, N., Harmuth, H. and Xia, G., 2013. Investigation of continuous casting slag films sampled on site and comparison with laboratory results. Journal for Manufacturing Science & Production, 13(1-2), pp.103-114.

Moore, D.E. and Lockner, D.A., 1995. The role of microcracking in shear-fracture propagation in granite. Journal of Structural Geology, 17(1), pp.95-114.

Morrison, R.D. and Cleary, P.W., 2008. Towards a virtual comminution machine. Minerals Engineering, 21(11), pp.770-781.

Mousavi, S.T., Richart, N., Wolff, C. and Molinari, J.F., 2015. Dynamic crack propagation in a heterogeneous ceramic microstructure, insights from a cohesive model. Acta Materialia, 88, pp.136-146.

Pehl, M., Arvesen, A., Humpenöder, F., Popp, A., Hertwich, E.G. and Luderer, G., 2017. Understanding future emissions from low-carbon power systems by integration of life-cycle assessment and integrated energy modelling. Nature Energy, 2(12), p.939.

Purwanto, H., Mizuochi, T., Tobo, H., Takagi, M. and Akiyama, T., 2004. Characteristics of glass beads from molten slag produced by rotary cup atomizer. Materials transactions, 45(12), pp.3286-3290.

Sadrai, S., Meech, J.A., Ghomshei, M., Sassani, F. and Tromans, D., 2006. Influence of impact velocity on fragmentation and the energy efficiency of comminution. International Journal of Impact Engineering, 33(1-12), pp.723-734.

Smith, D.S., Grandjean, S., Absi, J., Kadiebu, S. and Fayette, S., 2003. Grain-boundary thermal resistance in polycrystalline oxides: alumina, tin oxide, and magnesia. High Temperatures. High Pressures, 35(1), pp.93-99.

Tanemura, M., 2003. Statistical distributions of Poisson Voronoi cells in two and three dimensions. FORMA-TOKYO-, 18(4), pp.221-247.

Tromans, D. and Meech, J.A., 2002. Fracture toughness and surface energies of minerals: theoretical estimates for oxides, sulphides, silicates and halides. Minerals Engineering, 15(12), pp.1027-1041.

Tromans, D. and Meech, J.A., 2004. Fracture toughness and surface energies of covalent minerals: theoretical estimates. Minerals engineering, 17(1), pp.1-15.

Tromans, D., 2008. Mineral comminution: energy efficiency considerations. Minerals engineering, 21(8), pp.613-620.

Wang, B., Yu, Y., Lee, Y.J. and Bauchy, M., 2015. Intrinsic nano-ductility of glasses: the critical role of composition. Frontiers in Materials, 2, p.11.

Waples, D.W. and Waples, J.S., 2004. A review and evaluation of specific heat capacities of rocks, minerals, and subsurface fluids. Part 1: Minerals and nonporous rocks. Natural resources research, 13(2), pp.97-122.

Zavattieri, P.D. and Espinosa, H.D., 2001. Grain level analysis of crack initiation and propagation in brittle materials. Acta Materialia, 49(20), pp.4291-4311.

Chapter 6: CO$_2$ Mineralization

Stabilization of CO$_2$ into calcium and magnesium carbonates is the long-term fate for the majority of carbon in the atmosphere, hydrosphere, and pedosphere [Wilson, 2004]. Reactions of carbon dioxide with calcium and magnesium silicates to form calcium and magnesium carbonates is thermodynamically spontaneous and exothermic [Lackner et al., 1995]. For these reasons, there has been concerted effort over the past 30 years to realize a climate change mitigation technology based on CO$_2$ mineralization. Such technologies have examined CO$_2$ mineralization in natural geologic formations (in-situ), using intentionally mined natural minerals (ex-situ), and extant anthropogenic wastes. In-situ mineralization is often envisioned as a way to remove the leakage risk from CCS and to ameliorate safety concerns from the public. While some projects intentionally produce rapid in-situ mineralization [Gunnarsson et al., 2018], the majority of research is in accurately projecting the degree of mineralization that will naturally occur over the course of centuries [Kelemen et al., 2018]. For ex-situ and waste-based CO$_2$ mineralization, the rate of conversion is of central importance; unlike in-situ mineralization, there is no physical barrier separating non-stabilized CO$_2$ from the environment. Though the thermodynamics are favorable, the kinetics of CO$_2$ mineralization using calcium and magnesium silicates are slow [Mayes et al., 2018]. Ex-situ methods can therefore be further separated based on their method for managing the issue of CO$_2$ mineralization rate. Methods that do not alter the thermodynamic pathway are termed 'passive' while other methods are termed 'enhanced'. The vast majority of research has focused on enhanced methods, which can be further segregated into biotic and abiotic methods. Biotic methods focus on the addition of finely ground materials to the complex ecosystem of soil; this in turn may enhance dissolution of calcium and magnesium silicates while also facilitating improved soil health and thus carbon retention [Beerling et al., 2018]. Some work on utilizing slag in the environment exists [Horii et al., 2013], but environmental concerns (e.g., heavy metal leaching, pH alteration) [Koryak et al., 2002; Navarro et al., 2008; Roy et al., 2002] generally make such applications problematic. Abiotic enhanced mineralization includes chemical enhancement (e.g., pH-based dissolution and precipitation) [Azadarpour 3t al., 2015], alteration of the pCO$_2$ beyond that available in extant anthropogenic streams [Bourgeois et al., 2018], high temperatures [Farhang et al., 2016], and mechanical modification of the mineral structure [Li and Hitch, 2018] amongst others [Pan et al., 2012; Romanov et al., 2015; Yuen et al., 2016]. Unfortunately, the vast majority of studies on enhanced mineralization methods fail to perform a LCA that accounts for CO$_2$ emissions along the whole process chain (e.g., CO$_2$ emissions from chemical production, heating, etc.). When properly accounted (cf. Zimmermann et al., 2018) the majority of 'accelerated' slag-based CO$_2$ mineralization methods provide net CO$_2$ reductions at the process level, but a net increase in CO$_2$ at the level of the planet [Ncongwane et al., 2018]. A common tactic to improve net CO$_2$ mineralization extent is to rely on low carbon renewable energy (RE) sources (e.g., solar power with lithium ion battery storage: PV+LiB). This, often unstated, assumption may be suitable for processes directly relying on energy for 'enhancement' if the additional CAPEX of purpose-built RE is clearly considered. However, reliance on the grid to provide low carbon energy implies the process will be applied in a future energy system (i.e., not realizable in most locations for at least several decades) [Jacobson et al., 2017]. Moreover, depending on RE-based chemical or non-recoverable additive production inherently assumes on-site production with the associated increase in CAPEX, OPEX, and system complexity. The literature on enhanced CO$_2$

mineralization methods is starkly lacking in recognition of these realities, calling into question the technical and financial viability of these proposals.

The difficulty in achieving net CO_2 reduction using enhanced mineralization leaves passive CO_2 mineralization as the only technically viable option. Unfortunately, attempts to realize such goals have largely been deemed impractical due to the slow kinetics of the slag-CO_2 reactions [Huijgen and Comans, 2005]. Nevertheless, three decades of research (primarily focused on aqueous methods) has attempted to overcome the slow kinetics using various equipment and process designs. Despite this, the mineralization efficiency of the field remains relatively flat with the only clear and consistent improvement in performance coming from reduction of slag particle size (cf. **Fig.2-23**). The lack of clear signal leading to improved passive CO_2 mineralization may be due to unaccounted for properties of slag. Most ISM slags contain dozens of distinct mineral phases which are effectively ignored by researchers in preference for accounting of total calcium and magnesium content. However, it is already established that CO_2 mineralization rates using alkaline earth silicates must be evaluated on a mineral-by-mineral basis [Daval et al., 2010]. A few authors have attempted to calculate the mineral-specific reaction extent of common slag minerals [Ashraf and Olek, 2016; Bodor et al., 2013] but none have determined the diffusivity of CO_2 through the product layer of slag (D). Consequently, the results from CO_2 mineralization of slags in the literature are difficult to apply generally, to integrate into process optimization, or to analyze novel methods for process improvement. Furthermore, as the diffusivity of the disparate minerals is undefined, the interactions between minerals (e.g., blocking of reactions due to geometric constraints) remains undefined.

This thesis focuses on direct, gas-solid CO_2 mineralization without use of chemical or thermal enhancement. Additionally, the source of CO_2 is flue gas, absent any CO_2 capture or purification. Conceptually, slag is ground to a predetermined particle size distribution and carried along a covered conveyor. Flue gas flows countercurrent to the slag, converting gaseous CO_2 into calcium and magnesium carbonates. The temperature is passively maintained at roughly 30 ˚C by the heat content of the flue gas and the natural environment. The relative humidity within the covered conveyor is maintained at 90% by way of pans of still water. The covered conveyor reactor concept is shown in **Fig. 6-1**.
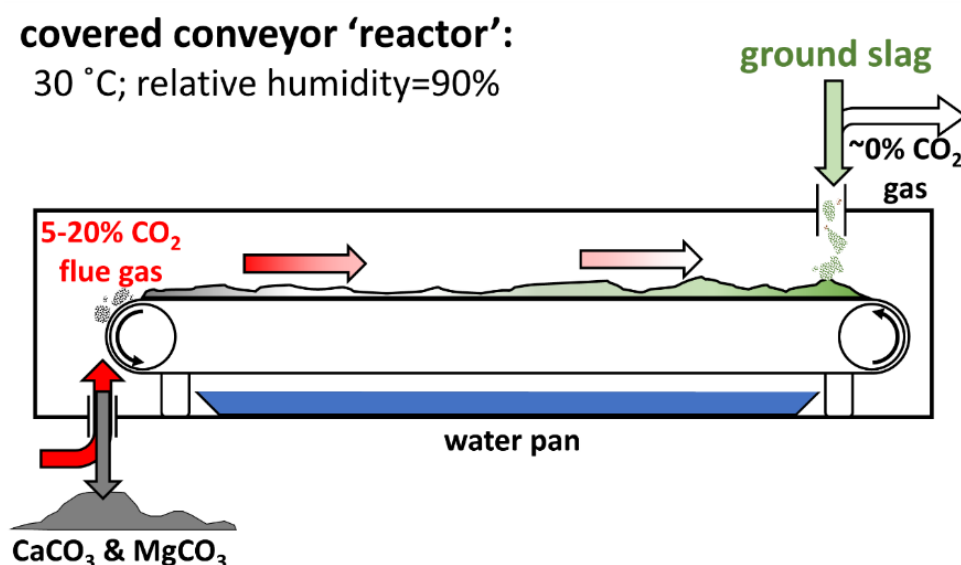

Fig. 6-1. The covered reaction conveyor concept for CO_2 mineralization of ISM slag.

Chapter highlights

- The shrinking core model was modified to account for the full particle size distribution and the roughness factor of powdered samples.
- Use of statistical metrics (e.g., surface area moment mean, BET surface area) will inherently produce erroneous predictions or results when compared to the full particle size distribution.
- The majority of minerals, and their amorphous counterparts, found in iron and steelmaking slag were synthesized via solid state sintering and verified via quantitative X-ray diffraction.
- Each mineral was left in a 5% and 20% CO_2 atmosphere at 30 ˚C and a relative humidity of 90% for up to 2 months.
- The CO_2 diffusion coefficient for each mineral was calculated, showing ~8 orders of magnitude difference.
- Amorphous compounds are particularly prone to low CO_2 diffusivities.
- Inclusion of Mg, Al, or Fe into a Ca-silicate structure dramatically reduces the CO_2 diffusion coefficient.
- The diffusion coefficient for a heterogeneous slag sample was calculated from the underlying mineral composition, mineral specific diffusion coefficients, and effective medium theory.
- Unreactive materials, or minerals with very low CO_2 diffusivity, can act to occlude high CO_2 diffusivity materials from reaction with CO_2, so-called 'mineral locking'.
- Mineral locking is a function of the ratio of the particle size to the grain size and the quantity of reactive material.
- Mineral locking can nearly eliminate the mineralization potential of a heterogeneous slag when the reactive species is less than 20% of the volume and the mineral grains are much smaller than the slag particles.

Publications relevant to this chapter

- Quantification of the CO_2 mineralization potential of ironmaking and steelmaking slags under direct gas-solid reactions in flue gas, International Journal of Greenhouse Gas Control Vol. 87C p.100-111 (2019), **Corey A. Myers**, Takao Nakagaki, and Kosei Akutsu.
- Experimental determination of CO_2 mineralization depth of slag minerals at CO_2 concentrations available in iron and steelmaking flue gases, 14th International Conference on Greenhouse Gas Control Technologies Melbourne Australia (October 2018), **Corey Myers** and Takao Nakagaki.

6.1. Mineral-specific product layer CO₂ diffusion coefficient

The gas-solid reaction of inorganic minerals with CO_2 is generally accepted to follow the tenets of the Shrinking Core Model (SCM) [Yagi and Kunii ,1955]. The SCM was introduced as a method for calculating gas-fluid reaction rate and extent relevant to many chemical systems. The simplifications within the SCM are as follows: the solid is considered a non-porous, smooth sphere, mass transfer occurs between the solid and a non-depletable fluid, the process occurs isothermally, and a shell of reacted material forms as the reaction progresses towards the center of the particle. If the reacted material leaves the particle then the theory is termed the Shrinking Particle Model; if a homogeneous distribution of pores is present, then it is termed the homogeneous model. The continued presence of a product layer (PL) and the general growth of the PL into pore spaces suggests the SCM is most appropriate for modeling slag-based CO_2 mineralization.

In SCM, three potential reactions can act as the rate-limiting mechanism: gas phase diffusion to the solid, diffusion through the product layer (diffusivity: D), or reaction between the gas and solid. Based on available data, the diffusion through the PL of slag minerals is orders of magnitude less than mineralization reactions or gas phase diffusion [Bhatia and Perlmutter, 1983; Stendardo and Foscolo, 2009]. The movement of the reaction interface is substantially slower than the rate of gas diffusion and the CO_2 mineralization reaction itself (i.e., pseudo steady state approximation); therefore, at any instant the boundary is assumed to be stationary, allowing for simple calculation of the concentration profile.

The key advantage of SCM is the ability to move directly between reaction rate ($\partial \xi / \partial t$) or extent ($\xi$) and diffusivity ($D$), and vice versa. This means that the effect of complex geometries can be removed from experimental data and the true $\partial \xi / \partial t$ can be parsed. In other words, once the D is known, the $\partial \xi / \partial t$ for any geometry can be determined. This provides the opportunity for system-level process optimization and unbiased comparison of minerals, equipment, and processes.

6.1.1. Modification to the Shrinking Core Model

Though a powerful theoretical framework, some of the simplifying assumptions of SCM are not appropriate for slag-based CO_2 mineralization and thus require modification for accurate quantification of D and application to calculation of $\partial \xi / \partial t$ and ξ. These failings are due to miscalculation of the SA from lack of consideration of the full particle size distribution (PSD) and a lack of consideration of the surface roughness factor (RF).

Particle Size Distribution.

In the simplest implementation of the SCM, a single particle is used to represent all of the particles. The reason for this application is primarily due to issues with measurement of polydisperse particle samples. Until recently, it was not possible to automate the counting of particles from micrographs using computers. This made the counting of particles a labor and time intensive task, particularly given that several thousand particles should be measured for each sample to generate an accurate representation of the population PSD [Vigneau et al., 2000]. As such, most researchers relied on either sieve-based or laser-based PSD determination. Under ideal conditions, sieve-based PSD provides a rough, piece-wise distribution. In reality, the accuracy of sieve-based analyses decreases with the size class of particles due to imperfect separation and increasingly easy loss of sample to the environment [Gadikota et al., 2014]. Moreover, assumptions must be made about the distribution of particle sizes within each sieve group. Notably, when materials are ground to micrometer scale, there is increased tendency to deviate from typical statistical distributions due to the interplay of mechanisms that operate on disparate scales (primarily fracturing and deformation) [Little et al.,

2017]. Laser-based PSD can measure particles at the micrometer scale but without information on the particle shape. As a result, laser-based systems must convert measured particles to an 'equivalent' sized sphere. This 'equivalent' size is the source of large errors in laser-based PSD, especially for non-spherical particles such as slag [Califice et al., 2013]. Laser-based systems typically report sizes in terms of the volume-moment mean diameter (X_{VM}) as defined in **Eq. (6-1)**. In **Eq. (6-1)**, X represents the diameter of each particle in the sample. This distribution focusses on the mass/volume of the particle. In processes where the surface area is critical, it is more common for the surface area-moment mean diameter (X_{SM}) to be utilized (**Eq. 6-2**). Such statistical metrics are inherently less accurate than the full PSD and are limited by the inability to convert back to a PSD.

$$X_{VM} = \frac{\sum X^4}{\sum X^3} \tag{6-1}$$

$$X_{SM} = \frac{\sum X^3}{\sum X^2} \tag{6-2}$$

In recent years, computer-based image analysis has increased to the point where individual particles can be distinguished from a dispersed sample and measured. This allows for the full PSD to be measured. Consideration of the full PSD alters the calculation of ξ in the SCM to **Eq. (6-3)**. In **Eq. (6-3)**, r_i is the radius of an individual particle, δ is the reaction depth, and n_i is the number of particles of radius r_i. In **Fig. 6-2** through **Fig. 6-4**, the errors resulting from using a statistical metric instead of the full PSD when applying the SCM are shown.

$$\xi = \sum_{r_i \geq \delta}^{r_i = r_{max}} \left\{ \left[\frac{r_i^3 - (r_i - \delta)^3}{r_i^3} \right] \times \left(\frac{\frac{4}{3}\pi r_i^3 n_i}{\sum_{r_i = r_{min}}^{r_i = r_{max}} \frac{4}{3}\pi r_i^3 n_i} \right) \right\} + \sum_{r_i = r_{min}}^{r_i < \delta} \left(\frac{\frac{4}{3}\pi r_i^3 n_i}{\sum_{r_i = r_{min}}^{r_i = r_{max}} \frac{4}{3}\pi r_i^3 n_i} \right) \tag{6-3}$$
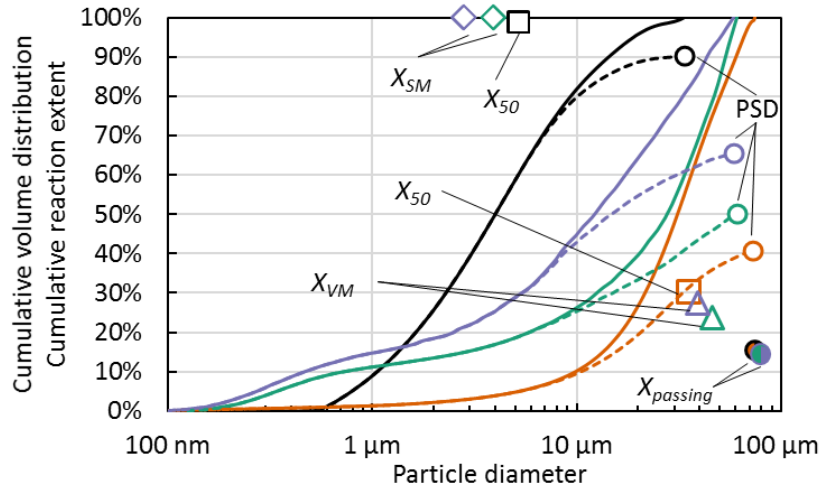
Fig. 6-2. Alteration of calculated reaction extent using SCM for a polydisperse sample that occurs when using summary statistics instead of the complete PSD. A uniform reaction depth of 2 μm was used. Solid lines are the cumulative volume distribution, dashed lines are the cumulative reaction extent. Particle size distributions are from Ashraf and Olek, 2016 (black and orange) and Santos et al., 2013 (purple and green data).
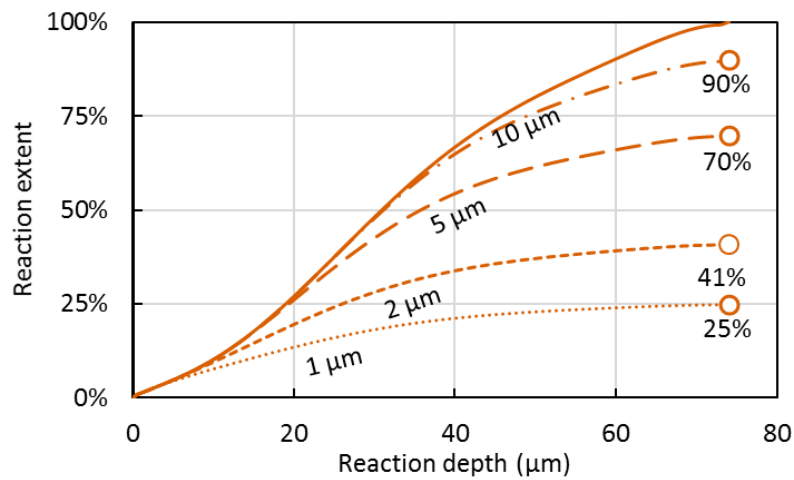

Fig. 6-3. Alteration of ξ as a function of δ when SCM is applied using the full PSD. The unreacted PSD data is from Ashraf and Olek, 2016.
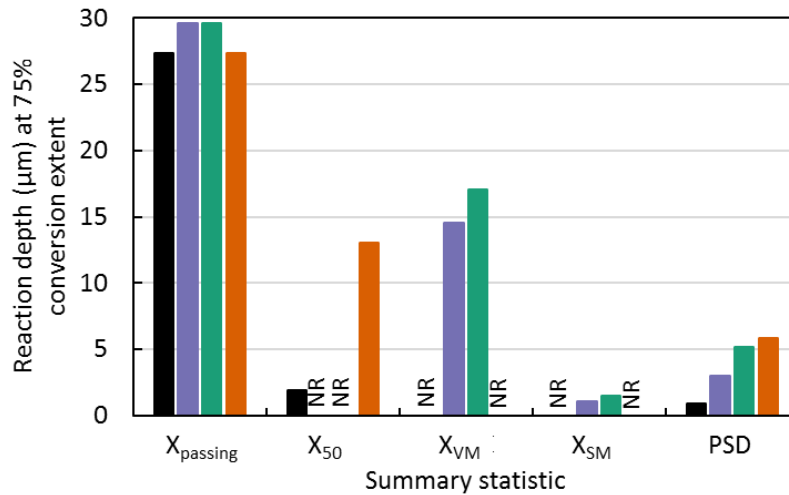
Fig. 6-4. Calculated δ when the sample $\xi = 75\%$ using the PSD from Ashraf and Olek, 2016 (black and orange) and Santos et al., 2013 (purple and green data). 'NR' indicates the data was not reported in the source papers.

As described in Chapter 2.2.5, the PSD of ground materials is typically not Gaussian, but rather lognormal [Kolmogorov, 1941]. The assumption of a Gaussian distribution leads to significant errors in the initial SA/V and its progression due to the underestimation of the number of small particles in the distribution.

Surface Roughness.

The SCM assumes a spherical particle, and therefore no change in the geometry of the reaction front with reaction (only a change in size). While this is appropriate for many manufactured products, evaluation of extant slag (or any ground mineral) shows a distinctly non-spherical shape due to the random nature of impact events and randomly oriented preferred fracture planes. The concept of sphericity is not completely misplaced as geometry and the stochastic nature of impacts will tend to favor rounded shapes over highly irregular shapes. However, fracturing of particles less than ~1 µm in diameter are generally less favored than distortion of the particle due to the brittle-to-ductile transition [Tromans and Meech, 2001]. Additionally, the fracture planes of minerals contain inherent roughness at the scale of nanometers. In traditional particle size analysis methods, the surface roughness is ignored or quantified using some form of adsorption testing (e.g., Brunauer–Emmett–Teller). Unfortunately, adsorption testing does not indicate how the surface area is arranged. Therefore, the evolution of the reaction front into the particles as CO₂ mineralization occurs cannot be modeled or quantified. Along with a number-based PSD, computer-based image analysis can also provide measurement of the projected area (A) and projected perimeter (P) of the particles. Combined this information allows for more precise quantification of particle shape. The PSD and innate non-sphericity allow for the smoothing effects reaction front progression to be calculated and accounted for in CO₂ mineralization rate equations. Using the A, the equivalent area circle radius (r'), equivalent area ellipse major radius (r^L), and minor radius (r^S) for each particle in a sample can be calculated. Using the box-counting method, the fractal dimension (f_D) of the overall sample can also be easily measured.

The aspect ratio for each particle ($AR = r^L/r^S$) was calculated and the volume-averaged summation across all n particles in the sample was performed as shown in **Eq. (6-4)**. Given the likely axis of stability in the gravitational field of the Earth, the ellipse volume (V_e) was calculated by

assuming the vertical dimension is equal to r^S per **Eq. (6-5)**. Assumption of spherical particles naturally overestimates δ (**Eq. (6-6)**) relative to ellipsoids (**Eq. (6-7)**) due to the change in SA/V, with larger AR giving larger errors. The RF was first calculated in 2D (**Eq. (6-8)**) and the sample roughness factor is calculated as the sample volume average (**Eq. (6-9)**).

$$AR_{sample} = \frac{\sum_n (AR_n \times V_{e,n})}{\sum_n V_{e,n}} \qquad (6-4)$$

$$V_e = \frac{4}{3}\pi r^L r^S r^S \qquad (6-5)$$

$$\delta = r' \left(1 - (1-\xi)^{1/3}\right) \qquad (6-6)$$

$$(r^S - \delta)^2 (AR r^S - \delta) = AR(r^S)^3 (1-\xi) \qquad (6-7)$$

$$RF = \frac{P/A}{P'/A} \qquad (6-8)$$

$$RF_{sample} = \frac{\sum_n RF_n \times vol_n}{\sum_n vol_n} \qquad (6-9)$$

In **Eq. (6-8)**, the perimeter of an equivalent area circle is $P' = 2\pi r'$. The volume of the sphere built from the equivalent area circle is given by vol. The conversion from 2D to 3D is accompanied by a multiplication by 1.5 given that particles are assumed roughly spherical (**Eq. (6-10)**).

$$\frac{SA/vol}{P'/A} \equiv 1.5 \qquad (6-10)$$

Roughness is a fractal property and should therefore be applied to scales much smaller than those visible under light microscopy. The appropriate application of RF can be determined by analyzing the scale at which a change in the f_D occurs (H). The f_D can be calculated by computer vision using the box-counting method. Application of RF should occur from H down to infinitely small sizes. Inclusion of RF to the smallest scales only effects the early stage $\partial \xi / \partial t$ because the volume contained in the outermost 'rough' features is small (**Fig. 6-5**). As the mineralization reactions progress, features of the reaction surface are removed at a rate correlating with the degree of deviation from a sphere (**Fig. 6-6**). The reduced time (t') to a given reaction extent due to surface roughness is applied to the SCM using **Eq. (6-11)**.
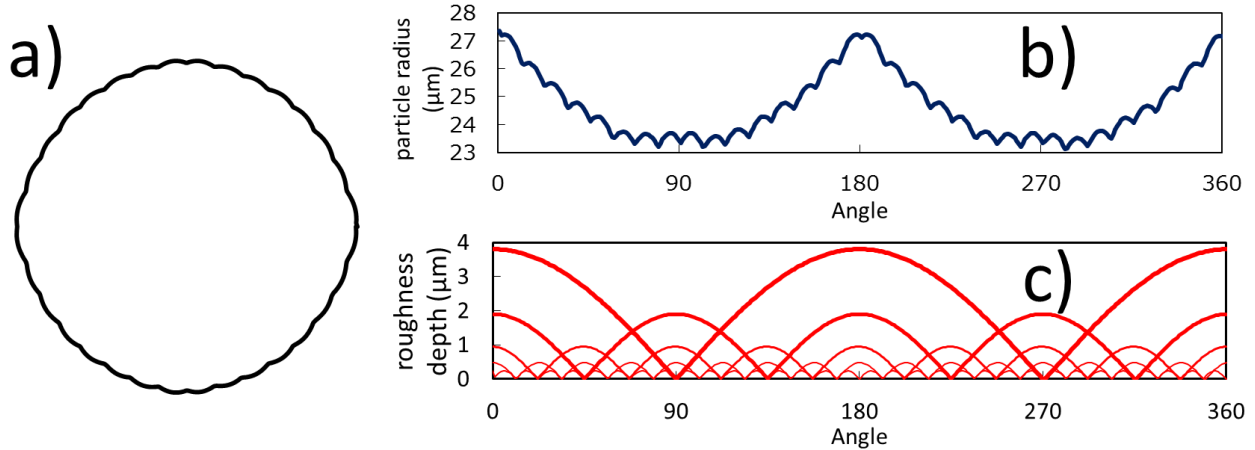
Fig. 6-5. The fractal nature of roughness and its volumetric impact on the overall SA/V as shown for a single rough particle a) in 2D, b) converted to an azimuthal decomposition of the radius, and c) as a Fourier decomposition of the radius.
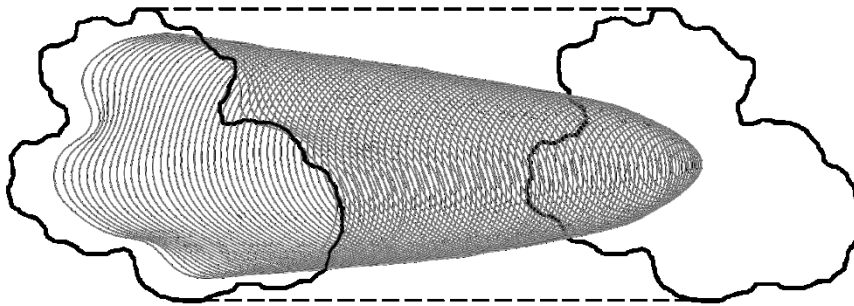

Fig. 6-6. The rounding of the reaction surface of a particle as it undergoes reaction.

$$t' = \frac{\frac{\rho R^2}{6DC_g}\left\{1 - 3\left(\frac{R-\delta}{R}\right)^2 + 2\left(\frac{R-\delta}{R}\right)^3\right\}}{(H/\delta)RF} \tag{6-11}$$

6.1.2. Mineral synthesis and verification

The majority of minerals found in ISM slag have no economic value and are thus not commercially available. Moreover, most are not common in nature. Therefore, all minerals were synthesized from the simple oxides. Stoichiometric mixes of powdered oxides were mixed by hand in a mortar and pestle for 1 hour and then pressed without binder into 10 mm diameter pellets at 500 GPa until pressure could be maintained for 3 minutes. Pelletizing was performed to enhance inter-particle contact and homogenization. After pelletizing, samples were placed in 99.9% alumina crucibles, typically stacking two pellets atop one another. Pellets were heated in an inert gas furnace (KDF 1700 electric muffle furnace); both N_2 and Ar atmospheres were used with no apparent difference between the produced samples. Samples were heated to an estimated solid-state sintering temperature (T_{sinter}), which was initially estimated as 95% of the T_L estimated from DNN. The heating protocol began with an initial 30-minute hold at 30 ˚C to purge the furnace of air. The temperature was increased at 5 ˚C/min to 350 ˚C and held for 1 hour. This initial hold was intended to decompose any Mg-carbonates that had formed during the mixing and pelletizing process due to

reaction with ambient CO_2. The samples were then heated at 5 ˚C/min to 550 ˚C and held for 1 hour to decompose any (Ca/Mg)-hydroxides. Finally, heating at 5 ˚C/min to 900 ˚C with a one-hour hold was used to decompose any $CaCO_3$. Heating from 900 ˚C to T_{sinter} occurred at 5 ˚C/min and T_{sinter} was held for 1 hour. Cooling of the sample was set to 10 ˚C/min to 30 ˚C. If the heating profile resulted in partial or complete melting of the sample (**Fig. 6-7**), new pellets were produced, and the process was repeated at a lower T_{sinter}. If the sample appeared unchanged (i.e., no indication of fusion), then the sample was reground, re-pressed, and reheated at a higher T_{sinter}. If visual inspection indicated fusion of the samples (e.g., apparent by removal of fines and/or fusion of pellets sitting atop one another) (**Fig. 6-8**), then the solid pellets were crushed in a hydraulic press, ground in a zirconia mortar and pestle, and analyzed by a Rigaku SmartLab® X-ray diffractometer for crystallinity and mineral composition. Analysis of XRD results was performed with the PDXL V.2 software package. When the target mineral did not exceed 60 mass% of the sample, the sample was reground, re-pressed, and re-sintered. This iterative process progressively enhanced the produced compounds towards the stoichiometric composition mineral. The overall process of mineral synthesis is displayed as a process flow diagram in **Fig. 6-9**. The sintering temperatures tested for each mineral and the qualitative results are provided in **Fig. 6-10**. The XRD graphs for the successfully synthesized minerals are provided in **Fig. 6-11**. The T_{sinter} for each mineral, the mineral purity of each sample, and the composition of any impurities is provided in **Table 6-1**.

Fig. 6-7. Partially melted samples, a) $Ca_3Al_2Si_3O_{12}$ at 1265 ˚C, b) $CaSiO_3$ at 1838 ˚C, and c) $Ca_3MgSi_2O_8$ at 1441 ˚C.
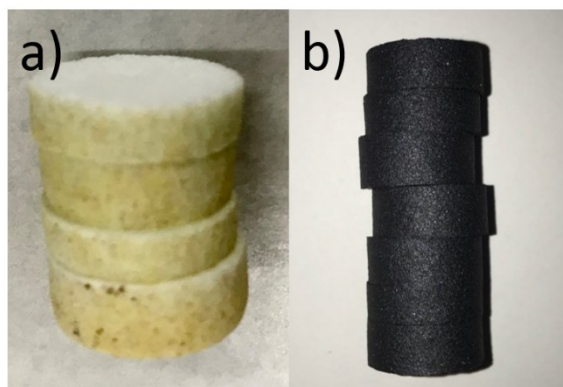

Fig. 6-8. Sintering of samples indicated by partial fusion of separate cylinders without change in shape for a) $CaMgSi_2O_6$ and b) $Ca_4Al_2Fe_2O_{10}$.
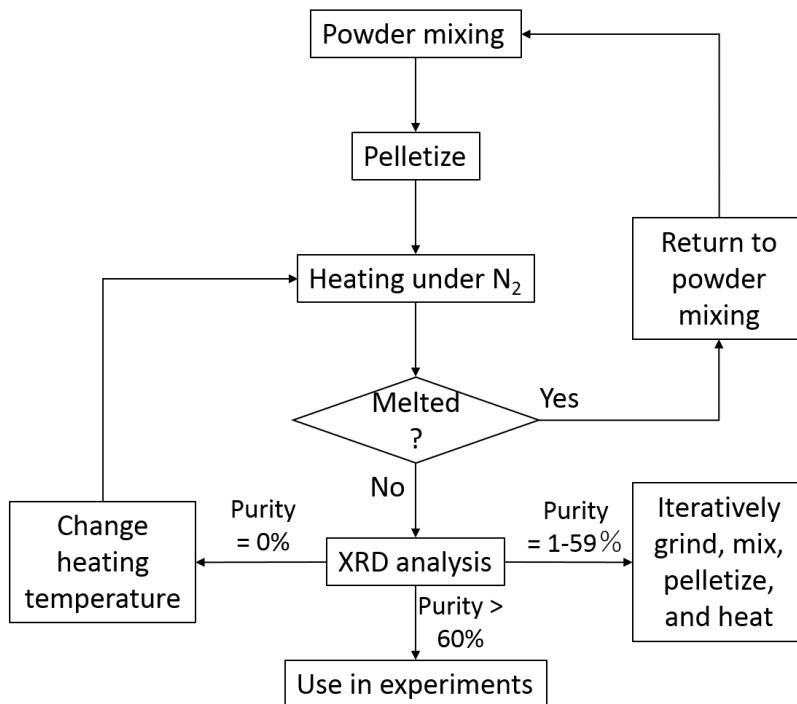
Fig. 6-9. The process flow diagram for mineral synthesis.
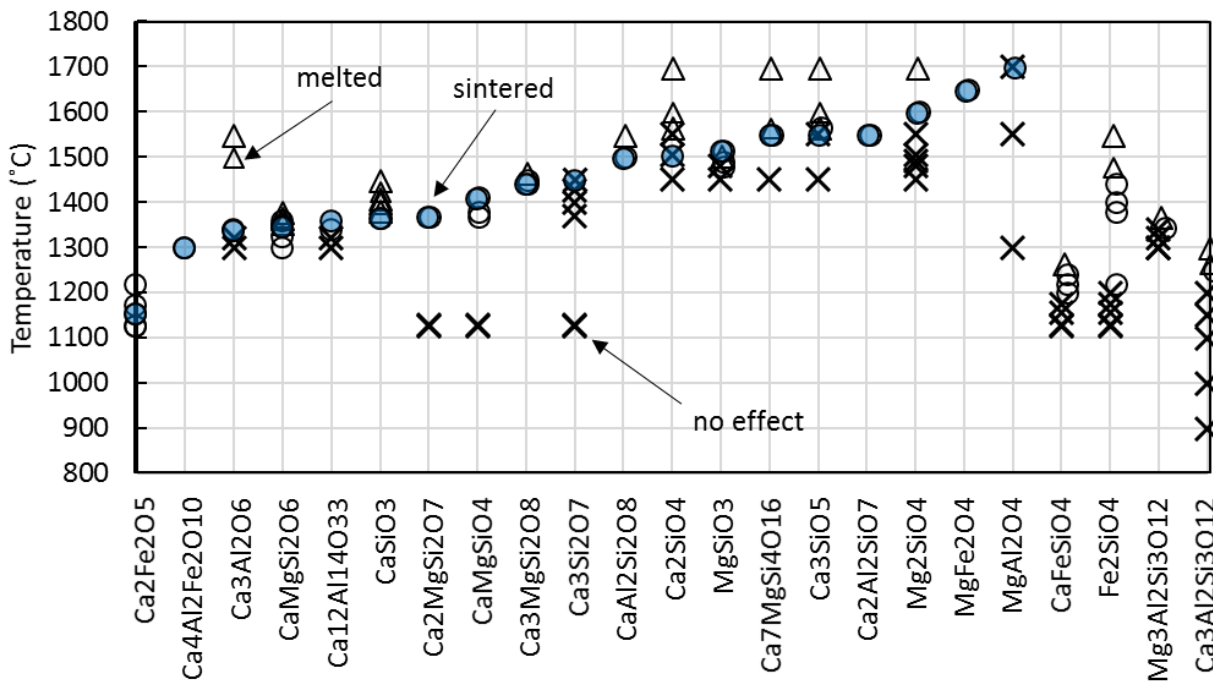
Fig. 6-10. The qualitative results of sintering. Blue circles indicate sintering that produced high purity crystals, white circles indicate low purity crystals, triangles indicate partial or complete melting, and a lack of fusion is indicated by Xs.
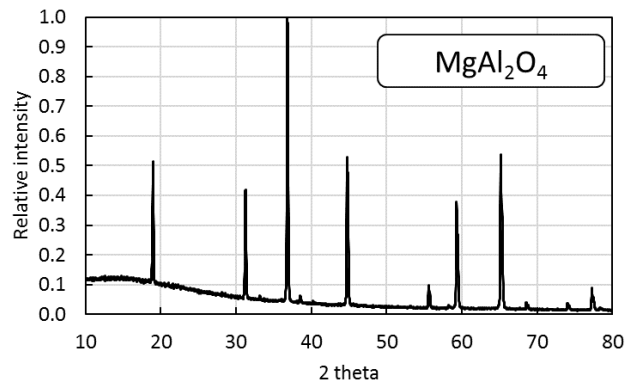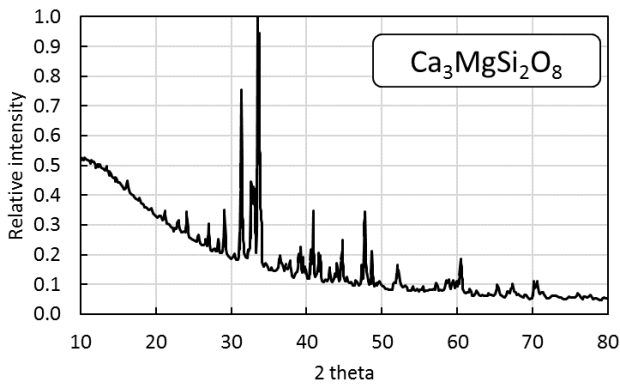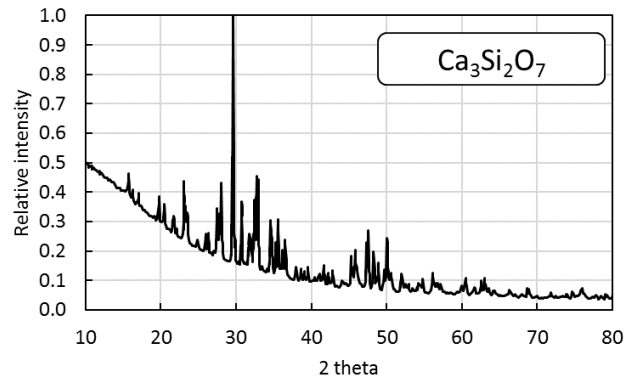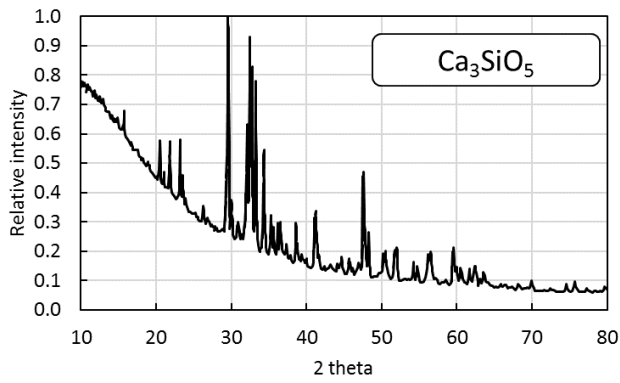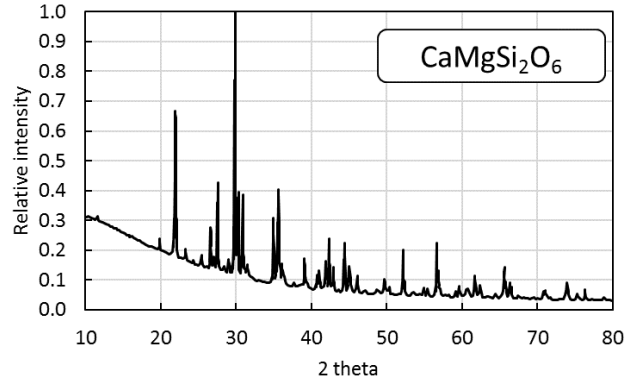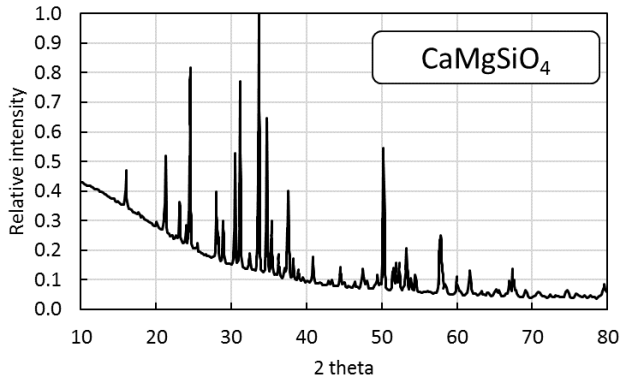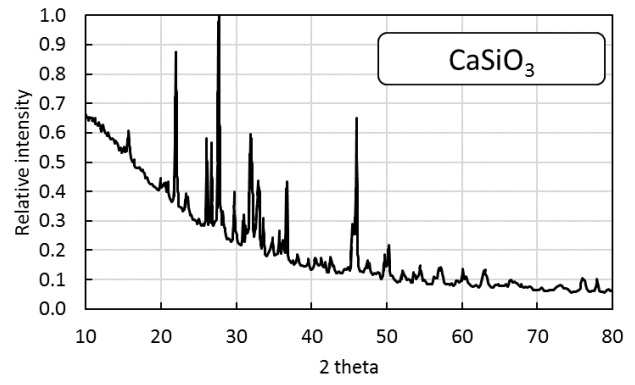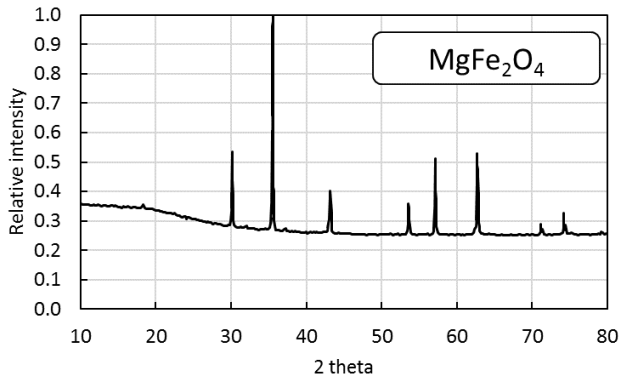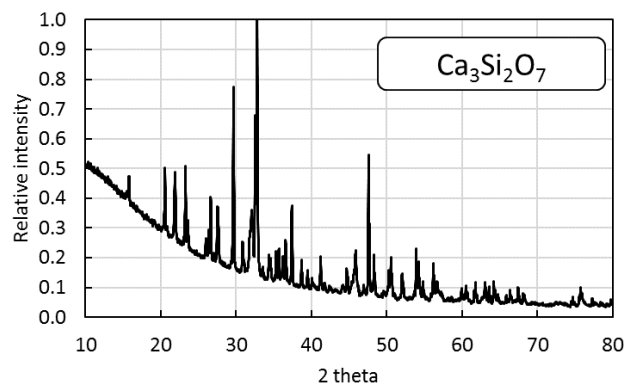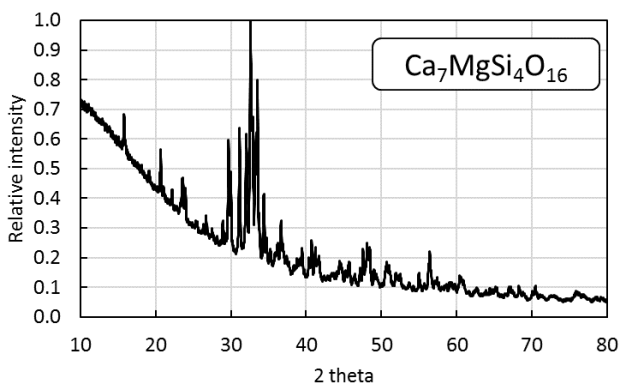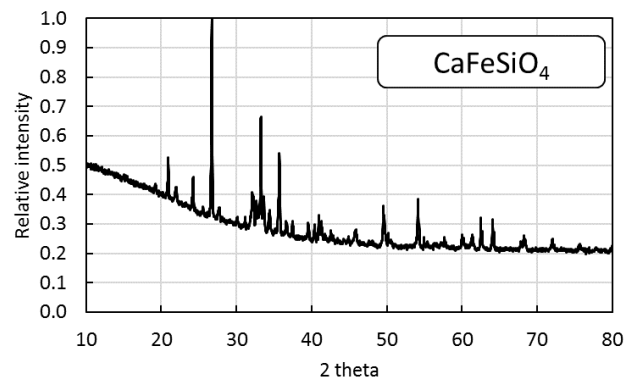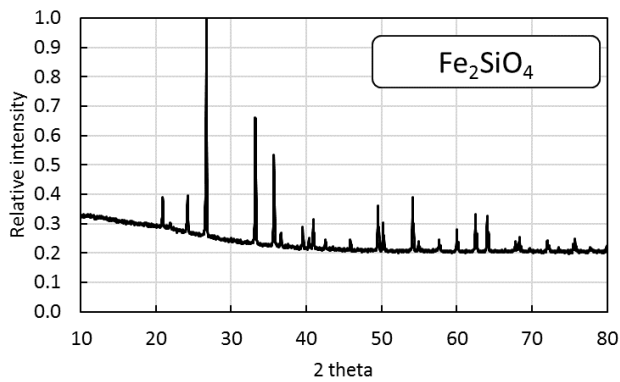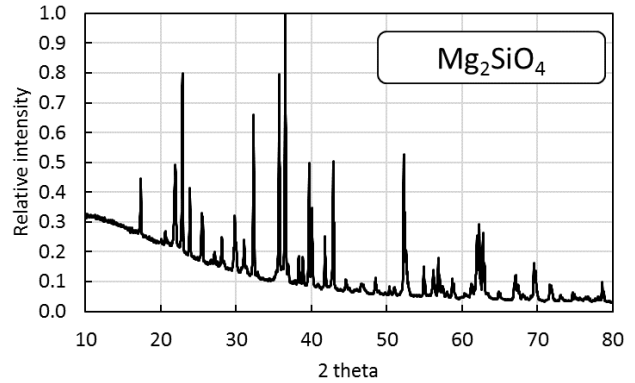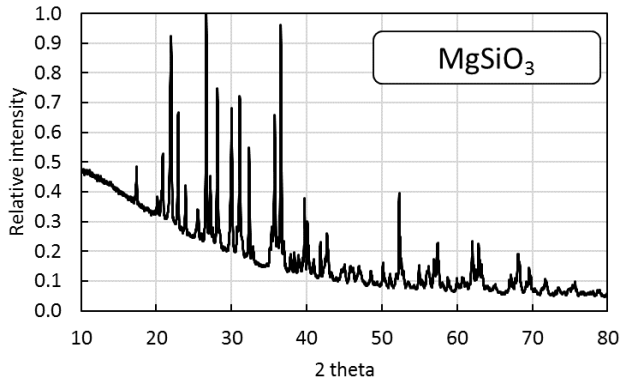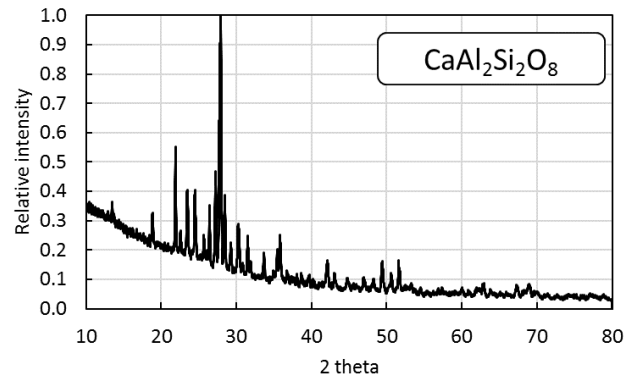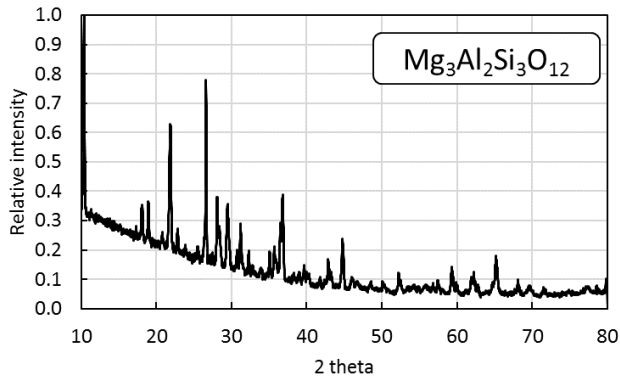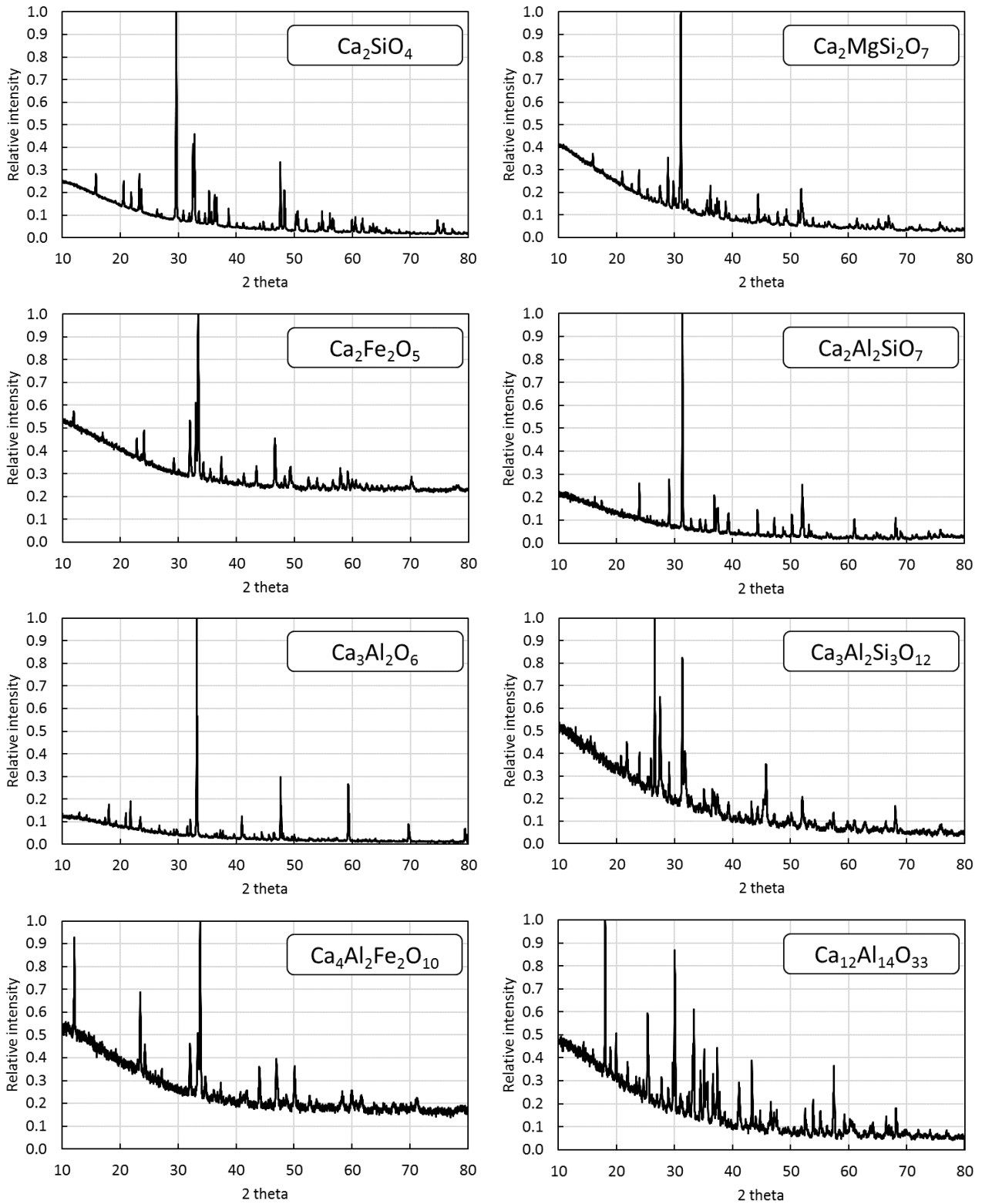
Fig. 6-11. XRD analysis for the 24 minerals successfully synthesized by solid-state sintering.

Table 6-1. The sintering temperature, purity, impurity composition, and shape characteristics of synthetic slag minerals.

	Mineral	T_{sinter} (°C)	Purity (mass%)	Impurities (mass%)
Oxides	CaO	[a]NA	100	[b]UD
	MgO	[a]NA	100	[b]UD
Ca-silicates	Ca_2SiO_4	1505	98.9	[b]UD
	$CaSiO_3$	1365	98.1	SiO_2
	$Ca_3Si_2O_7$	1449	77.0	$CaSiO_3$ (14.7) Ca_2SiO_4 (7.9)
	Ca_3SiO_5	1550	63.8	Ca_2SiO_4 (35.6) CaO (1.6)
Mg-silicates	Mg_2SiO_4	1600	91.5	MgO (5.3) SiO_2 (3.3)
	$MgSiO_3$	1515	83.4	SiO_2 (10.6) Mg_2SiO_4 (6.0)
	$CaMgSi_2O_6$	1347	83.9	SiO_2 (16.1)
	$CaMgSiO_4$	1410	78.2	$Ca_2MgSi_2O_7$
	$Ca_2MgSi_2O_7$	1368	78.0	$CaMgSi_2O_6$ (14.1) CaO (3.8) $CaSiO_3$ (3.3) MgO (0.8)
	$Ca_3MgSi_2O_8$	1441	68.9	$Ca_2MgSi_2O_7$
	$Ca_7MgSi_4O_{16}$	1550	no RIR	[b]UD
(Al/Fe)-minerals	Fe_2O_3	NA	100	[b]UD
	$Ca_3Al_2O_6$	1340	100	[b]UD
	$MgAl_2O_4$	1550	100	[b]UD
	$MgFe_2O_4$	1649	100	[b]UD
	$Ca_2Al_2SiO_7$	1550	100	[b]UD
	$CaAl_2Si_2O_8$	1500	100	[b]UD
	$Ca_2Fe_2O_5$	1155	92.2	CaO
	$Ca_{12}Al_{14}O_{33}$	1360	89.0	CaO

	$Mg_3Al_2Si_3O_{12}$	1345	39.8	$Mg_2Al_4Si_5O_{18}$ (39.8) $MgAl_2O_4$ (31.0) Mg_2SiO_4 (29.0)
Failed minerals	Fe_2SiO_4	[c]1127-1440 [d]1220-1440 [a]NA	0	[a]NA
	$CaFeSiO_4$	[c]1127-1265 [d]1200-1240 [e]1265	0	[a]NA
	$Ca_3Al_2Si_3O_{12}$	[c]900-1300 [d]1250 [e]1265	0	[a]NA

a: not analyzed; b: undetected; c: range of no indication of phase change; d: range of apparent sintering; e: onset of melting

6.1.3. Amorphous compound synthesis and verification

As many slags, intentionally or by chance, include glassy components, amorphous versions of the primary slag minerals were also synthesized and tested. Production procedure mirrored that of crystalline slags except in the heating and cooling protocol. Samples were intentionally heated above their T_L and held for 1 hour. It was attempted to keep the temperature as close to the T_L as possible to reduce the risk of dissolution of the alumina crucible, causing alteration to the melt composition. Additionally, due to the dynamics of the cooling process, it is beneficial to have as low a temperature as possible when cooling is begun, in order to inhibit the formation of crystals upon cooling. Cooling was performed by removing the crucible directly from the furnace and placing it on a heat resistant, insulating surface in room air (**Fig. 6-12**). Cooled, amorphous samples were crushed and analyzed by XRD to ensure no peaks indicating crystal phases were present. Synthesis was not attempted for minerals known to have melting points above 1700 ˚C. The XRD graphs for the produced minerals are provided in **Fig. 6-13**.

Fig. 6-12. Removal of liquid slag from the furnace for rapid solidification.
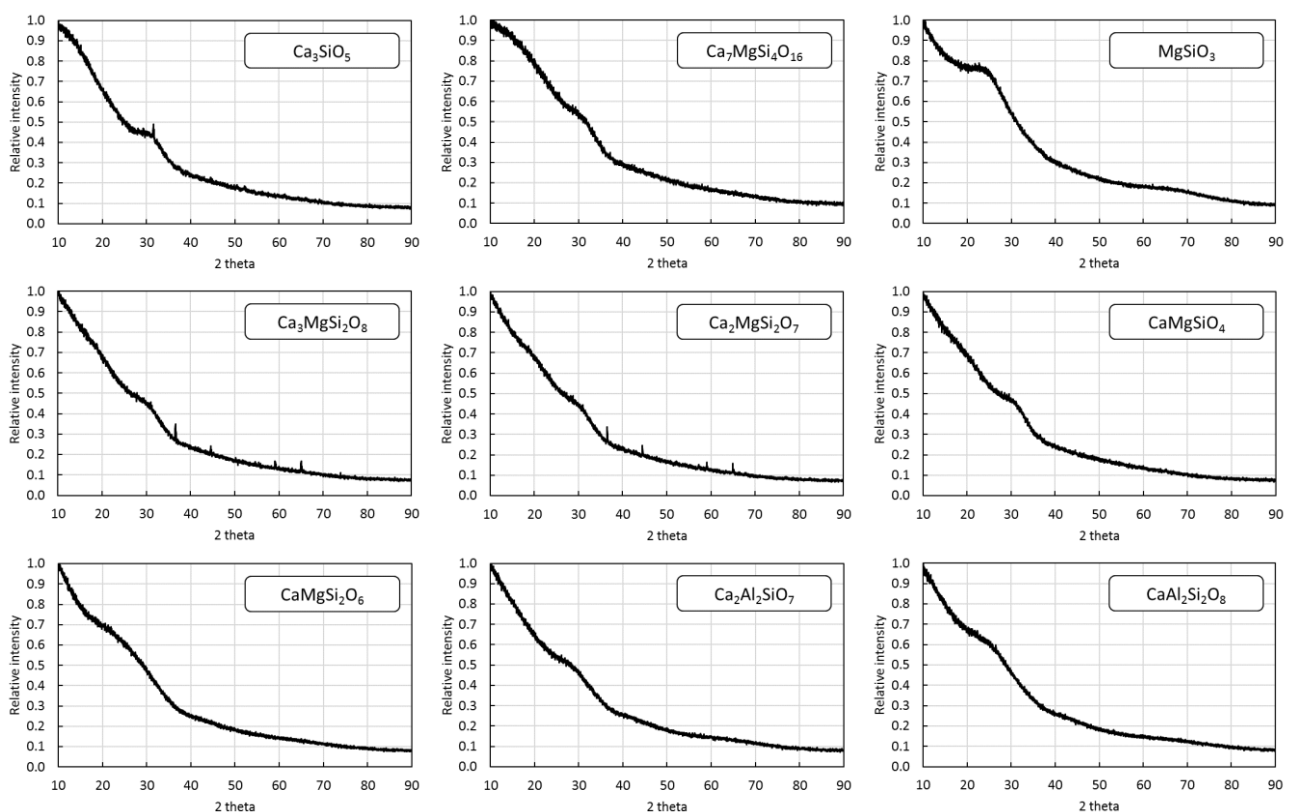
Fig. 6-13. XRD graphs of the synthesized amorphous solids.

6.1.4. Particle size distribution and roughness factor analysis

After synthesis, crystalline and amorphous samples were sieved to between 10 and 90 μm such that a large reaction rate signal could be observed in a relatively short time frame while also avoiding practical experimental issues that come with excessive SA and possible surface activation [Gadikota et al., 2014]. To quantitatively account for non-spherical particles and/or large surface roughness, computer vision analysis of optical micrographs was performed using the open source software ImageJ. In order to ensure the sample used in the measurements was representative of the population distribution, 40 subsamples were taken from each sample. Imaging was done at 400× magnification. Typically, direct imaging of particles requires 500-1500 particles to ensure an accurate distribution [Barreiros et al., 1996; Vigneau et al., 2000]. All samples exceeded this amount, with the

least number of particles being 1,966 obtained for $Ca_3Al_2O_6$ and the largest number of particles being 15,289 obtained for $Ca_2MgSi_2O_7$. To promote dispersion of particles (i.e., reduce the instances of particles sitting atop one another), samples were placed on a plastic plate; the electrostatic charge of the plate was sufficiently strong to disperse the small particles.

In the analysis by ImageJ, each micrograph was converted to a binary color scale. Next the built-in threshold function was applied to insert boundaries between touching particles. After thresholding, each micrograph was manually checked and edited to ensure overlapping particles were segregated and particles with the threshold applied were truly overlapping (**Fig. 6-14**). Once a satisfactory accounting of the particles was complete, the P, A, and r^L were measured by ImageJ.
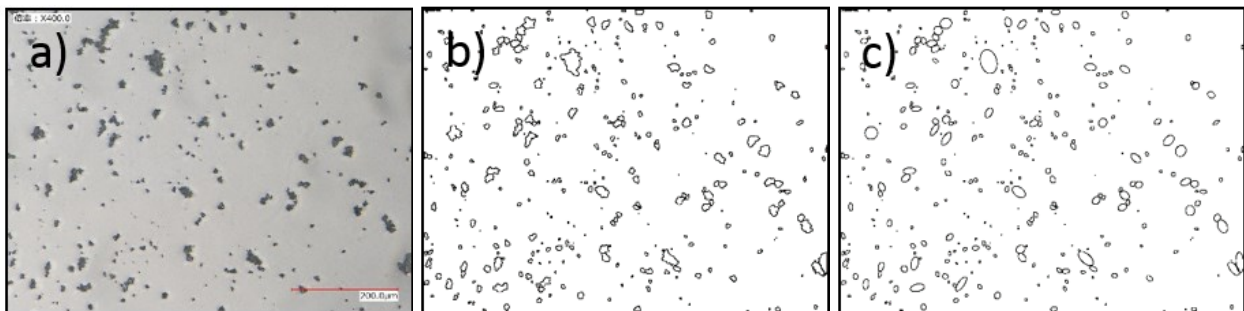
Fig. 6-14. The steps of the semi-automated image analysis performed by ImageJ with a) the initial image, b) the outline of the particles, and c) conversion to equivalent area ellipses.

An example of the dependence of AR on particle size for the most highly elongated mineral (Ca_2SiO_4) is shown in **Fig. 6-15**. Considering the PSD of the produced minerals, the error in the SCM estimation of δ due to non-sphericity (i.e., AR >1) is less than <10%. Moreover, the RF corrects for most of the effect of AR due to its application up to the point of fractal dimension divergence. It was found that the RF can be sufficiently approximated by multiplying the BET surface area by a mesoscale facture roughness related to the rate of stress application [Sadrai et al., 2006].
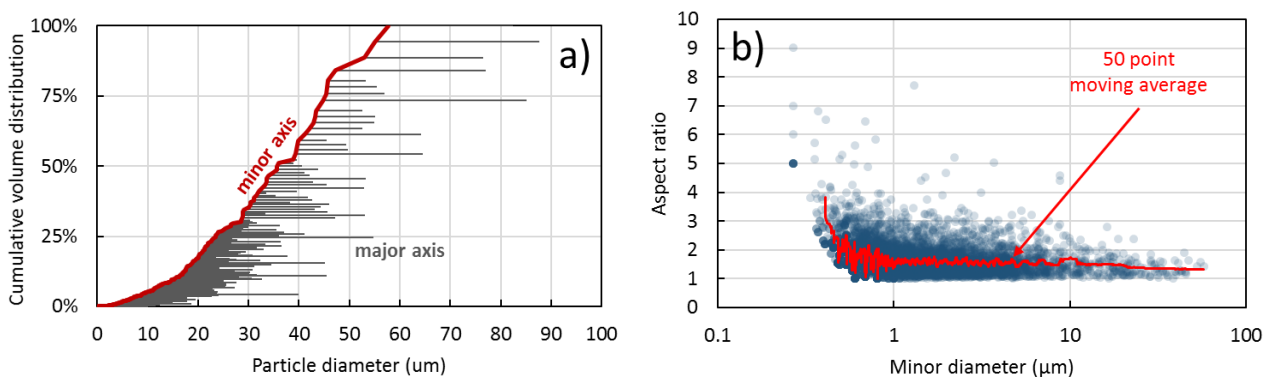
Fig. 6-15. The variation in AR as a function of particle diameter for the most elongated mineral tested (Ca_2SiO_4) showing a) the majority of particles have an $AR < 2$ and b) the bulk of high AR particles are small, and thus have a minimal effect on long term reaction rates.

The f_D for each mineral was calculated to determine the maximum length scale at which the RF should be applied (H). For most compounds H was between 1.9 and 3.8 µm. Simply put, this means the effects of surface roughness are only applicable to the first few micrometers of depth, after which

the depth of most of the irregular features have been smoothed away by the uneven progression of the reaction front. The AR, RF, H, and particle number for each sample are provided in **Table 6-2**.

Table 6-2. The sample-specific shape properties.

	Mineral	AR	RF	H (μm)	Particle #
Oxides	CaO	1.44	2.313	3.8	4932
	MgO	1.46	2.292	3.8	7745
Ca-silicates	Ca_2SiO_4	1.71	2.432	1.9	2641
	$CaSiO_3$	1.44	2.212	2.9	5221
	$Ca_3Si_2O_7$	1.56	2.322	3.8	7531
	Ca_3SiO_5	1.43	1.999	1.9	9283
Mg-containing silicates	Mg_2SiO_4	1.54	2.304	1.4	2604
	$MgSiO_3$	1.43	2.037	2.9	7766
	$CaMgSi_2O_6$	1.58	1.912	2.9	13555
	$CaMgSiO_4$	1.55	2.252	1.9	11694
	$Ca_2MgSi_2O_7$	1.62	2.180	2.9	5218
	$Ca_3MgSi_2O_8$	1.53	2.218	3.8	15289
	$Ca_7MgSi_4O_{16}$	1.48	2.097	1.4	3595
(Al/Fe)-containing minerals	Fe_2O_3	1.39	2.368	3.8	7868
	$Ca_3Al_2O_6$	1.43	2.425	2.9	1966
	$MgAl_2O_4$	1.41	2.234	3.8	9599
	$MgFe_2O_4$	1.39	2.087	1.9	14658
	$Ca_2Al_2SiO_7$	1.56	2.259	1.4	7920
	$CaAl_2Si_2O_8$	1.41	2.048	2.9	5263
	$Ca_2Fe_2O_5$	1.41	2.063	3.8	4886
	$Ca_{12}Al_{14}O_{33}$	1.40	2.157	2.9	6575

6.1.5. CO₂ incubator results

Mineralogically and geometrically characterized samples were subjected to CO_2 at 20 mol% and 5 mol% in an incubator at 30 ˚C with a relative humidity (RH) of 90% for 3-7 weeks. A high RH was maintained to ensure continued mineralization reactions [Longo et al., 2015; Smith et al., 2014] and was achieved by inclusion of a simple tray of water in the incubating chamber. For each mineral, a separate sample was reacted for each pre-designated time period. This was done to ensure that consistent results were achieved (i.e., remove noise due to empirical errors and sample variability).

Each sample was measured via mass change (Δm), thermogravimetry and differential thermal analysis (TG-DTA), C/H/N gas phase elemental analysis (CHN), X-ray fluorescence (XRF), and X-ray diffraction (XRD). Mass change provides a rough estimate of the quantity of CO_2 taken up by reaction with minerals but is unable to distinguish any water that was concurrently taken up by the sample. TG-DTA provides a rough estimate of water and CO_2 content by the different temperatures over which decomposition occurs. However, for some potential products (in particular Mg-carbonates), there is an overlap in the release temperatures for water and CO_2. Moreover, there is the possibility for diffusion-related lag in the release of water from deep in the sample during TG-DTA experiments (as evidenced by a non-zero slope between the water and CO_2 release temperatures in **Fig. 6-16**).
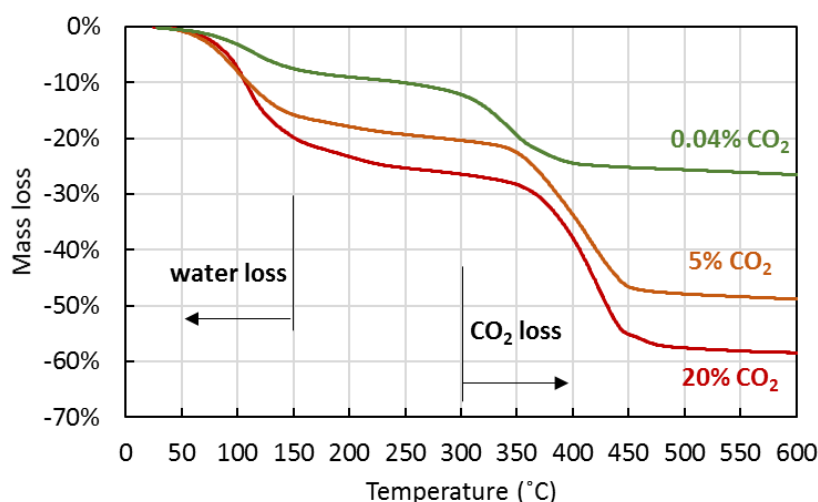
Fig. 6-16. TG-DTA analysis of MgO reacted with CO_2 over 21 days.

In all cases, TG-DTA gave an accurate assessment of the total mass loss and was therefore able to provide the true initial mass of the sample before CO_2 reaction (i.e., TG-DTA improves the estimate of Δm). Quantitative information on the composition of the gases released during heating was provided by C/H/N testing, thereby correcting for any overlap or diffusion-lag that occurs in TG-DTA analysis. X-ray fluorescence was used to quantify the amount of carbon in the sample post reaction and was used as an independent verification of the calculated results from Δm, TG-DTA, and C/H/N analysis. X-ray diffraction analysis was used to determine the mineralogical composition of the product layer materials but not used to calculate the reaction extent. The calculation scheme is provided schematically in **Fig. 6-17**. Examples of the evolution of the XRD analysis for CaO and MgO over the course of reaction with CO_2 are provided in **Fig. 6-18** and **Fig. 6-19**, respectively.
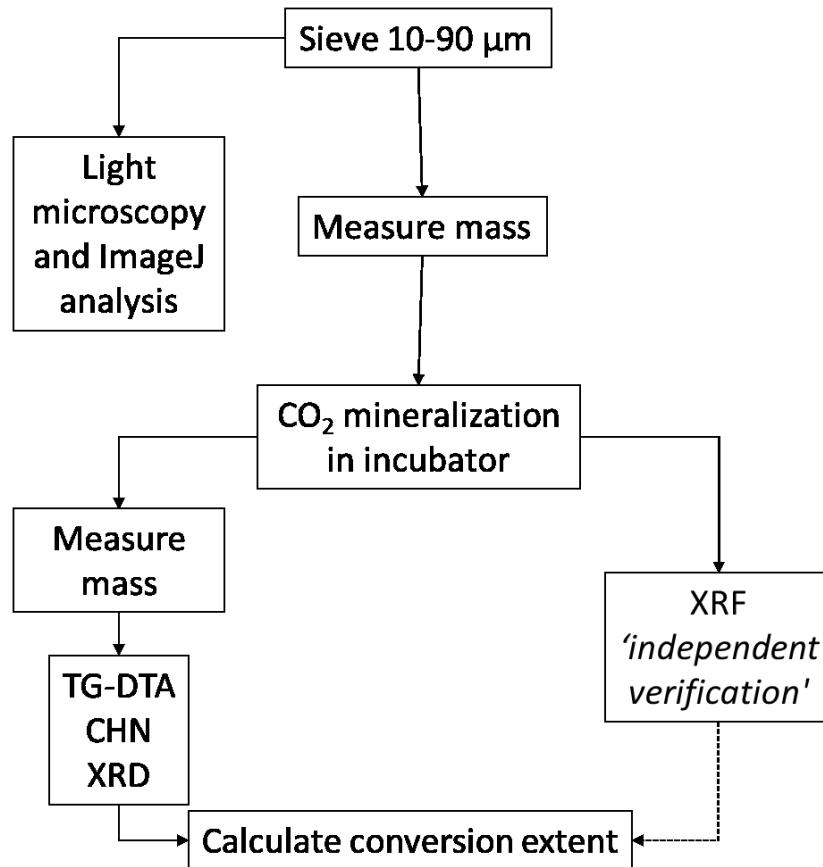
Fig. 6-17. The CO₂ incubation testing and analysis flow diagram.
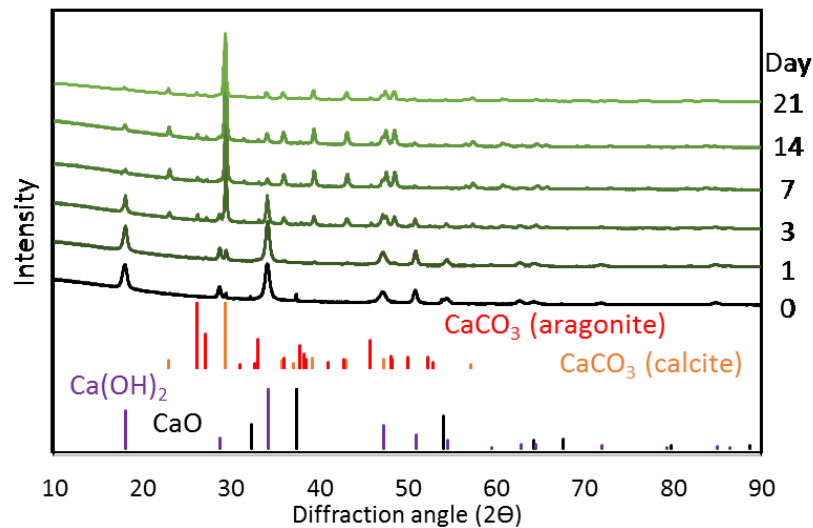
Fig. 6-18. The passive mineralization of CO_2 into various calcium carbonate polymorphs by reaction with CaO. Reactions occurred at 30 ˚C in a relative humidity of 90% and a volumetric CO_2 concentration of 20%.
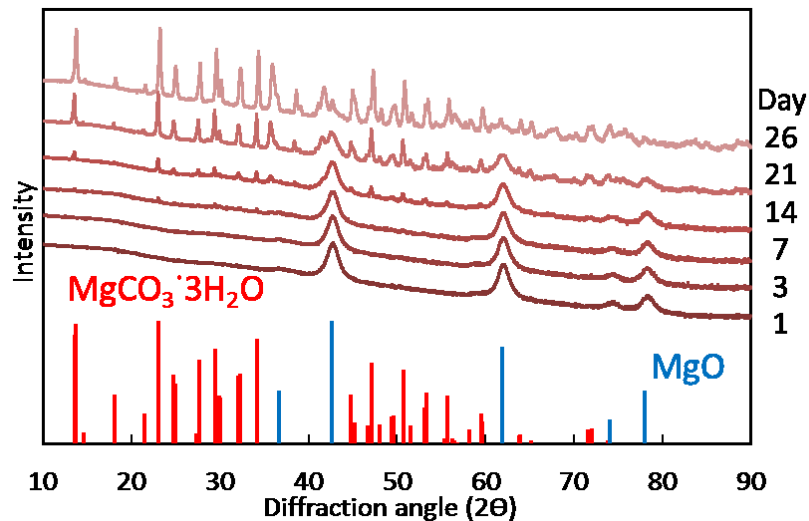
Fig. 6-19. The passive mineralization of CO_2 into Nesquehonite by reaction with MgO. Reactions occurred at 30 °C in a relative humidity of 90% and a volumetric CO_2 concentration of 20%.

The conversion extent (ξ) of the calcium and magnesium content of the minerals was calculated as the molar ratio of mineralized CO_2 to the amount of available Ca and Mg (i.e., assuming that Ca and Mg are homogeneously distributed through the sample). The ξ was used together with the particle size distribution and surface roughness to calculate then transient reaction depth (δ). Graphs of the reaction extent and depth over time for 20 mol% and 5 mol% CO_2 for crystalline compounds are given in **Fig. 6-20**.
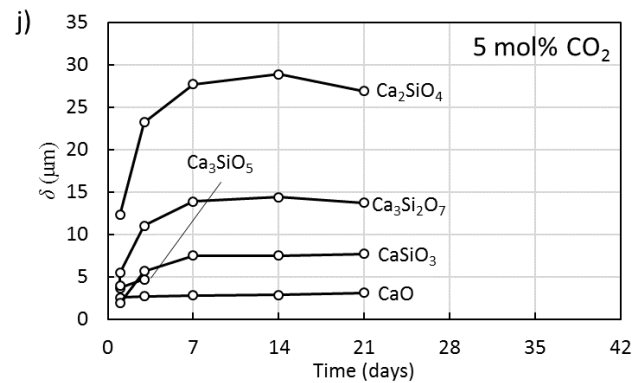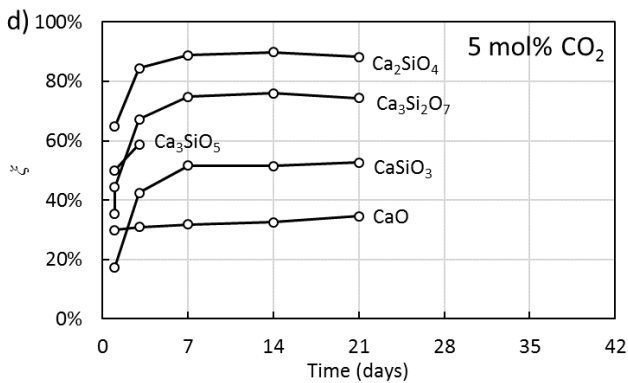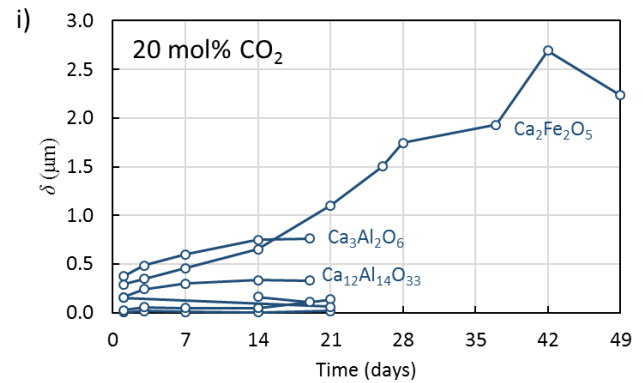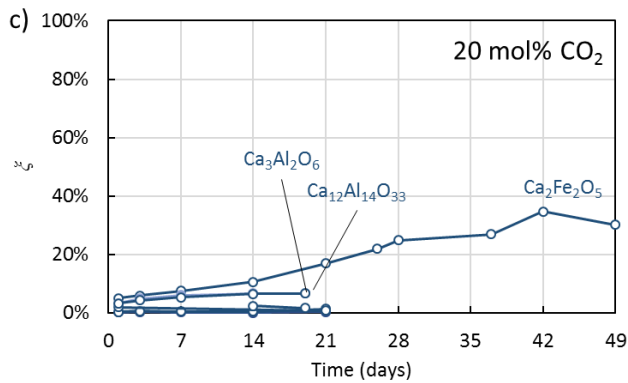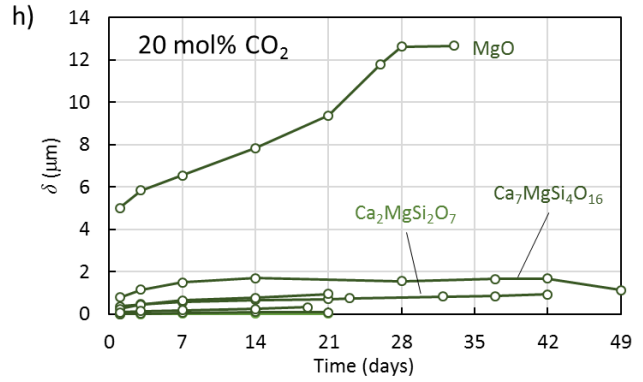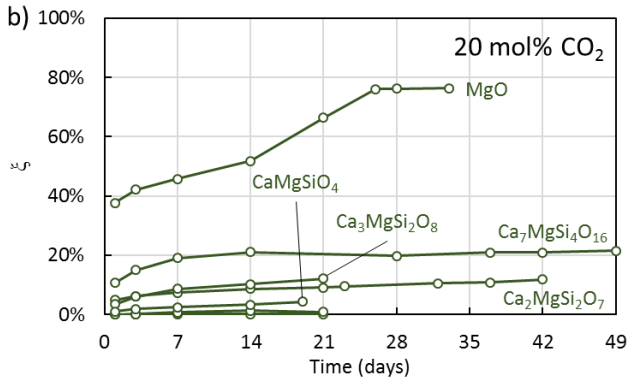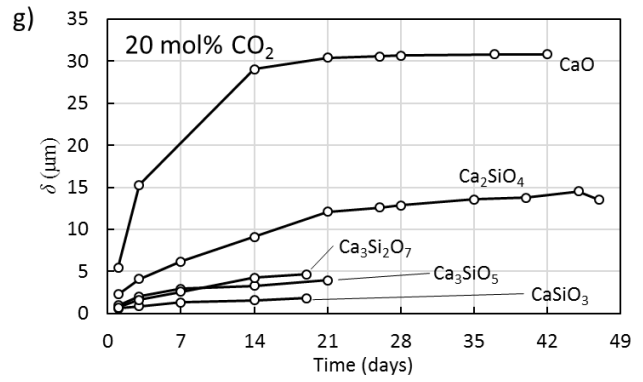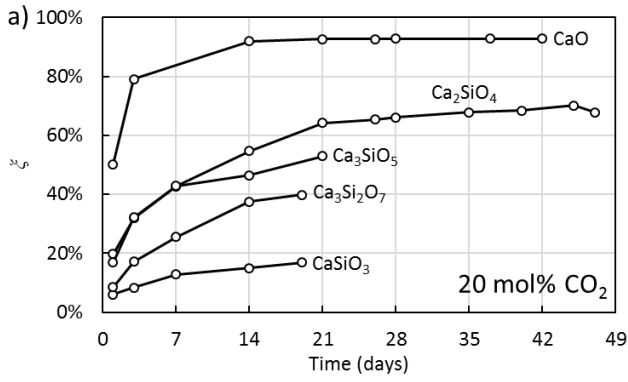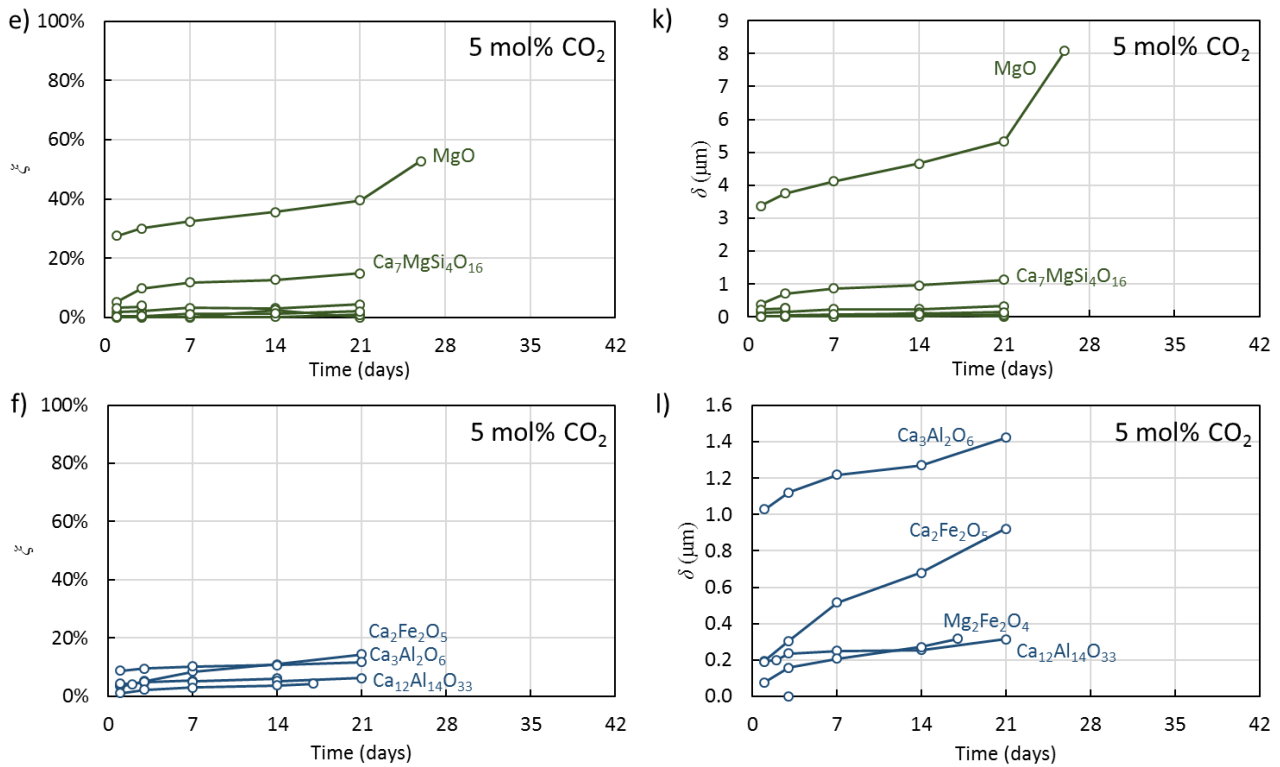
Fig. 6-20. The reaction extent over the course of testing for a) ξ of Ca-minerals at 20 mol% CO_2, b) ξ of Mg-minerals at 20 mol% CO_2, c) ξ of (Al/Fe)-minerals at 20 mol% CO_2, d) ξ of Ca-minerals at 5 mol% CO_2, e) ξ of Mg-minerals at 5 mol% CO_2, f) ξ of (Al/Fe)-minerals at 5 mol% CO_2, g) δ of Ca-minerals at 20 mol% CO_2, h) δ of Mg-minerals at 20 mol% CO_2, i) δ of (Al/Fe)-minerals at 20 mol% CO_2, j) δ of Ca-minerals at 5 mol% CO_2, k) δ of Mg-minerals at 5 mol% CO_2, l) δ of (Al/Fe)-minerals at 5 mol% CO_2. Note the changes in the magnitude of the vertical axis when δ is shown. All reactions occurred at 30 ˚C and a relative humidity of 90%.

Given that flux (J) asymptotically approaches 0 in the SCM, the transient J was calculated using **Eq. (6-12)** where the start and end of the reaction period are denoted by subscripts i and f, respectively. In **Eq. (6-12)**, the total moles available for reaction is denoted by mol_T and the SA calculation only includes particles whose radius is larger than δ_f. The J and its derivative (J') were graphed to determine the point at which the influence of mineralization reaction and gas phase diffusion were negligibly small in relation to the diffusion time; an example graph for $Ca_2MgSi_2O_7$ is provided in **Fig. 6-21**.

$$J = \frac{(\xi_f - \xi_i) \times mol_T}{(t_f - t_i) \times \sum_n 4\pi (R_n - \delta_f)^2} \tag{6 – 12}$$
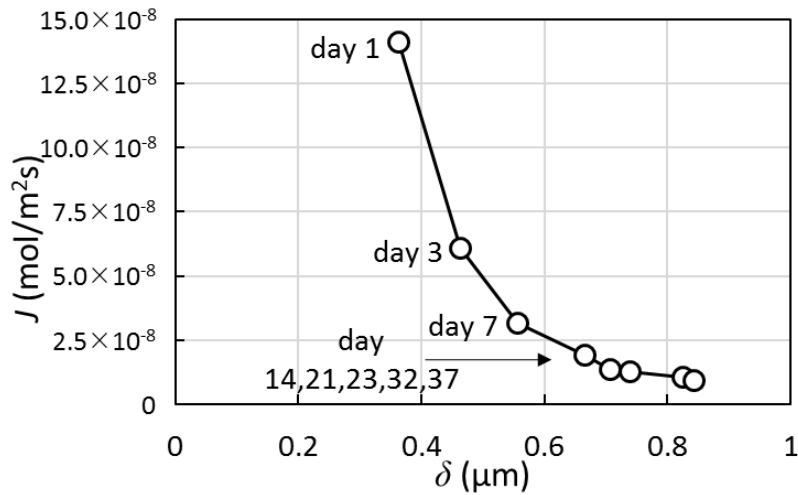
Fig. 6-21. The change in flux over the course of mineralization reactions for $Ca_2MgSi_2O_7$ in a 20% CO_2 atmosphere with a relative humidity of 90% at 30 ˚C.

After calculation of the time of constant flux, the D was then calculated using **Eq. (6-13)**, where the radius of the largest particle in the sample is given by R, t and δ are set by the instant of constant flux, ρ is the unreacted mineral density, and C_g is the density of CO_2 in the gas phase (kg/m³).

$$D = \frac{\rho R^2}{6t C_g}\left\{1 - 3\left(\frac{R-\delta}{R}\right)^2 + 2\left(\frac{R-\delta}{R}\right)^3\right\} \tag{6-13}$$

As some samples were not completely pure, the calculated D included the effect of multiple minerals. To account for the heterogeneous nature of these samples, the D was corrected using the tenets of Effective Medium Theory (EMT) applied in 3 dimensions per **Eq. (6-14)** [Wang et al., 2006].

$$\sum_m \left[\psi_m \frac{D_m - D_{bulk}}{D_m + 2D_{bulk}}\right] = 0 \tag{6-14}$$

In **Eq. (6-14)**, m represents each distinct mineral in the sample (including the target mineral). The volume fraction of each mineral is denoted by ψ_m. Starting from minerals with a single impurity of known D, the D of every compound was calculated iteratively until all D converged. The corrected D was applied using the SCM to each compound and the predicted reaction progressions were plotted against experimental results to verify the appropriateness of the SCM to the particular reaction. The initial and corrected D for each mineral is provided in **Table 6-3** along with the composition of the product layer. Differences in the D as a function of CO_2 concentration is likely due to the difference in the structures of the various carbonate polymorphs [Ni and Ratner, 2008]. For minerals that halted mineralization at a certain depth, the apparent depth of reaction is also provided. The D for each mineral is also graphed on ternary diagrams that cover the composition space of CaO-SiO_2-FeO, CaO-SiO_2-Al_2O_3, and CaO-MgO-SiO_2 (**Fig. 6-22**). These diagrams were chosen because they cover the majority of the minerals formed in ISM slag. The graphs are color-coded to display the $\log_{10}$ CO_2 diffusivity (high diffusivity is yellow, low diffusivity is purple).

285

Table 6-3. The diffusion coefficient and product layer composition for ISM slag minerals under different CO_2 concentrations. All reactions occurred at 30 ˚C in a relative humidity of 90%.

Source mineral	Product phase	CO_2	D (m²/s)	Depth (nm)
CaO	β-$CaCO_3$ (80.8%) λ-$CaCO_3$ (19.2%)	20%	4.407×10^{-12}	*NA*
	NA	5%	9.910×10^{-14}	
MgO	$MgCO_3 \cdot 3H_2O$ (95.7%) $MgCO_3$ (2.8%) others (1.5%)	20%	1.278×10^{-13}	*NA*
	Amorphous	5%	9.705×10^{-14}	
Ca_2SiO_4	β-$CaCO_3$ (77.7%) λ-$CaCO_3$ (22.3%)	20%	2.888×10^{-13}	*NA*
	λ-$CaCO_3$ (88.5%) β-$CaCO_3$ (11.5%)	5%	2.329×10^{-11}	
$CaSiO_3$	*NA*	20%	8.532×10^{-15}	*NA*
	λ-$CaCO_3$	5%	5.080×10^{-13}	
$Ca_3Si_2O_7$	*NA*	20%	6.516×10^{-14}	*NA*
	λ-$CaCO_3$	5%	1.398×10^{-12}	
Ca_3SiO_5	*NA*	20%	9.006×10^{-15}	*NA*
		5%	1.312×10^{-14}	
Mg_2SiO_4	$Mg_5(CO_3)_4 \cdot (OH)_2 \cdot 4H_2O$	20%	5.108×10^{-17}	*NA*
	NA	5%	3.757×10^{-17}	
$MgSiO_3$	*UD*	20%	1.145×10^{-18}	15
	NA	5%	5.295×10^{-19}	*NA*
$CaMgSiO_4$	$CaMg(CO_3)_2$ (83.3%) β-$CaCO_3$ (13.5%) λ-$CaCO_3$ (1.5%) $Mg_5(CO_3)_4 \cdot (OH)_2 \cdot 4H_2O$ (1.1%) Others	20%	4.186×10^{-16}	*NA*
	NA	5%	3.424×10^{-16}	
$CaMgSi_2O_6$	$CaCO_3$	20%	6.159×10^{-16}	*NA*
	NT	5%	*NT*	*NT*

Source mineral	Product phase	CO$_2$	D (m^2/s)	Depth (nm)
Ca$_2$MgSi$_2$O$_7$	CaMg(CO$_3$)$_2$ (46.3%) β-CaCO$_3$ (18.6%) MgCO$_3$ (13.8%) μ-CaCO$_3$ (9.2%) MgCO$_3$·3H$_2$O (7.0%) Mg$_5$(CO$_3$)$_4$·(OH)$_2$·4H$_2$O (5.0%)	20%	2.067 × 10^{-15}	*NA*
	NA	5%	1.917 × 10^{-15}	
Ca$_3$MgSi$_2$O$_8$	*NA*	20%	5.049 × 10^{-15}	*NA*
		5%	5.175 × 10^{-15}	
Ca$_7$MgSi$_4$O$_{16}$	λ-CaCO$_3$ (60.3%) CaMg(CO$_3$)$_2$ (26.1%) β-CaCO$_3$ (12.0%) MgCO$_3$·3H$_2$O (1.6%)	20%	5.975 × 10^{-15}	*NA*
	NA	5%	7.838 × 10^{-15}	
Fe$_2$O$_3$	*NT*	20%	*NT*	*NT*
	UD	5%	0	0
Ca$_3$Al$_2$O$_6$	*NA*	20%	1.512 × 10^{-15}	*NA*
	β-CaCO$_3$ (80.0%) λ-CaCO$_3$ (14.8%) μ-CaCO$_3$ (5.2%)	5%	1.906 × 10^{-14}	
MgAl$_2$O$_4$	*UD*	20%	3.392 × 10^{-18}	*NA*
	NA	5%	1.595 × 10^{-18}	
MgFe$_2$O$_4$	*NA*	20%	2.509 × 10^{-16}	*NA*
	MgCO$_3$	5%	9.954 × 10^{-15}	
Ca$_2$Al$_2$SiO$_7$	β-CaCO$_3$ (65.5%) λ-CaCO$_3$ (34.5%)	20%	4.363 × 10^{-17}	*NA*
	NT	5%	*NT*	*NT*
CaAl$_2$Si$_2$O$_8$	λ-CaCO$_3$ (98.5%) β-CaCO$_3$ (1.5%)	20%	0	60
	NT	5%	*NT*	*NT*
Ca$_2$Fe$_2$O$_5$	λ-CaCO$_3$ (78.1%) β-CaCO$_3$ (21.9%)	20%	4.612 × 10^{-15}	*NA*
	NA	5%	4.885 × 10^{-15}	

Source mineral	Product phase	CO$_2$	D (m^2/s)	Depth (nm)
Ca$_{12}$Al$_{14}$O$_{33}$	β-CaCO$_3$ (44.9%) λ-CaCO$_3$ (41.0%) μ-CaCO$_3$ (14.1%)	20%	2.011 × 10^{-16}	NA
	NA	5%	6.490 × 10^{-16}	
Ca$_4$Al$_2$Fe$_2$O$_{10}$	NA	20%	8.024 × 10^{-17}	NA
	NT	5%	NT	NT

Table 6-3 *continued*. The product layer depth and associated time of reaction used in determining the diffusion coefficient for ISM slag minerals.

Source mineral	δ (μm)	t (days)
CaO	30.999	66
	3.118	21
MgO	7.562	43
	4.836	26
Ca$_2$SiO$_4$	14.104	66
	26.903	21
CaSiO$_3$	1.823	19
	7.721	21
Ca$_3$Si$_2$O$_7$	4.649	19
	13.703	21
Ca$_3$SiO$_5$	3.982	21
	4.000	3
Mg$_2$SiO$_4$	0.066	21
	0.007	21
Mg$_2$Si$_2$O$_6$	0.146	21
	0.151	21
CaMgSiO$_4$	0.509	19
	0.237	21
CaMgSi$_2$O$_6$	0.329	14
	NT	
Ca$_2$MgSi$_2$O$_7$	1.351	61
	0.468	21

Source mineral	δ (µm)	t (days)
$Ca_3MgSi_2O_8$	1.258	21
	0.376	5
$Ca_7MgSi_4O_{16}$	2.674	66
	1.325	21
Fe_2O_3	~0	21
	NT	
$Ca_3Al_2O_6$	0.760	19
	1.422	21
$MgAl_2O_4$	0.035	21
	0.005	5
$MgFe_2O_4$	0.249	19
	0.739	17
$Ca_2Al_2SiO_7$	0.048	21
	NT	
$CaAl_2Si_2O_8$	0.060	21
	NT	
$Ca_2Fe_2O_5$	2.232	47
	0.922	21
$Ca_{12}Al_{14}O_{33}$	0.332	19
	0.314	21
$Ca_4Al_2Fe_2O_{10}$	0.166	21
	NT	

NA: not analysed; NT: not tested; UD: undetected
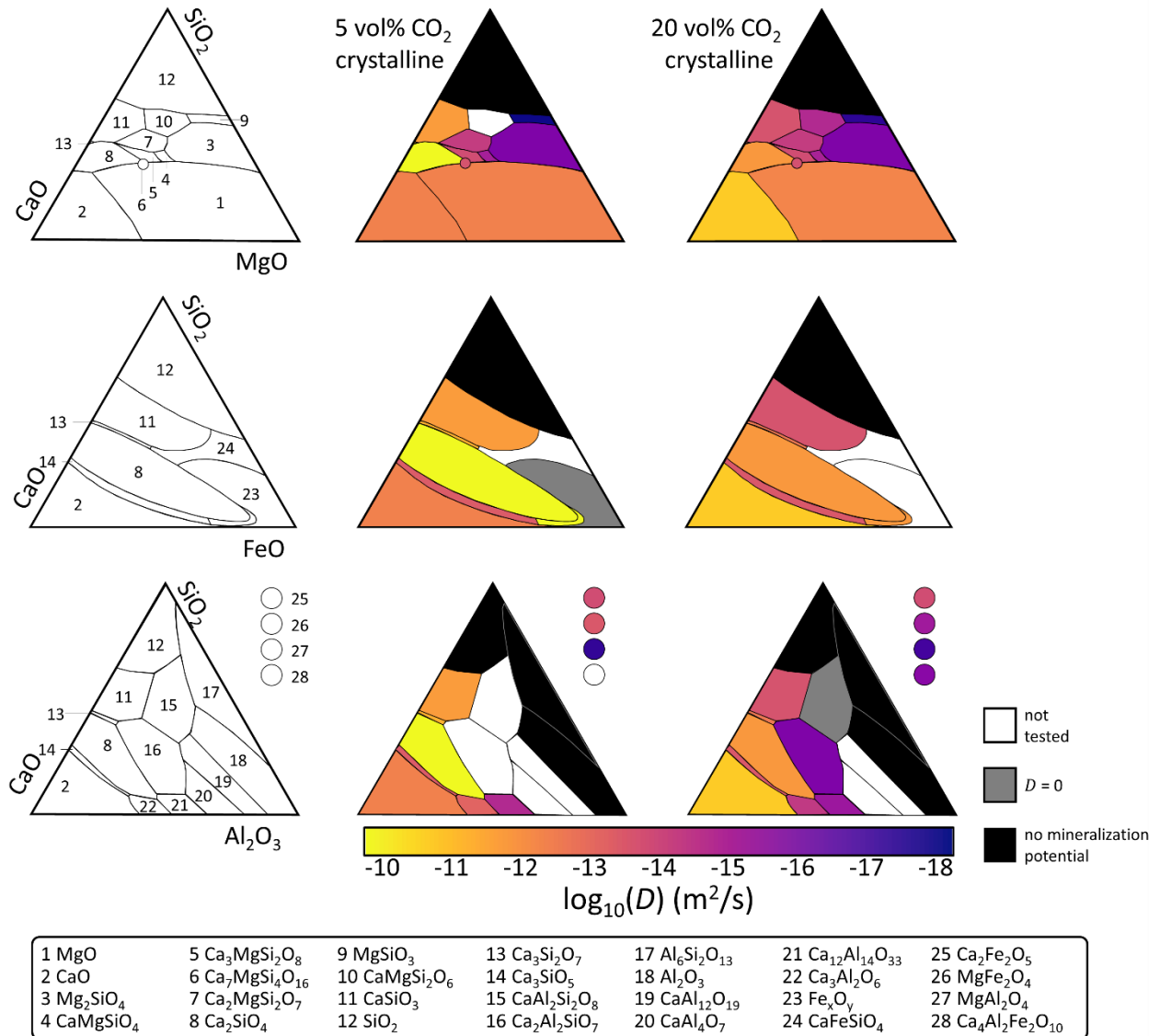
Fig. 6-22. The empirically determined $\log_{10} D$ (m²/s) for the main crystalline minerals of ISM slag at 30 ˚C and a relative humidity of 90%.

The empirically determined D for the amorphous phases is provided in **Table 6-4**. For minerals that halted mineralization at a certain depth, the apparent depth of reaction is also provided. The values are mapped to ternary diagrams in **Fig. 6-23**.

Table 6-4. The diffusion coefficient for amorphous compounds common to ISM slag. All reactions occurred at 30 ˚C and a relative humidity of 90%.

Glass composition	CO_2	D (m^2/s)	Depth (nm)	t (days)
Ca_2SiO_4	20%	1.179×10^{-17}	NA	21
$CaSiO_3$	20%	8.898×10^{-18}	NA	21
$Ca_3Si_2O_7$	20%	1.201×10^{-15}	NA	21
Ca_3SiO_5	20%	4.203×10^{-18}	NA	21
$MgSiO_3$	20%	0	0	21
$CaMgSiO_4$	20%	1.309×10^{-14}	NA	21
$CaMgSi_2O_6$	20%	0	0	21
$Ca_2MgSi_2O_7$	20%	5.689×10^{-15}	NA	21
$Ca_3MgSi_2O_8$	20%	8.253×10^{-18}	17	21
$Ca_7MgSi_4O_{16}$	20%	7.168×10^{-18}	19	21
$Ca_2Al_2SiO_7$	20%	3.148×10^{-17}	40	21
$CaAl_2Si_2O_8$	20%	1.205×10^{-17}	NA	21
$Ca_2Fe_2O_5$	20%	1.399×10^{-18}	NA	21
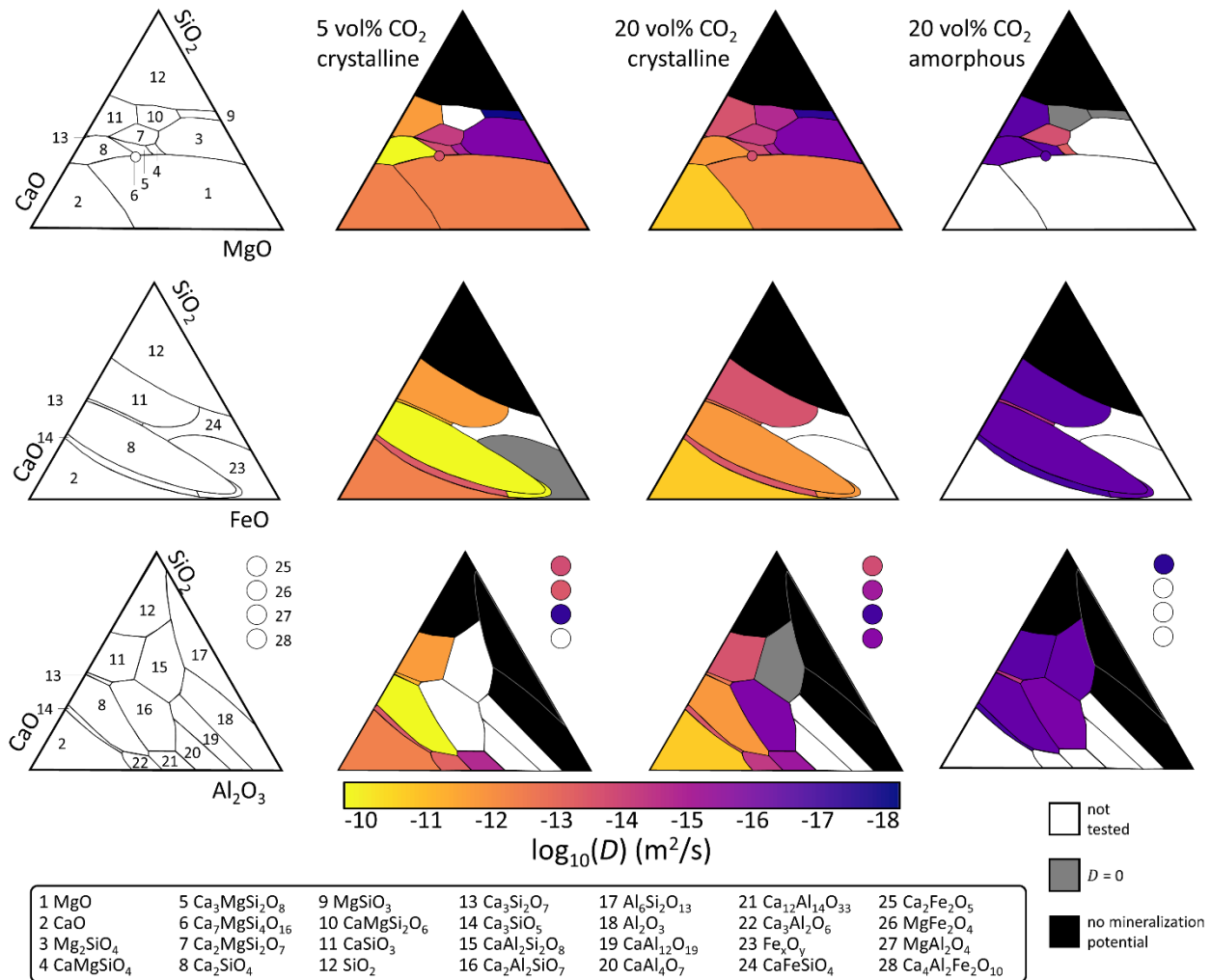
Fig. 6-23. The empirically determined $\log_{10}D$ (m²/s) for crystalline and amorphous compounds in ISM slag under a 90% relative humidity atmosphere at 30 ˚C.

6.2. Performance indices

The relative potential of the various minerals to reduce CO₂ emissions via mineralization is a function of the potential CO₂ mineralization per mole of mineral (capacity factor: CF), the diffusivity of the product layer to CO₂ (D), and the energy expenditure of grinding (γ). Given the relatively consistent quantitative connection and minor differences between γ_{IG}, γ_{GB}, and γ_{IM}, any of the surface energies could be selected. Fractures will inevitably deviate from straight line fractures when following grain boundaries, raising the effective energy expenditure per normalized length of travel; therefore, the γ_{IG} was chosen as most representative of actual grinding energy. The performance of each mineral was summarized by a rate and capacity indices. The rate index is calculated as $\log_{10}(D/\gamma_{IG})$, with faster mineralization per degree of grinding being represented by less negative values. The mineralization capacity index is calculated as CF/γ_{IG} and provides insight on the net CO₂ mineralization potential for a given amount of grinding. The (Ca/Mg)-bearing minerals are graphed on the mineralization index plane in **Fig. 6-24**. Several minerals halted CO₂ mineralization reactions at a certain depth, therefore D would be an inappropriate measure for these materials. They are graphed with $\log_{10}(D/\gamma_{IG}) = -20$ for easing viewing and are further denoted by boxes instead of

circles. It is clear from **Fig. 6-24** that (Al/Fe)-bearing minerals naturally group in the lower-left hand portion of the graph due to high grinding energies and low capacity caused by the extraneous cations. On the other hand, (Ca/Mg)-silicates are gathered to the upper right-hand portion of the graph due to the inherently higher capacity for CO_2 and the low grinding energy of the silicate structure.

1) Ca2SiO4	18) Mg2SiO4
2) Ca3Si2O7	19) Ca3Al2O6
3) CaO	20) Ca2Fe2O5
4) CaSiO3	21) MgFe2O4
5) Ca3SiO5	22) Ca12Al14O33
6) α-Ca3Si2O7	23) Ca2Al2SiO7
7) α-Ca2SiO4	24) α-CaAl2Si2O8
8) α-CaSiO3	25) Ca4Al2Fe2O10
9) α-Ca3SiO5	26) α-Ca2Fe2O5
10) MgO	27) MgAl2O4
11) α-CaMgSiO4	28) CaAl2Si2O8
12) α-Ca2MgSi2O7	29) α-Ca2AlSi2O7
13) Ca7MgSi4O16	30) α-Ca7MgSi4O16
14) Ca3MgSi2O8	31) α-Ca3MgSi2O8
15) Ca2MgSi2O7	32) α-MgSiO3
16) CaMgSi2O6	33) MgSiO3
17) CaMgSiO4	34) CaMgSi2O6

Fig. 6-24. Performance indices of the common crystalline ISM minerals. The diffusivities are only relevant for reactions in atmospheres of 5-20% volumetric CO_2 concentration at 30 ˚C and a relative humidity of 90%.

Amorphous compounds are compared to crystalline compounds in **Fig. 6-25** in terms of the diffusivity alone. For compounds that halted reaction at a small depth, the empirical D while mineralization reactions occurred was used for graphing. For compounds that showed no reaction, the D was set to -20 to facilitate graphing.
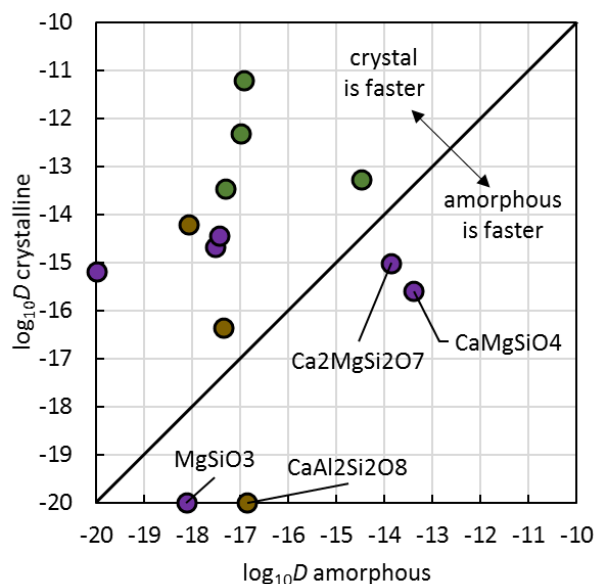
Fig. 6-25. The generally higher diffusivity seen among crystalline mineral compared to equivalent composition amorphous compounds. Results are only relevant at 30 ˚C, a relative humidity of 90%, and a CO_2 volumetric concentration of 20%.

A separate means to evaluate the performance of various compounds in terms of CO_2 mineralization is to plot the extent of grinding versus the time required to achieve near complete mineralization (defined as 99%). **Figure 6-26** provides such a graph for the crystalline minerals in ISM slags. The PSD is defined by its 99% volume passing diameter, atmospheres are 5 vol% CO_2, the relative humidity is 90%, and the temperature is 30 ˚C. Calcium silicates and (Ca,Mg)O are colored black, Mg-bearing compounds are colored green, and (Al,Fe)-bearing compounds are colored brown. Minerals are ordered top to bottom in the same order as they appear on the graph. Moving right to left along any mineral line indicates reducing the particle size and accordingly, the time to complete mineralization. Equivalently, at any particle size, minerals that are lower on the graph require less time to reach full mineralization. An equivalent graph for the amorphous compounds is given in **Fig. 6-27**. With the exception of $CaMgSiO_4$, $Ca_2MgSi_2O_7$, and $Ca_3Si_2O_7$, amorphous compounds exhibit roughly similar mineralization rates, which are significantly slower than their crystalline counterparts.
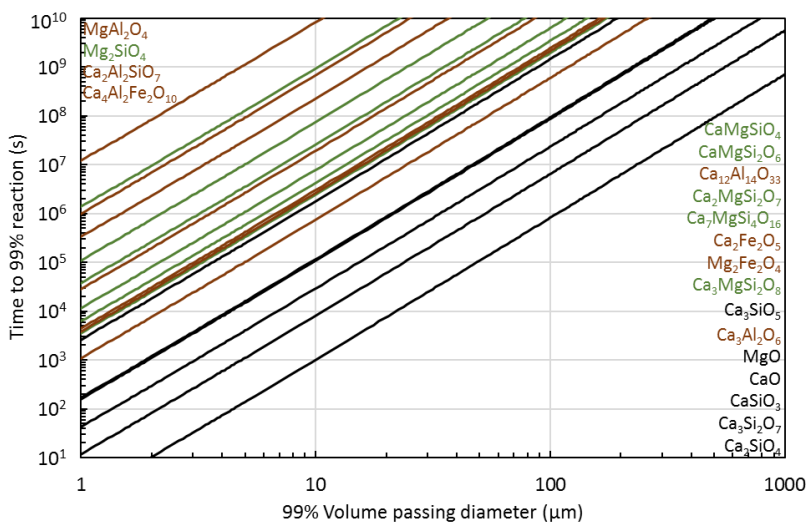
Fig. 6-26. Particle size versus complete (99%) mineralization time for crystalline ISM minerals. Reactions at 30 ˚C and a relative humidity of 90%.
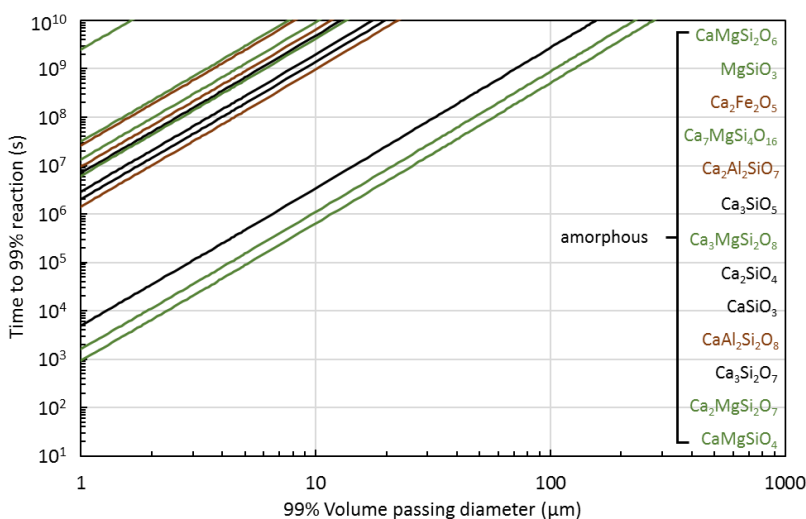
Fig. 6-27. Particle size versus complete (99%) mineralization time for amorphous ISM minerals. Reactions at 30 ˚C and a relative humidity of 90%.

6.3. Effective CO$_2$ diffusion coefficient

The CO$_2$ diffusivity of the heterogeneous bulk material (D_{bulk}) is well modeled by EMT with the assumption of spherical internal mineral grains. Numerically solving of **Eq. (6-15)** provides the relevant D_{bulk} [Wang et al., 2006].

$$\sum_m \left[\psi_m \frac{D_m - D_{bulk}}{D_m + 2D_{bulk}} \right] = 0 \tag{6-15}$$

6.3.1. Solid solutions vs mixed systems

During solidification, multiple mineral species can precipitate and remain in the final solid structure. It is also possible, through rapid solidification, to maintain slag in a mixed state. Thermodynamic models and empirical results indicate that Ca$_2$SiO$_4$ is typically the first compound to precipitate from molten melts with the remaining melt material being distributed between oxides of MgO, CaO, SiO$_2$, Al$_2$O$_3$, and FeO [da Rocha et al., 2018; Gautier et al., 2013; Kriskova et al., 2013]. By way of EMT, the D_{bulk} of mixtures of compounds were compared for equivalent composition solid solutions. In all instances, mixtures produced higher D than solid solutions **(Fig. 6-28)**. This phenomenon is especially strong when Mg, Fe, or Al are added to calcium silicates.
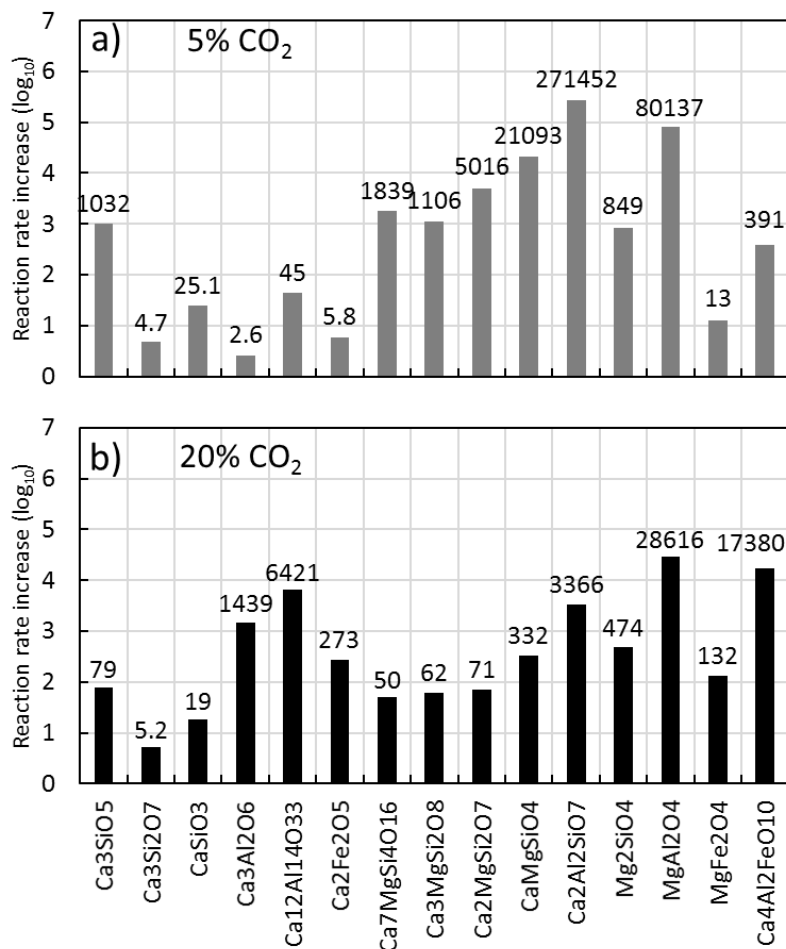
Fig. 6-28. The increase in reaction rate that comes with producing a mixture of solids instead of a solid solution under a) 5% CO$_2$ and b) 20% CO$_2$ atmospheres; 30 °C and a relative humidity of 90%.

6.3.2. Size distribution effects

The effects of EMT are only relevant as a bulk property. As the internal GSD approaches the PSD, the effects from the geometry of the sample will become less and less important. This behavior is evidenced by **Fig. 6-29**, showing the average value of a binary sample (D values of 1 or 0) as a function of the ratio of the PSD to the GSD.
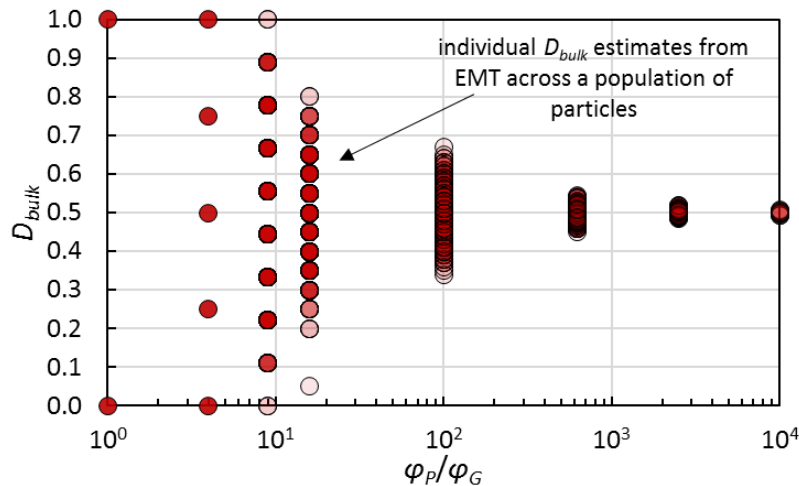
Fig. 6-29. Dependence of the results of EMT on the ratio of PSD to GSD.

6.4. Mineral locking

The overwhelming majority of ISM slags are polycrystalline solids, containing a variety of mineral compounds. Due to the substantial differences in diffusivity, this heterogeneity can substantially alter the bulk CO_2 diffusivity. Relatively unreactive minerals can effectively block the interaction of reactive minerals with CO_2 due to purely geometric effects. Even when reactions are not completely halted, the slower reacting portions can substantially slow the effective reaction rate of slag. This interference by surrounding compounds is terms 'mineral locking' (ML). Mineral locking involving only reactive species can be modeled by effective medium theory (EMT). However, if there exist unreactive minerals or minerals whose product layers have effectively blocked CO_2 diffusion, then portions of reactive minerals may be completely removed from CO_2 mineralization reactions. The degree of ML in a sample is determined by the concentration of the target reactive species (C_R) and the ratio of the PSD to the GSD (Ω). High concentrations are more likely to be connected to one another, providing a high diffusivity path for CO_2 to transit. Simple geometry makes it obvious that when PSD and GSD are of similar magnitude the potential for ML is reduced. The concept of ML is displayed in **Fig. 6-30**.
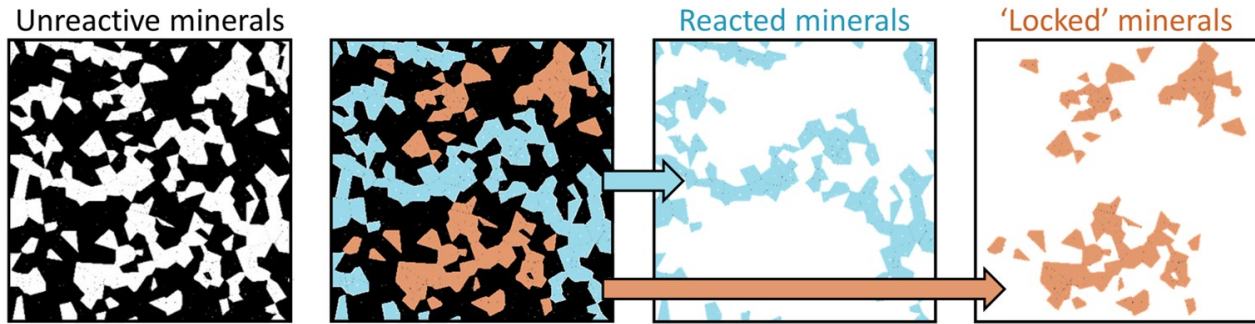
Fig. 6-30. A schematic displaying the effects of mineral locking.

Quantitative evaluation of ML is akin to the question of connectivity in percolation theory [Jerauld et al., 1984; Kirkpatrick, 1973]. A continuous chain of reactive minerals connected to the surface of a particle are not locked. Unfortunately, percolation theory remains a field that has not successfully generated formal proofs of the limits or trends in behavior. Most progress remains limited to the area of analysis of real world and in-silico systems. Theoretical work has stayed focused on platonic shapes in two dimensions ($\mathbb{R}^2$) and is thus not readily applicable to ISM slags [Bollobás and Riordan, 2006; Rossen, 1988]. Slag mineral grains are better approximated by voronoi tessellations, of course in 3 dimensions ($\mathbb{R}^3$). A result of the voronoi tessellation structure is that there exists a distribution in the number of faces per cell [Lazar et al., 2013]. This means that the potential paths of connection may be highly improbable and tortuous. Instead of attempting to model all possible paths of connection, the simple probability of connection can be used to greatly simplify the complexity of the problem. The wide distribution of probabilities can be removed through the knowledge that a huge number of particles will exist in any ground sample; therefore, even though highly unlikely events are expected, the effects will be diluted by the much larger number of typical events.

Simplified, probabilistic modelling of ML can be conceptually understood by separating each internal mineral grain into 3 parts of equivalent equal surface area. These border between areas is aligned normal to the radial direction of the slag particle, this results in three distinct sections. One section aligns with the radial direction and receives flux from the exterior of the particle. The second section lies parallel to the CO_2 flux. The third section aligns with the radial direction, with the CO_2 flux exiting from the inside of the grain towards the center of the sphere. **Figure 6-31** provides a schematic representation. The slag particle is divided into concentric shells (L) of depth equivalent to the diameter of the internal mineral grains. The probability that a grain in the i-th layer (L_i) is connected via an uninterrupted chain of reactive grains to the exterior of the particle is calculated by the relative content of the mineral (C_R) along with the number of faces per mineral grain (n_f) as described by **Eq. (6-16)**.

$$P_i = \left(\frac{n_f}{3}\right)^{L_i-1} \times C_R^{\,L_i-1} \qquad\qquad (6-16)$$
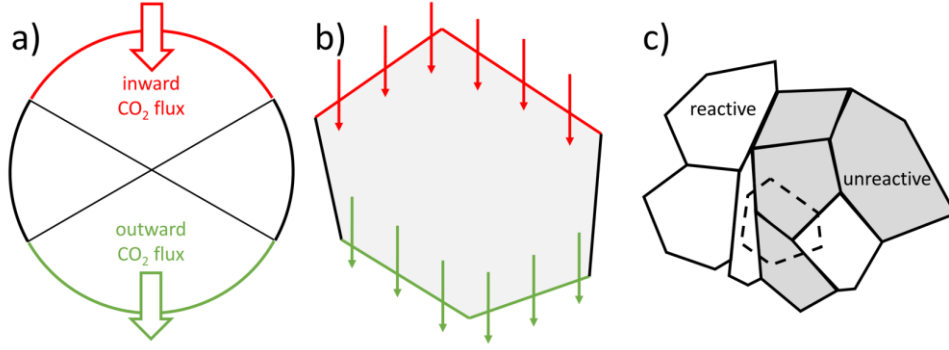
Fig. 6-31. Schematic of the simplified probabilistic analysis of ML with a grain modeled as a) spherical with equal surface area applied for CO_2 influx, parallel flow, and efflux, b) conversion to a voronoi cell, and c) the means by which bypass can occur in three dimensions.

In 2 dimensions, the number of faces is replaced by the number of edges, and the concentration is in terms of area instead of volume. The probability of connectivity in layer i (P_i) can then be multiplied by the C_R and the volume of shell i (or area in the case of $\mathbb{R}^2$). By summing the connected reactive content for all shells and dividing by the total quantity of the reactive material, the amount of 'connected' reactive material is determined. The calculation for ML in $\mathbb{R}^2$ and $\mathbb{R}^3$ is given by **Eq. (6-17)** and **Eq. (6-18)**, respectively.

$$ML(in\ \mathbb{R}^2) = 1 - \frac{\sum_i P_i C_R \pi \left[\left(\frac{\varphi_P}{2} - i\varphi_G - 1\right) - \left(\frac{\varphi_P}{2} - i\varphi_G\right)\right]^2}{C_R \pi \left(\frac{\varphi_P}{2}\right)^2} \qquad (6-17)$$

$$ML(in\ \mathbb{R}^3) = 1 - \frac{\sum_i P_i C_R \pi \left[\left(\frac{\varphi_P}{2} - i\varphi_G - 1\right) - \left(\frac{\varphi_P}{2} - i\varphi_G\right)\right]^3}{C_R \pi \left(\frac{\varphi_P}{2}\right)^3} \qquad (6-18)$$

6.4.1. Monte Carlo analysis

To assess the efficacy of the probabilistic ML model, a series of in-silico synthetic slags were generated and evaluated for ML. The synthetic slag consisted of 'reactive' and 'unreactive' grains in 2 dimensions. The grains were 'nucleated' at random sites within the reaction space via two separate random number generators. The grains then extended radially outward ('grew') until contacting other grains, setting up grain boundaries. The number of nucleating grains was used to control the GSD relative to the PSD (Ω) and the percentage of area occupied by reactive minerals (C_R). Each iteration of the analysis was run 5,000 times to ensure a statistically representative set of geometries (i.e., a Monte Carlo analysis). The results of the Monte Carlo Voronoi Cell in-silico experiments are provided in **Fig. 6-32**. The results agree with the basic intuition that there is increased connectivity between like grains (i.e., less ML) when their concentration increases. Likewise, a larger Ω results in more ML due to the increased number of consecutive connections required to maintain connectivity to the external surface.
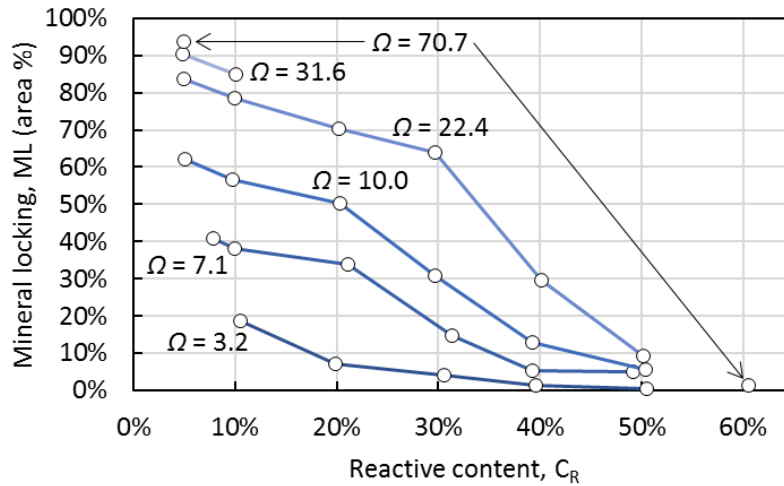
Fig. 6-32. The results of a Monte Carlo Voronoi Cell analysis of mineral locking in $\mathbb{R}^2$.

6.4.2. Probabilistic analysis in 2D and 3D

The probabilistic ML estimate in $\mathbb{R}^2$ is mapped against the in-silico experiments in **Fig. 6-33**. The probabilistic estimate was done using the average number of side lengths $\pm$ 1 standard deviation from Lazar et al. (2013). The results are unexpectedly accurate given the random nature of the voronoi tessellations and the large range of C_R and Ω examined. The encouraging performance of the probabilistic model in $\mathbb{R}^2$, along with its basis on basic geometry, prompted application to $\mathbb{R}^3$. Predicted ML in $\mathbb{R}^3$ for a range of C_R and Ω is provided in **Fig. 6-34**. It is immediately apparent that the extent of ML is less in $\mathbb{R}^3$ than in $\mathbb{R}^2$. This follows naturally from the extra degree of freedom provided by $\mathbb{R}^3$.
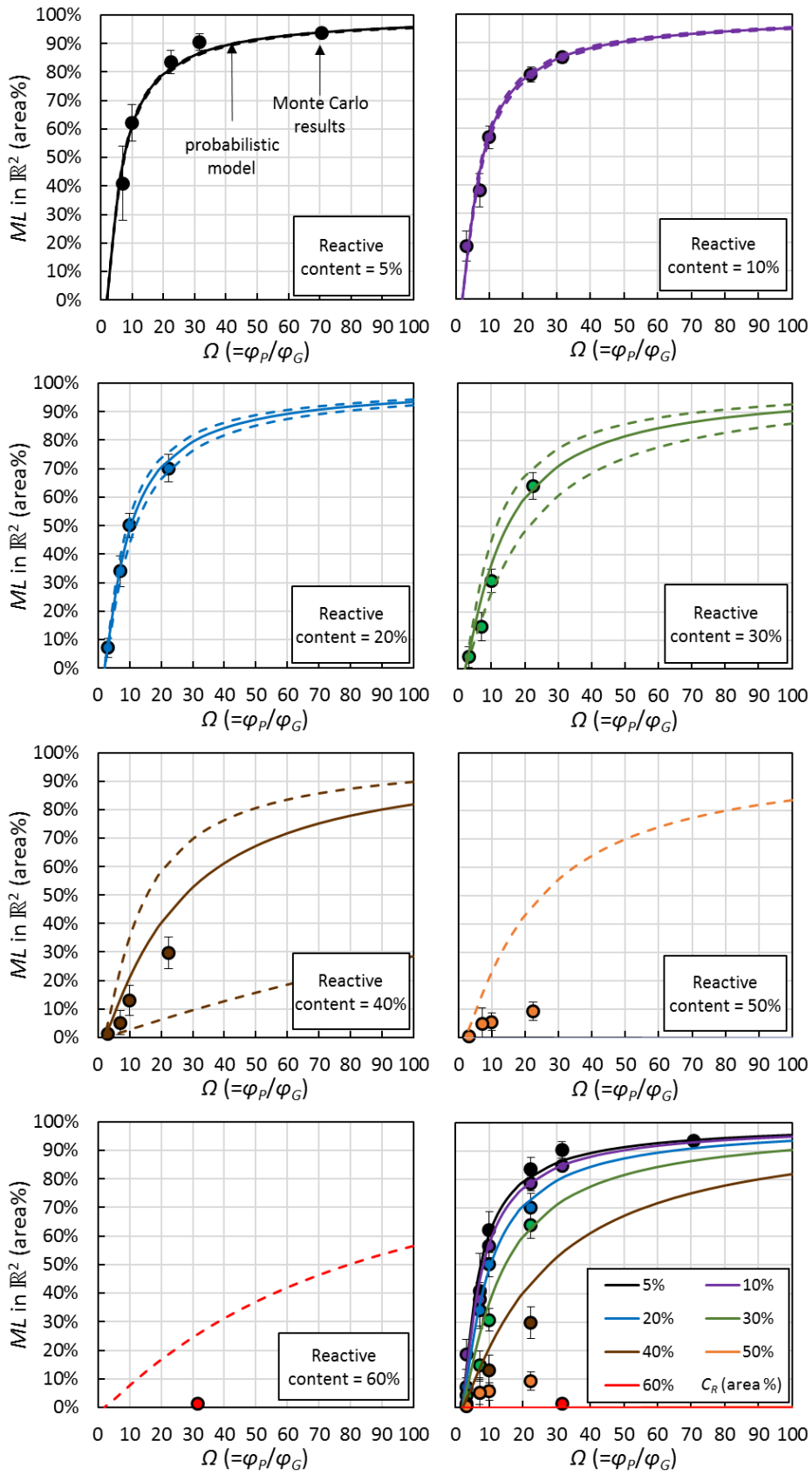
Fig. 6-33. The estimate of mineral locking compared to Monte Carlo Voronoi Cell results.
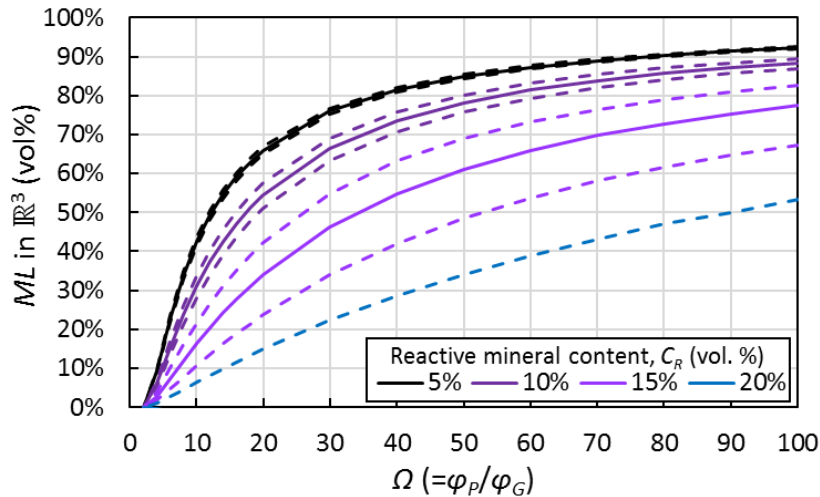
Fig. 6-34. Estimate of mineral locking extent in $\mathbb{R}^3$.

The extent to which ML is suppressed in $\mathbb{R}^3$ is made evident by **Fig. 6-35**, where it is graphed against the ML in $\mathbb{R}^2$ under equivalent situations. Even though it is somewhat suppressed in $\mathbb{R}^3$, ML can still severely stunt the CO_2 mineralization extent. When a reactive material falls to less than ~20% of the slag volume, its reaction speed will default to the reaction rate of the bulk material. Grinding helps to diminish ML but assurance of complete removal of ML requires C_R in excess of 20% or a $\Omega \leq 2$. Both situations are rare in the literature and thus should not be expected in most tests using slag received from ISM operators.
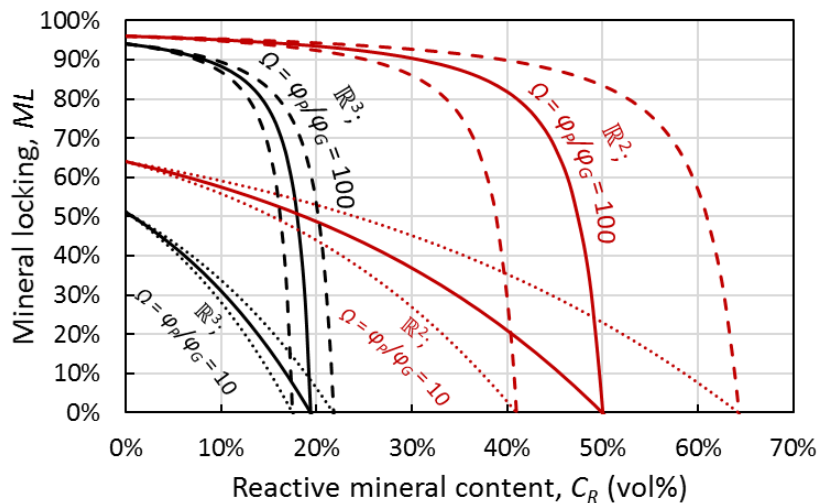
Fig. 6-35. The difference between mineral locking onset and extent in $\mathbb{R}^2$ and $\mathbb{R}^3$.

6.4.3. Size distribution effects

The parameters of Ω and ML require consideration of the complete distribution of particle and grain sizes. **Figure 6-36** shows both factors depend on what portion of the distributions are considered and from which end of the distribution they are analyzed. For example, a uniform GSD of 2 μm and reactive material content of 15% for a $X_{V,99}$ sample generates a total ML of 19.3%, which is applied only the larger particles in the distribution. However, the volume-averaged sample ML is dominated by the ML extent in larger particles. Slightly over 19.3% of the reactive material is sequestered due to ML; thus, the true amount of reactive material is reduced from 15% to 12.1%.
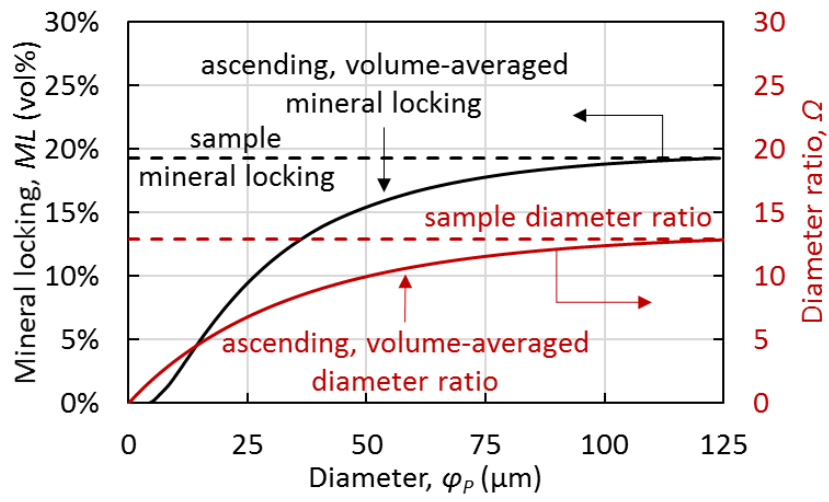
Fig. 6-36. The change in mineral locking that occurs across a size distribution.

Chapter-specific symbols and abbreviation list

A: Projected area

AR: Aspect ratio

BET: Brunauer–Emmett–Teller surface area

CCS: Carbon capture and sequestration

C_g: Concentration of CO_2 in the gas phase

C_R: Mineral concentration

CF: Capacity factor

CHN: C/H/N gas phase elemental analysis

D: Diffusivity of CO_2 through the PL

D_{bulk}: Bulk diffusivity of slag

D_m: Mineral-specific diffusivity

EMT: Effective medium theory

f_D: Fractal dimension

GSD: Grain size distribution

H: Largest scale at which f_D is applicable

i: Layer number

ISM: Iron and steelmaking

J: Flux

L: Shell depth

LCA: Life cycle assessment

ML: Mineral locking

n_f: Number of faces per mineral grain

n_i: Number of particles in a distribution

P: Perimeter

P_i: Probability of connectivity in layer i

PL: Product layer

PSD: Particle size distribution

PV+LiB: Solar photovoltaic power with lithium ion battery storage

$\mathbb{R}^2$: 2-dimensional space

$\mathbb{R}^3$: 3-dimensional space

RE: Renewable energy

RF: Surface roughness factor

RH: Relative humidity

r_i: Radius of an individual particle in a distribution

r^L: Major radius of equivalent area ellipse

r^S: Minor radius of equivalent area ellipse

r': Radius of equivalent area circle

SA: Surface area

SCM: Shrinking core model

t: time

t': Reduced time to reaction

TG-DTA: Thermogravimetry and differential thermal analysis

T_{sinter}: Sintering temperature
V: Volume
V_e: Ellipse volume
X: Particle diameter
XRD: X-ray diffraction
XRF: X-ray fluorescence
X_{SM}: Surface area-moment mean diameter
X_{VM}: Volume-moment mean diameter
$X_{V,99}$: 99% volume passing diameter

γ: Surface energy
δ: Reaction depth
$\partial \xi / \partial t$: Reaction rate
ξ: Reaction extent
ρ: Density of unreacted material
φ_G: Grain diameter
φ_P: Particle diameter
ψ_m: Volume percent of mineral m
Ω: GSD to PSD ratio
Δm: Mass change

References

Ashraf, W. and Olek, J., 2016. Carbonation behavior of hydraulic and non-hydraulic calcium silicates: potential of utilizing low-lime calcium silicates in cement-based materials. Journal of materials science, 51(13), pp.6173-6191.

Azdarpour, A., Asadullah, M., Mohammadian, E., Hamidi, H., Junin, R. and Karaei, M.A., 2015. A review on carbon dioxide mineral carbonation through pH-swing process. Chemical Engineering Journal, 279, pp.615-630.

Barreiros, F.M., Ferreira, P.J. and Figueiredo, M.M., 1996. Calculating shape factors from particle sizing data. Particle & particle systems characterization, 13(6), pp.368-373.

Beerling, D.J., Leake, J.R., Long, S.P., Scholes, J.D., Ton, J., Nelson, P.N., Bird, M., Kantzas, E., Taylor, L.L., Sarkar, B. and Kelland, M., 2018. Farming with crops and rocks to address global climate, food and soil security. Nature plants, p.1.

Bhatia, S.K. and Perlmutter, D.D., 1983. Effect of the product layer on the kinetics of the CO2‐lime reaction. AIChE Journal, 29(1), pp.79-86.

Bodor, M., Santos, R.M., Kriskova, L., Elsen, J., Vlad, M. and Van Gerven, T., 2013. Susceptibility of mineral phases of steel slags towards carbonation: mineralogical, morphological and chemical assessment. European Journal of Mineralogy, 25(4), pp.533-549.

Bollobás, B. and Riordan, O., 2006. The critical probability for random Voronoi percolation in the plane is 1/2. Probability theory and related fields, 136(3), pp.417-468.

Bourgeois, F., Julcour-Lebigue, C., Cassayre, L., Bailly, F., Cyr, M. and Touzé, S., 2018. Guiding mineralization process development with geochemical modelling.

Califice, A., Michel, F., Dislaire, G. and Pirard, E., 2013. Influence of particle shape on size distribution measurements by 3D and 2D image analyses and laser diffraction. Powder technology, 237, pp.67-75.

Daval, D., Sissmann, O., Corvisier, J., Garcia, B., Martinez, I., Guyot, F. and Hellmann, R., 2010. The effect of silica coatings on the weathering rates of wollastonite (CaSiO3) and forsterite (Mg2SiO4): an apparent paradox. Water–rock interactions. Taylor & Francis Group, London, pp.713-716.

Farhang, F., Oliver, T.K., Rayson, M., Brent, G., Stockenhuber, M. and Kennedy, E., 2016. Experimental study on the precipitation of magnesite from thermally activated serpentine for CO2 sequestration. Chemical Engineering Journal, 303, pp.439-449.

Gadikota, G., Swanson, E.J., Zhao, H. and Park, A.H.A., 2014. Experimental design and data analysis for accurate estimation of reaction kinetics and conversion for carbon mineralization. Industrial & Engineering Chemistry Research, 53(16), pp.6664-6676.

Gunnarsson, I., Aradóttir, E.S., Oelkers, E.H., Clark, D.E., Arnarson, M.Þ., Sigfússon, B., Snæbjörnsdóttir, S.Ó., Matter, J.M., Stute, M., Júlíusson, B.M. and Gíslason, S.R., 2018. The rapid and cost-effective capture and subsurface mineral storage of carbon and sulfur at the CarbFix2 site. International Journal of Greenhouse Gas Control, 79, pp.117-126.

Horii, K., Tsutsumi, N., Kitano, Y. and Kato, T., 2013. Processing and reusing technologies for steelmaking slag. Nippon Steel Technical Report, 104, pp.123-129.

Jacobson, M.Z., Delucchi, M.A., Bauer, Z.A., Goodman, S.C., Chapman, W.E., Cameron, M.A., Bozonnat, C., Chobadi, L., Clonts, H.A., Enevoldsen, P. and Erwin, J.R., 2017. 100% clean and

renewable wind, water, and sunlight all-sector energy roadmaps for 139 countries of the world. Joule, 1(1), pp.108-121.

Jerauld, G.R., Scriven, L.E. and Davis, H.T., 1984. Percolation and conduction on the 3D Voronoi and regular networks: a second case study in topological disorder. Journal of Physics C: Solid State Physics, 17(19), p.3429.

Kelemen, P.B., Aines, R., Bennett, E., Benson, S.M., Carter, E., Coggon, J.A., de Obeso, J.C., Evans, O., Gadikota, G., Dipple, G.M. and Godard, M., 2018. In situ carbon mineralization in ultramafic rocks: Natural processes and possible engineered methods. Energy Procedia, 146, pp.92-102.

Kirkpatrick, S., 1973. Percolation and conduction. Reviews of modern physics, 45(4), p.574.

Kolmogorov, A.N., 1940. Reprinted by Shiryayev, A.N., 1992. Selected works of A.N. Kolmogorov: Vol. 2, Probability theory and mathematical statistics. Kluwer Academic.

Koryak, M., Stafford, L.J., Reilly, R.J. and Magnuson, M.P., 2002. Impacts of steel mill slag leachate on the water quality of a small Pennsylvania stream. Journal of Freshwater Ecology, 17(3), pp.461-465.

Lackner, K.S., Wendt, C.H., Butt, D.P., Joyce Jr, E.L. and Sharp, D.H., 1995. Carbon dioxide disposal in carbonate minerals. Energy, 20(11), pp.1153-1170.

Lazar, E.A., Mason, J.K., MacPherson, R.D. and Srolovitz, D.J., 2013. Statistical topology of three-dimensional Poisson-Voronoi cells and cell boundary networks. Physical Review E, 88(6), p.063309.

Li, J. and Hitch, M., 2018. Mechanical activation of magnesium silicates for mineral carbonation, a review. Minerals Engineering, 128, pp.69-83.

Little, L., Mainza, A.N., Becker, M. and Wiese, J., 2017. Fine grinding: How mill type affects particle shape characteristics and mineral liberation. Minerals Engineering, 111, pp.148-157.

Longo, R.C., Cho, K., Brüner, P., Welle, A., Gerdes, A. and Thissen, P., 2015. Carbonation of Wollastonite (001) Competing Hydration: Microscopic Insights from Ion Spectroscopy and Density Functional Theory. ACS applied materials & interfaces, 7(8), pp.4706-4712.

Lottermoser, B.G., 2002. Mobilization of heavy metals from historical smelting slag dumps, north Queensland, Australia. Mineralogical Magazine, 66(4), pp.475-490.

Mayes, W.M., Riley, A.L., Gomes, H.I., Brabham, P., Hamlyn, J., Pullin, H. and Renforth, P., 2018. Atmospheric CO2 Sequestration in Iron and Steel Slag: Consett, County Durham, United Kingdom. Environmental science & technology, 52(14), pp.7892-7900.

Navarro, A., Cardellach, E., Mendoza, J.L., Corbella, M. and Domenech, L.M., 2008. Metal mobilization from base-metal smelting slag dumps in Sierra Almagrera (Almería, Spain). Applied Geochemistry, 23(4), pp.895-913.

Ncongwane, M.S., Broadhurst, J.L. and Petersen, J., 2018. Assessment of the potential carbon footprint of engineered processes for the mineral carbonation of PGM tailings. International Journal of Greenhouse Gas Control, 77, pp.70-81.

Ni, M. and Ratner, B.D., 2008. Differentiating calcium carbonate polymorphs by surface analysis techniques–an XPS and TOF‑SIMS study. Surface and Interface Analysis: An International Journal devoted to the development and application of techniques for the analysis of surfaces, interfaces and thin films, 40(10), pp.1356-1361.

Pan, S.Y., Chang, E.E. and Chiang, P.C., 2012. CO2 capture by accelerated carbonation of alkaline wastes: a review on its principles and applications. Aerosol Air Qual Res, 12(5), pp.770-791.

Power, I.M., Harrison, A.L., Dipple, G.M., Wilson, S.A., Kelemen, P.B., Hitch, M. and Southam, G., 2013. Carbon mineralization: from natural analogues to engineered systems. Reviews in Mineralogy and Geochemistry, 77(1), pp.305-360.

Romanov, V., Soong, Y., Carney, C., Rush, G.E., Nielsen, B. and O'Connor, W., 2015. Mineralization of carbon dioxide: A literature review. ChemBioEng Reviews, 2(4), pp.231-256.

Rossen, W.R., 1988. A new percolation statistic with unusual properties. Journal of Physics A: Mathematical and General, 21(9), p.L533.

Roy, A., Basu, S.K. and Singh, K.P., 2002. Modeling ecosystem development on blast-furnace slag dumps in a tropical region. Simulation, 78(9), pp.531-542.

Sadrai, S., Meech, J.A., Ghomshei, M., Sassani, F. and Tromans, D., 2006. Influence of impact velocity on fragmentation and the energy efficiency of comminution. International Journal of Impact Engineering, 33(1-12), pp.723-734.

Santos, R.M., Van Bouwel, J., Vandevelde, E., Mertens, G., Elsen, J. and Van Gerven, T., 2013. Accelerated mineral carbonation of stainless steel slags for CO2 storage and waste valorization: effect of process parameters on geochemical properties. International Journal of Greenhouse Gas Control, 17, pp.32-45.

Smith, R.S., Li, Z., Dohnálek, Z. and Kay, B.D., 2014. Adsorption, desorption, and displacement kinetics of H2O and CO2 on forsterite, Mg2SiO4 (011). The Journal of Physical Chemistry C, 118(50), pp.29091-29100.

Stendardo, S. and Foscolo, P.U., 2009. Carbon dioxide capture with dolomite: a model for gas–solid reaction within the grains of a particulate sorbent. Chemical Engineering Science, 64(10), pp.2343-2352.

Tromans, D. and Meech, J.A., 2001. Enhanced dissolution of minerals: stored energy, amorphism and mechanical activation. Minerals Engineering, 14(11), pp.1359-1377.

Vigneau, E., Loisel, C., Devaux, M.F. and Cantoni, P., 2000. Number of particles for the determination of size distribution from microscopic images. Powder Technology, 107(3), pp.243-250.

Wang, J., Carson, J.K., North, M.F. and Cleland, D.J., 2006. A new approach to modelling the effective thermal conductivity of heterogeneous materials. International journal of heat and mass transfer, 49(17-18), pp.3075-3083.

Wilson, M.J., 2004. Weathering of the primary rock-forming minerals: processes, products and rates. Clay Minerals, 39(3), pp.233-266.

Yagi, S. and Kunii, D., 1955, January. Studies on combustion of carbon particles in flames and fluidized beds. In Symposium (international) on Combustion (Vol. 5, No. 1, pp. 231-244). Elsevier.

Yuen, Y.T., Sharratt, P.N. and Jie, B., 2016. Carbon dioxide mineralization process design and evaluation: concepts, case studies, and considerations. Environmental Science and Pollution Research, 23(22), pp.22309-22330.

Zimmermann, A., Wunderlich, J., Buchner, G., Müller, L., Armstrong, K., Michailos, S., Marxen, A., Naims, H., Mason, F., Stokes, G. and Williams, E., 2018. Techno-Economic Assessment & Life-Cycle Assessment Guidelines for CO2 Utilization.

Chapter 7: Application of centrifugal, MYNA, and legacy slag processes

The centrifugal separation, MYNA, and passive CO_2 mineralization processes have the potential to reduce CO_2 emissions of ISM without modification to the metallurgical process. However, like any process related to climate change mitigation, a full analysis of interdependencies is necessary to quantify the magnitude of CO_2 reduction. Additionally, there is a large source of legacy slag that may be targeted for carbon dioxide removal from the atmosphere. The mineralogy and microstructure of such legacy slag is not amenable to the centrifugal or MYNA processes without first re-melting the slag; the energetic requirements of such activities obviously exceed the benefits. Moreover, a large portion of the legacy slag has been used in the construction industry as GGBS and aggregate. As negative emissions are related to the drawdown of legacy CO_2 from the atmosphere, the reaction of legacy slags with atmospheric CO_2 represents a negative emission; this is true whether they are labeled as slag, aggregate, or otherwise. The reaction of legacy slag will require grinding, and so the grinding of demolition materials does not represent an unexpected activity. A similar potential for negative emissions exists in other solid sources of calcium and magnesium, primarily mining residues, concrete demolition wastes, and natural rocks. As is the case with slag, these materials will require grinding in order to mineralize meaningful amounts of CO_2 in a timely manner. Therefore, the primary point of contention for all sources is calculation of the net CO_2 effect (i.e., reduction or emission). For the centrifugal process, the primary source of CO_2 emissions is from production of metal used to fabricate the centrifuge and the energy used to operate the centrifuge. The CO_2 reduction comes from the circular use of calcium oxide and the enhanced recovery of low oxidation state iron. For the MYNA process, passive CO_2 mineralization of legacy slags, and passive mineralization of other solids, the primary source of CO_2 is from the generation of energy required to grind the materials. The degree of grinding required is a function of the speed at which CO_2 mineralization is desired. Faster gross mineralization requires more grinding which reduces the net CO_2 mineralization. This negative feedback limits the net rate of CO_2 mineralization achievable. Thus, the CO_2 mineralization extent and rate lies upon an operational curve of the degree of grinding, which can be altered to fit specific goals.

Chapter highlights

- The centrifugal separation and solidification process can operate at very low energy expenditure due to the nature of the process being a simple liquid-liquid separation.
- The slow solidification followed by solid-state quenching (so-called, 'MYNA') can be used to generate materials which completely react with CO_2 within 1 hour under iron and steelmaking flue gas conditions (30 ˚C, 5-20 volume percent CO_2) so long as relative humidity (RH) is maintained near 90%.
- CO_2 mineralization using legacy slag, other waste materials, or natural rocks can be accomplished using simple grinding and the reaction conveyor.
- CO_2 mineralization using atmospheric CO_2 requires substantial gas-solid contact time; such a system can be achieved using greenhouses.
- Certain minerals, in particular Mg-silicates and amorphous compounds, are likely not good candidates for CO_2 mineralization due to their very low CO_2 diffusivity.

Publications relevant to this chapter

- Quantification of the CO_2 mineralization potential of ironmaking and steelmaking slags under direct gas-solid reactions in flue gas, International Journal of Greenhouse Gas Control Vol. 87C p.100-111 (2019), **Corey A. Myers**, Takao Nakagaki, and Kosei Akutsu.
- Effect of Solidification and Cooling Methods on the Efficacy of Slag as a Feedstock for CO_2 Mineralization, ISIJ International Vol. 58 No. 2 p.211-219 (2018), **Corey Adam Myers** and Takao Nakagaki.

7.1. Contemporary slag

For contemporary and future slag, operations beginning at the molten state (i.e., centrifugal separation or in-container solidification) allow for increased control of the solid-state properties. For centrifugal separation, the CO_2 release is directly determined by the energy used to operate the centrifuge and the CO_2 intensity of that energy. The energy associated with molten slag handling as part of in-container solidification is negligible as the process involves passive solidification within insulted containers. Both processes have embodied CO_2 emissions in the materials used to fabricate the equipment and containers.

7.1.1. Centrifugal process

The sources and sinks of CO_2 in the centrifugal process are shown in **Fig. 7-1** for conceptual reference. Carbon dioxide in red is indicative of releases from the centrifuge process or associated energy and materials. Carbon dioxide in green is indicative of partial or full removals due to the centrifugal process.
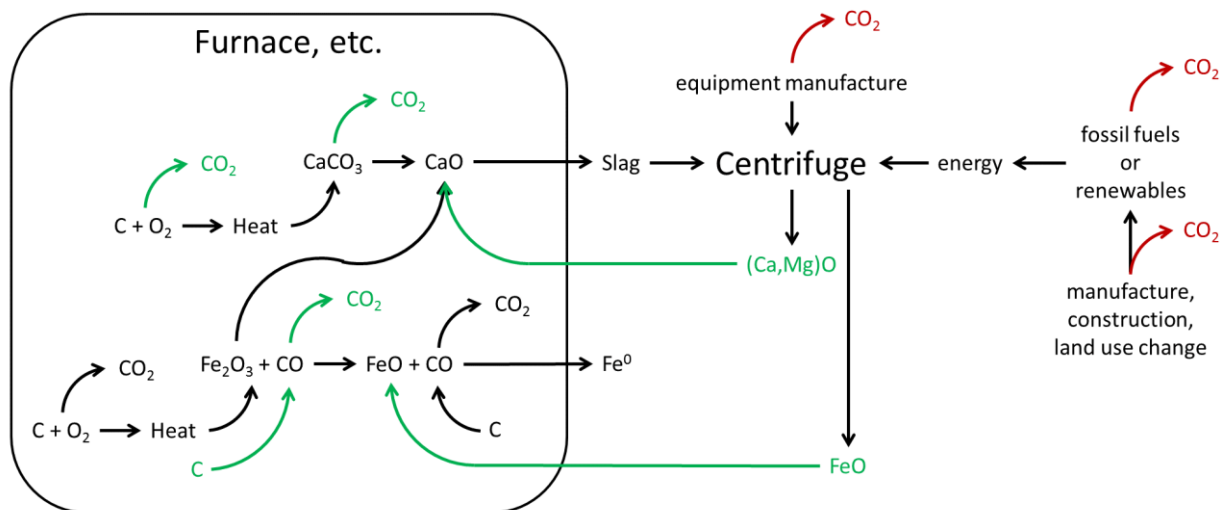
Fig. 7-1. Schematic of CO_2 emission sources (in red) and reduction sources (in green) in the centrifugal process and associated activities.

Centrifugal separation occurs in a relatively small volume container. This is done to expedite the separation process and to limit the energy draw during maximal rotational velocity. Given its small volume, centrifugal operations must be run nearly continuously (i.e., matching the filling and tapping rate of the furnaces). As such, the centrifuge requires a constant and reliable energy supply. This constraint means that current iterations of centrifugal separation will inherently rely on fossil fuel power. Power can be supplied in one of two fashions: 1) a dedicated power supply such as a generator, or 2) a battery pack that can at a minimum draw from the grid. A battery-based system could be paired with purpose-built RE (e.g., PV+LiB). However, the intermittent nature of RE (at times lasting days) means that a battery system needs to be able to draw from the grid. This method has the advantage of 'greening' over time as the CO_2 intensity of utility power decreases. The energy for operation of the centrifuge was calculated based on conversion of the 2D simulation into a 3D structure. Due to the overwhelming strength of the centrifugal force as compared to the gravitational force, differences in composition along the vertical axis were ignored. The geometry used in

calculation is shown schematically in **Fig. 7-2**. From this symmetric geometry the work required to rotate the centrifuge and internal slag (W_r) was calculated as the angular kinetic energy per **Eq. (7-1),** where the moment of inertia is given by I, the angular velocity by ω, and the initial and final conditions are denoted by the subscripts i and f, respectively. The work for each element of slag within the container, as well as the container itself, was calculated and summed.

$$W_r = \frac{1}{2}I_f\omega_f^2 - \frac{1}{2}I_i\omega_i^2 \qquad\qquad (7-1)$$
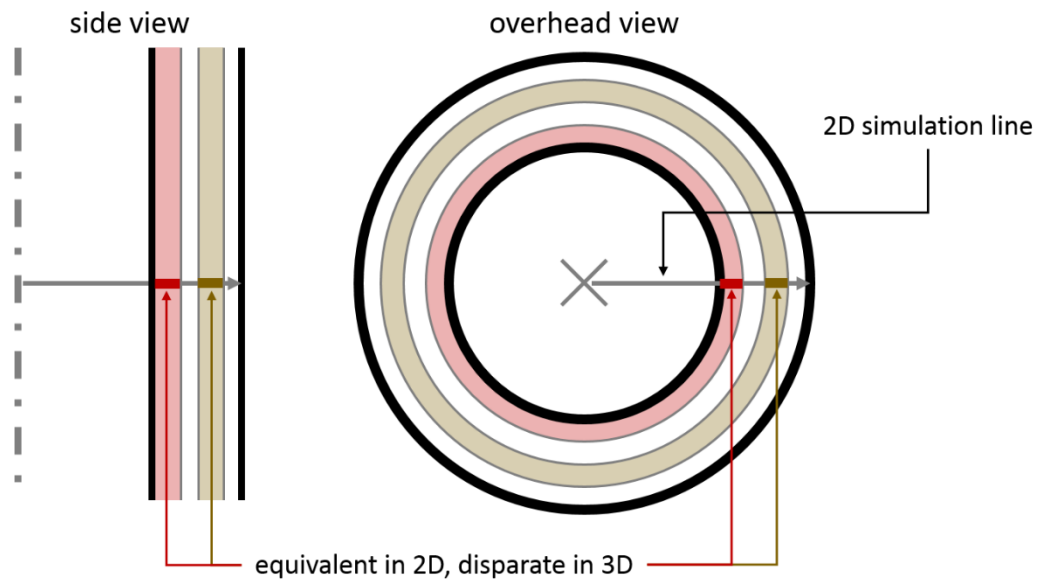
Fig. 7-2. Schematic of the geometry used to calculate the centrifugal work.

The centrifugal separation process was separated into two process for the purpose of performing the above calculation. The first process consists of the angular acceleration (i.e., alteration to ω). The second process involves the separation of elements within the container (i.e., alteration to I). Though separation and acceleration occur concurrently, the strong dependence of separation on centrifugal force (ergo on angular velocity) means that separation does not begin in haste until full angular velocity is reached.

Given the extreme angular velocity of the centrifuge, the energetic effect of air resistance on the outer edge and losses from friction at bearings was included in calculations. The additional torque required to overcome the viscous force of air on the centrifuge surface is dependent on the angular velocity, its geometry, and the properties of air. Air will naturally be heated by the centrifuge, lowering its viscosity and thus its drag effect on the centrifuge. However, the large temperature difference between the air and centrifuge surface will induce significant natural convection. Moreover, the advective effects of the centrifuge rotation will continuously clear the surface of the centrifuge of heated air. Given these effects, it was considered conservatively safe to assume a constant air temperature of 300 K and air pressure of 101.325 kPa. The geometry used in the drag calculation includes a heat and material shield around the centrifuge (spaced 50 mm from the outer edge of the centrifuge). This shield acts to reduce radiative heat loss and protects against potential ejection of molten slag from the centrifuge that may occur from imprecise filling (**Fig. 7-3**). The centrifuge was idealized as a perfect cylinder sans weld lips, flanges, and other surface imperfections.

Drag on the top and bottom of the cylinder was ignored along with drag during the acceleration period.
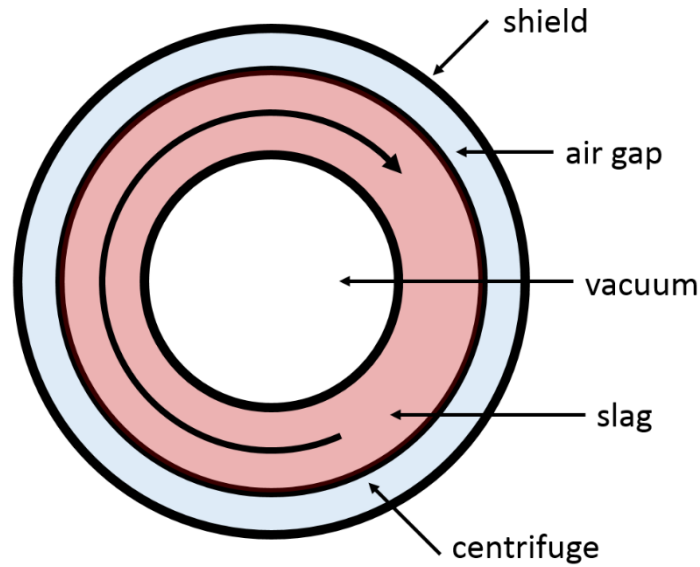
Fig. 7-3. The geometry used in the determination of air drag on the rotating centrifuge.

The flow regime (Taylor number: Ta) of air between the centrifuge and shield was calculated via **Eq. (7-2)**, where values >400 are considered turbulent [Fénot et al., 2011]. In **Eq. (7-2)** the external radius of the centrifuge is given by r_c, the hydraulic diameter is given by D_h and calculated by **Eq. (7-3)**, and the other values (ρ: density, μ: dynamic viscosity) are the properties of air. The inner surface of the shield is given by r_S. **Equation 7-2** can be interpreted as the ratio of the centrifugal force to the viscous force. The Reynold's number (Re) for concentrically rotating cylinders was calculated per **Eq. (7-4)** with the gap between the centrifuge and the shield given by $\Delta r = r_S - r_C$.

$$Ta = \frac{\omega^2 r_C \rho^2 \left(\frac{D_h}{2}\right)^3}{\mu^2} \tag{7-2}$$

$$D_h = \frac{2(r_S^2 - r_C^2)}{(r_S + r_C)} \tag{7-3}$$

$$Re = \frac{\rho \omega r_C \Delta r}{\mu} \tag{7-4}$$

Plotting the Re against the Ta of the centrifugal process reveals that the flow is turbulent under steady state operation. For concentrically rotating cylinders under turbulent flow conditions, the moment coefficient (C_M) was determined empirically by Tachibana et al., 1960 as **Eq. (7-5)**. The resultant moment on the centrifuge (M_C) is given by **Eq. (7-6)** and the additional energetic requirement to overcome drag (E_d) is given by **Eq. (7-7)** where H is the height of the centrifuge.

$$C_M = 0.146 \left(\frac{r_S \Delta r}{r_C^2} \right)^{0.25} Re^{-0.3} \tag{7-5}$$

$$M_c = 0.5 C_M \pi \rho \omega^2 r_i^4 H \tag{7-6}$$

$$E_d = M_C \omega \Delta t \tag{7-7}$$

The energetic consumption due to friction in the bearings (E_b) was calculated using **Eq. (7-8)** where μ_B is the friction coefficient of the bearing (set to 0.002 for thrust bearing), d is the bore diameter of the bearing (set to 113 mm), and F is the load on the bearing (i.e., the weight of the centrifuge and internal slag). The upper bearing was ignored due to its unloaded nature.

$$E_b = \frac{1}{2} \mu_B F d \omega \Delta t \tag{7-8}$$

It was assumed that the centrifuge was directly driven; thus, no power train losses were applicable. The total energy (E_T) to operate the centrifuge is then calculated by aggregating the above equations as **Eq. (7-9)**. The E_T was converted to CO_2 emissions ($CO_{2,o}$) by multiplication with the CO_2 intensity of energy generation (ϵ_E) via **Eq. (7-10)**. The ϵ_E for various common fuels and the major ISM locations is summarized in **Table 7-1**.

$$E_T = \frac{1}{2} I_i \omega_f^2 + \frac{1}{2} \omega_f^2 (I_f - I_i) - E_d - E_b \tag{7-9}$$

$$CO_{2,o} = E_T \epsilon_E \tag{7-10}$$

The gross CO_2 emissions reduction of the centrifugal process was calculated based on the material recovery results from simulations. Recovered CaO and MgO of purity exceeding 95% was assumed to be recycled to the furnace. A molar equivalent quantity of CO_2 was assumed to be directly avoided by this recycling activity. Additionally, a reduction in CO_2 emissions from reduced fuel usage was calculated. This reduction was calculated as the energy difference (E_h) of heating CaO as opposed to $CaCO_3$ from 300 K to 1223 K (complete $CaCO_3$ decomposition) along with the enthalpy of decomposition (ΔH_{dec}°) of calcium carbonate (**Eq. (7-11)**). The total moles of calcium and magnesium were converted to a mass of CaO (m) for calculation. The energy was converted to CO_2 by assuming coking coal as the fuel with a complete conversion of C to CO_2 and a molar heating value (ΔH_{coke}) of 0.312 MJ/mol; coking and other coal preparation operations were not considered (**Eq. (7-12)**).

$$E_h = \left(c_{P,CaCO_3} m_{CaCO_3} - c_{P,CaO} m_{CaO} \right) \Delta T + m_{CaCO_3} \Delta H_{dec}^\circ \tag{7-11}$$

$$CO_{2,h} = \frac{E_h}{\Delta H_{coke}} \tag{7-12}$$

Recovered low oxidation state iron was also considered in net CO_2 calculation. For the BF, the recovered iron is ostensibly Fe^0 and can thus be sent directly to the steelmaking process as scrap. The CO_2 offset of recovery of this material is then equivalent to the per mass CO_2 emissions of crude iron production ($\epsilon_{BF} = 1.447\ kgCO_2/kg - Fe$) [Freuhan et al., 2000]. For steelmaking processes, the recovered iron is ostensibly FeO and was assumed to be used as charge in ironmaking operations. The CO_2 offset was calculated as the stoichiometry of **Eq. (7-13)**. The energy required to heat FeO as opposed to Fe_2O_3 was not considered. The gross CO_2 emissions reduction for ironmaking and steelmaking then becomes **Eq. (7-14)** and **Eq. (7-15)**, respectively.

$$Fe_2O_3 + CO \rightarrow 2FeO + CO_2 \qquad (7-13)$$

$$Ironmaking: CO_{2,red} = \left[mol_{CaO} + mol_{MgO} + CO_{2,h} + (kg_{Fe}\epsilon_{BF})\right]MW_{CO_2} \qquad (7-14)$$

$$Steelmaking: CO_{2,red} = \left[mol_{CaO} + mol_{MgO} + CO_{2,h} + (mol_{FeO}/2)\right]MW_{CO_2} \qquad (7-15)$$

Table 7-1. The CO_2 intensities of various fuel sources and regions.

Energy source	CO_2 intensity (kgCO$_2$/kWh)
Natural gas[‡]	0.405
Diesel[‡]	0.715
Solar PV[§]	0.0052
Onshore wind[§]	0.0042
OECD[‡]	0.421
China[‡]	0.681
‡: [IEA, 2016]; §: [Pehl et al., 2017]	

The overall energy consumption of the centrifuging process was calculated to the point of complete solidification of the internal slag (conservatively set to 10 minutes for all slags). This resulted in 3.204, 4.033, and 3.760 MJ/m^3-slag for BF, BOF, and EAF slag, respectively. Assuming usage of the local grid, this is an equivalent CO_2 emission of 0.407, 0.512, and 0.477 kgCO$_2$/m^3-slag if applied in Japan and 0.606, 0.763, and 0.711 kgCO$_2$/m^3-slag if applied in China [MOE, 2018; IEA, 2016]. This degree of CO_2 emissions represents 0.036%, 0.033%, and 0.040% of the CO_2 reduction potential of BF, BOF, and EAF slag if applied in Japan and 0.054%, 0.049%, and 0.060% percent if applied in China. Energy recovery by regenerative breaking could be used to charge a battery system, lowering the total energy consumption and thus CO_2 emissions, though this option was not explored due to the relatively low CO_2 emissions and the extreme working environment. The energy required to transport slag from place to place within the process (e.g., from the centrifuge to the disparate usage sites) was considered comparable to current energetic demands of slag transport. As such, the CO_2 emissions associated with these ancillary tasks are captured in the total CO_2 emissions of ISM and therefore do not need to be separately calculated here.

Along with CO_2 emissions from operating the centrifugal process, there is a CO_2 debt from the production of the centrifugal equipment. This CO_2 debt was estimated by the production of the steel needed for fabrication of the centrifuge body and shield. Assuming a conventional steel production CO_2 intensity of 1.636 kgCO_2/kg-steel [Freuhan et al., 2000], the total CO_2 debt of building a centrifuge with 2 m^3 capacity is 2.983 tonnes CO_2. It is assumed that a centrifuge can last for 1 year of operation. This relatively long lifespan, despite being in contact with molten slag, is due to several details of the operation. Firstly, the inner surface of the outer shell of the centrifuge will be in contact primarily with FeO and Fe^0, due to the centrifugal action; dissolution by slag is thus limited. The inner surface of the inner shell will be free from contact with slag due to the centrifugal force (i.e., a small headspace at the completion of filling results in a small gap between molten slag and the centrifuge). The upper and lower caps to the centrifuge may require some form of protection from the molten slag (e.g., MgO refractory), but this detailed design has not yet been evaluated. The number of containers required is based on the timing of the tapping operations (cf. Chapter 4.1.2). Accounting for operating schedule, the maximum amount of slag that a centrifuge can treat ~185 kt/y (i.e., 6 centrifuges treating a continuously tapped BF furnace producing 4 megatonnes of steel per year). At a tapping schedule of 6 hours, the per centrifuge slag treatment quantity falls to ~9 kt/y. These two extremes determine the number of centrifuges required and therefore the amount of steel that must be produced for centrifuge fabrication. Applied globally, these two extremes generate ~31 and ~637 ktCO_2/y for the production of the centrifuge bodies. The global emissions reduction potential from centrifuging is 382 MtCO_2/y. The embodied CO_2 of the centrifuge bodies is thus three to four orders of magnitude less than the CO_2 reduction provided by centrifuging molten slag.

7.1.2. MYNA process

The sources and sinks of CO_2 in the MYNA process are shown in **Fig. 7-4** for conceptual reference. Carbon dioxide in red is indicative of releases from the MYNA process or associated energy and materials. Carbon dioxide in green is indicative of partial or full removals due to the MYNA process.
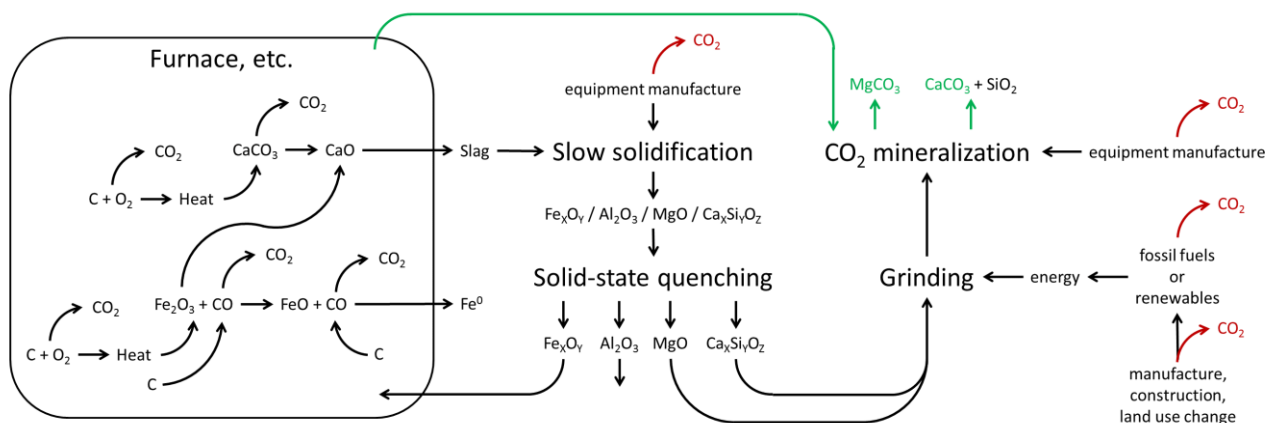
Fig. 7-4. Schematic of CO_2 emission sources (in red) and reduction sources (in green) in the MYNA process and associated activities.

The MYNA process provides an alternative to centrifugal separation for CO_2 reduction. The MYNA process is more akin to current slag treatment methods used in ISM facilities. Unlike the centrifugal separation method, the treatment of molten slag in the MYNA process does not incur an operational energy penalty. Instead, the operational energy penalty comes from the grinding of slag

necessary to achieve a pre-specified CO_2 mineralization rate. The energy penalty is therefore dependent on the specific mineralogy and GSD of slag. The process was evaluated for industry average BF, BOF, and EAF slags.

The in-container solidification process dictates the size of the mineral grains within each slag. The mineral grain sizes were predicted as discussed in Chapter 4.2.2. The mineral composition was estimated based on stability assumptions from empirical and theoretical studies, summarized in **Fig. 7-5**. The mineral composition is provided in **Table 7.2**.
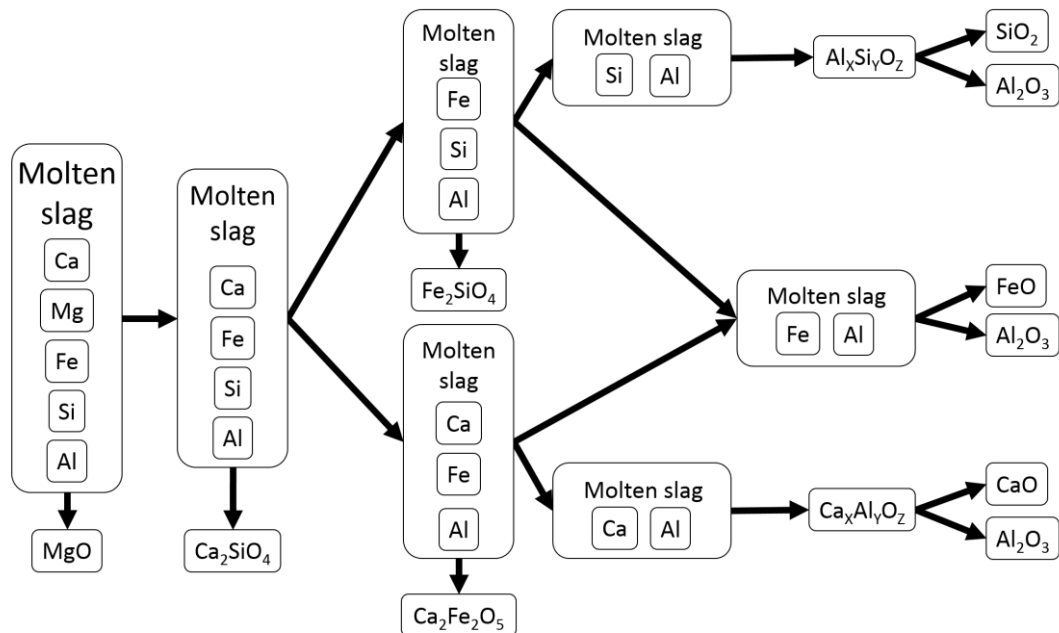
Fig. 7-5. The method of estimating the mineral phases that emerge in the in-container solidification process.

Table 7-2. The mineralogical compositions of BF, BOF, and EAF slag generated by slow solidification.

Mineral	BF	BOF	EAF*
MgO	11.9%	6.4%	8.1%
Ca_2SiO_4 (γ)	59.4%	41.1%	46.4%
SiO_2	18.1%	---	---
$Ca_{12}Al_{14}O_{33}$	---	5.5%	---
Al_2O_3	---	0.2%	6.6%
$Al_6Si_2O_{13}$	9.8%	---	---
$Ca_2Fe_2O_5$	---	46.8%	7.9%
FeO	---	---	30.9%
Fe_2SiO_4	0.8%	---	---
values do not sum to 100% due to rounding.			

After solidification, a single solid-state quenching step was performed. The liberation of materials due to quenching is dependent on the GSD, quenching rate, and mineral composition of the slag; however, an upper limit is 40% liberation. Multiple quenching steps would enhance

liberation but have not yet been demonstrated experimentally. The remaining slag plate is crushed to liberate the remaining 60% bound minerals. As conventional grinding methods produce random breakages, the extent of crushing needed for full liberation is smaller than the grain size (set to ½ the GSD). After quenching and crushing, the materials were assumed to be separated based on density and magnetism. The materials not containing magnesium or calcium (i.e., cannot contribute to CO_2 mineralization) are removed. Low oxidation state iron (i.e., Fe^0 or FeO) are recycled to the furnace. Aluminates and aluminosilicates are assumed to be used as aggregate in construction. The removal of non-reactive materials also removes their contribution to grinding energy. The calcium- and magnesium-bearing materials are further ground for reaction with carbon dioxide. In a system that optimizes reduction of process energy, each mineral could be ground separately, so as the optimal reaction speed-efficiency tradeoff is met. However, to reduce the capital expense of multiple grinders, it is assumed that all reactive materials are mixed for grinding and CO_2 mineralization. It should be noted that the large grain sizes produced by slow solidification eliminate that the inhibitive effects of mineral locking.

The time required to reach a given reaction extent as a function of the 99% volume passing diameter (X_{V99}) is provided in **Fig. 7-6**. The operational net CO_2 that results from grinding to enhance the rate of mineralization to a given extent is shown in **Fig. 7-7**. **Figure 7-7** was calculated assuming a diesel-powered grinder in order to mimic the likely CO_2 intensity of grinding equipment currently in use at ISM facilities.
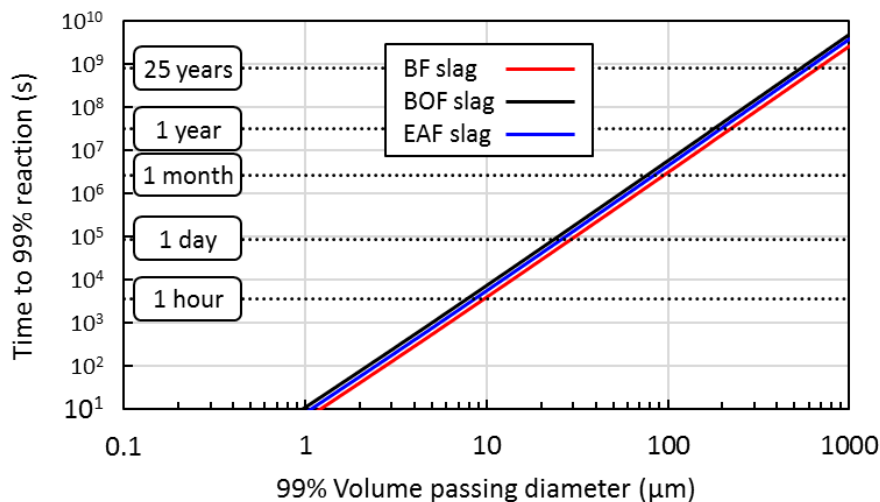

Fig. 7-6. The time to 99% reaction as a function of grinding diameter in terms of the 99% volume passing diameter ($X_{V,99}$). Mineralization reactions are assumed to occur at 5 vol% CO_2, 30 °C, and a relative humidity (RH) of 90%.
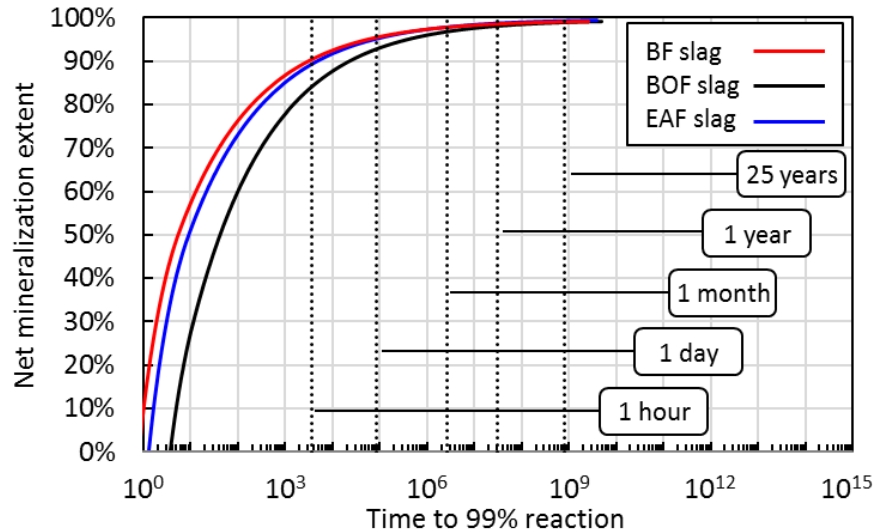
Fig. 7-7. The net mineralization extent that results from performing grinding in order to reach 99% reaction by a given time. Energy for grinding is derived from diesel. Mineralization reactions are assumed to occur at 5 vol% CO_2, 30 °C, and RH=90%.

The remarkably similar behavior of the three disparate compositions is primarily due to the ejection of most MgO and Al_2O_3 from calcium silicate species, the reduced grinding energy due to removal of non-reactive species while mineral grains are large, and the reduced need for grinding due to the production of mineral species with high CO_2 diffusion rates through their product layer. These effects become particularly pronounced after comparison to passive CO_2 mineralization of legacy slags (Chapter 7.2).

The energy required for transport and separation of slag was considered comparable to current operations. Thus, the associated CO_2 emissions are inherent to total CO_2 emissions of ISM and not separately accounted for here. The CO_2 emissions from grinding were described in Chapter 5 and the CO_2 mineralization rate was described in Chapter 6.

Along with CO_2 emissions from operating the grinding equipment, there is a CO_2 debt from the production of the solidification containers. This CO_2 debt was estimated by the production of the raw materials; namely, refractory bricks and steel. A 300 mm layer of refractory (simplified as MgO) is surrounded by a 20 mm steel shell. These dimensions are equivalent to slag torpedo-cars (used to transport molten slag), and thus considered conservatively safe. The chemistry of ironmaking slag means that alumina and alumina-silicate refractory is more resistant to chemical dissolution; however, inclusion of alumina and silica via dissolution into the slag would negatively impact the CO_2 mineralization rates. Therefore, all slag types were designed to be solidified in containers using MgO type refractory. Based on the results of Chapter 4.2.3, an internal container volume of 4.9 m^3 with an internal slag height of 10 cm was chosen. The CO_2 footprint of the steel was set as that of the modern BF-BOF process: 1.636 kgCO_2/kg-steel [Freuhan et al., 2000]. The refractory is expected to slowly dissolve into the slag due to its high temperature and basicity. However, any MgO dissolved into slag will be used for CO_2 mineralization. Therefore, the CO_2 footprint of the refractory brick was set as only the energy to heat $MgCO_3$ to its decomposition temperature, complete the decomposition to MgO and CO_2, and further heat the material to 900 °C to ensure purity [Waples and Waples, 2004]. The dissolution rate of the refractory bricks was assumed equivalent to that of modern day BOF

furnaces which require replacement of internal refractory every 35,000 heating cycles [Dhaka, 2017]. Assuming the 1 hour solidification time (per Chapter 4.2.2) equates to replacement of the refractory every 4 years with the additional CO_2 emissions from its production. The metal casing lifetime was assumed to be sufficiently long as to be negligible (i.e., embodied CO_2 emissions only occur once). Each container weighs 149 tonnes with an embodied emission of 122 tonnes of carbon dioxide. The recurring CO_2 emissions from manufacture of MgO refractory is 86 tonnes every 4 years. Given that the container size was made to match the BF slag production rate of 1.111 megatonnes/y, 9 containers are required. Assuming the slag is ground with a diesel-powered grinder such that complete reaction occurs within 1000 seconds (~17 minutes), the initial CO_2 debt from container construction is 'paid off' within ~22 hours of operation. Likewise, the recurrent CO_2 emissions from production of MgO refractory represents 0.006%, 0.007%, and 0.006% of the CO_2 mineralization potential of BF, BOF, and EAF slag, respectively.

An important distinction between the MYNA and centrifuge processes is the timing of the energy-intensive activity. Centrifugal separation must be run concurrent with slag production; likewise, in-container solidification must match slag production rate and CO_2 mineralization rate must match production rate. However, grinding can be temporally-offset from the solidification and mineralization processes. The ability to run grinding intermittently makes operating the process with RE (e.g., PV+LiB) technically simpler than the centrifuge process. The lower CO_2 intensity of RE alters the optimal grinding extent for the MYNA process. Purchase of RE with battery power drastically improves the net efficiency as is discussed in Section 7.3. However, the inherently high performance of the MYNA process means that the increased emissions reduction from usage of RE is minor.

7.2. Legacy slag

The sources and sinks of CO_2 in the legacy slag process are shown in **Fig. 7-8** for conceptual reference. Carbon dioxide in red is indicative of releases from the process, associated energy, and associated materials. Carbon dioxide in green is indicative of partial or full removals due to the process.
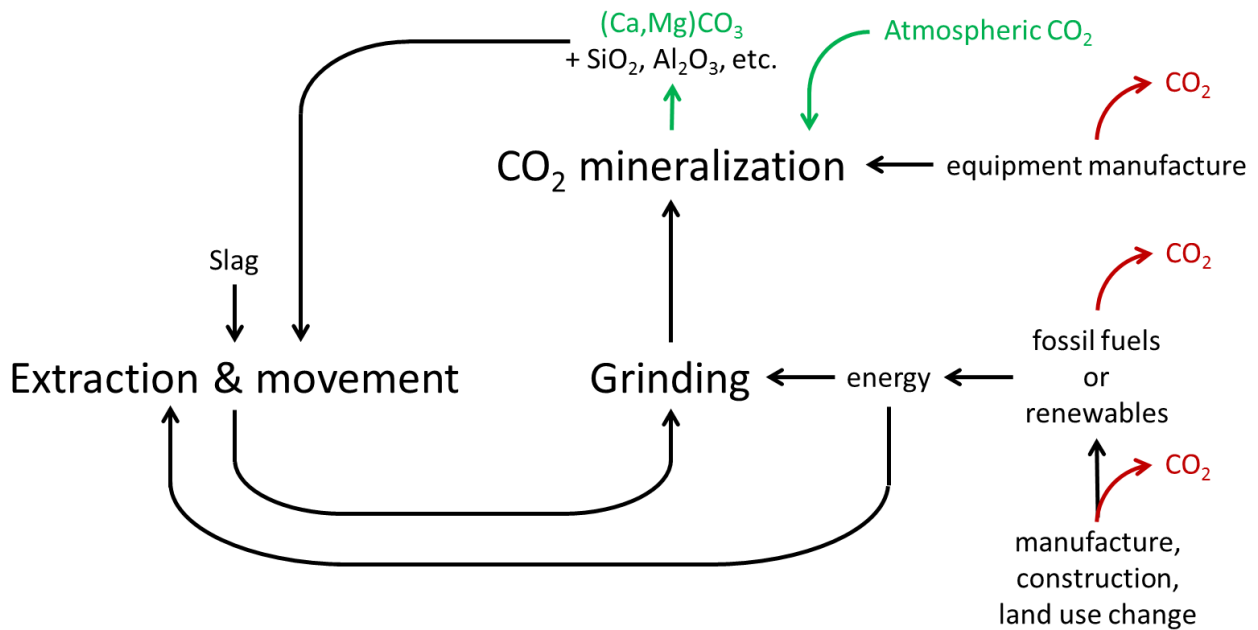
Fig. 7-8. Schematic of the CO_2 emission sources (in red) and reduction sources (in green) in the legacy slag process and associated activities.

Unlike contemporary slag, legacy slag is not available for alteration to the mineralogy, crystallinity, or GSD. As such, the process is a simple grinding of slag followed by contact with flue gases. Optimization of the process involves designing the extent and timing of grinding such that the rate of CO_2 mineralization is meaningfully rapid but not excessively energy intensive. The mixed mineralogy and small GSD of legacy slag means that effects from mineral locking and gangue content are important. The traditional implementation of rapid cooling means that a large portion of legacy slags are amorphous is nature. Given the unknown mineralogy of extant slag, a mix of hypothetical and empirical data was used in calculations. Published mineralogy for extant ironmaking slag and steelmaking slag [Gautier et al., 2013; Bodor et al., 2013; Liu et al., 2016] was used as a baseline. Additionally, given the common practice of generating so-called "glassy" slag, amorphous Ca_2SiO_4 was also modeled. Lastly, a Monte Carlo analysis of hypothetical slag compositions was run using the industry-average chemical compositions and varying the local chemical composition via a gaussian such that the output closely matched the observed spread in empirical mineralogy [Mombelli et al., 2016; Gautier et al., 2015]. The Monte Carlo slag compositions are displayed as ternary diagrams in **Fig. 7-9**. The mineralogical compositions used in analysis are provided in **Table 7-3** through **7-5**. These compositions are plotted using the performance indices from Chapter 6 in **Fig. 7-10**.

Fig. 7-9. The molten synthetic slag compositions created by Monte Carlo simulations for a) BF slags, b) BOF slags, and C) EAF slags.

Table 7-3. The mineralogical compositions of legacy steelmaking slag used in analysis of passive CO_2 mineralization.

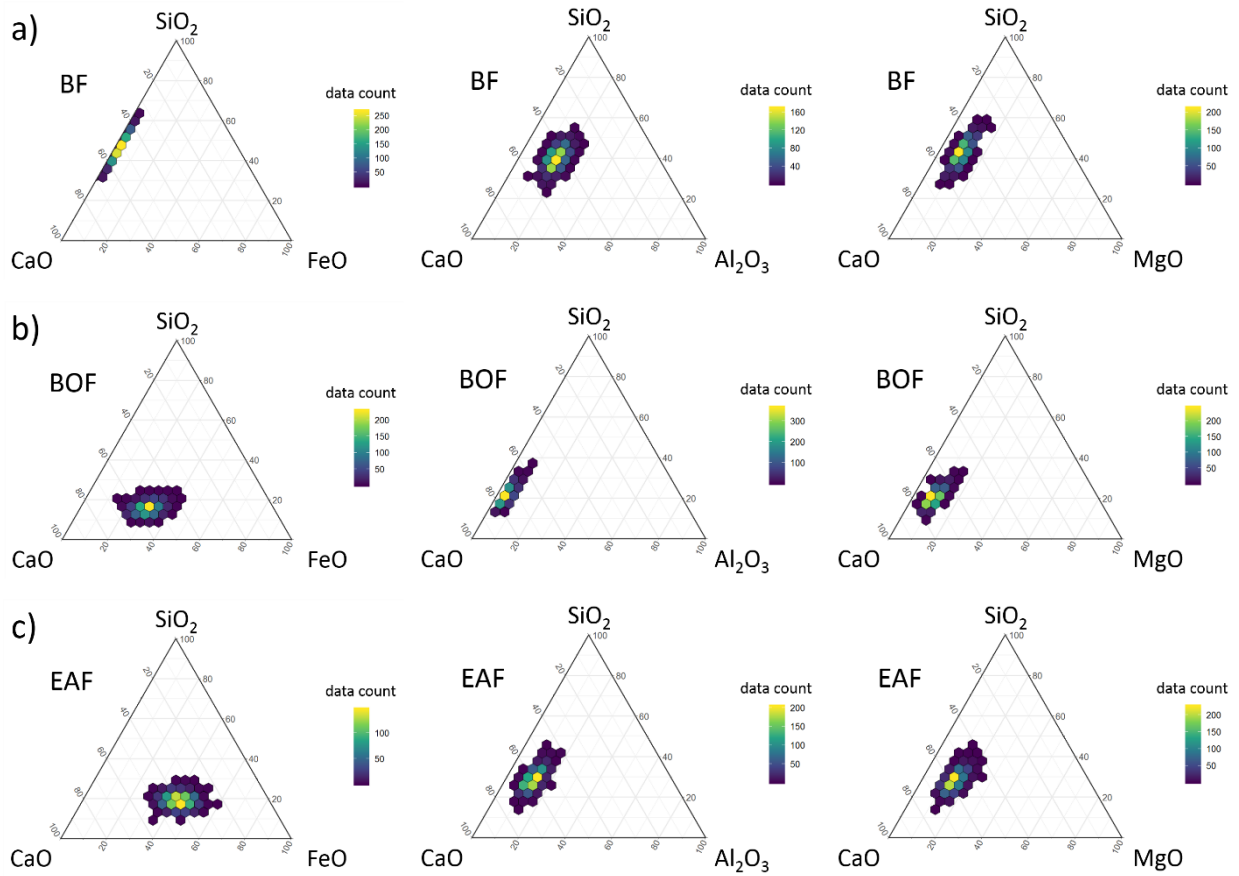| Mineral	Steel 1	Steel 2	Steel 3	Steel 4	Steel 5	Steel 6	Steel 7
MgO	2.79%	3.72%	6.73%	6.19%	4.22%	10.72%	4.67%
CaO	9.61%	15.78%	2.09%	8.56%	---	23.12%	12.06%
FeO	---	---	---	---	---	1.63%	---
Fe_3O_4	---	---	---	---	---	0.89%	---
$Ca_2Fe_2O_5$	31.49%	32.34%	---	---	41.12%	11.13%	38.69%
$MgSiO_3$	18.78%	5.19%	5.14%	11.28%	5.25%	0.38%	2.60%
$CaSiO_3$	7.70%	4.12%	1.41%	3.71%	---	0.84%	---
$Ca_3Si_2O_7$	---	---	11.35%	4.22%	---	---	---
$Ca_2MgSi_2O_7$	---	---	3.53%	2.84%	---	---	---
Ca_2SiO_4 (β)	25.36%	37.89%	4.70%	5.98%	---	32.52%	41.98%
Ca_2SiO_4 (γ)	4.27%	0.97%	19.25%	27.74%	---	---	---
$Ca_3MgSi_2O_8$	---	---	18.39%	7.27%	---	---	---
$Ca_7MgSi_4O_{16}$	---	---	27.41%	22.20%	---	4.31%	---
Ca_3SiO_5	---	---	---	---	49.41%	---	---
$CaAl_2Si_2O_8$	---	---	---	---	---	6.65%	---
$Ca_2Al_2SiO_7$	---	---	---	---	---	1.30%	---
$MgAl_2O_4$	---	---	---	---	---	1.45%	---
$MgFe_2O_4$	---	---	---	---	---	2.35%	---
$CaMgSiO_4$	---	---	---	---	---	2.57%	---

Table 7-4. The mineralogical compositions of legacy ironmaking slag used in analysis of passive CO_2 mineralization.

Mineral	Iron 1	Iron 2	Iron 3	Iron 4	Iron 5	Iron 6	Iron 7	Iron 8
$MgSiO_3$	---	---	---	---	---	---	---	10.17%
$CaSiO_3$	4.19%	4.22%	---	---	12.88%	---	25.34%	---
$Ca_3Si_2O_7$	---	---	2.39%	---	---	---	---	---
$Ca_3MgSi_2O_8$	---	---	---	31.01%	---	---	---	---
$Ca_7MgSi_4O_{16}$	---	---	10.51%	---	---	---	---	---
$CaAl_2Si_2O_8$	11.97%	2.51%	---	---	7.42%	15.37%	11.38%	---
$Ca_2Al_2SiO_7$	83.84%	93.27%	87.09%	68.71%	79.70%	83.47%	63.28%	85.90%
$MgAl_2O_4$	---	---	---	0.28%	---	1.16%	---	3.93%

Table 7-5. The mineralogical compositions of synthetic BF, BOF, EAF, and glassy slag used in analysis of passive CO_2 mineralization.

Mineral	Synthetic BF slag	Synthetic BOF slag	Synthetic EAF slag	'Glassy'
CaO	---	13.37%	0.10%	---
FeO	---	12.93%	6.61%	---
Fe_3O_4	---	---	0.47%	---
$MgFe_2O_4$	---	5.54%	49.10%	---
$Ca_2Fe_2O_5$	---	32.41%	0.24%	---
Al_2O_3	3.31%	---	---	---
SiO_2	1.13%	---	---	---
$CaSiO_3$	5.99%	---	0.53%	---
$Ca_2MgSi_2O_7$	3.60%	---	0.07%	---
Ca_2SiO_4	0.13%	35.76%	42.70%	---
Ca_2SiO_4 (amorphous)	---	---	---	100%
$Ca_3MgSi_2O_8$	38.77%	---	0.08%	---
$Ca_7MgSi_4O_{16}$	13.68%	---	---	---
$CaFeSiO_4$	---	---	0.10%	---
$Ca_2Al_2SiO_7$	10.23%	---	---	---
$CaAl_2Si_2O_8$	9.07%	---	---	---
Al_2SiO_5	14.10%	---	---	---
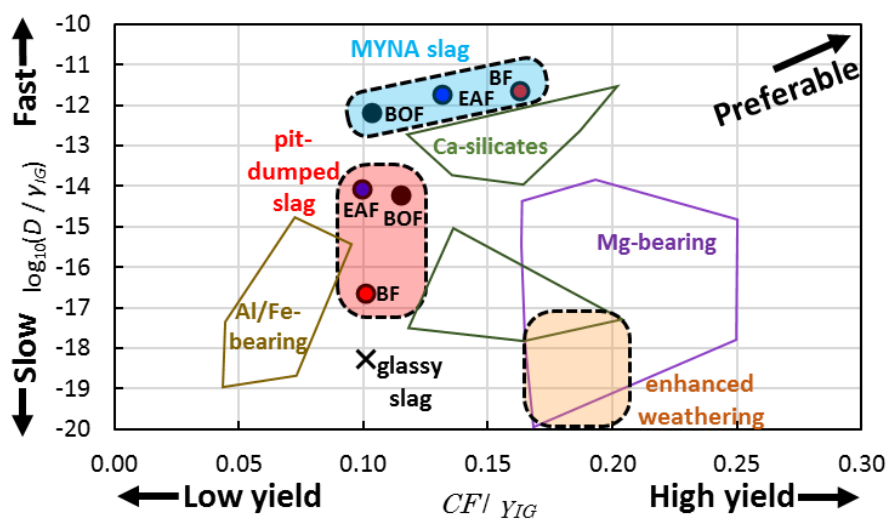
Fig. 7-10. Legacy slag graphed on the performance index map. Diffusivity values are only relevant at 30 ˚C and a RH=90%.

The effects of ML and the slow kinetics of many minerals in legacy slag means that the CO_2 uptake of legacy slag quickly falls as reactions proceed. To overcome this deceleration of CO_2 mineralization, the slag must be ground to the extent that such inhibitory effects are removed. However, such extensive grinding greatly reduces the net CO_2 efficiency of the process due to the need to generate extremely small PSD. Additionally, a decrease in comminution efficiency occurs when grinding below 1 μm due to increased plastic deformation of materials [Fuerstenau and Abouzeid, 2002]. As the diameter of mineral grains within legacy slag measures in the single micrometers, no separation of

unreactive materials is possible; thus, substantial grinding energy is applied to gangue compounds. Moreover, the inhibitory effects of ML remain pronounced until very small PSDs have been produced.

The time required to reach a given reaction extent as a function of the 99% volume passing diameter ($X_{V,99}$) for the legacy ironmaking and steelmaking slags is provided in **Fig. 7-11** and **Fig. 7-12**, respectively. The synthetic slags are included on the graphs to indicate the accuracy of the synthetic slag generation process. The synthetic BF, BOF, EAF, and glassy Ca_2SiO_4 are compared in **Fig. 7-13**. The operational net CO_2 that results from grinding to enhance the rate of mineralization to a given extent is shown in **Fig. 7-14**, **Fig. 7-15**, and **Fig. 7-16** for legacy ironmaking, legacy steelmaking, and the synthetic slags, respectively. These figures were calculated assuming a diesel-powered grinder for comparison with the MYNA process results.
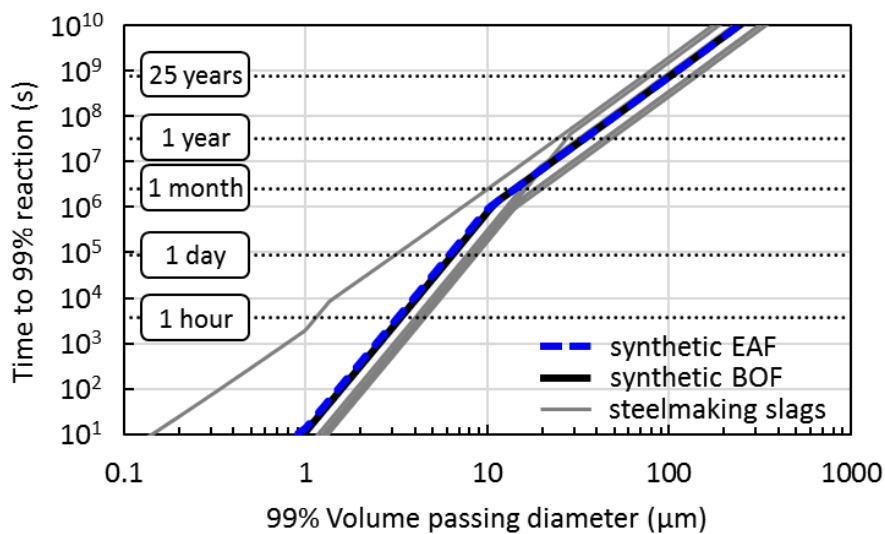
Fig. 7-11. The time to 99% reaction as a function of $X_{V,99}$ for legacy steelmaking slags at 5 vol% CO_2, 30 °C, and RH=90%. The synthetic pit-cooled BOF and EAF slags are also shown for comparison.
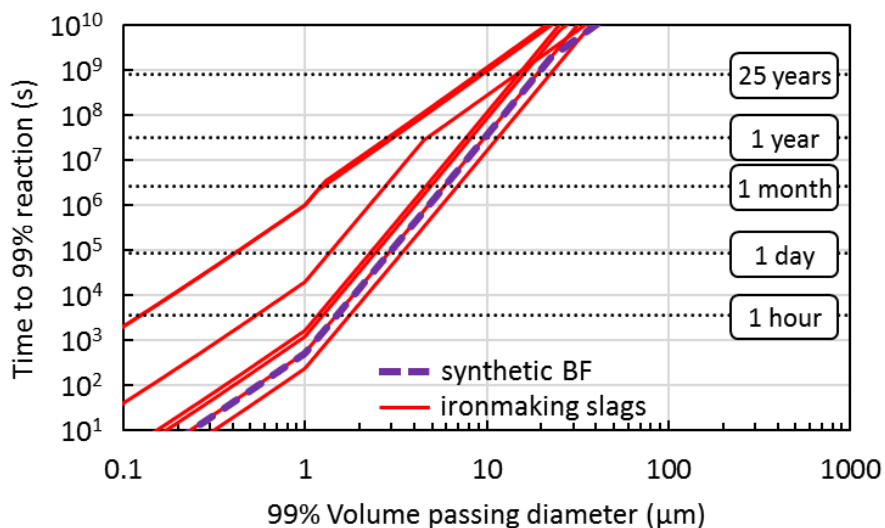
Fig. 7-12. The time to 99% reaction as a function of $X_{V,99}$ for legacy ironmaking slags at 5 vol% CO_2, 30 °C, and RH=90%. The synthetic, pit-cooled BF slag is shown for comparison.
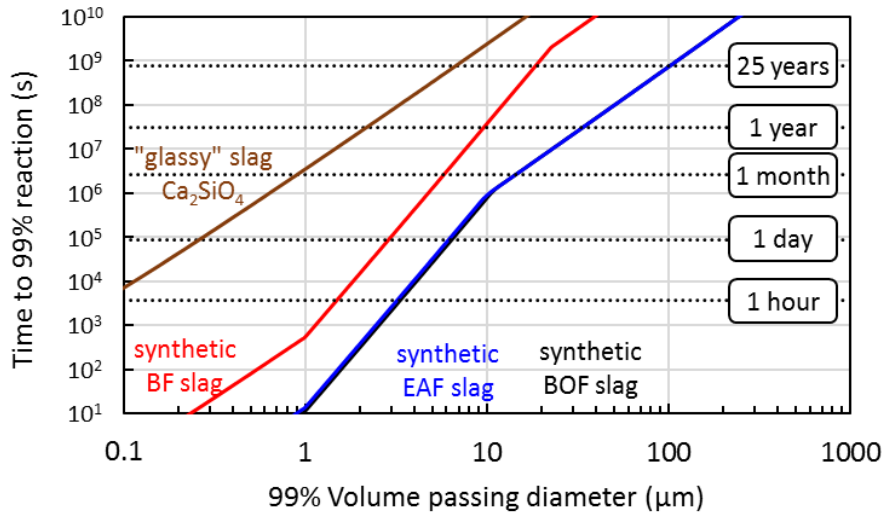
Fig. 7-13. The time to 99% reaction as a function of $X_{V,99}$ for synthetic BF, BOF, EAF, and 'glassy' slags at 5 vol% CO_2, 30 ˚C, and RH=90%.
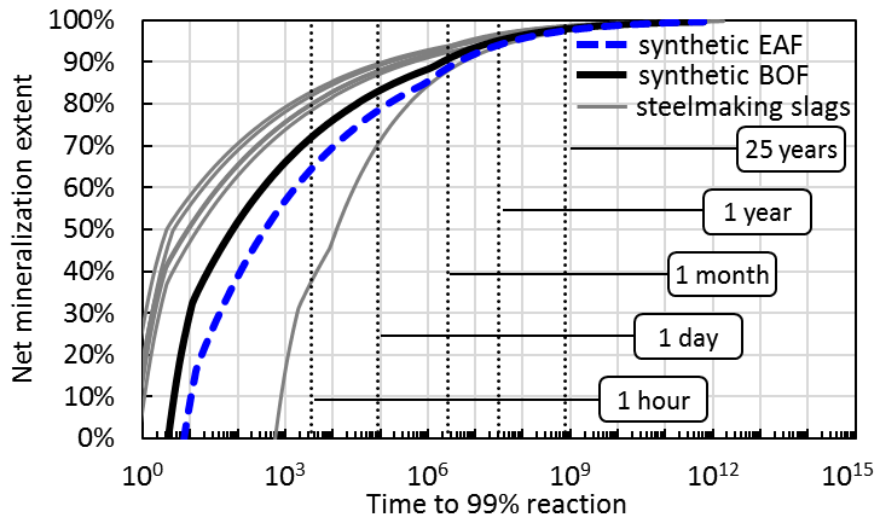
Fig. 7-14. The net mineralization extent for legacy steelmaking slags that results from performing grinding in order to reach 99% reaction by a given time. Energy for grinding is derived from diesel. Mineralization reactions occur at 5 vol% CO_2, 30 ˚C, and RH=90%.
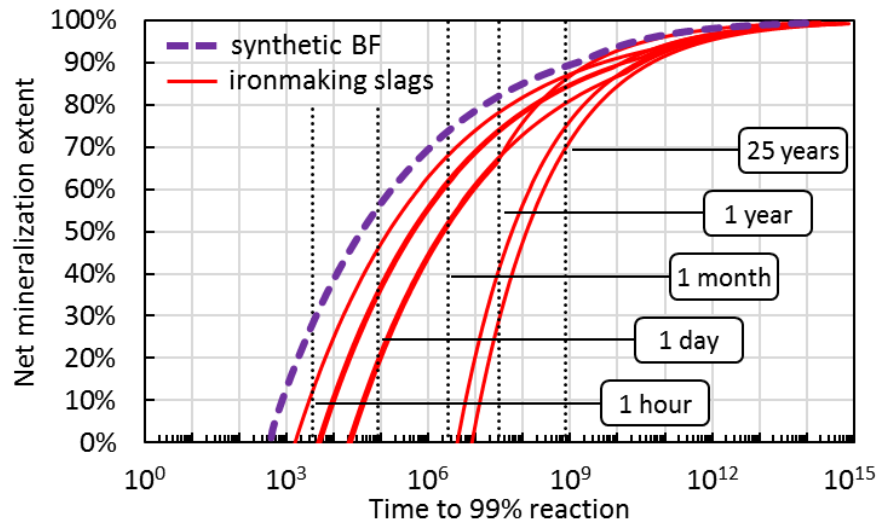
Fig. 7-15. The net mineralization extent for legacy ironmaking slags that results from performing grinding in order to reach 99% reaction by a given time. Energy for grinding is derived from diesel. Mineralization reactions occur at 5 vol% CO_2, 30 ˚C, and RH=90%.
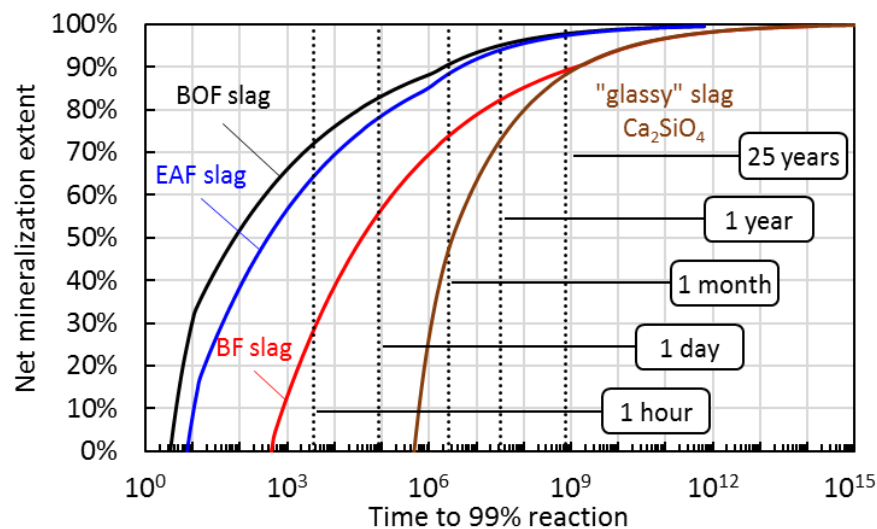
Fig. 7-16. The net mineralization extent for synthetic BF, BOF, EAF, and glassy slags that results from performing grinding in order to reach 99% reaction by a given time. Energy for grinding is derived from diesel. Mineralization reactions occur at 5 vol% CO_2, 30 ˚C, and RH=90%.

The results displayed in **Fig. 7-11** through **Fig. 7-16** highlight a few key features of running passive mineralization on legacy slags. First, it is interesting to note that steelmaking slags, in general, outperform ironmaking slags in term of net mineralization efficiency and rate. Steelmaking slags have historically been difficult to reuse do to issues in generating mineralogies and crystallinities appropriate for usage as an additive in cement manufacture. The use of steelmaking slags to cheaply offset CO_2 emissions may provide an attractive reuse pathway for this 'waste'. The source of faster reactions in steelmaking slags is the relative lack of Al-bearing species, which not only drastically reduce the effective diffusion coefficient, but also increase the specific grinding energy. The calcium ferrite species that typically prevent re-usage of steelmaking slags shows relatively rapid CO_2 mineralization. However, caution is warranted in broadly applying these results to all steelmaking

and ironmaking slags. For example, an apparent outlier with longer reaction times and lower reaction efficiencies exists amongst the steelmaking slags (**Fig. 7-11** and **7-14**). This BOF slag was rapidly solidified, generating fewer mineral species with a more mixed composition, though no amorphous phases. As legacy slags contain not only a variety of compositions, but have also undergone a variety of solidification rates, it should be expected that the performance of passive CO_2 mineralization will vary widely.

As with the rapidly cooled steelmaking slag, amorphous Ca_2SiO_4 showed a pronounced decrease in performance compared to polycrystalline ironmaking slag. This result suggests extreme caution for passive CO_2 mineralization using legacy or contemporary slags that have been rapidly solidified. As most ground granulated blast furnace slag (GGBS) and slag used as aggregate has been rapidly solidified for reasons of chemical and mechanically stability [Juckes, 2002], the slag that exists as part of current buildings and infrastructure is most likely subject to the low reaction rates and efficiencies shown in **Fig. 7-15** for legacy BF slag and **Fig. 7-16** for 'glassy' slag.

In order to robustly avoid the potential for net CO_2 emission when applying passive mineralization to legacy slag, usage of low CO_2 intensity energy is likely necessary. The legacy and synthetic slags are graphed together in **Fig. 7-17** using PV+LiB as the energy source. Notably, extremely rapid reactions of some ironmaking slags and glassy slags is a net CO_2 emitter. However, if slower reaction rates (e.g., ~days) are acceptable, then passive CO_2 mineralization should be applicable to functionally any legacy slag. Usage of RE shifts the problem from the CO_2 emissions of grinding, to the design and operation of equipment that can reliably generate sub-micrometer fines.
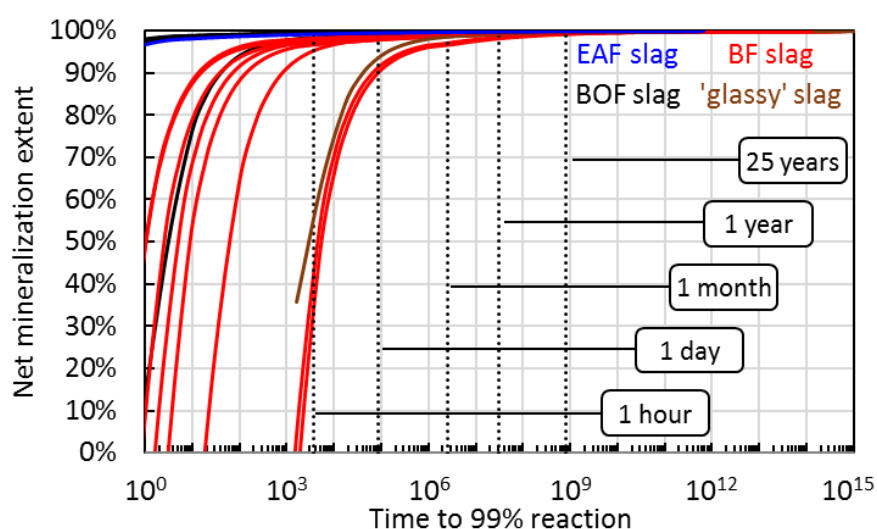
Fig. 7-17. The net mineralization extent for legacy and synthetic slags that results when power is supplied by PV+LiB. Mineralization reactions occur at 5 vol% CO_2, 30 ˚C, and RH=90%.

7.3. Other Sources

Additional sources of calcium and magnesium solids exist that may be appropriate for CO_2 mineralization. These sources are roughly separated into mining residues, demolition wastes (including cement kiln dust), and natural rocks. Mining residues have already undergone a fair amount of grinding and separation as part of mining operations and consist primarily of magnesium silicates. Demolition waste is dominated by concrete (i.e., cement-bound aggregate). A large portion of the cement raw materials and aggregate has come from ISM slag. Therefore, the mineralization

rate can be estimated by treating the cement binder as an additional mineral phase along with amorphous dicalcium silicate. The CO_2 mineralization rate of natural rocks can be directly estimated from the data of Chapter 5. However, the true mineral composition and GSD of extant rocks, not considered here, must be accounted for prior to implementing such operations. There are other industrial sources of calcium or magnesium bearing solids (e.g., fly ash, red mud), but their quantities are so small as to be negligible in terms of reducing the effects of climate change [Power et al., 2013].

7.3.1. Mining residues

The quantity of mining residues currently available for CO_2 mineralization efforts measures in the gigatonnes [Bodénan et al., 2014]. The majority of residues are dominated by silicate minerals, and predominately magnesium-bearing silicates of the Olivine and Pyroxene groups [Assima et al., 2014; Cavallo, 2017; Wilson et al., 2009; Vogeli et al., 2011; Zarandi et al., 2017] but also the Plagioclase group [Ghacham et al., 2015; Munz et al, 2012]. Extensive work has gone into CO_2 mineralization of mining residues, but the empirically slow kinetics [Assima et al., 2013a; Guyot et al., 2011; Kandji et al., 2017; Lechat et al., 2012] have pushed researchers to explore enhanced methods (e.g., chemical, mechanical, thermal treatment) [Fagerlund et al., 2009; Giannoulakis et al., 2014; Li and Hitch, 2018; Nduagu et al., 2012b] and tailoring processes to the minor amount of MgO and $Mg(OH)_2$ present in mine wastes [Assima et al., 2013a; Harrison et al., 2012]. But, as was the case with slag-based CO_2 mineralization, such 'enhancements' make net CO_2 emissions highly likely [Ncongwane et al., 2018; Nduagu et al., 2012a].

The empirical difficulties encountered by researchers can be attributed to the passivation effect of the product layer as discussed in Section 2.4.2. Efforts to rely on the rapidly reacting MgO or $Mg(OH)_2$ content of mining wastes are destined for failure due to the effects of mineral locking (Chapter 6.4). In order to accelerate reactions, the passivation layer must be removed. The large CO_2 footprint of chemicals production, CO_2 capture, and high temperatures makes 'enhanced' methods likely to become net CO_2 emitters. Mechanical removal of the passivation layer (or grinding to an extent at which the passivation layer is not meaningful) are necessary to make mining wastes a viable CO_2 mineralization feedstock. The central question becomes what rate of CO_2 uptake is acceptable. Given the immediacy of the impacts from climate change and the potential for passing climatic tipping points, rapid CO_2 drawdown is deemed necessary. The time to complete mineralization is plotted against the net CO_2 mineralization extent (i.e., including energy from grinding) using Olivine (Mg_2SiO_4) as representative of mine tailings in **Fig. 7-18**. **Figure 7-18a** plots the data assuming a diesel generator and **Fig. 7-18b** assumes use of PV+LiB. The efficiency of grinding is assumed to be 1% for diameters of 1 μm and scaled linearly to 0.1% to diameters of 100 nm. Efficiency is held constant at 0.1% for all diameters less than 100 nm.
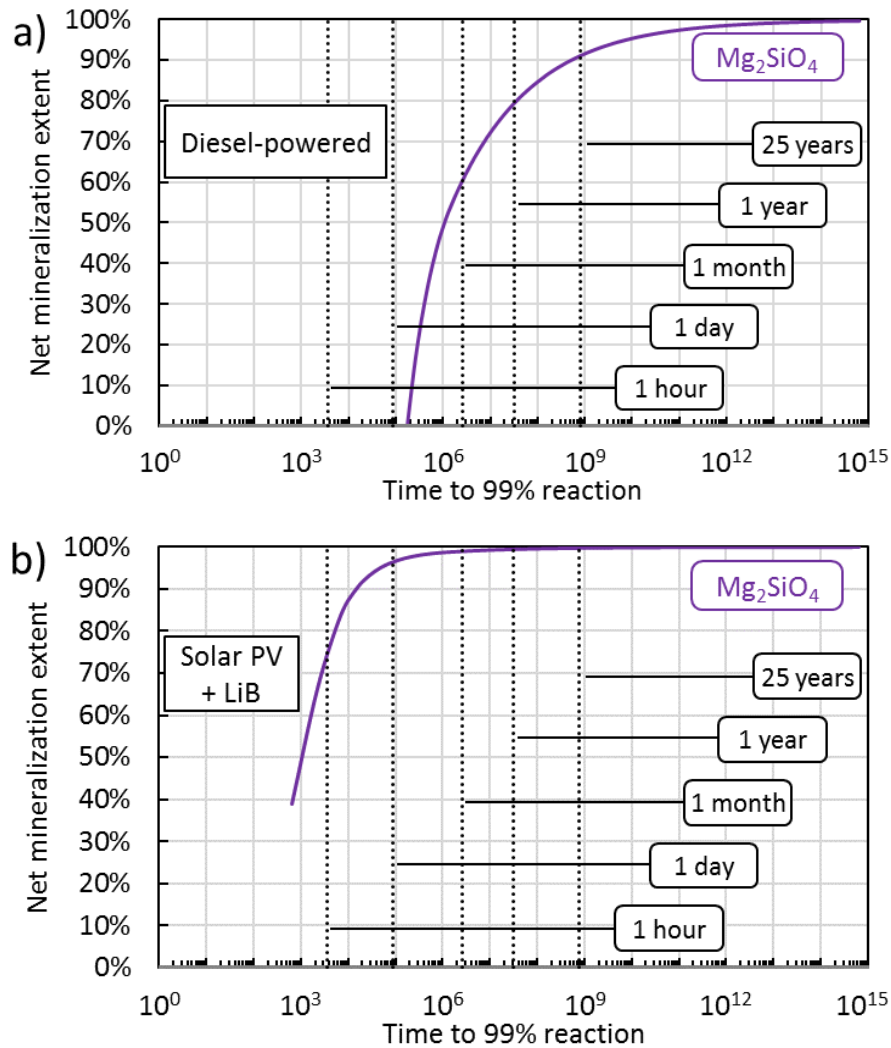
Fig. 7-18. The net mineralization achieved as a function of the desired reaction time using a) diesel-power and b) using PV+LiB. Mineralization reactions occur at 5 vol% CO_2, 30 ˚C, and RH=90%.

Figure 7-18 highlights the sensitivity of net CO_2 mineralization when using mining residues. For the process to be robustly 'net CO_2 negative' while using power supplied by fossil-fuel sources requires the willingness to wait years for significant mineralization extent. On the other hand, if the process is designed with purpose-built RE, then much more rapid net mineralization can be expected without losing efficiency. However, the impact of decreasing comminution efficiency at small grain sizes puts practical, but currently unquantifiable, limits on performance. Additionally, the rapid mineralization regimes generate copious amounts of very fine particulates, raising concerns over human health and environmental impacts. Likewise, the above estimates assume a pure Mg_2SiO_4 source; however, most mine waste contains a non-negligible quantity of material that does not mineralize carbon dioxide (e.g., iron oxides, silica). Gangue species (i.e., compounds unreactive to CO_2) are rarely reported in the literature on mineralization, but available data indicates mass contents between 18-33% are normal [Kandji et al., 2017; Vogeli et al., 2011]. Such gangue material increases the grinding energy per unit CO_2 mineralized and reduces the overall diffusion rate. The effects of 25% alumina silicate (Al_2SiO_5) content on the net CO_2 mineralization extent and rate are provided in **Fig. 7-19**.
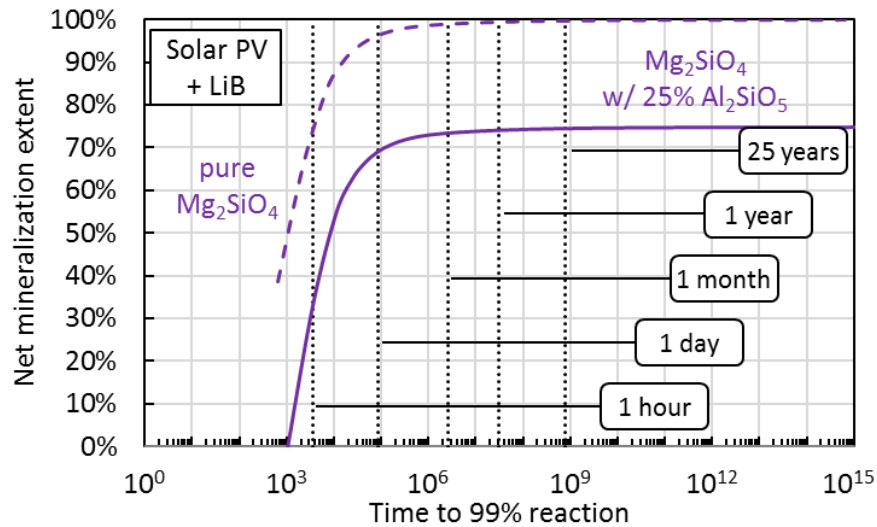
Fig. 7-19. The impact of gangue material on mineralization performance of mining residues. Mineralization reactions occur at 5 vol% CO_2, 30 ˚C, and RH=90%.

A major practical issue with the results of **Fig. 7-19** is the assumption of application of the materials in 5 vol% CO_2 gas stream. This assumption was made for comparison to ISM slag and also because this dissertation focusses on reducing the emissions from ISM. However, the inherently low performance of mining wastes means that they are unlikely to be utilized by ISM or other point source emitters for CO_2 mineralization. Moreover, mining wastes are rarely located close to such point sources, thereby incurring a CO_2 penalty of transportation. Though electric vehicles are rapidly expanding in the market, and electric trucking seems near, the underlying energy source for most electric vehicles is still the local utility power, thereby undermining the concept of low CO_2 transportation unless purpose built low CO_2 power is included. Given these practical constraints, it is more likely that mining wastes will simply be ground more extensively on-site and left for reaction with the atmosphere. The impact of the lower CO_2 concentration (415 ppm) on reaction rate is displayed in **Fig. 7-20**. **Figure 7-20** makes clear that even idealized systems using low CO_2 power for grinding will only draw down CO_2 at decent efficiencies over the course of years.
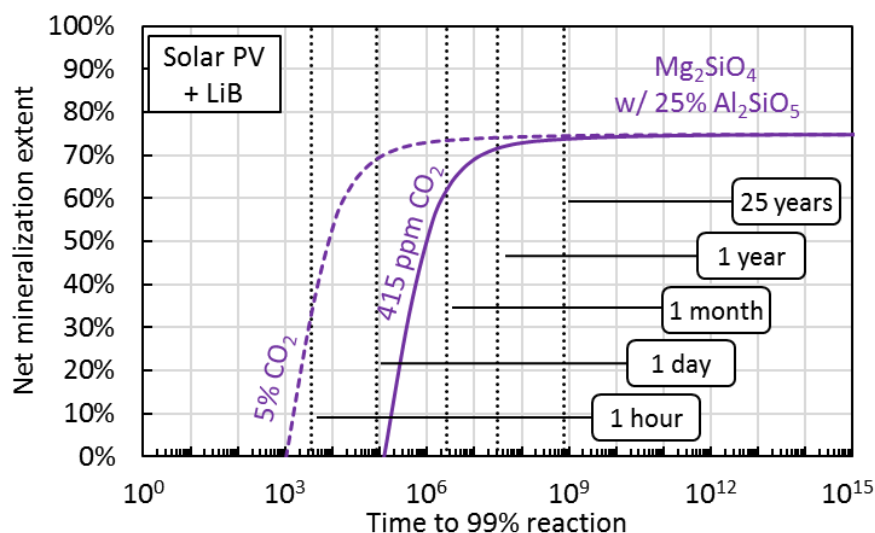
Fig. 7-20. The application of Mg_2SiO_4 ground via PV+LiB to CO_2 mineralization from the ambient atmosphere, including the effects of gangue material. Mineralization reactions occur at 30 ˚C and a RH=90%.

Enstatite ($MgSiO_3$) and Anorthite ($CaAl_2Si_2O_8$) are also common minerals encountered in mine tailings. $MgSiO_3$ effectively halts CO_2 mineralization at 15 nm and $CaAl_2Si_2O_8$ mineralization ends at 60 nm. As such, the mineralization extent for these compounds depends only on the degree of grinding and not (in the long term) on the exposure time allotted. Assuming these minerals are ground to the extent that the passivation layer depth equals the radius, the total generated SA and thus, energy expenditure can be calculated. If power is supplied by diesel, then each kilogram of $MgSiO_3$ that is ground results in a net release of 2.838 kilograms of CO_2. Likewise, each kilogram of $CaAl_2Si_2O_8$ that is ground to complete reaction has the net effect of releasing 1.140 kilograms of carbon dioxide. This analysis is overly optimistic, as the generated particles are treated as monodisperse (cf. **Fig.5-7b**) and the comminution efficiency is kept at 1%. Usage of PV+LiB results in net CO_2 reduction of 0.356 and 0.126 kgCO₂/kg-mineral for $MgSiO_3$ and $CaAl_2Si_2O_8$, respectively. However, accounting for the reduction in comminution efficiency for particles below 1 μm in diameter returns the process to a net CO_2 emitter of 0.360 and 0.132 kgCO₂/kg-mineral for Enstatite and Anorthite, respectively. Consideration of the full PSD further increases CO_2 release.

These results strongly suggest that mine wastes should not be expected to rapidly draw down atmospheric carbon dioxide unless power is exclusively supplied by extremely low CO_2 sources. Even with RE sources, some minerals are simply off-limits for application of gas-solid CO_2 mineralization. For those minerals that show promise, industrial grinding equipment integrated with PV+LiB is a prerequisite. Battery-powered mining equipment is now available in the market, meaning there does not seem to be any technical barriers inhibiting implementation. As the process reacts with atmospheric CO_2, there is no inherent mineralization rate required. This trait is advantageous given that the process depends on low CO_2 power to ensure net CO_2 mineralization. Conceptually, the process could be run semi-automatically, based purely on the availability of renewable energy.

7.3.2. Demolition waste

Demolition waste relevant to CO_2 mineralization consists primarily of concrete. Concrete consists of cement and aggregate. The calcium-silicate-hydrate structure of cement is complex and not amenable to crystallographic definition. Even so, analysis of the long-term reactions of cement with

atmospheric CO_2 have been performed [Pade and Guimaraes, 2007; Possan et al., 2017; Xi et al., 2016]. Results indicate that CO_2 diffusion through cement is Fickian, analogous to the slag minerals examined in Chapter 5. At a steady state of concrete production and building demolition, roughly half of direct CO_2 emissions from concrete production (i.e., from the decomposition of $CaCO_3$) are concurrently mineralized. General suggestions for improved CO_2 mineralization are analogous to those herein: grinding of demolition waste will enhance the quantity and rate of CO_2 mineralized. Unfortunately, none of the studies considered the CO_2 emissions associated with grinding operations. This CO_2 source cannot be accounted for here because the undefined structure of the calcium-silicate-hydrate network prevents utilization of the methods of Tromans and Meech from Chapter 5. Even so, the rapid observed diffusion rate for concrete indicates that the degree of grinding necessary to achieve rapid uptake is small and thus the CO_2 losses are negligible if RE is utilized. However, the historical use of amorphous slag as a cement additive and concrete aggregate may result in a dramatic slow down of CO_2 mineralization when the amorphous material is all that remains to be carbonated.

7.3.3. Natural rocks

Natural rocks capable of taking part in CO_2 mineralization technically include any compounds with magnesium or calcium content. Though the primary focus in the literature is on CO_2 mineralization using magnesium silicates [Hangx and Spiers, 2009; Lackner et al., 1995], the analysis of mining industry residues indicates the potential pitfalls of such a selection. Thus, the discussion of natural rocks is limited to the concept of purposefully mining and grinding rocks that have no other value in the current market. This criterion leaves Wollastonite ($CaSiO_3$) as the primary target for CO_2 mineralization (**Fig. 7-17**). Wollastonite is a much more attractive target in terms of rate and efficiency of CO_2 mineralization as compared to Mg_2SiO_4, $MgSiO_3$, and Al-bearing minerals. As is universally the case with passive CO_2 mineralization, low CO_2 energy supply is critical for making the process robustly net CO_2 negative (compare **Fig. 7-21a** and **7-21b**). Likewise, the amount of gangue material directly effects overall process efficiency (**Fig. 7-21c**). $CaSiO_3$ ground using low CO_2 energy may an attractive target for reducing point source emissions. Of course, locating a source of $CaSiO_3$ near the emission site will be necessary to maintain low CO_2 emissions from transportation. Assuming such advantageous citing is not available, reaction of $CaSiO_3$ under atmospheric CO_2 concentrations remains rapid.
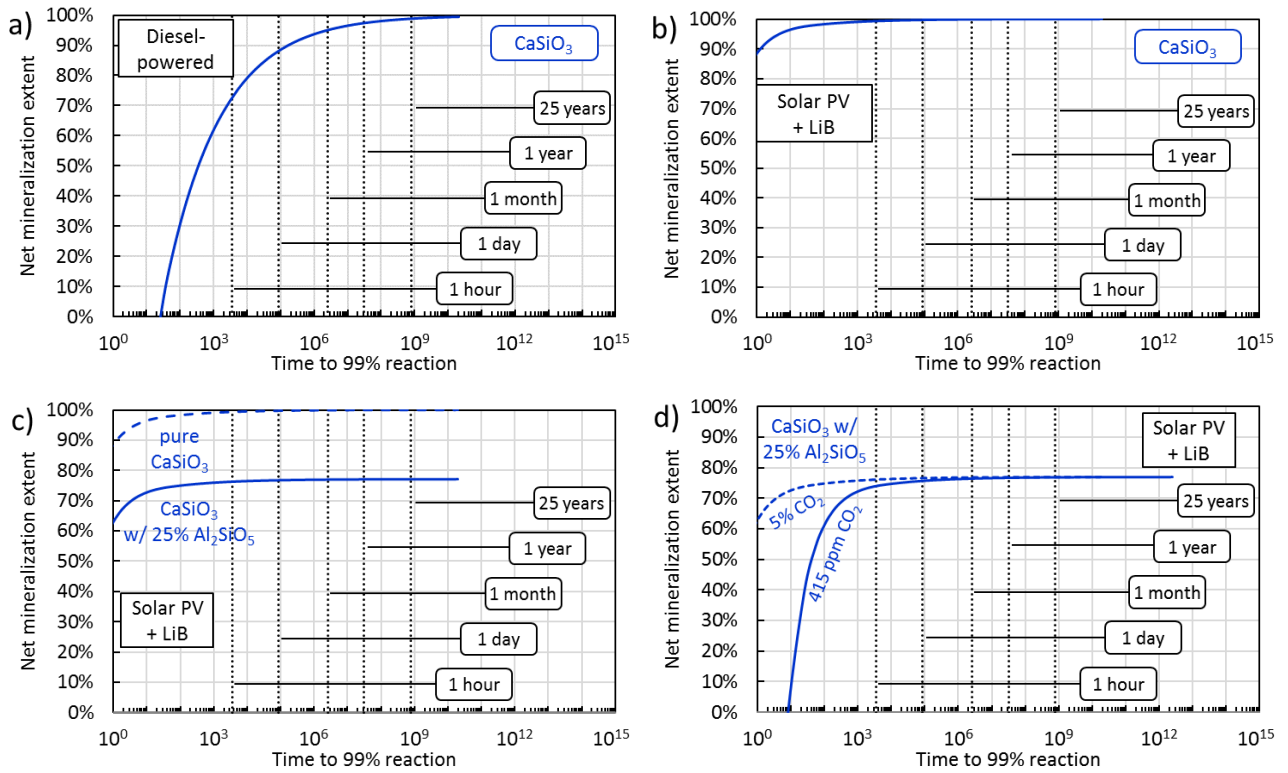
Fig. 7-21. The net mineralization of $CaSiO_3$ achieved as a function of the desired reaction time using a) diesel-power, b) using PV+LiB, c) accounting for inclusion of gangue, and d) operating at atmospheric CO_2 concentrations. Mineralization reactions occur at 30 ˚C and RH=90%.

Chapter-specific symbols and abbreviation list

2DS: 2 ˚C Scenario of Paris Agreement

BF: Blast furnace

BOF: Basic Oxygen Furnace

C_M: Moment coefficient

$CO_{2,O}$: CO₂ emissions

c_p: Specific heat

D_h: Hydraulic diameter

d: Bore diameter of bearing

E_b: Energy due to friction of bearings

E_d: Energy to overcome drag

E_h: Energy difference of heating CaO and CaCO₃

E_T: Total energy

EAF: Electric Arc Furnace

F: Load on bearing

f: Final condition

GSD: Grain size distribution

H: Height of centrifuge

I: Moment of inertia

i: Initial condition

IM: Inter-mineral grain fracture

ISM: Ironmaking and steelmaking

M_C: Moment of centrifuge

m: mass

MYNA: In-container solidification with solid-state quenching

PV+LiB: Solar photovoltaics with lithium ion battery storage

PSD: Particle size distribution

r_c: External radius of the centrifuge

RE: Renewable energy

Re: Reynold's number

r_S: Inner radius of shield

Ta: Taylor number

W_r: Work to rotate centrifuge and internal slag

X_{V99}: 99% volume-passing diameter

ϵ_E: CO₂ intensity of energy generation

ω: Angular velocity

ΔH_{coke}: Molar heating value of coke

ΔH_{dec}°: Enthalpy of decomposition

ρ: Density

μ: Dynamic viscosity

Δr: Gap between centrifuge and shield

μ_B: Friction coefficient of bearing

References

Assima, G.P., Larachi, F., Molson, J. and Beaudoin, G., 2013a. Accurate and direct quantification of native brucite in serpentine ores—new methodology and implications for CO2 sequestration by mining residues. Thermochimica acta, 566, pp.281-291.

Assima, G.P., Larachi, F., Beaudoin, G. and Molson, J., 2013b. Dynamics of carbon dioxide uptake in chrysotile mining residues–effect of mineralogy and liquid saturation. International Journal of Greenhouse Gas Control, 12, pp.124-135.

Assima, G.P., Larachi, F., Molson, J. and Beaudoin, G., 2014. Comparative study of five Québec ultramafic mining residues for use in direct ambient carbon dioxide mineral sequestration. Chemical Engineering Journal, 245, pp.56-64.

Bodénan, F., Bourgeois, F., Petiot, C., Augé, T., Bonfils, B., Julcour-Lebigue, C., Guyot, F., Boukary, A., Tremosa, J., Lassin, A. and Gaucher, E.C., 2014. Ex situ mineral carbonation for CO2 mitigation: Evaluation of mining waste resources, aqueous carbonation processability and life cycle assessment (Carmex project). Minerals Engineering, 59, pp.52-63.

Bodor, M., Santos, R.M., Kriskova, L., Elsen, J., Vlad, M. and Van Gerven, T., 2013. Susceptibility of mineral phases of steel slags towards carbonation: mineralogical, morphological and chemical assessment. European Journal of Mineralogy, 25(4), pp.533-549.

Cavallo, A., 2018. Serpentinitic waste materials from the dimension stone industry: Characterization, possible reuses and critical issues. Resources Policy, 59, pp.17-23.

Dhaka, R.K., 2017. Current Refractory Technology and Practices in the Steel Industry. United States Steel Corporation.

Fagerlund, J., Teir, S., Nduagu, E. and Zevenhoven, R., 2009. Carbonation of magnesium silicate mineral using a pressurised gas/solid process. Energy Procedia, 1(1), pp.4907-4914.

Fénot, M., Bertin, Y., Dorignac, E. and Lalizel, G., 2011. A review of heat transfer between concentric rotating cylinders with or without axial flow. International journal of thermal sciences, 50(7), pp.1138-1155.

Fruehan, R.J., Fortini, O., Paxton, H.W. and Brindle, R., 2000. Theoretical minimum energies to produce steel. Report to the US Department of Energy, Office of Industrial Technologies. Washington, DC.

Fuerstenau, D.W. and Abouzeid, A.Z., 2002. The energy efficiency of ball milling in comminution. International Journal of Mineral Processing, 67(1-4), pp.161-185.

Gautier, M., Poirier, J., Bodénan, F., Franceschini, G. and Veron, E., 2013. Basic oxygen furnace (BOF) slag cooling: laboratory characteristics and prediction calculations. International Journal of Mineral Processing, 123, pp.94-101.

Ghacham, A.B., Cecchi, E., Pasquier, L.C., Blais, J.F. and Mercier, G., 2015. CO2 sequestration using waste concrete and anorthosite tailings by direct mineral carbonation in gas–solid–liquid and gas–solid routes. Journal of environmental management, 163, pp.70-77.

Giannoulakis, S., Volkart, K. and Bauer, C., 2014. Life cycle and cost assessment of mineral carbonation for carbon capture and storage in European power generation. International Journal of Greenhouse Gas Control, 21, pp.140-157.

Guyot, F., Daval, D., Dupraz, S., Martinez, I., Ménez, B. and Sissmann, O., 2011. CO2 geological storage: The environmental mineralogy perspective. Comptes Rendus Geoscience, 343(2-3), pp.246-259.

Hangx, S.J. and Spiers, C.J., 2009. Coastal spreading of olivine to control atmospheric CO2 concentrations: A critical analysis of viability. International Journal of Greenhouse Gas Control, 3(6), pp.757-767.

Harrison, A.L., Power, I.M. and Dipple, G.M., 2012. Accelerated carbonation of brucite in mine tailings for carbon sequestration. Environmental science & technology, 47(1), pp.126-134.

Hartmann, J. and Moosdorf, N., 2012. The new global lithological map database GLiM: A representation of rock properties at the Earth surface. Geochemistry, Geophysics, Geosystems, 13(12).

IEA, 2016. CO_2 emissions from fuel combustion: 2016 edition.

Juckes, L.M., 2002. Dicalcium silicate in blast-furnace slag: a critical review of the implications for aggregate stability. Mineral Processing and Extractive Metallurgy, 111(3), pp.120-128.

Kandji, E.H.B., Plante, B., Bussière, B., Beaudoin, G. and Dupont, P.P., 2017. Geochemical behavior of ultramafic waste rocks with carbon sequestration potential: a case study of the Dumont Nickel Project, Amos, Québec. Environmental Science and Pollution Research, 24(12), pp.11734-11751.

Lackner, K.S., Wendt, C.H., Butt, D.P., Joyce Jr, E.L. and Sharp, D.H., 1995. Carbon dioxide disposal in carbonate minerals. Energy, 20(11), pp.1153-1170.

Lechat, K., Lemieux, J.M., Molson, J., Beaudoin, G. and Hébert, R., 2016. Field evidence of CO2 sequestration by mineral carbonation in ultramafic milling wastes, Thetford Mines, Canada. International Journal of Greenhouse Gas Control, 47, pp.110-121.

Li, J. and Hitch, M., 2018. Mechanical activation of magnesium silicates for mineral carbonation, a review. Minerals Engineering, 128, pp.69-83.

Liu, C., Zhang, Y.Z., Li, J., Li, J.G. and Kang, Y., 2016. Thermodynamic simulation on mineralogical composition of CaO–SiO 2–Al 2 O 3–MgO quaternary slag system. SpringerPlus, 5(1), p.1028.

MOE, 2018. National Greenhouse Gas Inventory Report of Japan 2018.

Mombelli, D., Mapelli, C., Barella, S., Di Cecca, C., Le Saout, G. and Garcia-Diaz, E., 2016. The effect of chemical composition on the leaching behaviour of electric arc furnace (EAF) carbon steel slag during a standard leaching test. Journal of environmental chemical engineering, 4(1), pp.1050-1060.

Munz, I.A., Brandvoll, Ø., Haug, T.A., Iden, K., Smeets, R., Kihle, J. and Johansen, H., 2012. Mechanisms and rates of plagioclase carbonation reactions. Geochimica et Cosmochimica Acta, 77, pp.27-51.

Nduagu, E., Bergerson, J. and Zevenhoven, R., 2012a. Life cycle assessment of CO2 sequestration in magnesium silicate rock–A comparative study. Energy Conversion and Management, 55, pp.116-126.

Nduagu, E., Romão, I. and Zevenhoven, R., 2012b. Production of Mg (OH) 2 for CO2 emissions removal applications: parametric and process evaluation. In 25th International conference on efficiency, costs, optimisation, simulation and environmental impact of energy systems (ECOS 2012), Perugia, Italy.

Pade, C. and Guimaraes, M., 2007. The CO2 uptake of concrete in a 100 year perspective. Cement and Concrete research, 37(9), pp.1348-1356.

Pehl, M., Arvesen, A., Humpenöder, F., Popp, A., Hertwich, E.G. and Luderer, G., 2017. Understanding future emissions from low-carbon power systems by integration of life-cycle assessment and integrated energy modelling. Nature Energy, 2(12), p.939.

Power, I.M., Harrison, A.L., Dipple, G.M., Wilson, S.A., Kelemen, P.B., Hitch, M. and Southam, G., 2013. Carbon mineralization: from natural analogues to engineered systems. Reviews in Mineralogy and Geochemistry, 77(1), pp.305-360.

Tachibana, F., FUKUI, S. and MITSUMURA, H., 1960. Heat transfer in an annulus with an inner rotating cylinder. Bulletin of JSME, 3(9), pp.119-123.

Waples, D.W. and Waples, J.S., 2004. A review and evaluation of specific heat capacities of rocks, minerals, and subsurface fluids. Part 1: Minerals and nonporous rocks. Natural resources research, 13(2), pp.97-122.

Wilson, S.A., Dipple, G.M., Power, I.M., Thom, J.M., Anderson, R.G., Raudsepp, M., Gabites, J.E. and Southam, G., 2009. Carbon dioxide fixation within mine wastes of ultramafic-hosted ore deposits: Examples from the Clinton Creek and Cassiar chrysotile deposits, Canada. Economic Geology, 104(1), pp.95-112.

Vogeli, J., Reid, D.L., Becker, M., Broadhurst, J. and Franzidis, J.P., 2011. Investigation of the potential for mineral carbonation of PGM tailings in South Africa. Minerals Engineering, 24(12), pp.1348-1356.

Xi, F., Davis, S.J., Ciais, P., Crawford-Brown, D., Guan, D., Pade, C., Shi, T., Syddall, M., Lv, J., Ji, L. and Bing, L., 2016. Substantial global carbon uptake by cement carbonation. Nature geoscience, 9(12), p.880.

Zarandi, A.E., Larachi, F., Beaudoin, G., Plante, B. and Sciortino, M., 2017. Ambient mineral carbonation of different lithologies of mafic to ultramafic mining wastes/tailings–A comparative study. International Journal of Greenhouse Gas Control, 63, pp.392-400.

Chapter 8: Impact towards climate change mitigation

A plethora of technologies, processes, and methods exist for the capture, utilization, and storage of CO_2 from both point sources and the atmosphere (cf. Chapter 1). Despite the range of options for fighting climate change, none have yet made an appreciable dent in pace of anthropogenic CO_2 emissions increase, much less towards a decrease in CO_2 emissions. A net CO_2 negative global society seems fanciful given the current trends; nevertheless, anthropogenic net CO_2 emissions much match the combined CO_2 sinks of nature and engineered systems by mid-century -with strong emissions reductions occurring immediately- for any chance to avoid the perils of an increasingly unlivable planet. From this globally-shared perspective, what is necessary in technologies to fight climate change are the following: 1) gigatonne-scale CO_2 reduction, 2) rapid scale-up to saturation, 3) passive safety, 4) neutral-to-positive impact on the natural environment, and 5) robustness against an altering economic/political/natural environment. Points 1 and 2 are the physical necessities of solving the climate change problem. Points 3 and 4 are necessary given the scale of the climate change problem without producing un-intended consequences of the same scale as climate change. Points 1 through 4 are solved in theory by conventional climate change mitigation methods (e.g., CCS), but points 1 and 2 have not come to pass due to point 5. All current climate change mitigation methods have relied on direct or indirect funding from the public sector to be implemented at scale. However, the spread of neoliberal economics has made the problem intractable in many of the major governments in the world, with short-term profits of corporations dumping CO_2 carrying more import in the chambers of government than the long-term stability of the environment for the good of human civilization.

Recognition of the current political failings is a prerequisite when designing a climate change mitigation technology or method. Dependence on a functioning government for appropriate levels of financial and regulatory support of a technology is no longer a sound assumption. Instead, a process must be able to rapidly produce gigatonne-scale CO_2 reductions even without assistance in the form of a price on carbon or emissions limits.

Chapter highlights

- Assuming no change in iron and steelmaking production, the centrifuge and MYNA processes operated using renewable energy to 2100 can cumulatively reduce CO_2 emissions by ~43 (32-54) and ~21 (16-27) Gt-CO_2, respectively.

- Legacy slag currently offers roughly ~8 (7-9) GtCO_2 mineralization potential.

- Legacy slag increases as the rate of diffusion of the centrifuge and MYNA processes decreases; legacy slag treatment using renewable energy to 2100 reaches ~16 (12-20) GtCO_2 for the centrifuge and ~23 (18-29) GtCO_2 for the MYNA process.

- Combined with legacy slag treatment, total CO_2 reduction to 2100 is on the order of 60 GtCO_2 for the centrifuge and roughly 45 GtCO_2 for MYNA.

- All processes generate a profit while reducing CO_2 emissions by the resale or reuse of materials.

- The centrifugal separation method generates high value FeO and (Ca,Mg)O which can be recycled to the furnace, this results in a profit of roughly $70/t-$CO_2$ emissions reduction.

- The MYNA process produces aggregate from slag, resulting in a profit of roughly $30/t-$CO_2$ emissions reduction.

- CO_2 mineralization of legacy slag produces aggregate, resulting in a profit of roughly $5/t-$CO_2$. The reduced profit in comparison to the MYNA method is primarily due to the higher degree of grinding required.

- Excluding the revenue from the sale or reuse of materials, the centrifugal, MYNA, and legacy slag methods still provide a lower cost for CO_2 emissions reduction than CCS, modifications to existing ISM methods, or new ISM processes.

8.1. Scale and rate

Though ultimately determined by economics and policy, the scale and rate of a climate change mitigation technology is limited in the extreme by the constraints of resources, energy, and space. The physical limit to the scale and rate of each process (centrifugal, MYNA, passive mineralization) and resource category (contemporary slag, legacy slag, industrial waste, natural rocks) is discussed herein. Potential combinations of technologies and resources is discussed at the end of this section.

8.1.1. Centrifugal process

Centrifugal separation and solidification requires molten slag and so is only applicable to newly-generated slag. The reduction in emissions from the process is due to a looping of CaO and MgO in the process and the enhanced recovery of low-oxidation iron species. Calcium and magnesium oxide act as a temporary carrier for silica, alumina, and other impurities - pulling them from the ore and coke prior to being separated in the centrifuge, with the $(Ca,Mg)O$ returning to the furnace for another round of duty. In the ideal scenario, the direct emission of CO_2 from decomposition of $(Ca,Mg)CO_3$ occurs only once in the lifetime of the ISM facility, with complete recycling thereafter. An energy load for heating of $(Ca,Mg)O$ to the furnace temperature still remains, but the energy needed for $(Ca,Mg)CO_3$ decomposition is removed. In an idealized scenario, after centrifugal separation, the hot, solid $(Ca,Mg)O$ is returned to the furnace with minimal heat loss. However, the generation of pelletized flux consisting of mixes of ore and lime mean that the generated $(Ca,Mg)O$ will likely return to ambient temperature prior to re-entering the furnace. A separate implementation of centrifugal separation is to mineralize the generated $(Ca,Mg)O$. While this is less efficient in terms of CO_2 reduction, it is also less intrusive to current ISM operations, and so may be the preference of the ISM industry. If mineralization of the $(Ca,Mg)O$ is implemented, then the CO_2 reduction is stoichiometric with a small penalty for operating the centrifuge and for applying grinding. However, the high net mineralization efficiency of these compounds means that very little grinding is necessary, and thus the CO_2 penalty is low.

The Fe^0 and FeO of slag is concentrated and purified from the melt prior to being returned to the furnace. This lowers the amount of reductant (i.e., coke) required for operation. The CO_2 emissions reduction from this conversion of slag into scrap is equal to the CO_2 chemically required to reduce iron ore (Fe_2O_3) to the said oxidation state and the coke usage to elevate the material to the appropriate temperature.

Operation of the centrifugal system functionally reduces CO_2 emissions immediately. The small CO_2 debt of centrifuge fabrication is paid off within a few cycles of the centrifuge. Likewise, the CO_2 embodied in replacement of the centrifuge body due to thermochemical dissolution is close to zero. The energetic load of running the centrifuge is also of so little consequence, that consideration of the CO_2 intensity of the energy source provides essentially no benefit. If $(Ca,Mg)O$ is recycled to the furnace, the avoided emissions are instantaneous. If $(Ca,Mg)O$ is used to mineralize CO_2, the rapid rate of reaction for these materials means that reductions occur within the first day, even if diesel power is used for grinding.

The requirement for molten slag limits the scale of CO_2 reductions to the magnitude of slag produced. In the current ISM industry, application of centrifugal separation would directly reduce emissions by 0.262-0.382 $GtCO_2/y$ globally, equivalent to 9.4-13.7% of the total CO_2 emissions of the industry. Recovery of low oxidation state iron compounds provides 0.077 $GtCO_2/y$ whereas the $(Ca,Mg)O$ content provides 0.305 $GtCO_2/y$ reduction if recycled to the furnace and 0.262 $GtCO_2/y$ if used for CO_2 mineralization. These values include the CO_2 emissions from operations and the

embodied CO_2 of constructing the centrifuges. The CO_2 intensity of energy for operating the centrifuges was scaled based on the quantity of slag produced by country [WSA, 2018] and its specific CO_2 intensity of energy production [IEA, 2016]. The operational CO_2 emissions for grinding was based on achieving complete reaction within 1 hour, using diesel-powered grinders.

It is unreasonable to assume that all ISM entities will immediately adopt centrifugal separation. To model the rate of uptake, it was assumed a single BF-BOF operator tested a 2 m^3 per batch centrifuge, receiving slag from a continuous tap. Starting in 2019, design and construction of the centrifuge and necessary ancillary equipment was assumed to take one year, followed by one year of testing. Assuming successful implementation, two additional 2 m^3 centrifuges were added each year until all slag at the integrated BF-BOF facility was handled by centrifuge. From this point, the technology was assumed to spread within the company in 4 m^3 increments for each furnace per year. Additionally, the technology was assumed to spread to other ISM companies at 4 m^3 per furnace per year beginning 5 years after the complete treatment of BF-BOF slag at the initial trial facility. The technology diffusion is plotted in **Fig. 8-1**; **Figure 8-2** plots emissions reductions to a 2020 baseline.
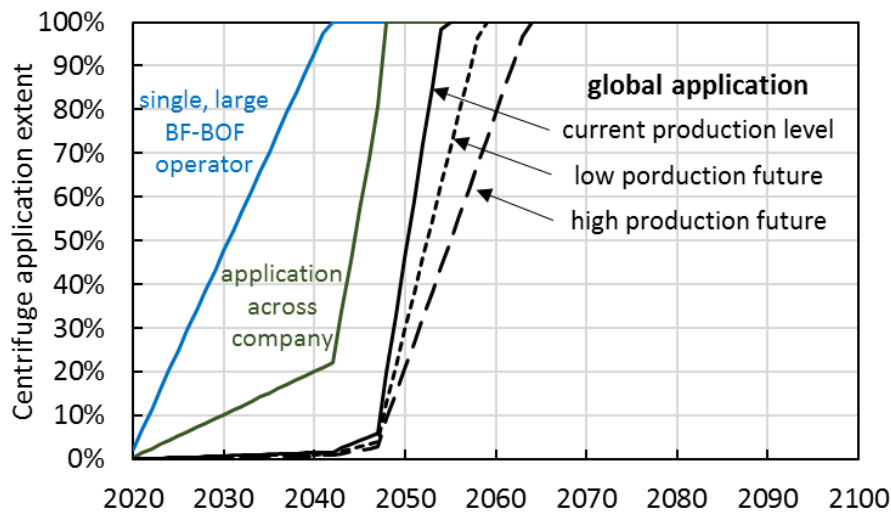

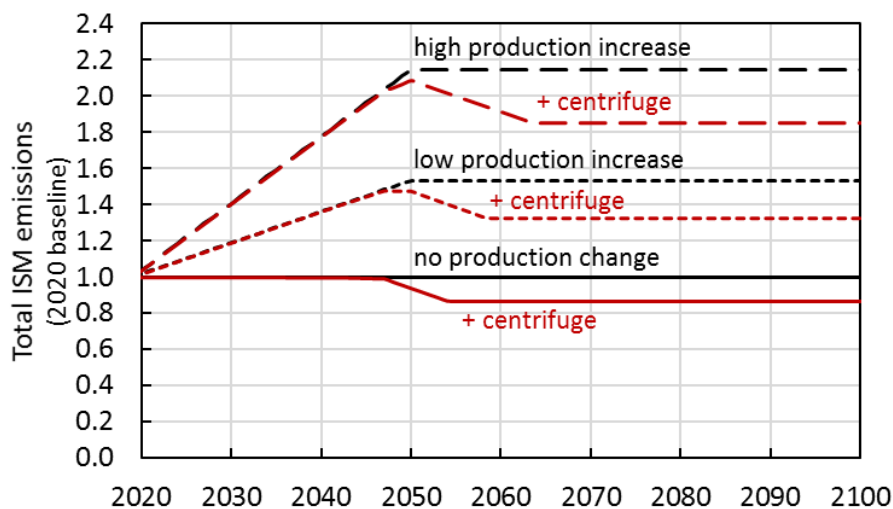**Fig. 8-1.** The assumed diffusion of centrifugal separation across ISM.

Fig. 8-2. The reduction in CO_2 emissions from diffusion of centrifugal separation across ISM.

8.1.2. MYNA Process

The MYNA process requires molten slag to operate, limiting the total scale of impact to that of future slag generation. The emission reductions are due to mineralization of CO_2 using the calcium and magnesium content of slag. These elements are originally sourced from carbonates, so the process acts as a virtual loop between solid carbonates in the environment. However, the heating and decomposition of carbonates requires energy addition which is not recovered in the MYNA process. As such, even with ideal efficiencies, the MYNA process does not completely offset the CO_2 emissions from fluxing agents. Though it is expected that the MYNA process will increase the recovery of iron oxides (i.e., via alteration of mineralogy during solidification and the generation of easily separable phases), this result requires empirical validation across a range of slag mineralogies in order to be claimed when calculating the net CO_2 reduction.

The process was assumed to be implemented using the low CO_2 concentration sinter and reheating flue gas streams. In order to prevent a build-up of slag on site, slag was assumed to be ground such that mineralization reaches completion within 1 hour. The calculated 99% volume passing diameters for BF, BOF, and EAF slag are 12.5, 13.5, and 15.7 µm, respectively. The process was assumed to be run using diesel power, such that ISM facilities could immediately implement the process using available equipment. This degree of grinding resulted in a net CO_2 reduction efficiency of 88.7%, 92.3%, and 93.1% for BF, BOF, and EAF slag, respectively. An additional CO_2 penalty exists for the initial production of the containers and the recurrent production of MgO refractory every 4 years. This reduced the net efficiency by 0.06% for the initial construction, and 0.04% for each recurrent cycle.

Global application of the MYNA process would reduce CO_2 emissions by 0.203 and 0.226 GtCO/y for grinding powered by diesel and PV+LiB, respectively. This value accounts for the embodied CO_2 in container construction and recurrent MgO insulation production. This represents 7.3-8.1% of the CO_2 emissions of ISM.

As was the case the case with centrifugal separation, it is unreasonable to expect an instantaneous adoption of the MYNA process. Adoption was assumed to occur in 2020 after one year of design and construction at a large integrated BF-BOF facility. The initial size was considered as a single 5 m^3 container with a one year test period. An additional 5 m^3 container was added once per year until all slag was treated by the MYNA method. From that point, the MYNA method was assumed to spread across the company and globally in 10 m^3/y increments at each facility. A 5 year delay between full utilization at a single facility and the start of global uptake was assumed for the spread to other companies. The resulting diffusion of the MYNA process is plotted in **Fig. 8-3** with the reduction in emissions related to a 2020 baseline provided in **Fig. 8-4**.

Fig. 8-3. The assumed diffusion of MYNA across ISM.
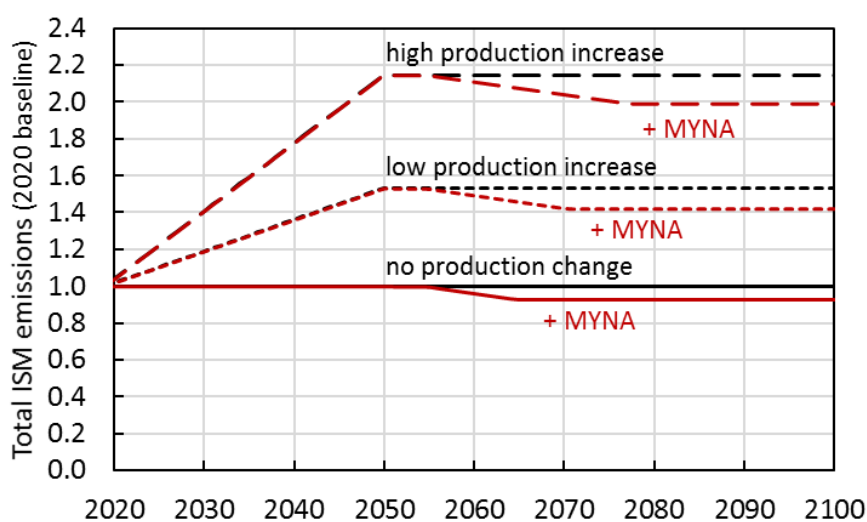
Fig. 8-4. The reduction in CO_2 emissions from diffusion of MYNA across ISM.

8.1.3. Legacy slag

From the perspective of implementing CO_2 mineralization, legacy slag is distinct due to its unknown and variable mineralogy, crystallinity, and grain size distribution. These unknowns make utilization of legacy slag precarious if the energy source is not low-CO_2. Moreover, much legacy slag is bound in buildings and infrastructure as aggregates or as part of the cement matrix. Therefore, there will be additional CO_2 emissions in the transport of these materials to the ISM facility if flue gas streams are envisaged as the CO_2 source. Given these complicating factors, grinding using purpose-built PV+LiB and exposure to atmospheric CO_2 concentrations were assumed. However, simple exposure of ground legacy slag to the ambient environment will likely not produce the desired CO_2 mineralization rates due to low relative humidity. Therefore, passive mineralization was achieved in an enclosed area, similar to a greenhouse.

In order to operate in a robustly net negative CO_2 manner, legacy slag was ground to a size that is fully mineralized after 1 year. It was assumed that no specific, consistent mineralogies and crystallinities of slags could be determined for a given slag pile. The composition was assumed to be

roughly similar to the industry average for pit-cooled BF, BOF, and EAF slags. For each slag type, the average of the performance for literature slag and synthetic slag was calculated at a reaction time of 1 year under atmospheric CO_2 concentrations. This resulted in an average 99% volume passing diameter of 3.60, 8.02, and 7.52 μm for BF, BOF, and EAF slags respectively. The resultant net CO_2 mineralization efficiency using diesel-powered grinders is 62.6%, 85.6%, and 82.2%, respectively. If PV+LiB powers the process, then the efficiency becomes 99.1%, 99.6%, and 99.5%, respectively. The total performance was then calculated by weighting each slag type against its global production quantity. Note that grinding of extraneous material (e.g., cement and other binders) is not included in the calculations; extraneous materials could be considered gangue, but the variety of extraneous materials and their potential for CO_2 mineralization makes this difficult to estimate.

It was estimated based on historical ironmaking and steelmaking production and general slag compositional data that post 1950 there has been 17.132 gigatonnes of BF slag, 2.308 gigatonnes of BOF and open hearth slag, and 0.736 gigatonnes of EAF slag produced. Using average slag compositions (with open hearth slags assumed roughly equivalent to BOF slags), there exists roughly a potential for negative emissions through CO_2 mineralization of legacy slag of 8.2 $GtCO_2$. Given the miniscule mineralization extent of minerals stored in pits or mounds [Lechat et al., 2016; Mayes et al., 2018; Nowamooz et al., 2018] and the integration of much slag as an aggregate or as GGBS, much of this potential likely remains unreacted. Accounting for the life cycle emissions of PV+LiB used to supply energy for grinding, utilization of this resource for passive CO_2 mineralization would result in a net mineralization of 7.852 $GtCO_2$. If diesel is used to power the grinding equipment, the total CO_2 mineralization drops to 5.097 $GtCO_2$. If applied to reduce 10% of ISM emissions, this resource would last for 16-23 years, dependent on source energy CO_2 intensity.

The diffusion of passive CO_2 mineralization of legacy slag requires less development and testing than the centrifugal or MYNA process, as the technology is simple grinding. The largest hurdle to process diffusion is the adoption of RE-powered, industrial scale grinding equipment. Though such equipment currently exists in the marketplace, it is not yet widely adopted. Displacement of current industrial in-pit excavators, crushers, and spreaders by battery powered models was assumed to require 5 years. During those 5 years, application of passive mineralization is achieved using diesel-powered systems. Though direct application of legacy slag to exhaust gas is preferable, it is assumed that a large portion of slag may be restrictively far from ISM facilities. As such, CO_2 mineralization is assumed to occur at atmospheric CO_2 concentrations. The size distribution was selected such that mineralization reactions would be completed within 1 year assuming the slag is primarily pit-cooled. The slag mounds are assumed to be spread globally across the 180 major ISM facilities. Projects are added at 4 per year until all sites are operating. The processing rate is set to exhaust the slag in 20 years, with operations occurring 240 days per year (5 days per week for 48 weeks per year) for 16 hours per day (2, 8-hour shifts). The resulting diffusion of passive mineralization to legacy slag is plotted in **Fig. 8-5** with the reduction in emissions related to a 2020 baseline provided in **Fig. 8-6**.
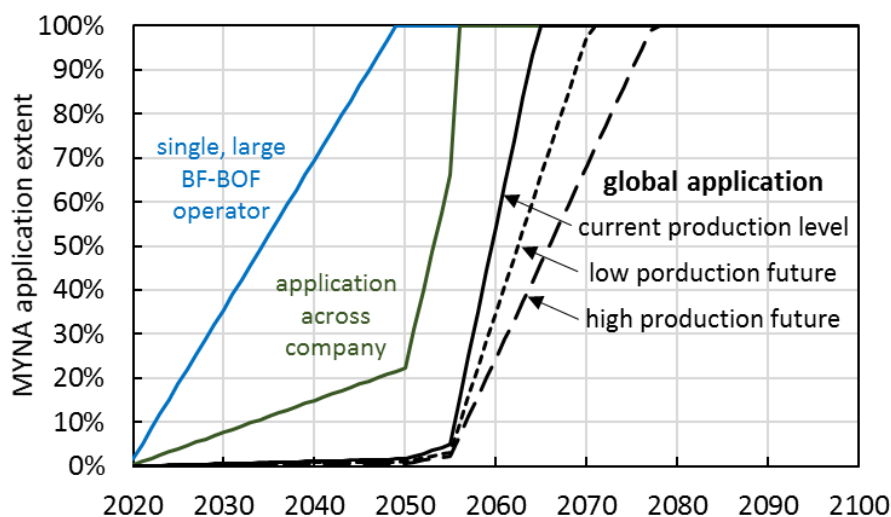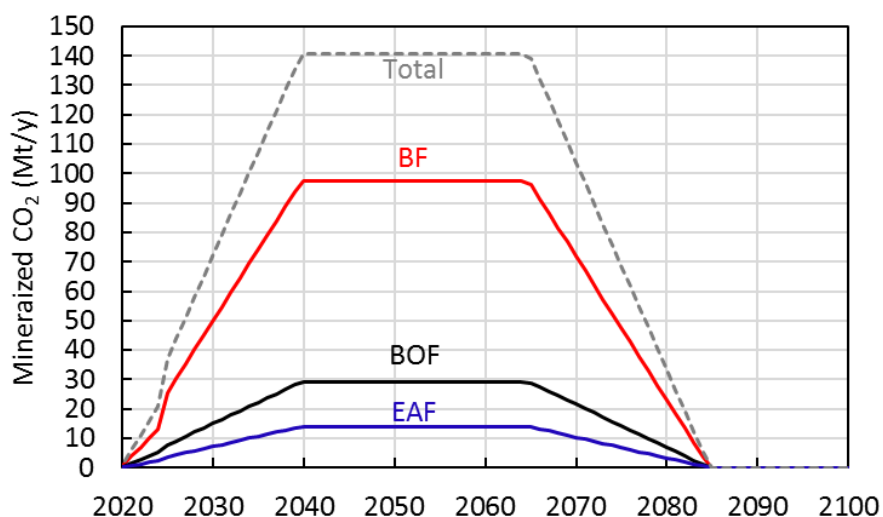
Fig. 8-5. The assumed diffusion of passive mineralization across ISM.
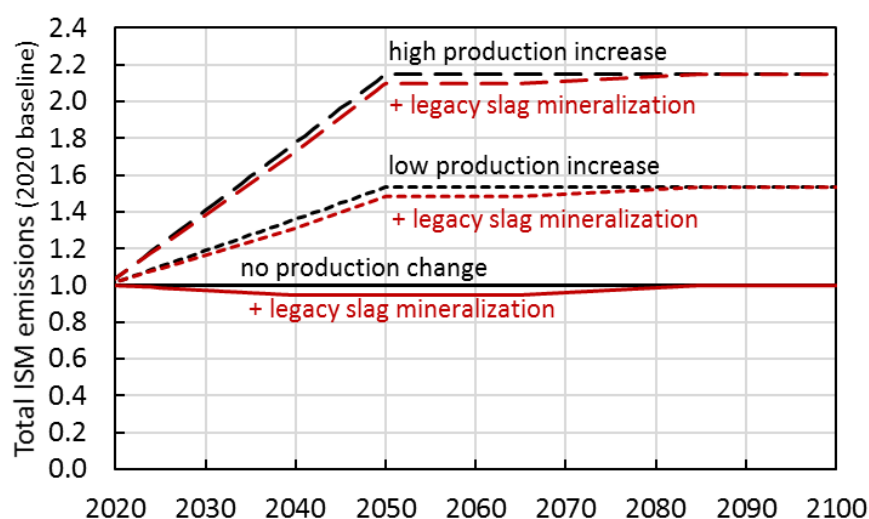
Fig. 8-6. The reduction in CO_2 emissions from diffusion of legacy slag-base CO_2 mineralization.

8.1.4. Other sources

The analysis of other calcium- or magnesium-bearing minerals for CO_2 mineralization pointed to the difficulty of transporting materials at low CO_2 emissions from their location to CO_2 point sources. As such, all other minerals are assumed to be ground and left to react with atmospheric carbon dioxide. Though the reactions are kinetically slowed by the reduction in CO_2 concentration, they also no longer must react with CO_2 at accelerated rates. So long as mineral piles are designed such that natural convection generates airflow (or piles are regularly overturned) and the relative humidity is kept high, CO_2 mineralization reactions will continue. Though the global supply of Mg-silicate mining residues is large, and potentially exploitable deposits represent a CO_2 sink greater than all anthropogenic emissions, the poor performance of the materials in passive CO_2 mineralization makes diversion of energy and capital towards these minerals difficult to recommend. The fact that a net emission of CO_2 occurs even when PV+LiB is used to supply energy for grinding $MgSiO_3$ or $CaAl_2Si_2O_8$ clearly indicates the precarious nature of depending on Mg-silicate resources for CO_2 mineralization. Though Mg_2SiO_4 performs better in hypothetical analyses, the ubiquitous nature of gangue natural

minerals means that the process may easily transition from reduction to emission without operators being aware of the change.

Calcium silicate minerals may provide opportunity for significant emissions reductions directly from the atmosphere. However, as is the case with any mineral deposit, it will be necessary to account for the actual mineralogical composition, including gangue material and amorphous phases. Without a detailed accounting of the minerals present, reasonable assumptions about a given mineral stocks can lead to predictions ranging from net CO_2 emission to highly efficient CO_2 reduction. As such, no estimates are given for the global potential for other minerals to reduce carbon dioxide, as such estimates would be effectively meaningless.

8.1.5. Aggregate effect

The total CO_2 reduction potential of each method and source is compiled in **Table 8-1**. The centrifugal and MYNA processes are sized to match slag production rate, while the legacy slag process operates via mineralization of atmospheric CO_2 over the course of 1 year. Slag produced during the scale-up and development periods of the centrifugal or MYNA processes is transferred to the legacy slag pile. Notable is the lack of impact that energy source has on the net CO_2 reduction of the centrifugal process. Equally notable is the major impact that energy source has on passive mineralization of legacy slags. It is clearly possible that a poorly-informed or designed passive CO_2 mineralization system targeting legacy ISM slags could generate large CO_2 emissions. The use of low CO_2 power functionally removes much of the sensitivity of the passive CO_2 mineralization process. **Figure 8-7** examines the mitigation impact of the centrifugal process in combination with passive CO_2 mineralization of legacy slags. In **Fig. 8-8**, the sensitivity of the centrifugal process to the reuse pathways of the products is examined. **Figure 8-9** examines the mitigation impact of the MYNA process in combination with passive CO_2 mineralization of legacy slags. In **Fig. 8-10** the effect of using diesel to power the processes in place of low-CO_2 power sources is graphed. Both pathways largely close the gap between current CO_2 emissions in ISM and the reductions necessary to meet the B2DS condition from the projection done by the IEA to meet 1.75 °C by 2100 [IEA, 2017]. Combining these methods with novel ISM processes (e.g., BF top gas recycling) should allow time for the ISM industry to develop the next generation of ISM facilities that can achieve radically lower emissions (e.g., electrolytic steelmaking, ISM+CCS).

Many failure points still exist in a system powered by RE. A lack of understanding of the mineralogy and crystallinity can result in unexpectedly low mineralization rates. Lack of control of the relative humidity can halt CO_2 mineralization, even for reactive minerals. Improper calculation of the PSD can cause unintended energy over-runs or overly large particles. Most of these problems are solved by the centrifugal and MYNA methods by way of generating easily separable solids with less mineralogical complexity. However, for passive mineralization of legacy slags, there exists no simple way to prevent such issues.

Table 8-1. The CO_2 reduction for each method and source.

		Centrifuge (grid)	Centrifuge (RE)	Centrifuge w/ CO_2 mineralization (grid)	Centrifuge w/ CO_2 mineralization (RE)	MYNA (diesel)	MYNA (RE)	Passive mineralization of legacy slag (diesel) [‡]	Passive mineralization of legacy slag (RE) [‡]
Current slag (MtCO$_2$/y)	**BF**	145.56	145.62	138.91	138.97	139.20	156.49	4043	6595
	BOF	142.00	142.03	98.22	98.24	43.23	46.75	841	995
	EAF	47.38	47.39	40.42	40.43	21.04	22.54	212	263
	Total	334.95	335.04	277.55	277.64	203.47	225.78	5097	7582
Total to 2100 (GtCO$_2$)		**42.999** (32.11-53.89)	**43.011** (32.12-53.91)	**35.630** (26.60-44.66)	**35.642** (26.61-44.67)	**19.322** (14.24-24.43)	**21.417** (15.77-27.06)	**Centrifuge 11.417** (8.4-14.0) **MYNA 16.632** (12.5-20.4)	**Centrifuge 16.117** (11.9-19.8) **MYNA 23.480** (17.6-28.8)
‡: total potential of current stocks									
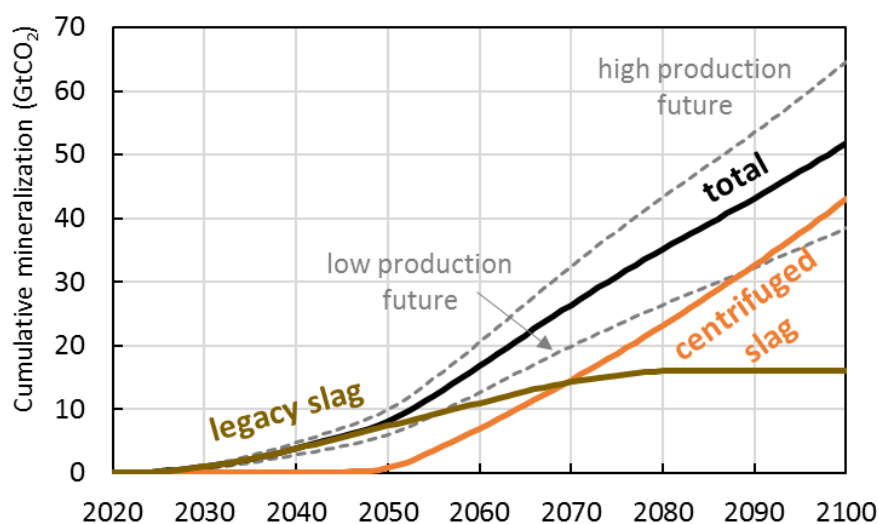
Fig. 8-7. Reduction in ISM CO_2 emissions due to slag centrifuging and CO_2 mineralization using legacy slag. All power is provided by PV+LiB.
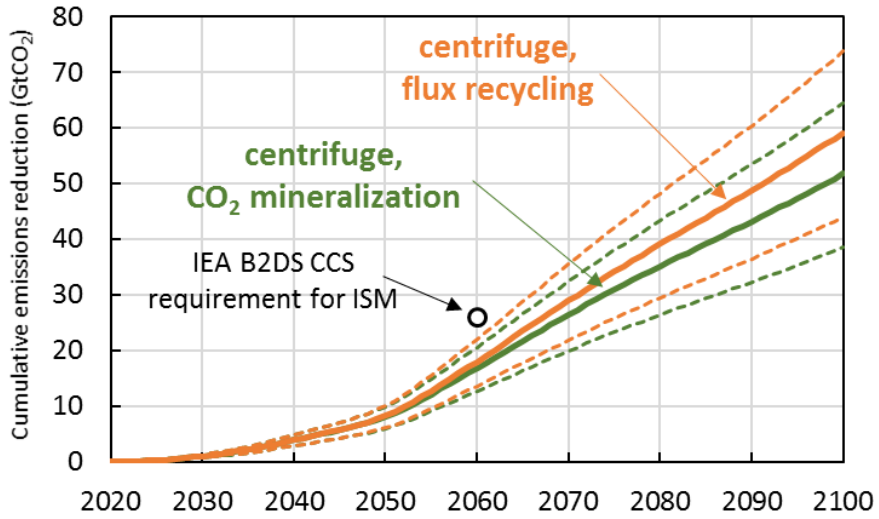
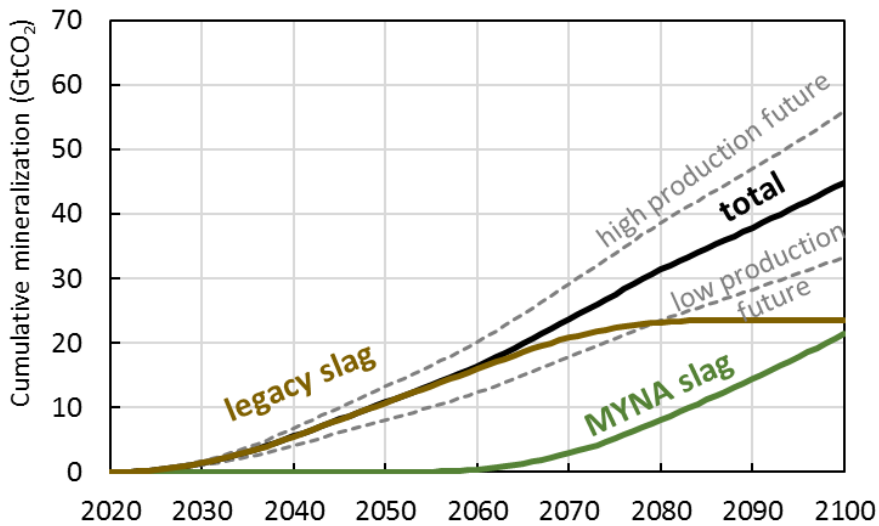**Fig. 8-8.** Cumulative CO₂ reduction from RE-powered centrifuging with legacy slag mineralization.

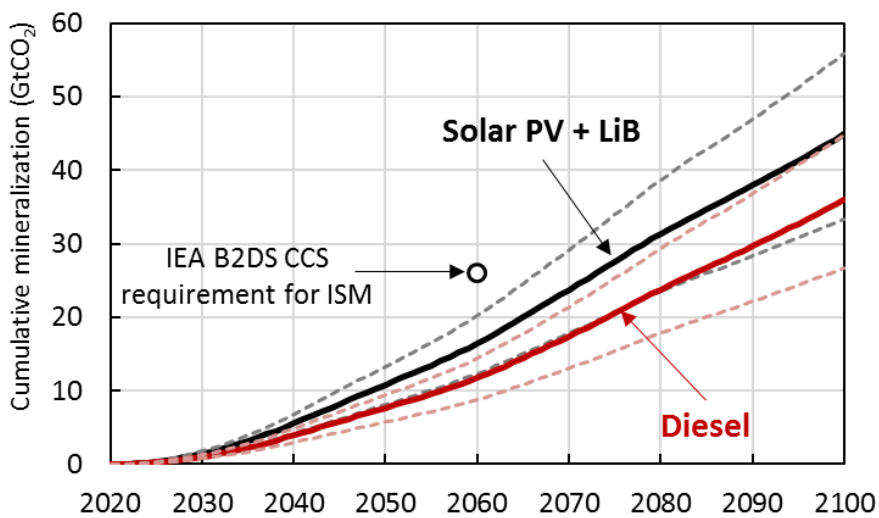**Fig. 8-9.** Cumulative CO₂ reduction from RE powered MYNA and legacy slag mineralization.

Fig. 8-10. Cumulative CO₂ reduction from MYNA and legacy slag mineralization based on power.

8.2. Cost

As noted in Chapter 1, the financial burden of technologically viable methods to fight climate change has been the primary factor preventing action. Moreover, as highlighted in Chapter 2, the ISM industry is exposed to international competition currently based primarily on the cost of production. As such, the proposed methods to reduce the CO_2 footprint of ISM were evaluated from an economic standpoint.

The CO_2 reduction methods proposed in this dissertation were purposely designed not to affect the operation of the ISM process; in other words, all processes occur after molten slag has been removed from the furnace and separated from the metallic melt. Therefore, the proposed processes do not alter the baseline cost of iron and steel production. An additional design point of the proposed processes is the ability to apply them at various sizes without major design changes. This allows for gradual increase in application extent, and learning-by-doing in low financial risk settings.

Estimation of the costs of the proposed processes is limited to the capital and operating expenses of the equipment. Other important costs (e.g., taxes, depreciation) were not calculated. Likewise, no assumptions of learning curves were made. All costs are reported in 2019 dollars.

8.2.1. Centrifugal process

Cost estimation for the equipment and operation of the centrifugal separation process is complicated by novelty of the method. The centrifuge system is simple, but unique: a metal body connected to a motor. There are no analogous, high temperature centrifuges found in the literature. Therefore, the cost of the centrifuge bodies was estimated by the cost of 2 m^3 internal volume cylindrical pressure vessels [Garrett, 1989]. Centrifuge bodies were assumed to be replaced each year. The motor to run the centrifuge was based on traditional fossil fuel motors, though an electric motor is envisioned. The motor was assumed to be replaced every 5 years. The ancillary equipment (e.g., bearings) and equipment to remove the solidified slag were assumed to double the capital cost of the centrifuge and motor system; ancillary equipment was assumed to have a 10-year lifetime. Power was supplied by the grid, with a backup PV+LiB system with storage capacity for 2 days of operations [Lazard, 2018]. Because ISM facilities already employee workers for slag treatment, the centrifugal systems is not envisaged to require additional manpower in comparison to current operations. The equipment and assumptions used in the cost estimate is provided in **Table 8-2** with a conceptual diagram provided in **Fig. 8-11**. The breakdown of costs and revenue streams is provided in **Fig. 8-12**.

The cost was calculated to be \$4.27/t-CO_2 avoided (±30% accuracy implies a range of \$3.28-\$5.55/t-CO_2). Nearly 100% of the cost is due to the capital expenditure into the centrifuge system. The operational expenses arise from the energy for centrifuging. Substantial recovery of expenses is possible through the recycling of (Ca,Mg)O as flux, FeO as ore, and Fe^0 as scrap. Accounting for this revenue, CO_2 reduction becomes profitable at \$71.10/t-CO_2 avoided (±30% accuracy of cost estimate implies a profit range of \$69.82-\$72.09/t-CO_2). The majority of these savings are from flux; the cost of fluxing agents was estimated as the cost of CaO in order to account for the costs of producing CaO from $CaCO_3$ at ISM sites. If the cost of flux is estimated as that of crushed stone (i.e., assuming that considerable pretreatment of the recovered Ca/MgO will still be required), the profit becomes \$22.34/t-CO_2 avoided (±30% accuracy of cost estimate implies a profit range of \$21.06-\$23.32/t-CO_2).

In addition to mineral recovery, energy could be recovered during the deceleration of the centrifuge. This energy could be used to charge a battery, thereby reducing the total energy consumption of the process. Likewise, in areas where a price on carbon exists, the reduced emissions would reduce costs. However, the patchwork nature of carbon prices and their susceptibility to

politics makes them a poor base on which to build a financial feasibility. A carbon price was not considered.
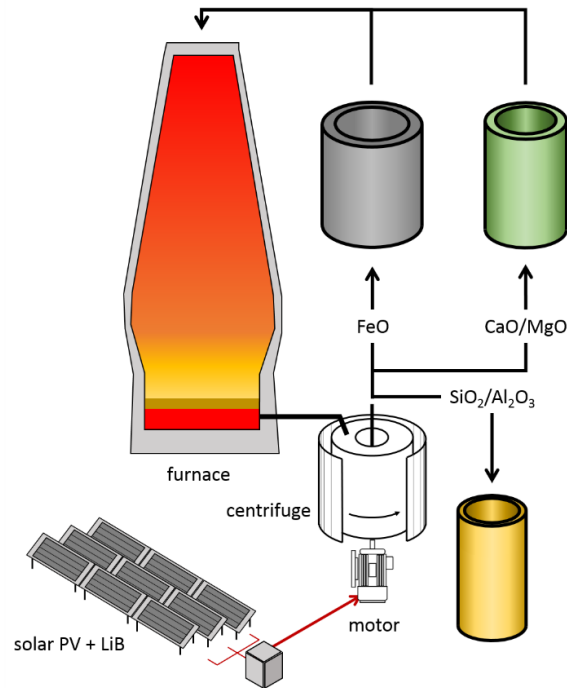

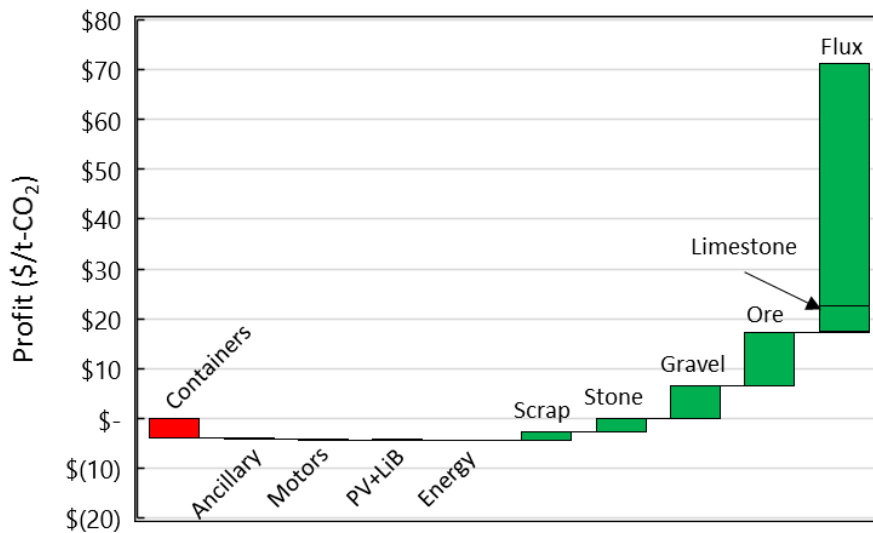**Fig. 8-11.** Conceptual diagram of centrifugal separation system.

Fig. 8-12. Cost and revenue streams in the centrifuge process.

Table 8-2. The cost and revenue analysis for the centrifugal process based on the operation of centrifuges to treat 1.111 Mtonne/y of slag for 20 years.

	Cost ($/unit)	Quantity	Comments
Capital Expenses	**$61,892,806**		
Centrifuge body	$458,242 [a,e]	6	$2m^3$ internal volume. 6.9 MPa pressure vessel. 2.46 tonne total mass. Monel 400 used for cost analysis though not necessarily appropriate for actual usage. Replaced annually.
Motor	$38,926 [a,e]	6	Priced using conventional motor, but an electric motor is envisioned. Replaced every 5 years.
Ancillary equipment	$497,169	6	Set equal to total cost of centrifuge body and motor due to unknown design. Replaced every 10 years.
PV+LiB backup	$315/MWh [b]	1.84 MWh	20-year life span. 2-day energy supply.
Process Expenses	**$368,617**		
Energy for centrifuge	$0.055/kWh [c]	0.953 kWh/m^3	Negligible effect of CO_2 intensity of energy supply allows for use of utility power.
Unit cost	**$4.27/t-CO₂**		**$3.28 - $5.55/t-CO₂**
Revenue	**$388,044,219 - $1,099,244,416**		
Scrap	$265/t [d]	4531 t/y	Fe^0 from BF slag.
Ore	$70/t [d]	111,021 t/y	FeO from BOF and EAF slag.
Lime	$123/t [d]	318,781 t/y	If recovered (Ca/Mg)O can be used without major pretreatment then lime is the assumed avoided cost. Otherwise, limestone is used to determine the avoided cost.
Limestone	$11.50/t [d]		
Crushed stone	$11.50/t [d]	175,059 t/y	Calcium silicates.
Gravel	$8.70/t [d]	548,925 t/y	Alumina, silica, and mixed compounds.
Unit revenue	**$26.61 - $75.37/t-CO₂**		
Unit profit	**$22.34 - $71.10/t-CO₂**		**$21.06 - $23.32/t-CO₂** **$69.82 - $72.09/t-CO₂**
a: Garret, 1989; b: Lazard, 2018; c: IRENA, 2018 ; d: USGS, 2018; e: Inflation calculated using the Marshall and Swift Process Industry Index.			

8.2.2. MYNA process

Cost estimation for the equipment and operation of the MYNA process is complicated by the unique slow solidification equipment. The cost of the containers was estimated by the cost of flat, non-pressure tanks made of 316 SS and the cost of 85% magnesia insulation for the interior insulating bricks [Garrett, 1989]. The comminution and movement of slag through the facility was modeled using data from small-scale mining operations [Stebbins, 1987]. A conveyer within ductwork was used to estimate the cost of the mineralization 'reactor'. At the end of the conveyor a front-end loader was assumed to be needed to transport reacted slag. As ISM facilities already employee workers for slag treatment efforts, no cost of additional labor was assumed. The equipment and assumptions used in the cost estimate are provided in **Table 8-3** with a conceptual diagram provided in **Fig. 8-13**. The breakdown of costs and revenue streams is provided in **Fig. 8-14**.

Operated for 20 years at a slag generation rate of 1.111 Mtonne/y, the cost of the MYNA process is $11.53/t-$CO_2$ mineralized (±30% accuracy implies a range of $8.87-$15.00/t-CO_2). Roughly 24% of the cost is due to initial capital expenditure which is dominated by the construction of a large duct to house the slag conveyor and flue gas for mineralization reactions. The primary operational expenses arise from the energy for grinding. Sale and reuse of the products from the MYNA process can substantially recover costs; namely, carbonated products can be sold as crushed stone, FeO can be reused as ore, and non-carbonated products can be sold as gravel. Accounting for this revenue, CO_2 reduction generates a profit of $32.59/t-$CO_2$ avoided (±30% accuracy of cost estimate implies a profit range of $29.13-$35.25/t-CO_2). The majority of these savings are from the crushed stone and ore.

In jurisdictions with a carbon price additional revenue/savings would occur by reduced ISM CO_2 emissions. However, the vacillatory nature of carbon prices and the lack of a global regulatory body makes reliance on such revenue precarious. A carbon price was not considered.
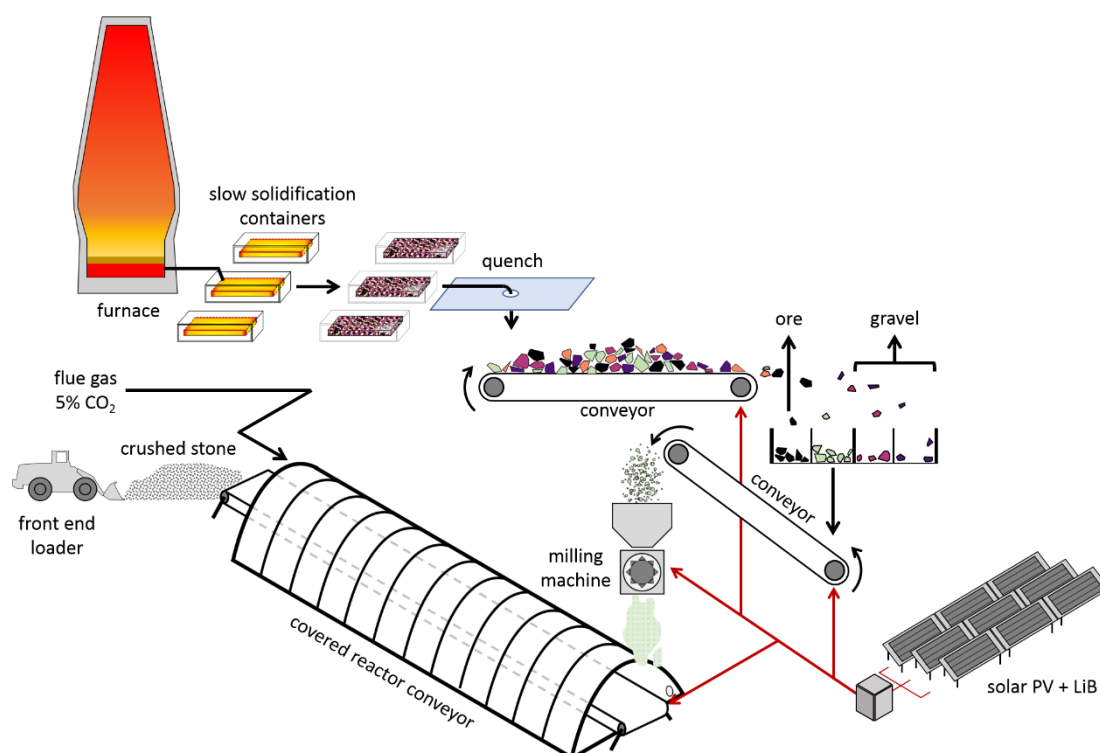

Fig. 8-13. Conceptual diagram of the MYNA system.

Table 8-3. The cost and revenue analysis for the MYNA process based on the treatment of 1.111 Mtonne/y of slag for 20 years.

|	Cost ($/unit)	Quantity	Comments
Capital Expenses	**$26,867,881**		
Solidification container	$47,397 [a,f] (shell: $23,404, internal refractory: $23,993)	45	9 containers needed at a time. Container lifetime of 4 years. External shell is 316 SS. Internal refractory priced as 85% magnesia.
Hopper	$6,371 [b,f]	1	Sized to match slag generation rate.
Crusher	$74,084 [b,f]	1	Sized to match slag generation rate.
Mill	$408,992 [b,f]	2	Sized to match slag generation rate.
Conveyor	$1,317/m [b,f]	100 m	91 cm wide conveyor.
Ductwork	$231,950/m [a,f]	100 m	6.35 m diameter, 3.174 mm thickness, mild steel.
Front-end loader	$378,026 [b]	1	For removal of mineralized slag at the end of the reaction conveyor.
PV+LiB backup	$315/MWh [c]	419 MWh	20-year life span. 2-day energy supply.
Process Expenses	**$83,217,823**		
Energy for hopper	$0.63/h [b,f]		
Energy for crushing and grinding	$0.055/kWh [d]	65 kWh/t	Negligible effect of CO_2 intensity of energy supply allows for use of utility power.
Energy for conveyor	$7.88/h [b,f]		
Energy for front-end loader	$21.41/h [b,f]		
Unit cost	**$11.53/t-CO₂**		**$8.87 - $15.00/t-CO₂**
Revenue	**$421,051,932**		
Ore	$70/t [e]	85,836 t/y	FeO.
Crushed stone	$11.50/t [e]	1,275,234 t/y	Carbonated products.
Gravel	$8.70/t [e]	50,876 t/y	Alumina, silica, and mixed compounds.
Unit revenue	**$44.12 /t-CO₂**		**$29.13 - $35.25/t-CO₂**
Unit profit	**$32.59 /t-CO₂**		**$29.13 - $35.25/t-CO₂**
a: Garret, 1989; b: Stebbins, 1987; c: Lazard, 2018; d: IRENA, 2018; e: USGS, 2018; f: Inflation calculated using the Marshall and Swift Process Industry Index.			
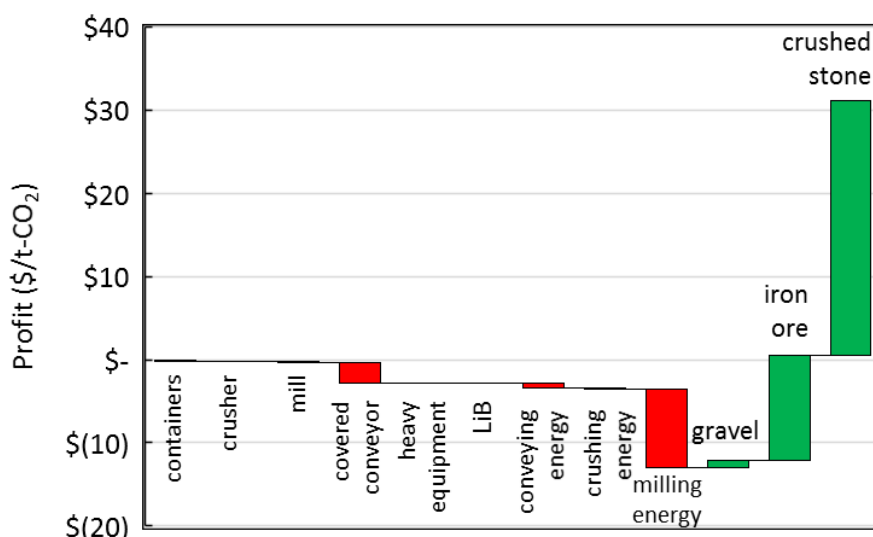
Fig. 8-14. Cost and revenue streams in the MYNA process.

8.2.3. Passive CO$_2$ mineralization

Cost estimation for the equipment and operation of passive mineralization of legacy slag was based primarily on the design of small mining operations [Stebbins, 1987]. The assumptions and equipment used in the cost estimate are provided in **Table 8-4** with a conceptual diagram provided in **Fig. 8-15**. The breakdown of costs and revenue streams is provided in **Fig. 8-16**.

The cost of passive mineralization of legacy slag is $26.47/t-CO$_2$ mineralized (±30% accuracy implies a range of $20.36-$34.41/t-CO$_2$). Only 4% of the cost is due to initial capital expenditure which is split rather evenly between a vinyl greenhouse for humidity control and equipment for moving and grinding slag. Operational expenses are dominated by energy generation for grinding. Grinding is assumed to occur only while energy is being generated by an on-site PV system. Sale of the products from passive mineralization can provide significant revenue. The mixed mineralogy and crystallinity of legacy slags means that it can likely only be reliably sold as a gravel substitute. Luckily, the mineralization process acts to trap potentially toxic metals that may be present in legacy slags [Hamilton et al., 2018]. Accounting for the revenue from resale, the CO$_2$ mineralization of legacy slags generates a profit of $4.35/t-CO$_2$; the ±30% accuracy of cost estimate implies that the process ranges from a cost of $3.59/t-CO$_2$ to a profit of $10.46/t-CO$_2$. A carbon price would naturally provide substantial increases in profit, but the poor track record of assured carbon prices led to its exclusion from this analysis.
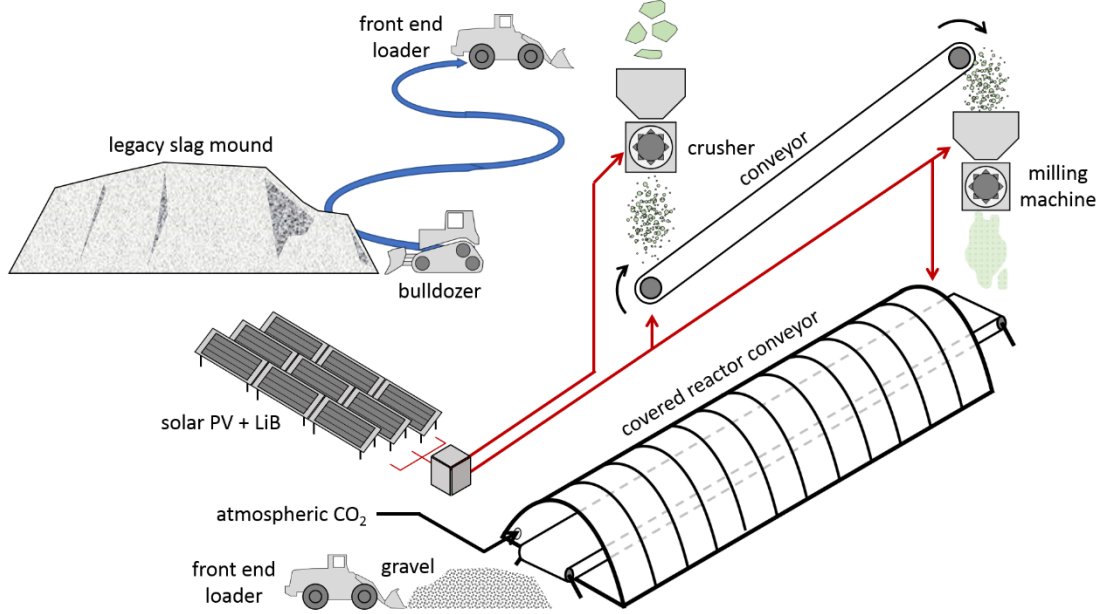
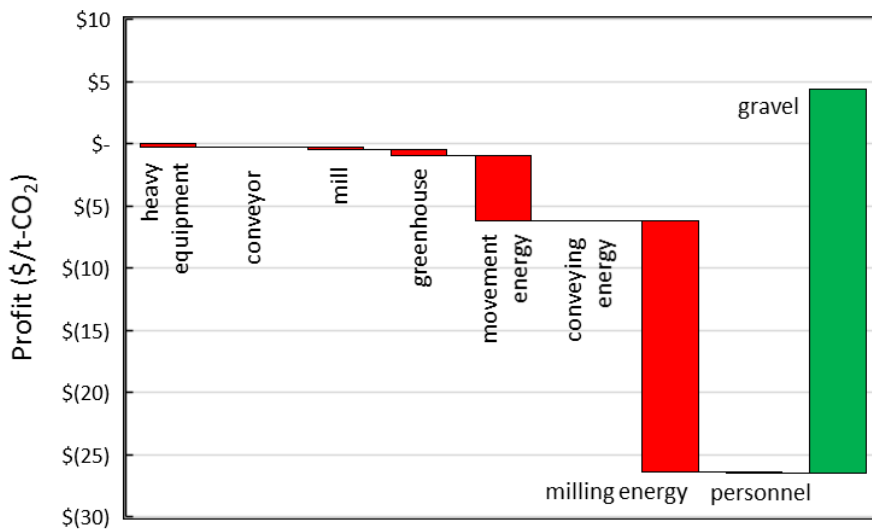**Fig. 8-15.** Conceptual diagram of the legacy slag system.

Fig. 8-16. Cost and revenue streams in the passive mineralization of legacy slag.

Table 8-4. The cost and revenue of using an 84 Mtonne legacy slag pile for CO_2 mineralization over the course of 20 years.

	Cost ($/unit)	Quantity	Comments
Capital Expenses	**$28,269,465**		
Bulldozer	$783,583 [a,e]	2	Necessary to breakthrough hard outer crust from weathering reactions.
Front-end loader	$908.568 [a,e]	4	For transporting slag from the pile to the grinding unit.
Hopper	$6,371 [a,e]	1	Sized to match grinding rate.
Feed conveyor	$532/m [a,e]	100 m	Sized to match grinding rate.
Mill	$414,182 [a,e]	11	
Conveyor	$532/m [a,e]	100 m	Sized to match grinding rate.
Front-end loader	$908.568 [a,e]	4	For transporting slag from the grinding unit to the greenhouse.
Greenhouse	$7.00/m^2 [b]	2.11 km^2	To maintain proper relative humidity.
Process Expenses	**$753,676,392**		
Energy for bulldozer	$139.42/h [a,e]		
Energy for front-end loaders	$1,874.32/h [a,e]		
Energy for hopper	$4.21/h [a,e]		
Energy for conveyors	$13.34/h [a,e]		
Energy for grinding	$0.055/kWh [c]	129 kWh/t	PV system reported as LCOE. No battery system required due to matching grinding to energy production.
Personnel	$100/h	10 workers/ shift	2 shifts of 8 hours a day, 5 days a week, 48 weeks a year.
Unit cost	**$26.47/t-CO$_2$**		**$20.36 - $34.41/t-CO$_2$**
Revenue	**$910,570,458**		
Gravel	$8.70/t [d]	104,662,201 t	Alumina, silica, and mixed compounds.
Unit revenue	**$30.83/t-CO$_2$**		
Unit profit	**$4.35/t-CO$_2$**		**$(3.59) - $10.46/t-CO$_2$**
a: Stebbins, 1987; b: Laate, 2013; c: IRENA, 2018; d: USGS, 2018; e: Inflation calculated using the Marshall and Swift Process Industry Index.			

In **Fig. 8-17** the sensitivity of the cost of treatment using the three proposed methods to the LCOE is plotted. As was the case for sensitivity to CO_2 intensity of energy, the centrifuge process is insensitive to LCOE. The MYNA process is less sensitive to LCOE then passive mineralization of legacy slags. This arises from the large grain sizes and more reactive minerals that are generated during the in-container solidification of the MYNA process.
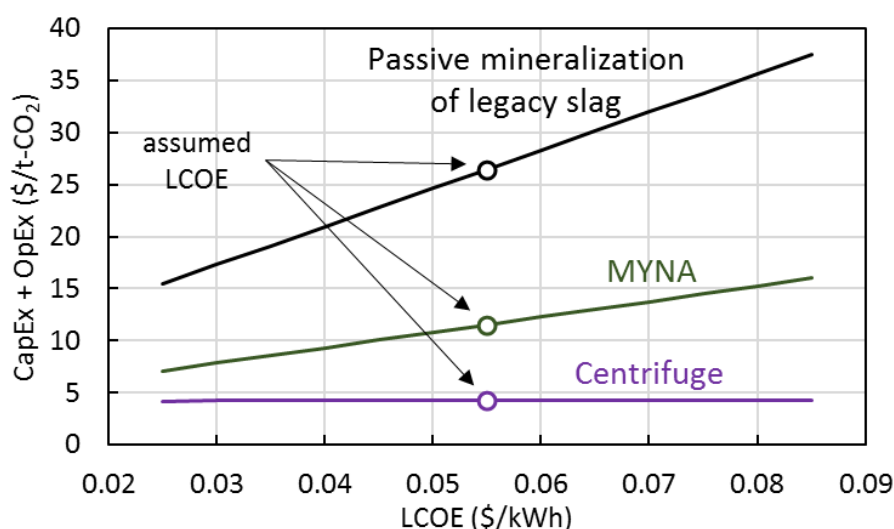
Fig. 8-17. The influence of LCOE on total process cost.

In **Fig. 8-18** the sensitivity of the profit to the LCOE is plotted. Unsurprisingly, the centrifuge process maintains a high profitability regardless of LCOE. The MYNA process is able to maintain profitability even at high energy costs, but the profit margin is less than the accuracy of the cost analysis. Passive mineralization of legacy slags becomes a net cost when the LCOE exceeds $0.066/kWh.
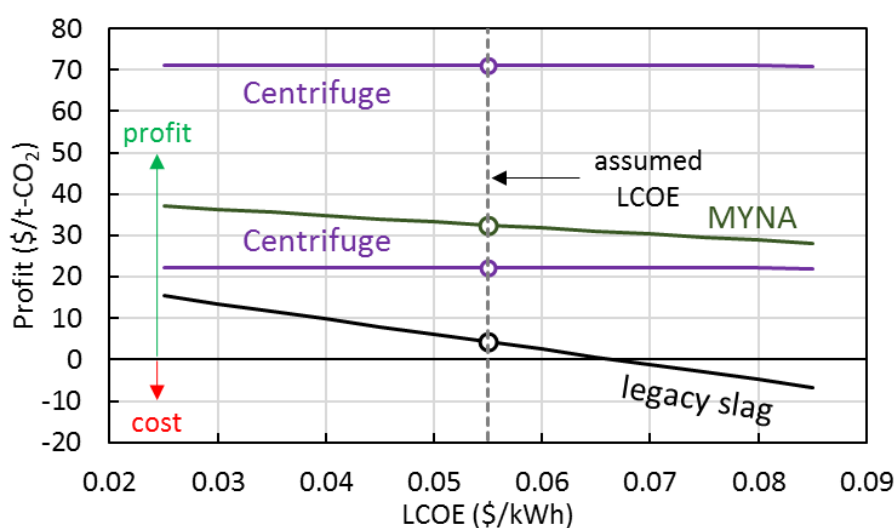
Fig. 8-18. The influence of LCOE on profit.

8.2.4. Comparison to extant CO$_2$ reduction options

The majority of research effort in reducing the CO$_2$ emissions of ISM is focused on capture and storage of CO$_2$ from the various flue gases and recycling of the BF topgas. Calculations of costs for retrofitting ISM facilities with CCS have yet to fully consider the potential pitfalls of flue gas heterogeneity, inclusion of species that may cause significant amine degradation, and the old and diverse nature of ISM equipment and processes. This means each retrofitting of CCS to ISM may be a 'first of a kind' plant (FOAK). Moreover, the ever-present weakness of CCS is the need for integration of sizing and timing of capture facilities with CO$_2$ transport infrastructure and storage sites. Putting

these concerns aside, the cost of retrofitting ISM with CCS averages $72.38/t-$CO_2$ [IEAGHG, 2018]. In the case of new builds, the average cost is $71.25/t-$CO_2$. This lack of substantial price decline is indicative of the mature nature of CO_2 capture technology. If waste heat from ISM is available the price of retrofits and new builds decline to $39.25/t-$CO_2$ and $51.25/t-$CO_2$, respectively. There is significant variation in cost estimates arising from the amount of CO_2 captured, the concentration of CO_2 in the gas stream, the geographic location of the plant, and whether plants are considered FOAK or 'nth-of a kind' (NOAK) [Biermann et al., 2018; Bui et al., 2018; Irlam, 2017; Leeson et. al, 2017]. Innovative ISM processes (some applied in conjunction with CCS) are projected to reduce CO_2 emissions at an average cost of $67.25/t-$CO_2$, dropping to $61.63/t-$CO_2$ if waste heat is available. The range of cost estimates are provided in **Fig. 8-19** along with the cost of the systems proposed in this dissertation.
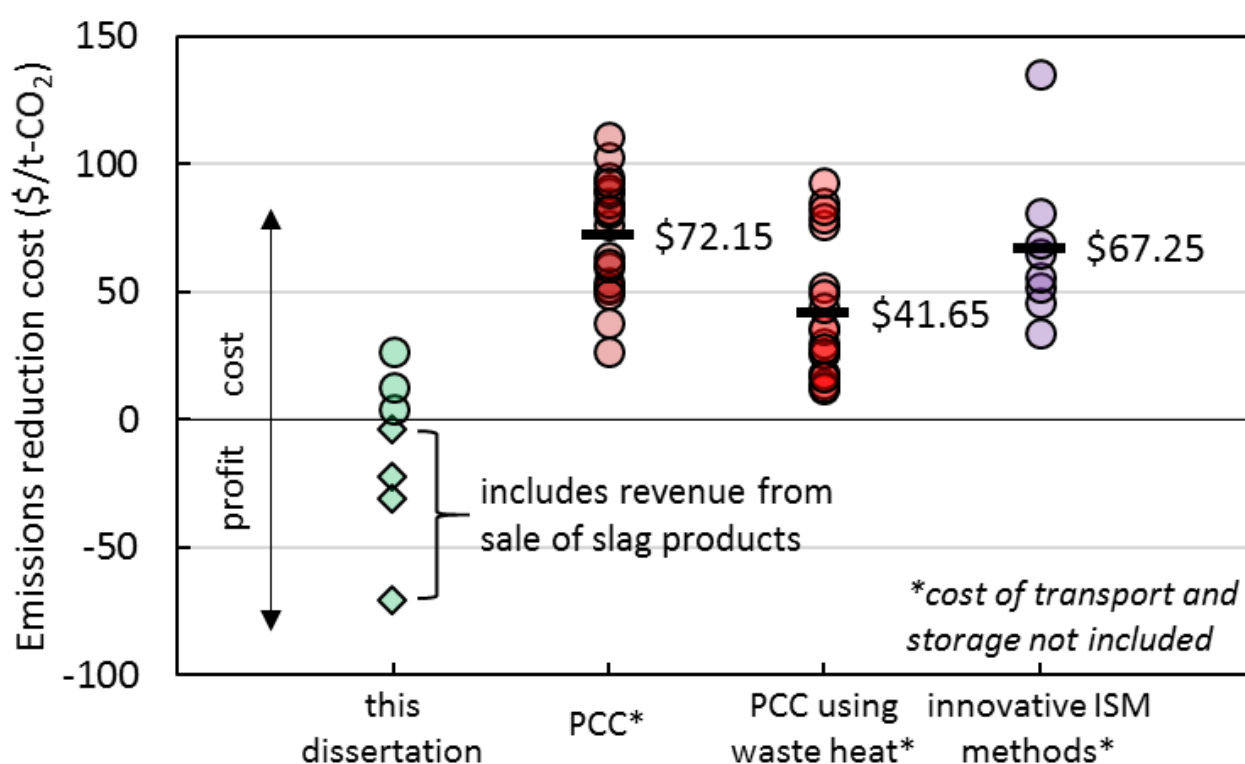
Fig. 8-19. The cost of various CO_2 reduction methods for ISM from the literature compared with those of this dissertation.

In the 1990's and 2000's a number of studies evaluated relatively passive CO_2 mineralization schemes using natural mineral and industrial wastes such as ironmaking and steelmaking slag [Huijgen, 2005; Huntzinger et al., 2009; Lackner et al., 1995; Lackner et al., 1997; Rawlins, 2008; Sipila et al., 2008; Zevenhoven et al., 2009]. This work tended to focus on geologically plentiful magnesium silicates and made insufficient efforts to determine the mineralogy and crystallinity of ISM slags. These decisions led to the conclusion that gas-solid CO_2 mineralization reactions were infeasibly slow, and thus pushed the research community to aqueous carbonation, chemical enhancement, high-temperature, and high-pressure processes. However, such 'enhanced' methods fail to robustly produce net CO_2 reductions when a LCA is properly performed. Therefore, cost estimates for these 'enhanced' systems are deemed meaningless and not reported here. Considering only non-chemical

processes without 'thermal pretreatment' or 'mechanical activation', and excluding the cost of CO_2 capture and transportation, the only detailed cost estimate for slag-based CO_2 mineralization is $119.84/t-$CO_2$ in 2019 dollars [Huijgen, 2005]. Of this cost, $34.24/t-$CO_2$ was directly associated with grinding energy and equipment, while the remaining costs were due to increasing reaction temperatures and pressures, heat exchangers, blowers, and other ancillary equipment. The assumed cost of electricity amounts to greater than $0.09/kWh in 2019 dollars. Adjusting for the price of current and near-future utility energy ($0.055/kWh), the cost of grinding would become $26.64/t-$CO_2$. Moreover, the study did not consider the mineralogy and crystallinity of the slag, resulting in the low conversion efficiency of 69%. It is notable that this reaction percent is predicted by the current dissertation based on slag type and desired reaction rate. If conversion was allowed to occur in 1 year instead of 1 hour, the conversion efficiency would increase to ~83% and the grinding costs would reduce to $19.89/t-$CO_2$ in 2019 dollars. This value is quite close to the cost of passive mineralization of legacy slag calculated in this dissertation ($20.36-$34.41/t-CO_2).

The profitable and scalable nature of the proposed centrifuge, MYNA, and passive mineralization methods are unique in the climate change mitigation field. These methods can be applied to the financial benefit of the iron and steelmaking industry while also reducing anthropogenic CO_2 emissions. The hope is that this pairing of financial and environmental benefits will lead to rapid adoption and potentially a new industry of profitable CO_2 reduction and removal technologies.

Chapter-specific symbols and abbreviation list

BF: Blast furnace

BOF: Basic oxygen furnace

CCS: CO_2 capture and storage

EAF: Electric arc furnace

ISM: Ironmaking and steelmaking

LCOE: Levelized cost of electricity

MYNA: In-container solidification with solid-state quenching

PSD: Particle size distribution

PV+LiB: Solar photovoltaic with lithium ion battery storage

RE: Renewable energy

References

Arasto, A., Tsupari, E., Karki, J., Sihvonen, M., and Lilja, J., 2013. Costs and potential of carbon capture and storage at an integrated steel mill. Energy Procedia, 37, pp.7117-7124.

Biermann, M., Normann, F., Johnsson, F. and Skagestd, R., 2018. Partial carobon capture by absorption cycle for reduced specific capture cost. Industrial & Engineering Chemistry Research, 57(45), pp.15411-15422.

Bui, M., Adjiman, C.S., Bardow, A., Anthony, E.J., Boston, A., Brown, S., Fennell, P.S., Fuss, S., Galindo, A., Hackett, L.A., Hallett, J.P., Herzog, H.J., Jackson, G., Kemper, J., Krevor, S., Maitland, G.C., Matuszewski, M., Metcalfe, I.S., Petit, C., Puxty, G., Reimer, J., Reiner, D.M., Rubin, E.S., Scott, S.A., Shah, N., Smit, B., Trusler, J.P.M., Webley, P., Wilcoxx J. and Mac Dowell, N., 2018. Carbon capture and storage (CCS): the way forward. Energy & Environmental Science, 11(5), pp.1062-1176.

Garrett, D.E., 1989. Chemical engineering economics. Van Nostrand Reinhold, New York.

Hamilton, J.L., Wilson, S.A., Morgan, B., Turvey, C.C., Paterson, D.J., Jowitt, S.M., McCutcheon, J. and Southam, G., 2018. Fate of transition metals during passive carbonation of ultramafic mine tailings via air capture with potential for metal resource recovery. International Journal of Greenhouse Gas Control, 71, pp.155.

Huijgen, W.J., Witkamp, G.J., and Comans, R.N., 2005. Mineral CO2 sequestration by steel slag carbonation. Environmental science & technology, 39(24), pp.9676-9682.

Huntzinger, D., Gierke, J., Komarkawatra, S., Eisele, T.C. and Sutter, L.L., 2009. Carbon Dioxide Sequestration in Cement Kiln Dust through Mineral Carbonation. Environmental science and technology, 43, pp.1986-1992.

IEA, 2016. CO_2 emissions from fuel combustion: 2016 edition.

IEA, 2017. Energy technology perspectives 2017: Catalysing energy technology transformations.

IEAGHG, 2018. Cost of CO2 capture in the industrial sector: Cement and Iron and Steel Industries. 2019-TR03.

IRENA, 2018. The power to change: Solar and wind cost reduction potential to 2025.

Irlam, L., 2017. Global costs of carbon capture and storage: 2017 Update. GCCSI.

Kuramochi, T., Ramirez, A., Turkenburg, W., and Faaij, A., 2012. Comparative assessment of CO2 capture technologies for carbon-intensive industrial processes. Progress in energy and combustion science, 38(1), pp.87-112.

Laate, E.A., 2013. The economics of production and marketing of greenhouse crops in Alberta. Alberta agriculture and rural development, Economics and competitiveness division, Economics branch.

Lackner, K.S., Butts, D.P., and Wendt, C.H., 1997. Progress in binding CO2 in mineral substrates. Energy conversion and management, 38, pp.S259-S264.

Lackner, K.S., Wendt, C.H., Butts, D.P., Joyce Jr., E.L., and Sharp, D.H., 1995. Carbon dioxide disposal in carbonate minerals. Energy, 20(11), pp.1153-1170.

Lazard, 2018. Lazard's levelized cost of storage analysis – Version 4.0.

Lechat, K., Lemieux, J.M., Molson, J., Beaudoin, G. and Hébert, R., 2016. Field evidence of CO2 sequestration by mineral carbonation in ultramafic milling wastes, Thetford Mines, Canada. International Journal of Greenhouse Gas Control, 47, pp.110-121.

Leeson, D., Mac Dowell, N., Shah, N., Petit, C. and Fennell, P.S., 2017. A techno-economic analysis and systematic review of carbon capture and storage (CCS) applied to the iron and steel, cement, oil refining and pulp and paper industries, as well as other high purity sources. International Journal of Greenhouse Gas Control, 61, pp.71-84.

Mayes, W.M., Riley, A.L., Gomes, H.I., Brabham, P., Hamlyn, J., Pullin, H. and Renforth, P., 2018. Atmospheric CO2 Sequestration in Iron and Steel Slag: Consett, County Durham, United Kingdom. Environmental science & technology, 52(14), pp.7892-7900.

Nowamooz, A., Dupuis, J.C., Beaudoin, G., Molson, J., Lemieux, J.M., Horswill, M., Fortier, R., Larachi, F., Maldague, X., Constantin, M. and Duchesne, J., 2018. Atmospheric carbon mineralization in an industrial-scale chrysotile mining waste pile. Environmental science & technology, 52(14), pp.8050-8057.

Rawlins, C.H., 2008. Geological sequestration of carbon dioxide by hydrous carbonate formation in steelmaking slag. PhD Thesis. Missouri University of Science and Technology.

Sipilä, J., Teir, S., and Zevenhoven, R. Carbon dioxide sequestration by mineral carbonation: Literature review update 2005–2007. Åbo Akademi University, report VT2008-1.

Stebbins, S.A., 1987. Cost estimation handbook for small placer mines (Vol. 9170). US Department of the Interior, Bureau of Mines.

Tsupari, E., Karki, J., Arasto, A., and Pisila, E., 2013. Post-combustion capture of CO2 at an integrated steel mill – Part II: Economic feasibility. International Journal of Greenhouse Gas Control, 16, pp.278-286.

USGS, 2018. Mineral commodity summary 2018.

Ho, M.T., Bustamante, A., and Wiley, D.E., 2013. Comparison of CO2 capture economics for iron and steel mills. International Journal of Greenhouse Gas Control, 19, pp.145-159.

World Steel Association, 2018. Steel Statistical Yearbook 2018.

Zevenhoven, R., Fagerlund, J., Wiklund, A., Nduagu, E., Forsman, A.M., Falt, M., Matilla, H.P., Eloneva, S. and Said, A., 2009. CO2 emissions mitigation in Finland by carbonation of silicate minerals and industrial wastes. International flame research foundation, 1, pp.15.

Chapter 9: Conclusions

9.1. Novel findings and significance

The motivation for this research was to provide technically feasible, rapidly adoptable, economically viable methods to reduce CO_2 emissions in the iron and steelmaking industry. To do so required development of cutting-edge analytical tools, extensive gathering of available data, and tedious experimentation to determine fundamental properties. However, the resulting processes and equipment are simple and rely on existing technologies. They also derive incentive not from political policy, but rather from self-motivated economics.

9.1.1. Molten state property prediction

The ability to predict the properties of molten slags at significantly higher accuracies and over a wider compositional space than conventional methods was demonstrated using deep neural networks. Due to the high risk of molten systems and the large capital investments of iron and steelmaking, the improved prediction of molten properties is especially beneficial. Experiments in the molten slag system are notoriously difficult, time consuming, and expensive. Moreover, the large number of chemical components in slag causes a combinatorial explosion which puts fundamental limits on the usefulness of experimentation. Deep neural networks allow the metallurgical industry to predict the properties of novel slag chemistries at the accuracy limit of the available data. Moreover, deep neural networks explicitly provide information on the degree of certainty of a given prediction relative to the database as a whole, thereby allowing for informed decisions about what experiments should be performed. Outside of iron and steelmaking, deep neural network predictions may find use in glassmaking, coal furnaces, and planetary modeling.

9.1.2. First accurate prediction of nucleation lag time

The physical mechanisms underlying the nucleation lag time remains an open debate in the literature with no predictions that fit all empirical data. The accurate prediction of nucleation lag time by a deep neural network represents the first step in understanding this phenomenon in detail. Bootstrapping the prediction with the viscosity reduced the prediction accuracy, while bootstrapping with the liquidus temperature increased the accuracy. As deep neural networks are simply a mapping of the underlying data, this result provide solid evidence that the viscosity is spuriously correlated with the nucleation lag time, but not a meaningful mechanistic lever the process. This back and forth between conventional theories and deep neural networks provides a blue print both for understanding hitherto intractable physical phenomenon and for untangling the internal workings of deep neural networks.

In addition to the scientific value of this result, highly accurate estimates of the nucleation lag time allows for a plethora of design and engineering activities that have, as of yet, been impossible. Three such examples appeared herein: centrifugal separation, calculation of the critical cooling rate, and prediction of the grain sizes that develop from slow solidification. Knowledge of the nucleation lag time is fundamentally for any process or field that deals with the liquid-to-solid phase change.

9.1.3. Novel centrifugal process

A simulation of centrifugal separation of mixed molten slag into pure phases demonstrated the promise in such a method in terms of CO_2 reduction. Supported by the estimates from deep neural networks, the simulation indicated that the current experimental centrifugal systems have yet to reach the true potential of the method. Due to constitutional supercooling, the nucleation lag time, and the rapid nature of centrifugal separation, high purity layers are generated and subsequently

solidify. This provides the potential to create a closed recycling of CaO and MgO in the iron and steelmaking processes, wherein silica, alumina and other impurities do not remain bound to calcium and magnesium, but rather are shuttled to a distinct, aggregate phase. Likewise, the centrifugal method provides the opportunity to recover the metallic and low oxidation state iron from slags, further lowering the CO_2 intensity of producing iron and steel.

9.1.4. Novel slow solidification method

A slag handling methodology at complete odds with conventional practices was developed. Namely, molten slag is slowly solidified in containers in order to generate large mineral grains which can be more easily separated. This separation of materials within slag was demonstrated to greatly increase the efficiency of subsequent slag treatment (i.e., quenching and CO_2 mineralization). Moreover, the method was shown to reduce the complexity of minerals that ultimately arise in slag, resulting in more rapid CO_2 mineralization.

9.1.5. Mineral-specific grinding energy calculation

The surface energies and critical stress intensities of the major minerals found in slag were calculated from considerations of crystal structure. This data greatly improves the accuracy of grinding energy predictions, allowing for nuanced system design and optimization. This data can be applied to the mining industry as well to help determine best practices and areas for improvement.

9.1.6. Quenching-based liberation

A novel comminution method of quenching high temperature, solid slag was generated. The method was shown to reduce grinding energy by up to 40% in a single quenching stage. Concurrently, the nature of the underlying mechanisms allows for increased liberation of the fractured materials.

9.1.7. Empirical determination of CO_2 diffusivity of minerals and glasses

The CO_2 diffusion coefficient for 21 crystalline minerals and 13 glasses taking part in gas-solid CO_2 mineralization was empirically determined. This covers the majority of minerals found in ironmaking and steelmaking slags, along with minerals commonly touted as CO_2 mineralization feedstocks. The results show a high variability between minerals in terms of diffusivity, resulting in very different operating parameters for CO_2 mineralization.

9.1.8. CO_2 mineralization performance indices for minerals

Combination of the data on the energy intensity of grinding and on empirical CO_2 diffusion constants was combined to generate performance indices for minerals used in CO_2 mineralization. In general, only calcium silicates, calcium oxide, and magnesium oxide are suitable for industrial CO_2 mineralization processes. Aluminum, iron, and magnesium drastically reduce the overall reaction rate of calcium and magnesium bearing compounds. Efforts to increase the reaction rate inherently require energy which thereby reduces the net CO_2 mineralization due to associated emissions. These indices suggest that the substantial research into mineralization of magnesium silicates is misplaced.

9.1.9. Probabilistic prediction of mineral locking in 3D

A hitherto unappreciated phenomenon of mineral locking was proposed and modeled in three dimensions. The analysis provides quantitative proof that target species of less than 20% of the slag or mineral volume are subject to severe blocking from the reaction environment by neighboring grains. This information suggests that many of the CO_2 research projects are destined to failure due to the unnoticed effects of mineral locking.

9.1.10. Modified shrinking core model

The classic Shrinking Core Model was modified to account for the full particle size distribution of a sample, demonstrating the substantial errors of monodisperse approximations. The model was

further modified to account for particle shape, surface roughness, and fractal effects. Equivalent corrections were made for calculation of mineral locking and effective diffusivity. These improved analytical methods can be applied to any field or industry that deals with gas-solid reactions.

9.1.11. Gigatonne-scale reduction of CO_2 emissions

The potential for three technologies to reduce the CO_2 emissions of iron and steelmaking were analyzed. Centrifugal separation and the MYNA process (in-container solidification with solid-state quenching) were shown to have the potential to reduce current global CO_2 emissions by hundreds of megatonnes a year. Application of passive CO_2 mineralization to legacy slags was demonstrated to be technically possible but potentially treacherous if fossil fuels were used to power grinding. Utilization of renewable energy, or other low CO_2 power sources, makes mineralization of CO_2 using legacy slags robustly net negative. Assuming a middle of the road increase in ISM over the 21st century, the centrifuging of slag combined with mineralization using legacy slags would result in a cumulative emissions reduction of 51.8-59.1 GtCO_2 by 2100. Alternatively, the MYNA process combined with mineralization using legacy slags could cumulatively reduce emissions by 36.0-44.9 GtCO_2 by 2100.

9.1.12. Caution regarding mining wastes

The rates of CO_2 uptake by mining wastes were shown to be too kinetically slow to risk gas-solid CO_2 mineralization in ambient conditions; this fact remains even when power is supplied by renewable energy. These results are important in guiding efforts of the negative emissions community which currently is focused primarily on Mg-silicates as a CO_2 mineralization feedstock. Though many alternative reaction pathways are being developed (e.g., aqueous, mixed with soil, etc.), all pathways involve extensive grinding; the results of this dissertation supply important information on the impact of grinding net CO_2 emissions.

9.1.13. Potential for enhanced weathering of certain minerals

In contrast to Mg-silicate rocks, high purity calcium silicate geologies may prove an attractive target for passive CO_2 mineralization. However, care is needed to control the relative humidity of the ambient atmosphere. Development of passive mineralization methods and equipment should begin with the iron and steelmaking industry using available technology and on-site resources. This knowledge base may be beneficial in developing technologies that allow for CO_2 mineralization using Ca-silicate mineral resources.

9.2. Open problems and future work

The various technologies and methods upon which this dissertation was built each have substantial room for further development and improvement. The simulation of molten slag centrifugal separation should be updated to account for a full heat balance; namely, heat loss to the container and environment, the latent heat of solidification, and heating from internal viscous friction. Additionally, the effects of pressure and shear on the nucleation and growth of solids in the slag should be accounted for in the centrifugal simulation. The assumed inherent cluster size should be evaluated by running the centrifuge simulation to match available experimental data. Once the physical mechanisms and associated assumptions have been thoroughly verified, the general shape and dimensions of the centrifuge should be optimized for material recovery. Such optimization will be complicated by the multiple physical mechanisms at play: travel distance, heat balance, centrifugal force, and likely shear. The considerable variation between steelmaking slags indicates that the process may be sensitive to minor compositional changes. Therefore, optimization will also need to focus on making a process that is robust against the minor alterations in composition that

occur in slag. It seems unlikely that energy will be a limiting factor to maintain net CO_2 mineralization, making the analysis purely about optimizing separation. The physical handling of molten and solidified slag will obviously require engineering design to bring the system to reality.

The MYNA process contains several subsystems that require further development. Conceptually, the slow solidification system is well supported by operational evidence and theory. However, the composition of minerals that precipitate under slow solidification remains an open question. The mineral composition was estimated based on empirical evidence from the literature and thermodynamic analysis. However, thermodynamic methods are limited in the compositional complexity which they can analyze, making these results somewhat tenuous. Likewise, empirical results rarely provide the detailed reporting necessary to develop deep neural network solutions. As such, estimation of the mineral composition of slowly solidified slag will likely have to proceed by empirical investigation.

The solid state quenching portion of the MYNA process is well founded on experimental and theoretical evidence. Realizing the system is within the capabilities of current iron and steelmaking facilities. However, the potential production of a liquid waste stream and the loss of a considerable amount of thermal energy deserves further evaluation. Given the slow solidification process generates mineral grain sizes on the order of a few hundred micrometers, the energetic requirements for grinding the slag for the purpose of separating the disparate compounds is small. Analysis may show that heat recovery from the high temperature slag -post slow solidification- followed by crushing for separation is more energetically favorable. This would have the added benefit of eliminating potential liquid waste streams from the process.

The covered conveyor/greenhouse systems used for CO_2 mineralization are simple and can be realized using extant technology and know-how. Of importance though, is matching the federate of ground slag to the exhaust gas flow rate such that the exiting flue gas has been effectively scrubbed of carbon dioxide. Such design must account for the mineralogical makeup, particle size distribution, grain size distribution, and the gas-solids interaction geometry. For legacy slag, the CO_2 source is assumed to be atmospheric, so low-energy methods to enhance gas-solids contact must be developed. For all systems, control of the relative humidity is of critical importance. Hitherto, the relative humidity has been controlled by water pans; however, such a set-up is sensitive to fluctuations in temperature and gas flow rates. Humidity control based on wetted solids (e.g., common salts) is a promising method to passively maintain humidity across the likely temperature ranges.

The above-mentioned areas for further development all seem within the realm of standard engineering design; in fact, this trait of using extant technologies was fundamental to the design of the systems. However, the foundation of this dissertation is reducing CO_2 emissions at a scale and on a timeline commensurate with reducing the worst effects of climate change. Quantitatively, that necessitates gigatonnes of CO_2 emissions reductions and negative emissions in the coming decades. Therefore, the largest open problem, and the course of future work, is to scale-up and spread these processes as quickly as possible. As evidenced by the underwhelming adoption of CCS technologies over the past decades, providing a technical solution is not sufficient to prompt wide-scale adoption. The processes put forward in this dissertation were purposefully designed to be simple, flexible, reliable, independent, and profitable. The next step is to prove these characteristics hold up in real world applications. An additional area of future focus is to extend the methods of this dissertation to other solid wastes (e.g., demolition waste) and promising natural minerals. Connected to the

mineralization of solids is the production of building and infrastructure materials which will grow in demand as the effects of climate change intensify. Thus, the utilization of the products of the processes described in this dissertation towards protection of the natural and built environment is an area that deserves specific study in the future.

Research Achievements

Journal Articles

- Quantification of the CO_2 mineralization potential of ironmaking and steelmaking slags under direct gas-solid reactions in flue gas, International Journal of Greenhouse Gas Control Vol. 87C p.100-111 (2019), Corey A. Myers, Takao Nakagaki, and Kosei Akutsu.
- Prediction of nucleation lag time from elemental composition and temperature for iron and steelmaking slags using deep neural networks, ISIJ International Vol. 59 No. 4 p.687-696 (2019), Corey Adam Myers and Takao Nakagaki.
- Effect of Solidification and Cooling Methods on the Efficacy of Slag as a Feedstock for CO_2 Mineralization, ISIJ International Vol. 58 No. 2 p.211-219 (2018), Corey Adam Myers and Takao Nakagaki.
- Application of quenching to polycrystalline metallurgical slags to reduce comminution energy and increase mineral liberation, In Proceedings of the 16th International Heat Transfer Conference Beijing China, IHTC Digital Library, p. IHTC-22437 (2018), Corey A. Myers and Takao Nakagaki.
- Enhanced recovery process of calcium oxide and metals from steelmaking slag with net carbon sequestration, Energy Procedia Vol. 114 p.6246-6255 (2017), Corey Myers, Takao Nakagaki, and Takuya Mitamura.

Review Articles

- CCS、CCUS のレビューと技術展望 〜コスト、量的寄与、リスクの観点から〜. 日本機械学会誌、第 122 巻　第 1203 号特集　二酸化炭素分離回収と貯留・固定および利用技術 p.8-13 (2019), Takao Nakagaki and Corey Myers.

International Conference Papers

- Application of quenching to polycrystalline metallurgical slags to reduce comminution energy and increase mineral liberation, In Proceedings of the 16th International Heat Transfer Conference, p. IHTC16-22437 (2018), Corey A. Myers and Takao Nakagaki.
- Experimental determination of CO_2 mineralization depth of slag minerals at CO_2 concentrations available in iron and steelmaking flue gases, 14th International Conference on Greenhouse Gas Control Technologies Melbourne Australia (October 2018), Corey Myers and Takao Nakagaki.
- Feasibility study of net CO_2 sequestration using seawater desalination brine with profitable polyproduction of commodities, 14th International Conference on Greenhouse Gas Control Technologies Melbourne Australia (October 2018), Yohei Tsubuku, Corey Myers, and Takao Nakagaki.
- Molten slag property estimation using deep neural networks for advanced material recycling, 1st International Conference on Energy and Material Efficiency and CO_2 Reduction in the Steel Industry Kobe Japan (October 2017), Corey Myers and Takao Nakagaki.

- Enhanced recovery process of calcium oxide and metals from steelmaking slag with net carbon sequestration, 13th International Conference on Greenhouse Gas Control Technologies Lausanne Switzerland (November 2016), Corey Myers and Takao Nakagaki.

Domestic Conference Papers

- CO_2 utilization via mineralization into construction aggregate using waste brine, In SCEJ 50th Fall Meeting Kagoshima (2018), Kohei Sato, Corey Myers, Yohei Tsubuku, and Takao Nakagaki.
- Improvement of HCl recovery efficiency in brine-based CO_2 mineralization using Mg. In SCEJ Regional Meeting Kanazawa (2017), Yohei Tsubuku, Corey Myers, Kei Shiraishi, and Takao Nakagaki.

Poster Presentations

- CCUS development supported by prediction via Deep Neural Networks, IEAGHG 2018 CCS Summer School Trondheim Norway (2018), Corey Myers.
- ディープ・ニューラル・ネットワークを用いた複雑な組成の液体物性の効率的な予測, 第 2 回 WIRP ワークショップ Tokyo Japan (2017), Corey Myers.

Official Reports

- 実践的モデルを活用した CCS 全体システムのコスト計算成果報告書 (2019), Takao Nakagaki, Corey Myers, Yohei Tsubuku, Naoya Ogiyama, Hirotaka Isogai, Daisuke Hasegawa, Kohei Sato.
- 地上設備を含めた CCS システム全体のコスト評価成果報告書 (2018), Takao Nakagaki, Corey Myers, Dabin Wang, Hyeongseok Park, Akira Ozeki, Yohei Tsubuku, Naoya Ogiyama, Daiichi Watanabe.

Patents

- 特願 2019-0243. 二酸化炭素固定化方法 （早稲田大学，出光興産，日揮の共願）(*patent pending*).

Awards

- "Most Outstanding Student", IEAGHG, 2018 CCS Summer School.
- "Best Essay Explaining Negative CO_2 Emissions", Carbon 180 (formerly: Center for Carbon Removal), Travel and attendance scholarship to 1st International Conference on Negative CO_2 Emissions, Gothenburg, Sweden 2018.
- "Best Presentation Award" for Master's Thesis 2016, Waseda University Graduate School of Environment and Energy Engineering, "Reducing the Carbon Footprint of the Iron and Steel Making Industry -Separation and Conversion of Constituent Elements of Slag-".

Acknowledgements

To the people of Japan and the Japanese government,
      thank you for providing a haven for research in this tempest of a world,
            thank you for unburdening my mind through your financial support.

To Professor Takao Nakagaki,
      thank you for always being a bit ahead, a bit faster, a bit cleverer,
            thank you for staying just out of reach of what I could accomplish,
                  thank you for holding me to a standard while letting me grow free.

To my reviewers, Professor Masafumi Katsuta, Professor Jin Kusaka, Professor Makoto Yoshida, Assistant Professor Nobuhiro Maruoka, and Mr. Nobuhiro Kobayashi,
      thank you for pushing me to sprint even when the end was in sight.

To my colleagues in Japan and abroad,
      thank you for the comradery and competition, I am sorry I had to show you up.

To my wife, Miwa,
      thank you for carrying my burden that I might stand,
            I surely would have crumbled without you,
                  this work is as much yours as it is mine.

To my family in America, living and deceased,
      thank you for encouraging my choice despite the pain of separation it brings us all,
            thank you for your weirdness, your kindness, and your love.

To my family in Japan,
      thank you for always protecting me from myself,
            thank you for surrounding me with the beauty of nature and the good of people.

To those who could have done it better, but did not have the opportunity,
      I have given all the spirit, effort, and cunning I have,
            it is a pittance, but it is the most I can offer you in restitution.

To those who will suffer and perish because I was not good enough or fast enough,
      please know that I carry your misery with me now and always,
            I will not stop fighting for you,
                  I will not stop fighting for our world.